UNIVERSITY OF CALIFORNIA,
IRVINE

Evolving Biological Technologies as Engineered Drinking Water Treatment Systems for Cyanotoxin Removal: Towards an Improved Predictive Understanding of the Microorganisms Involved

DISSERTATION

submitted in partial satisfaction of the requirements
for the degree of

DOCTOR OF PHILOSOPHY

in Environmental Engineering

by

Derek Conte Manheim

Dissertation Committee:
Associate Professor Russell Detwiler, Chair
Professor Sunny Jiang
Assistant Professor Kristen Davis

2019

Dedication

I would like to dedicate this dissertation research to all those in need of safe and clean drinking water resources worldwide. Hopefully, this research will continue to inspire others to advance the use of biological treatment technologies as sustainable and eco-friendly options for drinking water treatment.

TABLE OF CONTENTS

LIST OF FIGURES

LIST OF TABLES

ACKNOWLEDGMENTS

I would like to first gratefully acknowledge the assistance and guidance from my advisors, Dr. Russell Detwiler and Dr. Sunny Jiang. Without their direction and understanding, I would not have been able to complete this dissertation. I would also like to thank Dr. Kristen Davis and Dr. Stanley Grant who were also very instrumental in helping me shape this dissertation and for providing me with valuable feedback throughout my career here at UCI.

To my wife Francesca: I am sincerely indebted to your support, wisdom, and appreciation for my work here these past four years. I am so grateful to have you by my side and am so thankful for your ability to always surround me with love, positive thoughts and inspiration to succeed. I know that we will continue to accomplish so many great things together and I am so excited to see what the future has in store for us these upcoming years.

To my friends and family: I cannot describe or repeat enough how supportive you have been my entire life. Thank you for always believing in me and never doubting my success. You have taught me how and why to pursue the things that mean the most to you in life, and I am so grateful for that. You have also taught me to never be afraid of the person you will become and to always accept, respect, and cherish everything in life, no matter how small, unfamiliar, or insignificant it may be.

I also would like to acknowledge all of my colleagues and non-faculty members here at UCI that helped me along with my research, including Yuen Ming Cheung, Dr. Trevor Jones and Srikiran Chandrasekaran. Thank you for your time, help with thinking through and setting up experiments, and very helpful discussions to keep me on track.

CURRICULUM VITAE

Education

University of California, Irvine *Degree Conferred: 01/2019*
Ph.D., Engineering with a Concentration in Environmental Engineering
Dissertation Title: *Evolving Biological Technologies as Engineered Drinking Water Treatment Systems for Cyanotoxin Removal: Towards an Improved Predictive Understanding of the Microorganisms Involved*
Overall Graduate GPA: **4.0**

California Polytechnic State University, San Luis Obispo *Degree Conferred: 08/2012*
M.S., Civil and Environmental Engineering
Thesis Title: Improved Microalgal Biomass Harvesting Using Optimized Environmental Conditions and Bacterial Bioflocculants
Overall Graduate GPA: **4.0**

California Polytechnic State University, San Luis Obispo *Degree Conferred: 08/2012*
B.S., Environmental Engineering
Overall Undergraduate GPA: **3.50** (Cum Laude)

Experience

Ph.D. Candidate, *Applied Environmental Microbiology Laboratory, UCI, CA*
09/2014-Current

- Advancing biological technologies (i.e., biological filtration) as energy efficient, cost-effective treatment practices to specifically target cyanobacterial toxin (microcystin-LR/LA) removal from drinking water
- Research approach focuses on developing and calibrating both unstructured and structured kinetic models to effectively describe laboratory scale studies assessing growth kinetics and community dynamics of pure and mixed bacterial cultures degrading cyanobacterial toxins
- Actively involved in authoring several NSF, US EPA, and water industry proposals focused on funding my dissertation research
- Teaching assistant: "*CEE 60: Contemporary and Emerging Environmental Challenges*," and "*CEE 169: Environmental Microbiology for Engineers,*" both lower and upper division undergraduate classes, respectively
- Mentored students in the Undergraduate Research Program (UROP), assisted with their experimental design and research in the laboratory, and aided the presentation of their results at the UROP symposium
- Responsible for training, guiding, and supervising undergraduate and graduate research assistants to support the experimental workload of my dissertation research

Experience (Continued)

Research Associate, *Global Waste Research Institute, San Luis Obispo, CA*
08/2012–08/2014

- Performed a wide-ranging literature review, materials flow analysis, and assisted with field research for the California Air Research Board's future regulations regarding CFC, HCFC and HFC releases from appliance and construction based foams present in landfills throughout California
- Operated and managed an optical interferometer (*Bruker NP-Flex)* to characterize 3D surface texture of soil particles (sand or gravel), various geosynthetics (including geomembranes and geotextiles used for landfill lining applications), and other engineering materials
- Established testing procedures and developed correlations between surface texture characteristics and engineering response of these materials, presenting findings in scientific journals and conferences
- Coordinated with faculty/graduate students to support interdepartmental activities focused on surface texture quantification by providing a series of workshops and seminars to spread knowledge and applications of the interferometer across the campus research community

Teaching Associate, *Civil/Environmental Engineering Department, Cal Poly, CA*
08/2012–12/2012

- Taught laboratory sections for the senior-level Air Quality Measurements Course
- Applied knowledge and experience in air quality monitoring equipment, EPA air related sampling procedures and methods, and ambient air quality sampling techniques
- Responsible for equipment knowledge and setup, maintenance of laboratory supply inventory, editing and grading of student reports and lab books

Graduate Research Associate, *Civil/Environmental Engineering Department, Cal Poly, CA*
06/2011–08/2012

- Researched and aided in the development of improved, energy efficient harvesting methods of algae for production of biofuel from wastewater treatment ponds
- Improved the settling rate of two microalgae species for commercial algal biofuel production using both bacterial bioflocculants and field samples of wastewater pond sludge
- Directed and trained undergraduate lab assistants for development of research

City of Del Mar Ocean Lifeguard I, *San Diego, CA*
04/2007–06/2011

- Responsible for safety and oversight of 15,000 beachgoers per day in the summer season
- Certified in Advanced Emergency Medical Response, Swift Water Rescue, and Cliff Rescue
- Organized and planned fundraising events in the local community

Technical Skills and Certifications

- EIT Certified (#147377)
- Interferometry, Optics, Microscopy
- Programming: AutoCAD, C, C++, GIS, ArcGIS, MATLAB, Python, R
- Proficient in Microsoft Excel, Word, Outlook, and PowerPoint
- Flow cytometry and fluorescence activated cell sorting (FACS)
- qPCR, RT-qPCR, gene cloning
- Air quality (field) analysis: portable FID, stationary/dynamic flux chamber measurements
- Air quality (laboratory) analysis: Gas Chromatography, Ion Chromatography
- Water quality (lab) analysis: BOD, COD, TKN, Total Solids (TSS/VSS/TDS), TOC analysis, UPLC-MS, UPLC-MS/MS, HPLC-UV/VIS
- Soil/Groundwater monitoring and sampling
- Metagenomics and high throughput sequencing of 16S rRNA

Leadership, Involvement, and Awards

- Graduated from *Honors Program*, *Cal Poly*, SLO
- Awarded President's Honors List for 06/2010-06/2011 academic year
- Dean's List for 8 out of 14 quarters as an undergraduate student at Cal Poly, SLO
- Past member of *Society of Environmental Engineers* (Cal Poly, SLO)
- Past member of *National Society of Collegiate Scholars*
- Member of *Chi Epsilon* (National Civil Engineering Honor Society)
- Member of the Surfrider Blue Water Task Force
- Member of *Air and Waste Management Association*
- Associate Member of *American Society of Civil Engineers*

List of Recent Publications, Reports, and Conference Proceedings

2019

Manheim, D., Detwiler, R., and Jiang, S., (2019), "Optimal Design of Experiments for the Estimation of Unstructured Kinetic Model Parameters Describing Microcystin Biodegradation," *Water Research* (In Review).

Manheim, D., Detwiler, R., and Jiang, S., (2019), "A Reliable and Efficient Semi-Parametric, Moment Independent Approach to Global Sensitivity Analysis Based on Copulas," *Environmental Modelling & Software* (In Review).

Manheim, D., Detwiler, R., and Jiang, S., (2019), "Application of Unstructured Kinetic Models to Predict Microcystin Biodegradation: Towards A Practical Approach for Drinking Water Treatment," *Water Research*, 149(1), 617-631.

Manheim, D., Detwiler, R., and Jiang, S., (2019), "Accurate and Reliable Estimation of Kinetic Parameters for Environmental Engineering Applications: A Global, Multi-Objective, Bayesian Optimization Approach," *MethodsX* (In Press).

2018

Manheim, D., Jiang, S., and Cheung, Y. M., (2018), "The Effect of Organic Carbon Addition on the Community Structure and Kinetics of Microcystin Degrading Bacterial Consortia," *Water*, 10, 1523.

2017

Manheim, D., and Jiang, S., (2017), "Investigation of Algal Biotoxin Removal during SWRO Desalination through a Materials Flow Analysis," *Water*, 9(10), 730.

2016

Hanson, J., Sohn, A., Yesiller, N., and Manheim, D., (2016), "Emissions of Selected Greenhouse Gases from a Landfill," *Proceedings of the SWANA Western Regional Symposium*, April 11-14th, San Luis Obispo, California.

Yesiller, N., Manheim, D. C., Hanson, J. L., and Chyrsovergis, T., (2016), "Temperature dependent variation in surface texture characteristics of a textured geomembrane due to interface shear testing against a GCL," *Proceedings of the GeoAmericas 2016: 3rd Pan-American Conference on Geosynthetics*, April 10th-16th, Miami Beach, Florida.

2015

Hanson, J. L., Chrysovergis, T. S., Yesiller, N., and Manheim, D., (2015), "Temperature and Moisture Effects on Textured Geomembrane and Geosynthetic Clay Liner Interface Shear Strength," *Geosynthetics International,* 22(1), pp. 110-124.

Hanson, J. L., Flores, A. F., Yesiller, N., and Manheim, D., (2015), "Temperature Effects on Interface Shear Strength between Sand and Steel," *Proceedings of the International Foundations Congress and Equipment EXPO 2015,* March 17th-21st, San Antonio, Texas.

Yesiller, N., Manheim, D. C., Hanson, J. L., and Kopp, K., (2015), "Temperature Effects on Surface Texture of Geomembranes," *Proceedings of the XV Pan American Conference on Soil Mechanics and Geotechnical Engineering*, November 15th-18th, Buenos Aires, Argentina.

2014

Manheim, D. C., Yesiller, N., Hanson, J. L., Gourc, J. P., Carbone, L., Moraci, N., Carrubba, P., and Pavanello, P., (2014), "Investigation of Post-Shear Surface Texture Characteristics of Geomembranes," *Geosynthetics Conference 2015,* February 15th-18th, Portland, Oregon.

Manheim, D. C. and Yesiller, N., (2014), "Optical Interferometry Analysis of Virgin Geomembrane Specimens," G.W.R.I. Interferometer Report #2014-1, Cal Poly, San Luis Obispo.

Schnepf, J., Manheim, D. C., and Lathrop, A., (2014), "Surface Texture Analysis of Fresh Produce Using Optical Interferometry," Abstract presented in *International Association for Food Production 2014*.

2013

Manheim, D. C. and Nelson, Y., (2013), "Settling and bioflocculation of two species of algae used in wastewater treatment and algae biomass production," *Environmental Progress & Sustainable Energy (Special Issue),* 32(4), pp. 946-954.

Manheim, D. C., Yesiller, N., and Hanson, J. L., (2013), "Estimation of Potent Greenhouse Gas Release from Appliance and Building Wastes in the Landfill Environment," *Proceedings of the Global Waste Management Symposium 2014,* Orlando, Florida, pp. 1-4.

Manheim, D. C. and Yesiller, N., (2013), "Optical Interferometry Analysis of Smooth and Textured Geomembrane Specimens," G.W.R.I. Interferometer Report #2013-1, Cal Poly, San Luis Obispo.

Yesiller, N., Hanson, J. L., Manheim, D. C., and Sohn, A., (2013), "Emissions of Potent Greenhouse Gases from Appliance and Building Waste in Landfills: A Literature Review," Report submitted to *State of California Air Resources Board*.

Yesiller, N., Hanson, J. L., Nelson, Y., and Manheim, D. C., (2013), "Materials Flow Analysis: Estimated Emissions of Greenhouse Gases from Appliance and Building Waste During End of Life Processes Prior to Landfilling," Report submitted to *State of California Air Resources Board*.

2012

Manheim, D. C., (2012), "Improved Microalgal Biomass Harvesting Using Optimized Environmental Conditions and Bacterial Bioflocculants," M.S. Thesis. California Polytechnic State University, San Luis Obispo, CA. *Available on Cal Poly, San Luis Obispo Digital Commons: http://digitalcommons.calpoly.edu/theses/848*

ABSTRACT OF THE DISSERTATION

Evolving Biological Technologies as Engineered Drinking Water Treatment Systems for Cyanotoxin Removal: Towards an Improved Predictive Understanding of the Microorganisms Involved

By

Derek Conte Manheim

Doctor of Philosophy in Environmental Engineering

University of California, Irvine, 2019

Associate Professor Russell Detwiler, Chair

Harmful algae blooms associated with toxic cyanobacteria have been increasing in both frequency and severity as a result of global climate change. These blooms are responsible for the release of biotoxins, the most common and toxic of which are the microcystins (MCs), that are recalcitrant to the operations of conventional drinking water treatment plants (DWTPs). Bio-based technologies targeting MC removal, such as biofiltration systems, have been proposed as cost-effective and sustainable alternatives to advanced treatment technologies (i.e., ozonation). Biofilters rely on native bacterial communities endemic to the source water to metabolize microcystin as a carbon and energy source. However, biofilter treatment variability is an ongoing challenge, arising from variations in environmental conditions including temperature, pH, and the presence of other bioavailable nutrients. To effectively address this treatment variability, biofilters must be evolved into “engineered” systems, in which MC degrader bioactivity is promoted and treatment tightly controlled.

This dissertation has amalgamated a series of system modelling, experimental data collection efforts, unstructured kinetic modelling, as well as sensitivity and optimal experimental design (OED) analyses to arrive at an improved predictive understanding of MC biodegradation. The results of these efforts first indicated that the removal of biotoxins within biofilters is highly dependent on the pretreatment system and operations employed by the DWTP. The kinetics of MC biodegradation by degrading communities were bi-phasic, where the taxonomy of the communities and the kinetics of MC degradation were altered in the presence of an alternative carbon source. The kinetics of MC metabolism and bacterial growth of isolated degrading populations were well predicted by the Moser kinetic model, where up to 5 out of 6 parameters could be identified. A novel approach to global sensitivity analysis was developed to improve the accuracy and convergence efficiency of the sensitivity indices ranking the most influential parameters of the Moser model. Finally, the OED procedure designed a fed batch reactor experiment that drastically improved the practical identifiability of the parameters of the Moser model. The culmination of these analyses has laid the foundation for a comprehensive and practical kinetic model describing degrader growth and MC removal in bio-based treatment systems.

INTRODUCTION

The significance of marine and freshwater microalgae to sustain life on earth is ubiquitous, as these microorganisms contribute to nearly half of the global net primary production (Behrenfeld et al. 2006). Although these microalgae sustain vital ecosystem services on Earth, an imbalance in any one environmental condition, such as water temperature, pH, or availability of nutrients, often favors the dominance of a certain population that may cause more inherent detriment than good. Such is the case of the toxic or "harmful" microalgae that have existed on this earth for approximately 3.5 billion years. In contrast to their vital and historic role in net carbon cycling throughout the globe, the proliferation of harmful microalgae (approximately 2% of the total microalgal population on earth), that produce toxic secondary metabolites, pose impending threats to the wellbeing of humans as well as the structure and function of aquatic ecosystems alike (Hallegraef 2010, Paerl and Paul 2012).

Within the last decade, both the prevalence and duration of these harmful algal bloom events (HABs) has been increasing throughout fresh, estuarine, and marine water bodies across the globe as a direct consequence of global climate change and associated anthropogenic activities (Paerl et al. 2011, Paerl and Paul 2012, Paerl and Otten 2013). In 2007, Lake Taihu, located in the Northwest province of China, was severely impacted by a large scale HAB event associated with the cyanobacterium *Microcystis aeruginosa*, leaving approximately 2 million people without potable water for at least a one-week period (Qin et al. 2009a). More recently (2014), a similar magnitude cyanobacterial bloom occurred in Lake Eerie, leaving approximately a half million residents of Toledo, Ohio without water for

a three-day period, despite robust treatment efforts to remove the high concentrations of cyanobacterial toxins (Ho and Michalak 2015). The intrusion of toxic blooms of *Microcystis sp.* in the San Francisco Bay delta (and associated watersheds in the region) is yet another well studied estuarine predicament that is threatening agricultural water resources as well as the survival of the local fish population, the Delta smelt (Lehman et al. 2005, 2009). One of the largest harmful marine algal blooms in history (associated with the alga *P. nitzschia*, which produces the toxin domoic acid) was recorded in June 2015, affecting marine life from the tip of Monterrey Bay to the Alaskan coast, and temporarily shutting down commercial fisheries and shellfish harvesting operations (DiLiberto, 2015).

Clearly, the HAB events witnessed across the world have been and continue to be a predominant issue affecting freshwater availability and the balance of different aquatic ecosystems; but what are the contributing external drivers? Climate change in the Northern Hemisphere over the past 20 years has resulted in an increase in air and surface water temperatures and prolonged periods of drought, along with less frequent, but more intense, storm events (Scavia e al. 2002). Warmer water temperatures (>25 ºC) correlate with increased growth rates and productivity for most microalgae and increase the temporal lengths and spatial extents of vertical stratification in most water bodies (Paerl and Huisman 2009, Paerl and Paul 2012). Light availability and increased CO_2 emissions to the atmosphere as a result of more persistent periods of drought and continued combustion of fossil fuels and biomass also drives the productivity of most microalgae species upward (Paerl and Huisman 2009, Paerl and Paul 2012). More intense precipitation events, followed by periods of drought, create a flushing and confining effect that increases

the nutrient loading and eutrophication potential of water bodies, further exacerbating the possibility of HAB events.

Anthropogenic activities other than the combustion of fossil fuels, coupled with shifts in climactic patterns, synergistically initiate HAB events of great severity and duration. Increasing the use of fertilizers to support agricultural practices, containing the essential nutrients nitrogen and phosphorus (N & P) to sustain algal growth, have long exacerbated the frequency and longevity of HABs throughout coastal, estuarine, and inland water bodies (Anderson et al. 2002, Paerl and Huismann 2009, Kosten et al. 2012, Lehman et al. 2013). The use of fertilizers containing high levels of N and P has increased worldwide to support the growing population and the development of an increasingly urbanized environment. The resulting nutrient pollution has overwhelmed many inland and coastal watersheds and contributed to the severity and persistence of HAB events (Heisler et al. 2008). Comparably, the large freshwater footprint (and lack of water reuse) associated with the growing population has resulted in a relative scarcity of freshwater resources. As the inland freshwater bodies continue to be diminished rather than replenished, the proliferation of harmful algae is likely to be increased (Dahm 2010).

HABs specifically impair the quality of water due to the production and release of soluble, secondary metabolites including taste and odor compounds (MIB and Geosmin) and toxic compounds (microcystin, domoic acid, etc.) (Huiman et al. 2006, Otten and Paerl 2015). Favorable conditions for the production of toxins may include the increased prevalence of sunlight, a stable water column, elevated water temperatures, and increased abundance of necessary nutrients (N and P, “eutrophic” conditions), among many other co-varying factors depending on the aquatic environment (i.e., freshwater, estuarine or

saltwater) (Huismann et al. 2006, Davis et al. 2009). Environmental effects from HAB events are far reaching and range from complete changes to the ecosystem structure and function, such as the transition of a water body from mesoeutrophic to hypereutrophic, to complete death and intoxication of higher trophic organisms (i.e., fish or marine mammals) (Landsberg 2002, Jester et al. 2009a). The most direct human health effects associated with these toxins are repeated exposure from drinking water, contaminated fish or shellfish, or during recreational activities. These toxins can initiate both acute and chronic human health risks from different exposure events (depending on the toxicity, dose, and mode of action), and some toxins are known carcinogens (especially the hepatotoxins, microcystin-LR) (Dittman and Wiegand 2006, Bourne et al. 2006, Hoefel et al. 2009).

A significant problem with most toxins excreted by harmful algae are their relative stability in the environment, as they are very chemically non-reactive, characteristically low in molecular weight, and water soluble, thereby resistant to most conventional water treatment unit processes such as coagulation, flocculation, membrane treatment processes, and chlorine disinfection (Westrick et al. 2010, Cruz et al. 2011). In addition, a majority of these toxins are produced and stored internally and not released until unfavorable growth conditions or other "stressors," presenting yet another potential treatment challenge (Ross et al. 2006). Advanced oxidation processes (such as ozonation, high pressure UV treatment (photolytic oxidation)) and granular/powder activated carbon (GAC/PAC) have been introduced as reliable, widely accepted treatment alternatives to chemically/photolytically oxidize or adsorb these toxic compounds. However, the main drawback to these advanced treatment methods are the fact that they are energy intensive, cost ineffective, subject to some inherent treatment variability, and may contribute to unintentional cell lysis

(Westrick et al. 2010). The treatment variability and relatively high costs incurred for additional advanced treatment processes to remove these toxins has placed a progressive stress on both municipal water authorities and responsible government agencies to develop alternative and sustainable solutions to these increasingly frequent and severe events.

Biological treatment technologies, such as biological filtration (biofiltration), have been introduced in the past as viable water treatment alternatives for the removal of toxins produced from HAB events (Ho et al. 2006, Ho et al. 2007a, Ho et al. 2012a). These bio-based treatment technologies rely on the development of mixed microbial communities, as biofilm or suspended communities in the water column, from native bacteria endemic to the source water in an engineered reactor that facilitate natural rates of toxin degradation. Of the wide array of technologies available, biofiltration has been advocated as the most promising treatment configuration to remove microalgal toxins, where up to 100% removal of microcystin toxins has been reported for mature, laboratory scale reactors (Ho et al. 2007a). Biofilters have been characteristically designed as simple rapid, deep bed granular media filters (common to drinking water treatment practice), where medium to coarse, uniformly distributed silica sand (mono-media) is commonly used. Ultimately, the primary objective of biofiltration systems is to allow toxin degrading bacterial populations to form stable biofilm communities that can rapidly and reliably degrade toxins present in the influent water (Huck 2000, Ho et al. 2012a).

More recently, biofiltration has evolved into a widely accepted and practiced unit treatment process for the targeted removal of biological organic matter (BOM) and particulate matter (excess turbidity) to both increase the biological stability of the product

water in the distribution system and reduce disinfection byproduct formation, among many other objectives (Urfer et al. 1997, Huck 2000, Halle et al. 2009). Increased attention has also been given to model and optimize biofiltration processes to better comprehend the dynamics of the treatment efficiencies of BOM (Hozalski and Bouwer 2001a, 2001b, Rittman et al. 2002a). However, a general disconnect between the scientific community and the majority of water management utilities is evident, as biofiltration systems are not currently managed as true "biological" treatment systems in that conditions for microbial growth are not sustained or sometimes even acknowledged (67% of utilities actively manage or monitor these systems) (Evans et al. 2010b, Evans et al. 2013a, 2013b). Therefore, there has been a movement to standardize biofiltration treatment practices in the U.S. with the introduction of a monitoring and control toolbox aimed at existing water utilities to provide the scientific resources to modify the treatment efficiencies of existing systems (Evans et al. 2013a, 2013b).

The advent of "engineered" biofiltration is an innovative concept that focuses on developing new amendments to existing theory, design, and operation of traditional rapid sand, deep bed mono or dual media filtration systems (Huck 2000, Lauderdale et al. 2012). Amendments to the preexisting system operation may include nutrient addition (bio-stimulation), bacterial culture seeding (bioaugmentation), running the filters without chlorine or ozone residual, changing the backwash intensity and method, and manipulating filter contact times (Lauderdale et al. 2012). The current benefits of including engineered biological filtration units in the drinking water treatment unit process train range as a supplement to advanced pre-oxidation processes for excess particulate and dissolved organic carbon removal and are not primarily stand-alone treatment unit treatment

processes (Huck 2000, Evans et al. 2013a, 2013b). However, little experimentation or formal research has been conducted regarding 1) the entire breadth of amendments that can be made, 2) which of these amendments are most significant and applicable for different contaminants of interest, and more importantly, 3) what operational parameter or series of parameters can effectively control or predict treatment performance of the substrate of interest.

The primary challenge bio-based systems face is that the treatment efficiency of algal toxins for most biofiltration systems are recognized to be transient in nature, as the population of native microorganisms in the source water is constantly changing and environmental conditions (i.e., temperature, pH, nutrient content) are highly variable (Ho et al. 2006, Ho et al. 2012a). Many studies have investigated the degradation capability of isolated bacterial strains when exposed to cyanobacterial toxins; however, few studies have examined the complexity behind toxin degrading bacterial communities (Li et al. 2011a, 2011b, 2011c, Li et al. 2015, Mou et al. 2013). The biodegradation characteristics (i.e., efficiency and kinetics) of the bacterial consortia compared to the bacterial isolates are much more realistic to application in engineered systems, are very dynamic, and difficult to predict in natural settings. Therefore, one significant challenge is to maintain a reliable and robust microbial degrading population within these engineered systems, especially for algal toxin degradation, since past studies have indicated that the degrader population is rather diverse and not particularly high in abundance (Mou et al. 2013, Liao et al. 2013). Furthermore, although the degradation pathway has been characterized for cyanobacterial toxins, it is difficult to elucidate potential interactions between community members during toxin degradation. Other challenges may include the slow or often bi-phasic

degradation kinetics of certain toxins of concern previously observed for bacterial consortia (Ho et al. 2012a). Preliminary column experiments have demonstrated that microalgal toxin degrading populations were evidenced to have a lag phase on the order of days before toxin degradation commences, which may hinder the establishment of a reliable degrader community within a given biofiltration system (Ho et al. 2006, Bourne et al. 2006).

To effectively address the main challenges identified with biological treatment systems targeting algal toxins, and to evolve bio-based treatment from passive to completely "engineered" systems, a fundamental *predictive* understanding of the microorganisms involved is required. Therefore, the focus of this dissertation is to develop, verify, and improve upon several mechanistic models that can accurately and reliably predict algal toxin fate and biodegradation, with a focus directed toward drinking water treatment applications. These models are structured on four, progressively finer scales of analysis (i.e., the drinking water treatment facility, a biofilter in operation at a treatment facility, the toxin degrading bacterial communities underlying bio-based treatment, and isolated members of the toxin degrading communities) to offer some comprehensive insight into algal toxin fate and biodegradation in drinking water treatment systems (Figure 1). To set the stage for application of these predictive models, several leading research questions were developed to guide this dissertation research:

1) What is the fate and distribution of algal biotoxins within current drinking water treatment trains and what are the broader current human health risks and environmental impacts from the operation of these systems?

2) How does the toxin degrading bacterial community respond to different environmental stimuli, such as the presence of alternative substrates other than microalgal toxins (organic carbon)?
3) Can a comprehensive biofiltration model be developed that accurately predicts microcystin removal?
4) What unstructured kinetic model can best predict the coupled growth and toxin degradation kinetics of isolated, degrading bacterial populations (i.e., within a given community) and how accurate and reliable are model predictions and parameter estimates?
5) How can we improve the accuracy and reliability of these unstructured kinetic model predictions by focusing on improved parameter identifiability and experimental design?

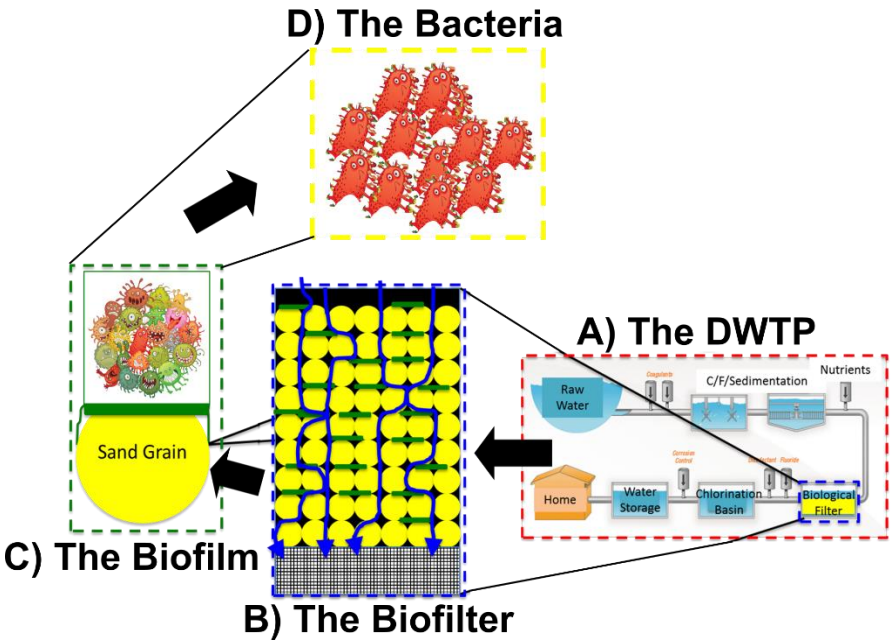

Figure 1. *Description of the main Ph.D. research agenda as a function of scale, ranging from the A) drinking water treatment facility (DWTP), B) a biofilter unit operating at a treatment facility, C) the algal toxin degrading microbial communities within the bio biofiltration units,*

and D) individual populations of algal toxin degrading bacteria existing within the greater community.

This dissertation research will combine a series of system modelling, experimental, computational modelling, and sensitivity/uncertainty analysis approaches in several interrelated studies to improve upon our predictive knowledge of the drinking water treatment train operations, as well as the bacteria and bacterial communities involved in algal toxin removal and biodegradation. In the first chapter of this dissertation, a system model will be developed based on the principles of probabilistic materials flow analysis to assess the fate and distribution of algal toxins in current drinking water treatment processes and to quantify the range in current toxin removal efficacies of these full-scale systems. Broader impacts of these treatment systems, such as potential acute human health effects from exposure to these toxins, will be assessed from the output of the system model.

The second chapter of this dissertation will involve a combined experimental-modelling approach to examine the dynamics of several isolated microcystin degrading bacterial communities exposed to an alternative organic carbon source (in addition to the toxin of interest).

Next, the third chapter of this dissertation will be focused on the development and verification of a 1-D computational model framework that predicts the removal of algal toxins within biofiltration systems.

The fourth and fifth chapters of this dissertation detail a formal model selection effort comparing several unstructured kinetic models used to predict coupled bacterial growth and substrate (toxin) degradation, as well as a complete review of parameter sensitivity and identifiability of the selected and calibrated models. A novel optimization procedure for optimal parameter estimation is further detailed in the fifth chapter.

The sixth chapter introduces a new method to improve existing sensitivity analysis techniques, where this method can be integrated into an optimal experimental design framework for improved parameter estimation and model predictive accuracy.

The seventh chapter of this dissertation investigates in what ways an experimental design can be improved to enhance parameter identifiability and certainty in the context of predicting microcystin biodegradation in engineered bio-based treatment systems. Finally, a summary of the main findings from each of these chapters and some future perspectives for further research are presented in the Conclusions and Future Directions section of this dissertation.

BACKGROUND/LITERATURE REVIEW

The background/literature review section of this dissertation focuses on familiarizing the reader with previous research and theory related to a) common freshwater microalgal toxins and their effects on human health, b) microalgal toxin biodegradation, c) biological and engineered biological filtration (i.e., concepts, operation, and design), as well as d) past studies exploring biofiltration as an option to target algal toxin removal performed on the laboratory scale. It is important to note that since the majority of this dissertation proposal focuses on cyanobacterial toxins (cyanotoxins), the discussion of toxins of concern is limited to the microcystin suite of toxins associated mostly with freshwater and some estuarine environments. Additional information about marine toxins of concern is presented in Appendix A for reference.

I. Cyanotoxins and Human Health

Of the broad class of freshwater microalgal toxins threatening the security and quality of water resources, the microcystin class are perhaps the most commonly observed and toxic (Edwards and Lawton 2009, Paerl and Otten 2013). Microcystins are a series of cyclic heptapeptides (7 amino acids) produced intracellularly by the freshwater cyanobacteria *Microcystis*, *Anabaena*, *Nostoc*, *Oscillatoria*, and *Planktothrix*. The molecular structure of microcystin-LR is composed of seven main amino acids including: 1) the ADDA group, 2) the D-glutamic acid group, 3) the N-methyldehydroalanine group, 4) the D-alanine group, 5), the leucine group, 6) erythro-β-methyl-D-aspartic acid group, and 7) the arginine group (Jones and Orr 1994, Bourne et al. 1996). There are over 100+ different microcystin congeners, each varying in the amino acid residue at positions 2 and 4 of the

cyclic ring structure, with the presence or absence of methylated groups on the methylaspartic acid, or the esterification of methyl-aspartic acid or iso-glutamic acid (Edwards and Lawton 2009, Figure 2).

Microcystin-LR is by far the most common and toxic of the microcystin congeners (present in 50-100% of total MC environmental samples) and consists of the amino acids leucine and arginine in positions 2 and 4 of the ring structure, respectively (Edwards and Lawton 2009, Figure 2). Two ionizable carboxylic acid groups on D-glutamate and D-erthyro-β-methylaspartic acid as well as one ionizable amino on the arginine group contribute to MCLR's high water solubility (Texiera and Rosa 2005). In addition, the ADDA group attached to MCLR's ring structure is relatively hydrophobic, which contributes to an appreciable solubility in organic solvents (Texiera and Rosa 2005).

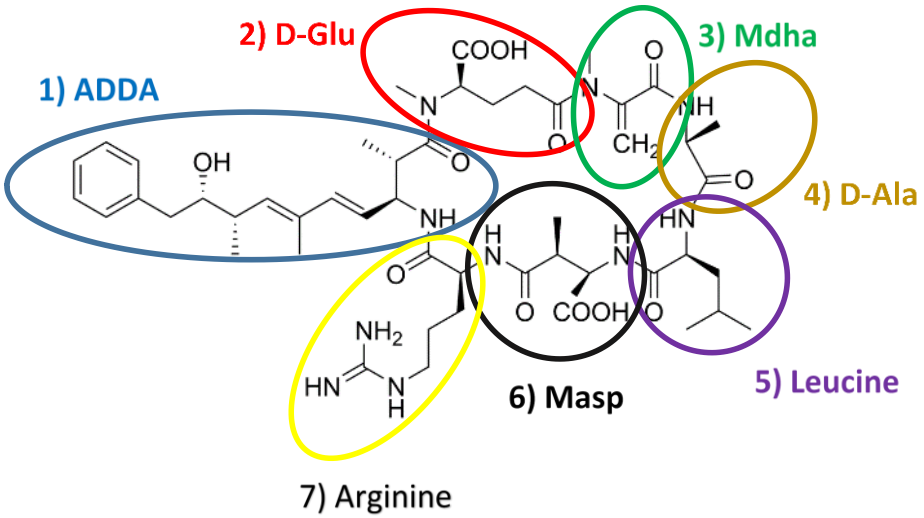

Figure 2. *Molecular structure of microcystin-LR with each amino acid identified with a different color.*

The mechanism of toxicity of microcystin-LR in humans is directly related to the inhibition of protein phosphatases PP1, PP2A, PP4, and PP5 which leads to tumor promotion (from an increase in protein phosphorylation in liver cells) and the

development of primary liver cancer (Nishiwaki-Matsushima et al. 1992). Potential exposure pathways to dissolved or particulate algal toxins include direct intake from drinking water, dietary exposure from contaminated shellfish or fish, as well as direct contact from recreational exposure events. Limited long-term epidemiological studies have been conducted linking the relationship of primary liver cancer to microcystin exposure in drinking water even though its carcinogenic potential has been widely studied in mammals (WHO 2003, Zhang et al. 2015a). Despite the carcinogenic potential of microcystin-LR, acute liver damage and eventual failure from microcystin exposure is also a serious threat to human health, where 50 patients were killed at a hemodialysis center in Brazil from an exposure event to microcystin contaminated water (LD50 of 5 mg/kg) (Jochimsen et al. 1998). Therefore, the WHO has adopted a guideline of 1 μg/L of dissolved microcystin for drinking water; however, as of yet, the US EPA has not instated any specific regulations on the appropriate levels of microcystin in drinking water (WHO 2003, US EPA 2016a). Although no specific regulations have been established, the US EPA recommends the WHO limit of 1 μg/L as a provisional, national guideline in drinking waters (US EPA 2015a). In recent years (2009), the US EPA has added microcystin-LR to its candidate contaminant list (CCL) under the Safe Drinking Water Act and guidelines have been created for water authorities and utilities to securely manage algal toxins during severe bloom events (US EPA 2015a).

II. Biodegradation of Cyanotoxins

Microcystin biodegradation has been well studied for individual isolates of native bacterial consortia present in the source water of HAB events, source water sediments, and

from full scale biological treatment unit processes in drinking water treatment facilities (Bourne et al. 1996, Saito et al. 2003, Eleutario and Batista 2010, Jimbo et al. 2010, Li et al. 2011a, Li et al. 2011b, Li et al. 2015a). The majority of the degrader isolates were from the family *Sphingomonadaceae* (under the phylum proteobacteria and alphaproteobacteria class) and included different strains of *Sphingomonas sp.* and *Sphingopyxis sp.* (Ho et al. 2012a, Dziga et al. 2013). However, the diversity of potential degraders is very high, as evidenced by the large number of isolates obtained from other bacterial classes, families and orders. For example, isolates were obtained from a variety of experimental studies belonging to the *Arthrobacter sp.*, *Brevebacterium sp.*, *Rhodococcus sp.*, *Methylobacillus sp.*, *Bacillus sp.*, *Stenotrophomonas* (Gamma-Proteobacteria), *Novosphingobium sp.* (Alpha-Proteobacteria), *Pseudomonas aeruginosa* (Gamma-Proteobacteria), *Ralstonia solanacearum* (Beta-Proteobacteria), *Paucibacter toxinivorans* , *Burkholderia sp.* , *Flavobacterium sp.*, *Sphingosinicella sp.*, *Rhizobium gallicum*, *Morganella morganii*, and *Microbacterium sp.* (some of the more commonly reported species) (Dziga et al. 2013, Rastogi et al. 2014). Even probiotic bacterial species were evidenced to possess some microcystin degrading capabilities, including *Lactobacillus sp.* and *Bifidobacterium* (Ho et a. 2012).

The corresponding biodegradation pathway of microcystin-LR has been identified using a strain of *Sphingomonas sp.* as a model example (Bourne et al. 1996, 2001). The biodegradation pathway was indicated to be a sequential three step process (Figure 3). First, a transporter protein coded by the *mlrD* gene cluster is responsible for bringing the microcystin toxin into the bacterial cell. The *mlrD* encoded transport protein also may facilitate the removal of degradation products of microcystin out of the cell. Consequently,

the enzyme microcystinase expressed by the *mlrA* gene cluster, hydrolytically cleaves the ADDA-arginine bond to open the cyclical structure of microcystin and form a linearized product, reducing the corresponding toxicity by 160 times (*M/Z* 1012) (Bourne et al. 1996, 2001). Next, the putative enzyme serine peptidase, is expressed by the *mlrB* gene cluster to further transform the linearized a-MCLR (cleaving at the Ala-Leu bond) to yield a tetrapeptide intermediate (NH2-Adda-Glu-Mdha-Ala-OH, M/Z of 614). Finally, the putative metallopeptidase enzyme, expressed by the *mlrC* gene cluster, breaks down the tetrapeptide intermediate into much smaller peptides and amino acids (Figure 2) (Bourne et al. 1996, 2001). Harada et al. (2004) described that one of the smaller peptides formed during the last enzymatic step was the ADDA group, but the complete range in potential amino acids and peptides form remains unknown.

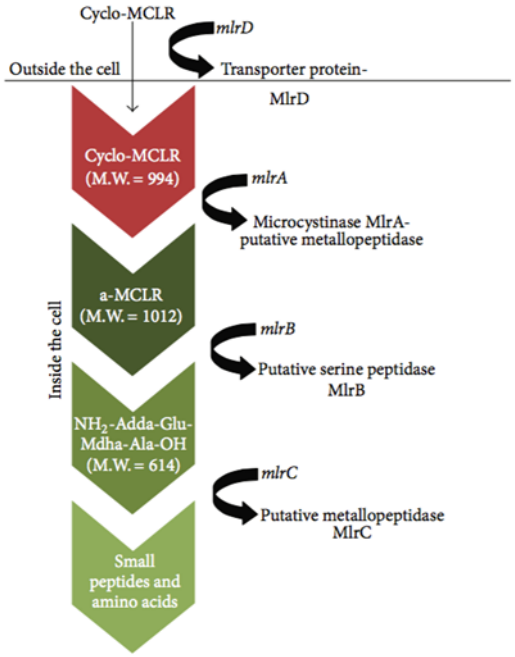

Figure 3. *Enzymatic pathway for the biodegradation of microcystin-LR*

Although the proposed pathway for *Sphingomonas sp.* has been confirmed by several studies in different strains and species (Imanishi et al. 2005, Kato et al. 2007,

Edwards and Lawton 2009, Hashimoto et al. 2009), it is apparent that many degrader isolates do not possess the *mlr*(A-D) gene sequences (Harada et al. 2004, Manage et al. 2009, Zhang et al. 2010, Lawton et al. 2011). Comparably, the expression of different *mlr* genes may differ across varying bacterial populations. Jiang et al. (2011) indicated that the *mlrB* gene lost its functional activity in the THN1 strain of *Novosphingobium sp.* In addition, other studies have reported contradictory or multiple functions of different enzymes. Dziga et al. (2012) and Shimizu et al. (2012) confirmed that the *MlrC* enzyme is involved in the initial hydrolytic linearization of microcystin-LR as well as the breakdown of the tetrapeptide product. Thus, it is clear that potentially many other biodegradation pathways exist both for microcystin-LR and the range of microcystin congeners across different bacterial genus and environmental conditions.

Based on the proposed biodegradation pathway and the relative importance of the *mlrA* gene to initiate the hydrolysis of the cyclic structure of microcystin, Hoefel et al. (2009) developed a sensitive and specific qPCR approach to target and quantify the abundance of the *mlrA* gene for *Sphingopyxis sp.* In general, the proportion of gene copy numbers was determined to be equivalent to the microcystin degrading activity observed in an experimental sand filter, validating the method (Hoefel et al. 2009). Ho et al. (2010) observed the same result as Hoefel et al. (2009), where *mlrA* gene copies were proportional to microcystin degradation efficiency in a laboratory sand column fed with activated sludge treated effluent.

The functional gene abundance (*mlrA*, *mlrB*, *mlrC*, *mlrD*), detected using this developed technique, was implied as a surrogate for microcystin degrader abundance for a number of more recent studies examining the presence of microcystin degraders within

biological drinking water treatment processes (Jimbo et al. 2010, Li et al. 2011a, Li et al. 2015a). Jimbo et al. (2010) demonstrated the year-round presence of microcystin degrading bacteria within a biofilm community from a water treatment facility in Japan using the qPCR technique, where degrader abundance ratios ranged from 0.0001 to 0.005% of the total bacterial population. Li et al. (2011a) observed high microcystin biodegradation potential of a bacterial consortia isolated from a biological treatment process during wintertime, which corresponded to an increase in the *mlrA* abundance over the degradation period. Li et al. (2015) concluded that the trends in degrader abundance (using *mlrA* qPCR) and biodegradation rates were rather similar over a one-year study period. Therefore, there is considerable evidence demonstrating that degrader abundance can be well approximated by the relative abundance of *mlrA* genes, which can be further used to assess the dynamics of microcystin degradation for native bacterial consortia.

Biodegradation of microcystin has been either expressed as zero order or first order kinetics in the existing literature. Zero order kinetics were derived from a linear approximation of the change in microcystin concentration over time (concentration independent), whereas first order kinetics were approximated from an exponential decrease in microcystin concentration over time (concentration dependent). Rates for zero order kinetics were generally vary variable across different bacterial geneses and species, ranging from 1.5 to 101,520 µg/L/day, with an average of 7,321 µg/L/day (five orders of magnitude variation, summary extrapolated from Dziga et al. 2013). These zero order rates corresponded to half-lives ranging from 0.1 hours to 18 days (average of 1.25 days). The significantly high variation in reported zero order biodegradation rates was most likely due to the different MC variants used, initial concentrations used for each variant, the varying

physiological conditions, methods used for MC detection, as well as culture densities employed in each reported study. In addition, the fact that isolated degrader cultures were used for the majority of these experiments may suggest that isolated populations may not perform the degradation as efficiently as compared to within a degrading consortium (highlighting the role of the bacterial consortia to improve degradation). Li et al. (2015) illustrated that the MCLR biodegradation rate did not vary as drastically as the range reported for a variety of isolate studies for a native bacterial consortium taken from a biological treatment process located at a drinking water treatment facility. The zero order biodegradation rates for this study ranged from 8 to 40 μg/L/day, with higher rates observed from mid to late autumn months following an algal bloom collapse.

First order biodegradation rate constants were compiled from a variety of studies, including batch and sand column degradation studies, as a comparison to zero order rates reached for studies in the literature (Chorus and Bartel 2006, Grutzmacher et al. 2010, Eleutario and Batista 2010, Ho et al. 2006, Ho et al. 2007a, Ho et al. 2012b, Li et al. 2015a). Overall, the first order approximations appeared to be much more reasonable (better fit to the data) than zero order kinetics and ranged from 1.3E-03/hr to 0.693/hr for these experimental studies, with an average of 0.0818/hr (three orders of magnitude difference). The corresponding half-lives for microcystin degradation ranged from 1 hour to 22 days, (average of 3 days) with less variation observed in the reported data than those summarized for zero order kinetics. The summary of half-lives for both zero order and first order experimental data shows that the degradation processes, in itself, is subject to a high variability, and even the fastest reported rates for degradation may not sustain the removal rates required by existing biofiltration systems. Similarly, the representation of the

degradation rates is extremely important to adequately predict toxin removals in full scale treatment systems.

III. Biological Filtration

General Theory of Biological Filtration

Biological filtration relies on physical, chemical, and biological treatment mechanisms for removal of algal toxins of concern, similar to its predecessor of deep bed filtration. The main objective of engineered biological filtration is to establish consistent hydraulic throughput and optimum removal efficiencies of a wide array of water quality constituents. In the case of algal toxin removal, adequate hydraulic and environmental conditions should allow the formation of microcystin degrading bacterial biofilm communities (that will concurrently degrade dissolved nutrients) that are stable over time (Ho et al. 2012a). Ultimately, a feedback "bioclogging" mechanism, combined with the accumulation of particulate and organic material or cell debris, influences the available pore space for water flow over time, which results in the requirement to backwash the filter grains and reestablish a relatively clean filter bed (Thullner et al. 2004, Engesgard et al. 2002, 2006). The backwash frequency and intensity are likely to be reduced as to not completely disturb the existing biofilm communities and to allow full and fast regeneration of the previous biofilm communities after filter start up (Emelko et al. 2006).

The efficiency of biological filtration is first governed by physical-chemical mechanisms of contact (transport) and attachment of bacterial and colloidal particles to the surface of the collector grains. Contact potential of either bacterial particles or colloids to filter grains is controlled by several physical transport mechanisms including straining, sedimentation, diffusion, hydrodynamic interactions, inertial impaction, and interception

(O'Melia and Stumm 1967, Huisman and Wood 1974, Keir et al. 2009). Straining relates to the mechanism of entrapment of bacterial particles or colloids that are too large to fit through the pore spaces of the sand grains and depends on the ratio of the diameter of the particle in question (d_p) to the representative grain diameter of the media (d_{10}) (O'Melia and Stumm 1967, Huisman and Wood 1974, Keir et al. 2009). Sedimentation refers to the physical settling of bacterial particles or colloids on the grain surface, due to density differences between the particle and fluid, and depends on the available surface area provided by the collector grains, the hydraulic loading rate, as well as the theoretical settling velocity predicted by Stoke's law (Yao et al. 1971, Huisman and Wood 1974, Keir et al. 2009). A comparison of the surface loading rate (HLR normalized by the theoretical surface area of grains) to the settling velocity gives some indication to the impacts of sedimentation for the removal of bacterial particles and colloidal matter (Huisman and Wood 1974).

Molecular diffusion relates to the random movement of generally submicron bacterial particles or colloids from areas of high concentration to low concentration and plays a role in mass transfer of particles or water quality constituents from the bulk solution of fluid to the biofilm or sand grain surfaces (Dullien 2012, Bear 2013). Contact between the particle or colloid of interest and the collector surface may also arise due to hydrodynamic actions, or the random, drift in motions associated with migration of spherical bacterial particles across non-uniform shear fields experienced in the soil pores (Keir et al. 2009). Interception occurs when the streamline of a particular bacterial particle or colloid exists within a given radius of the grain surface, resulting in an increased contact potential (Yao et al. 1971). Transport of bacterial particles to grain surfaces may also be

mediated by bacterial mobility (Keir et al. 2009). Finally, inertial impaction is related to contact with a grain surface as a result of the inertial forces of the particle/water quality constituent of interest that causes deviation from the fluid streamlines, thereby impacting the collector surface (Yao et al. 1971).

Once the bacterial particle or colloid of interest comes in contact with the filter grain surface, several mechanisms such as electrostatic interactions, London-Van der Waals forces, and the nature of the particle and grain surfaces influence the ultimate attachment and removal (O'melia and Stumm 1967, Keir et al. 2009). Electrostatic attraction between the particle and grain collector surface arise due to variations in the electric double layers of the particle or water constituent of interest, primarily as a function of ionic strength and pH (O'melia and Stumm 1967, Keir et al. 2009). Changes to the electric double layer may include adsorption of ions in solution or disassociation of functional groups, which may result in net attraction or repulsion to the media surface (O'melia and Stumm 1967). Most clean quartz or silica sands used in filtration applications carry a net negative surface charge, causing the initial deflection of net negatively charged bacteria, anions, and organic matter (Tufenkji and Elimelech 2005). However, as filtration progresses, charge reversal may occur due to oversaturation of the collector surface with positively charged particles, which increases relative adsorption of negatively charged species. Some studies have also described local heterogeneities in surface charge of the grain surface that influence bacterial attachment, even at high activation energies; therefore, the charge distribution on a surface collector should not be considered completely uniform (Tufenkji and Elimelech 2005). The nature of the bacterial particle surface, such as the presence of organic macromolecules (humic or fulvic acids) or steric interactions between adsorbed polymers

in solution and the grain surface, may also influence the ultimate attachment efficiency (Franchi and O'melia 2003, Bolster et al. 2001). London-Van der Waals dispersion forces are associated with dipole moments formed from the temporary asymmetrical distribution of electrons on atomic nuclei and are important attachment forces when the separation distance between the particle and grain surface is relatively small and the size of the molecules or particles of interest is relatively large (Grasso et al. 2002, Tufenkji 2007). Other forces influencing attachment include born and hydration forces. Born forces, repulsive in nature, occur when the electron clouds of two atoms or molecules overlap (McDowell-Boyer 1992, Keir et al. 2009). Hydration forces can arise due to a disruption or change in the molecules surrounding a surface, where repulsive hydration forces exist due to the affinity of water molecules to bind to hydrophilic surface groups on the media surface (hydroxyl groups and hydrated ions) (Elimelech, M., & O'Melia 1990).

The nature of the grain collector surface also plays a role in attachment of particles or water quality constituents of interest, including the relative hydrophobicity and associated interactions due to phase affinity. For example, if a surface is more hydrophobic it is more likely to bind with constituents that have a natural affinity to dissolve or interact in that phase, such as nonpolar molecules in octanol. The increase in hydrophobicity of the surface also reduces the Gibbs free energy of the surface, which may promote bacterial attachment (as the net repulsive force is reduced significantly) (Scholl et al. 2003, Chen and Strevett, 2003). Similarly, surface roughness or the presence of natural or contrived surface coatings (i.e., metal hydroxides) of the collector grain surface may increase particle attachment under saturated flow conditions (Bolster et al. 2001, Morales et al. 2009).

The summation of the interactions among these forces, both attractive and repulsive in nature, termed the resultant adhesive force, influences the ultimate attachment efficiency on the grain surface and varies according to the separation distance of the particle and grain surface (Keir et al. 2009). Generally, from DLVO theory, the interaction energy between the bacteria particle and grain surface is attractive at small separation distances, whereas the interaction energy is repulsive at larger distances from the surface. As the particle approaches the surface, an energy barrier is present (primary maximum) that must be overcome before the particle officially attaches (and reaches) the primary minimum energy state. In some cases, a secondary energy minimum is also present at larger separation distances that may play a significant role in the irreversible attachment of bacterial cells with relatively low thermal energies (Redman et al. 2004). Ultimately, the ionic strength and the pH of the medium have a large impact on the distribution of the theoretical interaction energy curve, where solutions with high ionic strength (decrease double layer thickness) and result in lower activation energies (easier access to the primary minimum). High or low pH may also result in protonation or deprotonation of functional groups, which may increase the contribution of electric double layer repulsion over other forces, thereby increasing the activation energy barrier. However, studies have demonstrated that the effect of pH under operational conditions (5-8) on bacterial attachment was diminished compared to the effect of ionic strength (Jewett et al. 1995).

Once a sufficient bacterial population is established on the filter media (termed the ripening period), biodegradation of different water quality constituents may commence. The proper functioning of the biofilm community depends on the availability of both electron acceptors (oxygen) and electron donors (organic carbon, microcystin, etc.) utilized

by heterotrophic bacteria as energy and carbon sources for development of new biomass or production of extracellular polysaccharides (EPS) or other cellular byproducts. Of course, the presence of autotrophic bacteria (nitrifiers) and inert biomass also affects the structure and function of the biofilm matrix (Rittmann 1987, Rittmann et al. 2002). The function of the EPS coating in the biofilm community is to provide protection against environmental stresses and dehydration as well as to maintain attachment to a given surface under a variety of hydrodynamic conditions (Vu et al. 2009). Substrate utilization of bacterial biofilm communities is generally limited by the mass transfer of both electron donors and acceptors from the bulk liquid in the pore space to the biofilm surface (Rittmann and McCarty 1980). Current models of biofilm subsistence have proposed that the mass transfer of either electron donors or acceptors to the biofilm surface depend on the diffusion coefficient in the pore space and the length of the diffusion layer film, which presents a resistance to mass transfer (Fick's first law) (Rittmann and McCarty 1980, Rittmann 1982a). As the EA or ED is transported to the biofilm surface, a spatial gradient of either EA or ED from the surface of the biofilm to the grain surface is established, creating a concurrent diffusive flux of either the EA or ED into the biofilm matrix (Fick's second law). The diffusive flux of substrate or electron acceptor into the biofilm matrix enables the growth of different microbial communities from the utilization of different substrates, which is often predicted using a Monod type, hyperbolic equation (where the substrate utilization is dependent on the specific microorganism concentration, cell yield, maximum growth rate, and half saturation constant). As long as there are no perturbations in the system, the biofilm community is assumed to reach steady state, where the net

accumulation or microorganisms balances the net decay or release of microorganisms (Rittmann and McCarty 1980, Rittmann 1982a).

The maintenance of the steady state biofilm depends on the rate of microbial detachment, as opposed to attachment, which can be physically, chemically, or biologically mediated. Of the myriad physico-chemical and biological mechanisms, erosion, abrasion, sloughing, predation, and filter backwashing are the main contributing factors (Liu and Tay 2001, Liu and Li 2008). Erosion of biomass within the biofilm results due to varying hydrodynamic shear conditions within the porous media and is analogous to bits and pieces of the matrix being "shed" from the existing biomass (Liu and Tay 2001). It has been previously demonstrated that conditions of high hydrodynamic shear in porous media lead to a thin, stable, smooth, and dense biofilm matrix, preferable for biological filtration applications (Liu and Tay 2001). Physical collisions with external particles also lead to abrasion of the biofilm matrix (Chaudharry et al. 2003). Sloughing is another physical detachment mechanism related to the sudden loss of a large portion of the biofilm matrix on the physical size order of the length of the biofilm matrix, most likely a function of the hydrodynamic conditions (Telgmann et al. 2004). The potential of grazing by native protozoa on heterotrophic bacterial populations within a biofilm is yet another potential detachment mechanism that may occur in drinking water treatment biofilters. A more direct way, from an operational standpoint, to induce bacterial detachment is the advent of a backwashing system using air scour or fluidized bed techniques to promote hydrodynamic shear and concomitant losses in biomass from filter grains (Emelko et al. 2006). The use of a backwashing process is often a necessary tool to ensure efficient volumetric throughput of water over the operational life of the filter system.

Microorganisms have also been known to actively detach from supporting media as a result of nutrient limitations, such as carbon or trace nutrient sources (Sawyer and Hermanowicz 1998).

Design and Operation of Conventional Biological Filtration Systems

The design of a conventional biological filtration system depends on the following criteria (but is not limited to): 1) media type and characteristics; 2) length of the media (L) and presence of alternating layers of media types (i.e., mono, dual media); 3) hydraulic (HLR), surface (SLR), and organic loading rates (OLR); 4) empty bed contact time ($EBCT$); 5) limiting substrate fluxes (J_{deep}) and concentrations (S_{min}); 6) as well as the filter backwash techniques (Huck 2000, Chaudharry et al. 2003). Other significant parameters that should be taken into account are the source water quality such as temperature, ionic strength, pH, as well as the concentration of residual oxidants, and whether ozonation is applied to treat the source water (from pre or post ozonation processes).

The most important criteria for biological filtration include a surface supporting quick microbial growth, larger surface area to support more biomass growth, and adequate surface texture to ensure biomass stability, in which the ultimate selection has major cost implications (Chaudharry et al. 2003, Urfer et al. 1997, Huck 2000). The media types for most conventional systems range from quartz or silica sands, to anthracite, or to granular activated carbon (GAC). The specific surface area (unit surface/unit volume filter) of sands is typically higher than GAC, due to the fact that bacteria are not able to colonize the microporous structures (1-100 nm) and the effective grain size for sand is lower than GAC (Urfer et al. 1997). Benefits of GAC over sand or anthracite include its macroporous structure and high surface roughness which promotes bacterial attachment and protects

bacterial detachment from hydrodynamic shear. Further, GAC also adsorbs chemical constituents in water, such as algal toxins, which sand or anthracite may fail to consistently remove (Urfer et al. 1997). In terms of performance, media selection (anthracite vs. sand) was determined not to have a significant effect on biodegradable organic matter (BOM) removal efficiency for full scale systems, despite the greater amount of biomass observed for full scale systems with GAC (Huck 2000). In addition, GAC-sand dual media systems were concluded to provide better aldehyde and carboxylic acid removals at colder temperatures, establish a BOM biofilm more rapidly, and provide increased protection against ozone or chlorine residuals than anthracite-sand systems. The greatest deterrent to GAC based systems is the initial capital cost and operational costs associated with regeneration compared to anthracite or sand (Huck 2000).

Media characteristics may include the uniformity coefficient (UC), representative grain diameter (d_{10}), and the grain size distribution of particles. In general, grains with low uniformity coefficient (1-1.4), medium to coarse grain size distributions (0.20 to 0.75 mm) and representative grain diameters are desirable for efficient biological filtration operation and water throughput. The depth of media for most conventional biofiltration systems ranges from 0.08 to 3.73 m, with an average depth of approximately 0.75 m for 21 WTPs surveyed in the U.S. (Evans et al. 2013a, 2013b). Little comparison has been made regarding the treatment performance of biological filters with varying grain sizes and depths, but it is expected there is an inherent tradeoff between treatment efficiency, media size, and water throughput. For example, if smaller representative sizes of sand were incorporated, treatment efficiency would most likely improve (due to an increase in specific surface area) at the expense of a smaller volume of water throughput. Clearly, the

greater depth of media would potentially increase treatment efficiency of water quality constituents but would require more physical resources and area to engineer. Lastly, a majority of biofilter systems in the U.S. are also configured as dual media as compared to mono and multi-media systems (Evans et al. 2013a, 2013b).

The theoretical design and operation of a biofilter can be improved through the use of several distinct "macroscopic" parameters including the hydraulic loading rate (*HLR*), the surface loading rate (*SLR*), the organic or substrate loading rate (*OLR*), and the empty bed contact time (*EBCT*) (Figure 4). These parameters are termed macroscopic in that they are relatively coarse (and at the continuum scale), where the level of control of the pore scale processes is variable. Hydraulic loading rate (*HLR*) is specified as the volume of water applied to the nominal surface area of the filter and is equivalent to the specific discharge in groundwater systems. Comparably, surface loading rates (*SLR*) are defined as the volume of water applied to the specific surface area of the filter grains. If spherical shapes are assumed the *SLR* can be approximated by Equation 1, where *Q* represents the volumetric rate of water application to the filter (m^3/sec). The organic loading rate (*OLR*) is defined as the HLR multiplied by the concentration of species in the water, to obtain a mass loading per time (Equation 2). The empty bed contact time (*EBCT*) is simply the length of the filter normalized by the hydraulic loading rate (Equation 3). Typical *HLR*s for conventional biofilter systems range from 5 to 30 m/hour, with corresponding *EBCT*s ranging from 5 to 20 minutes, similar to rapid sand filtration systems (Evans et al. 2013a, 2013b). A number of studies have demonstrated that *EBCT* is a significant operational and design parameter for biological filtration processes as compared to HLR alone (Carlson and Amy 1996, 1998). These studies also determined that for a given *EBCT*, BOM removal was

independent of the change in *HLR*, suggesting that external mass transfer (of nutrients or electron acceptors in the bulk liquid to the grain surface) does not play a large role in BOM removal (Urfer et al. 1997). Since BOM removal and influent concentration of BOM were directly proportional, increasing the *EBCT* was determined to have a less than proportional effect on BOM removal, but still positive nonetheless (Urfer et al 1997, Huck 2000).

$$Ss = \frac{6}{d}(1-\theta) * V_{reactor} \quad (1)$$

$$SLR = \frac{Q}{Ss} \quad (2)$$

$$OLR = HLR * C_w \quad (3)$$

$$EBCT = \frac{L}{HLR} \quad (4)$$

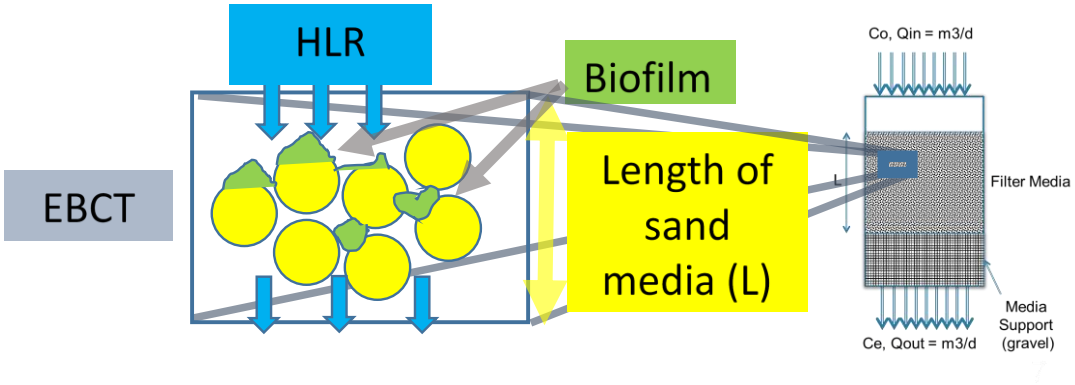

Figure 4. *A schematic of the drinking water treatment biofiltration process and associated coarse design/operational parameters*

Rittman (1982a, 1987, 1989) proposed additional, "microscopic" parameters, focused at the pore scale, to aid in fine tuning the design and operation of aerobic biological treatment systems. These microscopic parameters were developed from the theory of biofilm kinetics in biological reactor systems. The bulk of the theory is focused on a substrate flux (J_{deep}, the minimum flux to support a "deep biofilm") that enters the biofilm, which is dependent on the mass transfer rate of substrate from the bulk liquid to the biofilm surface, the corresponding substrate utilization rates by biomass in the biofilm, and

the length of the biofilm, if the biofilm is at steady state (no net growth or loss of microorganisms). The utilization of substrate in the biofilm by heterotrophic microorganisms creates a concentration gradient, driving a diffusive flux of substrate throughout the depth of the biofilm. Steady state biofilms were categorized into deep, shallow or fully penetrated in nature (Rittman and McCarty 1980). Biofilms that are considered deep (with sufficient thickness) often have a length scale where the concentration at the media surface can be assumed to be zero (and have the highest diffusive flux), whereas shallow and fully penetrated biofilms either have a concentration of substrate at the media surface that is nonzero or proportional to the concentration at the surface of the biofilm (Figure 5). From this theory, the biofilter can be designed to operate at the most efficient flux, J ($J>J_{deep}*3$ for heterotrophic organisms) and substrate concentration, S ($S>S_{min}$) to support an adequate population of degrading microorganisms (Equations 5, 6, and 7).

$$J = \frac{Q(S_0 - S_e)}{A_F V} \quad (5)$$

Where S_0 and S_e are the influent and effluent concentrations, Q is the volumetric flow rate of water, A_F is the theoretical biofilm surface area, and V is the volume of the reactor.

$$J_{deep} = \{2[S_{LF} - \ln(1 + S_{LF})]\}^{1/2} \quad (6)$$

Where S_{LF} is the concentration of the substrate at the biofilm surface (which can be equivalent to the concentration in the bulk solution for well mixed systems).

$$S_{min} = \frac{K_s * b'}{(Y\mu_{max} - b')} \quad (7)$$

Where K_s is the half saturation constant, b' is the overall first order biomass loss coefficient, Y is the yield of biomass per substrate consumed, and μ_{max} is the maximum bacterial growth rate.

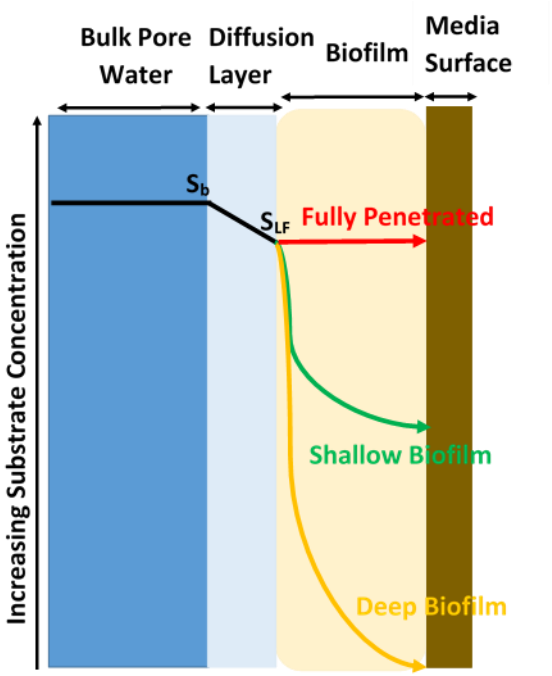

Figure 5. *Depiction of the Biofilm Theory Proposed by Rittmann and McCarty 1980*

Backwashing strategies present another design and operational parameter to control the accumulation of biomass and particulate matter in the biological filtration system (Huck 2000). In practice and in theory, it is optimal to carefully manage the existing biomass to maintain the system in operation as close to steady state as possible. However, at times during operation, there might be a sudden perturbation (such as a change in the organic loading rate) that causes a shift in biomass concentration away from steady state (either a net loss or accumulation of organisms) that results in clogging of the system (reducing the volume of water through the filter) or a breakthrough of considerable amount of bacterial or colloidal particles (increasing the turbidity of the effluent water). Long term performance of biological filtration systems is very reliant on a proper backwashing scheme and may depend on the amount of biomass vs. organic or inorganic particulate or colloidal matter (Rasheed et al. 1998, Ahmad and Amirtharajah 1998, Emelko et al. 2006, Liao et al. 2014). Optimal backwashing schemes for non-biological

filters are traditionally a combination of air and water at sub fluidization velocities to obtain collapse-pulse conditions, which results in efficient removal of colloidal and particulate matter (Urfer et al. 1997). As compared to non-biological filters, the strength of bacterial attachment was found to be significantly greater than colloidal/particulate attachment, which ultimately influences the design of an efficient backwashing scheme for biological filters (Ahmad and Amarathah 1998). A majority of studies have described little to no loss in total biomass from backwashing schemes with and without air scouring (Urfer et al. 1997). Emelko et al. (2006) more recently determined that backwashing with air scouring did not influence the consequent removal of BOM, even though some biomass was lost. Comparably, some studies have reported a relative decrease in biomass with chlorinated as compared to non-chlorinated backwash waters (while BOM removal efficiency remained unaffected), especially for anthracite media as compared to GAC (Huck 2000). Regardless of the scheme employed, backwashing is essential to ensure contact time is not altered and that substrate biodegradation efficiency is not reduced by the increased presence of inorganic or colloidal materials accumulating in the pore spaces.

Of the environmental conditions that may vary during operation of a biological filtration system, temperature has been determined to be one of the most critical. Theoretically, higher temperatures lead to increased microbial activity (faster growth and substrate utilization kinetics) as well as improved mass transfer of substrate. Several studies have reported that BDOC, gloxylate, and aldehyde removal efficiencies increased with increasing temperatures (Coffey et al. 1996, Daniel and Teefy 1995, Servais et al. 1992, Krasner et al. 1993), supporting theoretical inferences.

Oxidant residual, or the presence of free chlorine or ozone, is yet another key factor that can be more or less controlled or monitored before entering biological filtration systems (Urfer et al. 1997). In general, the presence of a residual oxidant may be deemed harmful for operation of biological filters, as some microorganisms in the degrading population are extremely sensitive to these types of disinfectants. In many cases, the media type may significantly decrease the deleterious effect of the oxidant on the biofilm communities. For example, GAC has been observed to react with Cl2 and decompose other oxidants, which explains why some studies have observed no effect of ozone or chlorine residual on biodegradation efficiency of certain compounds in GAC filters over anthracite filters (Boere 1991). Hydrogen peroxide (H202), traditionally used to accelerate ozone decay, may also show bactericidal properties at relatively high concentrations (Huck et al. 1991). Further, residual choramines were demonstrated to reduce bacterial populations in biofilters at certain concentrations (Ferguson et al. 1990). Above all, the oxidant residual should be carefully monitored and controlled as to not disrupt the bacterial populations within biofilm communities and to ensure optimal degradation efficiencies.

If ozonation is included in the pretreatment train, the design and operation of biological filters may be tailored to reduce the excess fractions of biodegradable carbon created. Ozonation has been observed to increase the biodegradable portion of organic carbon in NOM present in the source water, including the formation of hydroxyl, carbonyl, and carboxyl groups, loss of double bonds and aromaticity, and the shift from high to low molecular weight organics (Volk et al. 1993, Nishijima and Speitel 2004). The transformation of organic compounds generally favors the growth of bacteria, as the source waters are generally carbon limited (in terms of electron donor) as compared to both

nitrogen and phosphorus nutrients (Rittmann 1990). Several studies have indicated that the ozone-biofiltration process must be coupled in order to achieve stringent regulations on disinfectant byproduct formation (Hozalski et al. 1999). In addition, the biological activity in biofilters generally can reduce the carbon loading to pre-ozonation levels, often achieving up to 75% removal for certain compounds generated by ozonation (Urfer et al. 1997).

IV. The Movement Towards Engineered Biological Filtration and Algal Toxin Removal

A general shift in consensus among water quality authorities and utilities alike has been taking place nationwide concerning the role of biological filtration as a biological process during drinking water treatment practice. A recent survey of 77 water utilities across the U.S. indicated that approximately 39% of the filtration processes were operated as non-biological processes, whereas a greater majority (45%) responded that they intentionally operated their filtration process to increase biological activity (Evans et al. 2010b). The utilities differed in the biological filtration systems that they employed. Of the utilities operating their filtration processes in a biological manner, the greater majority used combined ozone, post biological filtration systems (44%) compared to biological perchlorate/nitrate removal (26%) and rapid biological filtration processes (18%). In addition, the majority of the rapid biological filtration processes were converted deep bed filtration systems that were not operated with chlorine dosing, suggesting that little previous optimization to improve treatment efficiencies in these systems has occurred (Evans et al. 2010b).

A difference also existed among utilities regarding the operation of their biological systems in an intentional or incidental manner as well as the assigned treatment objectives of these systems. Greater than 70% of the rapid biological filtration/ozone enhanced biofiltration processes were managed intentionally as biological filtration systems, whereas over 100% of GAC filtration systems were considered "incidental" in nature (Evans et al. 2010b). The primary treatment objectives of these systems were either: 1) turbidity or particulate removal or 2) assimilable organic carbon (AOC)/total organic carbon removal for reduction in disinfectant byproduct formation, with little emphasis on algal toxin removal (Evans et al. 2010b). A similar study of representative water treatment utilities in the U.S. concluded that the intentionally managed biological filtration processes did not effectively monitor the biological activity of their treatment systems, most likely due to the lack of available practical tools, where only pH, turbidity, and flowrate were the most common water quality parameters actually monitored (Evans et al. 2013a, 2013b). These studies also highlighted that there was little consistency among water utilities in the management of their biological filtration systems, partly due to the lack of available guidelines and universal monitoring techniques. Therefore, despite the movement, interest, and efforts to assimilate biological processes into conventional treatment trains among water treatment authorities and utilities, the monitoring and optimization of these filters to improve treatment efficiencies has been lagging behind the potential demonstrated by the research community.

The emergence of engineered biological filtration and the transition from operation of current systems from passive to active processes is an important stepping stone in the potential removal of algal toxins throughout current biological filtration systems

(Lauderdale et al. 2012). This concept of intentionally optimizing the biological activity of these systems stems from the desire to achieve removal of a wide array of water quality constituents, aside from the traditional turbidity and particulate removal expected by most passive, conventional processes. Current research on engineered biological filtration has been focused on addition of substances or nutrients to the filter system in a manner that optimizes both treatment efficiency and hydraulic throughput. The three most studied and recognized techniques to improve the biological activity of these systems range from biostimulation through nutrient addition, control of EPS production and stimulation of enzymes that oxidize organics through peroxide addition, as well as bioaugmentation through the addition of isolated consortia capable of degrading certain contaminants of concern (Lauderdale et al. 2012, Benner et al. 2013, McKie et al. 2015, Azzeh et al. 2015, Rahman et al. 2016).

Nutrients such as organic carbon, nitrogen, and phosphorus are key to support the growth and proliferation of microbial communities in any environment, suspended or immobilized. In most aquatic freshwater ecosystems, the amount of bioavailable carbon is often limiting, as well as bio available phosphorus (Yu et al. 2003a, 2003b, Rittmann 1990). In porous media, the production of extracellular byproducts of microbial communities, often termed EPS, can significantly clog pore spaces and reduce the hydraulic throughput over time. Thus, there has been considerable interest to optimize biofilter performance through nutrient addition to balance EPS production and enhance microbial growth. Optimum nutrient ratios of these constituents of approximately 100:10:1 (bioavailable organic carbon: ammonium nitrogen: orthophosphate phosphorus) have been reported to stimulate microbial activity and reduce EPS secretion (Flemming and Wingender 2001, Liu

et al. 2006). However, this reported ratio (100:10:1) is subject to inherent variation due to different growth conditions and microbial community composition, among many factors (Flemming and Wingender 2001, Scott et al. 2012).

Past studies that have investigated nutrient amendment scenarios on biofilter performance have provided mixed results, suggesting that the role of nutrient addition to supplement an engineered biofiltration process is not entirely consistent. Lauderdale et al. (2012) reported a 15% decrease in the filter headloss (15% increase in filter run times) with phosphoric acid amended biofilters over controls, which was postulated to be a result of the decrease in EPS production and stimulation of microbial activity (ATP levels) (greater than 30% for each). In addition, phosphorus amended biofilters corresponded with a significantly higher removal of DOC, manganese, and MIB than control biofilters (Lauderdale et al. 2012). Pharand et al. (2014) found no significant relationship between C:N/C:P ratios and biofilter performance as measured by DOC/AOC removal and biomass quantity/activity. Removal of AOC was still observed to be substantial under phosphorus limited conditions (C:P of 100:0.15) (Pharand et al. 2014).

The addition of phosphorus had a negligible effect on biofilter biomass and did not improve the removal of NOM, specifically biopolymers related to membrane fouling in a pilot scale biofiltration experiment (Rahman et al. 2016). The addition of phosphorus to pilot scale biofilters slightly increased the removal of DOC and humic substance, but this effect was observed to decrease over time (Rahman et al. 2016). Comparably, the effect of nutrient additions (nitrogen and phosphorus) to pilot scale GAC and anthracite filters did not demonstrate any significant differences in DOC, AOC, or DBP precursor compounds compared to a control biofilter (McKie et al. 2015). Azzeh et al. (2015) also did not observe

any beneficial results on DOC, biopolymer, or DBP precursor removal for biofilters amended with nitrogen and phosphorus (at ratios of up to 100:40:20). Finally, no significant differences were observed in filter run times, DOC removal, and head loss development for GAC filters amended with nitrogen and phosphorus (Wong et al. 2014). Yu et al. (2003b) observed an increase in bacterial growth potential (BGP) and COD removal (up to 21%) of pilot scale drinking water treatment biofilters amended with phosphorus, where phosphorus addition improved performance over organic carbon addition. The differences in treatment efficiencies and headloss development in biofilters from reported nutrient amendment strategies may be due to large variations in source water quality (available carbon, nitrogen, and phosphorus) and more importantly, the temperature of water for most experimental systems.

Hydrogen peroxide addition has been identified as another potential strategy to engineer biological filtration systems through a combined increase in oxidizing functions of native microbial consortia as well as a decrease in the bioclogging potential of porous media (Lauderdale et al. 2012). Hydrogen peroxide addition at certain prescribed doses to immobilized cultures has been shown to degrade biopolymers associated with the EPS matrix and to not disrupt the productivity of existing bacterial communities (Christensen et al. 1990). Other effects of hydrogen peroxide addition include the induction of microbial community expression of oxidoreductase enzymes that may decrease inactive biomass and EPS in the biofilm matrix (Pardieck et al. 1992).

Similar to nutrient amendment scenarios, the addition of hydrogen peroxide to actual biofiltration systems has demonstrated variable results. The supplementation of peroxide (at 1 mg/L for a 10-day period) increased the removal of DOC at a removal

efficiency 50% greater than a control biofilter operated on the pilot scale of analysis and provided complete removal of MIB and manganese (Lauderdale et al. 2012). Similar peroxide additions also decreased filter head loss by 60% compared to a control biofilter and did not affect the productivity of active biomass in the amended biofilter (Lauderdale et al. 2012). In contrast to the improved performance reported by Lauderdale et al. (2012), Mckie et al. (2015) indicated no improvement in treatment performance (DOC, AOC, DBP precursors, biopolymers) comparing GAC biofilters amended with and without hydrogen peroxide, which most attributed to the lack of available organic carbon in the drinking water treatment plant feed waters. Beneficial biofilter operation was observed by Azzeh et al. (2015) when peroxide was dosed between 0.1 to 0.5 mg/L, where head loss decreased between 9 and 48%, respectively. Urfer and Huck et al. (2000) observed no appreciable increase in biological acetate and formate removals for a sand-anthracite biofilter periodically dosed with hydrogen peroxide at (0.5 mg/L). The culmination of these results suggests that hydrogen peroxide may have a beneficial effect on treatment efficiencies of biological filters, especially when dosed continuously and at appropriate levels as not interfere with the biological stability of immobilized biofilm communities.

Bioaugmentation refers to the addition of supplemental microbial communities or isolated bacterial strains to drinking water treatment biological filters to either stabilize or enhance treatment efficiencies of contaminants or compounds of concern (Benner et al. 2013). Generally, degrading populations of certain micro pollutants or algal toxins within the source water are not particularly abundant within the microbial community and therefore not consistently metabolically represented or active. However, upon addition of these stimulated strains or consortia to the existing bacterial community, enhanced

mineralization of micropollutants/algal toxins or degradation kinetics may result. This improvement in degradation depends on whether microbes within the community actively use the algal toxin or micropollutant as a primary substrate or partake in co-metabolic degradation of the constituent of concern. The prior degradation ability allows the microbial community to mineralize the substrate as an energy and carbon source, whereas the latter degradation capacity is mediated by enzymes that the bacteria secrete which transform the algal toxin or micropollutant of interest into products that may be favorable for other populations within the complex microbial community (Banner et al. 2013). Several studies have demonstrated the utility of bioaugmentation for direct elimination of microalgal taste and odor compounds as well as microalgal toxins. McDowall et al. (2007, 2009) revealed that the addition of a geosmin degrading bacterial population increased the removal of geosomin by 75% compared to control sand biofilter columns with no bioaugmentation. The presence of an existing biofilm on the immobilized media, whether active or inert, improved the degradation capacity and efficiency of the seeded culture of geosmin degrading bacteria, most likely due to the greater attachment efficiency of these microorganisms within the EPS-biofilm matrix. Bourne et al. (2006) studied the degradation potential of an inoculated strain of a microcystin degrading bacterium to laboratory slow sand filters. No significant differences were observed in the biodegradation efficiencies and kinetics of microcystin-LR between slow sand filter columns inoculated with and without the isolated degrading strain. These results suggest the potential of degrading consortia over isolated degrading strains for improved algal toxin degradation in biological filtration systems, especially when the degrading population is under-represented and variable throughout the course of treatment.

The Potential of Engineered Biological Filtration of Algal Toxins

Although many studies have addressed the degradation efficacy of a variety of water quality constituents in biologically activated filters, including dissolved organic carbon, assimilable organic carbon, biopolymers, and DBP precursors, few have studied the direct potential of biofiltration of algal toxins of concern, especially at larger scales of analysis (Ho et al. 2006, Bourne et al. 2006, Wang et al. 2007, Ho et al. 2010, Ho et al. 2012a). These studies will be briefly reviewed to provide some context into previous work that has been conducted regarding the potential removal efficiencies and degradation kinetics of microcystin algal toxins in biological filtration systems.

Ho et al. (2006, 2007) was the first study to confirm that the complete removal of microcystin-LA/LR was indeed possible after an initial lag phase from laboratory rapid sand filters dosed with reservoir water containing native microbial consortia and packed with sand from existing full-scale filtration systems. Moreover, Ho et al. (2006) concluded that there were little differences in biodegradation efficiency of microcystin-LA/LR as a function of the empty bed contact time (EBCT) and hydraulic loading rate (HLR). In addition, pre-exposure to microcystin-LR/LA had a significant impact on degradation efficiency, where no lag phases were observed for columns inoculated with sand that was previously exposed to these microalgal toxins (Ho et al. 2006, 2007). The biodegradation efficiency was also improved when the sand was not autoclaved or cleaned (inactivated) prior to experimentation, demonstrating that the initial lag phase may be due to necessary cell attachment and biofilm acclimation prior to commencement of degradation (Figure 5) (Ho et al. 2007a). Comparably, sand sourced from different treatment plant locations developed varying degradation kinetics, indicating the variability in degrading

microorganisms present (Figure 5A). Initial concentrations of microcystin also did not affect the biodegradation potential in the laboratory columns, in which temperature was determined to be the limiting factor (higher temperatures corresponded to higher degradation kinetics) (Ho et al. 2007a).

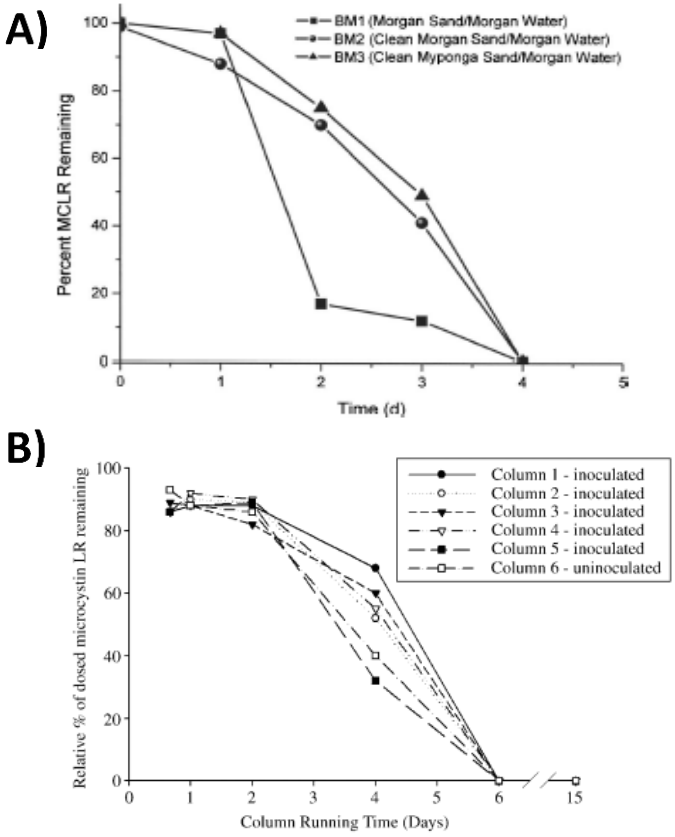

Figure 6. *Significant results from previous laboratory-based column biofiltration studies targeting microcystin removal from: A) Ho et al. 2007a and B)) Bourne et al. 2006.*

Bourne et al. (2006) researched the removal of microcystin-LR in laboratory slow sand filtration as opposed to rapid sand filtration column experiments. Hydraulic conditions, including EBCT and HLR, during these experiments were an order of magnitude higher (30 hours) or lower (0.0165 m/hr) than the previous experiments conducted by Ho et al. (2006, 2007). A series of five column experiments were inoculated with an isolated

degrading strain as compared to one treatment with just raw water from the drinking water treatment plant reservoir (Figure 5). The degradation kinetics for the slow sand filtration experiments were relatively similar for all treatments, where degradation commenced after a 2-4-day initial lag period. Microcystin-LR was completely eliminated in all columns by day 6 of the study, which was approximately two days longer than the rapid sand filter experiments, demonstrating the relative feasibility of rapid sand filters over slow sand filters for algal toxin removal. The efficient removal of microcystin analogues in biologically active GAC filters as well as in a wastewater environment has been established by previous studies, where kinetics and degradation behavior are of a similar nature to those presented above.

The studies that have been conducted and reviewed here have determined that the full removal of microcystin analogues can be achieved (on the laboratory scale of analysis); however, the main limitations to the degradation process include overcoming a lengthy lag phase in degradation resulting in toxin breakthrough for a timescale of several days as well as the establishment of a consistent and well-represented bacterial degrading consortium (Ho et. al 2012). The concepts described in the previous section regarding the establishment of engineered amendments to support the degradation kinetics and consistency in treatment of algal toxins have only been explored to a limited extent and could offer a solution to future operational challenges observed for full scale systems.

Chapter 1: Investigation of Algal Biotoxin Removal during SWRO Desalination through a Materials Flow Analysis

Abstract: The operation of seawater reverse osmosis (SWRO) desalination facilities has become challenged by the increasing frequency and severity of harmful algal blooms (HABs). The efficiency of algal toxins removal during SWRO and pretreatment processes has critical human health implications. Therefore, a probabilistic materials flow analysis (pMFA) was developed to predict the removal of algal toxins in source water by various pretreatment configurations and operations during SWRO desalination. The results demonstrated that an appreciable quantity of toxins exists in the SWRO permeate (ng/L–μg/L levels), the backwash of pretreatment, and final brine rejects (μg/L–mg/L levels). Varying the pretreatment train configuration resulted in statistically significant differences in toxin removals, where higher removal efficiencies were evidenced in systems employing microfiltration/ultrafiltration (MF/UF) over granular media filtration (GMF). However, this performance depended on operational practices including coagulant addition and transmembrane pressures of MF/UF systems. Acute human health risks during lifetime exposure to algal toxins from ingestion of desalinated water were benign, with margins of safety ranging from 100 to 4000. This study highlights the importance of pretreatment steps during SWRO operation in the removal of algal toxins for managing marine HABs.

1. Introduction

Seawater reverse osmosis (SWRO) technology has the potential to meet the growing worldwide demand for freshwater by securing the most abundant resource of surface water available on the planet: the ocean (Voutchkov 2013). As the stress increases on existing surface freshwater supplies due to population growth, agricultural development, global climate change, and industrial expansion, SWRO has become a more accepted approach to augment the world's existing freshwater supply, especially in arid regions such as the Middle East (Dawoud 2005, Ghaffour et al. 2013a). Coupled with recent advances in membrane technology and sustainable sources of energy for operation (such as solar or wind power), SWRO is transitioning from a viable alternative to an integral component of freshwater provisions for many coastal municipalities and industries worldwide (Schiffler 2004, Eltawil et al. 2009, Subramani et al. 2011, Ghaffour et al. 2013b).

Like any emerging or established technology, however, SWRO faces several important challenges to gain full acceptance as a reliable technology for freshwater supply (Ghaffour et al. 2013b). The increasing frequency and severity of harmful marine algal blooms (HABs), has posed a serious threat to full- scale SWRO desalination facilities operating worldwide (Laycock et al. 2012, Boerlage and Nada 2015, Seubert et al. 2012). Caron and co-workers (2010) acknowledged two important impacts of HABs on desalination facilities: (1) complete removal of algal toxins; (2) increased demand on pretreatment for membrane fouling prevention. Besides the elevated biomass, algal blooms also contribute to excess organic matter (AOM) and transparent extracellular particulate (TEP) that intensify the biofouling potential of SWRO membranes (Voutchkov 2010, Villacorte 2015a, 2015b).

Although HABs cannot be prevented entirely, engineering measures have been developed to overcome the issues encountered. Existing responses to HABs at SWRO facilities may include changes to the operation or design of pretreatment trains. Operational changes may include increasing coagulant/flocculant addition, reducing filtration (granular or membrane based) run times, and increasing backwashing intensity or cleaning frequency of filtration systems (Voutchkov 2010, 2013). More recently, amendments to the design of pretreatment trains may include integrating dissolved air flotation (DAF) systems or changing inline coagulation/flocculation systems to an individual unit treatment process with separate sedimentation tanks to improve algal cell removal (Villacorte et al. 2015b).

Increased awareness of the harmful effects of HABs on full- scale desalination processes has also prompted new monitoring techniques and associated numerical modeling efforts to predict HAB events, so plant engineers and operators can be better prepared to handle the negative effects of these bloom periods on plant operations (Caron et al. 2010, Villacorte et al. 2015b). Integrating online sensing systems—such as fluorescent light scattering (i.e. flow cytometry) and/or total organic carbon analyzers—with RO membranes also provides a direct way to both detect and assess the deleterious effects of HAB periods on permeate water quality (Huang et al. 2015a).

A topic often overlooked, however, is the fate of marine algal biotoxins throughout pretreatment and RO membrane operations in full- scale desalination facilities (Boerlage and Nada 2015, Meyerhofer et al. 2010). Most existing studies in the literature have been limited to examining removal of these marine algal toxins across RO membranes alone, concluding that the RO membranes remove a considerable portion (>99%) of dissolved

algal toxins (Laycock et al. 2012, Boerlage and Nada 2015, Seubert et al. 2012, Meyerhofer et al. 2010). However, these studies were restricted to the laboratory/pilot scale of analysis and did not consider the effects of pretreatment processes on toxin removal.

In addition, the associated human health risk from consumption of desalinated water during HABs has not been fully assessed (Laycock et al. 2012, Boerlage and Nada 2015, Seubert et al. 2012, Meyerhofer et al. 2010). Preliminary risk assessments have ascertained that the risk of acute intoxication from consumption of desalinated water is rather low (Laycock et al. 2012, Boerlage and Nada 2015, Seubert et al. 2012). However, these assessments were based on data acquired from laboratory-based studies and may severely underestimate the environmental and hydraulic conditions RO membranes face in practice. The environmental effects of the backwash water and brine rejects during HAB periods are even less understood and are under-reported in the scientific literature (Caron et al. 2010). Therefore, a probabilistic materials flow analysis (pMFA) was carried out in this study to gain a quantitative and holistic understanding of the removal of algal biotoxins during full- scale SWRO practice. Ultimately, the pMFA was developed to answer the following questions:

- What is the typical concentration of algal toxins in desalinated water and brine/reject water?
- What pretreatment designs and operations (if any) lead to improved algal toxin removals?
- What is the human health risk from drinking desalinated water during HABs?

To address these questions, a quantitative comparison of toxin removal efficiencies during pre-treatment for several conventional configurations was conducted to estimate

the toxin concentration in the RO permeate as well as the combined pretreatment backwash and brine reject. A formal risk assessment framework was adopted to estimate the acute human health risks from drinking desalinated water incorporating the posterior distributions of toxin concentrations from the pMFA output. Model parameter sensitivity and outcome confidence evaluations were conducted to ascertain the validity of the model predictions and to prioritize future data collection efforts.

2. Materials and Methods

2.1. pMFA Overview and Model Assumptions

A pMFA was used to simulate the fate of algal toxins through various treatment processes (Gottschalk et al. 2010a, 2010b). To best represent a realistic desalination system, the study was set in Coastal Southern California, a region actively exploring SWRO as a solution to supplement ever increasing drinking water demands, where at least six new facilities have been proposed (CDWR 2013). A hypothetical 50 million gallons per day (MGD) (1.89 × 105 m^3/day) SWRO desalination facility, located in Santa Monica Bay, CA, was used to set the theoretical control volume for the pMFA analysis. The system would operate with a conventional salt rejection rate of 99.5%, permeate recovery of 50%, and intake rate of 100 MGD (3.78 × 105 m^3/day). A period of 24 hours was set as the duration of the pMFA for facility operation, providing a daily perspective on marine algal toxin production and fate in a SWRO facility.

The conceptual pMFA diagram that includes 10 distinct pretreatment trains commonly used in a conventional full-scale desalination facility is shown in Figure 7 (T1–T10). At the intake, the marine algal toxins enter in either dissolved (extracellular, C_{E0} in

μg/L) or particulate (intracellular, C_{I0} in pg/cell) forms. The mass flow of intracellular (M_{I0}) and extracellular toxins (ME0) entering the facility is calculated using Equation (1) and Equation (2).

$$M_{I0} = C_A * V_I * C_{I0} \quad (1)$$

$$M_{E0} = C_{E0} * V_I \quad (2)$$

where C_A is the count of algal cells in intake water (cells/L), V_I is the intake volume, C_{I0} and C_{E0} is the intracellular toxin per cell (pg/cell) and extracellular toxin per liter (μg/L), respectively.

Following the intake into the desalination facility, conventional coagulation treatment is considered for each process train with no sedimentation; consequently, no mass of toxin is removed during this step. Treatment trains without the coagulation step were also used for comparison (Figure 7). In addition, comparisons were made for trains with and without DAF before treatment options of: pressurized microfiltration/ultrafiltration (MF/UF), submerged MF/UF (vacuum), gravity granular media filtration (GMF), and pressurized GMF. The volumetric inflow and backwash for each pretreatment process in the pMFA are detailed in Appendix A, Section 1.

For each pretreatment process a range of toxin removal efficiencies (transfer coefficients) were specified. These parameters included: (a) removal of intracellular toxins within intact cells during pretreatment processes (K_1); (b) removal of dissolved toxins during pretreatment processes (K_2); and (c) removal of dissolved toxins across the RO membrane (K_3). An additional model parameter was specified to account for the release of intracellular toxin to dissolved toxin as a result of algal cell breakage during each pretreatment process (K_B).

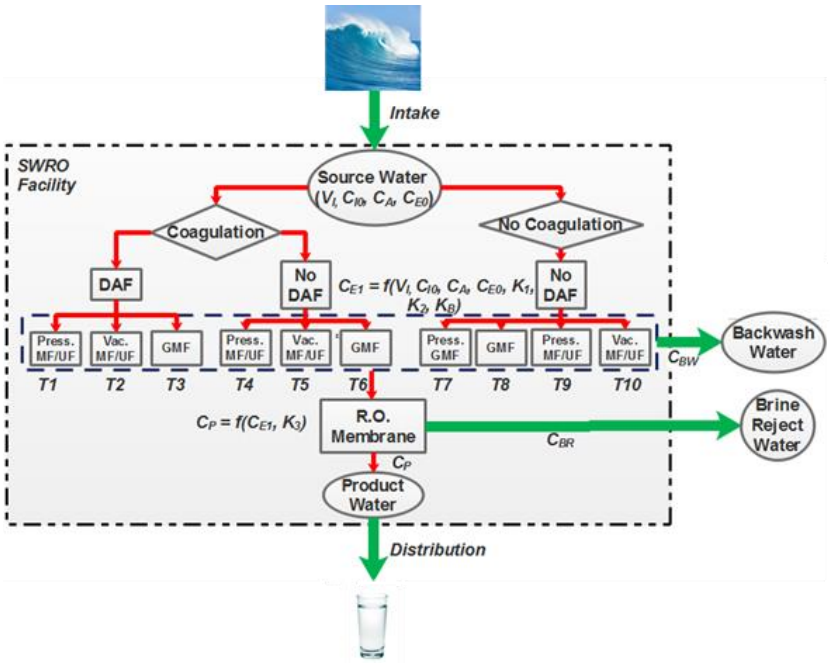

Figure 7. *Conceptual pMFA diagram for the full-scale SWRO desalination facility. The boundaries of the SWRO facility are indicated by the dashed black line, while pretreatment unit processes trains (T1-T10) are grouped by the dashed blue line. The arrows indicate toxin mass flow rates expressed in µg/day, simplifying to a mass of toxin (in µg) on the timescale of one day. The red arrows specify mass flows within the desalination facility control volume, whereas the green arrows indicate mass flows of toxins out of the control volume.*

The core calculations of the pMFA for the combined pretreatment and RO membrane processes included three main steps. First, the mass of intracellular toxin in intact algal cells (MNB, µg) and that released (MB, µg) due to the cell breakage fraction, KB, were determined (Equations (3) and (4)).

$$M_{NB} = (M_{I0} - K_B * M_{I0}) \quad (3)$$

$$M_B = (1 - M_{NB}) \quad (4)$$

Next, the dissolved toxin concentration (C_{E1}, µg/L) and backwash toxin concentration (C_{BW}, µg/L) after treatment by a given unit treatment process were calculated using the dissolved toxin (K_1) and cellular toxin (K_2) removal coefficients and the volume of intake water (V_I, L) and backwash water (V_{BW}) (Equations (5) and (6)).

$$C_{E1} = \frac{(M_{E0} - (K_1 * M_{E0}) + M_B) + (M_{NB} - K_2 * (M_{NB}))}{V_I} \quad (5)$$

$$C_{BW} = \frac{(K_1 * M_{E0}) + (K_2 * M_{NB})}{V_{BW}} \quad (6)$$

Finally, the concentration of dissolved toxin in the RO permeate water (C_p, µg/L) and RO brine water rejects (C_{BR}, µg/L) were calculated considering the removal efficiency across the RO membrane (K_3), the volume of permeate water (V_p, L) and brine/reject water (V_{BR}, L) (Equations (7) and (8)). The mass of extracellular toxin entering final RO treatment (M_{E1}, µg) was calculated assuming that all intact cells remaining (M_{NB}, µg) were ruptured due to the high-pressure RO membrane process.

$$C_p = \frac{(M_{E1} - K_3 * M_{E1})}{V_p} \quad (7)$$

$$C_{BR} = \frac{(K_3 * M_{E1})}{V_{BR}} \quad (8)$$

Several assumptions were included to reduce the model complexity: (1) no biological removal mechanisms were involved due to the lack of published information and the complexity of predicting removal; (2) toxins were dissolved into solution upon cell breakage; and (3) no generation or storage mechanisms for any treatment train processes were considered—flow that entered each treatment process had to leave either in the backwash/concentrate waters or water flowing through the RO membrane.

2.2. Algal and Toxins Concentrations

Algal bloom data at the Santa Monica Pier were taken from the Southern California Coastal Ocean Observing System (SCCOOS, http://www.sccoos.org/), which reports common bloom formers including *Akashiwo sanguinea*, *Alexandrium species*, *Dinophysis* species, *Prorocentrum* species, *Lingulodinium polyedrum*, *Pseudo-nitzschia* species, *Cochlodinium* species, and *Phaeocystis* species. It is important to note that the *Pseudo-*

nitzschia cell abundance data included in the SCCOOS database is not currently identified down to the species level (Seubert et al. 2013). Instead, cell abundance is classified into two different size fractions by light microscopy: the *Pseudo-nitzschia delicatissima* class (frustule widths >3 μm) and the *Pseudo-nitzschia seriata* class (frustule widths <3 μm) (Seubert et al. 2013). Of these genera listed, only some species of *Alexandrium* (producer of saxitoxin, STX), *Dinophysis* (producer of okadaic acid, OA), *Lingolidinium polyedrum* (producer of yessotoxin, YTX), and *Pseudo-nitzschia* (producer of domoic acid, DA) produce toxins (Caron et al. 2010). Therefore, only DA, STX, OA, and YTX were included in the pMFA. The toxic effects of each toxin are described in Appendix A, Section 2.

SCCOOS data from a three-year period (2012–2015) were first used to create an overview of the frequency and severity of blooms in the region, similar to the time-period specified by Seubert and co-workers (2013) (Figure A1). To simplify the pMFA analysis, we did not separate bloom periods into either major or minor events as previously described (Seubert et al. 2013, Allen et al. 2008, Kim et al. 2009). Instead, a constant chlorophyll-a threshold using the overall mean of the 3-year data (~12 μg/L) was incorporated to identify significant events (comparable to the definition for minor blooms in Allen et al. (2008)). From this analysis, eight significant bloom events were identified (chlorophyll-a >12 μg/L). DA producing species exhibited the highest cell abundance and variation over each of the eight bloom periods (Table 1), confirming blooms off Southern California were greatly dominated by *Pseudo-nitzschia sp.* (Caron et al. 2010, Schnetzer et al. 2007). STX (*Alexandrium*) and YTX (*L. polyedrum*) producing species were the least abundant and variable in cell numbers during the bloom periods (Table 1 and Figure A2).

The statistical distributions of cell concentrations from the bloom periods appeared to be nonparametric (after excluding 0 and non-detects), with higher frequency of observations at the lower range in cell concentrations (see Appendix A, Figure A3). Therefore, to adequately predict cell concentrations in pMFA simulations, an inverse empirical concentration distribution function (ECDF) was developed relating the probability of occurrence (x-axis) versus the concentration (log10) of species observed from field data (see Appendix A, Figure A4). To account for the probability of non-detects, a uniform random number generator between 0 and 1 was first used. The selection was then sent to sample the corresponding cell concentration from the interpolated, inverse ECDF.

In comparison with algal cell concentrations, data on dissolved toxin concentrations surrounding Santa Monica Pier was sparse. Limited dissolved toxin concentrations (DA, STX) reported at the intake of a Southern and Central California SWRO pilot facilities (Seubert et al. 2012, Meyerhofer et al. 2010) indicated lower (0–10 μg/L) ranges than those observed in coastal and inland marine or estuarine environments (0–150 μg/L) (Allen et al. 2008, Kim et al. 2009, Schnetzer et al. 2007). These data were perhaps not collected during a substantial algal bloom. Thus, coastal and inland marine measurements (Trainer et al. 2007, Bargu et al. 2008, Lefebvre et al. 2008) collected off the west coast of the continental U.S. were considered more representative of severe HAB scenarios and were used in this analysis (Table 1). However, dissolved toxin concentrations for OA and YTX were compiled from work by Mackenzie and co-workers (2004), which were collected off the coast of New Zealand (Table 1).

Table 1 *- Concentration of dissolved marine toxins, toxin producing algal cells and intracellular toxin per cell used in the pMFA simulations.*

Environmental Variable	Distribution	Unit	Specified Range or Value	Mean	SD	Reference
Dissolved toxins						
DA	Uniform	µg/L	60–135.6	-	-	(Trainer et al. 2007, Bargu et al. 2008)
STX	Uniform	µg/L	0.150–0.800	-	-	(Lefebvre et al. 2008)
OA	Uniform	µg/L	1.31–4.67	-	-	(MacKenzie et al. 2004)
YTX	Uniform	µg/L	23.7–126	-	-	(MacKenzie et al. 2004)
Algal cell conc.[1]						
Alexandrium sp.	ECDF	cells/L	374–748	524	205	
Dinophysis sp.	ECDF	cells/L	123–3886	1112	1120	
L. polyedrum	ECDF	cells/L	374–748	481	183	
Pseudo-nitzschia delicatissima	ECDF	cells/L	374–48,578	15,170	35,896	
Pseudo-nitzschia seriata	ECDF	cells/L	374–563,500	22,280	92,575	
Intracellular toxin conc.						
Alexandrium sp.	Uniform	pg/cell	57.9	-	-	(Jester et al. 2009b)
Dinophysis sp.	Uniform	pg/cell	2.7	-	-	(MacKenzie et al. 2005)
L. polyedrum [2]	Uniform	pg/cell	0.005	-	-	(Howard et al. 2008)
Pseudo-nitzschia delicatissima	Uniform	pg/cell	117	-	-	(Schnetzer et al. 2007)
Pseudo-nitzschia seriata	Uniform	pg/cell	117	-	-	(Schnetzer et al. 2007)

[1] All algal cell concentrations were retrieved from SCCOOS Database; [2] This value was collected from laboratory-grown cells.

Only dissolved concentrations obtained by grab sampling as opposed to passive sampling methods (SPATT) were included in this analysis given that it is not currently possible to directly compare or extrapolate SPATT measurements (µg/g resin) to ambient concentrations (µg/L). SPATT integrates sampling both spatially and temporally and, in many cases, has been evidenced to be more sensitive than grab sampling methods (Kudela et al. 2015, Lane et al. 2010). Although adsorption profiles and extraction efficiencies of these toxins (DA, STX) to/from SPATT resins have been extensively studied and verified in the laboratory setting, this knowledge is not applicable to uncontrolled conditions in the field setting, leading to instances of moderate variability in replicate field measurements

(coefficients of variation (COV) 15–37%) (Lane et al. 2010). This observed variability in SPATT measurements further supports reliance on grab measurements reported from field studies, where COV for replicate measurements are <10% for ELISA kits (per manufacturer instructions, ABRAXIS, Warminster, PA, USA). Uniform probability distributions were used in the modeling effort due to the lack of published information reporting dissolved toxin concentrations (Table 1).

The intracellular toxin concentrations reported from most field and laboratory studies were highly variable in the scientific literature (Schnetzer et al. 2007, Jester et al. 2009b, MacKenzie et al. 2005). Intracellular toxin concentrations of DA as determined from laboratory cultures of *Pseudo-nitzschia* species, for example, were observed to vary over 9 orders of magnitude (Trainer et al. 2012). Field reported values of intracellular toxin concentrations were less common and were also highly variable due to different physical, chemical, and biological factors influencing bloom dynamics in field settings (see Granelli and Turner (2006) for additional information). Due to the lack of understanding of the intracellular concentration of most species (which likely varies with environmental conditions, the phase of the algal bloom, etc.), the highest reported intracellular concentration from field reports was used as the model input to represent a worst-case scenario (Table 1). A deterministic value of intracellular toxin concentration was further used to continue with the conservative, worst-case scenario approach. In the absence of field studies, YTX intracellular toxin concentrations were obtained from a laboratory study of *L. polyedrum* isolated from coastal Southern California waters (Howard et al. 2008).

2.3. Intracellular and Dissolved Toxin Removal Efficiencies

The removal efficiency of intracellular toxin was directly related to the removal of toxin producing algal cells during each pretreatment process. Algal cell removals through GMF systems were compiled based on pilot or full-scale SWRO studies reported in the literature (Table 2) (Meyerhofer et al. 2010, Leparc et al. 2007, Bar-Zeev et al. 2009, Sabiri et al. 2012, Remize et al. 2009, Bar-Zeev et al. 2012, Bar-Zeev et al. 2013, Plantier et al. 2013, Guastalli et al. 2013). A pooled mean and standard deviation of algal cell removal for GMF systems with and without coagulation was calculated and fitted to a normal probability distribution (Table 2). However, a uniform probability distribution was used for predicting cell removal in pressurized GMF systems due to the lack of data in the published literature (Table 2).

For MF/UF systems, the range in algal cell removal efficiencies was also summarized from pilot and full-scale SWRO plant studies [38, 43 –46]. Uniform probability distributions were used in the pMFA model for MF/UF systems considering the small number of reported observations from the literature (Table 2).

Table 2 *- Intracellular and dissolved toxin removal efficiencies used in the pMFA simulations*

Treatment Trains	Specified Range	Reference
Cell Removal		
GMF *With* Coagulation	79–93% [1]	(Bar-Zeev et al. 2009, Remize et al. 2009, Bar-Zeev et al. 2013)
GMF *Without* Coagulation	48–98% [1]	(Sabiri et al. 2012, Bar-Zeev et al. 2012, Plantier et al. 2013)
GMF *Pressurized*	74–99.2%	(Meyerhofer et al. 2010, Leparc et al. 2007, Guastalli et al. 2013)
MF/UF *With* Coagulation	99–99.9%	(Meyerhofer et al. 2010, Guastalli et al. 2013)
MF/UF *Without* Coagulation	95–100%	(Remize et al. 2009, Campinas and Rosa 2010, Castaing et al. 2011, Frappart et al. 2011, Zhang et al. 2011a)
DAF	43–93%	(Guastalli et al. 2013, Kim et al. 2011, Zhu et al. 2014)
RO	-	-
Algal Cell Breakage [2]		
GMF *With* Coagulation	0–10%	This study

GMF *Without* Coagulation	0–25%	This study
GMF *Pressurized*	75–100%	This study
MF/UF *With* Coagulation	75–100% (pressure driven); 15–35% (submerged)	This study
MF/UF *Without* Coagulation	50–100% (pressure driven); 15–35% (submerged)	This study
DAF	-	-
RO	-	-
Dissolved toxin removal [3]		
GMF *With* Coagulation	0–34%	This study
GMF *Without* Coagulation	26–50%	This study
GMF *Pressurized*	6.6–40%	This study
MF/UF *With* Coagulation	24.7–76.7%	This study
MF/UF *Without* Coagulation	3–32.7%	This study
DAF	-	-
RO	99.4–99.9%	(Laycock et al. 2012, Seubert et al. 2012, Meyerhofer et al. 2010)

[1] The mean and standard deviation are 86% and 11%, respectively for cell removal by GMF with coagulation; and are 72% and 21%, respectively for cell removal by GMF without coagulation. The mean and deviation were not calculated for the remaining parameters in the table due to limited data availability; [2]Estimated based on transmembrane pressure used in each pretreatment process (see Appendix A, Section 3.6 for details); [3]Estimated based on toxin physical-chemical properties and reference toxin removal rates (see Appendix A, Sections 3.1–3.4 for details).

DAF algal cell removals were obtained from reports of a mixture of laboratory, pilot, and full-scale experiments (Guastalli et al. 2013, Kim et al. 2011, Zhu et al. 2014). The reported range in algal cell removal efficiencies ranged between 43–93%, likely due to the variations in algal cells encountered and doses/types of coagulants used (Table 2). Again, uniform probability distributions were used in the pMFA model for predicting algal cell removals in DAF systems.

An important consideration during pretreatment for cell removal is algal cell breakage that transforms intracellular toxins into dissolved toxins. The magnitude of the ranges in algal cell breakage was developed according to Voutchkov (2010) (see Appendix A, Section 3.6) and differed for each pretreatment process (Table 2). The wide ranges in cell breakage used here reflect the expected variability in breakage among different species and groups (diatoms versus dinoflagellates) of marine microalgae. However, the increments of the ranges (set to quartiles, i.e. 25–50%, 75–100%) were relatively similar for different

treatment processes as a conservative factor in all pMFA simulations. Since DAF processes use air bubbles to float the algal cells to the surface, no algal cell breakage was expected. In addition, due to the small molecular size, water solubility, and polarity of the toxins, little to no removal of dissolved toxins was expected in the DAF process.

An extensive literature search indicated a lack of data on the dissolved marine algal toxin removal rates through SWRO pretreatment trains. However, removal efficiencies of dissolved microcystin-LR (MC-LR) toxins produced by cyanobacteria that impact drinking water safety have been reported in both GMF and MF/UF processes. Therefore, the removal efficiencies of each targeted marine algal toxin were estimated based on a comparison of the physical-chemical properties (including size, structure, polarity and charge) of each with those of MC-LR (Table 2) (see Appendix A, Section 3 and Tables A6–A8 for additional validation). Uniform probability distributions sampled the range of dissolved toxin removal efficiencies in both GMF and MF/UF processes.

Dissolved marine algal toxins rejection rates by the RO membrane have been reported by Laycock and co-workers (2012) and Seubert and co-workers (2012) in laboratory and pilot scale studies. The removal efficiencies for RO ranged from 99.0 to >99.9% for all toxins studied (Table 2) (see Appendix A, Section 3.5 and Table A9 for additional validation). It is important to note that 100% removal was not assumed in this study as the analytical detection limits ranged from 0.1, 0.2–0.5, to 0.02 (μg/L) for OA, DA, and STX, respectively. Thus, the analytical methods used in these studies were not able to detect trace masses of these toxins in the sub-micron to nanogram range or lower (Laycock et al. 2012, Seubert et al. 2012). Uniform probability distributions were used to sample the range of dissolved toxin removals across the RO membranes.

2.4. pMFA Simulation Algorithm

A Monte Carlo based simulation method was the main approach for the pMFA using 10,000 iterations per run to achieve statistical rigor (Finley and Paustenbach 1994). The algorithm developed to run the simulations was based on the following procedure using MATLAB (*Mathworks* Inc. , Natick, MA, USA, r2015b): (1) randomly sample the system input of toxins (intracellular and dissolved), toxin removal and generation (from cell breakage) efficiency of each treatment processes from the prior initial distribution; (2) run the pMFA model using this unique combination of toxin input and plant operation efficiency; (3) store the output concentration of toxins in the permeate water and backwash/brine water; (4) repeat this process using a different draw of initial toxin input and operation efficiency from the prior distribution until the number of iterations had been reached.

2.5. Statistical and Sensitivity Analysis

A one-way analysis of variance (ANOVA) was conducted to assess the statistical significance of the results from the pMFA simulations for toxin concentration distributions (TCDs) in both the permeate and combined backwash/brine water. The one-way ANOVA specifically tested the hypothesis of whether the means of the resulting posterior probability distributions were equal (assuming the TCDs were normally distributed). A Tukey honestly significant difference post hoc analysis method was further incorporated to assess the statistical significance of the data (for significant ANOVA outcomes only) by comparing individual means of toxin concentration from different pretreatment trains using variables from the ANOVA output.

A sensitivity analysis was conducted to determine which environmental inputs and treatment efficiencies were the most influential contributors to the predicted posterior TCDs, both in the permeate and backwash/brine waters. The sensitivity analysis was separated into two categories: (a) the sensitivity of the pMFA simulations related to the environmental inputs and (b) the sensitivity of the model related to the treatment efficiencies (Gottschalk et al. 2010a, 2010b, Finley and Paustenbach 1994, Norton 2008). The rank of importance was developed for both environmental input and treatment efficiency to assess the confidence in the model through comparison of sensitivity and relative order of uncertainty (Gottschalk et al. 2010a, 2010b). The sensitivity of the posterior toxin distribution related to each removal efficiency or environmental input was calculated using Equation (9) (Gottschalk et al. 2010a, 2010b).

$$S = \left[\frac{\frac{\Delta X_{mean}}{X_{mean}}}{\frac{\Delta P_{mean}}{P_{mean}}}\right] * \sigma \qquad (9)$$

S is the sensitivity value (unitless), σ is the standard deviation of original environmental input or removal efficiency values, X_{mean} is the mean of the posterior toxin distribution in the permeate waters using the original values, ΔX_{mean} is the difference in means between the original posterior distribution and the changed posterior distribution, P_{mean} is the mean of the original prior data probability distribution, and ΔP_{mean} is the difference in means between the original prior probability distribution and the changed prior probability distribution.

2.6. Determination of Human Health Risks from Marine Algal Toxins

A quantitative chemical risk assessment was conducted by incorporating the predicted concentrations of algal toxins remaining in permeate waters following U.S.

Environmental Protection Agency (EPA) guidelines (Fowle and Dearfield 2000). Human exposure to the algal toxin through ingestion of desalinated water was evaluated through daily intake rate established by U.S. EPA guidelines (Fowle and Dearfield 2000).

Since all of the target toxins display acute toxicity in humans, a thresholding effect based on acute reference doses (RfD) was used. Although RfDs have been established for shellfish by the U. S. Food & Drug Administration and European Food Safety Administration (EFSA), the relevance of these doses may not carry equal weight when applying them to drinking water exposure scenarios. For drinking water purposes, we re-analyzed the RfDs for shellfish consumption, assuming the same LOAEL (lowest observed adverse effect level) or NOAEL (no observed adverse effect level) and uncertainty factors widely used in the shellfish RfD calculations by the EFSA (Paredes et al. 2011) (see Appendix A, Section 4 for a complete derivation of RfD values).

From the estimated RfDs, an acceptable level (AL, also known as a maximum contaminant level goal) of each toxin in drinking water was calculated using the RfD, body weight (BW, 70 kg), relative source contribution (RSC), and drinking water intake rate (IR, 2 L/day) (Equation (10), (Cotruvo 1988, Donohue and Zavaleta 2003)). A complete derivation of AL values can be found in Appendix A (Section 4).

$$AL = \frac{RfD * BW * RSC}{IR} \tag{10}$$

The RSC represents the relative expected contribution of exposure from drinking water compared to other potential routes of exposure, in which the recommended range is between 0.2 and 0.8 (Howd et al. 2004). For this study, we chose a conservative value of 0.5 to equally account for other potential routes of exposure other than drinking water such as ingestion of algal toxins in shellfish or fish.

A quantitative estimate of the relative risk of acute human illness was further evaluated using a calculated margin of safety (MO) (AL normalized by the concentration of algal toxin predicted in the permeate water) (Cotruvo et al. 2011, Trussell et al. 2012). A range in MOs was calculated using one standard deviation confidence intervals of the mean toxin concentration in the permeate water. MOs greater than 1 indicated that the relative risk was low, where higher MOs (>1000) suggested that the relative risk was minimal to none (Cotruvo et al. 2011, Trussell et al. 2012).

3. Results

3.1. Comparison of Algal Toxin Removal Efficiencies

The pMFA model outputs indicated TCDs followed normal probability distribution in RO permeates for all pretreatment train configurations. STX concentration distributions were shown as representations for all other toxins (Figure 8). These normal probability TCDs were the basis of comparison for the removal efficiency of various pretreatment configurations.

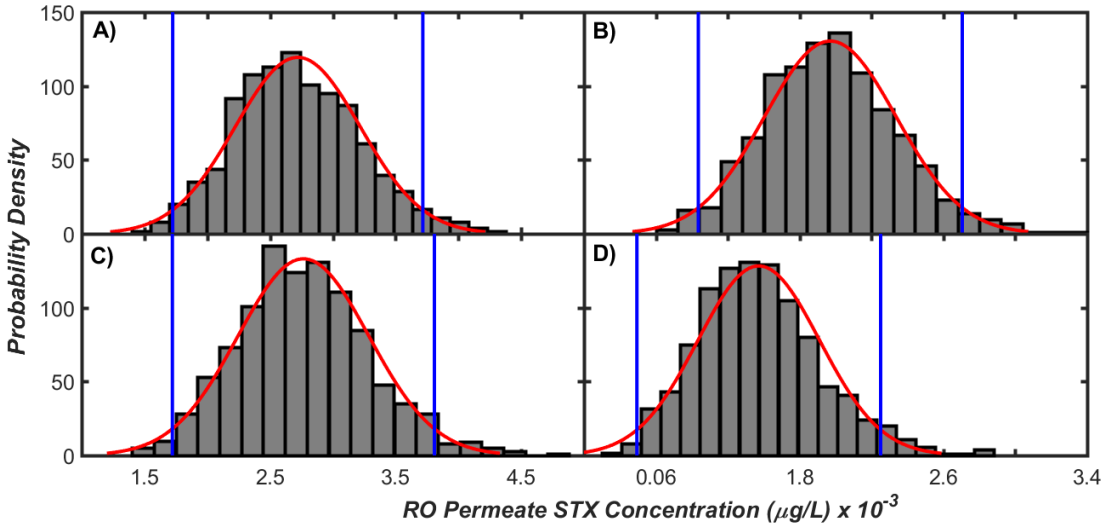

Figure 8. *STX toxin concentrations in the RO permeate for: (a) GMF processes without coagulation (T8), (b) Pressurized MF/UF processes without coagulation (T9), (c) GMF processes with coagulation (T6), and (d) Pressurized MF/UF processes with coagulation (T4).*

The pMFA results demonstrated that a low, but detectable quantity, of algal toxins was present in the permeate water, despite 99.0–99.9% removal across the RO membranes. Concentrations of DA in the permeate were the most significant out of all algal toxins, ranging from 0.5 to 2.8 µg/L, whereas concentrations of STX were considerably lower (1–5 ng/L) (Figure 9). Despite the differences in concentrations observed, the risk of acute intoxication from STX is comparable in magnitude to DA due to the dramatic difference in toxicities of each compound (which are further discussed in Section 3.3).

In general, MF/UF pretreatment processes with coagulation/DAF outperformed the toxin removal by GMF processes, with mean toxin removal efficiencies ranging from 47 to 57% (Figure 9). This performance depended on whether the MF/UF pretreatment processes included coagulation practices as coagulation greatly improved the toxin removal for all GMF pretreatment trains (Figure 9).

Treatment processes without coagulation (for both MF/UF and GMF) demonstrated relatively large treatment variability, as noted by the large interquartile ranges and increased number of outliers from these results (Figure 9). Again, reliable treatment performances (represented by low statistical variability) were observed for both MF/UF and GMF systems with coagulation (Figure 9).

Submerged MF/UF systems demonstrated a slightly improved treatment performance as compared to pressurized MF/UF systems when comparing the means of the TCDs in the permeate water. The treatment variability of both processes, however, was equivalent and overlapping (Figure 9). Similarly, adding a DAF process for most MF/UF systems was redundant, as the treatment performance and variability for MF/UF systems with and without DAF (with coagulation) were nearly identical for all toxin types.

The concentrations of each algal toxin in the combined backwash/brine waters were higher in magnitude than those observed in both the inlet and permeate waters (Figure 9). Similar to the permeate water, DA concentrations in the backwash/brine waters were the highest in magnitude among all toxin types, ranging from 400 to 1200 μg/L (0.4 to 1.2 mg/L), followed by YTX with concentrations ranging from 100 to 550 μg/L. OA and STX concentrations in the backwash/brine waters were much lower in magnitude for all pretreatment process, ranging from 5 to 20 μg/L and 1 to 7 μg/L, respectively. The range in toxin concentration of the combined brine/backwash waters increased considerably (at least 2 to 10 times more concentrated) compared to the inlet range in toxin concentration, which greatly depended on the treatment train configuration (see Appendix A, Figures A8 and A9).

The reduction in toxicity of the permeate waters for both GMF/MF/UF treatment processes employing coagulation corresponded to an appreciable increase in toxicity of the backwash/brine waters (Figure 9). Submerged vacuum MF/UF systems (with and without coagulation/DAF) resulted in the lowest magnitude of TCDs in the backwash/brine waters for all toxin types, followed by pressurized MF/UF and GMF systems (Figure 9). Similar to the observation for permeate waters, the inclusion of a DAF system had a negligible effect on TCDs in the combined backwash/brine waters (Figure 9).

The variability of the TCDs in the backwash/brine waters was slightly lower for GMF systems employing coagulation compared to systems without coagulation, slightly higher for pressurized MF/UF systems (with and without coagulation), and relatively unchanged for vacuum MF/UF systems (with and without coagulation) (Figure 9). These trends were summarized using all toxin types by examining absolute changes in COV

values. In addition, these trends described above were apparent when comparing the interquartile ranges (IQRs) for OA and YTX toxins among the treatment configurations for pressurized and vacuum MF/UF systems, and the IQRs for STX among configurations for GMF systems with and without coagulation (Figure 9, Panels B vs. C). The variation for STX toxins in the backwash/brine waters was high under pressurized GMF systems (T7, Figure 9). Additional results of algal TCDs, toxin concentration factors in backwash and brine reject are presented in Appendix A, Sections 5.1–5.3 and in Figures A8–A10.

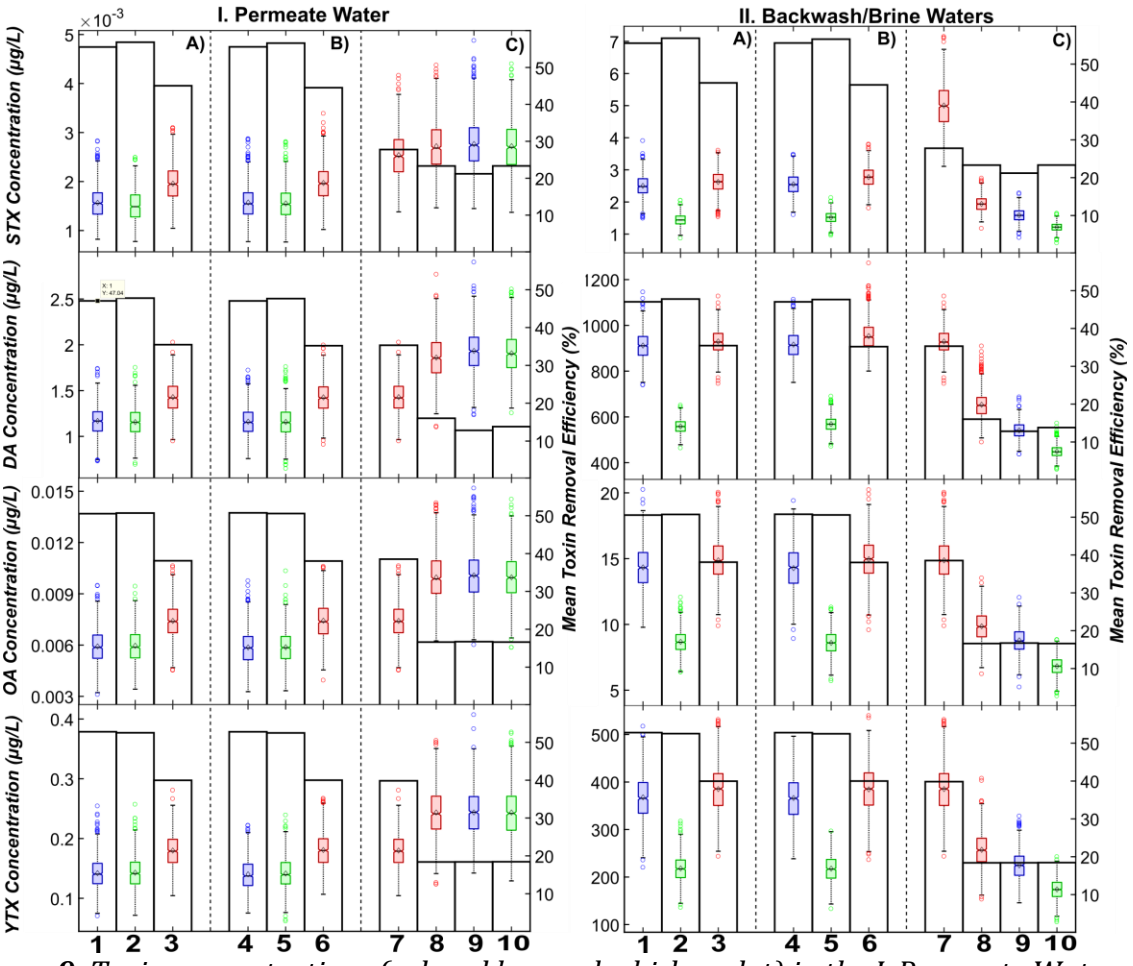

Figure 9. *Toxin concentrations (colored box and whisker plot) in the I. Permeate Water and II. Backwash/Brine Waters for all treatment trains (labeled 1–10 for train T1–T10). Results are grouped into trains employing (A) DAF, (B) Coagulation, and (C) No Coagulation. Blue, green and red colors represent trains including pressurized MF/UF, vacuum MF/UF, and GMF treatment processes, respectively. The secondary y-axis portrays the mean toxin removal efficiency (shown as open bars) predicted for each treatment train.*

The one-way ANOVA demonstrated an overall significant difference in the means of the TCDs in the permeate water resulting from 10 pretreatment train configurations (overall $p < 0.05$). Similarly, the TCDs in the backwash/brine water from 10 treatment processes were all significantly different (overall $p < 0.05$). The overall results for the one-way ANOVA were equivalent for all toxin types (STX, DA, OA, YTX) for both the permeate and backwash/brine waters.

Varying results were obtained for the comparison of individual TCDs in the permeate and backwash/brine waters from different pretreatment processes (p values ranged from <0.05 to 1) (Figure 10). Significant differences were identified when comparing treatment trains with and without coagulation ($p < 0.05$), and trains of no-coagulation vs. those with DAF systems ($p < 0.05$). However, for all processes and most toxins, there was generally not a significant difference in TCDs from processes employing coagulation vs. DAF systems (average $p > 0.1$) (Figure 10).

Significant differences were also identified when comparing across all GMF vs. MF/UF trains ($p < 0.05$) (Figure 10). However, the comparison across all pressurized vs. vacuum driven MF/UF systems did not yield statistically significant outcomes ($p > 0.1$) for most toxins. A "within" treatment comparison of trains employing GMF (i.e. T3 vs. T6 vs. T7 vs. T8), or pressurized MF/UF (T1 vs. T4, vs. T9), or vacuum driven MF/UF (T2 vs. T5 vs. T10) revealed a large variability of p values, with values mostly below the 0.05 statistically significant threshold (Figure 10). The p values for all the pairwise comparisons are presented in Appendix A as well as a complementary figure summarizing the Tukey post hoc comparison tests for the backwash/brine waters (Section 6, Table A11, Figure A11).

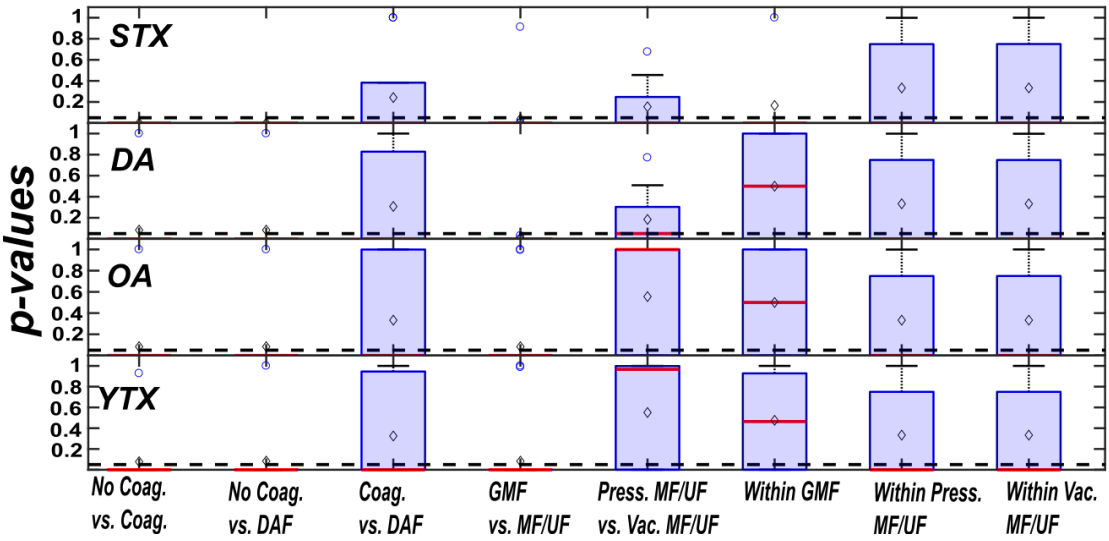

Figure 10. *Box and whisker plots of p-values summarizing the Tukey post hoc comparison tests for the permeate waters categorized by each toxin (i.e. STX, DA, OA, YTX). The black dashed lines illustrate the significance level (0.05), while the red lines and black diamonds indicate the median and mean of p-values for each group, respectively. Open circles represent outlying p-values from each comparison group.*

3.2. Sensitivity Analysis

Of the model inputs included in the pMFA, the output TCDs were most sensitive to the input algal cell concentration and far less sensitive to the dissolved toxin concentration and intracellular toxin concentration per algal cell (Figure 11A). Dissolved YTXs was the only examined toxin contributing to a noticeable fraction of model sensitivity, ranging from 12 to 14% of the model outcomes (Figure 11A). The most sensitive parameters for toxin removal efficiency varied according to the pretreatment configuration (Figure 11B). Algal cell removal efficiencies were more sensitive parameters for GMF (T3, T6, T7, T8) processes as compared to MF/UF (T1, T2, T4, T5, T9, T10) processes. Contrarily, the resulting TCDs from MF/UF processes were largely affected by the dissolved toxin removal and algal cell breakage parameters over all other removal efficiency parameters for all toxin types (Figure 11B).

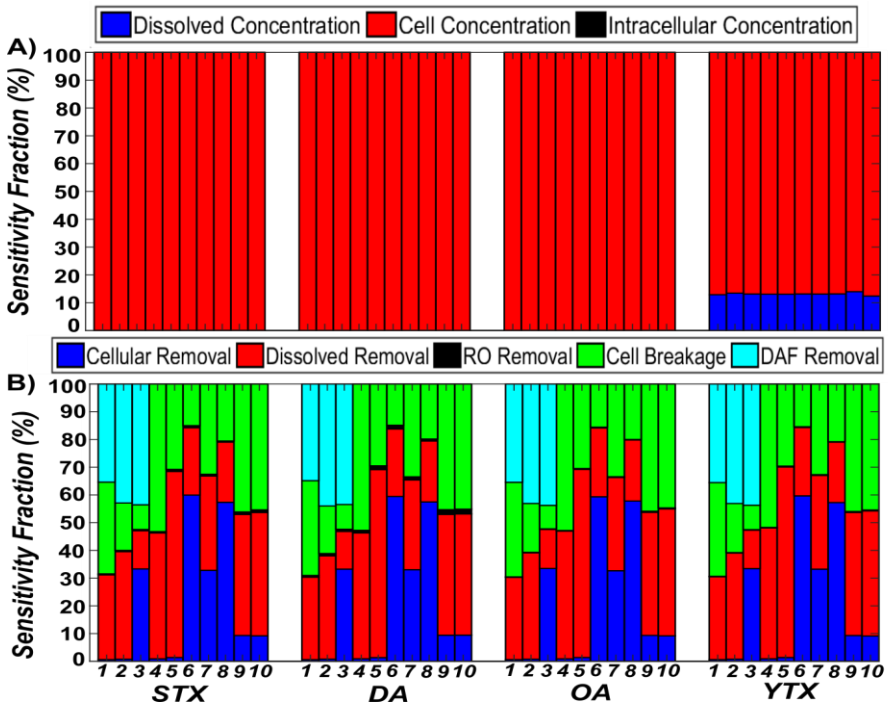

Figure 11. *Sensitivity fractions of (A) model inputs, and (B) removal efficiency parameters as a function of algal toxin type and pretreatment processes (labeled as 1–10 for treatment train T1–T10).*

3.3. Acute Human Health Risks

Acute human health risks were assessed by comparing the calculated AL in drinking water to cumulative probability distributions (CDF) of effluent toxin concentrations in the permeate water. The ALs for STX, DA, OA, and YTX in drinking water were 3.32, 525, 1.40, and 292 µg/L, respectively. The simulation results proved that the simulated CDF would never exceed the prescribed AL threshold, based on the acute RfD (Figure 12). The tight confidence intervals for these CDF estimates indicated that the certainty in these estimates was high (data not shown). Therefore, the pMFA results demonstrated that the human health risk from ingesting permeate water during algal bloom periods was minimal to none, with greater than 95% certainty. This conclusion is confirmed when comparing the tabulated MO values for each pretreatment process (Figure 12A). All of the MO values are

above 1, indicating that there was minimal risk present when consuming permeate water during algal bloom periods (Figure 12A).

The low magnitude of the MO for OA toxins, however, showed that OA toxins contribute most to the drinking water risk during bloom periods in Southern California, followed by DA, YTX, and STX, respectively (Figure 12). This result may seem counterintuitive at first given that the DA toxin loading to the facility is the highest out of all algal toxins and is the most sparingly removed toxin during pretreatment and across the RO membranes. However, a much lower acute RfD (about four orders of magnitude) and AL in the permeate water were estimated for OA as compared to DA. Comparably, the difference in permeate toxin concentrations predicted by the pMFA simulation were only about 2 orders of magnitude different. Therefore, due to the larger difference in acute RfD values between the toxins, the acute RfD was the most influential parameter affecting risk calculations, resulting in a higher risk for toxins that are less prevalent in Southern California's coastal waters.

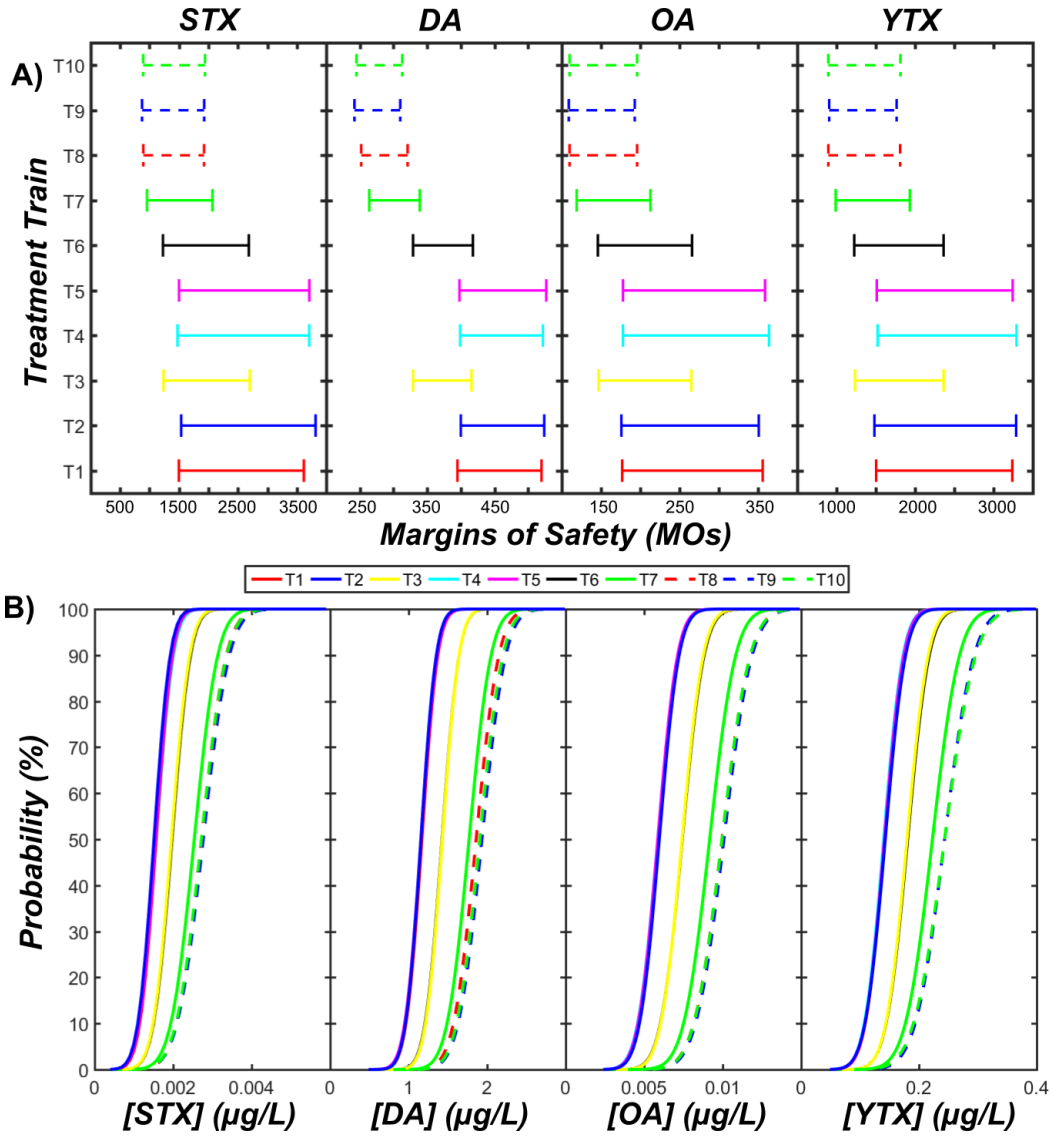

Figure 12. *Summary of (A) margins of safety (MOs) for various algal toxins in the permeate water and (B) cumulative probability distributions of toxin concentrations in the permeate water.*

4. Discussion

4.1. Contribution of the Study

This study is the first attempt to estimate marine algal toxin concentrations in the permeate water and combined brine/backwash waters from a full-scale SWRO facility. The removal of algal toxins in full-scale pretreatment systems is important because desalination plant managers and designers can directly benefit from reduced toxin loadings

to the RO membranes. Since complete (100%) removal of algal toxins by RO treatment is rarely achieved in full-scale practice, reduction of the toxin loadings reaching the RO membranes can significantly decrease the toxin concentrations in the permeate water and the associated human health risks. To illustrate this point, we compare the operation of a hypothetical situation where a "baseline" pretreatment system is not optimized for toxin removal against the performance of an "optimal" pretreatment configuration presented herein. For the baseline system, if we considered minimal to no removal of DA during pretreatment and 99% RO removal efficiency, a concentration of 200 μg/L of DA in the inlet would result in 2 μg/L in the permeate, which translates to an MO of 263. If, however, we assumed an optimal pretreatment system removing 57% DA before reaching the RO membrane, the new MO (610), or the risk of acute illness from ingesting produced water, would be reduced by a factor of approximately 2.

Another potential benefit of optimizing pretreatment practices for marine biotoxin removal is to avoid toxin breakthrough across the RO membrane due to changes in the RO toxin removal efficiency over time. In full-scale practice, it is likely that the RO toxin removal efficiency will vary over the course of operation due to changes in RO membrane properties and feed water composition. For example, formation of a fouling layer on the surface of RO membranes during operation may alter toxin transport, especially for the small molecular weight and polar (more hydrophilic) toxins DA and STX (Xu et al. 2006, Ng, and Elimelech 2004, Verliefde et al. 2009). Cake enhanced concentration polarization, charge interactions, or other mechanisms may lead to increased or decreased rejection of these toxins, depending on the concentration of the toxins in the feed water, the physico-chemical characteristics of the toxins, the membrane (i.e. pore size, hydrophobicity, etc.), as

well as the extent and type of membrane fouling (Verliefde et al. 2009). In addition, high concentrations of these toxins on the RO membrane surface may serve as exogenous carbon and nutrient sources for bacteria escaping pretreatment processes, potentially intensifying the biofouling potential of the RO membranes (Stewart et al. 1998).

Although the primary purpose of SWRO pretreatment is to remove excess turbidity, TSS, microorganisms and TOC for RO membrane fouling protection, this study has demonstrated that the SWRO pretreatment selection, design, and operation can have a significant impact on the removal of algal biotoxins. STX, DA, OA, and YTX removal efficiencies were subject to variation, ranging from 15 to 57% for all algal toxins and pretreatment processes. The predicted removal efficiencies (up to 57%) accounted for nearly one quarter to one half of the overall removal of algal biotoxins, where the other three quarters to one half of removal can be accounted for by the RO membranes. The fraction of toxin removal predicted by the pMFA during pretreatment was higher than initially expected, especially for pretreatment processes not designed to target the removal of these toxins. These results suggest that modifications to the operations of SWRO pretreatment processes, rather than the design, could have the most pragmatic and far-reaching impacts on biotoxin removal. Amendments to plant operations, such as coagulant addition, would not hinder but provide additional benefits other than toxin removal, such as removal of TSS, other colloidal particles, and dissolved organic matter. The most significant proof to this supposition was the magnitude of change observed between all systems (both GMF and MF/UF) operating with and without coagulation and the statistically significant differences in TCDs in the permeate or backwash waters both among and within these treatment trains. In both GMF and MF/UF systems, coagulation

was critical to (1) reduce the variability in permeate TCDs and (2) increase the magnitude of mean toxin removal efficiencies.

Another potential operational change considered in this study was to assess the operation of MF/UF systems at lower transmembrane pressures in submerged configurations. Although submerged MF/UF systems (<0.4 bar) had higher mean toxin removal efficiencies and lower variability in treatment than the pressurized systems (>0.4 bar), the TCDs in the permeate and backwash waters were not significantly different between the systems. Therefore, the selection of submerged systems over pressurized systems in pretreatment design for biotoxin mitigation may not be as critical as expected initially.

Amending the design of the SWRO pretreatment system with a DAF system demonstrated mixed results from the pMFA simulations regarding toxin removal efficiencies. On one hand, statistically significant reductions in TCDs were observed for DAF systems compared to systems operating without coagulation, whereas no statistically significant differences were found between systems operating with DAF and those with coagulation. It was likely that the above discrepancies observed in the results of the pMFA were due to: (1) the high variability of reported removal efficiencies of algal cells in DAF systems (i.e. 43–93%) and (2) the scarcity of studies (N = 3) examining algal cell removal in DAF systems [42,47,48]. The high variability in reported algal removal efficiencies from DAF systems results directly from the site-specific algal species composition during the evaluation period for each study (Voutchkov 2010). Voutchkov (2010) stated that removal of chlorophyll-a is often lower for DAF treatment systems as most of the influent water (up to 50–75% at the intake) comprises picoplankton, which are sparsely removed by DAF

processes. Future studies should consider reporting both reductions in chlorophyll-a and algal species profiles as determined by microscopy for standardizing their reported results. An equally important aspect to consider in future study (that was neglected in this study) is the removal of dissolved toxins in DAF systems. Previous studies have indicated considerable biopolymer and humic acid removal in these systems (Voutchkov 2010, Guastalli et al. 2013, Zhu et al. 2014); therefore, the removal of other soluble organics, such as algal toxins, would greatly improve the accuracy of future pMFA simulations.

Future design of pretreatment systems and configurations should consider the impact of HAB periods on plant operations. The results highlighted a great difference in treatment potential between GMF and MF/UF systems, with MF/UF systems demonstrating improved performances. This difference in performance was attributed to the high range in algal cell removal and small cell removal variability reported in the literature for MF/UF processes. Subpar removal of algal biotoxins by GMF systems can be attributed to the colloidal size of most marine microalgae associated with harmful algal bloom periods. Most conventional sand filtration media has an effective size range of 0.4 to 0.6 mm (400 to 600 μm), which is much larger than the corresponding width and length dimensions of dinoflagellates and diatoms (10 to 100 μm) (Voutchkov 2013). Marine microalgae are negatively charged and may not adsorb to the negatively charged surface of the filter media or organic material already adsorbed to the grain surface. Similarly, the high filtration rates often applied during GMF may prevent the conglomeration and straining of algal cells.

It is also necessary to consider the differences in dissolved toxin removal for both GMF and MF/UF processes in the future. Using more hydrophobic membranes has proven to increase adsorption of algal toxins, including MC-LR, through partitioning of these toxins

based on phase affinity of the membrane surface (Lee and Walker 2006, Gijsbertsen-Abrahamse et al. 2006, Lee and Walker 2008). Equally critical is the potential for dissolved toxin adsorption (mainly by electrostatic interactions) to or phase affinity for the compressible organic cake layer formed at the surface of the membrane (Castaing et al. 2011, Babel and Takizawa 2010).

Potential benefits of GMF systems—such as increased biological activity—may increase the removal of dissolved toxins over MF/UF systems. Voutchkov (2013) has stated that the removal of soluble organics in some second stage GMF systems can account to 20–40% by biological filtration processes alone. Biological treatment has the potential to remove dissolved organic carbon and TEP of the source water without requiring expensive cleaning/purchase of coagulants or cleaning chemicals, energy intensive backwashing (increase in filter run times), and can reduce the replacement frequency of membranes over the duration of operation (Bar-Zeev et al. 2012, Bar-Zeev et al. 2013, Jeong et al. 2013, Naidu et al. 2013, Simon et al. 2013).

Other than pretreatment design and operation, the design of a proper seawater intake system represents a significant amendment for future SWRO facilities to mitigate the effects of HABs (Voutchkov 2010, Villacorte et al. 2015a, Villacorte et al. 2015b). Although a majority of current SWRO facilities operate with an open (surface water) intake system, the use of subsurface systems (wells and galleries) can significantly reduce the influent suspended solids, bacteria, dissolved organic carbon, and toxic/non-toxic algae present in the source water (Dehwah et al. 2015, Missimer et al. 2013). Subsurface intakes are well suited for coastal regions where the geology is favorable (i.e. the presence of permeable rocks, limestones, dolomites or gravels), which may limit the widespread application of

these intake systems to future SWRO facilities intending to alleviate the deleterious effects of HABs (Missimer et al. 2013).

4.2. Uncertainty and Variability

Since there is little experimental data to verify the effluent pretreatment concentrations predicted by the pMFA, a certainty/variability analysis was performed to elucidate the accuracy of the model predictions. Algal breakage fractions represented the highest model uncertainty. The algal cell breakage fractions were informed estimates made by extrapolating experimental data summarized in Voutchkov (2010). However, algal cell breakage behavior is influenced not only by operational practices (shear in pumps or valves, transmembrane pressure), but also algal cell type and species (diatom or dinoflagellates) and other biotic factors such as cell age (Vandanjon et al. 1999, Hamm et al. 2003, Subhash et al. 2005, Losic et al. 2007, Lau et al. 2007, Ladner et al. 2010, Michels et al. 2010). We reduced this high uncertainty in our model by structuring the distribution of breakage coefficients to encompass a relatively large range, and by incorporating uniform probability distributions for selecting breakage coefficients during each simulation.

The dissolved toxin removal coefficients were also subject to a moderate to high uncertainty when extrapolating from MC-LR observations summarized from the literature. This extrapolation was based on the octanol-water distribution coefficients either experimentally derived or modeled from molecular structure alone (see Appendix A, Section 3.1). We focused primarily on collecting experimental observations of octanol water distribution coefficients over modelled predictions to first reduce the relative uncertainty in dissolved toxin removals. In addition, we focused on collecting field and pilot

studies examining the dissolved removal of MC-LR over laboratory studies to further reduce the uncertainty of pMFA simulations.

The sensitivity results indicated that algal cell removal was the most sensitive parameter for GMF systems, whereas dissolved toxin removal and algal cell breakage were the most sensitive parameters for MF/UF systems. Given these results, there is higher certainty in the GMF simulations over the MF/UF simulations. However, if we analyze the entire system, the algal cell concentration was the most sensitive input. When model inputs were grouped with the removal efficiency parameters in the sensitivity analysis, greater than 99% of the model output still depended on the algal cell concentration alone (data not shown). This is a significant conclusion given that the uncertainty of the algal cell concentration is low compared to all other model inputs or parameters. Based on this result, the model predictions can be afforded relatively high levels of confidence, despite the uncertainty observed for some of the model removal efficiency parameters.

To improve the pMFA model predictions, several areas of data collection should be improved and prioritized. The first and foremost step would be to collect algal toxin data from a full-scale SWRO facility at different points in the treatment train for a prolonged time period (i.e. 3 years). This data collection effort would allow a clear comparison between pMFA model predictions and real-world data, potentially providing the opportunity to optimize removal efficiency parameters and compare these removal efficiency estimates to those observed in practice. Ultimately, from this data collection, a true quantitative estimate of the certainty of model predictions can be reached. An additional area of research would be to study the algal cell breakage magnitude for different pretreatment configurations during various stages of algal blooms and analyzing

the dissolved removal of algal toxins during various pretreatment processes. This study extrapolated treatment efficiencies of dissolved toxins from MC-LR removal data, based on similarity or differences in physical and chemical properties. The new research should be integrated with the field data collection effort to develop an improved understanding of toxin removal during SWRO pretreatment.

4.3. Human Health Effects

The lifetime risk of acute human illness from ingesting permeate waters during algal blooms was determined to be minimal using a quantitative chemical risk assessment framework. The AL was determined based on the acute RfD developed by the EFSA. Most of these doses (STX, DA, OA) were based on LOAEL from actual human shellfish poisoning events and should be more reliable than animal testing data (YTX). In addition, the RfD developed by the EFSA considered two to three uncertainty factors (extrapolating from LOAEL to NOAEL, accounting for intra-species variation), depending on the toxin, which further decreases the margin of acceptable risk. Based on these facts, we are confident in the human health effect conclusions presented in this study.

Although we have thoroughly addressed the acute human health risks from exposure to algal toxins, the chronic, accumulated, or compounding human health risks associated with exposure to low levels of these toxins in desalinated drinking water are relatively unknown. For example, several studies have indicated that repetitive exposure to low level doses of OA through shellfish consumption may be correlated to an increase in the incidence of colorectal cancers in exposed human populations (Manerio et al. 2008, Cordier et al. 2000, López Rodas et al. 2006). Developmental and neurological effects of chronic (low-level) DA exposure on infants and young children are a concern, as DA has

been shown to cross the placenta, enter the blood brain barrier of infants, and collect in amniotic fluid in mammals (Levin et al. 2005, Levin et al. 2006, Lefebvre and Robertson 2010, Lefebvre et al. 2012, Costa et al. 2010). Chronic DA exposure has also been linked to cognitive impairment in mice (Lefebvre et al. 2017). More reliable chronic DA exposure epidemiological studies on humans, however, have been rarely reported. A recent study by Grattan and co-workers concluded that there was a possible, but not clinically significant, connection between long term, low level exposure to DA (through razor clam consumption) and memory (Grattan et al. 2016). Future studies should consider the development of chronic RfDs of algal biotoxins in desalinated drinking water for lifetime exposure human health risk assessments.

The effect of concentrated brine and backwash waters on both human health and the surrounding environment during harmful algal bloom periods should be a topic of equal concern for future study, as the results from pMFA simulations indicated a relatively high concentration of algal biotoxins in the combined backwash/brine waters (up to mg/L levels). Besides ingestion of finished drinking water, humans may be at risk when exposed to elevated concentrations of algal biotoxins either through recreational exposure pathways or consumption of contaminated seafoods. The ingestion of contaminated shellfish harvested near the zone of dilution at the desalination brine discharge point may pose the most critical human health risk, as benthic shellfish are chronically exposed to elevated concentrations of biotoxins from the combined backwash/brine discharge. An important question would be to assess whether the background concentration of dissolved toxin during HAB periods contributes more to shellfish bioaccumulation than the actual SWRO discharge itself. Studies should equally weigh the potential biomagnification of algal

biotoxins in the surrounding ecosystem as another environmental issue emanating from concentrated SWRO brine discharge.

5. Conclusions

The primary objective of this study was to quantify the removal of algal toxins during SWRO using a pMFA approach. The main conclusions drawn from this study are:

- A detectable quantity of algal toxins is present in the permeate water, despite almost 99.0–99.9% removal predicted across the RO membranes (in the ng/L to µg/L range);
- A relatively high concentration of algal toxins was predicted for the combined backwash and RO reject waters (in the µg/L to mg/L range);
- MF/UF systems with coagulation generally had the highest predicted toxin removals (and least variability) over all GMF systems/operations (up to 57% of the entire removal across SWRO);
- There is a low to negligible risk of acute intoxication from ingesting desalinated water during algal bloom periods (margins of safety ranged from 100 to 4000).

6. List of Abbreviations

SWRO	Seawater Reverse Osmosis
RO	Reverse Osmosis
HABs	Harmful Algal Blooms
pMFA	Probabilistic Materials Flow Analysis
MF/UF	Microfiltration/Ultrafiltration
GMF	Granular Media Filtration
DAF	Dissolved Air Flotation
TEP	Transparent Extracellular Particulate
MGD	Million Gallons per Day (international unit)
SCCOOS	Southern California Coastal Ocean Observing System
STX	Saxitoxin

DA	Domoic Acid
OA	Okadaic Acid
YTX	Yessotoxin
ECDF	Empirical Cumulative Distribution Function
SPATT	Solid Phase Adsorption Toxin Tracking
MC-LR	Microcystin-LR
ANOVA	Analysis of Variance
RfD	Acute Reference Dose
EFSA	European Food Safety Administration
EPA	Environmental Protection Agency
AL	Acceptable Level
LOEL	Lowest Observed Effect Level
NOAEL	No Observed Adverse Effect Level
RSC	Relative Source Contribution
MO	Margin of Safety
TCD	Toxin Concentration Distribution
IQR	Interquartile Range
COV	Coefficient of Variation
CDF	Cumulative Probability Distribution Functions

Chapter 2: The Effect of Organic Carbon Addition on the Community Structure and Kinetics of Microcystin-Degrading Bacterial Consortia

Abstract: Microcystin (MC), a hepatotoxin that is associated with cyanobacterial blooms in freshwater lakes, threatens the quality of drinking water resources. Biodegradation of MC using biofiltration is emerging as a cost-effective solution for drinking water treatment. This study reports isolation of five MC-degrading microbial consortia and investigation of their community structure and kinetics in the presence or absence of a readily-bioavailable organic carbon source. The results indicated that the presence of a bioavailable organic carbon source caused: (1) the proliferation of community members previously unobserved in each consortium cultured without ethanol; (2) a shift in abundance of representative taxa; (3) a fluctuation in genera affiliated with MC-biodegradation; and, (4) a unique response in simulated diversity among consortia. These changes to each microbial consortium were paralleled by a significant decline in MC degradation kinetics. Overall, this study highlights the importance of integrating environmental conditions into the design and operation of biofiltration systems for MC biodegradation.

1. Introduction

Harmful cyanobacterial blooms have increased in both frequency and severity worldwide as a result of climate change, population growth, and rapid urbanization (Paerl and Paul 2012). These blooms are termed "harmful" in that many cyanobacteria are responsible for the production and release of toxins that are harmful to humans and existing aquatic ecosystems (Huisman et al. 2006). The most common freshwater genera of harmful cyanobacteria include *Anabaena*, *Nostoc*, *Oscillatoria*, *Planktothrix*, and *Microcystis*, which produce a suite of biotoxins, including microcystin (MC) (Huisman et al. 2006). MCs are a class of heptapeptides, which are formed from seven amino acids, in which their mono-cyclical structure imparts a high stability in the environment (Edwards and Lawton 2009). Although approximately 100 structural congeners have been identified, MC-LR (L and R standing for Leucine and Arginine, respectively, for two of the variable amino acids in the cyclical structure) is the most common and toxic MC (Cheung et al. 2013, US EPA 2015a). Due to its acute toxicity, both the WHO (World Health Organization) and US EPA (United States Environmental Protection Agency) have adopted a guideline of 1 μg/L of dissolved MC for drinking water (US EPA 2015a).

MC-LR, along with other common structural variants observed in the environment (i.e., LA, RR), is water soluble, chemically-stable, and low in molecular weight, which renders it resistant to most conventional drinking water treatment processes (Westrick et al. 2010). Biological filtration (biofiltration), which relies on the development of biofilm communities on immobilized media (i.e., sand) to degrade cyanotoxins, has been proposed as an alternative, cost-effective, and sustainable drinking water treatment technology to

target MC removal (Li et al. 2011a, 2011c, 2015, Ho et al. 2007b, 2012, Huck et al. 2000, Urfer et al. 1997).

Previous studies have demonstrated the complete biodegradation of MC-LR within laboratory scale biofiltration systems following a preliminary lag phase of removal (Ho et al. 2006, 2007a, Bourne et al. 2006, Dziga et al. 2014). However, the toxin removal efficiency and extent of this lag phase can vary significantly with bacterial composition, nutrient concentration, and other environmental parameters that are associated with the source water. Efforts to evolve biofiltration from a passive process into a more standardized, controlled, and perhaps "engineered", biological treatment process for targeted removal of pollutants will require a better understanding of the physiology and genetics of MC-degrading bacteria (Huck et al. 2000, Urfer et al. 1997, Ho et al. 2007a, Rittmann et al. 1989, Lauderdale et al. 2012, Dziga et al. 2013).

Significant efforts have been made to isolate and characterize the specific MC-degrading bacterial populations during algal bloom events in the source water and sediments, and from full scale biological treatment units in drinking water treatment facilities (Li et al. 2011a, 2011c, 2015, Dziga et al. 2014, Bourne et al. 1996, Saito et al. 2003, Eleuterio and Batista 2010, Jimbo et al. 2010). However, these studies have not fully explored how these isolates function in mixed bacterial communities, nor the influences of mutualistic or antagonistic interactions on biodegradation kinetics. Several previous studies, however, have considered the effects of environmental stimuli (i.e., varying organic carbon concentrations) on MC-degrading bacterial consortia under aerobic conditions (Li et al. 2011a, 2011b, 2011c, 2017, Eleuterio and Batista 2010, Christoffersen et al. 2002, Yang et al. 2008, Ho et al. 2010). Research showed that addition of organic carbon sources

(i.e., glucose, acetate, or uncharacterized dissolved organic carbon (DOC)) significantly inhibits MC degradation kinetics of bacterial consortia (Li et al. 2011c, Eleuterio and Batista 2010, Li et al. 2011b, Ho et al. 2010). Catabolite repression is postulated as a mechanism underlying this inhibition, where MC-degrading populations may prefer more energetically-favorable (easily metabolized) over more energetically-intensive substrates, such as MC (Jones et al. 1994b). Other (fewer) studies have demonstrated that the addition of an alternative organic carbon source facilitates MC degradation rates, where the organic carbon was postulated to stimulate the growth and energy availability for production of the necessary enzymes required for MC-degradation by these bacterial populations (Zhang et al. 2015b, Surono et al. 2008). In addition, several studies have reported a net neutral effect with the addition of alternative organic carbon sources (Li et al. 2011a, 2011c, 2017, Christoffersen et al. 2002). The community structure of the microbial consortia that was involved in MC biodegradation was shown to change with environmental conditions (Li et al. 2011a, Christoffersen et al. 2002, Mou et al. 2013, Tsao et al. 2017). For example, Mou and co-workers (2013) reported that *Methylophilales* (*Methylotenera* genus) and *Burkholderiales* (*Bortadella*, *Burkholderia*, *Cupriavidus*, *Ralstonia* genera) were the most significant taxa in microcosms containing MC. There was significant enhancement of the broad class of metabolic functions when these MC-degrading populations were exposed to MC (Mou et al. 2013).

Consequently, insight into the changes in community structure in response to a shift in environmental condition, and the influence of such change on MC degradation kinetics can better inform engineered strategies to improve MC removal under various environmental conditions. In this study, we report the comparison of community structure

of five MC-degrading consortia in the presence or absence of organic carbon besides MC. We asked, "how and to what extent does the MC-degrading community structure and degradation kinetics change in response to an organic carbon addition?" We expect that the MC degradation kinetics of the consortia will be strongly driven by changes in the community structure with the addition of an exogenous carbon source, as changes to the presence or absence of community members should directly correlate with changes in representative specific metabolic pathways that are involved in MC degradation.

2. Materials and Methods

2.1. Isolation of Microcystin-Degrading Bacterial Consortia

One lake surface water sample (LSB) and four bed sediment samples (10B, 11B, 12B, 14A) were collected from a drinking water reservoir in Southern California that experiences periodic cyanobacterial blooms. Bed sediment samples were centrifuged (10,000 g for 10 min) to remove coarse sands. Both the surface water and supernatant from the sediment samples were filtered through a 1 μm pore size glass fiber filter to remove large protozoa and zooplankton potentially present in the samples.

The initial isolation of each consortium (i.e., Generation A) involved the addition of 5 mL of the filtrate from each environmental sample into a flask containing 20 mL of M9 minimal media (per liter media contains: 12.8 g of Na_2HPO_4-$7H_2O$, 3.0 g of KH_2PO_4, 0.5 g of NaCl, 1.0 g of NH_4Cl, 0.25 g of $NaNO_3$, 0.002 g of $MgSO_4$, 0.001 g of $CaCl_2$, pH of 7.3) with 200 μg/L of MC-LR, and 316 mg/L of ethanol. The composition of the initial medium used for isolation was kept consistent with the composition used for enrichment to effectively acclimatize each consortium to the conditions expected during laboratory culturing. This isolation period, which was maintained for seven days prior to further enrichment, also

allowed for each consortium to consume any residual organic carbon present in the initial samples that may have affected batch biodegradation results that were acquired during future experimentation.

To enrich for MC degradation consortia, two parallel tracks of experimentation were conducted (Generation B) (Figure 13). The first track involved the addition of 5 mL of the previous culture (Generation A) into a flask containing 20 mL of M9 minimal with 200 μg/L of MC-LR (a congener common to Southern California lakes) (Izaguirre et al. 2007). The seeding concentration of MC (200 μg/L) represented a higher range than that typically detected in the environment, but it was within the range of commonly used concentrations in enrichment studies to elicit a detectable response from the isolated consortia. The second parallel track of enrichment cultures (again with 5 mL of previous culture) was set up to include 316 mg/L of ethanol in addition to the M9 media and MC-LR, to serve as the comparison of MC biodegradation kinetics and community composition of each MC-degrading consortia. We expect that predicted MC-degrading half-lives and changes in the composition and abundance of the bacterial consortia will be the most effective and practical means to compare changes among MC-LR-degrading communities in the presence and absence of ethanol.

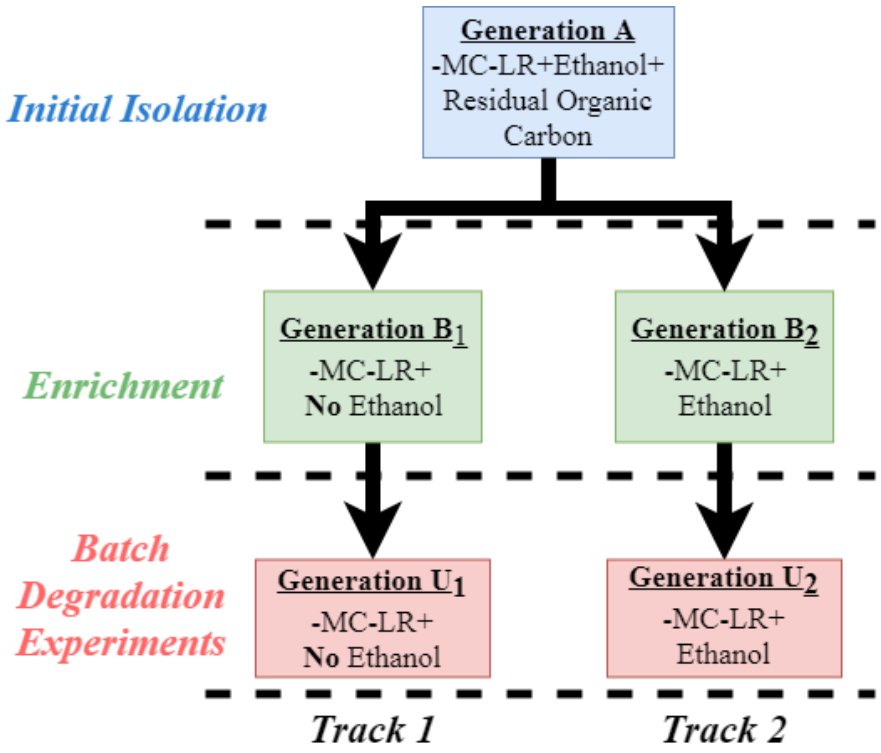

Figure 13. *Flow-chart of the experimental design employed in this study. Following initial isolation of 5 consortia from different locations within a reservoir, a parallel track of enrichment was set up to investigate the effect of ethanol addition on MC-LR biodegradation kinetics. The letters (A-U) indicate the relative generation age of each consortium during each track of enrichment (1–2).*

The selection of ethanol as an organic carbon substrate was two-fold: (1) MC-LR was supplied in ethanol from the manufacturer (Cayman Chemical), thus it requires no further purification to include ethanol as an organic supplement; (2) ethanol is an energy-excess substrate (compared to glucose). Ethanol is readily metabolized by most bacteria in the environment and potentially serves as a preferential substrate, as indicated in multiple studies (Babel and Müller 1985, Lovanh et al. 2002). The use of ethanol represents the availability of labile and simple forms of dissolved organic carbon that become readily available in freshwater ecosystems during harmful algal bloom (HAB) periods (Nguyen et al. 2005, Zhou et al. 2014). As labile, dissolved organic carbon does not solely originate from cyanobacteria during these bloom periods, the concentration of ethanol (316 mg/L)

was set to a similar order of magnitude to resemble the higher range of total dissolved organic carbon concentrations that were reported by the USA EPA's National Lake Assessment survey (ranging from 2–516 mg/L) (US EPA 2016b). This concentration of ethanol is reflective of dissolved organic carbon concentrations expected during worst case bloom conditions in lakes or reservoirs throughout the USA. In addition, this concentration of ethanol was considered to be non-inhibitory based on a thorough comparison of ethanol tolerances across common bacteria in the environment (i.e., E. coli), which indicated that the selected concentration was approximately 79–132 times lower than the threshold of growth inhibition (Ingram 1986, 1990, Wang et al. 2013, Jin et al. 2014).

Sub-culturing of the isolated bacterial consortia involved transferring 5 mL of the previous culture into a new sterile tissue flask with 20 mL of M9 minimal media spiked with 200 μg/L of MC-LR with or without ethanol. As MC was initially supplied in ethanol, a temperature controlled (4 °C), rotary evaporator was used to obtain ethanol free suspensions of MC (for Track 1 enrichment cultures only). Sub-culturing frequency was intentionally kept to a minimum (every two weeks) to prevent potential shifts in microbial community composition prior to performing batch degradation experiments; thus, each consortium was transferred approximately twenty times (Generation U) (Figure 1). It is important to note that, although five consortia were initially isolated (Generation A: 10B, 11B, 12B, 14A, LSB), ten distinct consortia were ultimately obtained with the experimental enrichment conditions employed. We make the important distinction between consortia enriched with (i.e., 10B-WE) or without ethanol addition (10B-NE) to avoid any further confusion.

MC concentrations in the flasks were monitored using an ADDA-ELISA kit (ABRAXIS, Warminster, PA, USA) to evaluate the MC degradation potential of the enriched samples. UPLC-MS/MS (Waters Quattro Premier QqQ) was also used initially for the quantification of MC. The correlation coefficients for all ELISA and UPLC-MS/MS tests ranged from 0.99 to 1, indicating that the results for each assay were reproducible (Appendix B, Figures B1 and B2). In addition, ELISA and UPLC-MS/MS measurements for initial experiments indicated good agreement (data not shown). Only the ELISA kit was used later for MC detection and quantification due to the high sensitivity at the low MC concentration range employed (0.1 µg/L detection limit). The flasks that showed a significant removal of MC (at or below the detection limit) within the seven-day enrichment period were deemed as MC-degrading consortia and used in later investigations.

2.2. Batch Degradation Experiments

Batch degradation experiments were carried out to quantify the MC degradation kinetics in each consortium using three experimental replicates. Culture conditions during batch degradation tests were identical to sub-culturing conditions, except for an additional washing step, in which the 5-mL consortium culture was pelleted and washed three times to remove any residual MC or ethanol present in the transfer culture. The washed cells were finally re-suspended in 5 mL of sterile M9 media and were transferred to the testing flasks. The initial optical density (OD at 600 nm) for experiments with and without the presence of ethanol was 0.002 and 0.0002, respectively. Although there was a detectable change in OD for the consortia amended with ethanol, the consortia without the addition of ethanol had a negligible change in OD. Flow cytometry was used to verify the growth of

bacterial cells for each consortium cultured without the addition of ethanol (see Appendix B, Section 2 for details).

All of the flasks were shaken at 120 rpm in the dark at ambient temperature (24 °C), where 500 µL of sample was taken every 24 h for an eight-day period to quantify the concentration of MC-LR using an ADDA-ELISA kit following the manufacturer-recommended protocols.

2.3. Kinetic Model of Microcystin Biodegradation

Visual examination of the MC degradation kinetics revealed a 24-hour lag phase for all batch experiments, which indicated that simple zero or first order kinetics were not adequate to predict MC degradation kinetics. A bi-phasic kinetic model that was proposed by Ouiroga and co-workers (1999) for the biodegradation of surfactants was adopted to model the removal of MC by each consortium as a function of time because it directly accounted for bacterial growth on MC along with substrate (MC) consumption (Equation (1)). In this model, the substrate utilization kinetics depend on the concentrations of degrading microorganisms (X), the substrate available (C), and the rate of substrate consumption (K) by degrading microbes to produce new biomass and other products.

$$\frac{dC}{dt} = -KCX \tag{1}$$

The analytical solution to Equation 1 results in (see Appendix B, Section 4 for derivation):

$$C = \frac{h(S_0-q)-q(S_0-h)e^{pt}}{(S_0-q)-(S_0-h)e^{pt}} \tag{2}$$

where the substrate MC concentration (C) is related to its initial concentration (S_0), the maximum MC available for biodegradation (h, in µg/L), the non-biodegradable portion of

MC (q, in μg/L), and the maximum specific growth rate of the degrading microorganisms (p, in 1/day).

The fitting of the experimental data to the bi-phasic kinetic model was carried out using the *DREAM$_{ZS}$* (Differential Evolution Adaptive Metropolis, sampling from past states) (v1.0) software package (Laloy and Vrugt 2012, Vrugt 2016). Details of this approach are presented in Appendix B, Section 5. The goodness of the model-data fit was compared through the assessment of two quantitative metrics, the r^2 value and the RMSE (root mean square error), as calculated during the fitting process. The distribution in posterior parameters derived from *DREAM$_{ZS}$* was used to estimate the MC degradation half-lives for comparison among different consortia and under different conditions.

2.4. Analysis of Bacterial Community Structure

The bacterial community structure of each bacterial consortia was analyzed using the 16S rRNA gene amplicon on a Roche 454 genome sequencer FLX+ (454 GS-FLX+, RTL Genomics, Lubbock, TX, USA). The pyrosequencing analysis was conducted immediately following one particular replicate of the eight-day batch biodegradation experiments. A 1 mL sample volume of the batch degradation experiment was pelleted (10,000 g for 15 min), supernatant discarded, and shipped on dry ice to the RTL laboratory for further analysis. Both the DNA extraction and amplicon sequencing were performed by RTL Genomics (Lubbock, TX, USA). The 16S rRNA gene universal eubacterial primers 939F (5'-TTGACGGGGGCCCGCACAAG-3') and 1492R (5'-TACCTTGTTACGACTT-3') were used to amplify approximately 550 bp of the variable regions V6 to V8. The pyrosequencing reads were analyzed using Quantitative Insights into Microbial Ecology (QIIME) (v. 1.9.1) (Caporaso et al. 2010), following the program's instruction. The bacterial community

structure and taxonomic abundance for samples with and without the presence of ethanol were compared using the statistical analysis of taxonomic and functional profiles (STAMP) bioinformatics software (v.2.1.3) (Parks et al. 2014). The statistical significance of the taxonomic abundance on the order level between the samples was determined using a two-sided G-test with Yates and Fisher's correction and Bonferroni multiple test correction. The difference in taxonomic abundance was deemed to be significant if the calculated p-value between the samples was below 0.05. Rarefaction plots, Beta diversity metrics (unweighted/weighted Unifrac distances), and jackknifed Beta diversity (principal coordinate analysis) were carried out using scripts provided by the QIIME module.

"True" as opposed to "raw" Alpha diversity indices were adopted in this study to facilitate comparisons of the abundance and presence or absence of species within the MC degrading communities with or without ethanol addition (Jost 2006, 2007, 2009, Tuomisto 2010, Chao et al. 2014). Common "raw" Alpha diversity measures, such as Shannon entropy, evenness, or Simpson's dominance suffer from difficult interpretation and comparison, since they do not share a common mathematical grounding (i.e., common units, derivation) or favorable mathematical properties (i.e., the "replication" principle) (Chao and Jost 2008). In a seminal study, Hill (1973) introduced a unified basis of calculation to transform the existing "raw" measures to "true" Alpha diversity measures with the advent of a single variable: the diversity order, q (Equation (3), where S is the total number of species and p_i is the relative proportion of the ith species within a given community). Lower diversity orders ($q < 0$) place more emphasis on the frequency of rarer species within a given population, whereas higher diversity orders ($q > 1$) weigh the frequency of dominant species more heavily (Jost 2006, Chao and Jost 2008, Hill 1973).

When q is equal to unity (corresponding to Shannon entropy), an equal weight is placed on the frequency of rare and dominant species (Jost 2006, Chao and Jost 2008, Hill 1973). Intuitively, a zero-order (q = 0) diversity value corresponds to the species richness within a given community (Jost 2006, Chao and Jost 2008, Hill 1973). It is important to note that the units of all true Alpha diversity orders are in number of species (or genera, depending on the taxonomic level), also termed "effective number of species", which provides a unified basis for comparison across diversity orders (Chao and Jost 2008).

$$D^q = \left(\sum_{i=1}^{S} p_i^q\right)^{\frac{1}{(1-q)}} \quad (3)$$

As biological or technical replicates of the metagenomic analyses were not conducted in this study, a series of Monte Carlo (MCA) simulations was conducted to simulate the statistical variability in "true" Alpha diversity indices. These simulations were based on an empirical, non-linear relationship that was developed between the taxon mean relative abundance and standard deviation of replicate measurements that were reported across similar metagenomic analyses in the scientific literature (see Appendix B, Section 6, Table B5, Figures B7 and B8). After running a sufficiently large number of MCA simulations (N = 20,000), normal distributions in true Alpha diversity metrics across several diversity orders (q = −1, 0, 1, 2, 3) were reached (Figures B9 and B10). For each MC degrading community, the significance of changes in true Alpha diversity metrics (across all diversity orders) with the addition of ethanol were simultaneously assessed using a one-way analysis of variance (ANOVA) with Bonferroni multiple comparison test correction (Pallmann et al. 2012). In addition, both the direction and magnitude of the differences between the resulting statistical distributions of the Alpha diversity metrics were

quantified using an effect size (*ES*) calculation (Equation (4), where $\mu_{we/ne}$ and $\sigma_{we/ne}$ refer to the mean and standard deviation of normal distributions with or without ethanol addition) (Coe 2002).

$$ES = \left(\frac{\mu_{we-}\mu_{ne}}{\sqrt{\frac{\sigma_{we}^2 + \sigma_{ne}^2}{2}}} \right) \quad (4)$$

Metagenomic stability, which is defined as the persistence of individual operational taxonomic units (OTUs) across different MC degrading communities profiled, of the microbial communities was evaluated using the QIIME generated output (OTU vs. abundance) from the genera level of analysis (after removing OTUs that comprised less than 0.1% of the total communities) (Linz et al. 2017, Woodhouse et al. 2018). Stability values were simply the coefficient of variation (*CV*) ($(\sigma/\mu) \times 100\%$) of the abundance across each microbial community with or without ethanol addition, where the values for OTUs less than 200% are considered to be stable (Woodhouse et al. 2018). In this study, we report an aggregate stability value for MC degrading consortia (with or without ethanol) by calculating the proportion of OTUs that are statistically "stable" out of the total number of OTUs present.

3. Results

3.1. Microcystin Biodegradation Kinetics

As shown in Figure 14, all five isolated consortia possess the ability to degrade MC within three to seven days in the presence or absence of ethanol with a one-day lag phase. This degradation was clearly biologically mediated as control experiments (without bacterial inoculum) demonstrated slow and relatively insignificant MC removal over the eight-day period investigated (Figure B4). The shape of the MC-LR degradation curves was

nearly identical for each isolated consortium across three experimental replicates (shown by the small standard deviation for each point of measurement), indicating that the degradation kinetics were consistent and repeatable. Although multiple measurements were taken within the first 24 h, only measurements that were taken at evenly spaced 24-hour intervals were included in Figure 14 to reduce the noise in the graphs. For consortia 12B and 14A without ethanol, a sharp decline in MC concentrations at day 2 was followed by a rapid rebound at day 3. Notably, this trend was apparent for all experimental replicates and was it not considered an error in measurements. It is also important to mention that although most of the MC concentrations appear in Figure 14 to be near zero after four days, the substrate concentrations rarely approached the limit of detection (0.1 μg/L). These results suggest that a portion of the MC substrate was potentially non-biodegradable. Similar results were presented by Eleuterio and Batista (2010) while using an ELISA quantification method, with measured MC residuals ranging up to 2 μg/L.

OD600 and flow cytometry results confirmed cell growth during the degradation experiments for MC consortia with and without ethanol addition, respectively. Flow cytometry results indicated that initial cell concentrations were on the order of 10^6–10^7 for consortia without ethanol addition (cells/mL). However, growth rates were highly variable across individual replicates for consortia without ethanol addition, with final cell concentrations ranging from 10^8–10^9 cells/mL (Figure B3).

The bi-phasic model accurately predicted the experimental results, as noted by the narrow widths of the 95% total predictive uncertainty intervals and the close proximity of the experimental data points to the best fitting solutions for all consortia analyzed (Figure 14). The r^2 is approaching 1 in 8 of the 10 degradation experiments, indicating a good fit of

the model to the experimental data (Figure 14, Table B2). Wider uncertainty intervals were observed for consortia 12B and 14A under some of the testing conditions, with r^2 ranging from 0.68 to 0.79, indicating less accurate model predictions. The wider predictive uncertainty intervals were attributed to unknown factors that were not currently considered in the model structure. The parameter estimability was relatively high across all experiments (as indicated by the defined shape of posterior parameter distributions); however, significant correlations were observed between the *h* (maximum available MC for degradation) and *p* (maximum specific growth rate) parameters, suggesting non-unique values of these parameters for these cases (Table B4, Figure B6).

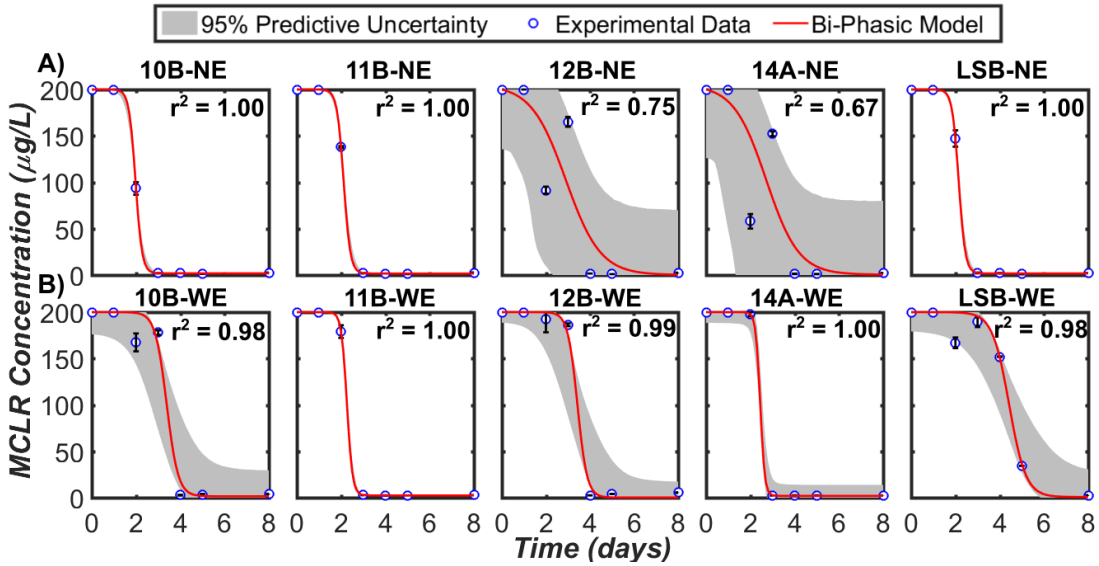

Figure 14. *MC-LR biodegradation by microbial consortia isolated from five environmental samples (10B, 11B, 12B, 14A, and LSB) in the absence (NE—no ethanol) (A) or presence (WE—with ethanol) of ethanol (B). Error bars are standard deviations for three experimental replicates at each measurement point (excluding t_0 and t_{24}). Light grey shading indicates the 95% total predictive uncertainty intervals of the kinetic model, while the red line indicates the best fit of the model to the experimental data.*

The presence of ethanol slowed the degradation kinetics of MC-LR in all five consortia, as indicated by the longer respective mean half-lives (Table 3). This decline in MC biodegradation kinetics was statistically-significant for all consortia (p-value < 1 ×

10^{-8}) based on the distribution of half-lives that was generated by the *DREAM*$_{ZS}$ model-data fitting procedure (N = 25,000 samples). Greater variations in predicted degradation kinetics were observed in some cases (i.e., 12B and 14A without ethanol), as indicated by the moderately high standard deviation of predicted half-lives (Table 3).

Table 3 *- Summary of half-lives and t-test significance for MC-LR degrading consortia without ethanol (NE) and with (WE) ethanol addition. The mean and standard deviation of the posterior distributions of half-lives are provided for reference.*

Consortia ID	Half-Life (Day)		*t*-Test
	NE	WE	*p*-Value
10B	1.98 ± 0.003	3.28 ± 0.371	$<1 \times 10^{-8}$
11B	2.14 ± 0.017	2.30 ± 0.016	$<1 \times 10^{-8}$
12B	2.74 ± 0.765	3.37 ± 0.367	$<1 \times 10^{-8}$
14A	2.14 ± 0.835	2.47 ± 0.046	$<1 \times 10^{-8}$
LSB	2.16 ± 0.016	4.41 ± 0.307	$<1 \times 10^{-8}$

3.2. Community Analysis of Microcystin-Degrading Consortia With and Without Ethanol Addition

Pyrosequencing yielded, on average, greater than 2,000 reads per sample (Table B9). Rarefaction curves indicated that the sequencing depth was adequate to accurately characterize the microbial communities in each consortium (Figure B12). As shown in Figure 15A, the taxonomic composition and relative abundance of each MC-degrading community varied by the sampling location. In descending order, *Pseudomonodales*, *Burkholderiales*, *Xanthomonadales*, and *Rhizobiales* were the most representative bacterial orders in the degrading consortia in the absence of ethanol (Figure 15A). *Rhizobiales* was a more representative order in the consortia isolated from bed sediment (10B, 11B, 12B, 14A), as compared to the lake water (LSB). However, *Xanthomonadales* was more representative in the lake water consortium as compared to the sediment consortia (Figure

15A). In addition, *Rhodospirillales* dominated the community composition of the 12B sediment consortia as compared to other sediment consortia.

In the presence of ethanol, the general taxonomic composition and relative abundance of each MC-degrading community changed noticeably, especially for the 10B and 12B consortia (Figure 15B). Specifically, the presence of bacterial populations within the *Rhizobiales* order declined greatly in the 10B, 11B, and 12B consortia. Moreover, the *Rhodospirillales* order declined to a great extent in the 12B consortium cultured with ethanol (Figure 15B). The relative abundance of the order *Burkholderiales* was noticeably depressed (and replaced by either *Xanthomonadales* or *Pseudomonadales*) in the 10B and LSB consortia cultured with ethanol. Relative abundances of *Xanthomonadales*, *Burkholderiales*, *Sphingomonadales*, and *Caulobacterales* increased considerably in the 14A consortium that was cultured with ethanol (Figure 15B). In addition, previously unobserved taxa within the orders of *Actinomycetales*, *Flavobacteriales*, *Cytophagales*, *Sphingobacteriales*, *Rhodobacterales*, and *Euglenozoa* were detected in the 12B consortium treated with ethanol (Figure 15B). Comparably, previously unobserved bacterial populations within the orders *Chlamydiales*, *Cytophagales*, *Rickettsiales*, *Legionellales*, and *Sphingobacteriales* were primarily detected in the 10B consortium treated with ethanol (Figure 15B).

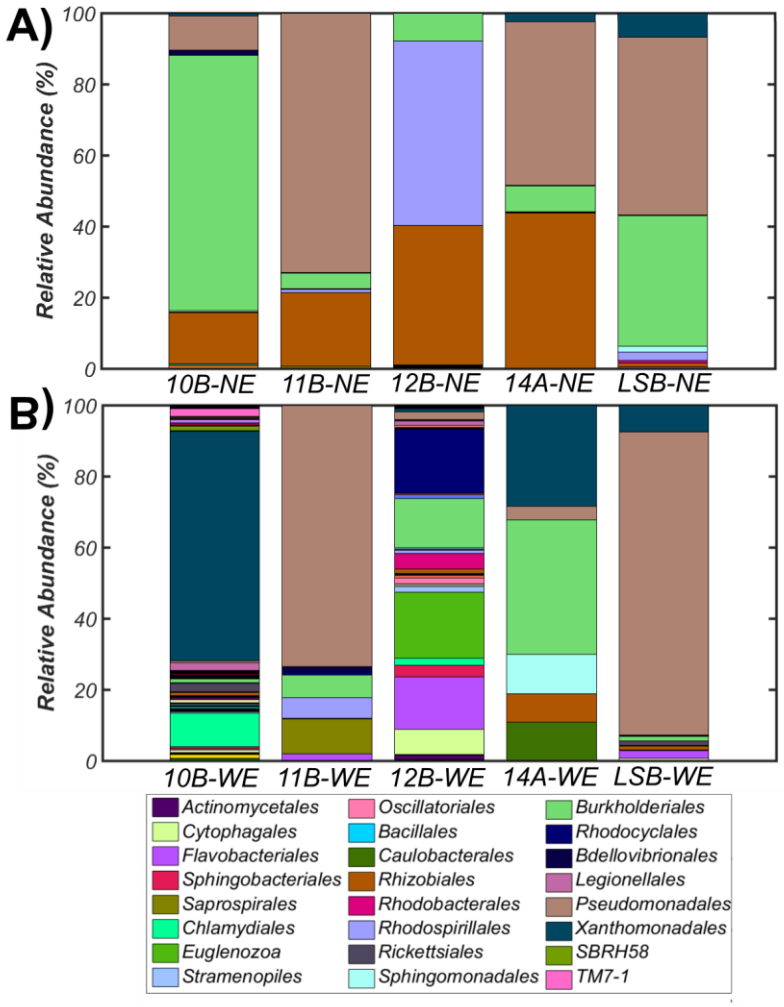

Figure 15. *General taxonomic differences in MC-LR degrading consortia isolated from lake sediment (10B, 11B, 12B, 14A) or surface water (LSB) analyzed on the order level in the (A) absence (NE) or (B) presence (WE) of ethanol. The pyrosequencing analysis was conducted immediately following the eight-day batch biodegradation experiments.*

Statistically-significant differences in taxonomic composition and abundance were observed when comparing the consortia cultured in the presence or absence of ethanol (Figure 16). For most of the MC-LR degrading consortia (three out of five consortia or above), the dominant community shifts in the presence of ethanol included an increment in bacterial orders of *Xanthomonadales*, *Pseudomonadales*, and *Burkholderiales*, and a decrement in *Sphingomonadales*, *Rhodospirillales*, and *Rhizobiales* (Figure 16). In addition, consortia with ethanol had many new community members not found in the absence of

ethanol, including the bacterial orders *Cytophagales*, *Sphingobacteriales*, *Flavobacteriales*, *Saprospirales*, *Chlamydiales*, *Rhodobacterales*, *Rhodocyclales*, *Methylophilales*, *Legionellales*, and *Rickettsiales* (Figure 16).

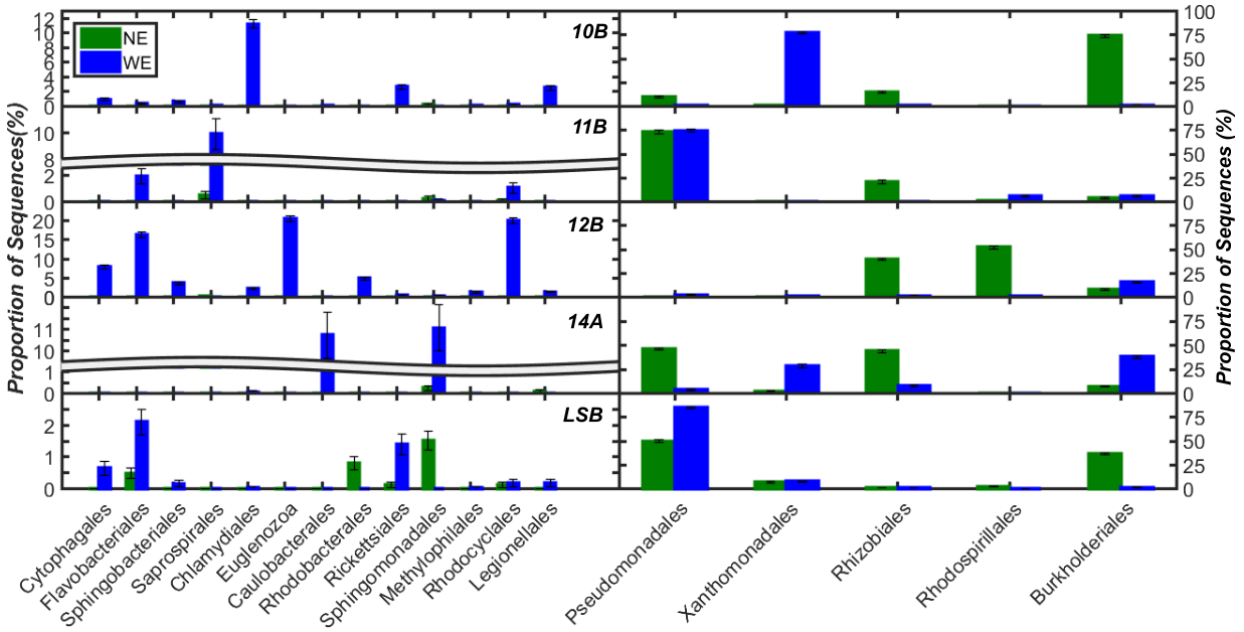

Figure 16. *Statistically-significant differences in relative abundance of the phylogenetic orders for all MC-LR-degrading consortia treated with (WE) and without ethanol (NE) (p-value < 0.05, Bonferroni corrected). Error bars represent 95% confidence intervals for relative abundances. X-axes are split to compare differences in relative abundances among isolated consortia. Y-axes are split for the 11B and 14A consortia to better visualize changes of underrepresented taxa.*

Simulated distributions in Alpha diversity metrics achieved from the MCA analysis were used to interpret changes in the within consortium bacterial community taxonomic composition and abundances in the presence of ethanol (Table 4). The range in *p*-values resulting from the multiple comparison test ($<1 \times 10^{-8}$ to 4.80×10^{-8}) demonstrated a statistically significant difference in simulated true Alpha diversity metrics across all diversity orders for the 10B, 12B, 14A, and LSB consortia in the presence of ethanol (Table 4). However, differences in simulated true Alpha diversity metrics were not statistically significant for the higher diversity orders (q = 2 and 3) when comparing the 11B

consortium (Table 4). In addition, the aggregate metagenomic stability of consortia, or the persistence of different OTUs across communities, increased for MC degrading communities in the presence of ethanol (from 53.7% to 65.7%, not depicted in Table 4).

Table 4 *- Summary of significant differences (p-values) in Alpha diversity metrics between MC-LR degrading bacterial consortia with and without ethanol addition as a function of diversity order.*

	Consortia ID				
Diversity Order	**10B**	**11B**	**12B**	**14A**	**LSB**
D^{-1}	$<1 \times 10^{-8}$	$<1 \times 10^{-8}$	$<1 \times 10^{-8}$	$<1 \times 10^{-8}$	$<1 \times 10^{-8}$
D^{0}	$<1 \times 10^{-8}$	$<1 \times 10^{-8}$	$<1 \times 10^{-8}$	$<1 \times 10^{-8}$	4.80×10^{-8}
D^{1}	$<1 \times 10^{-8}$	5.04×10^{-5}	$<1 \times 10^{-8}$	$<1 \times 10^{-8}$	$<1 \times 10^{-8}$
D^{2}	$<1 \times 10^{-8}$	1	$<1 \times 10^{-8}$	$<1 \times 10^{-8}$	$<1 \times 10^{-8}$
D^{3}	$<1 \times 10^{-8}$	1	$<1 \times 10^{-8}$	$<1 \times 10^{-8}$	$<1 \times 10^{-8}$

To address how and to what extent the true Alpha diversity indices were shifting with ethanol treatment, both the direction and magnitude of changes in the simulated distributions of true Alpha diversity metrics were investigated by incorporating an effect size calculation. Figure 17 compares the direction and magnitude of the effect sizes calculated between distributions in simulated Alpha diversity metrics with and without ethanol addition. The diversity orders are grouped into classes that give heavier (q = −1, 0), equal (q = 1), and lesser (q = 2, 3) weight to the frequencies of rare over abundant genera in each calculation.

The results of the effect size calculations indicated that, in the presence of ethanol, there was an increase in simulated Alpha diversity for the sediment consortia (10B, 11B, 12B, 14A) and a decrease in simulated Alpha diversity for the lake water consortia (LSB) when both rare and abundant genera were weighted equally (q = 1, “neutral”), which is equivalent to Shannon’s entropy value (Chao and Jost 2008). The magnitude of this shift in Alpha diversity (q = 1) varied across each consortium, with the lake water consortium

(LSB) demonstrating the largest change in magnitude (and 10B/11B the smallest change) (Figure 17). For the sediment consortia (10B-14A), there was a mixed response in the direction and magnitude of the shifts in lower (q = −1, 0) and higher order (q = 2, 3) diversity indices. Lower order diversity indices for both the 10B and 12B consortia increased by a similar level of magnitude, whereas higher order diversity indices increased for the 11B, 12B, and 14A consortia, albeit by different magnitudes (Figure 17). Comparably, a large depression in higher order diversity indices was observed for the lake water consortia (LSB) (Figure 17). These results signified that changes to the overall Alpha diversity of each consortium were attributed to: (a) more rare phyla for 10B and 12B consortia, as well as (b) more abundant phyla for 14A and LSB consortia. Due to the lack of statistical significance in higher order indices (Table 4) and similar magnitude changes among low and high diversity orders, inconclusive results were obtained for the 11B consortium (Figure 17).

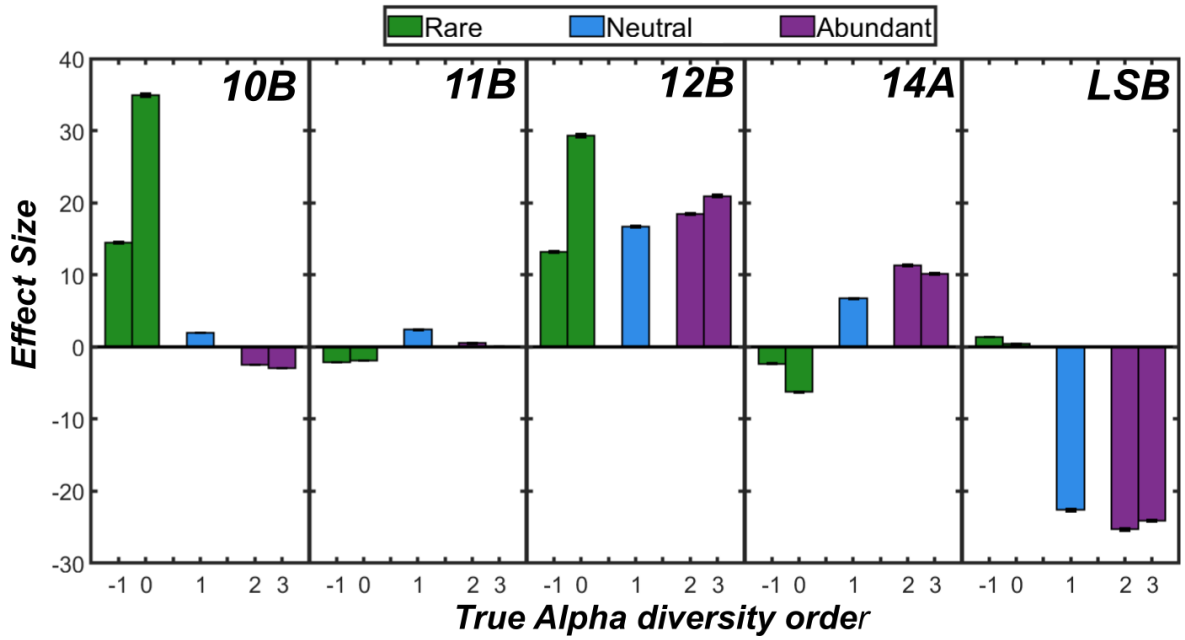

Figure 17. *Differences in effect size (direction and magnitude) as a function of true Alpha diversity order comparing MC-LR-degrading consortia treated with (WE) and without*

ethanol (NE). To clarify, the effect size is the difference in means of the distributions in diversity orders calculated for communities with ethanol as compared to without, normalized by the "average" standard deviations from both distributions $\left(\frac{\mu_{we}-\mu_{ne}}{\sqrt{\frac{\sigma_{we}^2+\sigma_{ne}^2}{2}}}\right)$*. Error bars represent 95% confidence intervals calculated for the effect sizes (Coe 2002). The diversity orders are grouped (and color coded) according to the weight placed on the frequency of rare versus abundant species during calculation. For example, diversity orders that place heavier weight on the frequencies of rare over abundant genera in each calculation (q = −1, 0) are colored in green.*

Beta diversity metrics were analyzed to compare differences in the bacterial phylogenetic composition between consortia degrading MC-LR with and without ethanol (Table 5). Statistically significant differences were observed in the phylogenetic composition for 10B, 12B, and LSB-isolated consortia that were treated with and without ethanol (p-value < 1×10^{-8}). However, the phylogenetic composition was not statistically significant when comparing the 11B and 14A consortia with and without the presence of ethanol (p-value = 1) (Table 5). These consortia demonstrated the highest phylogenetic similarity (p-value = 1) out of all the pairwise comparisons, indicating that the taxonomic composition of some MC-degrading consortia might be less sensitive to changes in the availability of alternative organic carbon sources (Table 5). Overall, the majority of consortia that were treated with ethanol (3/5) demonstrated statistically significant changes in phylogeny, which suggests that the composition of MC-degrading communities in the environment will be affected by the availability of alternative organic carbon sources.

Table 5 *- Summary of Beta diversity metrics and significance testing for MC-LR degrading bacterial consortia without (NE) and with (WE) ethanol addition. Beta diversity metrics were computed between each consortium (i.e., 10B) with and without the presence of ethanol. The corrected Bonferroni p-value was used to ascertain whether the phylogenetics of each consortium were in fact statistically significant.*

Consortia ID	Unweighted Unifrac Distance	Weighted Unifrac Distance	Bonferroni Corrected *p*-Value
10B	0.957	0.218	$<1 \times 10^{-8}$
11B	0.425	0.075	1
12B	0.921	0.382	$<1 \times 10^{-8}$
14A	0.775	0.218	1
LSB	0.561	0.112	$<1 \times 10^{-8}$

4. Discussion

This study has successfully isolated five MC-degrading bacterial consortia from lake surface water and bed sediments in the absence of a cyanobacterial bloom. The metagenomic analyses indicated highly diverse and distinct bacterial populations in each consortium, suggesting that many different MC-degrading and non-degrading populations may co-exist in each consortium. A comparison of common genera observed in the pyrosequencing results (in the absence of ethanol) to MC-degrading isolates reported in the literature indicated that species of the genera *Sphingopyxis*, *Sphingomonas, Acinetobacter, Aeromonas, Novosphingobium Pseudomonas*, *Stenotrophomonas*, *Ochrobactrum*, *Rhodococcus*, and *Steroidobacter* in the consortia may potentially comprise the MC-degrading populations (Figures B13–B16, Table B10) (see (Li et al. 2017) for an updated summary). Of these genera identified, *Sphingopyxis*, *Sphingomonas*, *Stenotrophomonas*, and *Novosphingobium* have been affiliated with MC degrading species utilizing the well-known *mlr* gene pathway (Table B10). However, this identification of degrading populations is only tentative because MC-degradation by alternative pathways (other than *mlr*) may also exist, but are currently unknown (Mou et al. 2013, Lezcano et al.

2016). As these alternative pathways are still yet to be determined, MC-degradation may be performed by a much greater number of bacterial genera than those that were identified in past research.

A comparison of the MC-degradation rates observed in this study with a compilation of half-lives reported for both MC-degrading bacterial isolates (n = 146) and microbial consortia (n = 167) indicated comparable degradation rates with those reported for consortia (Figure B18). However, the range of half-lives observed in all consortia including the present study are longer than those of MC-degrading bacterial isolates reported previously (Figure B18). In comparison with previous study designs that were focused on MC degrading microbial consortia (Eleuterio and Batista 2010, Tsao et al. 2017, Lezcano et al. 2016), this study is significantly different in which we have isolated the MC-degrading consortia by sub-culturing in minimal media enriched with MC. We have demonstrated the stability and unique individual characteristics of each isolated consortia for MC-degradation. These isolated consortia provide the opportunity to identify the effect of specific environmental conditions on MC-degradation kinetics without other interfering factors that could skew the results (i.e., the presence of uncharacterized dissolved organic matter from field samples or algal extracts). This approach was advantageous, because it allowed a parallel track of manipulation of consortia, where we could simultaneously enrich consortia with and without the presence of an organic carbon source that was supplemented with MC as the sole carbon/energy source from the onset of isolation to the batch degradation experiments performed. The large range of degradation rates reported in the literature likely reflects the complexity of environmental conditions and degradation community responses.

As the complexity of the environmental conditions was tightly controlled in this study, the main driver of observed differences in MC degradation kinetics was the initial diversity of each microbial community. High diversity, of both potential MC degrading and non-degrading populations alike, ultimately led to the isolation of distinct bacterial communities with rather unique MC biodegradation kinetic profiles. Ultimately, the trophic status of the lake of origin (i.e., productivity and nutrient availability) is an integral factor affecting bacterial community diversity (Hengy et al. 2017, Huang et al. 2017, Wobus et al. 2003, Bouzat et al. 2013, Winters et al. 2014). Although true diversity indices were presented in the results, the "raw" Shannon H values that were calculated from microbial communities in this study for both lake and sediment samples were on the same order of those reported in meso to fully eutrophic lake systems (i.e., 3–4) (Table B8) (Hengy et al. 2017, Huang et al. 2017, Wobus et al. 2003, Bouzat et al. 2013, Winters et al. 2014). These results may suggest that MC-degrading bacterioplankton community diversity may increase with trophic status (from oligo to fully eutrophic) of freshwater lakes. However, as indicated by (Newton and McLellan 2015, Yannarell and Triplett 2005, Zwirglmaier et al. 2015), the relationship between trophic status and community diversity of bacterioplankton is not so clear-cut, as other studies have reported contradictory trends (Yannarell and Triplett 2005, Zwirglmaier et al. 2015). Furthermore, it is still unclear how diversity may influence MC biodegradation kinetics in the environment as the temporal stability of these bacterioplankton communities is relatively unknown (i.e., do they achieve a relative steady state?). It is more likely that in an open system, such as the environment, the influence of community diversity on MC biodegradation may be diminished as highly variable environmental factors (such as zooplankton predation or hydrodynamics) result

in rapid succession, growth, and elimination of different populations comprising the MC-degrading community.

Ethanol addition resulted in a statistically significant increase in the simulated first order true Alpha diversity metrics for all sediment consortia along with a statistically significant decrease in first order metrics for the lake water consortium (LSB). As this first order index equally accounts for the frequency of rare and abundant genera in its calculation, it is often viewed as a surrogate of overall changes in community Alpha diversity (similar to Shannon entropy) (Chao and Jost 2008). More detailed examination of changes in the lower and higher order indices indicated that changes in the overall diversity were more affiliated with either changes in the abundance and/or presence of rare genera (for 10B and 12B) or dominant genera (for LSB and 14A). Notably, differences in true diversity orders also provide evidence as to the relative importance of species evenness and richness components to the overall diversity of each community (Chao and Jost 2008). For example, as the order of diversity approaches positive infinity, the richness component of diversity in the mathematical calculation becomes completely insignificant (and vice versa when approaching negative infinity) (Chao and Jost 2008). This interpretation suggests that changes in the overall diversity of LSB and 14A consortia were likely more influenced by changes in community evenness as opposed to richness (and vice versa for 10B and 12B consortia). In the case of the LSB and 14A consortia, the observed change in diversity (attributed to evenness over richness) either resulted in an increase in the dominance of certain community members or an increase in equitability among certain community members, respectively (which is supported by diversity profiles presented in Figure B11).

This wide variety of simulated responses in Alpha diversity metrics across each consortium was unique, as it defined several potential scenarios that organic carbon addition could trigger within MC degrading communities, which may include: (a) an increase in equitability of certain members within the community (as in 14A); (b) an enrichment (increasing richness) of previously unobserved community members (as in 10B or 12B); (c) the dominance of a few or more representative taxa within a given community (LSB); or, (d) resilience to changes in community composition (11B). Statistically significant differences in Beta diversities for 10B and 12B consortia further support the notion that the richness increased for these consortia, resulting in MC-degrading communities that were phylogenetically dissimilar with and without the addition of ethanol. It is also important to mention that, as the metagenomic stability increased with the addition of ethanol, the proportion of OTUs shared across each consortium also increased, suggesting that some of these previously unobserved community members (comprising this increase in richness) were of similar phylogenetic identity among both the 10B and 12B consortia. Moreover, the lack of a significant change in higher order Alpha diversity metrics (q = 2, 3) and Beta diversity metrics for 11B confirms some form of resiliency for the 11B consortium to changes in supplemental organic carbon concentrations.

Changes to the Alpha diversity metrics of each community have critical implications in terms of the sustenance, decline, or enhancement of community member interactions involving MC and carbon source metabolism in the environment. If, for example, scenario (c) defined above occurs for a given community, the average variety of interactions among individuals could decline, as the rare species that may be responsible for some more

obscure metabolic functions (i.e., microcystin biodegradation) might be replaced by an array of fast growing, superabundant species with more generalized metabolic functions (i.e., organic carbon metabolism) (Chao and Jost 2008). It was unclear in this study, however, whether these changes in Alpha diversity metrics consisted of primarily non-degrading or MC-degrading community members. Although we did not specifically differentiate between non-degrading or degrading community members in this study (by measuring total 16S rRNA and *mlrA* gene copy numbers), similar competitive interactions between potentially non-degrading and MC-degrading populations within the greater community in the presence of additional organic carbon have been proposed and documented by Li and co-workers (Li et al. 2011b, 2011c).

The MCA analysis provided a valuable technique to analyze the statistical significance of changes in the true Alpha diversity of each community with and without ethanol addition. Even though the results generated significant differences in true Alpha diversity metrics, it is important to recognize that these are simulated distributions, with some given uncertainty, that must be assessed accordingly. To reduce the uncertainty that is associated with these simulations, we selected studies from the literature solely analyzing the 16S rRNA of bacterial communities, with an emphasis being placed on soil and water samples only (see Table B5 for a complete summary). Most of these studies used identical platforms (454 pyrosequencing) and analysis pipelines (QIIME), which makes the extrapolation of their uncertainty and measurement error to our results very credible. In addition, these studies incorporated both biological and technical replicates in their experimental designs, which allowed our simulations to account for potential heterogeneity in community composition expected from the sampling location in addition

to uncertainty that is associated with the combined measurement and analysis processes. The main uncertainty in our simulations was derived from the relative lack of abundance data (with replication) exceeding 30% mean relative abundance (on the genera level) that was reported in the literature. This lack of data resulted in high predictive uncertainty for the expected standard deviation among replicates at mean relative abundances exceeding this value (>30%). However, since most of the abundance data on the genera level of analysis observed in our study was below this threshold, many of the simulated distributions in diversity orders had low variability (COVs < 22%, Tables B6 and B7). These results confirm that the MCA simulations were indeed valid and adequately reflected the uncertainty that is associated with actual 16S rRNA experimental replications.

Another contribution of the study was the introduction of a bi-phasic model that accounts for coupled bacterial growth and substrate degradation to describe MC biodegradation kinetics. Our results showed a more accurate estimation of MC-biodegradation kinetics, as compared to simple zero or first order models previously used to describe MC-biodegradation kinetics. This kinetic model also accounted for portions of non-biodegradable substrate observed experimentally and resulted in relevant ranges in maximum specific growth rates (Okpokwasili and Nweke 2006). We observed a sudden drop of MC and a rapid rebound of MC concentration in two degradation experiments (12B and 14A consortia without ethanol), which cannot be fully explained by the current model. These degradation kinetic profiles may be attributed to biosorption or passive uptake (facilitated diffusion) of MC either onto or into non-degrading cells, both of which have been reported for polycyclic aromatic hydrocarbons (PAHs) in the environment (Bugg et al. 2000). This explanation is similar to that proposed by Jones and co-workers (1994b),

attributing some initial removal of MC to non-specific absorption of fast growing, non-MC-degrading bacterial populations. Future investigations should be directed to adequately explain the deviation from the bi-phasic kinetics that was observed in this study and to comprehend why a portion of the MC substrate was non-biodegradable.

The sampling times and frequency for MC quantification during batch experiments, which was limited to uniform, one-day intervals, was a potential drawback of the experimental design that should be adequately discussed. As observed in Figure 14, the degradation kinetic profiles were quite similar for the 11B consortium (with and without ethanol) and very few data points were collected during the most dynamic portions of the experiment (i.e., few intermediate concentrations between 0–200 μg/L were measured). With few of these intermediate data points available for calibration, there is some uncertainty in the degradation response during critical time periods of each experiment. To review this uncertainty, another MCA was conducted by simulating experimental datasets with a greater number of time points included during model calibration as compared to the original dataset (Appendix B, Section 12). We found that including a high number of sampling points during the most dynamic time of experimentation did not significantly alter our main conclusions (i.e., ethanol still significantly slows MC biodegradation). This result was attributed to the inability of the model to mechanistically account for highly variable MC-degradation kinetics (similar to results that are presented for 12B-NE and 14A-NE in Figure 14). This uncertainty can be greatly reduced in future experiments by properly designing the sampling times and frequencies of each experiment a priori. Ultimately, application of optimal experimental design techniques with global sensitivity

analysis can improve parameter identification and the validity of statistical hypothesis tests (Rodriguez-Fernandez et al. 2007, Chu and Hahn 2010, 2013).

The isolation of MC-degrading populations in the absence of an on-going or proceeding a HAB implies that lake bacteria harbor the degradation capability in the absence of MC. These bacteria likely possess diverse metabolic pathways that allow for quick adaption to changing environmental conditions through effective, sometimes simultaneous, consumption of different sources of organic carbon. Egli (1995, 2010) has summarized the diversity of bacteria able to consume multiple carbon sources simultaneously under simulated oligotrophic conditions. Jones and co-workers (1994b) detailed the isolation of a *Sphingomonas* strain (ACM-3962) that was capable of degrading both complex carbon sources present in a peptone, yeast extract media as well as MC, supporting that MC degrading bacteria may exhibit simultaneous consumption patterns. Overall, the spatial and temporal persistence of MC-degrading bacterial populations within Southern California lakes, afforded by their diverse metabolic pathways, supports the potential application of biofiltration technologies. Shotgun metagenomic sequencing, as compared to 16S rRNA alone conducted in this study, could provide a more in depth understanding of the diverse array of functional genes that are present in these isolated MC-degrading consortia and offer some insight as to how this functional profile changes in the presence or absence of certain environmental stimuli.

However, the high sensitivity of each isolated consortia to the presence of an alternative, bioavailable carbon source, poses a significant challenge to the advent of biofiltration technology for MC removal from drinking water. Biofiltration systems targeting MC removal rely on the formation of stable bacterial communities that can

rapidly assimilate MC toxins along with other bioavailable nutrients. The results of this study provided initial evidence that the presence of alternative carbon sources (other than MC) offsets the stability of the degrading communities and retards MC biodegradation kinetics, thereby increasing MC treatment variability. In the presence of an alternative organic carbon source, there was a statistically-significant shift to the bacterial community composition, which was paralleled by a statistically-significant decline in MC-LR degradation kinetics. These results confirm previous findings by Giaramida and co-workers (2013), Li and co-workers (2011a, 2011b), and Eleuterio and Batista (2010). In addition, the pyrosequencing results identified the previously unobserved members in each community (i.e., *Cytophagales*, *Flavobacteriales*, and *Rickettsiales*) and changes in the abundance of representative taxa (i.e., *Pseudomonadales*, *Burkholderiales*, or *Xanthomonadales*). The sequencing data also detected both a statistically significant increase and a decline in existing bacterial genera that were previously affiliated with MC degradation (i.e., *Stenotrophomonas* and *Sphingopyxis*, respectively) in the presence of an organic carbon source across most consortia (Figure B17). These results may suggest different, more complex patterns of substrate utilization or preference among various individual MC-degrading populations within each consortium. Given these relatively unique community responses to ethanol addition that were observed among several isolated MC-degrading consortia, site and season specific biofiltration strategies, such as nutrient amendment (biostimulation), could be tailored to both (1) stabilize the natural MC-degrading community structure and (2) enhance metabolic functions that are related to individual MC-degrading populations comprising the greater community.

Importantly, the disparity in initial seeding concentrations between MC and ethanol employed in this study was targeted to reflect realistic nutrient conditions in most lake and reservoir environments. In these freshwater environments (throughout a range in trophic levels), MC will not be the primary carbon and energy source being metabolized by degrading bacteria, since it is often present in low background concentrations (ng/L to ug/L) and not secreted until algal bloom senescence or collapse (Merel et al. 2013, Francy et al. 2015). Instead, the presence of other bioavailable dissolved organic carbon (DOC), including other non-toxic cyanobacterial oligopeptides or exudates, represents the primary carbon and energy source for both competing degrading and non-degrading bacterial populations (Eleuterio and Batista 2010).

Furthermore, the relatively high magnitude of MC (200 µg/L) and ethanol (~300 mg/L) concentrations that were employed in this study were selected to represent worst case bloom conditions. Past sampling of lakes and reservoirs throughout the United States (U.S.) has indicated that concentrations of total MC rarely exceed 200 µg/L (Merel et al. 2013, Francy et al. 2015, Billam et al. 2006, Heiskary et al. 2014, Hollister and Kreakie 2016, Loftin et al. 2016, Howard et al. 2017), whereas total dissolved organic carbon (DOC) concentrations ranged from 0.2 to 516 mg/L (US EPA 2016b). It is important to note a considerable portion of the readily bioavailable fraction of the total DOC pool may be attributed to secreted algal organic matter, especially in HAB impacted environments (Nguyen et al. 2005, Zhou et al. 2014). Thus, the shifts in community composition and kinetics of MC degrading consortia when exposed to labile organic carbon observed in this study are reflective of shifts in composition and kinetics of degrading communities during collapse or senescence of a significant bloom event in the environment.

We further recognize the limitations of the current experimental approach because isolation based-studies have the tendency to alter MC degradation kinetics from that in the environmental setting. Culturing these isolated communities on MC as the sole carbon and energy source may have had the most significant impact on changing the original physiological state and structure of the natural community (Mou et al. 2013). Moreover, sub-culturing, which is necessary for maintaining the viability of each consortium, may have led to unintended shifts in the community composition and kinetics of substrate metabolism from initial isolation (Jiao et al. 2016). However, regardless of these unintended effects from enrichment and culture maintenance, in the absence of an in-situ tracking mechanism to follow the dynamics of different MC-degrading populations in the natural environment, isolating a consortium and studying its degradation kinetics under controlled laboratory conditions is necessary.

Improvement in the experimental design can be achieved by quantifying the total *mlr* MC-degrading population in each consortium or natural environment through the tracking of the known MC-degradation gene, i.e., *mlrA* gene, by quantitative PCR (qPCR). The *mlrA* gene copy number may be correlated with the period of lag phase in the degradation curve, such that MC-degradation can only be observed after the *mlrA* gene level reaches a certain threshold concentration. Determining the ratio of *mlrA* to 16S rRNA gene copy in each consortium or the natural environment may elucidate the difference in the degradation kinetics that was observed among different consortia. Confidence in the results would have been greatly improved if the presence of these MC-degrading populations could be directly evaluated through tracking *mlrA* gene expression by reverse transcription quantitative PCR (TR-qPCR). These analyses would have provided crucial

quantitative indications as to the active degradation bacteria. Lastly, tracking the *mlrA* and 16S rRNA gene copy number in each consortium could provide some explanation as to the high variability in growth rates experimentally observed using OD600 and flow cytometry. It is important to acknowledge here that the *mlrA* gene detection protocols that are described above will not quantify the total abundance of degrading populations within each consortium. Many previous studies have indicated that alternative degradation pathways (i.e., xenobiotic degrading) may exist and contribute to the removal of MCs in addition to the *mlr* pathway identified (Mou et al. 2013, Lezcano et al. 2016). Despite these limitations in quantifying total degrader abundances, the initial consortia composition (i.e., the proportion of MC-degrading vs. non-degrading populations) was a primary factor governing observed differences in cell growth kinetics across replicate experiments.

5. Conclusions

The results that are presented in this study exemplify the intimate link between MC-biodegradation and alternative organic carbon sources in the environment. In the presence of a readily available organic carbon source (ethanol), a statistically significant change to the taxonomic composition of the MC-degrading communities was observed. The following specific, statistically significant changes in taxonomic composition were detected with the addition of an organic carbon source: (1) an increase in the abundance of members that were previously unobserved in each community without ethanol; (2) a shift in the abundance of representative taxa (including *Rhizobiales*, *Pseudomonadales*, *Xanthomonadales*, and *Burkholderiales*); (3) a variation in the abundance of genera previously affiliated with MC biodegradation (i.e., *Sphingopyxis* and *Stenotrophomonas*); and, (4) an increase or decline in simulated Alpha diversity for sediment and lake water consortia, respectively. Changes in

simulated Alpha diversity metrics in the presence of ethanol generally agreed with trends in experimentally observed Beta diversity metrics. These changes to the community structure in the presence of an organic carbon source were paralleled by a statistically significant decline in MC biodegradation half-lives, as predicted through the application of a bi-phasic kinetic model.

The instability of the MC degrading communities in the presence of an organic carbon source presents a significant challenge to the advent of MC remediation technologies, such as biofiltration. Depending on the environmental conditions of the lake or reservoir (i.e., the trophic status), among many factors, high MC treatment variability will be expected in practice as other available DOC, as opposed to MC, may be considered as the primary carbon/energy source for many degrading populations within these greater bacterial communities. However, before biofiltration strategies to address these issues can be fully considered, the underlying mechanisms driving these changes must be further elucidated and disentangled. In addition to potential substrate competition between MC and available DOC, the potential higher order interactions between community members may change significantly in the presence of an alternative organic carbon source. Future studies should consider the isolated study of these potential mechanisms that are indicated above to more clearly identify why changes in MC-degrading bacterial community structure and degradation kinetics occurred in the presence of an alternative organic carbon source.

In addition to temperature and pH, changes in nutrient availability, such as the concentration of alternative organic carbon sources, is likely one of the many environmental factors that govern MC-biodegradation kinetics in the environment. The outcome from this study highlights the challenges in advancing biofiltration into a truly “engineered” treatment

system, as MC removal kinetics may be highly variable under different environmental conditions. As of current, biofiltration may serve as a pretreatment or post treatment system to reduce dissolved MC concentrations in drinking water. Additional treatment barriers, such as ozonation or activated carbon, are necessary to protect the safety and quality of drinking water resources.

Chapter 3: Development and Verification of a Mechanistic Model to Predict Microcystin Removal in Biological Filters

Abstract: Accurate and reliable mechanistic modelling of drinking water biological filtration treatment systems is critical to obtain insight into contaminant removal efficiency and the identification of efficient operational strategies and design practices to enhance contaminant removal. However, modelling any biological treatment system is extremely complex, where challenges reside in how to efficiently and accurately capture the key underlying processes to include in the model structure, while at the same time avoiding overparameterization and unnecessary complexity. In this chapter, a novel, steady state 1-D mechanistic model (MC-BIOFILT) was developed to adequately predict microcystin (MC) removal in biofiltration systems. This model considers the growth limiting substrate (MC) and MC-degrading bacterial cells, both in aqueous (suspended) and solid biofilm forms, as the three primary state variables affecting MC transformation. MC transport and removal was modelled by incorporating physico-chemical adsorption, advection, dispersion, as well as biodegradation by the aqueous and immobilized MC degrading populations. MC-degrading bacterial cell transformation was governed by growth (following Monod kinetics), attachment of aqueous cells to immobilized media, detachment of biofilm to aqueous cells, and decay (in addition to advective and dispserive transport). This model also captures bioclogging as a potential mechanism affecting physical transport of cells and MC substrate. A series of numerical verification experiments ascertained that the numerical solver is both accurate and stable, agreeing with all analytical solutions tested against. In addition, preliminary laboratory experiments have effectively calibrated the adsorptive and dispersive characteristics of MC transport. Future study will aim to expand

MC-BIOFILT to two dimensions and further paramterize the transport and transformation of MC-degrading bacterial cells, both in aqueous and solid biofilm forms. Moreover, a series of model validation experiments will be performed to ensure that the structure and calibrated parameters of MC-BIOFILT can adequately reproduce the real-world performance of biofiltration systems targeting MC removal.

1. Introduction and Background

Mechanistic models describing the full scope of underlying physical, chemical, and biological processes taking place during biological filtration of drinking water are critical to accurately and precisely predict the removal of toxic and noxious water quality constituents, including algal biotoxins (Rittmann and McCarty 1980, Zhang and Huck 1996, Hozalski and Bouwer 2001a, Rittmann and Stilwell 2002, Qiongqiong et al. 2008). Developing mechanistic models of these treatment systems can expand our current understanding of the governing theory describing these underlying processes, leading to improvements in full scale design and operation. Ultimately, models describing biological treatment processes may further both the operator's and engineer's comprehension of the performance of these systems under a variety of environmental, operational, and hydraulic conditions expected in practice (Rittmann et al. 2002).

Of all the advantages complex computer simulations can bring, often the most difficult question is how to efficiently structure the model based on scientific theory to produce accurate and repeatable representations of reality, within a certain level of acceptable statistical confidence. Biological treatment systems are notoriously some of the most complex systems to model, as these processes are highly variable in space and time and depend on countless physical and metabolic interactions among existing microbial

populations, many of which cannot be detected or monitored (i.e., in real time) using advanced bio-molecular techniques (Kirk et al. 2015, Azeloglu and Iyengar 2015, Rittmann et al. 2002). The environmental variables driving these microbiological treatment systems (such as pH, water temperature, nutrient concentrations) are also dynamic, wide-ranging, and difficult to monitor (Kirk et al. 2015, Azeloglu and Iyengar 2015, Rittmann et al. 2002). Moreover, the scientific theory governing the fate, distribution, and subsistence of these microorganisms and nutrients sustaining the growth of these microorganisms is a combination of several disciplines, where uncertainty may arise from multiple assumptions or conventions tailored by each. Finally, there are issues with scale up of the numerical simulations of these systems, where the behavior of one system on the laboratory scale is often not in agreement with the behavior of the system on a larger scale (Hozalski and Bouwer 2001b).

Despite the challenges identified above, the advancement in computing power over the last decade has enabled the development of new mechanistic biological models (i.e., in systems biology) that can mathematically account for the high complexity of these systems (Faust and Raes 2012, Song et al. 2014). However, many of the mechanistic, systems biology models that have been developed to describe microbial growth and community (i.e., metabolic) interactions may suffer from over-parameterization and inclusion of unnecessary complexity (Banga and Balsa-Canto 2008, Chis et al. 2011b, Villaverde and Banga 2014). Overparameterization refers to the fact that any mathematical model, no matter how far away from the true representation of reality, can fit the experimental data, given that the number of parameters in the model structure is sufficient to fit the data (Chis et al. 2011b, Villaverde and Banga 2014). But, are the parameters in the model realistic or

even physically relevant? Can each parameter be measured independently of the system at hand? Is all the complexity included in the model structure absolutely necessary to reproduce the experimental data? After considering these key questions, it is apparent that a model structure that minimizes the number of physically relevant parameters (all of which can be measured independently), avoids unnecessary complexity, and ensures computational efficiency is advantageous in the long run.

As of current, little research has been conducted regarding the development of numerical simulations to predict algal toxin removal in biological filters. However, a significant amount of modelling work has been conducted regarding the removal of organic compounds (more specifically biodegradable dissolved organic carbon or assimilable organic carbon) in these filtration systems (Rittmann and McCarty 1980, Billen et al. 1992, Laurent et al. 1999, Zhang and Huck 1996, Hozalski and Bouwer 2001a, 2001b, Rittmann et al. 2002, Rittmann and Stilwell 2002, Qiongqiong et al. 2008). Rittmann and McCarty (1980) was one of the pioneering studies to model biofilm processes and apply the same principles in drinking water treatment filtration applications. The model developed in their study assumed that a steady state biofilm could exist in porous media, where a thickness of biofilm could be predicted from a general bulk substrate concentration existing in the interstitial pore space. Standardization of this model for drinking water treatment applications was presented in Rittmann (1990) that developed operational principles and guidelines for drinking water treatment biological filtration systems based on four model parameters and normalized loading curves. Details of the actual model parameters, theoretical approach, and loading curves developed were presented in the background section for reference.

Billen et al. (1992) developed the CHARBROL model for simulation of biodegradable dissolved organic matter (BDOC) in the granular biological activated carbon process during drinking water treatment. The CHARBROL model took into consideration three different fractions of biodegradable organic carbon with different assimilation capacities (i.e., rapid/slow degradation) and showed that BDOC removal was directly proportional to the influent BDOC concentration at specific empty bed contact times (EBCTS) (Billen et al. 1992).

Zhang and Huck (1996) introduced another steady state biofilm model for analyzing the removal of assimilable organic carbon (AOC) in plug flow biological reactors, which was similar to that proposed by Rittmann and McCarty (1980). This study determined that the dimensionless empty bed contact time, which is a function of the actual empty bed contact time, specific surface area of the medium, and the ease of biodegradation/diffusion in the biofilm, is an effective predictor for effluent AOC concentrations, which appropriately described the linear experimental relationship observed between influent AOC concentration and effluent AOC concentration.

Hozalski and Bouwer (2001a, 2001b) presented the first transient biofilm model that was applied and validated to predict biodegradable organic matter (BOM) removal in drinking water treatment practice. The Hozalski and Bouwer model incorporated substrate (BOM) transport, aqueous cell transport/growth, as well as biofilm thickness growth/loss mechanisms. An innovative feature in the model developed by Hozalski and Bouwer (2001a, 2001b) was the introduction of an instantaneous biofilm loss term from the backwashing process.

More recently, a comprehensive biofiltration model based on similar principles to Rittmann and McCarty (1980) was developed by Rittman et al. (2002) to predict the removal of multiple species of water quality constituents as mediated by several types of bacteria within a biofilm community (heterotrophs, autotrophs, etc.). This model, called the Transient State Multiple Species (TSMS) took into account the dynamics of biofilms during drinking water treatment by considering four different bacteria types (heterotrophs, ammonia oxidizers, nitrite oxidizers, inert biomass), seven chemical species (biodegradable organic matter, ammonium nitrogen, nitrite/nitrate nitrogen, soluble microbial products, dissolved oxygen), eight distinct chemical reactions to describe the utilization of these species in the biofilm, substrate transport of species in the biofilm/porous media, growth, decay, lysis of biomass, and biofilm detachment processes.

Qiongqiong et al. (2008) developed a relatively simple steady state, analytically based simulation of biological filtration of natural organic matter (NOM) to Hozalski et al. (2001a,2001b) for drinking water treatment applications without considering diffusion of substrate within the biofilm or mass transfer limitations of substrate transport from the bulk liquid to the surface of the biofilm (which was fundamental to most previous models proposed by Rittmann et al.). The model introduced by Qiongqiong et al. (2008) considered the transport of natural organic matter (NOM), aqueous cells (attachment only), and growth/detachment of solid biomass cells (and no effects such as backwashing).

The main drawback to these previously developed models is the fact that they attempt to integrate microscopic (pore scale) approaches into a macroscopic (continuum based) model structure. The microscopic approaches that are included are generally focused on substrate mass transport to the biofilm surface as well as diffusive transport of substrate

throughout the biofilm. The parameters associated with the microscopic transport, including the molecular diffusion coefficient in liquid and in the biofilm for most water quality constituents, are generally difficult to constrain and measure independently. Moreover, the significance of these parameters, from an operational or design standpoint is rather limited outside the realm of research. Thus, it may be more beneficial to "back out" and consider only the macroscopic level of processes occurring within the porous media of a biological filter, to not only simplify the processes occurring, but to provide a realistic framework for design, operation, and monitoring.

Importantly, all of the currently published biological filtration models do not consider important feedback processes between the microorganism growth and the hydraulic conductivity or porosity of the media. This mechanism, also referred to as "bioclogging," is a critical process affecting the development of the flow field throughout the course of the filter operation (Thullner et al. 2002a, 2002b). The study of bioclogging has been introduced in the groundwater field and is especially relevant for bioremediation processes, as it produces heterogeneity in the availability of electron donors (i.e., organic carbon) and acceptors (i.e., oxygen) over time. In effect, the formation of a biofilm on immobilized media from microorganisms within the influent water will block the pore space over time and result in a channeling or the development of preferential flow paths. This biological-physical feedback process affects the dynamic availability of substrate within a biological filter, which ultimately influences the stability of these biofilm communities. Including this bioclogging feedback process will also provide valuable information on the development of head loss across the filter over time for optimal hydraulic performance.

A more pertinent aspect that has not yet been introduced in these previous simulations is the advent of modelling the change in community structure of the microorganisms over time that are actually present and performing the degradation. A critical assumption that each of these previous studies has made is that all microorganisms are capable of degrading any given substrate at any given time, which may be far from the case in the dynamic environment of a biofilter. Although Rittmann et al. (2002), Rittmann and Stilwell (2002) has considered the fluctuation in abundance and distribution of different communities (autotrophs, heterotrophs, inert biomass) these studies do not attempt to define what populations within these communities are actually performing the task at hand. This assumption may drastically overestimate the actual treatment efficiency of the system, given that the presence of certain bacteria to perform the degradation are transient in nature, and may change due to different environmental stimuli (nutrients) or hydraulic conditions (fluctuations in the HLR). Including this change in the bacterial community structure may also better reflect the removal of algal toxins in biological filtration systems, as the removal efficiencies of toxins greatly depends on the presence of microorganisms that are specific to the degrading process (Ho et al. 2012a).

Therefore, considering the previous limitations in mechanistic biofiltration models presented in the scientific literature, the focus of this chapter will be to develop and validate an efficient and reliable one- and two-dimensional numerical model that can simulate the biodegradation of microcystin within a biological filter. The numerical simulations will be verified using developed analytical solutions and parameters calibrated using a sequence of experimental, laboratory-based investigations. Ultimately, the primary objective after developing this model will be to achieve an improved predictive

understanding of the most important biological treatment mechanisms and to identify key operational and design parameters that improve the reliability and efficiency of algal biotoxin removal in biofiltration systems.

2. Experimental and Mechanistic Modelling Approach

2.1 Overview of the Mechanistic Model

The mechanistic model developed in this research to predict biological filtration of microcystin toxins integrated theory and principles from contaminant fate and transport, colloid/deep bed filtration, and bioclogging. A macroscopic approach was adopted to model each of the unique processes occurring during biological filtration. The core conceptual structure of the mechanistic model accounts for water flow through saturated porous media, microcystin transport and degradation, aqueous biomass transport and transformation (attachment, growth), as well as solid biomass transformation (decay, growth, detachment) (Figure 18). The governing equations for all the representative processes are first assumed to be at steady state, as the time scale for biomass growth is considerably longer than the time scales associated with water flow, and microcystin/aqueous cell transport. However, since the time scales of both microcystin and aqueous biomass transport are equivalent, the numerical solutions predicting the fate/transformation of these species were coupled. The specific structure of the numerical solution strategy will be further discussed after a brief review of the governing ordinary and partial differential equations for fluid flow, microcystin/aqueous biomass transport, and solid biomass transformation processes.

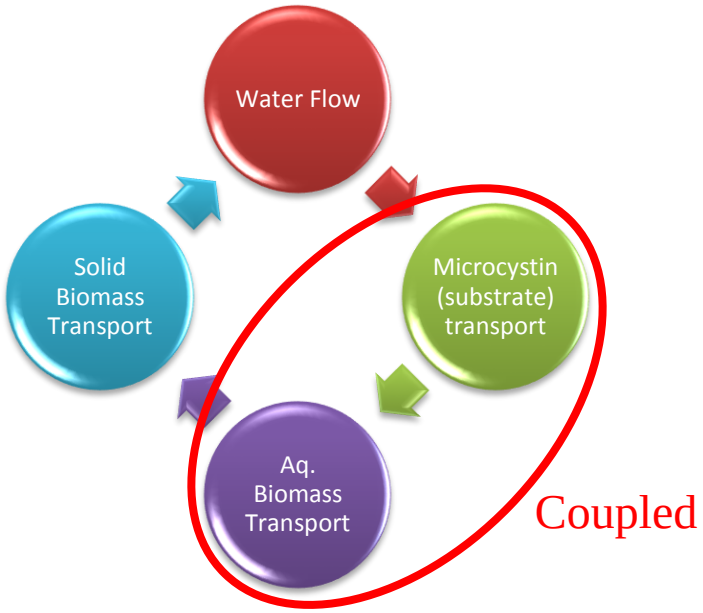

Figure 18. *The main conceptual structure of the mechanistic model developed in this study.*

Saturated water flow was accounted for in the computational model by solving the steady state groundwater flow equation (for confined flow, change in storage is negligible, Equations 1 and 2), assuming that the media was isotropic and homogenous. This assumption was valid as biofilter media has a high uniformity coefficient, and typically consists of medium-coarse silica sand (Evans et al. 2013a, 2013b). Equation 1 is often referred to as the 1D Laplace equation, where T_{xx} refers to the transmissivity of the porous media (m^2/day), h the head (m), and Ss the specific storage of the media (unitless). It is important to note that the x-direction signifies water flow in the vertical direction, which is assumed to be from the top to the bottom of the biofilter.

$$T_{xx}\frac{\partial^2 h}{\partial x^2} = S_s\frac{\partial h}{\partial t} \quad (1)$$

$$T_{xx}\frac{\partial^2 h}{\partial x^2} = 0 \quad (2)$$

The steady state fate and transport of microcystin-LR substrate concentration (C), aqueous bacteria cells (X_a), and solid biomass (X_s) were taken into account from existing

contaminant transport theory (Kildsgaard and Engesgaard 2001, Bear and Cheng 2010, Bear 2013). The three fundamental equations describing the steady state (left hand size is equivalent to zero) transport of these species throughout porous media were defined below in Equations 3-5 (in 1D, units are given in length (L), time (T), and mass (M)). The equation for microcystin transport (3) was modified assuming linear sorption characteristics of the porous media. We also considered nonlinear Monod kinetics (as described in the upcoming section) for microbial growth, attachment of suspended biomass, detachment of solid biomass, and decay of suspended and attached biomass.

$$R\frac{\partial C}{\partial t} = D\frac{\partial^2 C}{\partial x^2} - v\frac{\partial C}{\partial x} - \frac{\mu_{max}}{Y}\frac{C}{K_s+C}\sigma_a X_a - \frac{\mu_{max}}{Y}\frac{C}{K_s+C}\sigma_s X_s I_{bio}\frac{\rho_{Bulk}}{n} \quad (3)$$

$$\frac{\partial X_a}{\partial t} = D\frac{\partial^2 X_a}{\partial x^2} - v\frac{\partial X_a}{\partial x} + \mu_{max}\frac{C}{K_s+C}\sigma_a X_a - k_d X_a + \frac{\rho_{Bulk}}{n}k_{det}X_s - k_{att}X_a \quad (4)$$

$$\frac{dX_s}{dt} = \mu_{max}\frac{C}{K_s+C}\sigma_s X_s I_{bio} - k_d X_s - k_{det}X_s + \frac{n}{\rho_{Bulk}}k_{att}X_a \quad (5)$$

Where C is the concentration of microcystin-LR (M/L^3), t is the time (T), x is the filter depth (L), X_a is the concentration of bacterial aqueous species (M/L3), X_s is the concentration of solid biomass (M/M), D is the longitudinal dispersion coefficient (L^2/T), v is the interstitial pore water velocity (L/T), μ_{max} is the maximum specific growth rate (1/T), Y is the yield coefficient, K_s is the half saturation constant (M/L^3), k_d is the first order decay coefficient (1/T), k_{det} is the first order detachment coefficient (1/T), k_{att} is the first order attachment coefficient (1/T), ρ_{bulk} is the bulk density (M/L^3), n is the porosity (unitless), R is the retardation coefficient (unitless), and σ_a and σ_a represent the fraction of the total bacterial populations that are active microcystin degraders (explained in section 2.2).

The I_{bio} term was included from bioclogging theory to represent the maximum available space for biomass to grow given some initial clean bed porosity (Kildsgaard and

Engesgaard 2001) (Equations 6 and 7). In Equations 6 and 7, X_{max} represents the maximum theoretical biofilm mass that can fit in the available pore space, which is a function of the clean bed porosity (n, unitless), the bulk density of the porous media (ρ_{bulk}, M/L^3) and the density of the solid biofilm ($\rho_{x,s}$, M/L^3). The I_{bio} term should theoretically be included to account for the subdued transport of nutrients to the solid biomass only as a result of clogging of the available pore space. The three equations presented in the following section were used to estimate the corresponding change in hydraulic conductivity from a given change in solid biomass (X_s).

$$I_{bio} = \frac{X^{max} - (X_s)}{X^{max}} \quad (6)$$

$$X^{max} = n\frac{\rho_{x,s}}{\rho_{bulk}} \quad (7)$$

2.2 Describing Bacterial Growth, Decay, Biofilm Attachment, and Biofilm Detachment

As compared to first order kinetics, the Monod model is a more realistic expression of microbial growth and is based from experimental observations expressing the bacterial growth rate (dX/dt) as a hyperbolic function of the limiting primary substrate concentration (S or C) (Figure 19). At low initial substrate concentrations, the relationship between microbial growth rate and substrate concentration is linear, whereas the relationship between microbial growth rate and substrate concentration at much higher substrate concentrations is not concentration dependent (and asymptotic). Two model parameters are required to make this prediction between bacterial growth rate and primary substrate concentration, including the maximum growth rate (μ_{max}) and the half saturation constant (K_s, the substrate concentration corresponding to half of the maximum growth rate). In addition, the yield coefficient (Y) is required in the substrate utilization

kinetics, which relates the amount of biomass produced for each mass unit of substrate consumed (Shuler and Kargi 2002, Kargi 2009).

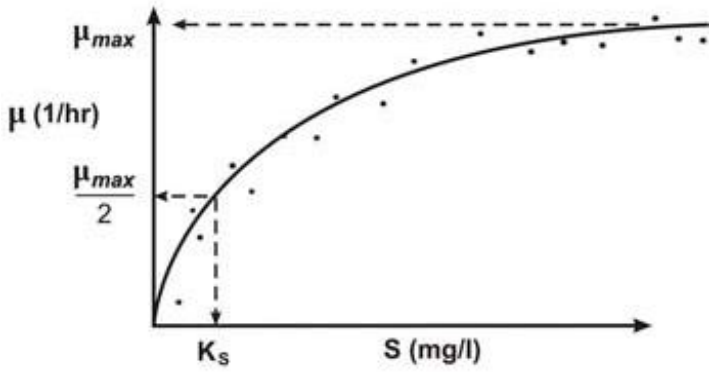

Figure 19. *The Monod model of bacterial growth and substrate utilization.*

The bacterial growth and substrate utilization rates can be expressed mathematically by Equations 8 and 9 below, where each ODE is coupled and dependent on the maximum growth rate, microorganism concentration (X), the half saturation constant, and the current substrate concentration (C).

$$\frac{dX}{dt} = \mu_{max} X_{a,s} \left(\frac{C}{Ks+C}\right) \tag{8}$$

$$\frac{dC}{dt} = -\frac{\mu_{max}}{Y} X_{a,s} \left(\frac{C}{Ks+C}\right) \tag{9}$$

It is important to note that the biokinetic parameters (μ_{max}, K_s, and Y) will vary with the type of microbial biomass considered (i.e., solid versus aqueous biomass), and the model was constructed to explicitly account for this difference. Again, one of the main differences between the aqueous and solid biomass fractions of degrading bacteria was that the solid biomass (X_s) represents the weight of biomass normalized by the weight of solids (i.e., sand grains).

An innovative concept proposed in the structure of this mechanistic model is explicitly accounting for the presence of bacteria within the biofilm community that can

actually perform the specialized function of microcystin (MC) degradation. As it is expected that the MC-degrader population may change significantly over time and when exposed to different environmental and hydraulic conditions, it will be important to account for the fraction of the total bacteria population that can readily metabolize MC. A new model parameter, $\sigma_{a,s}$, will relate the fraction of microcystin degrading population to the total bacterial population for both aqueous and suspended biomass. As observed in Equations 10 and 11 (where aqueous biomass is portrayed), this parameter will be added to the Monod model describing growth and MC degradation to scale both the active solid and aqueous bacterial biomass that is actually growing on the microcystin (i.e., $X_{a,d}$ or $X_{s,d}$) to the total bacterial population (X_a or X_s) within the transport equations introduced above.

$$\sigma_a = \frac{X_{a,d}}{X_a} \tag{10}$$

$$\frac{dX_a}{dt} = \mu_{max} \frac{C}{K_s + C} \sigma_a X_a \tag{11}$$

The predictive model proposed in this research will consider the transport of aqueous bacteria as an integral component to the development of biofilms (solid biomass) that mediate degradation of microcystin toxins. The first and foremost mechanism in which biofilms form and proliferate is related to bacterial attachment. As mentioned in detail throughout the background chapter of this dissertation, many electrochemical forces and interactions between the bacterial particles and the sand grain (collector) surfaces, as well as hydrodynamic forces, influence the extent (reversibility) of attachment and frequency of contact with the grain surface.

In this study, we consider the attachment of bacteria as a linear first order process, similar to models presented for a variety of porous media, deep bed filtration, and colloid

filtration studies (Kildsgaard and Engesgaard 2001, Brovelli et al. 2009). The first order attachment coefficient can be calculated according to existing theoretical relationships developed throughout deep bed and colloid filtration theories and depends on two main parameters, the collision efficiency $\propto$ and collector efficiency η (Equation 2) (Rajagopalan and Tien 1976, Ren et al. 2000, Schiebe et al. 2007). The collector efficiency represents the probability of bacterial contact with a given grain surfaces, whereas the collision efficiency represents the lumped probability of bacterial attachment upon contact with the grain surface (due to chemical adsorption and all other lumped forces or means).

$$k_{att} = \frac{3(1-\theta)v_p \propto \eta}{2d_g} \quad (12)$$

Where θ is the porosity, v_p is the pore water velocity, d_g is the representative grain diameter (d10), $\propto$ is the collision efficiency, and η is the grain collector efficiency.

The grain collector efficiency (η) can be estimated using the following theoretical relationship developed from deep bed filtration theory (Equation 13, Rajagopalan and Tien 1976):

$$\eta = 4A_s^{1/3}N_{Pe}^{-2/3} + A_s N_{Lo}^{1/8} N_R^{15/8} + 0.00338 A_s N_G^{1.2} N_R^{-0.4} \quad (13)$$

The A_s, N_{Pe}, N_{Lo}, N_R, N_G dimensionless numbers above can be defined in the following equations.

1) A_s is a dimensionless number that quantifies the effects of nearby particles on contact efficiency (Equation 14):

$$A_s = \frac{2(1-\gamma^5)}{2-3\gamma+3\gamma^5-2\gamma^6} \quad (14)$$

Where γ is the porosity constant defined below (Equation 15):

$$\gamma = (1-\theta)^{1/3} \quad (15)$$

2) N_{Pe} is a dimensionless number that quantifies effect of diffusion on particle grain interactions (Equation 16):

$$N_{Pe} = \frac{3\mu\pi v_p d_g d_p}{kT} \quad (16)$$

Where μ is the viscosity of water, v_p is the pore water velocity, d_g is the representative grain diameter, d_p is the diameter of the bacterial particle, k is the Boltzmann constant, and T is the fluid temperature.

3) N_{Lo} is a dimensionless number that quantifies London-Van der Waals attraction for bacterial adhesion on grain surfaces (Equation 17):

$$N_{Lo} = \frac{4H}{9\pi\mu d_p^2 v_p} \quad (17)$$

Where H is the Haymaker constant, v_p is the pore water velocity, μ is the viscosity of water, and d_p is the diameter of the bacterial particle.

4) N_R is a dimensionless number that quantifies the interception of bacteria for grain/particle collisions (Equation 18):

$$N_R = \frac{d_p}{d_g} \quad (18)$$

Where d_p is the diameter of the bacterial particle and d_g is the representative grain diameter (d10).

5) N_G is a dimensionless number that quantifies amount of sedimentation of bacteria on the grain surface (Equation 19):

$$N_G = \frac{g(\rho_p - \rho_f)d_p^2}{18\mu v_p} \quad (19)$$

Where ρ_p is the density of bacterial particles, ρ_f is the density of the water, v_p is the pore water velocity, μ is the viscosity of water, g is the gravitational acceleration constant, and d_p is the diameter of the bacterial particle.

6) The collision efficiency ($\propto$) can be estimated either in the laboratory or fitted empirically from experimental data.

Bacterial transport is further affected by potential decay (cell lysis or death) and release of bacterial cultures from sand grain surfaces that may occur due to reversible detachment mechanisms (Rittmann et al. 1982b, Engesgard et al. 2002, Brovelli et al. 2009). Reversible detachment mechanisms may include release of bacteria due to hydrodynamic conditions within the porous media and fluid shear. Therefore, we extend the aqueous bacterial transport model to include bacterial detachment and decay mechanisms and assume a linear, first order coefficient for each, similar to the attachment mechanism proposed.

Rittman et al. (1982b) developed an empirical relationship to estimate the first order detachment coefficient as a function of fluid shear, which was later adopted by Brovelli et al. (2009). This quantitative estimate of the reversible biomass loss is also adopted in this proposed research to predict the bacterial detachment properties of the porous media (Equation 20).

$$k_{det} = C_d \left[\frac{\mu(1-\theta)^3 v_p}{\theta^3 {d_g}^2 M} \right] \quad (20)$$

Where *Cd* is a unitless, empirical parameter (2.29E-06), μ is the viscosity of water, θ is the porosity, v_p is the pore water velocity, *M* is the specific surface area of the porous media, and *dg* is the representative grain diameter (d_{10}).

2.3 Accounting for Bioclogging of Biofilter Media

Bioclogging of a porous medium can be defined as a reduction in pore space due to the growth of microorganisms which has a direct effect on the available volume for fluid flow (Thullner et al. 2002a, 2002b, Thullner 2010). Bioclogging is considered in this study as a critical mechanism that affects the volumetric throughput of water in a given biological filtration unit due to the growth of biofilms on immobilized porous media. Several theoretical models have been developed to predict the mechanisms associated with bioclogging in porous media and differ according to the scale studied (i.e., macroscopic vs. microscopic). Microscopic models generally consider the distribution of biomass growing on a particular surface, which have been proposed to range from continuous biofilms, discrete micro-colony structures, and plugs near pore throats (Clement et al. 1996, Thullner 2010). The biofilm approach assumes continuous and uniform biomass growth on porous media, whereas the micro-colony approach assumes discrete (patchy), heterogeneous colony communities that contribute to pore clogging (Taylor and Jaffé 1990, Vandevivere and Baveve 1992). Other microscopic models assume that porous media can be defined as a bundle of parallel pores (capillary tubes) and biomass grows on the inside lining of the tubes, contributing to plug formations (Vandevivere 1995). Macroscopic models do not address this initial distribution of biomass or propose any specific growth patterns of biomass and take a spatially averaged approach to measuring biomass (Clement et al. 1996). Clement et al. (1996) argued that macroscopic models were theoretically more

sound as discrepancies for microscopic models in combining representative elementary volume (REV) scale models with continuum-based models of fluid flow (Darcy flow) may arise.

This study will integrate the classic macroscopic approach analytically derived by Clement et al. (1996) to predict the effects of bioclogging on biofilter operation. This model was also adopted by other more current studies for 2D analysis of the effects of bioclogging on fluid flow through porous media (Kildsgaard and Engesgaard 2001, Brovelli et al. 2009, and Seifert and Engesgaard 2012). This macroscopic approach first assumes that biofilm growth in the porous media simply affects the initial porosity, regardless of the colony distribution. Therefore, the total volume of the pore space occupied by biomass ($n_{X,s}$) can be approximated by the following expression (Equation 21):

$$n_{X,s} = \frac{X_s \rho_{bulk}}{\rho_{X,s}} \tag{21}$$

Where X_s is the concentration of solid biomass (kg biomass/kg soil), ρ_{bulk} is the bulk density of the soil (kg soil/m3 total volume), and $\rho_{X,s}$ is the density of biomass (kg biomass/m^3 biomass).

The biomass affected porosity (n) can then be derived assuming some initial clean bed porosity (n_{clean}) (Equation 22):

$$n = n_{clean} - n_{X,s} \tag{22}$$

The relation between permeability (k, hydraulic conductivity) and porosity can then be derived from either the Van Genuchten or Brooks-Corey soil-water retention functions (Clement et al. 1996). This resulting mathematical relationship relating hydraulic conductivity change and porosity change is presented in Equation 23 for reference. The

advantage of this analytical relationship is that no model fitting parameters are required, as the biomass density and solid biomass concentrations can be determined experimentally.

$$\frac{k}{k_{clean}} = \left(1 - \frac{n_{X,s}}{n_{clean}}\right)^{19/6} = (1 - aX_s)^{19/6} \quad (23)$$

Where a is a scaling factor, $a = \frac{\rho_{bulk}}{n_{clean}(\rho_{X,s})}$, and k is the hydraulic conductivity.

2.4 Numerical Implementation of the Mechanistic Biofiltration Model (MC-BIOFILT)

The numerical solution of the steady state groundwater equation involved a finite volume discretization technique (centered difference for dispersive term) and explicit matrix solution. Similarly, the two coupled transport equations (microcystin/aqueous cells) were solved numerically using a cell centered, finite volume-based discretization technique. A centered difference approximation was used to approximate the dispersion term and a first order upwind scheme was applied to approximate the advective term. Since the transport equations included a non-linear term (Monod Kinetics), a Picard iteration was introduced to iteratively solve for the correct numerical solutions. In addition, the microcystin and suspended biomass transport equations were coupled and solved simultaneously using an explicit matrix solution. Finally, the solid biomass growth was solved using a 4th order Runga Kutta scheme over the defined time step.

The numerical solutions were primarily developed for an infinite step pulse type boundary condition at the filter inlet obeying the following criteria. Future experimental methods will incorporate a time limited step pulse type boundary condition at the inlet of the column for comparison (Equations 24 and 25).

$$C(x = 0, t) = C_0 \quad (24)$$
$$C(x, t = 0) = 0 \quad (25)$$

The boundary condition at the outlet of the column was determined as follows (Equation 26):

$$C(x = L, t) = \frac{\partial C}{\partial X} \tag{26}$$

The specific structure of the numerical model solution can be more clearly explained graphically (Figure 19). The user first specifies all of the necessary input to run the model, including the physical characteristics of the filter (length/width/number of computational points), the operational characteristics of the filter (hydraulic loading rate (HLR)), temporal dimensions (run time, T, number of time steps), microbial associated parameters (specific growth rate, yield coefficient, initial microorganism concentrations), media characteristics (bulk density, dispersion coefficient, d_{10}), influent water characteristics (viscosity, initial concentration of MCLR, density), and other physical parameters. Although the user specifies the number of time points/filter run time, the time step is automatically updated during the model evaluation (solid biomass solver) to correspond to a maximum increase in 0.05% of the initial biomass concentration. This prevents unnecessary large jumps in solid biomass concentration.

The first step in the model evaluation process is to solve for the steady state head and velocity field across the filter. After the steady state velocity field is determined, the steady state transport of microcystin and aqueous cells is solved simultaneously. Next, the solid biomass is solved for using the initial time step as a guess. If the resulting change in biomass is too large (> 0.05% of initial), the time step is reduced, and a new biomass is solved for, where the time step value is updated (as indicated above). With the new biomass concentration, one of three relationships between solid biomass/porosity and hydraulic conductivity is used to update the hydraulic conductivity field, which further

changes the steady state head field in the next model evaluation. Once the filter run time is reached, the model outputs the concentration, aqueous biomass, hydraulic conductivity and solid biomass fields.

The main assumptions introduced with this model include the following: 1) the water quality does not change during operation (i.e., temperature/influent microcystin concentration/biomass composition is stationary); 2) microcystin is the limiting substrate available for growth (nitrogen and phosphorus are available to sustain growth, organic carbon does not affect growth); 3) substrate is readily available in the pore space and to microorganisms in the biofilm matrix (no mass transfer resistance or diffusion limitations in the biofilm) 4) electron acceptor concentration (oxygen for heterotrophic bacteria) is never limiting and no mass transfer limitations or diffusive transport within the pore space/biofilm; 4) dispersion coefficients are constant in time (do not update with velocity field); 5) no immobile zones exist within the porous media (OK for homogenous/isotropic media); 6) Monod kinetics can adequately approximate growth and substrate utilization kinetics (no lag phases); 7) only MC-degraders can degrade microcystin (growth rates are not identical in suspension and in immobilized biofilms). These assumptions allow the model to capture the breadth of fundamental processes occurring within the biological filter (bacterial attachment, growth, decay, detachment, and transport) without adding too much complexity and avoiding over parameterization.

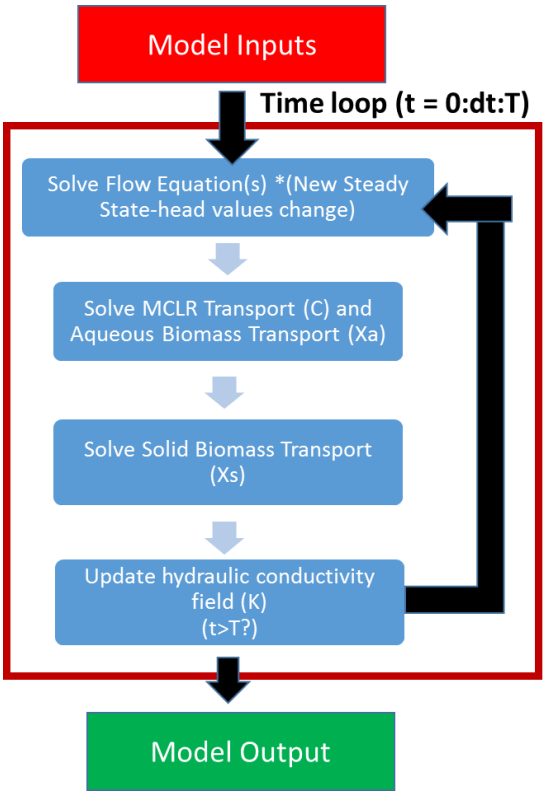

Figure 20. *Detailed structure of the MC-BIOFILT model evaluation procedure.*

3. Preliminary Results and Discussion

3.1 1-D Model Verification Studies

A series of detailed model verification studies were carried out to compare the numerical solutions developed in *MATLAB* (*Mathworks*, Inc., r2015b) to analytical solutions that had been previously derived. These verification studies encompassed comparisons of the numerical output to: a) first order reaction, analytical models, b) non-linear reaction, analytical models, and c) coupled reaction, analytical models. By considering this full range in model verification studies, it was expected that the behavior of the numerical model (i.e., the stability and accuracy) would be adequately characterized.

3.1.1 First Order Reaction Models: Analytical Verification Study #1

In the initial model verification study, a set of steady state, first order analytical solutions were applied for preliminary comparison with numerical model simulations. For

the initial model verification procedure, we only included first order biodegradation, no dispersion, and advection transport and reaction processes (Equations 27 and 28).

$$0 = -v\frac{\partial C}{\partial x} - K1(C) - K2(C) \quad (27)$$

$$C(x) = C_0 e^{(\frac{-K1-K2}{v})x} \quad (28)$$

Where K1 and K2 correspond to the following (Equations 29 and 30):

$$K1 = \frac{\mu_{max}}{Y} * X_a \quad (29)$$

$$K2 = \frac{\mu_{max}}{Y} * \frac{\rho_{bulk}}{\emptyset} * I_{bio} * X_s \quad (30)$$

In Equations 29 and 30, X_a and X_s are vectors (in the vertical direction of the filter) and are specified by some important initial conditions. For simplicity, we assumed that X_s was uniformly distributed with depth (x) and X_a was constant at the inlet, with no initial presence throughout the depth of the biofilter.

Table 6 summarizes the distribution of model parameters incorporated in this initial round of model verification study. The hydraulic loading rates (HLRs) considered represent the full range of HLRs encountered in practice (min, median, and max) (Evans et al. 2013a, 2013b). Microbial growth associated parameters were also selected from median reported values from studies examining the microbial growth characteristics of biofilm communities degrading organic carbon substrates in laboratory scale filtration units (Rittmann et al. 1986). Similarly, media characteristics were chosen based on the similarity to those expected in full scale practice (Evans et al. 2013a, 2013b). The comparisons between numerical and analytical models were made at three different Courant ($Cr = \frac{v\Delta t}{\Delta x}$, where v is the interstitial pore water velocity, Δt the time step, and Δx the grid size) numbers to assess the degree of numerical dispersion of the analytical solution for different hydraulic

loading rates. Peclet numbers ($Pe = \frac{v\Delta x}{D}$, where Δx is the grid size, v the interstitial pore water velocity, and D is the dispersion coefficient) were not listed here given that the initial comparisons did not include the effects of dispersion.

***Table 6**- Summary of Values used in the Initial Numerical/Analytical Solution Comparisons*

Variable Name	Symbol	Nominal Value	Units
Filter length	x	1	m
Number x computational points	$nxpoints$	100	unitless
Initial concentration	C_0	10	µg/L
Aqueous biomass concentration	Xa	6E-05	Kg cells/m^3
Solid biomass concentration	Xs	8E-06	Kg cells/Kg grains
Cell Maximum Growth Rate	μ_{max}	8.3E-03	1/second
Half Saturation Constant	K_s	1.2E-03	Kg MCLR/m^3
Yield coefficient	Y	0.2	Kg cells/Kg MCLR
Bulk density of sand	ρ_{bulk}	1.6E03	Kg/m^3
Porosity of sand	∅	0.3291	m^3 voids/m^3 total
Hydraulic Conductivity of Sand	K	4.69	m/hr
HLR	q	0.0061,6.10,50.10	m/hr
Interstitial velocity of fluid	v	0.01	m/sec
Courant Number	Cr	0.3710,370.7, 3,448	unitless
Peclet Number	Pe	N/A	unitless

Overall, for first order degradation scenarios, the numerical approximation to the analytical solution were valid for all three *Cr* number scenarios with corresponding sum of squared residuals (SSRs) (L2 norm) ranging on the order of magnitude from 1E-15 to 1E-18 (Figure 21). Simulations with the lowest flow rate and Cr number demonstrated the highest SSR (worst accuracy), whereas simulations with the highest flow rate were

improved (best accuracy) (Figure 21). Generally, higher Cr numbers resulted in a higher magnitude of numerical dispersion due to the fact that the upwind differencing scheme was only first order accurate. However, since the Cr number was changing in magnitude with the increase or decrease in velocity (not grid spacing), the poor accuracy of the numerical model was likely affected by the high magnitude of first order degradation for simulations with low interstitial pore water velocities.

The magnitude of the microbial growth rates was then altered to investigate to what extent the above observation was true, in that higher maximum growth rates result in higher discrepancies between the numerical approximation and the analytical solution. The magnitude of the maximum growth rates was changed from 8.3E-05, to 8.3E-03, to 8.3E-01 per second, while all other growth conditions were kept constant (i.e., half saturation constant and yield coefficient). In general, the numerical approximations to the analytical solutions were valid for all cases, with SSRs ranging from E-20 to E-13 (Figure 22). However, higher growth rates (8.3E-01) resulted in higher discrepancies between the numerical approximation and analytical solution (under-prediction of the exponential decay). Therefore, the accuracy of the numerical solution seems to be directly proportional to the magnitude of the growth rate and indirectly proportional to the hydraulic loading rates, where the most discrepancy can be expected at low interstitial velocities and high microbial growth rates.

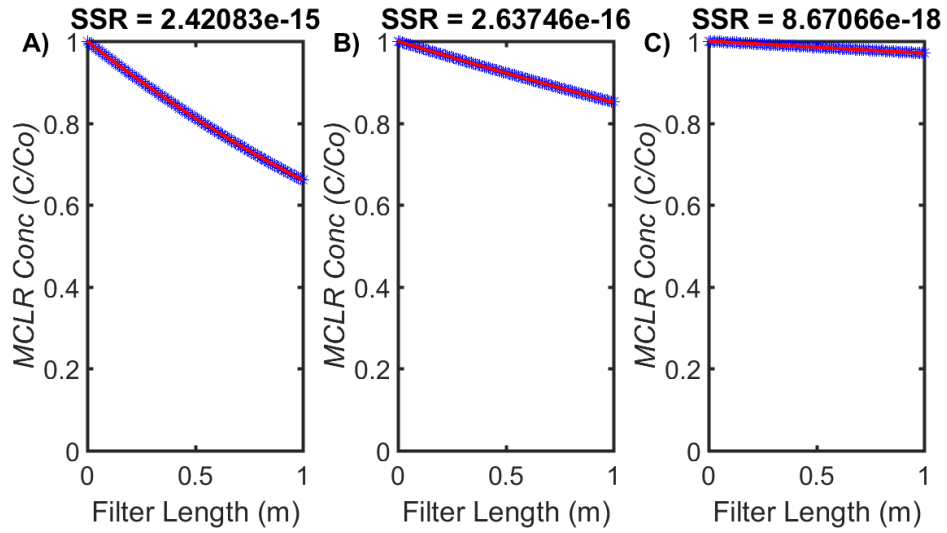

Figure 21. *Numerical approximation (red line) to analytical solution (blue *) comparisons and SSR for different hydraulic loading rates, a) Cr = 0.3707 b) Cr = 370.7 and c) Cr = 3,448.*

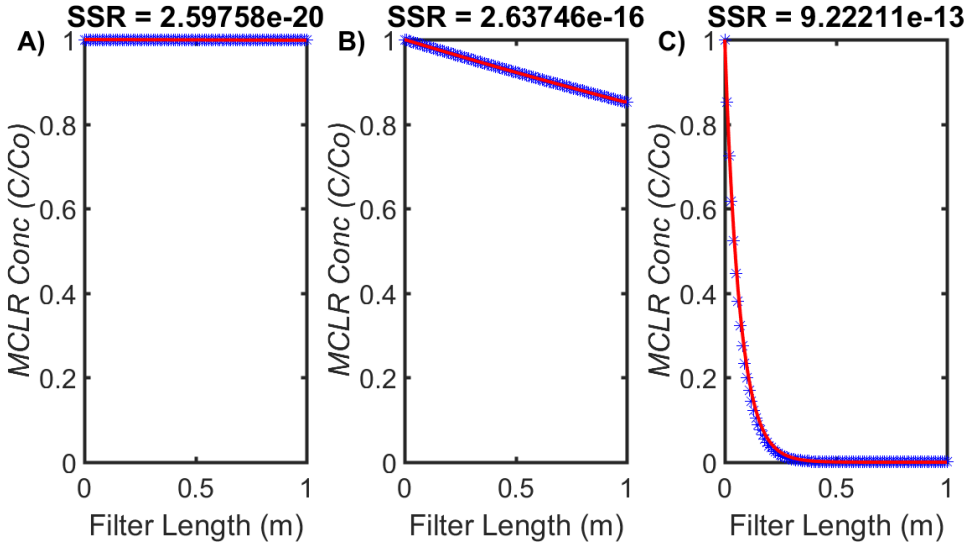

Figure 22. *Numerical approximation (red line) to analytical solution (blue *) comparisons and SSR for different microbial growth rates, a) μmax = 8.3E-05 b) μmax= 8.3E-03 c) μmax = 8.3E-01.*

An analytical solution was then obtained for the steady state dispersion, advection, and first order reaction equation (Equations 31 and 32). This particular analytical solution was derived assuming that the form of the second order ordinary differential equation can be reduced to a quadratic equation in which the roots can be solved for analytically (Yudianto and Yuebo 2010). The full derivation can be referenced in Yudianto and Yuebo

(2010), where the resulting analytical solution is presented below (Equation 32). Here K_{net} refers to the combination of K1 and K2, representing the contributions from both aqueous and solid biomass to the overall first order biodegradation rate.

$$0 = D\frac{\partial^2 C}{\partial x^2} - v\frac{\partial C}{\partial x} - K1(C) - K2(C) \quad (31)$$

$$C(x) = C_0 e^{\frac{v}{2D}x\left(1-\sqrt{1+\frac{4K_{net}D}{v^2}}\right)} \quad (32)$$

The agreement between numerical approximations of the steady state ADRE and the analytical solution derived above (Equation 32) will now be reviewed for different combinations of the Cr and Pe numbers. When varying the Cr numbers, the hydraulic loading rates were changed with a constant dispersivity value (α = 0.0103 m). Contrarily, when varying the Pe numbers, the magnitude of the dispersivity (αmin = 2.7E-04 m, αmed = 2.11E-03 m αmax = 0.2 m) was changed while holding the hydraulic loading rate constant (HLR = 6.10 m/hr). The values of the min, median, and maximum dispersivities were summarized from the literature for clean bed, uniform sand column experiments with length scales at or below 3 m (determined using a conservative tracer). These dispersivity values were considered most relevant for the expected laboratory and field conditions for validating the model output. The corresponding Pe numbers from the dispersivity values and constant HLR were 3,704, 474, and 5 for the verification study. Under both of these schemes (i.e., varying Cr or Pe), the effect of increasing and decreasing the maximum growth rates will be discussed. Identical conditions for the model input for the previous verification study were adopted in this analysis (Table 6).

Changing the Cr numbers with dispersion included (at a realistic Peclet number) had little effect on the resulting microcystin transport across the filter compared to without dispersion (Figures 21 and 23). The distribution of microcystin-LR across the filter and the

agreement of the numerical simulation and the analytical solution for simulations with dispersion included are very similar to results without dispersion at a realistic Pe number to full scale biofiltration systems (Pe = 370.70). Changing the maximum growth rate at the different Cr numbers with dispersivity fixed also has little effect on the resulting distribution of microcystin-LR across the filter and the agreement of the numerical and the analytical solutions as compared to the results with no dispersion included.

Increasing the dispersivity values (low Pe number, ~5) had a noticeable effect on the transport of microcystin across the simulated filter compared to without dispersion (Figures 21 and Figure 24). Including dispersion with the first order reaction term increased the removal efficiency across the filter as opposed to without dispersion. This result was in agreement with what was expected conceptually as dispersion increases the mixing potential and availability of microcystin substrate for the degrading bacterial community. The overall agreement of the numerical and analytical solutions was excellent, with a very low SSR observed for all Pe numbers and either advection or dispersion dominated systems (Figure 24).

Some discrepancies were observed between the numerical and analytical solutions at much lower Pe numbers that are unrealistic for the system under this study (Pe < 0.01, corresponding dispersivity values > 1 m). These discrepancies between the numerical approximation and analytical solutions were most likely due to the handling of the boundary condition at the filter effluent. For the numerical simulations, the solution assumes that the gradient at the previous grid block is equivalent to the gradient at the boundary, which may result in an under prediction of the effluent concentration, especially at steep gradients near the boundary (brought on by dispersion). This under prediction at

the boundary affects the resulting distribution of predicted microcystin concentration across the filter, resulting in a slightly altered numerical approximation.

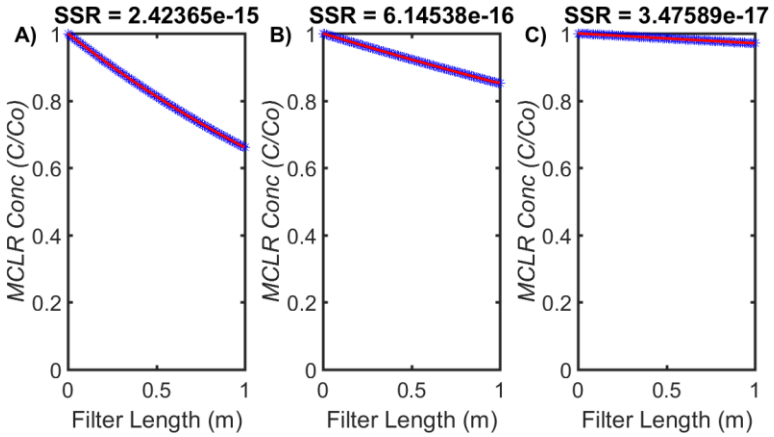

Figure 23. *Numerical approximation (red line) to analytical solution (blue *) comparisons and SSR for different hydraulic loading rates holding dispersivity constant, a) Cr = 0.3707 b) Cr = 370.7 and c) Cr = 3,448.*

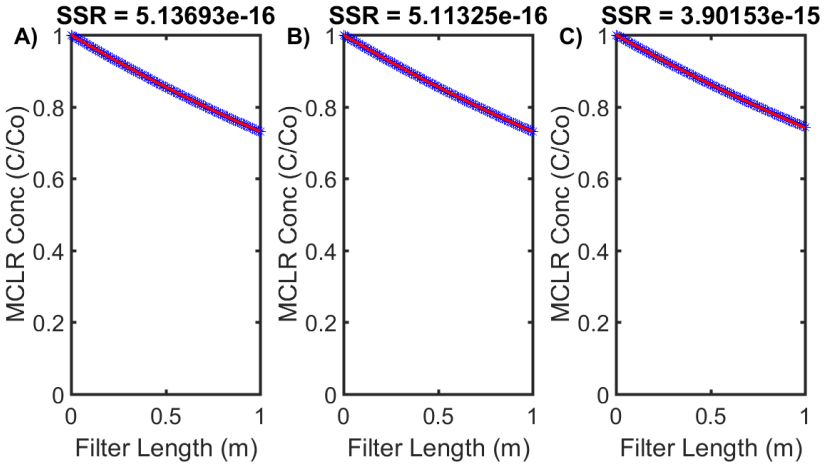

Figure 24. *Numerical approximation (red line) to analytical solution (blue *) comparisons and SSR for different dispersion coefficients holding HLR constant, a) Pe = 3,704 b) Pe = 474 and c) Pe = 5.*

3.1.2 Non-Linear Reaction Kinetics: Analytical Verification Study #2

Following the verification of the first order reaction analytical solutions, non-linear reaction kinetics were considered to approximate both microbial growth and substrate utilization (of microcystin) according to the Monod model. We first begin the derivation of the steady state analytical solution using the transport equation for microcystin (including

advection and dispersion), considering growth of both aqueous and solid biomass as reaction components, where Monod's nonlinear mathematical relationship between substrate and bacterial growth rate is considered (Equation 33).

$$0 = D\frac{\partial^2 C}{\partial x^2} - v\frac{\partial C}{\partial x} - \frac{\mu_{max}}{Y}X_a\left(\frac{C}{Ks+C}\right) - \frac{\mu_{max}}{Y}\frac{\rho_{bulk}}{\emptyset}I_{bio}X_s\left(\frac{C}{Ks+C}\right) \quad (33)$$

To develop useful analytical solutions to the nonlinear terms in Equation 33, we first considered the maximum and minimum ranges of the hyperbolic function describing bacterial growth rate as a function of substrate concentration. In addition, we considered situations in which dispersion was neglected, since most current biofiltration units are moderately advectively dominated systems (Pe = 97.10). Finally, the concentration of degrading microorganisms remained constant for the development of the first analytical solution and the growth of aqueous biomass in the filter was only considered (solid biomass was neglected).

At low substrate concentrations (C<<Ks), the relation between bacterial growth rate and substrate concentration was linear and first order. This resulted in a first order approximation for the nonlinear reaction terms in Equation 33 (Equation 34). However, at high substrate concentrations (C>>Ks), the bacterial growth rates were constant and not related to substrate concentration (zero order). The resulting expression for the nonlinear reaction terms is now zero order at high substrate concentrations (Equation 35).

$$\frac{dC}{dt} = \frac{-v_m}{Ks}(C) \quad (34)$$

$$\frac{dC}{dt} = -v_m \quad (35)$$

Where, $v_m = \frac{\mu_{max}}{Y}X_a$.

Modifying Equation 33 with Equations 34 or 35 (and neglecting solid biomass and dispersion terms) and then integrating the resulting equations results in the following

analytical solutions (Equations 36 and 37) for low and high substrate (microcystin) concentrations, respectively.

$$C = C_0 e^{-k_1 x} \quad (36)$$

$$C = C_0 - k_0 x \quad (37)$$

Where, $k_0 = \frac{v_m}{v}$ and $k_1 = \frac{v_m}{v*Ks}$.

Another analytical solution was applied for intermediate ranges in substrate concentration where the Monod kinetic model is more non-linear than at either extreme low or high substrate concentrations. Parlange et al. (1984) detailed an analytical solution to Equation 33 at steady state (neglecting dispersion and solid biomass growth) that includes nonlinear reaction kinetics for a constant concentration inlet boundary condition (Equation 38). Both Bekins et al. (1998) and Goudar and Strevett (2000) further described a Lambert W solution to iteratively solve for S as a function of v_m (μ_{max}), K_s, S_0 (initial susbtrate concentration), and distance (x) (Equation 38).

$$C = K_s * W\left\{\frac{C_0}{K_s}\exp\left(\frac{C_0 - v_m x}{K_s}\right)\right\} \quad (38)$$

Unlike the preliminary first order degradation verification studies above, the non-linear comparison studies required a more detailed investigation of the expected range in growth characteristics of microcystin degrading bacteria. Thus, microbial growth parameters relevant to bacteria native to surface waters were first compiled and used in the absence of data for growth parameters of microcystin-degrading bacteria. The minimum, median, and maximum ranges for each of these growth parameters are presented and were varied in this verification study, ranging from a difference of three to five orders of magnitude (Table 7). Lastly, the biomass concentration (using dry weight) of the aqueous bacteria entering the filter was determined from median values of carbon

contents of bacteria cells presented in the literature as well as an average influent cell concentration of 1E09 cells/mL (Table 7).

Table 7*- Summary of Microbial Growth Parameters Used in Verification Studies for Non-Linear Monod Kinetics*

Variable Name	Symbol	Units	Nominal Value
Cell Maximum Growth Rate	μ_{max}	1/second	1.74E-06 3.89E-05 3.83E-04
Half Saturation Constant	K_s	Kg MCLR/m^3	5.0E-07 1.68E-03 1.21E-01
Yield coefficient	Y	Kg cells/Kg MCLR	0.13 0.371 0.545
Inlet Aq. Biomass Concentration	X_a	Kg cells/m^3	0.01

The rate of substrate utilization by a fixed concentration of microorganisms ($v_m\left(\frac{C}{K_s+C}\right)$) was plotted as a function of substrate concentration (C) to determine the appropriate ranges in substrate concentrations where the above analytical solutions (Equations 36, 37 and 38) would be valid for the min, med, and max ranges in growth parameters (Figure 25). The resulting solutions demonstrated relatively limited ranges where the above analytical solutions would be valid for both first and zero order approximations of the nonlinear substrate utilization kinetics (for all ranges in the growth parameters, min, med, and max) (Figure 25B and 25C). From inspection of both subfigures, it is evident that the first order approximation threshold is well below 50 μg/L of microcystin, somewhere in the range between 0-5 μg/L, whereas the zero-order approximation threshold is approximately 0.5E07-1E07 μg/L of microcystin. The initial concentration ranges for first, non-linear, and zero order approximations were determined

to be 0.01, 100, and 1,000-10,000,000 for all ranges in growth parameters based on the trends observed in Figure 25. The initial concentration ranges were varied for the high concentration of substrate due to the distinct differences in substrate locations where the zero-order approximation was valid (Figure 25C).

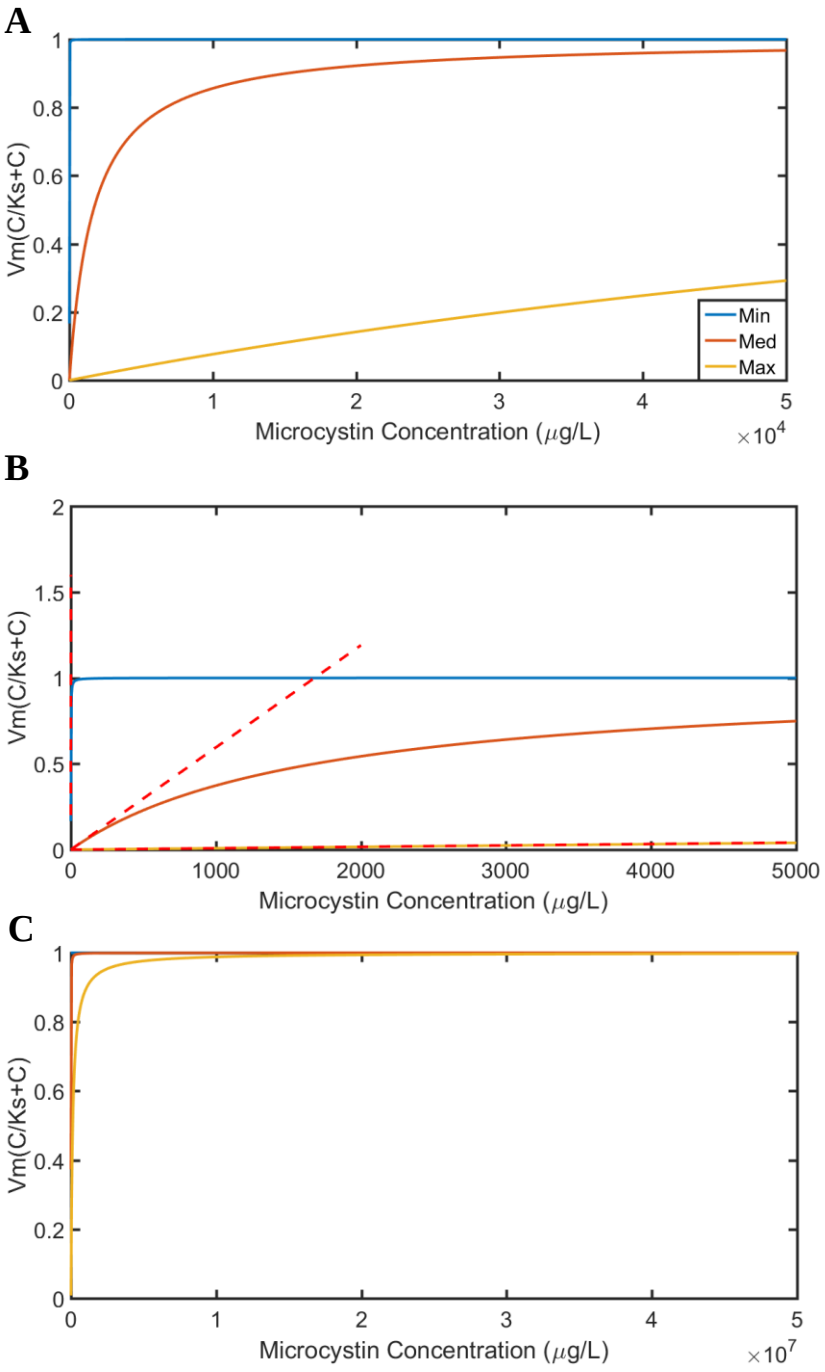

Figure 25. *Dimensionless Monod curves for a) substrate utilization rate as a function of microcystin concentration, b) determining the first order approximation threshold (red dotted lines are linear approximations), and c) determining the zero-order approximation threshold.*

The analytical and nonlinear numerical solutions were first compared at low substrate concentrations (C << Ks) using the analytical solution described in Equation 36 at

a singular Courant (Cr) number reflecting a minimum operational HLR of a full scale biofiltration system (HLR_{min} = 0.3 m/hr) (Figure 26). At low substrate concentrations, the highest removal efficiency of microcystin was achieved for the lowest magnitude bacterial growth parameter combinations followed by the median and maximum value combinations (Figure 26). Agreement between the analytical solutions and the numerical approximations was excellent for each case (SSRs above E-18). The removal of microcystin was generally faster at lower magnitude combinations of growth parameters since the rate of bacterial growth (at low substrate concentrations) was directly proportional to the μ_{max}/K_s ratio, where this ratio was largest for the parameter combinations that were the smallest in magnitude (Table 7).

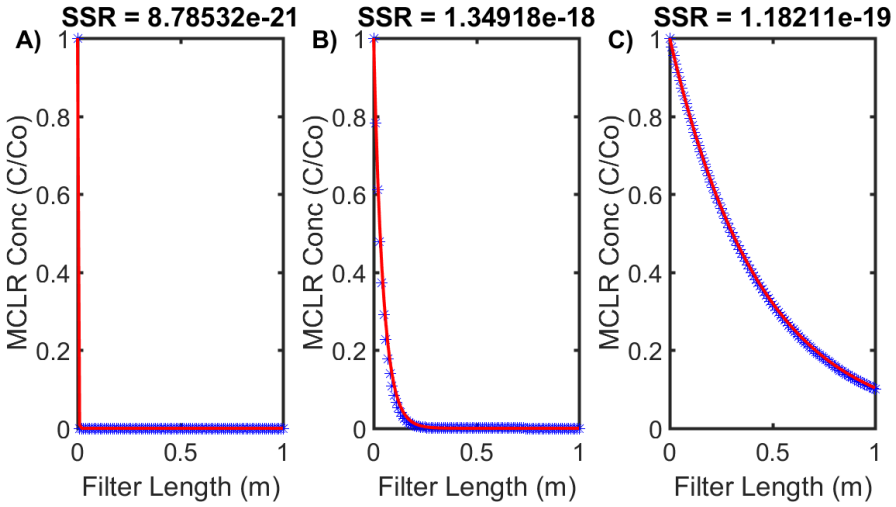

Figure 26. *Comparison of analytical and nonlinear numerical solutions for a) minimum, b) median, and c), maximum bacterial growth parameters at a minimum HLR (0.3 m/hr) and low substrate concentration (C<<Ks).*

At high substrate concentrations (C >> Ks), a reduction in the removal efficiency of microcystin was observed as compared to at lower substrate concentrations (Figure 27). This result was due to the fact that at higher concentrations, the substrate utilization kinetics are not dependent on the concentration of substrate, rather the maximum growth

rate. Therefore, as the substrate concentration increases, the rate of utilization will not increase (as maximum growth rate is fixed), which will result in less removal at higher and higher concentrations above the "high" concentration threshold (where C >> Ks).

The best removal efficiency at high concentrations of microcystin was demonstrated by the simulation with the lowest maximum growth rate (Figure 27). This result was due to the fact that the initial substrate concentration was much less for this simulation than the simulation with the highest maximum growth rate (on the order of 1,000 compared to 10,000,000). Comparably, at lower HLRs, the removal efficiency increased as there was an increase in contact time for degradation to occur across the filter between the substrate and suspended microorganisms. The relatively good agreement between all numerical approximations and analytical solutions also indicated that the nonlinear approximation of the growth kinetics was valid. The relatively high values of the SSR compared to previous experiments (on the order of 1E-05 vs. 1E-18) were due to differences in the scales of the substrate concentrations that were under comparison (g/L vs. μg/L) as opposed to actual discrepancies between the numerical model simulations and the analytical solutions.

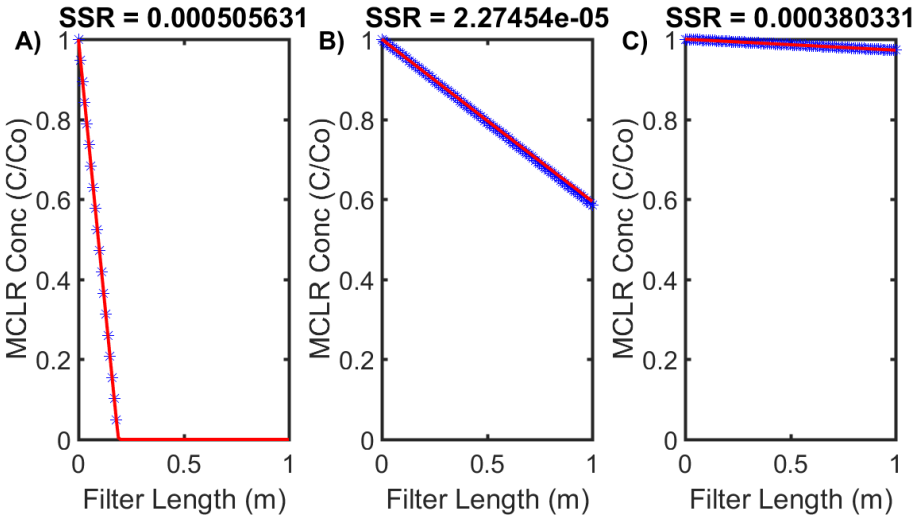

Figure 27. *Comparison of analytical and nonlinear numerical solutions for a) minimum, b) median, and c), maximum bacterial growth parameters at a minimum HLR (0.3 m/hr) and high substrate concentration (C>>Ks). Initial substrate concentrations were varied between 1000, 100,000, and 10,000,000 µg/L, respectively.*

The numerical approximation of the Monod equation at intermediate values of substrate concentration (100 µg/L) was very similar to the analytical solution using the Lambert W method (Figure 28). These results indicated that the numerical approximation using the Picard iteration was robust enough to successfully approximate even the most nonlinear portions of the Monod hyperbolic equation. The resulting microcystin removal efficiencies across the filters were almost equivalent to the removal efficiencies at low microcystin concentrations, but were slightly lower in magnitude (Figure 28). This result suggests that the concentration tested for moderate and maximum growth conditions (100 µg/L) may not have been in the distinct nonlinear portion of the Monod model, and may be closer to the linear approximation threshold. Nonetheless, the good agreement with the Lambert W solution demonstrated that the numerical solution to the nonlinear model was still accurate, with low SSR values observed for each simulation at moderate/high growth conditions (Figure 28).

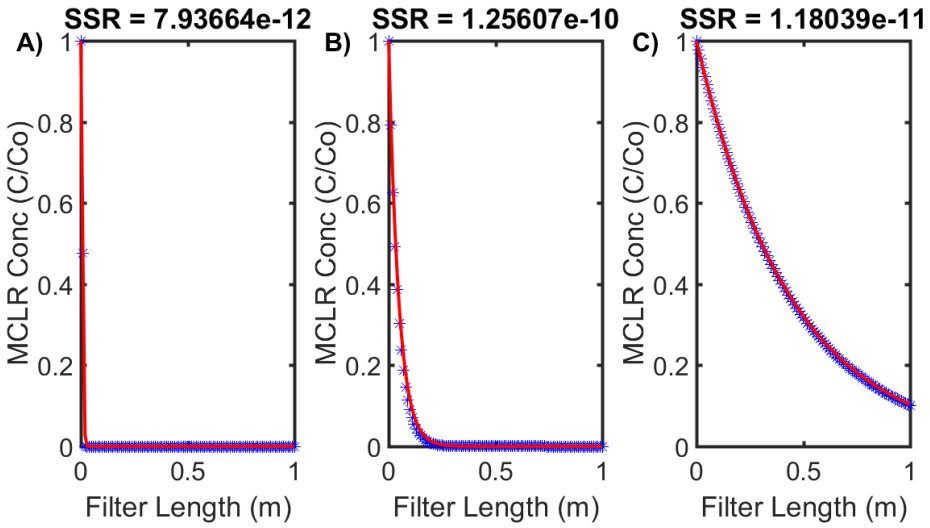

Figure 28. *Comparison of analytical and nonlinear numerical solutions for a) minimum, b) median, and c), maximum bacterial growth parameters at a minimum HLR (0.3 m/hr) and moderate substrate concentrations (C~Ks).*

3.1.3 Coupled Non-Linear Reaction Kinetics: Analytical Verification Study #3

The development of the coupled numerical solver was based on a verification study of the coupled rate expressions for microbial growth and substrate depletion following Monod kinetics. The simple rate expression for microbial growth in the presence of a certain growth limiting nutrient is presented in Equation 39 (Shuler and Kargi 2002, Kargi 2009). The amount of the cellular products and biomass depends on the amount of microorganisms present as well as the concentration of growth limiting substrate at any given time, t (or position, x) (Kargi 2009). The expression is autocatalytic in that more biomass (X) is produced in the reaction as well as certain extracellular products (P).

$$C + X \rightarrow P + nX \tag{39}$$

The rates of cell biomass formation and substrate utilization are based on Monod kinetic rate expressions (Equations 40 and 41) and are coupled by the yield coefficient (Equation 45). The analytical solutions of the coupled rate expressions presented were achieved by integrating the kinetic expressions below (Equations 42 and 43). The full

derivation of the analytical solutions is omitted in this chapter but is presented in Shuler and Kargi (2002) and Kargi (2009) for reference.

$$\frac{dX}{dt} = f(C,X) = \frac{\mu_{max} * C}{K_s + C} X \tag{40}$$

$$-\frac{dC}{dt} = g(C,X) = -\frac{1}{Y_{X/S}} \frac{dX}{dt} = -\frac{\mu_{max} * C}{Y_{X/S}(K_s + C)} X \tag{41}$$

After integration of Equation 40, the following analytical solution is reached for determining biomass concentration *X* as a function of several parameters, with time (t) replaced by the position (x) normalized by the interstitial pore water velocity (v).

$$\frac{(K_s Y_{X/S} + C_0 Y_{X/S} + X_0)}{(Y_{X/S} C_0 + X_0)} ln\left(\frac{X}{X_0}\right) - \frac{(K_s Y_{X/S})}{(Y_{X/S} C_0 + X_0)} ln\left\{\frac{(Y_{X/S} C_0 + X_0 - X)}{(Y_{X/S} C_0)}\right\} - \mu_{max} \frac{x}{v} = 0 \tag{42}$$

Where K_s is the half saturation constant (µg/L), $Y_{X/S}$ is the yield coefficient (unitless), μ_{max} is the maximum specific growth rate of the bacteria (1/sec), C_0 is the initial substrate concentration (µg/L), X_0 is the initial microorganism concentration (kg/m^3), x is the depth along the filter (m), and v is the interstitial pore water velocity (m/sec).

Similar integration of Equation 41 results in the analytical solution for determining substrate concentration *C*, as a function of several parameters (Equation 43). Again, time (t) replaced by the position (x) normalized by the interstitial pore water velocity (v) for comparison purposes.

$$\frac{(K_s Y_{X/S} + C_0 Y_{X/S} + X_0)}{(Y_{X/S} C_0 + X_0)} ln\left\{\frac{(Y_{X/S}(C_0 - C) + X_0)}{(X_0)}\right\} - \frac{(K_s Y_{X/S})}{(Y_{X/S} C_0 + X_0)} ln\left(\frac{C}{C_0}\right) - \mu_{max} \frac{x}{v} = 0 \tag{43}$$

Where K_s is the half saturation constant (µg/L), $Y_{X/S}$ is the yield coefficient (unitless), μ_{max} is the maximum specific growth rate of the bacteria (1/sec), C_0 is the initial substrate concentration (µg/L), X_0 is the initial microorganism concentration (kg/m^3), x is the depth along the filter (m), and v is the interstitial pore water velocity (m/sec).

The analytical solutions to Equations 40 and 41 require a constraint on the maximum growth of the microorganisms (X_{max}) given some initial microorganism concentration (X_0), substrate concentration (C_0), and yield coefficient (Y) to be valid. This constraint is also coupled with the fact that the substrate concentration can realistically never be less than 0 (Equation 44).

$$X_{max} = (Y * C_0) + X_0 \tag{44}$$

Plotting the normalized results for the substrate and microorganism concentration as a function of position and interstitial pore water velocity results in two s-shaped profiles, one increasing (biomass concentration) to the maximum theoretical limit and the other decreasing (substrate concentration) to zero (Figure 29). The parameters used to generate the plot of the coupled analytical solutions are similar to Table 6 above, although the pore water velocity is much lower to show the characteristic nonlinear S-shape of the solutions. These analytical solutions and initial conditions will be used as the basis for comparison with the coupled numerical solver.

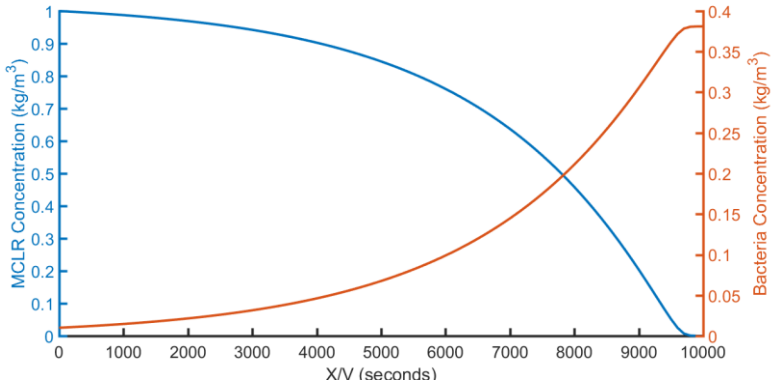

Figure 29. *Example of coupled analytical solution for substrate utilization and bacterial growth kinetics.*

For the model-analytical coupled solution testing, the initial conditions were kept identical to those presented in Table 6, except for the initial concentration of microcystin, which was maintained at 1,000 µg/L. The testing was conducted at one operational HLR (0.3 m/hr, which was often the limiting case), similar to the previous sections, for the range of bacterial growth conditions reported (low, moderate, and high) (Figures 30-32). At the low HLR used in this comparison, the behavior of the coupled numerical solution was erratic at times. Using coarse grid spacing (number of xpoints ~ 100) generally resulted in negative results for the 1D concentration field. The negative concentrations were due to the inability of the numerical solution to capture the nonlinearity of the analytical solution close to the x-axis. Since these results were unrealistic, the grid spacing was refined (decreased significantly) to solve this issue.

The main tactic to refine the grid spacing involved first determining a theoretical maximum time t_{max} and corresponding length scale (L_{max}) for a given set of microbial growth conditions (which was mainly dependent on the magnitude of Y, C_0, and X_0) where substrate concentrations approached zero. The L_{max} value was determined a priori to running the numerical model simulations and was based on an iterative solution given that the functions in Equations 40 and 41 never truly converge (and approach infinity). The L_{max} values were then related to the number of computational points required (to prevent negative numbers) for each bacterial growth condition (low, moderate, high) (Table 8). It seemed that L_{max} values below the specified depth of the computational domain (1 m) resulted in much lower grid spacing requirements for accurate numerical approximations. The difference in required grid spacing is only slightly different for moderate and low growth conditions as well, where 10,000 computational points appears to be the limit

MATLAB can handle in order to produce a computationally efficient numerical solution. Future work will consider a parameter space based on C_0, X_0, and Y in which different L_{max} values will result. This procedure will help to define specific ranges where higher grid spacing will be necessary to ensure optimal numerical approximations for a wide range in bacterial growth conditions.

Table 8*- Summary of theoretical L_{max} values and corresponding grid spacing for different bacterial growth conditions*

Growth Condition	Lmax (m)	Computational Points (Nxpoints)	Grid Spacing (dx)
Low	0.1904	10,000	1.904E-05
Moderate	0.6357	10,000	6.36E-05
High	6.73	100	0.01

Refining the grid spacing solved the issue of negative concentrations observed for substrate utilization, where good numerical approximations of the analytical solutions resulted for all of the bacterial growth conditions simulated (Figures 30-32). Low growth conditions (lowest values of K_s, μ_{max}, and Y) indicated the quickest removal of substrate across the filter as compared to high growth conditions (largest values of μ_{max}, K_s, and Y). In addition, moderate growth conditions demonstrated the characteristic asymptotic trend, where bacteria growth leveled off as substrate concentrations were exhausted. These results indicated that the coupled numerical solver developed in this research could efficiently and accurately replicate the derived coupled, analytical solutions when the grid spacing was automatically defined by the user. Future model efforts will develop user independent grid spacing refinement based on specified ranges in L_{max} that correlate with different grid spacing for improved numerical model performance. Moreover, results demonstrated that the magnitude of bacterial specific growth rate alone does not

determine the treatment efficiency of a given biological filtration system, where a specific combination of growth-related parameters may increase treatment efficacy. Proper analytical solutions will additionally be developed to ensure functioning of the 2D numerical implementation of this mechanistic model. Similar approaches to those developed herein will be adapted to develop these future 2D comparisons.

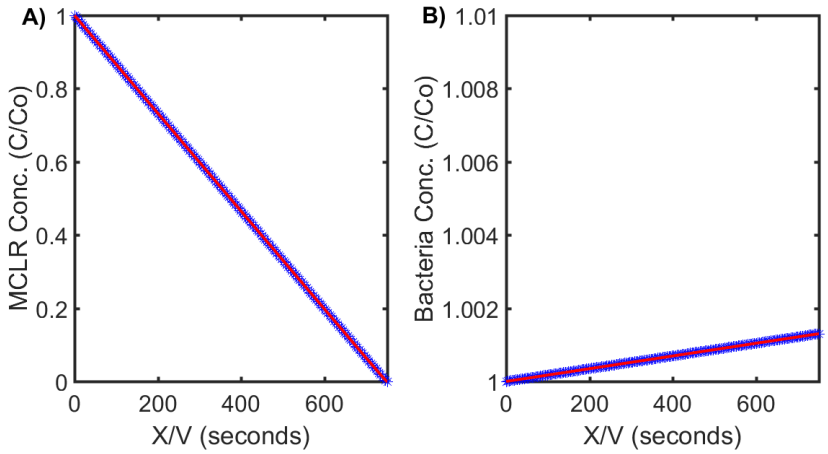

Figure 30. *Comparison of coupled numerical and analytical solutions for low bacterial growth conditions and low operational HLR (0.3 m/hr): a) substrate utilization and b) bacterial growth kinetics (blue asterisks are analytical solutions; red lines are numerical approximations).*

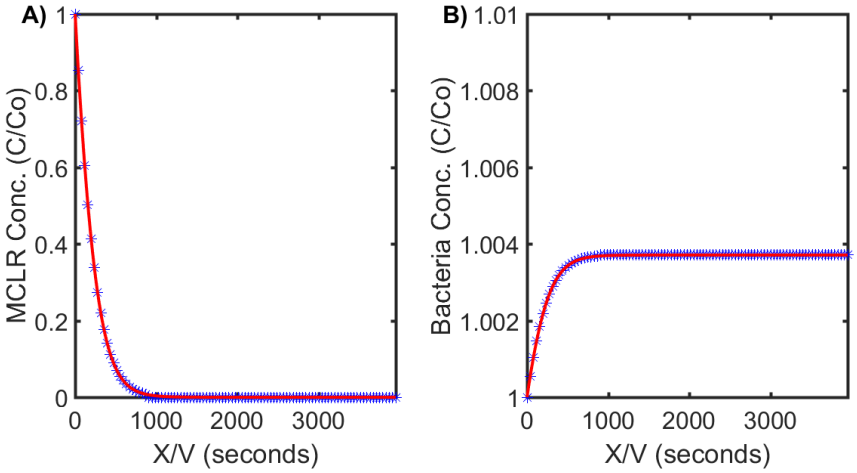

Figure 31. *Comparison of coupled numerical and analytical solutions for moderate bacterial growth conditions and low operational HLR (0.3 m/hr): a) substrate utilization and b) bacterial growth kinetics (blue asterisks are analytical solutions; red lines are numerical approximations).*

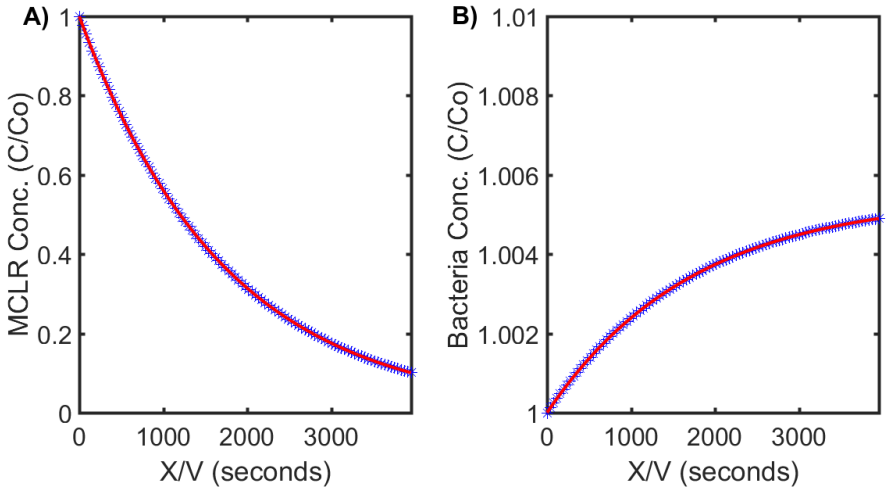

Figure 32. *Comparison of coupled numerical and analytical solutions for high bacterial growth conditions and low operational HLR (0.3 m/hr): a) substrate utilization and b) bacterial growth kinetics (blue asterisks are analytical solutions; red lines are numerical approximations).*

3.2 Calibration of Mechanistic Model Parameters

As the mechanistic model developed in this research was purely theoretical, it was necessary to parameterize the model using a series of laboratory-based experiments. The experiments that were actually conducted were primarily geared toward understanding the fate and transport of microcystin, where future experiments will be directed toward exploring the model parameters governing the fate and transport of MC degrading bacterial cells. Here, we briefly review the results of physico-chemical adsorption experiments and flow through, one-dimensional column tests designed to calibrate and understand the adsorption and dispersive characteristics of MC when transported through sandy, porous media.

3.2.1 Physico-Chemical Adsorption of MC-LR

The focus of this section of the results was to ascertain the physico-chemical adsorption potential of purified microcystin-LR onto cleaned silica sand filter media of the

same characteristics used in practice. The specific characteristics of silica sand grains chosen shared common traits such as the effective grain diameter (D10), uniformity coefficient (UC), and porosity/hydraulic conductivity to sands used in biofiltration practice.

Batch equilibrium experiments were performed to test whether the assumption of first order microcystin adsorption kinetics can be sustained in the proposed model. The batch equilibrium experiments consisted of adding a specified amount of sand with a certain initial concentration of microcystin-LR (~ 200 µg/L of LR standard) and measuring the amount of remaining microcystin after a 24 hour "equilibrium" time period has passed (OECD 2000).

Results from preliminary batch adsorption experiments confirmed the reduced adsorption potential of microcystin-LR onto cleaned silica sand (Figure 33). The batch adsorption kinetics were also linear, as indicated by the higher correlation between microcystin initial concentration in the water (Cw) and that adsorbed to the media surface (Cs). These results were similar to Grützmacher et al. (2010) who also observed a relatively insignificant adsorption potential and linear adsorption kinetics of microcystin-LR onto clean quartz sand.

It was also realized that the pre-cleaning procedure (sand preparation) may have produced an undesirable effect on the adsorption characteristics due to unforeseen changes in the surface properties of the sand. Previous procedures involved acid washing the sand with diluted hydrochloric acid (20%), washing with milli-Q water until pH was in a desired range, incubating at 500 °C (to remove excess organics), followed by autoclaving. Two of the procedures (incubation at 500 °C) and autoclaving were researched to significantly change the properties of the sand surface (including potential electrostatic

properties and surface morphology). Therefore, future experiments will include a revised sand pre-conditioning procedure with reduced incubation temperatures (to 60 °C overnight) and elimination of the autoclaving step.

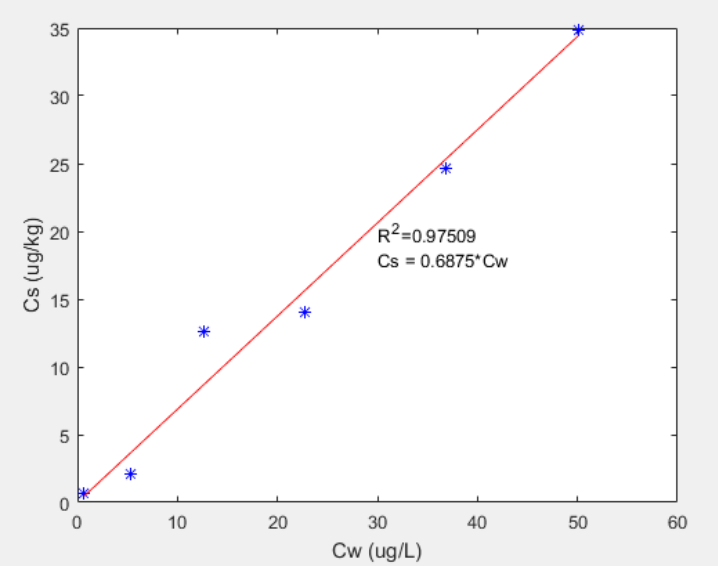

Figure 33. *Experimental adsorption potential of microcystin-LR onto cleaned silica sand.*

3.2.2 Dispersion of MC-LR in 1-D Column Experiments

In this section, the physical transport of microcystin-LR through sandy, porous media was studied through application of a series of 1-D flow through column experiments. The objective of these experiments was to calibrate the dispersive characteristics of MC when transported through sandy media that is used in biofiltration practice to assist in parameterizing the mechanistic model. Flow through laboratory scale column experiments were conducted with microcystin-LR and fully saturated columns packed with pre-conditioned (using identical procedures described above) sand media. The initial experiments used hydraulic empty bed contact times (EBCT) that were similar to the median value of those used in full scale practice (15 minutes) (Evans et al. 2013a, 2013b).

This EBCT (for a media length, L of 15 cm) corresponded to a hydraulic loading rate (flow rate of water applied normalized by the superficial area) of approximately 9 mL/minute.

Sodium chloride (NaCl) breakthrough curves were first evaluated, before the column was inoculated with MC, to study the dispersive characteristics of the media at the applied flow rate. A sodium chloride solution of 500 mg/L concentration was pulsed through the column at 9 mL/min for a six-minute time period and effluent conductivities were measured for twenty second intervals using a previously calibrated conductivity probe-flow cell device. In addition, flow rates were monitored at the effluent of the column for the duration of the experiment. Before tracer tests were run, careful attention was taken to first de-air the column (by flowing several pore volumes of de-aired, deionized water through the column) and that all fittings/tubing were cleared of any air bubbles prior to analysis (including the flow cell device).

The experimental data acquired was then fitted to an analytical solution of the one dimensional advection-dispersion equation (ADE) for a time limited pulse boundary conditions (assuming R = 1 for a conservative tracer such as salt) using a differential evolution (DE) algorithm previously developed to estimate the dispersivity (α) of the media (Equation, Van Genuchten and Alves (1982), Bear (2013)). It was assumed that the molecular diffusion term was negligible at the high interstitial velocities employed in these experiments, leading to a dispersion coefficient that was solely dependent on the dispersivity of the media. The L2 norm (sum of square residuals) was used as the basis for the objective function (OF) for the fitting procedure, and the evolutionary algorithm was chosen for its simplicity and efficiency to locate the true minimum of the proposed OF. Two

parameters were chosen for the fitting process including the interstitial pore water velocity (v) and the dispersivity of the media (α).

1) *For elapsed time $t \leq t_0$,*

$$C(x,t) = \frac{1}{2}\, erfc\left(\frac{Rx-vt}{\sqrt{4DRt}}\right) + \frac{1}{2}\exp\left(\frac{vx}{D}\right)\, erfc\left(\frac{Rx+vt}{\sqrt{4DRt}}\right) \quad (45)$$

Where t is the elapsed time (seconds), x is the spatial distance (15 cm), R is the retardation factor defined below (assuming linear sorption), v is the interstitial pore water velocity (m/sec), D is the dispersion coefficient (defined in Equation 46 below) (m^2/sec), α is the dispersivity of the media (cm) and *erfc* is the complimentary error function.

$$D = \alpha v \quad (46)$$

Where the pore water velocity (v) is equivalent to the Darcy velocity (HLR) normalized by the porosity of the media (Equation 47):

$$v = \frac{q}{\theta} \quad (47)$$

2) *For elapsed time $t>t_0$,*

$$C(x,t) = C(x,t) - C(x,t-t_0) \quad (48)$$

Where the retardation factor can be defined as follows and *C(x, t)* is the same function derived in Equation 45) above:

$$R = 1 + \frac{\rho_{bulk}}{\theta} K_d \quad (49)$$

Where ρ_{bulk} is the bulk density of the soil (kg/m^3), θ is the porosity of the soil (unitless), and K_d is the first order sorption term (m^3/kg).

The results of the salt tracer break through curve indicated that the silica sand media was not very dispersive, as the time limited pulse seemed to retain its theoretical rectangular shape and the height of the pulse was not attenuated to a significant degree (Figure 34). This observation was confirmed quantitatively, as the average fitted

dispersivity α-value was 0.00361 meters, with an average SSR of 0.2590 achieved by the fitting process. This value of dispersivity was determined to be acceptable through comparison of many published studies of similar sand characteristics, column attributes (length), and experimental conditions (pore water velocity) (i.e., Padilla et al. 1999, Avnimelech et al. 2001, Grützmacher et al. 2002, 2010, Chorus and Bartel 2006). The compilation of these studies determined that the maximum dispersivity value was 0.19 m and the median value was 0.00211 m; therefore, the magnitude of the value obtained from this study was in the appropriate range expected for a sand media with relatively high hydraulic conductivity and porosity.

Moreover, the fitted pore water velocity (v) value obtained (6.475E-08 m/sec) was similar to the average velocity determined experimentally (6.0 E-08 m/sec) over the course of the entire experiment. The breakthrough curve was further integrated to determine whether the mass that was dosed to the column was conserved. Results indicated that the mass measured (30.59 mg) was relatively equivalent to the magnitude of theoretical mass dosed to the column (26.92 mg), although a slight discrepancy was observed. Although the analytical model seemed to overshoot the top portion of the experimentally determined breakthrough curve, the low OF observed indicated that there was a reasonably good fit to the experimental data. Future predictions will take into account the 95% confidence intervals of the analytical model to further survey whether the model predictions completely capture the experimental data achieved.

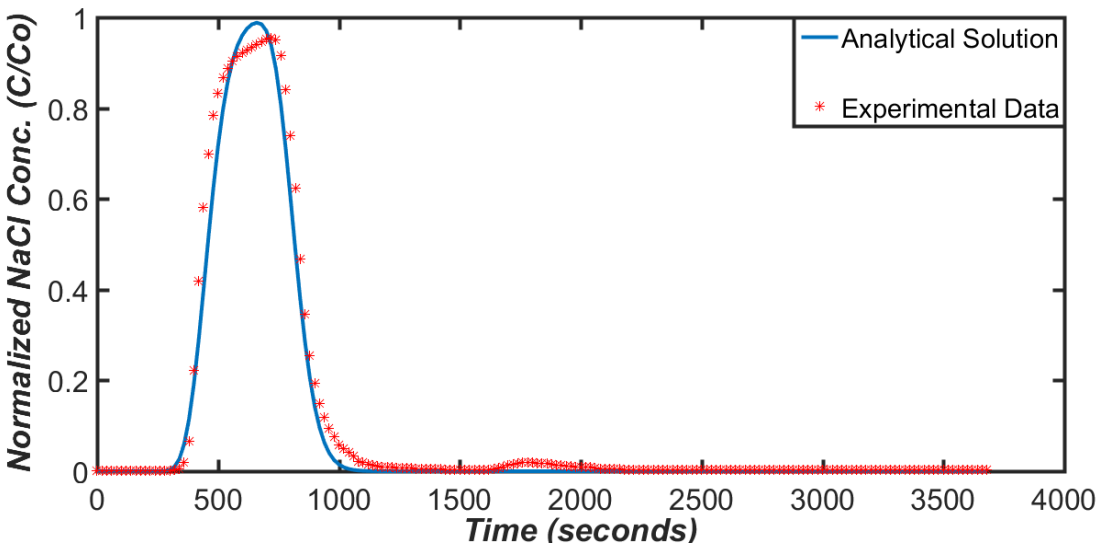

Figure 34. *Model-data fitting results for NaCl conservative tracer.*

After full analysis of the conservative tracer BTC, the fate and transport of a pure microcystin-LR standard was experimentally determined. Equivalent experimental conditions applied in the conservative tracer column study were applied in the microcystin-LR non-conservative tracer study (9 mL/min hydraulic loading rate, 6-minute injection time, 15 cm media length) to be as consistent as possible. The concentration of the pulse of microcystin was set at 125 µg/L, where a higher value was used (as compared to field dissolved concentrations expected) to ensure that the toxin was detected by the ELISA analysis. Samples were collected at the outlet of the column, however, for every two-minute intervals, as opposed to 20 seconds, as the ELISA tests for microcystin-LR concentration are quite lengthy and complex.

As observed in the resulting BTC, the temporal resolution selected was sufficient enough to calibrate the experimental data to the analytical model (Figure 35). In these initial experiments, the *R* value was still set to 1 in the analytical model, even though the tracer was assumed to be non-conservative. The experimental R value was then

determined by comparing the ratio of the magnitude of fitted pore water velocities (i.e., v_{MCLR}/v_{NaCl}) instead of using another parameter to fit the model. This procedure was undertaken to avoid possible overfitting to the experimental data and to be as consistent as possible for comparison purposes with the experimental data obtained from the conservative tracer breakthrough curve.

The results of the MC-LR breakthrough curve indicated that the arrival time of the MC-LR pulse was almost identical to the salt tracer at the outlet of the column (Figure 35). The fitted average pore water velocities were relatively the same magnitude between the chloride and microcystin-LR tracers, as the mean experimental retardation factor was determined to be 1.075. Assuming that the bulk density of the sand was approximately 1.60E3 kg/m^3 and that the experimentally determined porosity (0.3777) was appropriate, the back-calculated K_d value was determined to be 1.77E-05 m^3/kg. The magnitude of this value is approximately one order of magnitude lower than that observed experimentally under batch conditions (6.88E-04 m^3/kg). These results may suggest that a fraction of the microcystin-LR pulse may travel much more efficiently through the column, whereas other fractions may become trapped or diffuse into immobile zones of the media. This supposition is confirmed when considering that the microcystin-LR tracer was subject to a higher residence time in the column, as indicated by a small tail in the BTC between 1000 to 1500 seconds (Figure 35). Thus, the attenuation of the height of the breakthrough curve was presumed to be a result of the dispersive effects within the column over adsorptive effects, as the retardation factor was relatively small and the fitted average dispersivity values were two orders of magnitude higher for the microcystin-LR tracer (0.0157 m) as compared to the salt tracer (0.00361 m). Similarly, the slight tail in the BTC data further

indicated that dispersion (perhaps molecular diffusion) may play a more noticeable than anticipated role in microcystin-LR fate and transport along with advection at similar EBCTs employed to those in the field.

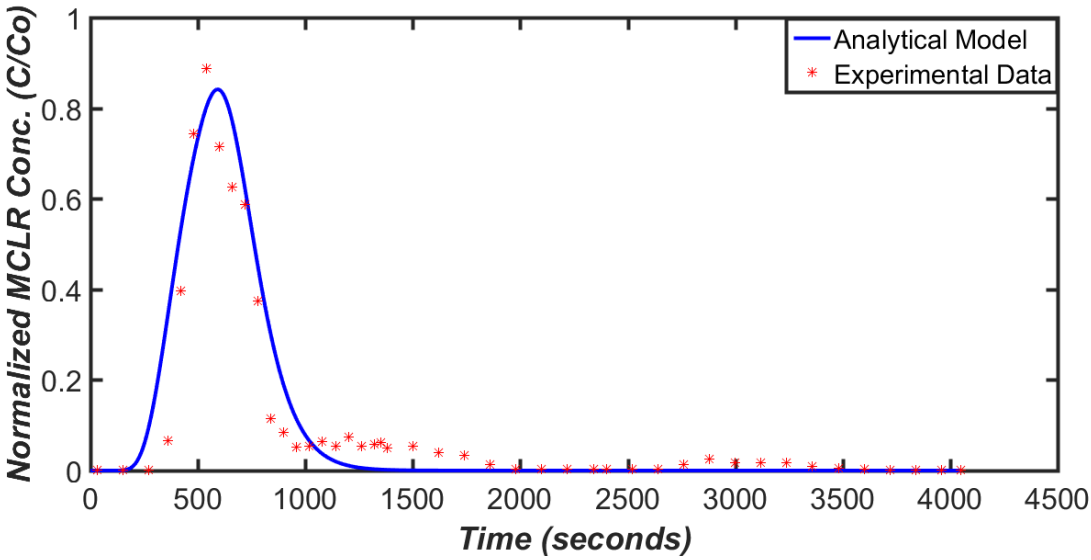

Figure 35. *Model-data fitting results for microcystin-LR non-conservative tracer.*

4. Conclusions and Future Directions

This chapter presented preliminary results detailing the development of a mechanistic model that can accurately and reliably predict microcystin removal in biological filters. The structure of this mechanistic model accounted for both substrate (microcystin) and bacterial cell transport throughout the filter depth. Substrate (microcystin) transport was assumed to be effectively predicted by considering first order, linear physico-chemical sorption, advection, dispersion, and biodegradation by aqueous (suspended) cells and solid biofilm growing on the biofilter media. Bacterial cells were also assumed to be affected by advective and dispersive transport, and attachment and detachment of cells to the filter media was described using a combination of existing deep bed filtration theory and empirical models. Importantly, this model can distinguish

between different growth rates of aqueous versus immobilized (solid biofilm) cells and accounts for the growth of bacterial populations that can actually perform MC biodegradation. The unique feedback mechanism of bioclogging was also captured in this model, where the hydraulic conductivity of the biofilter media declined as the solid biofilm grew in the available pore space.

The primary results of this chapter focused on the development and testing of a 1-D version of the mechanistic model on a series of analytical test functions to verify that the numerical solver was in fact stable and accurate. For the most part, the numerical solutions were in excellent agreement with the analytical solutions tested for various initial conditions and biofilter hydraulics. Although there were some instabilities observed in the coupled numerical solver, these issues were fixed through introducing a new discretization scheme that was shown to drastically improve the stability and accuracy of the numerical simulations.

Calibration of the adsorptive and dispersive behavior of MC when transported through saturated, sandy filter media were also summarized in this chapter as an initial attempt to parameterize the physical-chemical transport characteristics of the mechanistic model. Minimal adsorption of MC-LR was observed during batch biodegradation experiments, and the adsorption isotherm obtained was linear in nature (supporting initial assumptions made in the derivation of the mechanistic model). Conservative tracer experiments performed in 1-D flow through column experiments indicated that the sandy media was not very mechanically dispersive for non-reacting solutes and similar to measurements presented in the scientific literature. However, non-conservative flow through experiments using MC-LR showed that dispersion was not negligible and more

influential than adsorption, where contributions from molecular diffusion of MC-LR in addition to the dispersivity of the media may be important to consider when modelling MC transport through sandy, porous media.

Even though a steadfast attempt was made to develop, verify, and calibrate the 1-D mechanistic model in this chapter, the model was determined to be not parameterized well enough to make accurate and reliable predictions of MC removal. Regarding the bacterial transport throughout the filter, there was very high uncertainty surrounding the parameters governing the transport, attachment, detachment, growth, and decay of these MC degrading bacterial populations. Future experimental efforts will be directed to effectively isolate and independently study these processes and to obtain more accurate and defined parameter estimates compared to those presented in the literature. For example, the bacterial density (ρ_p), the bacterial diameter (d_p), the collision efficiency ($\propto$), as well as the first order decay coefficient (K_d) are all important model parameters describing bacterial attachment and decay. In addition, it will be important to parameterize the growth kinetics of both aqueous and immobilized biofilms degrading MC through application of unstructured models, such as the Monod model, and to determine the fraction of MC degraders existing within the total population through use of biomolecular techniques.

Another inherent limitation to this study was the inability to describe lateral fluid flow within the biofilter, which is important to consider if bioclogging is included within the scope of this mechanistic model. The 1D model should be expanded to at least 2 dimensions to ascertain the effects of bioclogging on biofilter performance, including the stability of the degrading biofilm communities. An interesting research question to address

would be the effect of preferential flow path formation due to bioclogging of the porous media, and how changes to the hydraulics affects treatment performance over long time periods of filter operations (i.e., days to weeks). For example, 2D numerical simulations could investigate whether there is a way to promote more torturous, "fingerlike" preferential flow paths (which increase residence time and lateral flow) as opposed to straight "channeling" of water throughout the filter. Simulations could assess how the initial distribution of biomass, both laterally and vertically, as well as the hydraulics affect the development of these different types of flow paths within the biofilter.

Lastly, after expanding the model to multiple dimensions and performing necessary calibration-based experiments to parameterize this mechanistic model, it will be critical to validate the numerical simulations against real world, laboratory scale experiments. These experiments could involve the application of 2D flow cells where biofilm attachment, growth and detachment could be carefully monitored and even quantified through novel, optical, in-situ techniques. In addition, biomolecular techniques, such as high throughput 16S rRNA sequencing could be performed to determine the key differences between the aqueous versus the solid biofilm MC degrading bacterial communities, which could provide insight as to why these communities are kinetically distinct. Ultimately, these final validation experiments will enable this mechanistic model to provide an improved predictive understanding of the most important biological treatment mechanisms and to identify key operational and design parameters affecting the reliability and efficiency of algal biotoxin removal in biofiltration systems.

Chapter 4: Application of Unstructured Kinetic Models to Predict Microcystin Biodegradation: Towards A Practical Approach for Drinking Water Treatment

Abstract: Biological drinking water treatment technologies offer a cost-effective and sustainable approach to mitigate microcystin (MC) toxins from harmful algal blooms. To effectively engineer these systems, an improved predictive understanding of the bacteria degrading these toxins is required. This study reports an initial comparison of several unstructured kinetic models to describe MC microbial metabolism by isolated degrading populations. Experimental data was acquired from the literature describing both MC removal and cell growth kinetics when MC was utilized as the primary carbon and energy source. A novel model-data calibration approach melding global single-objective, multi-objective, and Bayesian optimization in addition to a fully Bayesian approach to model selection and hypothesis testing were applied to identify and compare parameter and predictive uncertainties associated with each model structure. The results indicated that models incorporating mechanisms of enzyme-MC saturation, affinity, and cooperative binding interactions of a theoretical single, rate limiting reaction accurately and reliably predicted MC degradation and bacterial growth kinetics. Diverse growth characteristics were observed among MC degraders, including moderate to high maximum specific growth rates, very low to substantial affinities for MC, high yield of new biomass, and varying degrees of cooperative enzyme-MC binding. Model predictions suggest that low specific growth rates and MC removal rates of degraders are expected in practice, as MC concentrations in the environment are well below saturating levels for optimal growth. Overall, this study represents an initial step towards the development of a practical and comprehensive kinetic model to describe MC biodegradation in the environment.

1. Introduction

The quality of freshwater resources has become progressively challenged by the increasing frequency and severity of harmful cyanobacterial blooms (Paerl and Huismann 2009, Paerl and Paul 2012, O'Neil et al. 2012). Bloom events associated with toxic species of the *Microcystis*, *Anabaena*, *Planktothrix*, and *Nostoc* genera result in the release of biotoxins into receiving reservoirs or lake ecosystems (Huismann et al. 2006, Merel et al. 2013, Schmidt et al. 2014). The microcystin (MC) class of cyanobacterial toxins, composed of seven amino acids in a cyclical structure, are the most common and toxic in the environment. Over one hundred structural congeners of MC have been identified to date (Huismann et al. 2006, Puddick et al. 2014). MCs are both hepatotoxic and known human carcinogens, prompting the World Health Organization (WHO) and US EPA to develop guidelines for total MCs in drinking water of 1 μg/L (US EPA 2015a).

Of the broad class of MC toxins produced during cyanobacterial blooms, MC-LR (L and R standing for Leucine and Arginine, respectively, for two of the variable amino acids in the cyclical structure) is the most common and toxic (Edwards and Lawton 2009, Cheung et al. 2013). The high stability of the cyclical structure of MCs leads to their persistence in the environment and poses a human health threat through exposure to recreational and drinking water. Although conventional drinking water treatment technologies, such as coagulation, flocculation, and sedimentation can effectively remove intracellular MCs from source water, the extracellular fraction is sparingly removed (Westrick 2008, Westrick et al. 2010). Advanced treatment technologies to remove total MCs from drinking water, such as granular activated carbon (GAC) or ozonation are

effective, yet energy intensive, costly, and subject to some treatment variability (Westrick et al. 2010, Ho et al. 2012a).

Bioremediation strategies, such as biological filtration (biofiltration), which specifically target the removal of MCs from drinking water, have advanced as a viable alternative (Li et al. 2011c, Li et al. 2011b, Li et al. 2015a, Ho et al. 2007b, Ho et al. 2012a). Bio-based treatment strategies rely on the metabolism of MCs as auxiliary or sole carbon, energy, and nutrient (nitrogen) sources by microbial communities indigenous to the source water (Li et al. 2011c, Ho et al. 2012a, Li et al. 2017). However, high variability in indigenous bacteria composition, temperature, pH, and the presence of exogenous nutrients pose formidable barriers to consistent removal of MC in these systems (Li et al. 2017).

To overcome these limitations and progress toward "engineered" bio-based MC remediation systems, an improved predictive understanding of MC biodegradation is required. A practical approach is to model MC biodegradation using existing theory from the fields of biochemical engineering, bioremediation, and wastewater treatment (Esener et al. 1983, Kovárová-Kovar and Egli 1998, Alexander 1999, Shuler and Kargi 2002, Tchobanoglous et al. 2003, Okpokwasili and Neweke 2006). Unstructured kinetic models (i.e., the Monod kinetic equation) to describe biodegradation in field and laboratory settings, have gained wide acceptance in applications ranging from the prediction of microbial degradation of contaminants in the environment to treatment system design (Simkins and Alexander 1984, Rittmann et al. 1986, Suarez and Rifai 1999, Al-Khalid and El-Naas 2012, El-Naas et al. 2014). The popularity of unstructured kinetic models in these

engineering applications stems from the avoidance of unnecessary complexity and computational burden associated with many structured models (Esener et al. 1983).

Despite the practicality of unstructured kinetic models, the great number of models available describing different growth mechanisms, uncertainty associated with parameter estimates, and difficulties arising from non-linear regression during model calibration often limit their use in an environmental context (Koch et al. 1982, Robinson 1985, Grady et al. 1996, Kovárová-Kovar and Egli 1998, Knightes and Peters 2000). Of the number of challenges, identifying the mechanisms to include (i.e., the appropriate model) and arriving at accurate and reliable parameter estimates are primary issues undermining the predictive utility of unstructured kinetic models. For example, a broad range of unstructured model frameworks, from theoretical single, rate limiting enzyme catalyzed reactions (i.e., Monod 1949) to those that account for transport and uptake of substrate (i.e., Powell 1967), have been developed to describe microbial growth. In addition, reaching uncorrelated estimates of the maximum specific growth rate (μ_{max}) and half saturation constant (K_s) parameter values of many unstructured kinetic models has remained a well-known challenge over the years (Nihtilä and Virkkunen 1977, Holmberg 1982, Robinson and Tiejde 1983, Liu and Zachara 2001).

In this study, we address the following questions as a preliminary step toward the development of a practical and comprehensive MC biodegradation model in natural or engineered treatment systems. Importantly, we anticipate that the unstructured kinetic modelling framework reviewed herein will serve as a foundation for future modelling efforts focused on integrating more complex mechanisms to better reflect MC biodegradation in environmental settings:

1) What underlying mechanisms in existing unstructured kinetic growth model frameworks most reliably describe MC biodegradation kinetics?
2) What range in parameters (i.e., μ_{max}, K_s) are associated with these MC degrading organisms and how do they compare to other xenobiotic, micropollutant, or other organic chemical degrading organisms?
3) What is the relative level of confidence and certainty in the model predictions and estimated parameters?
4) Which parameters of these models are most sensitive, and can we identify any parameters that are non-influential?

In addressing these questions, we seek to compare the predictive performance of, and obtain reliable parameter estimates for, several unstructured kinetic models describing MC biodegradation. To this end, experimental data was mined from the literature describing growth and MC metabolism of various isolated degrading bacterial populations using MC as the sole carbon and energy source. An optimization framework merging global, single-objective, multi-objective, and Bayesian methods was developed and applied to these datasets to quantify the predictive and parameter uncertainty associated with each model. A combination of Bayes information criteria as well as a Bayesian approach to hypothesis testing and parameter correlation allowed for an objective approach to model selection, model predictive accuracy quantification, and an assessment of the strength of dependencies between calibrated parameters. Finally, a variance-based approach to global sensitivity, explicitly accounting for dependencies between estimated parameters, was employed to assess the influence of model parameters on model predictions describing cellular growth and MC metabolism.

2. Materials and Methods

A roadmap is presented to first illustrate the workflow of the Materials and Methods section (Figure 35). First (Section 2.1), we present a brief overview of the unstructured kinetic modelling framework as well as a complete description of the experimental data collection effort. Section 2.2 introduces the primary components of the model-data fitting approach, which is thoroughly detailed in a companion paper (Manheim and Detwiler 2018). Bayes information criteria, that were used to objectively compare and select the appropriate model describing MC biodegradation, are reviewed in Section 2.3. Furthermore, the Bayesian approach to hypothesis testing and correlation analysis, which quantified differences in model predictive accuracy and the strength of dependencies between calibrated parameters, is presented in Section 2.4. Lastly, the variance-based approach to global sensitivity analysis (GSA), quantifying the influence of input parameters on the model output variance, is introduced in Section 2.5.

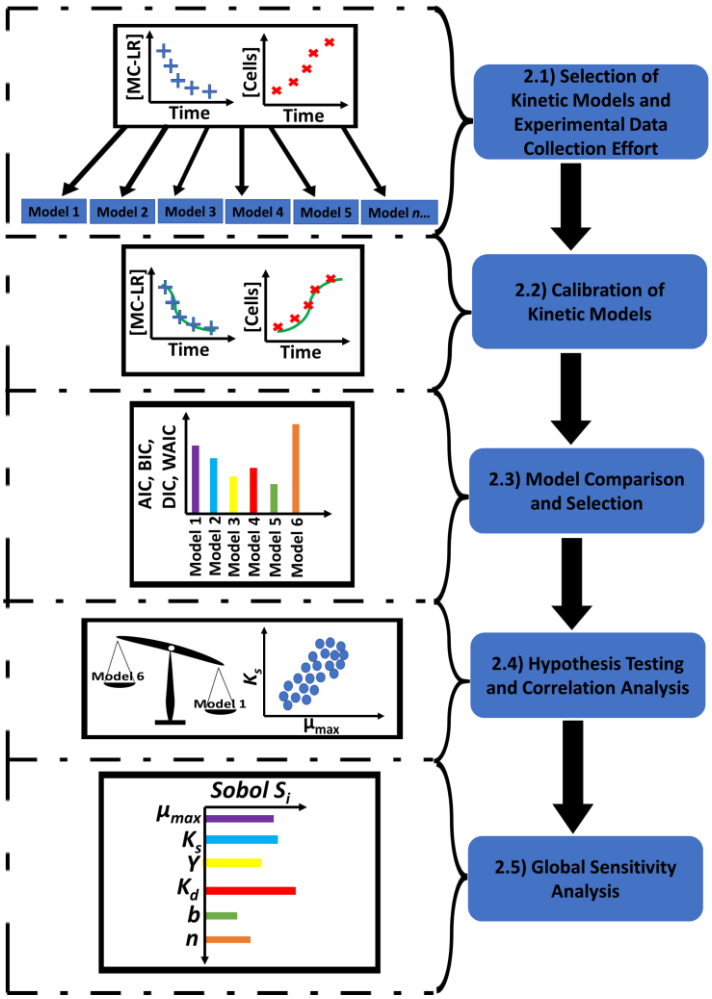

Figure 36. *A roadmap of the primary methods used in this research starting from the model selection and experimental data collection effort (Section 2.1) to the calibration (Section 2.2), model comparison and selection methods (Section 2.3), moving to the Bayesian hypothesis testing (Section 2.4), and ending in a GSA (Section 2.5).*

2.1 Summary of Selected Unstructured Kinetic Models and Data Collection Effort

A total of eight unstructured kinetic models were reviewed in this study to predict MC biodegradation. The main assumption of these unstructured kinetic models is that bacterial growth is limited by a single substrate (i.e., MC). Coupled substrate depletion and bacterial growth kinetics for these models are described by two ordinary differential equations (ODEs) (Eq. 1 and 2), where the endogenous decay of bacterial cells during growth is explicitly considered (Rittmann et al. 2002, Bodegom 2007):

$$\frac{dC}{dt} = -\frac{1}{Y}\mu X \quad (1)$$

$$\frac{dX}{dt} = \mu X - k_d X \quad (2)$$

Where C is the limiting substrate concentration (mg/L), X is the biomass concentration (mg/L), μ is the specific growth rate of bacterial cells (1/hr), Y is the cell yield coefficient (unitless), and k_d is the endogenous decay coefficient (1/hr). Importantly, $X = b*S$, where b is a linear scaling factor used to convert optical density or cell concentration data (S) into biomass concentrations (X).

Table 9 contrasts the unstructured kinetic models surveyed in this study to define the nonlinear relationship between limiting substrate concentration (C) and specific growth rate (μ). Here, we briefly compare the differences in mathematical structure and mechanisms accounted for by each model:

- The classical model of Monod (Monod 1949), analogous to the Michaelis Menten enzyme kinetic model, defines the specific growth rate (μ) as a hyperbolic function of substrate concentration (C) with three main parameters: the maximum specific growth rate, half saturation constant, and the yield coefficient (μ_{max}, K_s, and Y) (Table 9);
- The Tessier model (Tessier 1942) describes the specific growth rate as an exponential function of the substrate concentration, μ_{max}, and K_s (Table 9);
- The Contois model (Contois 1959) accounts for changes in population density that affect the net specific growth rate through inclusion of the biomass concentration, X, into the existing Monod framework (Table 9);

- The Blackman model (Blackman 1905) defines a first-order relationship between specific growth rate (μ) and substrate concentration at low substrate concentrations and a zero-order relationship at higher substrate concentrations (above a threshold concentration, *2*K_s*) (Table 9);
- The Moser (1958) model accounts for potential interactions between binding sites on the enzyme molecule by integrating a tunable parameter n into the Monod framework (analogous to Hill's enzyme kinetic equation, Panikov and Pirt 1978).
- Powell (1967) considered the effect of passive diffusion of a given substrate as the main rate limiting step affecting bacterial growth, deriving the equation in Table 9;
- Dabes et al. (1973) derived a "three-parameter" model describing bacterial growth on a single limiting substrate by considering that only two of the long series of catalyzed, reversible enzyme-substrate reactions involved in substrate metabolism had slow reaction rates (Table 9);
- By simplifying cellular processes to a coupled system of anabolic and catabolic reactions, Heijnen and Romein (1995) developed a universal microbial growth and substrate uptake model (Table 9).

***Table 9**- Summary of unstructured kinetic models implemented in this study*

Model #	Reference	Model Structure	Main Parameters
1	Monod (1949)	$\mu = \frac{\mu_{max} S}{K_s + S}$	μ_{max}, K_s
2	Tessier (1942)	$\mu = \mu_{max}[1 - \exp\left(\frac{-S}{K_s}\right)]$	μ_{max}, K_s
3	Contois (1959)	$\mu = \frac{\mu_{max} S}{K_s X + S}$	μ_{max}, K_s
4	Blackman (1905)	$\mu = \mu_{max}$ if S >= 2Ks $\mu = \frac{\mu_{max}}{2K_s} S$ if S < 2Ks	μ_{max}, K_s

5	Dabes et al., (1973)	$\mu = \mu_{max} \frac{1+\frac{S}{K_S}+\propto}{4\propto}\left[1-\left\{1-\frac{8\propto\frac{S}{K_S}}{(1+\frac{S}{K_S}+\propto)^2}\right\}^{1/2}\right]$	$\mu_{max}, K_s, \propto$
6	Powell (1967)	$\mu = \mu_{max} \frac{1+\frac{S}{K_S}+\propto}{2\propto}\left[1-\left\{1-\frac{4\propto\frac{S}{K_S}}{(1+\frac{S}{K_S}+\propto)^2}\right\}^{1/2}\right]$	$\mu_{max}, K_s, \propto$
7	Moser (1958)	$\mu = \frac{\mu_{max} S^n}{K_s + S^n}$	μ_{max}, K_s, n
8	Heijnen and Romein (1995)	$\mu = \mu_{max}\left[\frac{\frac{S}{K_s}}{\frac{S}{K_s} - 1 + 2^{1/n}}\right]^n$	μ_{max}, K_s, n

Experimental data were obtained from four studies quantifying MC biodegradation kinetics of isolated bacterial populations (Table 10) (Valeria et al. 2006, Wang et al. 2010, Xiao et al. 2011, Zhang et al. 2015b). These studies isolated bacterial populations from the *Sphingomonas*, *Sphingopyxis*, and *Bacillus* genera, which are representative of the main populations involved in MC degradation via the well-known *mlr* pathway (Bourne et al. 1996, Bourne et al. 2001, Li et al. 2017). The few studies that cultured isolated bacteria using MC as the sole carbon and energy source were selected because they agreed with the main model assumption described above.

Each study performed batch degradation experiments, where the initial bacterial inoculum and MC concentrations were controlled (200 µg/L-42 mg/L) (Table 10). These studies promoted aerobic biodegradation of MC (i.e., through shaking) and were temperature controlled (23-30 °C) (Table 10). Very few studies were observed in the literature that reported bacterial growth in conjunction with MC degradation, where those that did only reported optical density (Wang et al. 2010, Xiao et al. 2011, Zhang et al. 2015b) or cell count measurements (Valeria et al. 2006). As the units of cell concentration in Equation 2 are defined in mass per volume (mg/L), optical density and cell

concentration measurements were converted to cell biomass concentrations during model fitting.

Table 10 *- Summary of experimental conditions in each study selected*

Study #	Reference	Taxonomic Identity	Culture Conditions	MC Variant (Media)	Initial MC Conc. (mg/L)	Initial Bacterium Conc.
1	Zhang et al., 2015	*Bacillus nanhaiencis* strain JZ-2013	Batch growth, shaken at 30 °C	LR (M9)	15	OD (600 nm) ~0.514
2	Wang et al., 2010	*Sphingopyxis sp.* USTB-05	Batch growth, shaken at 200 rpm, 30°C	RR (Modified MSM)	42.3	OD (600 nm) ~0.004
3	Valeria et al., 2006	*Sphingomonas* sp. CBA4	Batch growth, shaken at 23±2 °C	RR (MSM)	0.200	1.20E06 CFU/mL
4	Xiao et al., 2011	*Sphingopyxis sp.* USTB-05	Batch growth, shaken at 200 rpm, 30°C	LR (Modified MSM)	28.8	OD (600 nm) ~0.019

2.2 Model-Data Fitting Approach

Bivariate experimental datasets subject to model calibration in this study described time varying concentrations in MC and biomass. Both the sparse and noisy data as well as the highly non-linear nature of the models presented a complex optimization problem (Manheim and Detwiler 2018). We applied a combination of single objective (SO) global optimization, multi-objective (MO) global optimization, and strictly Bayesian based evolutionary algorithms to determine an accurate and defined range in model parameters (Figure 37, refer to Chapter 5 of this dissertation).

A SO algorithm (AMALGAM-SO, Vrugt et al. 2009) was first applied to ascertain the location of the global minimum and the best fits for extremely biased solutions (i.e., fitting

one variable and not the other). An MO optimization approach (using the NSGA-III algorithm) was applied to both confirm the SO results and to define an optimal region in the search space where the corresponding solutions were unbiased (i.e., the "compromise" solution space) (Wohling et al. 2008, Deb and Jain 2014) (Figure 37). Finally, an Approximate Bayesian Computation (ABC) approach (using the DREAM-ZS algorithm, Laloy and Vrugt 2013) was adopted to quantify the uncertainty associated with the parameter estimates and the model predictions (Sadegh and Vrugt 2014) (Figure 37). Optimization results using this method are summarized in a supplementary dataset for reference (see Supplementary Material in online version). In addition, a range in model parameters (i.e., μ_{max}, K_s, Y) was compiled from relevant biodegradation literature to confine the search space to a realistic range in values (Appendix C, section 1).

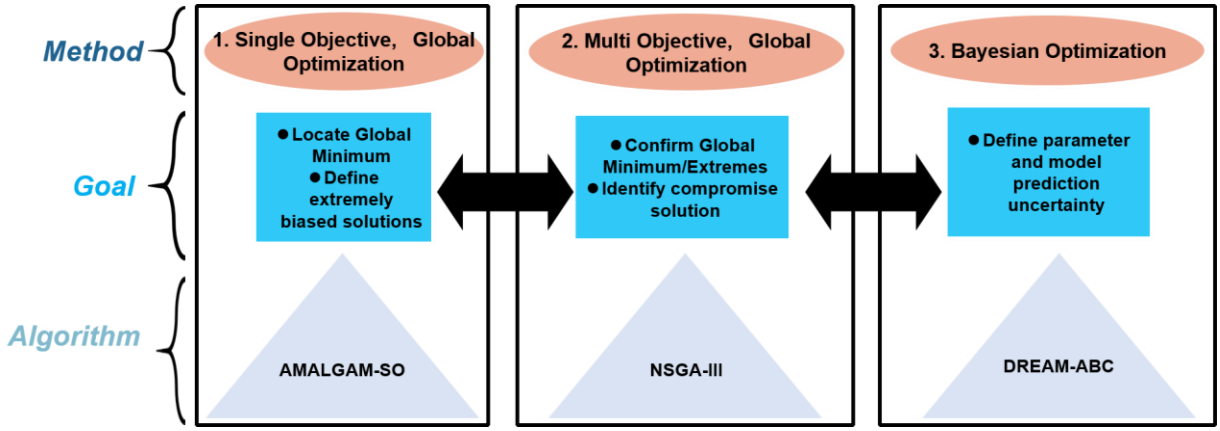

Figure 37. *The primary optimization methods, goals, and algorithms used in this study for parameter estimation.*

2.3 Bayesian Model Comparisons and Selection

A Bayesian framework for model predictive accuracy was applied to compare and select the best performing models (Gelman et al. 2014). Two popular approaches have been detailed in Gelman et al. (2014) and Christensen et al (2011). The first approach calculates several information criteria (i.e., AIC, BIC, DIC, WAIC, which are defined in

Appendix C, Section 2) that have been developed to assess model predictive accuracy. Smaller values of each information criterion indicate better model performance. The second approach is to define the log pseudo marginal likelihood (LPML) of selecting a certain model given the data (Geisser and Eddy 1979). Higher values of the LPML criterion indicate better model performance. Details concerning the calculations involved, an overview of the ranking method, and summary of the results are presented in Section 2 of Appendix C.

2.4 Bayesian Significance Testing and Correlation Analysis

A quantitative framework for Bayesian hypothesis testing, termed Bayesian Estimation Supersedes the T-test (BEST) was adopted in this study to compare the predictive accuracy of the best and next best performing models (Kruschke 2011, Kruschke 2013). Using the BEST framework, we tested the hypothesis that the predictive accuracy of both models was equivalent. The BEST method relies on a Bayesian approach to fit a t-probability distribution to the distribution in log-likelihoods obtained from the calibration procedure of both models (using the DREAM-ZS algorithm, Appendix C, section 3). Next, three probability distributions are derived from the difference in posterior distributions of central tendencies (means), variabilities (standard deviations), and effect sizes (see Appendix C, section 3). The effect size is a statistical parameter used to quantify the size of the difference between two different populations and is calculated using a combination of the means/standard deviations between both distributions $\left(\frac{\mu_1 - \mu_2}{\sqrt{\frac{\sigma 1^2 + \sigma 2^2}{2}}}\right)$ (Coe 2002). Based on the degree of overlap between the distribution in each of these differences (using a 95% highest density interval) with a defined region of practical equivalence (ROPE, -0.1 to 0.1

for all distributions) around the null value (0), the initial hypothesis can be accepted or rejected (Kruschke 2011, Kruschke 2013).

The correlation among different model input parameters was assessed using a Bayesian counterpart to Pearson's linear correlation model. A bivariate normal distribution was used as the main model framework to estimate several probability distributions in Pearson's correlation coefficient (ρ) between different model input parameters. The DREAM-ZS algorithm was used to fit the bivariate distribution model to the posterior distributions in model parameters achieved from the optimization procedure (using two parameter values at a time) (Appendix C, section 4).

2.5 Global Sensitivity Analysis (GSA)

GSA has progressed into one of the most powerful and robust approaches to investigate the influence of different model input parameters on output predictions (Saltelli et al. 2008, Razavi and Gupta 2015, Razavi and Gupta 2016a, Razavi and Gupta 2016b, Gupta and Razavi 2017). GSA investigates the model response when varying each input parameter across its entire uncertainty range, thereby allowing a comprehensive outlook on parameter sensitivity (see Saltelli et al. 2008 for more complete details).

A variance based global sensitivity analysis (VBGSA) accounting for dependent model input parameters was applied in this study to analyze the effects of different model input parameters on predicted responses (Mara et al. 2015). This method allows the GSA to be conducted unobstructed from the correlations that may be present between input parameters, allowing unique sensitivity indices to be derived. Sobol's first and total order effect indices can be reliably calculated to rank the influence of different model parameters on resulting predictions. The "first" order effect index (S_i) represents the independent

contribution of an individual parameter to the total model output variance, while the "total" order effect index (ST_i) denotes the combined interactive contributions of an individual parameter with all other parameters to the total model output variance (Saltelli et al. 2008). The specifications and calculations of the sensitivity estimation procedure are summarized in Appendix C (section 5).

3. Results

3.1 Bayesian Model Comparison and Selection

The top three best performing models, based on a ranking system using all summarized criteria (AIC-LPML), varied across each study (Figure 38, Tables C4-C7). The results highlighted the consistent and accurate performance of the Moser model for three of the four datasets investigated, as the AIC-WAIC criteria and LPML values were consistently lowest and highest for this model (Figure 38, Table C4-C7). Results for Study 4 indicated the only exception to this trend, where the Heijnen model performed the best (i.e., lowest DIC-WAIC and highest LPML, Figure 38). The Contois model performed reasonably well for Studies 1 and 2 (lower AIC-WAIC and higher LPML), and the performance of the Blackman kinetic model was worth considering based on results presented for Studies 3 and 4 (i.e., lower overall AIC-WAIC and higher LPML, Figure 38). However, the Monod model demonstrated poor predictive performance across all studies (i.e., higher overall AIC-WAIC and lower LPML Figure 38, Tables C4-C7).

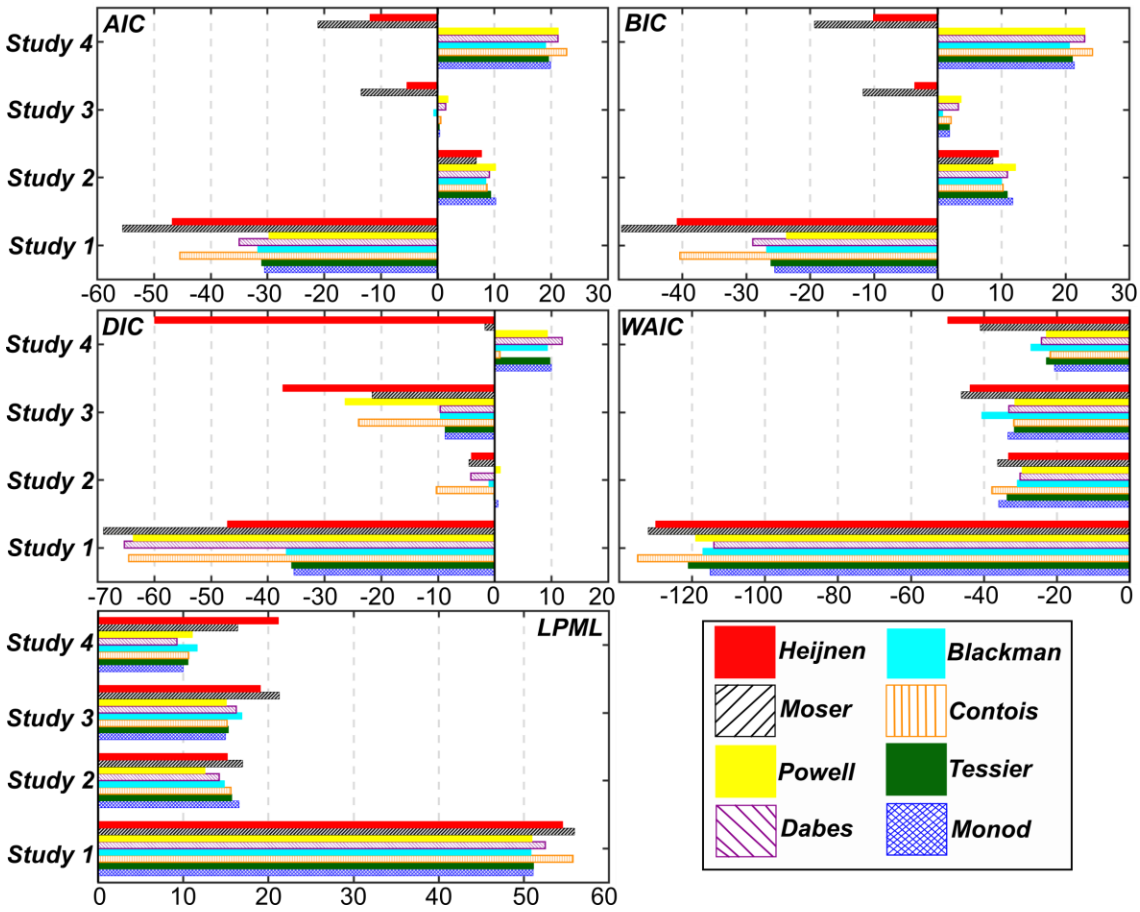

Figure 38. *Comparison of unstructured kinetic model predictive accuracy using Bayesian information criteria (AIC-WAIC) and Log Pseudo Marginal Likelihood (LPML) values calculated for each study and model. Lower values of AIC, BIC, DIC, and WAIC or higher values of LPML are associated with improved model predictive accuracy. According to all AIC/BIC, and LPML as well as most DIC/WAIC calculations, the Moser and Heijnen model predictions outperform all other models for Studies 1-3 and 4, respectively.*

The quantitative strength of evidence in favor of the Moser or Heijnen models for predicting MC biodegradation was assessed using the BEST approach (Kruschke 2011, Kruschke 2013). Through Bayesian fitting of a t-distribution to the log likelihood values obtained from the initial calibration procedure, a posterior distribution in means and standard deviations was reached for both competing models. The difference in this posterior distribution of means $(\mu_1 - \mu_2)$, standard deviations $(\sigma_1 - \sigma_2)$, and effect sizes

$\left(\frac{\mu_1 - \mu_2}{\sqrt{\frac{\sigma 1^2 + \sigma 2^2}{2}}}\right)$ between the best and next best performing model provides quantitative evidence of the magnitude of the difference in predictive accuracies between the competing models.

Figure 39 details the probability densities of the difference in means, standard deviations, and effect sizes between the best and next best performing models for each study. For Studies 1-4, the best and second-best performing models were as follows: Moser and Contois; Moser and Contois; Moser and Heijnen; as well as Heijnen and Moser. The results demonstrated that the predictive accuracies of the best and next best performing model were significantly different for each study, which is supported by the following evidence: 1) the distributions of the difference in means and standard deviations between the competing models were centered well away from zero; 2) the 95% highest density intervals (HDI) of the differences in means/standard deviations did not overlap the "null value" (0); 3) the magnitude of the differences in effect size was large; and 4) the 95% HDI of the effect sizes were well outside the range of the ROPE [-0.1, 0.1] interval (Figure 39, Kruschke 2011; Kruschke 2013). These results confirm that: 1) there is statistically significant evidence in favor of the Moser or Heijnen models and 2) that model selection (and associated growth mechanisms included) greatly influences predictive performance of MC biodegradation.

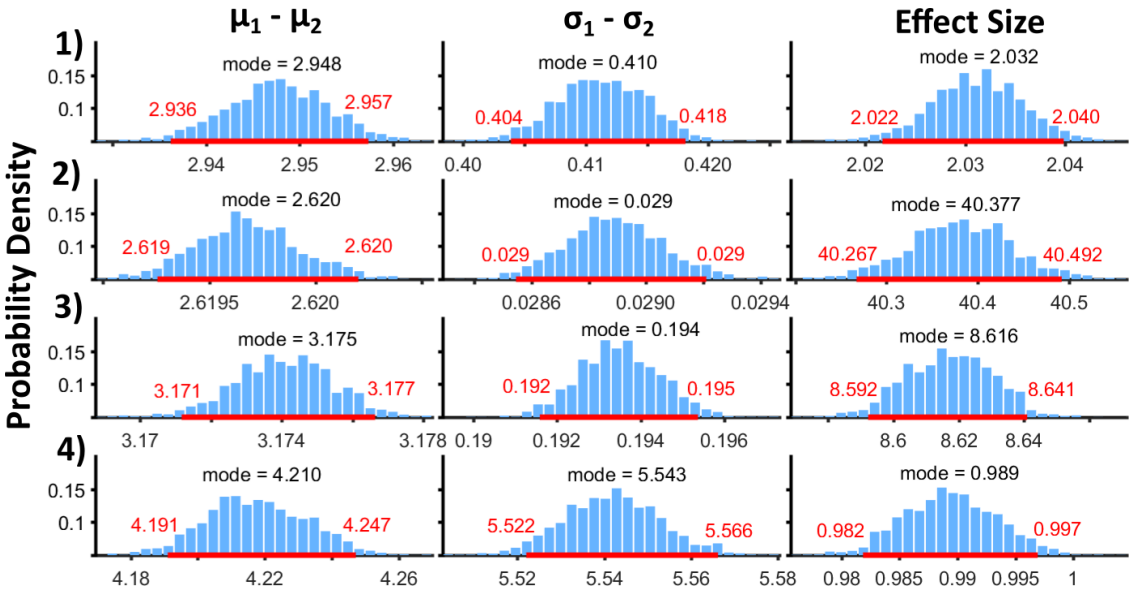

Figure 39. *Statistical differences in densities of model predictive accuracies (log likelihoods) associated with the best performing vs. the next best performing kinetic models for Studies 1-4. Using the BEST approach, the distribution in predictive accuracies (log-likelihoods) for the best and next best performing models is fitted to a t-distribution, returning a posterior distribution in means, standard deviations, and effect sizes. The difference in the posterior distributions of fitted means (column "μ_1-μ_2"), standard deviations (column "σ_1-σ_2"), and effect sizes (column "Effect Size") between the best and next best performing model forms a final distribution that determines the quantitative strength of evidence in favor of the best performing model. Both the 95% highest density intervals (in red) and the modes (black) of each final distribution are indicated on each figure.*

3.2 Model-Data Fits and Parameter Distributions

Both the Moser (Studies 1-3) and Heijnen (Study 4) models were able to accurately reproduce MC biodegradation and biomass growth for each of the four studies reviewed, as the experimental data fell within the 95% total predictive uncertainty intervals (Figure 40). The accuracy of, and certainty in, model predictions were highest for Study 1 (*Bacillus nanhaiencis* strain) and lowest for Study 2 (*Sphingopyxis sp.* strain), as noted by the width of the uncertainty intervals, the proximity of the best fitting prediction to the experimental data, as well as the RMSE and minimum objective function values (Figure 40, Table C8).

Parameter uncertainty was in all cases higher for the biomass growth data as compared to the substrate consumption data, as demonstrated by the wide 95% uncertainty

intervals (Figure 40). This result can be explained by both the high parameter uncertainty associated with the yield coefficient (Y) and endogenous decay rate (k_d) parameters (Table 11) and moderate to high sensitivity of the predicted cell concentrations to these model parameters (Figure 43). When an input parameter to a given model is both highly uncertain and influential, the total predictive uncertainty of this model will be higher, resulting in a wide range of predictions in biomass growth (Figure 40).

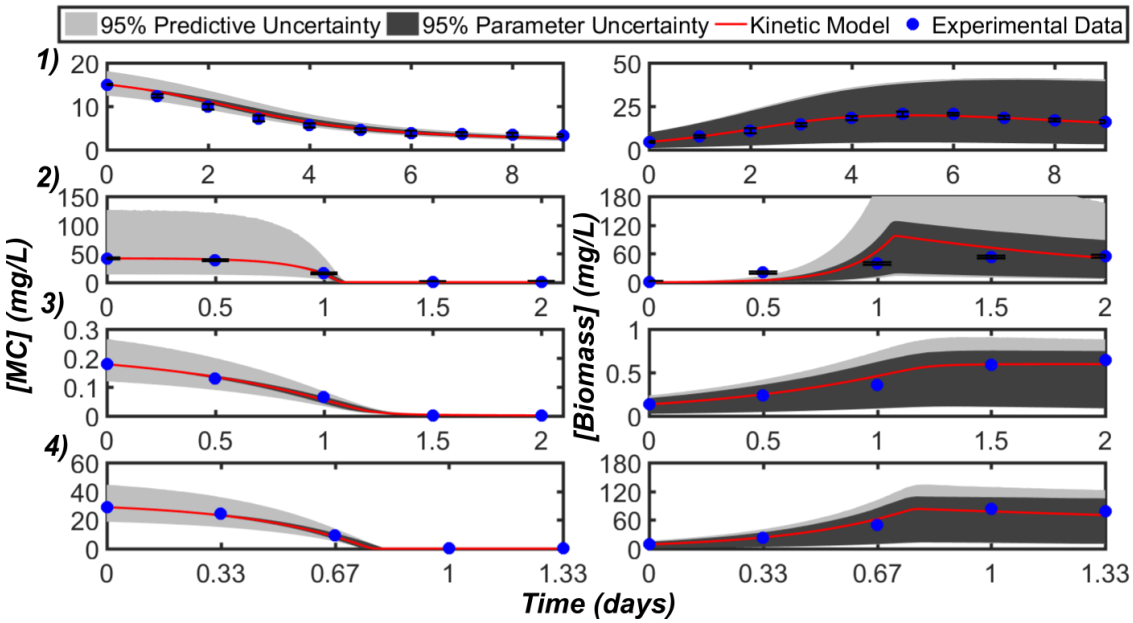

Figure 40. *Kinetic model-experimental data fitting results of the best performing model for Studies 1-4 portraying MC removal (first column) and corresponding biomass growth (second column). Studies 1-3 were fit using the Moser model, whereas Study 4 was fit using the Heijnen model. The red line indicates the best fitting model prediction, while the blue dots represent the experimental data points (along with the standard deviation of replicate experiments). The light grey shading indicates the 95% predictive uncertainty interval and the dark grey shading represents the 95% uncertainty interval associated with the parameter estimation. Narrower total and parameter uncertainty intervals are indicative of improved model predictive accuracy. All experimental data points were observed to fall within the uncertainty intervals, indicating that the predictions afforded by either model can reproduce the experimental data with great certainty.*

The posterior distributions in best performing model parameters were fairly normally distributed for μ_{max}, k_d, b, and n model parameters, indicating that they were well

identified during model-data calibration (Figure 41). This result was further supported by the small 95% credible interval widths and COV values obtained for these model parameters (Table 11). The half-saturation constant (K_s) could not be uniquely identified for Studies 1 and 4; however, K_s was well distinguishable given the experimental data from Studies 2 and 3 (supported by the small 95% credible intervals and COVs), although the distributions were very right-skewed (Figure 41). The yield coefficient values (Y) could not be uniquely identified for all studies investigated, as all parameter values approached the upper realistic boundary (Figure 41). The best performing parameter values were present close to the peak of each posterior distribution, further verifying that the distributions converged around the best compromise solution (Figure 41).

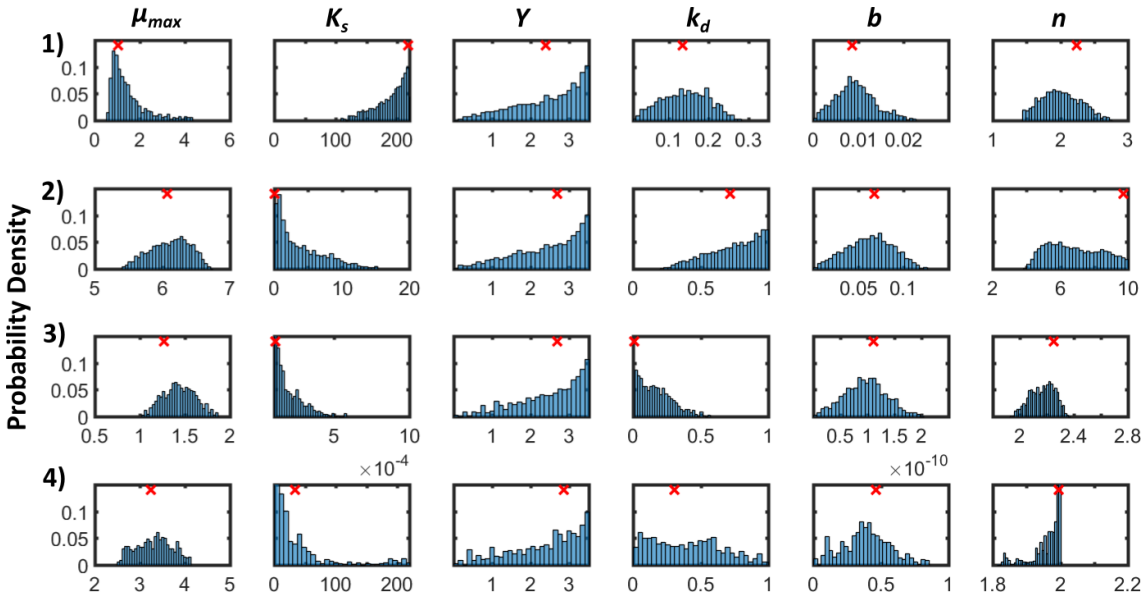

Figure 41. *Posterior distributions in best performing model parameters for Studies 1-4 obtained from the DREAMZS_ABC algorithm. Studies 1-3 were fit using the Moser model, whereas Study 4 was fit using the Heijnen model structure. Distributions that appear normally distributed indicate uniquely identifiable parameters, whereas flat or left/right skewed distributions indicate issues with unique identification (and possible correlation with other parameters). The red 'x' indicates the best fitting model parameter (MAP) value for each study. In most cases, the MAP falls on the location with the highest probability density.*

Diverse kinetic and physical growth characteristics were evidenced for each MC degrading bacterium included in this study, especially when comparing maximum specific growth rate and half-saturation constant model parameters (Table 11). Maximum specific growth rates on MC were not necessarily proportional to MC affinities (i.e., K_s). For example, the *Sphingopyxis sp. USTB-05* (Study 2) strain was characterized by a relatively low affinity for MC (moderate-high K_s), but had the highest maximum specific growth rate of the studies investigated. Comparably, the *Sphingomonas sp.* evidenced a very high affinity for MC as a substrate but had the lowest maximum specific growth rate of the studies investigated (Table 11). Great differences in the magnitude of conversion constants (*b*) implicated highly varying cell densities and physiologies for each MC degrading bacterium. Across all studies, the magnitude of the yield coefficient (*Y*), endogenous decay rate (k_d), and *n* values were relatively comparable (Table 11).

Table 11*- Summary of best performing model parameter values including the mean (μ), standard deviation (σ), coefficient of variation (COV), and 95% credible intervals.*

Parameter	**μ_{max} (1/day)**			
Study	1	2	3	4
μ	1.48	6.11	1.43	3.31
σ	0.799	0.290	0.177	0.392
COV	54	5	12	12
95% Credible Interval	[0.659, 3.80]	[5.53, 6.59]	[1.11,1.78]	[2.64,4.02]
Parameter	**K_s (mg/L)**			
Study	1	2	3	4
μ	188	3.93	0.000194	30.1
σ	26.2	3.52	9.37E-05	47.4
COV	14	90	48	157
95% Credible Interval	[127, 219]	[0.159,12.3]	[0.00010,0.00043]	[1.54,196]
Parameter	**Y (mg biomass/mg substrate)**			
Study	1	2	3	4
μ	2.43	2.42	2.47	2.36
σ	0.859	0.860	0.836	0.906
COV	35	36	34	38

95% Credible Interval	[0.525, 3.48]	[0.536,3.48]	[0.588,3.48]	[0.433,3.48]
Parameter	**k_d (1/day)**			
Study	1	2	3	4
μ	0.140	0.739	0.172	0.406
σ	0.0584	0.1908	0.1191	0.258
COV	42	26	69	64
95% Credible Interval	[0.0318, 0.245]	[0.329,0.991]	[0.014,0.450]	[0.0278,0.925]
Parameter	***b* ((g DW/L) / OD or (g DW/L) / (CFU/mL))**			
Study	1	2	3	4
μ	0.0094	0.0620	9.6E-11	0.389
σ	0.0044	0.0257	3.85E-11	0.176
COV	47	41	40	45
95% Credible Interval	[0.00173, 0.0191]	[0.012,0.109]	[2.01E-11, 1.72E-10]	[0.0621,0.751]
Parameter	***n* (unitless)**			
Study	1	2	3	4
μ	2.00	6.82	2.17	1.96
σ	0.289	1.573	0.090	0.042
COV	14	23	4	2
95% Credible Interval	[1.49, 2.57]	[4.37,9.73]	[1.98, 2.31]	[1.84, 2.00]

3.3 Parameter Correlation Analysis

The parameter correlation analysis indicated that for all studies (1-4), there was a strong, positive, linear correlation between μ_{max} and k_d as well as between b and Y model parameters (Figure 42), where distributions in Pearson's correlation coefficient varied between 0.53 to 0.92 (for μ_{max} and k_d) as well as between 0.80 to 0.90 (b and Y). Study 1 demonstrated a strong, negative, and non-linear correlation between μ_{max} and n model parameters. Studies 2-4 indicated a moderate, negative, and linear correlation between μ_{max} and b model parameters. Studies 2-3 observed a strong, negative, and slightly non-linear correlation between n and K_s values (Figure 42). Across all studies, the mostly negative correlations between parameters n and K_s/μ_{max} were non-linear given that the n value parameters were used as exponents in the original model structures (for Moser and Heijnen). The presence of multiple strong positive and negative linear and nonlinear

correlations was a factor that likely prohibited the unique identification of all six model parameters given the experimental data from all studies.

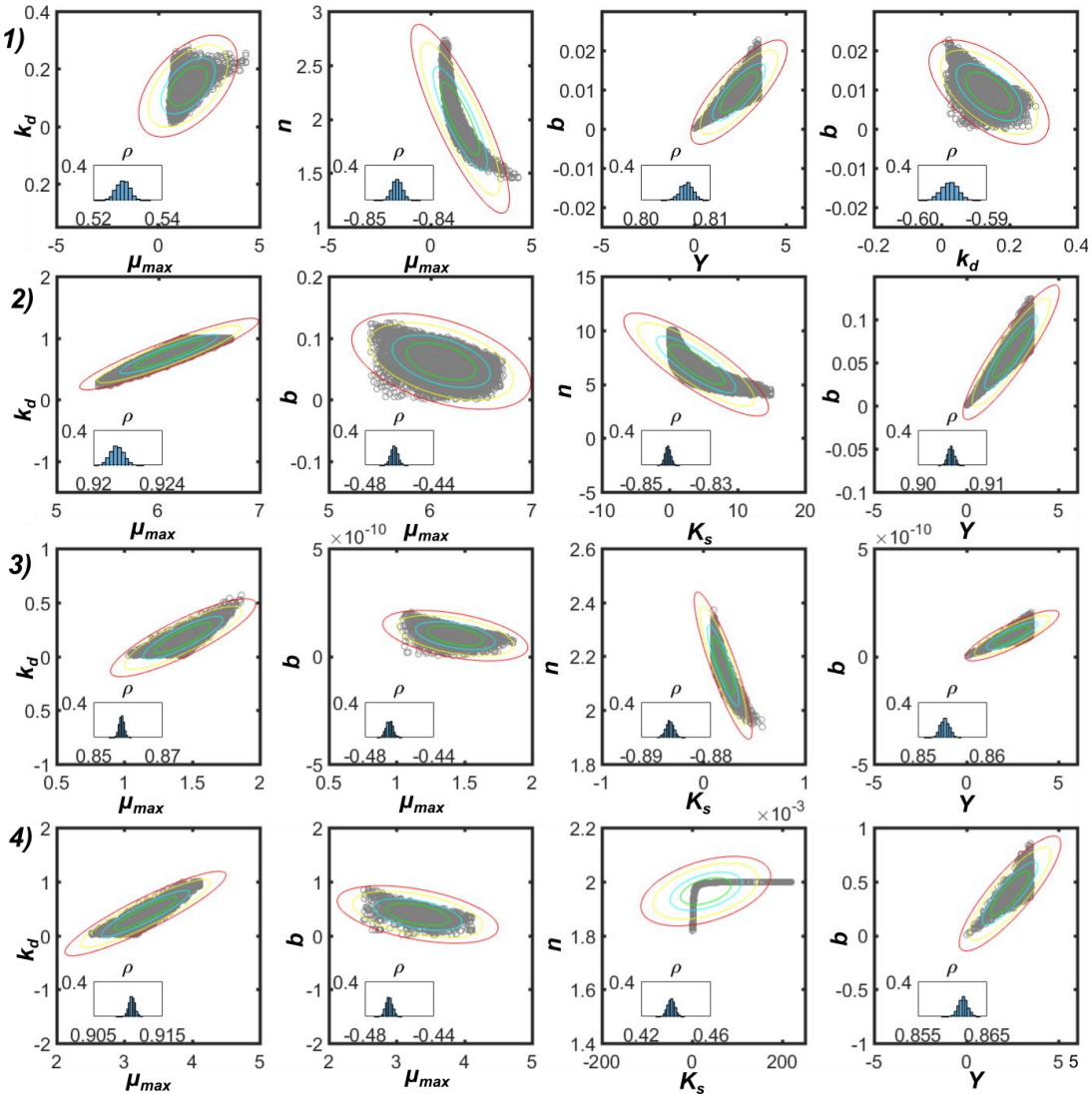

Figure 42. *Bayesian analysis of the strongest (i.e., ρ > 0.40, ρ < -0.40) linear correlations between best performing model parameters for Studies 1-4. The 99%, 95%, 75%, and 50% highest density ellipses are overlaid on the scatter plots in red, yellow, cyan, and green, respectively. The inlet plots depict the distribution in Pearson's correlation coefficient obtained from the Bayesian correlation analysis. Although the pairwise combinations of strongest linear correlations were not always equivalent across all studies, strong positive correlations (higher values of Pearson's ρ) were generally evidenced for μ_{max} vs. k_d and Y vs. b, whereas negative correlations were generally observed for μ_{max} vs. b. Some nonlinearity in the correlations were also evidenced for model parameters that involved exponents in the original model structure (i.e., n)*

3.4 Global Sensitivity Analysis

The results of the VBGSA indicated a diverse range in input parameter sensitivities across all studies using Sobol's first and total order effect indices as the primary means of comparison (Figure 43). It is important to note that Sobol's first order effect indices closer to 1 indicated that the model output was more sensitive to the corresponding input parameter, whereas indices closer to 0 indicated little to no sensitivity. Comparably, values of Sobol's total order effect index closer to or higher than 1 were indicative of a parameter that was highly interacting with other model parameters (and not interacting when values approached 0).

Based on a unique ranking system (described in Appendix C, section 5.3), the general parameter rankings across studies (using either first- or total-effect indices), from most to least influential, depended primarily on the variable of interest (i.e., substrate or cell biomass concentrations) (Figure 43). Using the first-order indices (S_i) as ranking criteria, predicted substrate concentrations were generally most influenced (in descending order) by k_d (1), b (2), and μ_{max} (3), with less influence observed from Y (4), K_s (5), and n (6) (Figure 43I). Predicted cell biomass concentrations were most influenced (in descending order) by parameter values of k_d (1), μ_{max} (2), and K_s (3), with less influence observed from Y (4), b (5), and n (6) (Figure 43II). Using the total order effect indices (ST_i) as ranking criteria, interactive effects on substrate concentration predictions were higher for k_d (1), K_s (2), Y (3) and less significant for n (4), μ_{max} (5), and b (6) model parameters (Figure 43I). Comparably, interactive effects on cell biomass concentration predictions were higher for k_d (1), μ_{max} (2), K_s (3) and less significant for Y (4), b (5), and n (6) model parameters (Figure 43II).

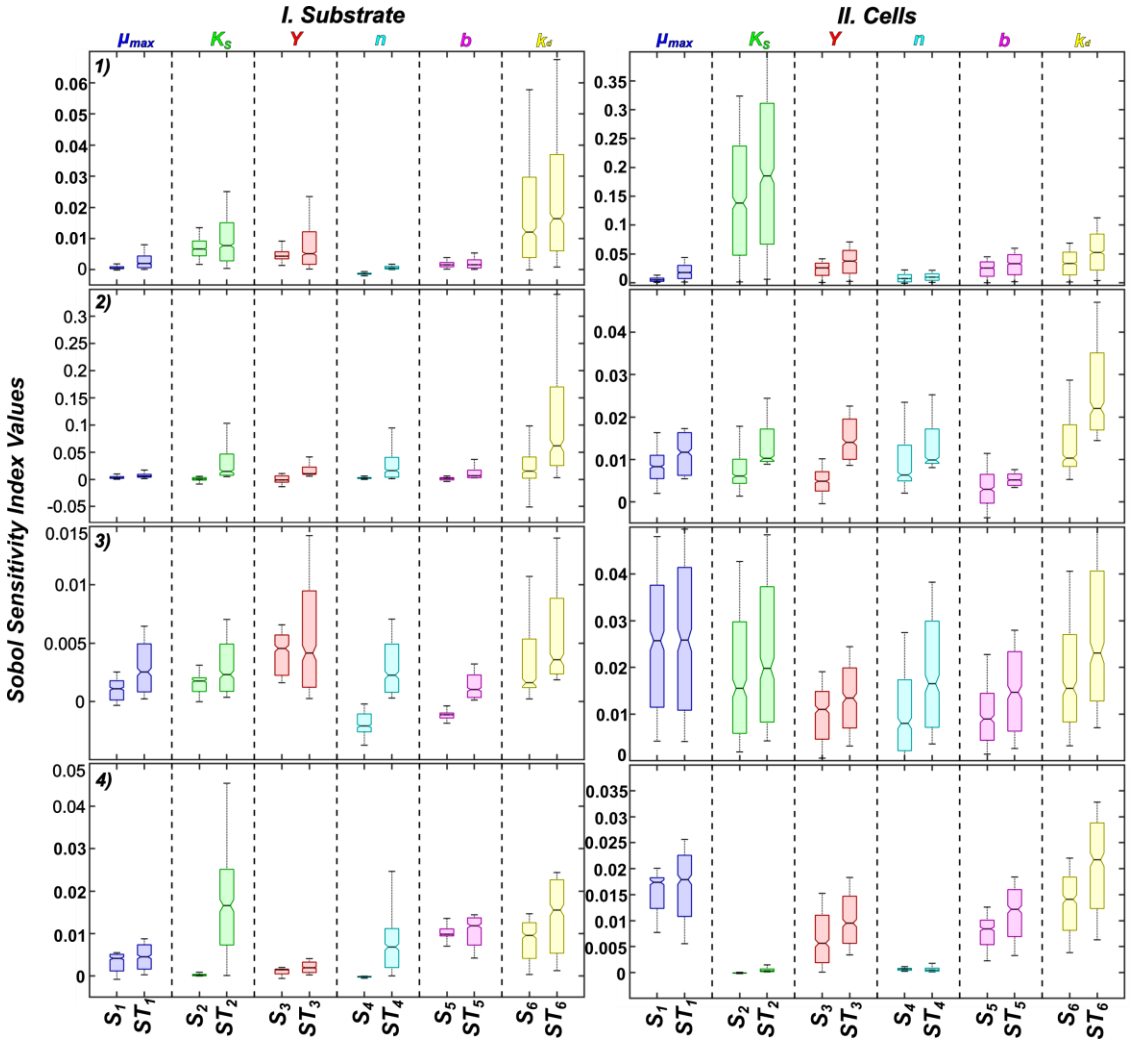

Figure 43. *VBGSA results summarized for Studies 1-4, presenting Sobol's first and total order effect indices. Here, "first" order represents the independent contribution of an individual parameter to the total model output variance, while "total" order denotes the combined interactive contributions of an individual parameter with all other parameters to the total model output variance. We note that by implementing the method of Mara et al. (2015), the sensitivity indices are determined free of any correlations present between input parameters. Values of the first order effect closer to 0 or 1 indicate that the model output is barely or highly sensitive to the corresponding input parameter, respectively. Values of the total order effect closer to 0 or 1 (or above) indicate that the parameter is hardly or highly interactive with all other model parameters, respectively. The boxplots represent the distribution in sensitivity indices across all simulated time points. Colors correspond to individual parameter values. Panel column I presents the sensitivity results for model predictions involving substrate concentration, whereas Panel column II presents results for model predictions involving cell biomass.*

4.0 Discussion

4.1 Study Contribution

This is the first study, to the best of our knowledge, to apply and compare several unstructured kinetic growth models to describe MC biodegradation. Coupled bacterial growth and MC removal kinetics were both accounted for in all unstructured models, which is a significant step forward from previous simplistic zero- and first-order kinetic models to describe MC biodegradation. Each unstructured model was successfully calibrated to existing experimental data through a novel optimization approach to determine an accurate and defined range in bio-kinetic parameters. These parameters can eventually, through further refinement, model complexity, and experimentation, be applied to the design of biological water treatment systems and prediction of the fate and persistence of MC in the environment.

The results from this study represent a preliminary step toward the development of a practical and comprehensive unstructured kinetic model that can predict the environmental behavior of these microorganisms. Clearly, accounting for different environmental factors in the model structure, such as temperature, pH, or the presence of other carbon substrates (as discussed in Section 4.5) will better capture the environmental variability expected in practice. As the complexity of these models is expected to increase in future studies to account for various environmental factors, we argue that issues associated with model selection, uncertainty estimation, nonlinear regression, and parameter identification will likely intensify. The approach presented herein for model selection and calibration provides a robust foundation for developing MC biodegradation models for increasingly complex environmental conditions.

4.2 The Physical Case for Moser Kinetics

The statistical results presented in this study have demonstrated that the Moser model provided superior MC biodegradation predictions compared to other common unstructured kinetic models. However, we have not emphasized the physical relevance underpinning the structure of the Moser model. As initially proposed by Blackman (1905), many studies have advocated that the Monod model is a theoretical extension of the "bottleneck concept," postulating that a single rate limiting "master" reaction controls the kinetics of metabolism of any substrate (Monod 1949, Dabes et al. 1973, Panikov 1995). In the simplified case of Monod kinetics, the maximum forward rate of one reaction in the cell is order of magnitudes smaller than the maximum forward rate of any other enzyme catalyzed reactions involved in transport and/or metabolism. This concept simplifies the description of bacterial growth into a Michaelis Menten (or Hill) type rate equation, depending on one enzyme and reaction of interest (Dabes et al. 1973, Panikov 1995).

We have shown statistically that accounting for the mechanisms of saturation, binding affinity, and binding interactions between this hypothetical enzyme and MC substrate complex can accurately and reliably predict MC biodegradation. A "master" rate-limiting reaction dictating MC biodegradation kinetics is further supported by the fact that the model comparison process did not select for a more complex, multiple reaction type derivation as provided by Dabes et al. (1973). Importantly, the mechanism of "saturation" involves binding of substrate molecules to the active sites on the enzyme to capacity; "binding affinity", the relative strength of attraction or attachment between an enzyme and substrate molecule; and "interactions", the degree of inhibition or facilitation between binding sites on a given enzyme (Panikov and Pirt 1978, Cohlberg 1979, Panikov 1995).

Given this theoretical justification to the Moser model, it is interesting to explore which "master" reaction may be the most well justified rate limiting step in the MC biodegradation pathway. MC biodegradation involves four primary genes/enzymes, including *mlr*A, *mlr*B, *mlr*C, and *mlr*D (production of the enzyme microcystinase (*Mlr*A), enzyme *Mlr*B, enzyme *Mlr*C, and enzyme *Mlr*D) (Bourne et al. 1996, Bourne et al. 2001). *mlr*A is responsible for the initial linearization of cyclical MC, *mlr*B and *mlr*C for further breaking down linearized MC into smaller peptide and amino acid products, and *mlr*D for actively transporting MC into the cell (Bourne et al. 1996, Bourne et al. 2001).

It is probable that the linearization of cyclical MC may be the rate limiting step in this pathway, given that the cyclical structure is highly resistant to degradation and may require a large cellular energy input to synthesize adequate quantities of microcystinase (Dziga et al. 2012). Experimental evidence of the enzymatic activity of microcystinase has indicated that Hill kinetics best describe the linearization reaction as compared to Michaelis-Menten enzyme kinetics. Dziga and co-workers (2012) results align with the statistical results observed from this study, which advocated the Moser model over the Monod model. In addition, the kinetic parameters measured for microcystinase (V_{max} = 95 day^{-1}, Ks = 158 mg/L, n = 1.57) were on the same order of magnitude of those observed for various MC degrading bacteria in this study, further strengthening our initial presumption.

4.3 Physical Significance of Model Parameter Estimates

The physical significance of the Moser model parameters is also important to review. The results demonstrated that all MC degrading bacteria possessed similar ranges in maximum specific growth rates (1-7 per day), which are comparable to the lower range in maximum specific growth rates reported for fast growing, heterotrophic

microorganisms in activated sludge systems (Kovárová-Kovar and Egli 1998, Tchobanoglous et al. 2003). These results imply that these MC degrading organisms may grow relatively quickly in the environment if MC is readily available.

Very significant differences in K_s values were estimated between MC degrading bacteria in this study. Since the inverse of the half saturation constant can be defined physically as an enzyme's relative binding affinity for a substrate (Kovárová-Kovar and Egli 1998), there are possibly marked preferences in MC as a substrate among various MC degrading bacteria. Across all MC bacteria reviewed, the *Sphingomonas* species had the lowest reported half saturation constant, which resulted in much higher specific growth rates at lower substrate concentrations. Smaller K_s values for MC substrates may signify a high specificity of microcystinase enzymes for MC as a substrate, or differences in enzyme regulation at the molecular level (i.e., induction vs. constitutive production), among many factors. A high affinity for a given substrate may be a physiological adaptation to improve an organism's capability to scavenge for several carbon sources under low nutrient conditions present in many oligotrophic environments (Noel and Narang 2009, Egli 2010).

Yield coefficient (Y) parameter estimates were very high among all MC degrading bacteria. It is important to note that the yield coefficients estimated in this study are "observed" or "apparent" values, not entirely corrected for the presence of maintenance costs (Esener et al. 1983, Bodegom 2007). For perspective, estimated yield coefficients from the literature for the biodegradation of organic and synthetic pollutants were observed to rarely exceed 1 (i.e., 100% conversion of substrate to biomass) (Doran 1995, Suarez and Rifai 1999, Shuler and Kargi 2002). Higher values of the yield coefficient

estimated in this study may suggest that MC is a superior carbon source for the creation of raw cellular material as compared to the supply of the MC degrading cell's other functions. The *n* parameter values for both the Moser and Heijnen models were typically greater than 1 for most studies. For the Moser model structure, this result signifies that the interactions between binding sites for MC degrading enzymes are cooperative in nature. Analogous to the Hill model for enzyme kinetics, cooperative interactions imply that the binding potential of MC substrate molecules to the enzymes involved increases as the number of previously bound substrate molecules increase (Panikov and Pirt 1978).

The endogenous first-order decay coefficient (k_d) represents the amount of energy diverted to a cell's maintenance requirements in the absence of substrate from the environment, and usually involves oxidation of a cell's internal reserves (Rittmann et al. 2002, Bodegom 2007). Results from this study indicated that first order decay parameter estimates are relatively high for MC degrading populations (0.1 to 0.7 per day), on the same order of magnitude of those estimated for mixed bacterial populations in activated sludge (Tchobanoglous et al. 2003). These results imply that in the absence of MC or other carbonaceous substrates, a swift decline in populations may ensue in the environment.

4.4 Initial Kinetic Model Predictions

A significant implication from initial predictions using the Moser model is that most bacterial growth rates are far from saturated in the environment if MC is used as a sole carbon and energy source (Figure 44), as at least two of the bacterial strains (*Bacillus nanhaiencis*, *Sphingopyxis sp. USTB-05*) will be growing at very low specific growth rates (6E-04 to 0.2 per day). Since specific growth rate is directly proportional to substrate removal rate, we would expect slow biological removal of MC in the environment. However,

when MC is supplied at much higher concentrations, as has been typically conducted in a laboratory setting (i.e., in the mg/L range), the removal rates of MC would be expected to drastically increase (1-4 orders of magnitude). Therefore, biological drinking water treatment strategies for MC removal will have to consider the disparity in specific growth rates of these organisms when faced with low concentrations of MC generally observed in the environment. A promising solution to ensure high specific growth rates of degrading bacteria and quick elimination of MC in bio-based drinking water treatment systems is through bio-stimulatory practices, like the addition of nutrients (i.e., nitrogen or phosphorus), which can perhaps maintain a stable and productive, year-round community of MC-degrading and non-degrading microorganisms (Tyagi et al. 2010, Lauderdale et al. 2012, McKie et al. 2015, Li et al. 2017).

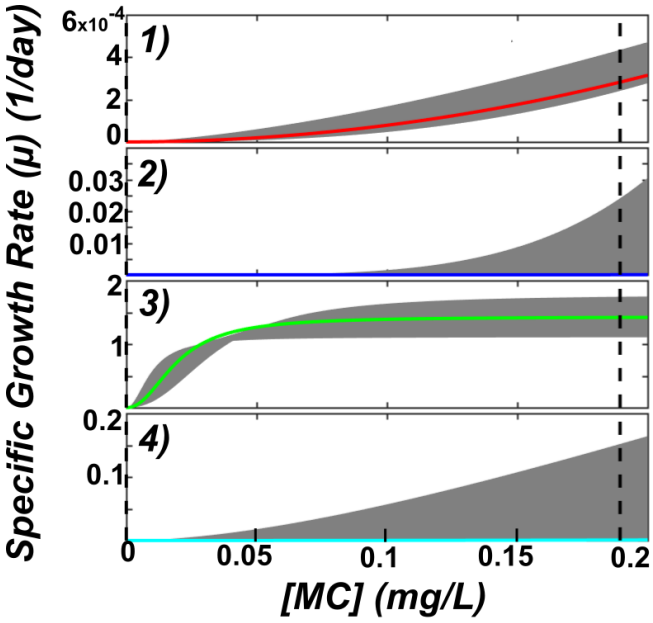

Figure 44. *Predicted specific growth rates of several MC degrading bacteria in the environment as a function of substrate concentration using the Moser (1-3) and Heijnen (4) models. The black dashed lines in indicate the minimum/maximum concentrations of MC expected in the environment. The grey region and colored lines indicate the predictions associated with the lowest/highest 95% credible interval and the mean of the posterior distribution of parameter values.*

4.5 Unstructured Kinetic Model Limitations

Even though the unstructured kinetic models were shown to accurately characterize MC biodegradation in an ideal setting, we recognize multiple limitations to the simplifying assumptions used. First, MC may not be the primary growth limiting substrate metabolized by these degrading bacteria, since it is often present in low background concentrations (ng/L to µg/L) and not secreted until bloom senescence or collapse (Merel et al. 2013, Francy et al. 2015). In most freshwater environments, the presence of other bioavailable dissolved organic carbon represents the primary carbon and energy source for these bacteria (Egli 1995, Eleuterio and Batista 2010, Egli 2010). All unstructured kinetic models can be aptly modified to account for other inhibiting or stimulating substrates these bacteria may encounter in the environment (Yoon et al. 1977, Reardon et al. 2000, Reardon et al. 2002). Future studies should consider the application of competitive multi-substrate models to better describe MC biodegradation in the environment.

Clearly, the temperature (23-30 ºC) and pH (~7) employed in the batch biodegradation experiments examined in this study are ideal cases of what would be encountered in the environment. As MC degrading bacterial growth rate is highly sensitive to water temperature (25-30 ºC optimal, Li et al., 2017), the predictions afforded by the current unstructured models would likely overestimate the rates of MC biodegradation in the environment. Unstructured kinetic models have been successfully tailored to account for temperature (Heitzer et al. 1991, Rosso et al. 1993, Kovárová-Kovar et al. 1996), pH, or both (Rosso et al. 1995) by either considering cardinal pH and temperature properties of bacteria (mostly *E. coli* strains) or deviations of the Arrhenius equation (Alagappan and Cowan 2004). Future studies should consider integrating these previous concepts into

existing unstructured kinetic model frameworks to account for the effects of temperature and pH.

Another limiting factor to address is the fact that these unstructured kinetic models only consider the growth of isolated MC degrading populations. In the environment, these populations are part of a much more complex and interactive network of mixed microorganisms. Single organism derived unstructured model parameters are frequently applied to wastewater treatment design and engineering to characterize the behavior of complex microbial communities (Tchobanoglous et al. 2003). However, more complex mixed population models can be applied based on these single population parameter estimates and theorized interactions among certain populations, including, for example, Lotka-Volterra competition models (Faust and Raes 2012, Song et al., 2014).

The scaling factor (b) required to convert either cell concentration or OD to biomass was identified as another limitation of the kinetic models reviewed. In this study, we assumed that there was a direct, linear relationship between OD or cell counts and dry weight biomass, which is generally the case for pure microbial cultures in practice (Kim et al. 2012, Myers et al. 2013). This assumption resulted in biomass concentrations of MC degraders ranging from 1 to 180 mg/L at stationary phase of growth. Typical dry weight biomass for activated sludge systems range from 3000 to 6000 mg/L, whereas the biomass concentrations ranged from 8 to 50 mg/L for species of bacteria degrading mixtures of BTEX compounds and PAHs (Tchobanoglous et al. 2003, Reardon et al. 2000, Reardon et al. 2002, Knightes and Peters 2000, Knightes and Peters 2003). Thus, since the ranges in biomass predicted for this study are of similar order of magnitude to bacteria degrading

petroleum hydrocarbons and far from activated sludge biomass concentrations, the use of a linear relation between OD or cell counts and biomass is well justified.

Yet another limitation of unstructured kinetic models is the assumption that the cell composition (and physiological state) remains constant during growth (i.e., "balanced growth") (Bailey and Ollis 1976). In the environment, growth of MC degrading organisms is expected to be "non-balanced," where cellular composition is transient with respect to fluctuations in environmental conditions (Ramkrishna et al., 1967, Fredrickson et al. 1971). Structured kinetic models can account for changes in physiological state and more comprehensively describe bacterial growth in the environment but may suffer from issues such as high complexity and computational burden (Ramkrishna et al. 1967, Fredrickson et al. 1971, Panikov 1995).

4.6 Improving Parameter Identifiability: The C_0/X_0 ratio

A complete set of unique parameter estimates was not obtained for most studies. This result indicates there were more limitations in the quality of the experimental data collected, which resulted from inadequacies in the experimental design. Many studies have stressed the importance of the initial substrate to biomass (C_0/X_0) ratio when designing experiments (Dang et al. 1989, Chudoba et al. 1992, Grady et al. 1996). These studies have determined that the C_0/X_0 ratio has a drastic effect on the growth behavior and extent of physical adaptation an organism may undergo (Grady et al. 1996). In general, low C_0/X_0 ratios (< 0.025 on a COD basis) were reflective of the original environmental behavior of the bacterial population ("extant" behavior), while larger C_0/X_0 ratios (> 20 on a COD basis) resembled the "intrinsic" characteristics of the population under study (Dang et al. 1989, Grady et al. 1996).

Applying these criteria to our results (see Supplementary Information, section 8), the experimental conditions in Studies 1, and 3-4 resembled more "extant" behavior (C_0/X_0 ratios ranged between 1-3), whereas the experimental conditions for Study 2 were more "intrinsic" (C_0/X_0 were above 20). This concept helps explain why there were drastically different kinetic parameter estimates for two experiments conducted for the same species of *Sphingopyxis* degrading a different MC congener (RR vs. LR), as different C_0/X_0 ratios were used (Study 2 vs. Study 4). Maintaining this C_0/X_0 parameter at a low value is more useful for identifying parameters that will be used to predict MC removal in an environmental setting, whereas high values are more useful in an engineered setting to observe the full kinetic degradation potential of a certain MC degrading population.

The C_0/X_0 ratio also affects the parameter identifiability for a given experiment (Grady et al. 1996). Classically, there has been much controversy over how to best design a batch biodegradation experiment to obtain independent estimates of μ_{max}, K_s, and Y model parameters (Nihtilä and Virkkunen 1977, Holmberg 1982, Robinson and Tiejde 1983, Liu and Zachara 2001). For example, Robinson and Tiejde (1983) found that uncorrelated estimates of μ_{max} and K_s could be reached when performing the batch experiment in the mixed order region of the specific growth rate vs. substrate theoretical curve (at $C_0/X_0 >$ 20).

Good separation of μ_{max} and K_s was observed for our results, and these parameters could be uniquely estimated for Studies 2 and 3. The experimental conditions for Studies 2 and 3 were reflective of very high C_0/X_0 ratios (Study 2 ~150 and Study 3 ~1000) (Table C9), confirming the importance of this ratio on improving parameter identifiability. However, a significant number of correlations were observed between the scaling

parameter (*b*) and (*Y*) across all studies, resulting in non-unique estimates of *Y*. This result was concerning as the sensitivity analysis indicated that *Y* is an interactive and relatively influential parameter when predicting both substrate and biomass concentrations. Future MC biodegradation experiments should eliminate the use of this scaling parameter by directly measuring the biomass concentration, through dry or wet weight, protein content, or even ATP-based methods (Velten et al. 2007, 2011) to avoid unnecessary correlations developed between the scaling parameter and all other remaining parameters observed in this study.

5.0 Conclusions

Engineered biological treatment systems targeting the removal of MCs rely on an in-depth predictive understanding of bacterial growth. We must admit that unstructured kinetic models are not in any way comprehensive representations of the true complexity of most biological processes. However, the models reviewed in this study provided an accurate and practical approach to characterize MC biodegradation kinetics. Based on this rigorous comparison of a broad range in unstructured kinetic models, the following main conclusions were drawn from this study:

1) The underlying kinetic model structure (and associated growth mechanisms accounted for) has a statistically strong effect on model predictive accuracy and precision for MC biodegradation. In this study, the Moser model and Heijnen and Romein model were the most reliable and consistent out of all models reviewed.
2) Unique parameter estimates for MC biodegradation depend on the quality of experimental data, which is highly influenced by the experimental design (i.e., C_0/X_0

ratio). Using a new, global optimization approach, unique parameter estimates were obtained for at least three (and up to five) parameters using different experimental datasets.

3) Model predictions were generally most sensitive to the parameter values of k_d, μ_{max}, K_s, and b in the absence of correlations. Model predictions were also affected by interactions between multiple parameters. Values of k_d, μ_{max}, K_s, and Y demonstrated moderate to high levels of interactions with other parameters. These results prioritize the proper identification of k_d and Y in future studies, which were not identifiable for certain studies reviewed herein.
4) Well below saturating concentrations of MC in the environment result in minimal to no growth of MC degrading bacteria, where sub-optimal MC removal kinetics are expected in treatment practice.

We envision the results from this study as a stepping stone toward the development of a practical and comprehensive unstructured kinetic model that can reliably predict MC biodegradation in the environment. The MC-degrading bacterial populations reviewed in this study are likely underrepresented members of a more complex and dynamic community, where the clear majority of community members are less inclined to (or cannot) utilize MC as a primary carbon and energy source. However, we stress that the predictive knowledge of the isolated kinetic behavior of these bacteria metabolizing MC as a sole organic carbon source can be integrated into more complex unstructured kinetic modelling frameworks that consider multiple interacting substrates and population members as well as different environmental conditions (i.e., temperature, pH). We expect that future studies will adopt a similar model surveying and calibration approach to

identify the necessary mechanisms to describe more complex environmental behavior of bacteria involved in MC biodegradation.

Chapter 5: Accurate and Reliable Estimation of Kinetic Parameters for Environmental Engineering Applications: A Global, Multi Objective, Bayesian Optimization Approach

Abstract: Accurate and precise predictions of bacterial growth and metabolism from unstructured kinetic models are critical to the proper operation and design of engineered biological treatment and remediation systems. As such, parameter estimation has progressed into a routine challenge in the field of Environmental Engineering. Among the main issues identified with parameter estimation, the model-data calibration approach is extremely crucial, yet an often overlooked and difficult optimization problem. Here, a novel and rigorous global, multi objective, and fully Bayesian optimization approach that overcomes challenges associated with multi-variate, sparse and noisy data, as well as highly non-linear model structures commonly encountered in Environmental Engineering practice is presented. This optimization approach allows an improved definition and targeting of the compromise solution space for all multivariate problems, allowing efficient convergence, and a Bayesian component to thoroughly explore parameter and model prediction uncertainty. This global optimization approach well outperforms, in terms of parameter accuracy and precision, standard, local non-linear regression routines and overcomes issues associated with premature convergence and overfitting of different variables in the calibration process.

1. Introduction and Background

Unstructured kinetic models, such as the well-known Monod model, have become widespread in the field of Environmental Engineering, ranging from air pollution control, water and wastewater treatment, and bioremediation to effectively describe and parameterize bacterial growth in engineered systems (Bailey and Ollis 1976, Kovárová-Kovar and Egli 1998, Alexander 1999, Tchobanoglous et al. 2003). These models provide a relatively simplistic, practical, and unified basis to predict microbial metabolism or transformation of nutrients, toxic chemicals, or production and synthesis of biochemicals throughout different media ranging from air, soil, and water (Alexander 1999, Simkins and Alexander 1984). Often, these models do not have a firm theoretical basis (as most were initially empirically derived) and holistically portray the cell, through various biokinetic parameters (i.e., the maximum specific growth rate, half saturation constant), as an enzyme "unit" that functions similar to the behavior described by different enzyme-kinetic models such as the Michaelis-Menten (Monod) or Hill (Moser) equations (Bailey and Ollis 1976, Esener et al. 1983, Shuler and Kargi 2002). Despite these over-simplifications, unstructured kinetic models have reliably and accurately reproduced experimental data from all fields mentioned above and form the foundation for design and operational practice of biological based treatment and remediation systems (Tchobanoglous et al. 2003).

Although these unstructured kinetic models are popular from a practical viewpoint, the uncertainty associated with parameter estimates and model predictions and difficulties arising from non-linear regression for model calibration often limit the use of these kinetic models in an environmental context, which is the focus of this developed method (Kovárová-Kovar and Egli 1998, Koch 1982, Robinson 1985, Grady et al. 1996, Knightes

and Peters 2000). Bayesian statistical techniques can offer insight into the uncertainty associated with model parameters and with the model structure itself (i.e., epistemic errors). Of the number of challenges identified, arriving at unique, accurate, and precise parameter estimates is a primary issue that often undermines the predictive utility of unstructured kinetic models. For example, reaching uncorrelated estimates of the maximum specific growth rate and half saturation constant of many unstructured kinetic models has remained a well-known challenge over the years (Nihtilä and Virkkunen 1977, Holmberg 1982, Robinson and Tiedje 1983, Liu and Zachara 2001).

Issues previously encountered with parameter estimation in bioremediation practice result from inadequacies in the experimental design, quality of experimental data collected, and the model-data calibration procedure (Baltes et al. 1994, Banga et al. 2004, Dette et al. 2005, Strigul et al. 2009). The model-data calibration procedure is extremely critical to obtain reliable parameter estimates and is often an overlooked, challenging non-convex optimization problem (Knightes and Peters 2000, Banga et al. 2004). Generally, difficulties arise during model-data calibration as: 1) the experimental datasets analyzing biodegradation of pollutants are often multivariate, sparse, and noisy in nature; and 2) the unstructured kinetic models used to describe these datasets are highly non-linear (Knightes and Peters 2000, Banga et al. 2004, Marsili-Libelli 1992, Vanrolleghem and Keesman 1996, Motulsky and Christopoulos 2004). Here, we emphasize that multi-variate datasets present more challenges, such as overfitting, where one variable may be given more weight during the calibration process.

It is concerning that many past biodegradation studies (e.g., Simkins and Alexander 1994, Knightes and Peters 2000, Knightes and Peters 2003) have relied on deterministic,

local nonlinear regression techniques for parameter estimation, as techniques based on gradient descent (like FMINCON provided by MATLAB's optimization toolbox) suffer from a lack of exploration of the search space and become trapped in local solutions. To overcome these exploration and convergence issues, stochastic, global optimization methods, including evolutionary algorithms (i.e., differential evolution), can be applied as robust solutions to this parameter estimation problem. Evolutionary algorithms (i.e., differential evolution), that are built on randomly evolving a population of individuals based on their fitness, are well known in the optimization field as effective and reliable global minimization approaches (Back 1996, Deb 2001). Although the application of these approaches in the field of bioremediation is still rather limited, several recent studies have applied variants of evolutionary algorithms, such as particle swarm, to investigate kinetic parameters describing the biodegradation of BTEX compounds (Trigueros et al. 2010).

In this research method, we describe a novel and rigorous approach to accurately and reliably estimate parameters in unstructured kinetic models given multi-variate experimental datasets based on a global, multi objective and fully Bayesian optimization procedure. In the following section (2), we give an overview of the workflow behind our approach, introduce key elements of the unstructured kinetic models and datasets used for model-data fitting comparison, and provide an in-depth description of the methods involved for improved parameter estimation. Finally, in Section 3, we demonstrate the utility of this research method by comparing the performance of the algorithms used in this optimization approach to local, non-linear regression methods.

2. A Global, Multi Objective, and Bayesian Optimization Approach to Parameter Estimation

The main workflow for this research method is detailed in Figure 37, which portrays a sequential three step approach to improved parameter estimation. These steps are reversible in the sense that the current step should be verified or rely on information from a previous step of the workflow (Figure 37). The most critical improvement this workflow brings is a) an improved definition and targeting of the compromise solution space for multi-variate calibration problems to avoid overfitting of different variables and b) a Bayesian component to explore parameter and model prediction uncertainty. Here, the compromise solution space is designated as the set of solutions (that are centered around the global optimum or the best compromise solution) that represent the optimized tradeoffs between different objective functions (Figure 45). The global optimum is equivalent to the best compromise solution of the compromise solution space, located at the solution (in the objective function space) closest to the nadir or apex of a curve formed between the set of compromise solutions (Figure 45). The extreme solutions, contrarily, are found when one variable, such as cell or substrate concentration, is fitted at a time as opposed to simultaneously (Figure 45A and C). The extreme solutions exist at the beginning and end of the curve that passes through the compromise solution set (Figure 45).

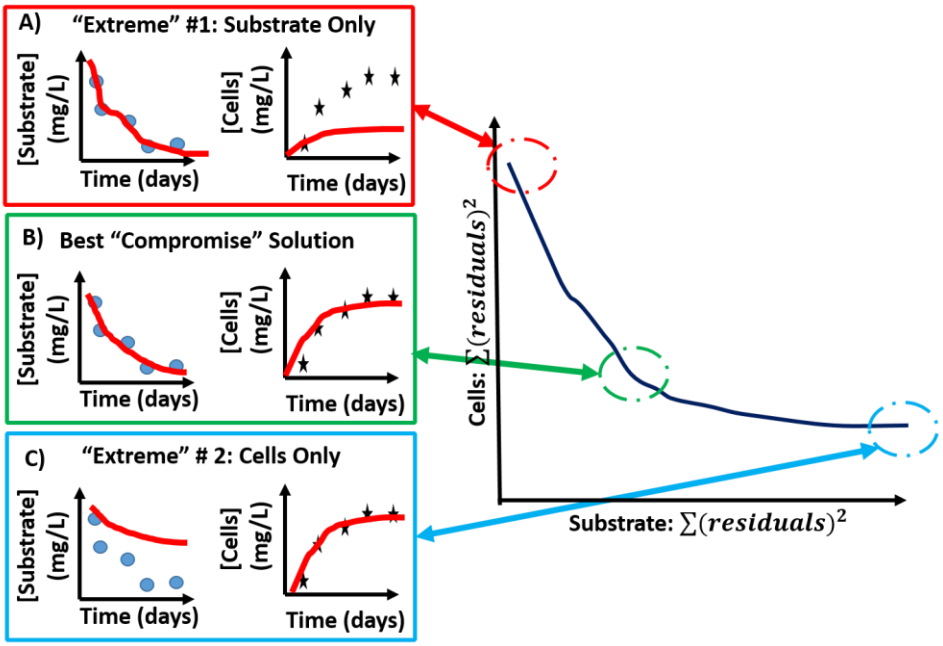

Figure 45. *Graphical representation of the extreme solutions (A and C) as well as the compromise solutions (B) terminology referred to in this research method. The dark blue line in the righthand figure represents the compromise solution space.*

In the first step of the workflow, a single objective, stochastic optimization algorithm is used to both locate the global optimum (i.e., the best compromise solution) and the "extreme" solutions. In the following step, a multi-objective, stochastic optimization algorithm is used to target the best compromise solution, in which results from the previous, single objective step are used to verify proper convergence of the multi-objective approach (Figure 37). Although initially three SO and MO algorithms were applied in this approach, we recommend that only the best performing algorithms listed in Figure 2 are necessary for proper convergence and parameter estimation. Finally, an Approximate Bayesian Computational (DREAM-ABC) approach is applied to develop a posterior distribution in parameters using the verified "best" compromise solution to target the correct compromise solution space around the global minimum.

2.1 Overview of Unstructured Kinetic Models and Datasets for Model-Data Fitting Comparisons

In this study, parameter estimation was performed for a variety of unstructured kinetic growth models describing microcystin (MC, a cyanobacterial toxin present in drinking water) biodegradation by isolated, homogenous bacterial populations (Manheim et al. 2019). Each of these models describes the specific growth rate of degrading bacterial cells (μ) as a non-linear, positively increasing function of substrate concentration (C) (where interested readers are referred to Manheim et al. 2019 (or previous chapter) for a complete description of the mathematical formulations and parameters included). As an example, the well-known Monod model describes the specific growth rate of bacterial cells as a hyperbolic function of the substrate concentration (Equation 1). The maximum specific growth rate, half saturation constant, and the yield coefficient (μ_{max}, K_s, and Y) describe the maximal growth rate of a bacterial population when the substrate is non-limiting, the bacterial population's relative affinity for a specific substrate, and the yield of new bacterial biomass per substrate consumed (Monod 1949). Other unstructured kinetic models, such as the Moser model, possess a similar mathematical framework to the Monod model, but incorporate additional parameters (such as C^n, where n is an additional model parameter) to describe other important underlying physical processes (Panikov and Pirt 1978).

$$\mu = \frac{\mu_{max} C}{K_s + C} \tag{1}$$

During a batch biodegradation experiment (i.e., where MC is the sole limiting carbon source, aerobic, temperature/pH controlled), the time dependent change in substrate concentration (C) and bacterial degrading biomass (X) can be described by the following

coupled set of ordinary differential equations (Equations 2 and 3), where the endogenous decay of bacterial cells is explicitly considered (Rittmann et al. 2002, Bodegom 2007):

$$\frac{dC}{dt} = -\frac{1}{Y}\mu X \quad (2)$$

$$\frac{dX}{dt} = \mu X - k_d X \quad (3)$$

where C is the limiting substrate concentration (mg/L), X is the biomass concentration (mg/L), μ is the specific growth rate of bacterial cells (1/hr), Y is the cell yield coefficient (unitless), and k_d is the endogenous decay coefficient (1/hr). Importantly, $X = b*S$, where b is a linear scaling factor used to convert optical density or cell concentration data (S) into biomass concentrations (X).

Experimental datasets for model-data fitting comparisons performed in this study were acquired from four different studies evaluating MC biodegradation of isolated, homogenous bacterial populations (Valeria et al. 2006, Wang et al. 2010, Xiao et al. 2011, Zhang et al. 2015b). These studies isolated bacterial populations from the *Sphingomonas* (designated Study 3, Valeria et al. 2006), *Sphingopyxis* (designated Studies 2 and 4, Wang et al. 2010 and Xiao et al. 2011), and *Bacillus* genera (designated Study 1, Zhang et al. 2015b), which are representative of the main populations involved in MC degradation (Bourne et al. 1996, 2001, Li et al. 2017). In accordance with the assumptions introduced above for Equations 2 and 3, each of these studies performed batch degradation experiments, where the initial bacterial inoculum, MC concentrations, temperature, pH, and the availability of oxygen and nutrients were tightly controlled (see Manheim et al. 2019 for a complete description and comparison). Across all experiments, both the substrate (MC) and bacterial biomass concentrations were quantified daily for a 1.3-10-day time period using HPLC (for

MC) and optical density (OD 600 nm) or plate counts (for biomass) as general quantification methods.

As an example, Figure 40 highlights the experimental results obtained from each study overlaid with the best fitting unstructured kinetic models determined from a Bayesian model comparison and selection process (Manheim et al. 2019). Studies 1-3 were fit using the Moser model, whereas Study 4 was fit using the Heijnen model (Heijnen and Romein 1995). As observed in Figure 40, all experimental data points were observed to fall within the uncertainty intervals, indicating that the predictions afforded by either model can reproduce the experimental data with great certainty. Overall, the relatively few time points for data collection and some data points with moderate variability (i.e., Study 2) were reflective of the general sparse and noisy nature of many datasets associated with batch biodegradation experiments.

2.2 Global, Single Objective Optimization (GSO) Approach

The GSO approach involved the application of an extensively tested series of SO evolutionary optimization algorithms, including Self-Adaptive Differential Evolution (saDE) (Qin and Suganthan 2005, Qin et al. 2009b), the multi-algorithm evolutionary based AMALGAM-SO optimizer (Vrugt et al. 2009), and an advanced variant of the LSHADE (cnEpSin) series of algorithms (Awad et al. 2016). The saDE algorithm was directly coded in MATLAB (Mathworks, Inc., r2015b) based on the description presented in Qin et al. (2009b), whereas MATLAB production codes were acquired for the AMALGAM-SO and LSHADE-cnEpSin algorithms. Exact details of the mechanism used behind each optimization algorithm are presented elsewhere (see Qin et al. 2009b, Vrugt et al. 2009, or Awad et al. 2016 for specific information). Although only one algorithm is generally

sufficient for use in future optimization problems, we observed some utility in benchmarking at least three different stochastic approaches to ensure that the global minimum was in fact reached. If the user is considering selecting only one of these algorithms, we recommend running multiple independent repetitions (changing the initial random seed), to ensure that the optimizer consistently reaches the global minimum solution.

Prior to applying each algorithm to the experimental datasets acquired, fifteen of the CEC 2005 benchmark functions were used to rigorously test and compare the optimization performance of each GSO. From this initial testing period, the AMALGAM-SO algorithm demonstrated the most reliable performance, followed by the LSHADE (cnEpSin) and saDE algorithms, respectively (Appendix D, Section 1). In addition, optimal run conditions and control settings for each algorithm were identified based on this prior testing and were kept consistent when applied to the experimental data acquired herein.

The formal Gaussian Log-Likelihood function was used as the primary objective function for GSO and GMO optimization approaches, similar to the approach presented by Knightes and Peters (2000, 2003). In this study, we assumed that the error residuals for each variable were independent, normally distributed (with zero mean), and exhibited constant variance (homoscedastic). A formal check of these three main assumptions is presented in Appendix D, Section 2 of this dissertation for reference. In addition, we assumed that the covariance between the variables (i.e., cell and substrate concentration) was negligible given that the number of experimental data points was limited for each study (ranging from 5-10 for each dependent variable) (Motulsky and Christopoulos 2004). This assumption not only simplified the objective function calculation but proved to

provide more reliable parameter estimates compared to using a form of the objective function that considers covariance between the dependent variables (data not shown). The Gaussian Log-Likelihood objective function (OF_1) to minimize thus reduces to a function of the sum of square residuals (SSR_1 and SSR_2) and the overall standard deviation for each variable (σ_{Y1} and σ_{Y2}) after making these necessary simplifying assumptions (Equation 4) (Knightes and Peters 2000, Bard 1974).

$$OF_1 = \frac{1}{{\sigma_{Y_1}}^2}\ (SSR_1) + \frac{1}{{\sigma_{Y_2}}^2}\ (SSR_2) \tag{4}$$

Although standard deviations were given in each dataset for each observation, we decided to fit each model using the average of replicate experiments, given that the number of repetitions was low for each study (three or less) (Motulsky and Christopoulos 2004). This assumption also eliminated the requirement for including the overall standard deviations for each variable as weight in Equation 4 above. To reduce bias related to the magnitude of the model predictions, the logarithm (base 10) of model predictions was used in calculation of the objective function values (Knightes and Peters 2000, 2003).

2.2.1 GSO Run Conditions and Control Settings

Standard run conditions were set for each SO algorithm to ensure fair performance for each model-dataset calibration. These run conditions included a fixed number of function evaluations (500,000) and equivalent termination criteria. The termination criteria for saDE and LSHADE- cnEpSin were dependent on three criteria: a) exceeding the maximum function evaluations; b) meeting the following tolerance: if the range of the objective function values of the population members was less than 1E-08; c) or meeting the following tolerance: if the range of the parameter values of all population members was less than 1E-02. Termination and restart criteria for AMALGAM-SO was identical to that

described in (Vrugt et al. 2009). However, global termination criteria were introduced so that if successive runs resulted in similar objective function values meeting a predefined tolerance, the search was stopped. Specifications of the exact run conditions and control settings used in each of these algorithms are specified in Appendix D, section 1.1.

2.3 Global, Multiple Objective (GMO) Optimization Approach

The GMO approach involved the use of three different evolutionary algorithms including the improved NSGA-III genetic based algorithm (Deb and Jain 2014), the multi-algorithm, multi objective AMALGAM optimizer (Vrugt and Robinson 2007), and the RVEA algorithm (RVEA) (Cheng et al. 2016). These MO algorithms were selected based on a formal comparison of at least ten different MO algorithms benchmarked on a suite of well-known MO test functions (Appendix D, Section 3). The PLATEMO test platform was incorporated in this MO test comparison as a useful tool for benchmarking different algorithms (Tian et al. 2017). Results of a formal benchmarking on standard, MO test functions indicated that the NSGA-III algorithm performed the best of the initial algorithms screened using a range of selection criteria (i.e., accuracy and convergence, diversity, and number of non-dominated solutions), followed by the AMALGAM-MO and RVEA algorithms (Appendix D, Section 3). Similar to the SO approach, optimal run conditions and control settings for each MO algorithm were identified and kept consistent when applied to the experimental data acquired herein.

2.3.1 GMO Run Conditions and Control Settings

Standard run conditions were set for each MO algorithm to ensure fair performance for each model-dataset calibration. These run conditions included a fixed number of generations (20,000) to run each MO algorithm, which was determined by successively

running an increasing number of generations until the change in the non-dominated solution sets was deemed negligible (after 5 independent repetitions) (data not shown). In addition, the population size was fixed to N = 100 for each algorithm. The AMALGAM-MO, NSGA-III and RVEA algorithms were run with identical control settings as specified in Appendix D, Section 3.1. It is important to note that the NSGA-III and RVEA algorithms were run using the *MATLAB* code developed by the PLATEMO user interface (Tian et al. 2017).

2.4 Bayesian Optimization Approach

A posterior distribution in parameter estimates was reached through the DREAM-ZS (Differential Evolution Adaptive Metropolis, sampling from past states) (v3.0) software package (Laloy and Vrugt 2012). Unlike the previous approaches, we chose a likelihood free method using Approximate Bayesian Computation (ABC) to specifically target and facilitate convergence to the compromise region of the search space (Sadegh and Vrugt 2014). The specific objective function (OF_2) incorporated in this study to maximize was similar to that presented by Sagdeh and Vrugt (2014), which is based on the distance between the observed and predicted summary statistics (m) and some predefined tolerance, ε_j (Equation 5). Importantly, the sum of squared residuals (for both cell and substrate data) from the compromise solution obtained by the best performing GMO were chosen as the observed summary statistics (S_j, Equation 5) to guide the ABC method. In this approach, the sum of squared residuals (L2 norm) obtained during the ABC optimization procedure (for fitting both cells and substrate) represented the simulated summary statistics ($\widehat{S_j}$).

$$OF_2 = \min_{j=1:m}\{\varepsilon_j - \rho(S_j, \widehat{S_j})\} \quad (5)$$

Where $\rho(S_j, \widehat{S_j})$ simply represents the distance between the observed and simulated summary statistics: abs$(S_j - \widehat{S_j})$. The specific DREAM-ZS run conditions and control settings applied for the ABC algorithm are summarized in Table D10 for reference (Appendix D, section 4).

The overall convergence statistic of Rubin and Gelman (1992) was summarized for each study (1-4 identified in Section 2.1) to verify that the DREAM-ZS -ABC algorithm was running through enough generations to reach a stable estimate of the posterior distribution in parameters (Figure 46). Convergence was assessed over a wide range in model structures to obtain insight into the performance of the ABC algorithm against various non-linearities, including (1-8) the Monod kinetic model (Monod 1949), Tessier kinetic model (Tessier 1942), Contois kinetic model (Contois 1959), Blackman kinetic model (Blackman 1906), Dabes kinetic model (Dabes et al. 1973), Powell kinetic model (Powell 1967), Moser kinetic model (Moser 1958), and the Heijnen and Romein kinetic model (Heijnen and Romen 1995).

For all studies and models investigated (a-d, 1-8), convergence was generally reached after 150,000 generations (corresponding to 900K overall for 6 chains), where the R-statistics converge to a stable value below the 1.2 threshold for each model structure reviewed (Figure 46). Across all studies, the Contois model demonstrated the largest number of necessary generations until convergence was reached, due to the more complex non-linear structure of the model (Figure 46). In some cases (Study 4), the Dabes kinetic model also demonstrated poor convergence using the ABC method. These results indicated

that reliable posterior distributions in parameters have been achieved after approximately 150,000 to 200,000 generations.

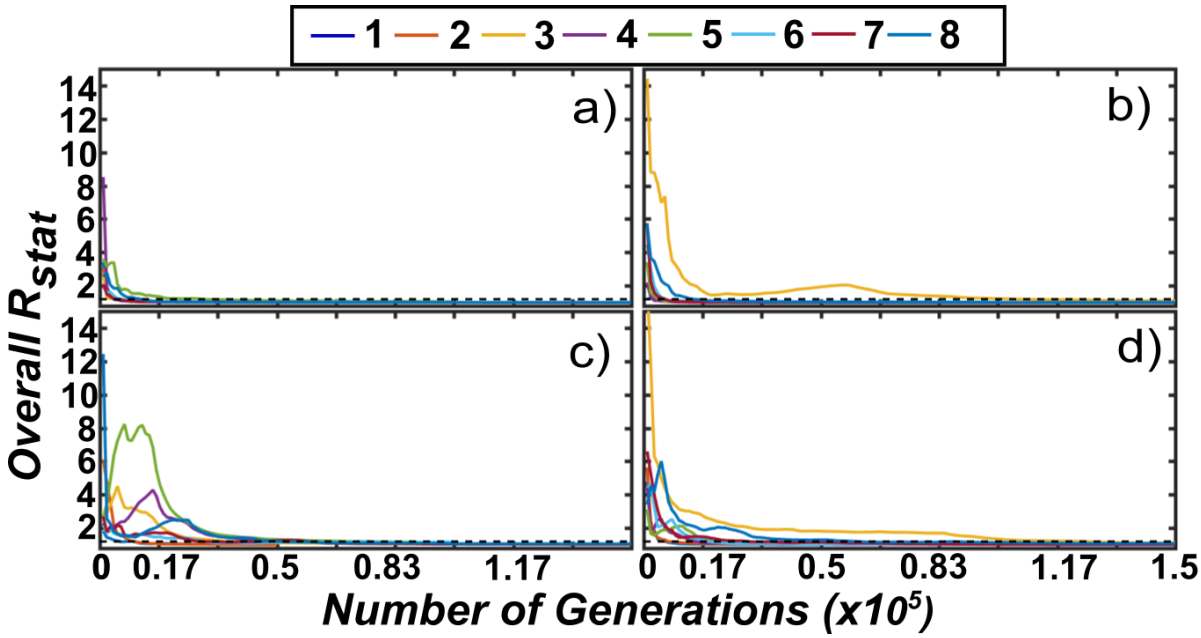

Figure 46. *Evolution of the overall Gelman and Rubin R-statistic for the DREAM-ZS (ABC) algorithm when applied to models 1-8 for each corresponding dataset. The letters a-d correspond to Studies 1-4 and numbers 1-8 correspond to the Monod, Tessier, Contois, Blackman, Dabes, Powell, Moser, and Heijnen model structures. The dashed line indicates the convergence threshold of 1.2.*

3. The Case for Global Optimization: Research Method Validation

Finally, we highlight the importance of global optimization techniques to provide accurate and robust parameter estimates for all nonlinear regression problems as compared to standard, localized optimization methods. We expect that the global optimization approaches adopted in this study can handle the difficulty of fitting multivariate, sparse, and noisy data by avoiding local optima solutions and locating compromise solutions that avoid overfitting one variable in a multivariate dataset. Here, the results of the *FMINCON* constrained nonlinear optimization tool provided by *MATLAB* (and commonly used for parameter estimation in past studies) are compared to the best

performing global optimization algorithms used in this study. We limit this comparison of the optimization algorithms to parameter estimation of the Moser model structure, a common unstructured kinetic growth model, for experimental data detailing MC biodegradation and cell growth from a variety of laboratory studies introduced in section 2.1 (Valeria et al. 2006, Wang et al. 2010, Xiao et al. 2011, Zhang et al. 2015b). The Moser model structure contains six parameters to be calibrated, including the maximum specific growth rate (μ_{max}), the half saturation constant (K_s), the yield coefficient (Y), the first order endogenous decay rate (K_d), a linear cell concentration to biomass conversion parameter (b), and the exponent parameter (n) in the Moser model (Equations 2, 3, 6). For each approach and Study (defined as 1-4, as indicated in Section 2.1), five independent repetitions were used to evaluate the mean and variance in the parameter estimates and objective function values.

$$\mu = \frac{\mu_{max} S^n}{K_S + S^n} \tag{6}$$

The run and control settings for the *FMINCON* method in *MATLAB* were kept as equivalent to those used for the global optimization algorithms to ensure impartiality. For all studies, identical bounds used in the global optimization algorithms were applied to the *FMINCON* approach for constraining the feasible parameter space, where all other constraints were set to null values. Furthermore, the *FMINCON* approach used identical experimental datasets to those used for the global optimization routines, and the search was commenced using randomly initialized (uniformly distributed) starting points within the feasible parameter space. As recommended by *MATHWORKS*, the "interior-point" optimization approach was implemented in FMINCON as this algorithm has demonstrated

success on both large, sparse problems as well as small, dense optimization problems (Byrd et al. 1999). To provide some insight into the performance of other available algorithms, the "active set" optimization setting was also selected in this comparison (Powell 1978). All the run settings for each algorithm (i.e., interior-point or active set) were kept at default values except for the stopping criteria. The stopping criteria were defined as follows: stop if a) the number of function evaluations was exceeded (500,000); b) the number of iterations was exceeded (500); c) the function tolerance (value of the objective function) was reached (1E-20); d) the step tolerance was reached (1E-20); or e) the constraint tolerance was reached (1E-20). It is important to note that the number of iterations (comparable to generations for the global optimization algorithms) was set to 500, which is considerably lower than the number stipulated for most global approaches, as most *FMINCON* searches stagnated within this window and performing additional iterations was deemed unnecessary. Moreover, the magnitude of the tolerances was set to very low values to ensure that the *FMINCON* search avoided premature convergence.

As demonstrated in Table 12, considerably different parameter estimates were obtained between the *FMINCON* and best performing SO, global optimization algorithms. The *FMINCON* approaches resulted in significantly larger variation in parameter estimates as compared to the global optimization approaches (Table 12). The high variation in estimates is most likely due to the nonlinear solver in FMINCON becoming stuck in local optimal solutions and prematurely converging. In most cases using the FMINCON algorithms, the search was terminated due to the step size tolerance, indicating that these methods have difficulty thoroughly exploring and exploiting the search space. These local optimization methods were also extremely sensitive to the initial values the parameters

were set to, where some repetitions demonstrated considerable improvement over others. However, the global optimization algorithms consistently reached the same global optimum, as confirmed by the low standard deviation of all parameter estimates (Table 12). These results imply that the global optimization methods, despite their stochasticity, are the most robust nonlinear regression techniques investigated, where reliable parameter estimates can usually be achieved with high probability.

***Table 12**- Parameter estimates for FMINCON and best performing global, single objective optimization algorithms. The mean and standard deviation are presented for each parameter and approach.*

Study	Approach	μ_{max}	K_s	Y	K_d	b	n
1	FMINCON-Active Fit	15.8	155	3.08	1.16E-01	1.79E-01	9.89
		13.9	52.3	4.71E-01	1.81E-01	3.57E-01	2.11 E-01
	FMINCON-Interior Point	18.60	152	2.52	4.44E-02	2.89E-02	9.84
		7.0	76.2	5.65E-01	2.02E-02	2.62E-02	1.38 E-01
	AMALGAM-SO	1.08	220	2.15	1.28E-01	8.06E-03	2.19
		6.53E-03	1.05E-02	1.39	8.00E-04	5.23E-03	6.40E-03
2	FMINCON-Active Fit	13.38	71.0	2.93	4.23E-01	8.61E-02	6.28
		9.6	47.9	1.07	4.81E-01	7.70E-02	2.96
	FMINCON-Interior Point	8.30	104	2.12	4.68E-01	7.65E-02	5.41
		4.28	65.1	5.13E-01	2.33E-01	2.40E-02	1.41
	AMALGAM-SO	6.23	1.21E-01	2.49	8.09E-01	5.98E-02	9.61
		1.80E-01	5.07E-02	1.44	1.23E-01	3.62E-02	5.92E-01
3	FMINCON-Active Fit	19.9	120	0.86	1.00E-02	2.68E-08	2.47
		16.0	63.8	1.42	5.16E-05	4.13E-08	3.02
	FMINCON-Interior Point	11.9	40.9	2.16	1.00E-02	4.15E-08	9.09E-01
		12.3	52.8	1.80	4.72E-07	5.34E-08	1.29E-01
	saDE	2.06	4.78E-02	2.90	3.38E-02	1.31E-10	1.59
		9.32E-01	6.38E-02	4.08E-01	3.81E-02	2.38E-11	5.39E-01
4	FMINCON-Active Fit	16.4	48.2	1.45	2.28E-01	5.82E-01	3.37
		20.8	83.9	1.38	3.05E-01	8.17E-01	3.76
	FMINCON-Interior Point	13.0	64.3	1.90	2.60E-01	7.56E-01	5.88
		19.9	75.6	1.16	2.40E-01	7.10E-01	3.43
	AMALGAM-SO	2.89	1.80E-04	2.69	9.35E-02	5.09E-01	2.59

1.68E-01	2.23E-04	1.37	1.22E-01	2.65E-01	1.12E-01

In terms of predictive accuracy, the global optimization methods demonstrated superior performance (Table 13). Out of all approaches, the best performing global optimization methods returned the smallest mean objective function (total sum of squared residuals) values and largest log-likelihood values (data not shown), with small standard deviations observed in general. The FMINCON optimization methods, contrarily, suffer from poor predictive accuracy, as mean values were significantly larger than those obtained by the global optimization approaches.

The ability of the SO algorithms to reach the best compromise solution was further compared using the percent contribution of substrate and cell concentration fitting error to the overall fitting error (% Subs or % Cells) (Table 13). This analysis is simply dissecting Equation 4 presented above (without standard deviations of the measurements included, σ_{Y1} and σ_{Y2}) into a contribution to the overall objective function (OF_1) from fitting either the cell concentration or MC substrate experimental data. Here, we benchmark the SO algorithms with the solution obtained using the MO approach. The MO global optimization results indicated the following percent contribution (% Subs/Cells) for the best compromise solution for each study (1-4): 87.5/12.5; 15.4/84.6; 82.9/17.1; 90.3/9.7. It is important to note that the best compromise solutions do not result in a proportional tradeoff (i.e., 50/50%) between fitting the cell and substrate concentration data. Instead, for most studies (1,3,4) the compromise solutions showed a better fit to the cell concentration as compared to the substrate concentration data, as the cell data indicated a higher contribution to the overall objective function.

The results demonstrated that for Studies 2 and 3, the compromise solutions reached were far different than the compromise solutions defined above for the *FMINCON* algorithms. However, although the accuracy was not high, the relative tradeoff between fitting the substrate vs. cell concentration data was similar to that obtained by the multi objective approach for studies 1 and 4 using the FMINCON algorithms (Table 13). As expected, the SO global optimization approaches always provided comparable compromise solutions to those obtained by the multi objective optimization approaches.

Table 13*- Objective function estimates for FMINCON and best performing global, single objective optimization algorithms. The mean and standard deviation are presented for each parameter and approach.*

Study	Approach	MinOF	Subs %	Cells %
1	FMINCON-Active Fit	7.61	88	12
		4.17	12	12
	FMINCON-Interior Point	8.61	96	4
		8.86E-01	1	1
	AMALGAM-SO	3.29E-02	88	12
		1.96E-05	0	0
2	FMINCON-Active Fit	5.12	73	27
		3.78	29	29
	FMINCON-Interior Point	1.88	58	42
		1.87	35	35
	AMALGAM-SO	5.97E-01	16	84
		1.04E-03	0	0
3	FMINCON-Active Fit	3.01	46	54
		2.74	23	23
	FMINCON-Interior Point	1.53	29	71
		4.74E-02	3	3
	saDE	2.17E-01	88	12
		1.26E-01	5	5
4	FMINCON-Active Fit	6.14	85	15
		11.2	14	14
	FMINCON-Interior Point	15.2	86	14
		13.8	15	15
	AMALGAM-SO	4.12E-02	88	12
		8.12E-03	6	6

Since a strong dependence of the local optimization methods on the initialization location in the search space was observed, we investigated whether the performance would be enhanced if the initialization was set very close to the global optimum solution. For this run of experiments, we narrowed the search space of the local optimization methods to an arbitrarily small hypercube (i.e., six-dimensional space) around the global optimum solution (see Appendix D, Section 5). The parameters were still randomly initialized in this smaller subspace using uniform random sampling and each local optimization method was run using identical settings as described above. Again, for each approach and Study (1-4), five independent repetitions were used to evaluate the mean and variance in the parameter estimates and objective function values.

Even within a very close vicinity to the global optimum solution, the results showed that the local search methods prematurely converged to a local solution located around the global optimum (Table 14). This result is evident as the magnitude of most parameter values are not the same when comparing the best performing global optimization and the *FMINCON* optimization results for each study (Table 14). Although the local optimization results of the constrained test cases still indicated that the global solution was not reached, the performance of the *FMINCON* algorithms was far superior to the case where the search boundaries were less constrained (Table 12 vs. Table 14).

In addition, there was a noticeable difference in performance between the two variants of the *FMINCON* algorithms, when comparing the mean absolute error calculated between the optimal parameter set (out of five repetitions) from the best performing global and local optimization parameter estimates and the standard deviation of parameter estimates. In general, the performance (benchmarked using the mean absolute error) using

the *FMINCON* Interior Point method was improved over the Active Set method for Studies 1 and 2, whereas the Active Fit method was better than the Interior Point method for Studies 3 and 4 (data not shown). Moreover, the Interior Point method demonstrated a less variable performance compared to the Active Fit method, as the standard deviation of most parameters using the Interior Point method were lower than those obtained using the Active Fit method (Table 14). These results confirm that even when the search is constrained further, local optimization methods are still not equipped with the adequate tools to thoroughly explore the feasible search space as compared to global optimization methods. Similarly, the performance of local search routines was observed to be highly sensitive to the gradient descent method selected as well as the control settings specified for optimization.

Table 14*- Parameter estimates for FMINCON and best performing global, single objective optimization algorithms when the search space was constrained. The mean and standard deviation are presented for each parameter and local optimization method. The best parameter set achieved for the global optimization methods after 5 repetitions are presented for reference.*

Study	Approach	μ_{max}	K_s	Y	K_d	b	n
1	FMINCON-Active Fit	1.0776	219.511	2.740	0.12884	0.0102	2.189
		2.05E-03	3.64E-01	4.02E-02	6.80E-04	1.34E-04	6.44E-04
	FMINCON-Interior Point	1.0720	219.578	2.723	0.12461	0.0103	2.183
		5.48E-05	5.00E-03	8.67E-04	4.72E-05	2.87E-06	2.31E-04
	AMALGAM-SO	1.0784	220.000	2.796	0.12852	0.0104	2.189
2	FMINCON-Active Fit	6.301	0.0896	3.304	0.8611	0.0767	9.551
		1.01E-01	9.93E-04	2.17E-01	5.19E-02	1.95E-03	2.69E-01
	FMINCON-Interior Point	6.370	0.0810	3.453	0.8657	0.0760	9.630
		8.40E-02	7.94E-04	1.73E-01	9.21E-03	1.80E-03	1.89E-01
	AMALGAM-SO	6.357	0.0822	3.451	0.8981	0.0780	10.000
3	FMINCON-Active Fit	1.235	0.000100	1.777	0.0125	7.80E-11	2.268
		1.55E-02	0	2.82E-02	3.39E-03	2.74E-12	1.48E-03
	FMINCON-Interior Point	1.227	0.000100	1.782	0.0100	7.90E-11	2.268
		3.42E-03	1.39E-15	4.06E-02	2.54E-06	2.24E-12	1.45E-04
	saDE	1.231	0.000100	1.740	0.0100	7.66E-11	2.268

4	FMINCON-Active Fit	2.771 4.12E-02	0.000101 2.97E-06	3.341 4.28E-02	0.0240 5.26E-03	0.6440 3.92E-02	2.615 8.67E-03
	FMINCON-Interior Point	2.756 3.23E-02	0.000104 4.73E-06	3.353 2.70E-02	0.0241 3.88E-03	0.6618 3.36E-02	2.614 4.74E-03
	AMALGAM-SO	2.789	0.000100	3.351	0.0295	0.6380	2.617

Another significant improvement achieved from this research method workflow resulted from the integration of likelihood free Bayesian optimization approaches (i.e., Approximate Bayesian Computation) as a final step, which allowed an enhanced targeting of the compromise solution space as compared to formal Gaussian Likelihood approaches. To demonstrate the benefits of likelihood free approaches, we briefly compared the convergence and parameter identifiability of the Bayesian optimization methods using both likelihood free and formal Gaussian likelihood methods. The simplest form of the Gaussian Log-Likelihood function was used (similar to Equation 4) and corresponded to option # 11 presented in Table 2 of the DREAM software package theory and implementation (Vrugt (2016)). The Moser model structure was used to compare both methods, as previous results (Figure 46) demonstrated that a higher number of generations were required to reach convergence when calibrating this model structure using the ABC approach (for most studies). All the control settings for both approaches were kept identical as described in Table D10. Similar to previous testing, five independent repetitions were used for each study/model combination to assess the variability in performance between the two Bayesian optimization approaches.

Although the formal convergence efficiency (using the overall R statistic of Gelman and Rubin 1992) was not significantly improved using the DREAM-ABC approach (Figure D5), the parameter identifiability was drastically enhanced for all studies (Figure 47). As

observed in Figure 47, which presents the mean of all parameter values across each Markov chain at each generation, the DREAM-ABC algorithm gradually converged to a stable posterior parameter distribution after approximately 50,000 generations, while the posterior parameter distribution obtained using the Gaussian Likelihood method was highly variable (Figure 47). This enhanced performance may be partly attributed to the inability of the DREAM approach to account for multiple objective functions using the built-in objective functions available. Although the user is free to create a custom objective function, there is no way to explicitly optimize two or more objective functions simultaneously. Similar improvements in parameter identifiability using the DREAM-ABC approach were observed using the experimental data from all other Studies (Appendix D, Section 7). Thus, despite the greater computational effort required to define the compromise solution space using this new approach (i.e., Steps 1-2 of this workflow), ultimately, more reliable as well as meaningful parameter and model prediction uncertainty estimates can be achieved.

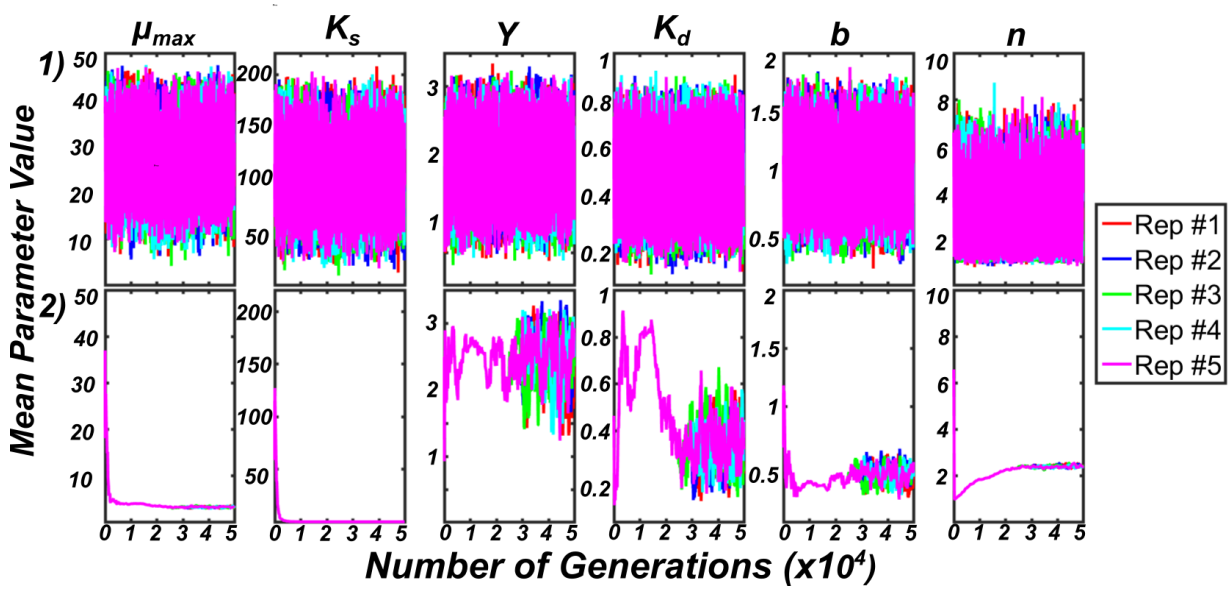

Figure 47. *Evolution of the mean (across all Markov chains) parameter values for both the 1) DREAM-ZS (Gaussian Likelihood) and 2) the DREAM-ZS (ABC) algorithms when calibrated against the Moser model using the fourth experimental dataset. The results of five independent repetitions are presented, as differentiated by the color scale of the legend.*

4. Conclusions

Given the observed differences in parameter precision, accuracy and bias observed between both approaches (i.e., local vs. global), the choice of optimization method is imperative to arrive at reliable parameter estimates for unstructured kinetic models describing biodegradation. In this study, we have proved global optimization approaches to be far superior to nonlinear regression routines provided by *MATLAB*'s optimization toolbox. Additional advantages of this optimization method workflow include the ability to handle multi-variate datasets, which often present problems with overfitting of certain variables. As evidenced above, global optimization approaches arrived at the best compromise solutions with higher probability than local methods. This method workflow also allowed a thorough review of both parameter and model prediction uncertainty through integration of an ABC approach. Ultimately, the Bayesian component of this

method was found to be a powerful diagnostic tool for model comparison and selection purposes commonly encountered in the Environmental Engineering field.

Chapter 6: A Reliable and Efficient Semi-Parametric Approach to Moment Independent Global Sensitivity Analysis Based on Copulas

Abstract: As models used to describe environmental systems have become increasingly complex following advances in computing power, the need for accurate and reliable methods to quantify the sensitivity of parameters underlying these models has never been greater. Sensitivity analysis can improve model predictive certainty by identifying key parameters that highly influence the model output, whereby focused experimental efforts for parameter identification can then be realized. This study presents a novel moment independent approach to global sensitivity analysis based on the application of parametric copula models to describe the joint probability distribution function between model input(s) and output(s) required for estimation of the sensitivity indices. Application of this method to a range in analytical functions demonstrated great improvements in accuracy compared to existing, fully non-parametric methods. Further application of this method to an environmental model confirmed that this method could model high nonlinearity, weak dependency, and non-monotonicity between model input(s) and output(s) alike.

1. Introduction

At the onset of the 21st century, the growing surge in computing power has fueled a rapid rise in the complexity associated with many mechanistic models used to describe environmental processes. As the structures of these models have become more parameterized and intricate, advanced approaches are necessary to assess the uncertainty associated with model predictions, parameters, and inputs alike (Tarantola et al. 2002, Mattot et al. 2009). Ultimately, environmental model predictions influence decision making processes, which require a rigorous assessment of associated uncertainties to ensure confidence in the resulting decisions (Refsgaard et al. 2007, Ascough et al. 2008, Mattot et al. 2009, Warmink et al. 2010).

Of the wide range in available uncertainty analyses, global sensitivity analysis (GSA), which is aimed at evaluating the sensitivity of model outputs to the full range of inputs (i.e., parameters or state variables), has evolved into a necessary step in the development and application of mechanistic models describing a wide range in environmental processes (Baroni and Tarantola 2014, Song et al. 2015, Pianosi and Wagener 2015, Pianosi et al. 2016, Manheim et al. 2019). GSA can identify and quantify, for example, how influential a given model parameter is when predicting a certain response and can even describe the degree of interactions between various parameters (Saltelli et al. 2008, Wei et al. 2015, Gupta and Razavi 2017). Quantifying the sensitivity of model parameters is crucial to assessing whether a model is overparameterized, and, if not, which parameters have the largest impact on overall model predictive uncertainty (Saltelli et al. 2008, Iooss and Lemaître 2015, Borgonovo and Plischke 2016).

In response to the increasing attention to quantify the sensitivity associated with model inputs, a broad number of classes to perform GSA have been advanced in the scientific literature, including derivative based, variance based, moment independent, and more recently, response surface methodologies (Wei et al. 2015, Razavi and Gupta 2015). Perhaps the most common and well-recognized class of GSA approaches (i.e., the method of Sobol) are those based on evaluating how a given parameter influences the output variance of a model, termed "variance-based" indices (Sobol 2001, Saltelli et al. 2010). However, despite their popularity, it has been repeatedly argued that the variance of the model output should not be the sole metric of uncertainty (Borgonovo 2007, Borgonovo et al. 2012, Pianosi and Wagener 2015). It has been further argued that variance-based methods do not consider the entire probability distribution function (PDF) of the model output, and do not consider highly skewed or even multi-modal nature of the outputs of many environmental models (Borgonovo and Plischke 2016). Thus, the moment independent (MI) class of GSA methods, which considers how a given shift in a parameter affects the full probability distribution of the model output, provides a more comprehensive outlook on model parameter uncertainty and sensitivity.

Borgonovo (2007) was the first to establish a reliable and computationally tractable moment independent sensitivity index termed the delta-sensitivity index (δ_i). Although several other MI indices have been promulgated by other authors (Liu & Homma 2009, Wei et al. 2013b, Zhai et al. 2014, Pianosi and Wagener 2015), Borgonovo's delta index remains the most applicable and intuitive index, despite the higher computational cost and difficulty in estimation associated with its calculation (Borgonovo 2007, Plischke et al. 2013). Given a model ($y = f(x)$) and its input parameters $x = (x_1, x_2, x_3, x_i)$, the delta sensitivity index

corresponding to the *i*th input parameter, (δ_i), is estimated by measuring the average shift ($S(x_i)$) between the unconditional probability density of the model output, $f_y(y)$, (when all model parameters are varied simultaneously) with that of the conditional probability density achieved when holding one of the parameters constant and varying the remaining model parameters, $f_{y|x_i}(y)$ (Equation 1). The average shift between both densities is represented mathematically by the expectation (E) of the uni-dimensional integral (where the dimensions are equivalent to the number of parameters or the dimensions of a problem, d), that can be generally approximated using quasi Monte Carlo methods (Castaings et al. 2012, Wei et al. 2013a) (Equations 1 and 2, where i ranges from 1 to d).

$$S(x_i) = \int \left| f_y(y) - f_{y|x_i}(y) \right| dy \quad (1)$$

$$\delta_i = \frac{1}{2} E_{x_i}[S(x_i)] \quad (2)$$

Although the MI class of GSA approaches has been viewed as a reliable and intuitive GSA methodology, MI methods are still notoriously difficult and computationally expensive to estimate for more involved applications, such as optimal experimental design (Chu and Hahn 2010, Yun et al. 2018, Feng et al. 2018). The MI method of Borgonovo (2007) as introduced above, for example, requires an estimate of both the unconditional and conditional probability densities of the model output, with a resulting computational complexity of $(dn_2+1)n_1$, where d is the problem dimension, n_1 and n_2 are the number of samples required for the outer and inner loop calculations, respectively (Borgonovo 2007). Clearly, this "double loop" method suffers from the "curse of dimensionality," as the complexity is dependent on the number of dimensions of the problem, d.

To reduce the computational burden inherent with this method, several studies have focused on avoiding the calculation of the conditional probability densities entirely,

thereby avoiding a "double loop" approach to estimation (Wei et al. 2013a). These studies have derived an equation to calculate δ_i based on the mathematical relationship between the conditional probability distribution as well as the marginal and joint probability densities of the model input parameter and model output. The application of the resulting equation was then reduced to a "single loop" approach, eliminating the "curse of dimensionality," and reducing the computational burden to n_1, hereafter referred to as n (Equation 3).

$$S(x_i) = \int \left| \frac{f_y(y) f_{x_i}(x_i)}{f_{x,y}(y,x_i)} - 1 \right| dy \tag{3}$$

The primary challenges faced by these improved MI approaches, however, were identified as accurately approximating either: the probability distribution function (PDF) of a given model output ($f_y(y)$); or 2) the joint probability distribution of a given model input and the model output ($f_{x,y}(y,x_i)$) (Equation 3) (Wei et al. 2013a, Wei et al. 2014). Previously, these probability distributions (of the marginal and joint PDFs) were estimated non-parametrically, using fast and relatively reliable implementations of either 1D or 2D kernel density methods (KDE) (Botev et al. 2010, Wei et al. 2013a, Wei et al. 2014). The accuracy of these methods could be improved if a semi-fully parametric and easily generalizable MI method can be achieved to approximate both the marginal and joint PDFs. More recent approaches to this end, ranging from the Edgeworth series expansion (Yun et al. 2018), to fractional moments combined with maximum entropy methods (Zhang et al. 2014, Zhang et al. 2015c), for estimating the PDF of the model output $f_y(y)$ have been conceived. Despite the advent of these improved approaches, a semi-fully parametric and reliable approach to estimate the joint PDF required in Equation 3 for use in MI sensitivity analysis has not yet been reached.

The advent of copulas to describe the joint PDFs formed by the model output and input parameters has previously been introduced as a reliable and efficient method for MI sensitivity analysis (Wei et al. 2014). The main advantage of using copulas are that they can easily decompose the joint PDF into that based on the marginal PDFs of both the model output predictions and input parameters as well as the correlation structure inherent between both input and output distributions (Joe 1997, Nelsen 2007). In the previous approach developed by Wei et al. (2014), a nonparametric method (using a 2D-kernel density estimation) was implemented to estimate the copula density describing the dependency between the input parameters and output model predictions. Although this fully non-parametric approach was deemed satisfactory for estimating the dependence structure between model input and outputs, similar to what was proposed above, the reliability (in terms of accuracy and precision) of this method could be improved by progressing toward a more parametric and defined estimate of the copula.

In this study, we present a novel, semi-parametric method for calculating the Borgonovo delta-indices in MI sensitivity analysis based on the use of parametric copulas. This method approximates the joint PDF between the model inputs and output using a parametric copula model, while still approximating the marginal PDFs using a stable 1-D KDE method (which is non-parametric, hence we refer to this method as "semi-parametric"). The use of a parametric copula model to describe the joint PDF between model input/output is expected to provide several key advantages (i.e., easily formulated, parameterized, and sampled), the most important of which is an increase in accuracy, as parametric Copula models provide a direct means to predict the joint PDF as a function of the input marginal cumulative densities of each variable. Since parametric models rely on

proper training and calibration of model parameters to predict future states, we also expect that a small fraction of initial samples will be required to reliably calibrate and predict the dependency structure between variables, thereby greatly reducing the computational burden required for analysis (Villarini et al. 2008). Of course, one of the main limitations inherent to parametric copula methods is the ability to generalize and model many different dependency structures (Chen and Huang 2007). Thus, we introduce a monotonization, variable transformation technique (Mohseni Ahooyi et al. 2014) to allow greater flexibility and improved accuracy of parametric copula methods to describe a wide range in dependencies existing between model inputs/outputs required for MI sensitivity analysis.

We compare this newly developed, semi-parametric approach to the existing non-parametric copula (Wei et al. 2014), single loop (Wei et al. 2013a), and improved non-parametric importance sampling single loop methods (Derennes et al. 2018) on a series of test functions ranging from a model with strictly linear inputs/output relations, to a model with highly nonlinear input/output relations, as well as a model exhibiting highly nonlinear, nonmonotonic input/output relationships. We demonstrate how explicitly defining the correlation structure using a parametric copula can lead to improvements in both accuracy and efficiency over methods that solely rely on non-parametric estimates of the dependency structure. The use of this semi-parametric method will also detect and describe nonmonotonic and complex dependencies between model outputs and inputs that non-parametric methods may not be able to effectively describe.

2. Materials and Methods

In Section 2.1 of the Materials and Methods, we first describe the background behind our semi-parametric, copula-based method, including the theory behind the variable monotonization (Rolling Pin) methods. Section 2.2 then describes the full numerical implementation of this approach, giving a step by step tutorial on how we calculated the delta sensitivity measures using this method. In Section 2.3, we introduce the test problems and run conditions for each of the MI methods compared in this study. Section 2.4 reviews the main approach taken to quantify the goodness of fit of each copula model reviewed. Section 2.5 presents the primary method to evaluate the tail concentration functions of each parametric copula model to assess the abilities of each model to handle the tail dependencies formed between model inputs and outputs. Section 2.6 addresses the methods used to evaluate copula symmetry and the technique applied to asymmetrize the Frank copula. Section 2.7 describes the approach to compare the semi-parametric method developed in this study to existing, fully non-parametric approaches. Finally, Section 2.8 presents the framework for applying this new method to an unstructured kinetic model describing microcystin biodegradation (i.e., the Moser model).

2.1 Description of the Semi-Parametric Copula Method

2.1.1 The Rolling Pin Method

The semi-parametric copula method for MI sensitivity analysis presented in this study can be described in seven principal steps (Figure 48). The first step in the workflow of the algorithm involves monotonization of the dependence structure between the model input parameters and the model output response (Figure 48). Integration of the Rolling Pin method, which “rolls out” the dependencies between model input parameters and output

predictions, offers the following advantages: 1) it can resolve issues with nonmonotonicity by always ensuring some optimal degree of linearity among the transformed variables; 2) it can allow the user to flexibly model unknown dependence structures with a known structure and may alleviate issues with selecting the correct parametric model; as well as, 3) it can capture highly nonlinear dependencies between different variables (Mohseni Ahooyi et al. 2014, 2015).

The heart of the Rolling Pin method relies on the monotonization of the model outputs to develop a strictly positive, linear and monotonic relationship to ensue between the model input parameters and output predictions (Equation 4).

$$Z_i = (1 - \alpha_i)Y + \alpha_i X_i \quad (4)$$

Where Y is the model output, α_i is the ith monotonization parameter (for i = 1 to d input parameters), X_i is the ith "reference variable", in this case the model input parameter in standard normal space, and Z_i is the ith transformed (monotonized) value of the model output. Different values of Z_i were obtained by changing the value of the reference variable (X_i), depending on which dependence structure was being analyzed (i.e., Y vs X_1, Y vs. X_2, Y vs. X_i). It is important to note that the model inputs (X_i) were not monotonized (with corresponding α values of 0) and only the corresponding model output (Y).

Mohseni Ahooyi et al. (2014, 2015) specified that the variables that will be monotonized (in this case the model output, Y) should be normalized to avoid scaling issues. Importantly, we found that performing this normalization of the model output led to incorrect approximations of the Borgonovo MI sensitivity indices (data not shown). Thus, no conversions or transformations of the model output were performed in this algorithm. However, the model input parameter values were transformed from uniform space to

standard normal space before monotonization. Since the model inputs were uniformly and randomly distributed, this initial conversion consisted of finding the uniform CDF values (*UCDF*, using a QMC sequence generator), then performing a standard normal inversion to calculate the transformed values ($\varphi^{-1}(UCDF)$). In this study, we found that using Sobol's low discrepancy QMC sequences for training/fitting the parametric Copula worked very well.

The efficacy of the Rolling Pin method was found to be extremely dependent on the correct choice of the monotonization parameter(s), α_i. Mohseni Ahooyi et al. (2014) specified several methods to determine or optimize values of this parameter, including a maximum log-likelihood (ML) approach. We found that the ML approach was most reliable compared to the other methods presented in Mohseni Ahooyi et al. (2014, 2015) and was adopted herein. The LSHADE-EpSin algorithm (without local search) developed by (Awad et al. 2016) was used for global optimization of the monotonization parameters required by the Rolling Pin method. Details behind the ML optimization method, LSHADE-EpSin control settings, as well as the objective function constructed for running the ML optimization are presented in Appendix E, section 1 for reference.

2.1.2 KDE Estimation of PDF/CDFs of Transformed Variables

After optimizing the monotonization parameters using the ML approach, the model output was transformed according to Equation 4. The PDF and CDF of the transformed model output was then estimated using the standard KDE approach provided in the statistics toolbox of MATLAB (Mathworks, r2015a). Nonparametric estimation of the cumulative, $F(x)$, and probability, $f(x)$, densities using this approach depends on proper selection of the smoothing function ($K()$) as well as the bandwidth (h) (Equations 5 and 6).

Here, x_i defines the centers of each kernel used to estimate the probability or cumulative densities and the bandwidth specifies the relative influence (or weight) of each kernel. A Gaussian kernel smoothing function and the rule of thumb bandwidth selection method were used in this study for stable estimation of the CDFs/PDFs of the transformed variables.

$$f(x) = \frac{1}{nh} \sum_{i=1}^{n} K\left(\frac{x - x_i}{h}\right) \tag{5}$$

$$F(x) = \int_{-\infty}^{x} K(t)\, dt \tag{6}$$

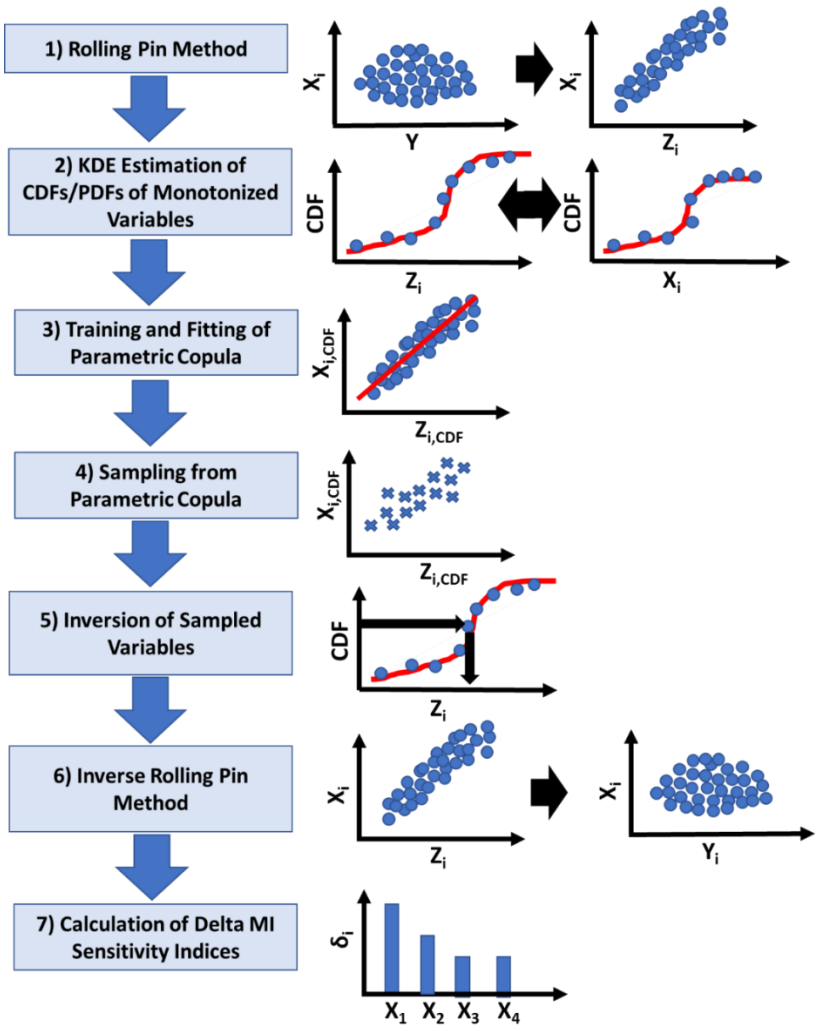

Figure 48. *Workflow and representative illustrations of the semi-parametric method based on Copulas for MI sensitivity analysis.*

2.1.3 Training and Fitting of the Parametric Copula Models

The next step of this algorithm was to construct multiple bi-variate parametric Copula models to estimate the joint PDFs between the model inputs and output variable (Step 3, Figure 48). In this method, we surveyed several parametric Copula models (Table 15), including the elliptical (i.e., Gaussian, t-distributions) and the one-parameter family of Archimedean Copulas (i.e., Frank, Clayton, Gumbel) (Joe 1997, Nelsen 2007). The parametric Copulas surveyed differ according to their mathematical formulation and can flexibly model different ranges in linear to nonlinear dependencies between variables (Table 15). In addition, it is important to note the strict ranges in model parameters that can be used to calibrate each parametric Copula model (Table 15).

Other than the mathematical formulation, the models reviewed also differed in their ability to model correlations present among extreme values, otherwise known as the tail dependencies, which can be assessed through comparison of the tail dependence coefficients (Table 15). For example, the *t*-distribution is more likely to capture extreme value correlations (albeit placing equal weight on both tails) as compared to the Gaussian Copula (Table 15). Unlike other Archimedean Copulas, the Frank Copula can model both positive and negative dependence structures existing between variables (if the number of dimensions ≤ 3) but is characterized by weak tail dependence (Table 15) (Joe 1997, Nelsen 2007). Both the Clayton and Gumbel copulas can capture lower or upper tail dependencies, respectively, where the strength of this dependency is dependent on the magnitude of the model parameter θ, defined in the equations presented in Table 15.

***Table 15**- Summary of bivariate parametric Copulas surveyed in this study, including the mathematical formulation, parameter ranges, and tail dependencies of each.*

Copula Model	Mathematical Description	Parameter Range	Tail Dependence Coefficients λ_L, λ_U	
Gaussian	$\int_{-\infty}^{\emptyset^{-1}(u)} \int_{-\infty}^{\emptyset^{-1}(v)} \frac{1}{2\pi\sqrt{1-\theta^2}} e^{\left(\frac{2\theta xy - x^2 - y^2}{2(1-\theta^2)}\right)} dxdy$	$\theta \in [-1,1]$	0	0
t-distribution	$\int_{-\infty}^{t_{\theta_2}^{-1}(u)} \int_{-\infty}^{t_{\theta_2}^{-1}(v)} \frac{\Gamma(\frac{\theta_2+2}{2})}{\Gamma(\frac{\theta_2}{2})\pi\theta_2\sqrt{1-\theta^2}} e^{\left(1+\frac{x^2-2\theta_1 xy+y^2}{\theta_2}\right)^{\frac{(\theta_2+2)}{2}}} dxdy$	$\theta_1 \in [-1,1]$ $\theta_2 \in (0,\infty)$	$2t_{v+1}\left(\frac{\sqrt{v+1}\sqrt{1-\theta}}{\sqrt{1+\theta}}\right)$	
Frank	$\frac{-1}{\theta} ln\left[1+\frac{(e^{-\theta u}-1)(e^{-\theta v}-1)}{e^{-\theta}-1}\right]$	$\theta \in$ R\0	0	0
Clayton	$\max(u^{-\theta}-v^{-\theta}-1,0)^{\frac{-1}{\theta}}$	$\theta \in [-1,\infty)\backslash 0$	$2^{\frac{-1}{\theta}}$	0
Gumbel	$e^{-[(-\ln(u))^{\theta}+(-\ln(v))^{\theta}]^{\frac{1}{\theta}}}$	$\theta \in [1,\infty)$	0	$2-2^{\frac{1}{\theta}}$

A critical aspect of the semi-parametric method developed in this study was the potential to substitute different parametric Copula models to better reflect the dependency structures existing within the problem of interest. Ultimately, for each test problem, a unique parametric Copula model was selected over other candidate models using the goodness of fit as the main metric for comparison. The steps taken to evaluate the best performing Copula model are explained in detail in (Section 6) and the results of the initial model calibrations are reviewed in Section 3.1. A canonical maximum likelihood estimation (CMLE) method, which is provided as a routine in MATLAB's statistics toolbox (r2015b), was ultimately used for fitting each parametric copula model to the QMC training points originally selected in Step 1 (see Appendix E, section 2 for full details).

2.1.4 Sampling from the Parametric Copula Models

The elliptical Copulas (i.e., Gaussian and t distributions) were sampled using the inverse CDF method, whereas the conditional distribution method (CDM, Joe 1997, Nelsen 2007) was primarily used for sampling from the constructed parametric Archimedean Copulas. The inverse CDF method is explained in detail in Appendix E, section 3. The CDM

algorithm, which is also conveniently built into MATLAB's statistics toolbox, relies on a closed form of the inverse conditional CDF of each parametric Copula. Details of how this algorithm was implemented are also available in Appendix E, section 3.

Three variants of this sampling scheme were also investigated and compared in Section 3.3 of the Results to improve the accuracy and precision of the semi-parametric method developed in this study (see Appendix E, section 4). Here, we have focused on the use of two classes of sampling schemes, those that sample directly from the Copula model, as well as those that re-sample from the samples previously obtained from the Copula model. The sampling scheme variants included the following: 1) using QMC sequences with the CDM method introduced above; 2) using QMC sequences with the Marshall-Olkin sampling algorithm (if the selected Copula was Archimedean) (Marshall and Olkin 1988, 1997, Hofert 2008); or 3) implementing a density-based re-sampling (Kurowicka and Cooke 2006) technique after initially sampling from the parametric copula (Appendix E, section 3). Importantly, for all test problems, the number of samples taken from the copula was equivalent to the number of QMC samples used to train/construct the parametric copula. The effect of each sampling scheme was compared across three test functions using a range in QMC sample numbers (n = 256, 512, 1024, 2048, 4096, 8192, 16384, 32768, 65536, 131072) to construct and the same number to sample each copula. Ten independent realizations were conducted to assess statistical precision of all sampling schemes.

2.1.5 Inversion of Sampled Variables and Inverse Rolling Pin Method

After sampling from each parametric Copula, it was necessary to transform the sampled CDF values back to values of the monotonized model outputs. This inversion was

accomplished using the KDE estimates determined in Step 2 (Figure 48), employing the inverse CDF option built into MATLAB's statistics toolbox. In addition to this inversion, a second round of KDE estimation was required to determine the PDF values of the monotonized, newly sampled model outputs. This step was necessary to offset the instability observed from the previous KDE inversion. Again, for the input parameters, the inversion was accomplished using a standard normal inverse CDF and the PDF values were determined using the standard normal PDF evaluated at the initial sampling points.

Lastly (Steps 5 and 6, Figure 48), the joint PDF values were de-monotonized using the equation developed in Mohseni Ahooyi et al. (2014) (Equation 7), where again *c()* represents the Copula PDF taking as input the CDF values (F_X/F_Y) of both the model input parameters ($X_{i,k}$) and monotonized model outputs ($Z_{i,k}$); f_x/f_z signify the marginal PDF values of both the model input parameters and monotonized model outputs; and α_2 represents the monotonization parameter optimized using the global optimization approach described in Step 1 ($\alpha_1 = 0$, Figure 48).

$$f_{x,y}(Y_1, X_1) = c\left(F_{Z,i}(Z_{i,k}), F_{X,i}(X_{i,k})\right) * f_{z,i}(Z_{i,k})(1-\alpha_2) * f_{x,i}(X_{i,k})(1-\alpha_1) \quad (7)$$

2.1.6 Calculation of the MI Borgonovo Delta Sensitivity Indices

As described in Step 7, Figure 48, the final step was to calculate the Borgonovo delta moment independent indices. Similar to Equation 3, the Monte Carlo estimate can be obtained given that the number of samples is sufficiently large to converge to a stable solution. Equation 8 presents the final calculation involved to estimate the delta MI sensitivity measures from the marginal densities of the model input parameters and de-monotonized outputs as well as the joint PDF estimated in Steps 1-4 above. It is important to note that f_y represents the marginal PDF of the *de-monotonized* model outputs, which

was achieved using the inverse of Equation 4 above. An additional KDE estimate (using the same approach outlined in Section 2.1.2) was necessary to determine the PDF values of the de-monotonized model outputs for use in Equation 8.

$$\delta_i = \frac{1}{2N} \sum_{k=1}^{N} \left| \frac{f_y(Y_{i,k}) f_{x_i}(X_{i,k})}{f_{x,y}(Y_{i,k}, X_{i,k})} - 1 \right| \tag{8}$$

2.2 Numerical Implementation of the Semi-Parametric Copula Method

We now present an example numerical implementation of the semi-parametric copula method, focusing on a step by step tutorial on how the delta indices were estimated. This is not meant to be a comprehensive explanation of the steps involved (see Section 2.1), but rather as a guide to how best implement this method numerically. The numerical implementation steps follow the structure presented in Figure 48 and include sub-steps to provide sufficient details on optimal implementation approaches. We provide a general framework so that effectively any parametric Copula can be integrated into this MI sensitivity method.

Step 1: Generate a MC sampling scheme, run the model and obtain the model output, and carry out the Rolling Pin method.

Step 1A: Generate a uniform, random quasi Monte Carlo sampling matrix (A) using Sobol's low discrepancy sequences as follows (Equation 9):

$$\mathrm{A} = \begin{bmatrix} {x_1}^{(1)} & {x_2}^{(1)} & {x_3}^{(1)} & \cdots & {x_d}^{(1)} \\ {x_1}^{(2)} & {x_2}^{(2)} & {x_3}^{(2)} & \cdots & {x_d}^{(2)} \\ {x_1}^{(3)} & {x_2}^{(3)} & {x_3}^{(3)} & \cdots & {x_d}^{(3)} \\ \vdots & \vdots & \vdots & \cdots & \vdots \\ {x_1}^{(n)} & {x_2}^{(n)} & {x_3}^{(n)} & & {x_d}^{(n)} \end{bmatrix} \tag{9}$$

The sampling matrix should be n number of samples long by d (number of input parameter) samples wide.

Step 1B: Obtain the vector of model outputs (Y) by running the model multiple times using the A matrix generated in Step 1.

$$Y = \begin{bmatrix} y^{(1)} \\ y^{(2)} \\ y^{(3)} \\ \vdots \\ y^{(n)} \end{bmatrix} \tag{10}$$

Note: the model output vector should be n number of samples long by 1 samples wide if it is a scalar model output (Equation 13). After running the model, be sure to transform the initial uniform, random model input parameters into standard normal space for use in the Rolling Pin Method.

Step 1C: For each input parameter X_i, use the Rolling Pin method and MLE optimization approach (Section 2.1.1) to monotonize the model input parameter and output dependence structure (obtaining Z_i monotonized model outputs).

Step 2: Use MATLAB's built in KDE toolbox to estimate the CDFs and PDFs for each monotonized model output, Z_i. Make sure to store these KDE estimates.

Step 3: Using the CDF estimates of the input parameters and monotonized model outputs, train and construct the parametric copula by applying the CMLE approach (Section 2.1.3) available in MATLAB's statistical toolbox. This step should be repeated a total of d times, resulting in d different parametric Copula models (and d different θ_{opt} parameter values). Please note that any parametric Copula can be tailored to the problem of interest.

Step 4: Sample from the parametric Copula n number of times using the CDM algorithm (Section 2.1.4) that is also built into MATLAB's statistical toolbox. Note that this sampling requires the corresponding θ_{opt} used in the previous step.

Step 5A: Invert the samples obtained in Step 4 back to the monotonized model output space using the inverse CDF estimated in Step 2.

Step 5B: Use MATLAB's built in KDE toolbox to estimate the PDFs for each monotonized, newly sampled model output, Z_i. Obtain estimates of the PDF of the input parameters using the standard normal distribution.

Step 6A: Invert the monotonized model outputs back to the original model output space using the inverse of Equation 4 and run a final KDE (using MATLAB's statistics toolbox) on this output to obtain the PDF values of the de-monotonized model outputs.

Step 6B: Calculate the joint PDF of the de-monotonized input/outputs using Equation 7, making sure that the correct monotonization parameter values, marginal PDF, and copula PDF calculations are used.

Step 7: Calculate the delta sensitivity indices using Equation 8 above incorporating the joint PDF and marginal PDFs of the model input parameters and de-monotonized outputs.

2.3 Investigation of Three Analytical Test Problems

The semi-parametric copula approach to MI GSA developed in this study and several competing algorithms were benchmarked on a series of analytical test functions including: a linear, strictly non-linear and non-linear, nonmonotonic test problem (Table 16). Analytical test case 1 is a simple additive combination of six standard normal distributions, resulting in a linear dependence structure between model input parameters and output. For this problem, the model input factor ranking is as follows: $X_6 > X_5 > X_4 > X_3 > X_2 > X_1$ (Table 16).

Analytical test case 2, with high non-linearity, is considerably more difficult to solve than test case 1. In this problem, the model inputs are uniform randomly distributed [0,1],

and the dependency between model inputs and output is generally positive, monotonic (exponential). The importance of the input variables can be controlled by the parameter *bi*, where in this case the following factor ranking results: X_1 >X2>X3>X4>X5>X6 (Table 16).

The well-known Ishigami function, which serves as analytical test case 3, is a very challenging non-linear and non-monotonic problem consistently used in the field of GSA to benchmark various approaches. Here, the dependence between the first input variable and the output is non-linear and positive, monotonic; however, the dependence between the second or third input variables and the output are nonlinear, but non-monotonic. The input distribution of the model inputs to this function are uniform random [-π, π], with similar parameters (a, b) implemented in this study to define the degree of interactions between input parameters (Table 16). The sensitivity ranking for this function using MI sensitivity methods generally indicated the following input ranking: X_2>X_1>X_3.

Table 16*- Summary of analytical test functions for comparison of various MI sensitivity approaches used in this study*

Test Case	Test Function	Mathematical Description	Input Distributions	Parameter Definitions	Ref.
1	Linear	$Y = 1.5X_1 + 1.6X_2 + 1.7X_3 + 1.8X_4 + 1.9X_5 + 2X_6$	$X_i \sim N(0,1)$	None	Borgonovo et al. 2011
2	Non-Linear	$Y = \exp(\sum_{i=1}^{6} b_i X_i) - \prod_{i=1}^{6}\left[\frac{\exp(b_i)-1}{b_i}\right]$	$X_i \sim U(0,1)$	b_i = [1.5,0.9, 0.7,0.5,0.3,0.1]	Helton and Davis 2002
3	Non-Linear, Non-monotonic (Ishigami)	$Y = \sin(X_1) + asin^2(X_2) + bX_3^4\sin(X_1)$	$X_i \sim U(-\pi, \pi)$	a = 5, b = 0.1	Ishigami, and Homma 1991

Approximate analytical solutions to the three test cases described above were achieved in this study using a QMC approach to MI GSA. In this approach, we incorporated Botev and co-workers (2010) method to accurately estimate the PDF values of both the

model output and conditional distributions. The delta sensitivity indices were then estimated using the double integration approach and PDF solutions identified above (Equation 14) as originally proposed in Borgonovo (2007) for a sufficiently large number of QMC samples. A summary of the approximate analytical solutions derived in this study is presented in Table E2 for reference.

$$\delta_i = \int f_{x_i}(x_i) \int \left| f_y(y) - f_{y|x_i}(y) \right| dy \, dx \tag{11}$$

2.4 Parametric Copula Goodness of Fit (GOF) Testing

Differences in the underlying mathematical structure of each parametric copula model reviewed in this study to describe a variety of dependence relationships encountered in environmental models further affects the estimation of reliable MI sensitivity indices. Thus, the overall abilities of different copula models to fit a range in dependence structures was compared through application of a goodness of fit (GOF) approach initially developed by Genest and Rivest (1993) (see Appendix E, section 6). This approach was based on calculating the Cramér-von Mises distance (hereafter referred to as CM statistic) between an empirical Kendall Distribution Function (KDF) and the parametric copula KDF, in which smaller values of this metric are indicative of a better performing parametric Copula model. We also compared the GOF achieved from the parametric Copula models surveyed in this study to a non-parametric Copula method, similar to that developed in Wei et al. (2014). Results of the Copula GOF testing were compared across the test functions described above using a range in initial QMC sampling numbers (n = 256, 4096, and 16384) to construct each Copula and ten independent realizations were conducted to assess statistical precision of all methods.

2.5 Parametric Copula Tail Dependency Testing

In addition to overall GOF, the tail dependence was critical to review, as the correlation among certain variables in some environmental models may increase or decrease heading toward the upper or lower tails of the copula distributions. The ability of each parametric (and non-parametric) copula model to fit the tails of each dependency structure was assessed through application of the tail concentration function (TCF) (see Appendix E, section 7). In general, the TCF conveys the probability of selecting a Copula pair ($C(u, u)$) as a function of the distance from the lower or upper tails (u) (Patton 2013, Durante et al. 2015). The tail fitting performance was again evaluated using a modified Cramér-von Mises distance (hereafter referred to as CM_{TCF}) calculated between the empirical TCF and the parametric TCF (Durante et al. 2015), where lower values are indicative of an improved tail GOF. Similar to the Copula GOF testing, results of the Copula tail dependency testing were compared across three test functions using a range in QMC sample numbers (n = 256, 4096, and 16384) to construct each Copula and ten independent realizations were conducted to assess statistical precision of the tail fits for all parametric copula models.

2.6 Evaluation of Copula Symmetry

Copula symmetry is an important prerequisite to check before modelling any dependence structure since most parametric Copula model derivations are based on the assumption of symmetry (Joe 1997, Nelsen 2007). Symmetry is often defined by mathematically reviewing the concept of exchangeability, where variables are deemed exchangeable if the order of the dependency structure has little effect on the Copula cumulative density evaluation (i.e., $C(u, v) = C(v,u)$) (Liebscher 2008, Durante 2009, Genest

et al. 2012). Often, the degree of exchangeability can be estimated through application of a modified Cramér-von Mises metric (S_n) calculated between the empirical Copulas formed for $C_n(u, v)$ and $C_n(v,u)$, where smaller values are indicative of a more symmetric dependency structure (Appendix E, section 8). In this study, statistical significance of the S_n metric was reviewed for test functions 2 and 3 only (as the linear additive case was always symmetrical) using a modified Monte Carlo resampling approach (evaluated at n = 256, 1024, and 4096 across ten independent realizations) presented in Genest et al. (2012) (see Appendix E, section 8).

In the case of asymmetric dependency structures existing between model inputs and output, Archimedean copulas can be modified to explicitly account for any degree of asymmetry using several transformation approaches. Here, we relied on the Khoudraji transformation (Genest et al. 1998, Vandenberghe et al. 2010), which is applied by multiplicatively combining two different copula model structures, in this case, the independence and Frank copula models (see Appendix E, section 8 for complete derivation). MI sensitivity indices were calculated using samples obtained from the asymmetrized Frank Copula as part of a modified semi-parametric approach. Complete details on how the asymmetrized Frank copula was implemented numerically are presented in Appendix E, section 8. The asymmetric Frank copula approach to MI sensitivity index estimation was compared to the symmetric Frank copula approach for Test Cases 2 and 3, where a range in QMC sample numbers (n = 256, 512, 1024, 2048, 4096, 8192, 16384, 32768, 65536, 131072) were used to construct and sample each copula across ten independent realizations to compare statistical precision of both methods.

2.7 Comparison of the Semi-Parametric Method to Existing Algorithms

The semi-parametric copula method presented in this study was thoroughly compared against three previous fully non-parametric approaches to MI sensitivity analysis, including: Wei and coworkers (2014) copula-based approach, Wei and coworkers (2013a) single loop approach, as well as a more recent approach to the single loop method using non-parametric importance sampling (NPIS) (Derennes et al. 2018). These methods were carefully coded in MATLAB (r2015b) based on the descriptions presented in each study and are available as Supplementary Materials to this study.

Each method was run for the following range of Sobol QMC samples (using the same sequence starting point): 2^8, 2^9,2^{10},2^{11},2^{12},2^{13},2^{14},2^{15},2^{16}, and 2^{17} in which 10 independent runs were performed for each method to assess the statistical precision. The accuracy of each approach was benchmarked using the absolute error (ABE), calculated between the approximate analytical solution ($\delta_{i,A}$) and the solution obtained after each run ($\delta_{i,E}$) (Equation 12). The precision of each approach was assessed using the standard deviation of all delta indices acquired across runs (Equation 13). In this study, we describe "convergence efficiency" as the number of model evaluations required to reach the following level of precision: the width of the empirical 95% confidence intervals across runs should be less than 0.05 (Sarrazin et al. 2016).

$$ABE = \sum_{i=1}^{N} \left| \delta_{i,E} - \delta_{i,A} \right| \tag{12}$$

$$SD = \sqrt{\frac{1}{N} \sum_{k=1}^{N} \left(\delta_k - \bar{\delta} \right)^2} \tag{13}$$

2.8 Application to an Environmental Model

To demonstrate the advantages of and elucidate the main mechanisms behind this newly developed approach, the semi-parametric approach was applied to a common unstructured kinetic model applied in the field of biodegradation: the Moser model. The Moser model describes the dynamics of bacterial growth (X) and substrate (contaminant) utilization (C) in the environment and was successfully applied to predict the biodegradation of microcystin, a toxin produced by freshwater cyanobacteria, by isolated bacterial populations (Equations 14-16) (Manheim et al. 2019).

$$\frac{dC}{dt} = -\frac{1}{Y}\mu X \tag{14}$$

$$\frac{dX}{dt} = \mu X - k_d X \tag{15}$$

$$\mu = \frac{\mu_{max} C^n}{K_s + C^n} \tag{16}$$

The Moser model defines the specific growth rate of bacterial cells (μ) growing on a defined substrate as a hyperbolic function of substrate concentration (C) with four main model parameters: the maximum specific growth rate (μ_{max}), half saturation constant (K_s), the cell yield coefficient (Y), and a parameter to theoretically account for potential interactions between binding sites on the degrading enzyme molecule (n) (Moser 1958). In addition, the endogenous decay of bacterial cells during growth is explicitly considered (k_d) (Rittmann et al. 2002, Bodegom 2007).

The MI sensitivity indices were estimated for this environmental model using the detailed simulation framework described in Appendix E, section 9. The semi-parametric method was run using identical Steps as presented in Section 2.2, over a wide range in

initial QMC samples (n = 2^8, 2^9,2^{10},2^{11},2^{12},2^{13}) using ten independent realizations to assess the variability of the estimated MI sensitivity indices.

3. Results

3.1 Selection of an Appropriate Parametric Copula through GOF testing

The overall GOF results demonstrated that as the number of QMC samples used to construct each copula was increased, the resulting error generally increased, indicating that the GOF declined (Figure 49). In addition, the best performing parametric copula varied according to each test function. For the linear, additive test function, Test Case 1, the Gaussian copula demonstrated the best overall GOF (especially for greater QMC samples), followed by the t-distribution, Frank, Clayton, and Gumbel Archimedean copulas (Figure 49). Regardless of the input variable-model output dependency investigated, however, the Frank Copula generally outperformed all other copulas for the first test function when the number of QMC samples was small (n = 256) (Figure 49).

The Frank Copula demonstrated superior overall GOF on both the non-linear test function, Test Case 2, as well as the non-linear, non-monotonic test function, Test Case 3 (Figure 49). For these test functions, lower values of the CM statistic were generally observed for the Frank Copula for most of the input variables and QMC samples (excluding input variables 2 and 3, for example). The Gaussian Copula also performed reasonably well for Test Cases 2 and 3 when comparing the resulting CM statistics (Figure 49).

The GOF for the Gumbel and Clayton Copulas, which are equipped to explicitly model tail dependence, was generally poor across all test functions (Figure 49). However, for test function 2, the Clayton Copula GOF was more reliable, especially for the 1st and 6th model input variables (Figure 49). In addition, the performance of the non-parametric

method was noteworthy, especially for the third test problem, where it even outperformed some of the parametric copula methods (input variable 1, Figure 49).

Across all test functions, the variability of the GOF over ten independent realizations, as conveyed by the standard deviation (plotted as error bars on each bar plot), was generally lower for the Archimedean copulas (Gumbel, Clayton, Frank) as compared to the elliptical copulas (Gaussian, *t*-distribution). The primary reason for this difference in statistical precision was that the elliptical Copulas were randomly sampled to develop the parametric KDF, as compared to the Archimedean Copulas, where an explicit expression was available to calculate the parametric KDF.

Furthermore, as the number of QMC samples used to construct each copula increased, the variability was observed to decrease (Figure 49). This result was as expected given that if more information concerning the dependency structure is available to construct each Copula, the resulting predictions from each copula model should be more precise. It is also important to note that although the GOF was generally high, the variability of the non-parametric copula method was comparable to or even slightly larger than that of the elliptical Copulas across all test functions (Figure 49). Thus, the Frank Archimedean copulas benefitted from both high accuracy and statistical precision as compared to the non-parametric Copula method.

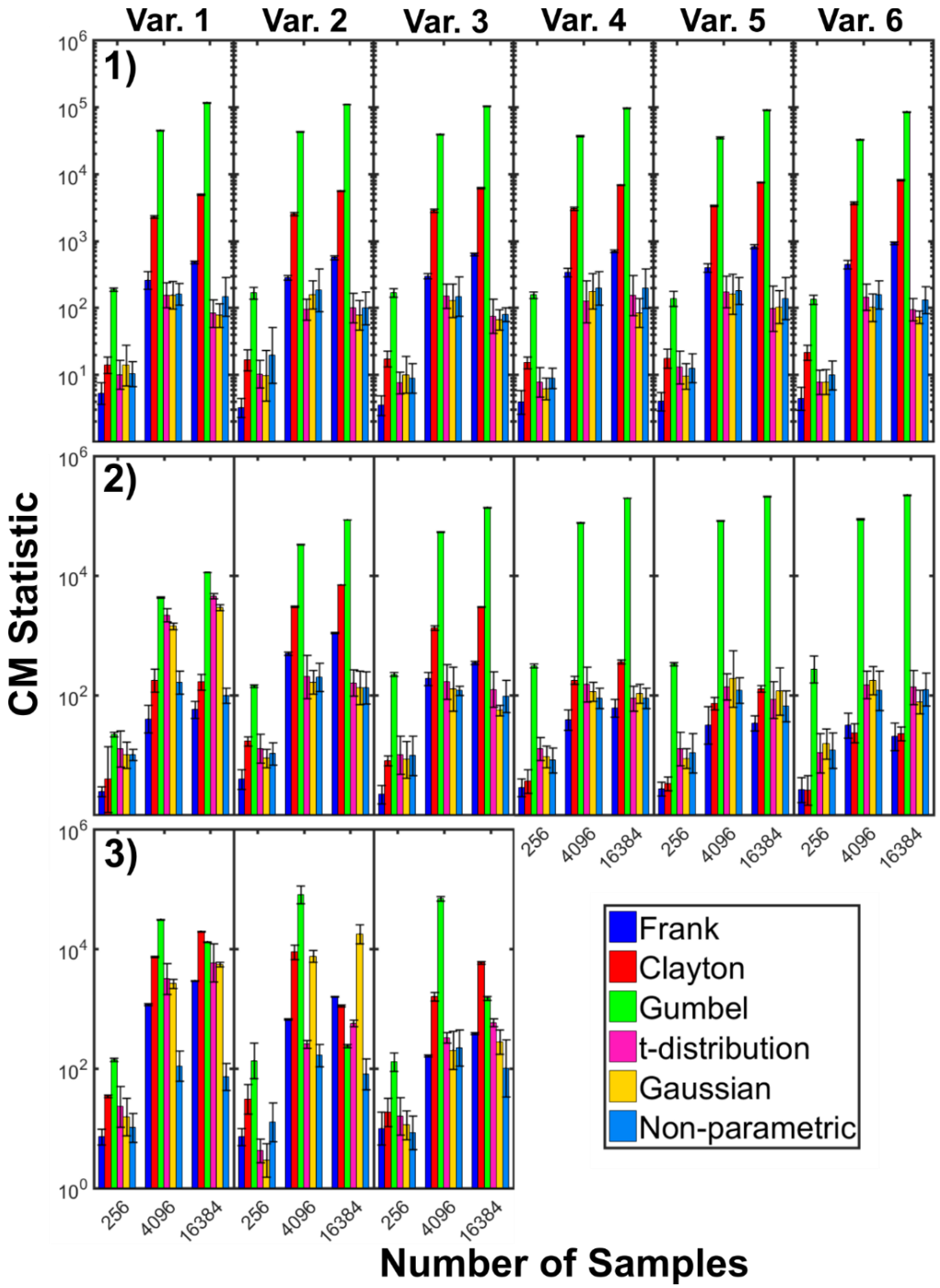

Figure 49. *Comparison of overall GOF of several parametric (and one non-parametric) Copula models. The bar charts indicate the mean of the Cramér-von Mises distance statistic after ten independent realizations were performed, and the error bars represent the standard deviation of these realizations. Results are presented row-wise for Test Functions 1, 2, and 3, where the number of samples used to construct each Copula was varied from n = 256, 4096, to 16384. The columns depict the results for different model input variables (i.e., comparing input 1 vs. model output). The legend coloring further depicts which copula model was used. The y-axis is plotted on a log10 scale to better differentiate between the results.*

3.2 Comparison of Tail Dependencies

The TCF results demonstrated that as the number of QMC samples used to construct each copula was increased, the resulting error generally decreased, indicating that the tail GOF increased (Figure 50). Again, when analyzing the results of the most influential model parameters, the tail GOF of each copula varied across each test function, with the Gaussian, Frank, and the t-distribution performing the best for Test Case 1, 2, and 3, respectively (Figure 50). The non-parametric copula method struggled with providing good TOF metrics for Test Cases 1 and 2; however, tail GOF results greatly improved for Test Case 3 (Figure 50). These results analyzing the tail GOF are somewhat aligned with those obtained for the overall GOF for each copula, except results presented for Test Case 3.

Across all test functions, the t-distribution elliptical copula, which places equal emphasis on both the upper and lower tails, was able to more closely replicate the unique tail dependencies as compared to all remaining parametric copulas. The improved performance of the t-distribution copula can be attributed to the underlying mathematical structure, which allows adaptation to differences in the strength of the dependencies that may exist at the upper and lower ends of the bivariate probability distribution. However, the ability of the t-distribution to improve the tail GOF was limited in some test cases in which asymmetry in the dependencies may have been present between the upper and lower tails. For example, for Test Case 2, the strength of dependency in the lower tail may have been greater than the upper tail, as the Clayton copula (which places more emphasis on the lower tails) performed very well. In addition, for Test Case 3, the strength of dependency may have been somewhat greater in the upper tail as compared to the lower tail given that the Gumbel copula performed well. Overall, the relative asymmetry between

upper and lower tail dependence was relatively weak as both the Frank and t-distributions (which place none to equal emphasis on both tails) outperformed both the Clayton and Gumbel copulas (Figure 50).

The variability of the CM_{TCF} metrics, as defined by the inter-quartile range of the boxplots (and the extent of the whiskers) was observed to decline significantly as the number of QMC samples used to construct each copula increased (Figure 50). This result was in concordance with the reduction in variability observed for the overall GOF presented in the previous section and makes sense intuitively, since more information is provided during the calibration process. The magnitude of the CM_{TCF} metric variability was equivalent to the tail fitting performance of each copula and varied according to each test function. For example, the variability of the Clayton function was relatively high for the first and third test cases, where tail GOF performance was poor; however, as tail GOF increased, as in Test Case 2, the variability was reduced significantly (Figure 50). This trend was similar for the other copula models, including the non-parametric method (Figure 50).

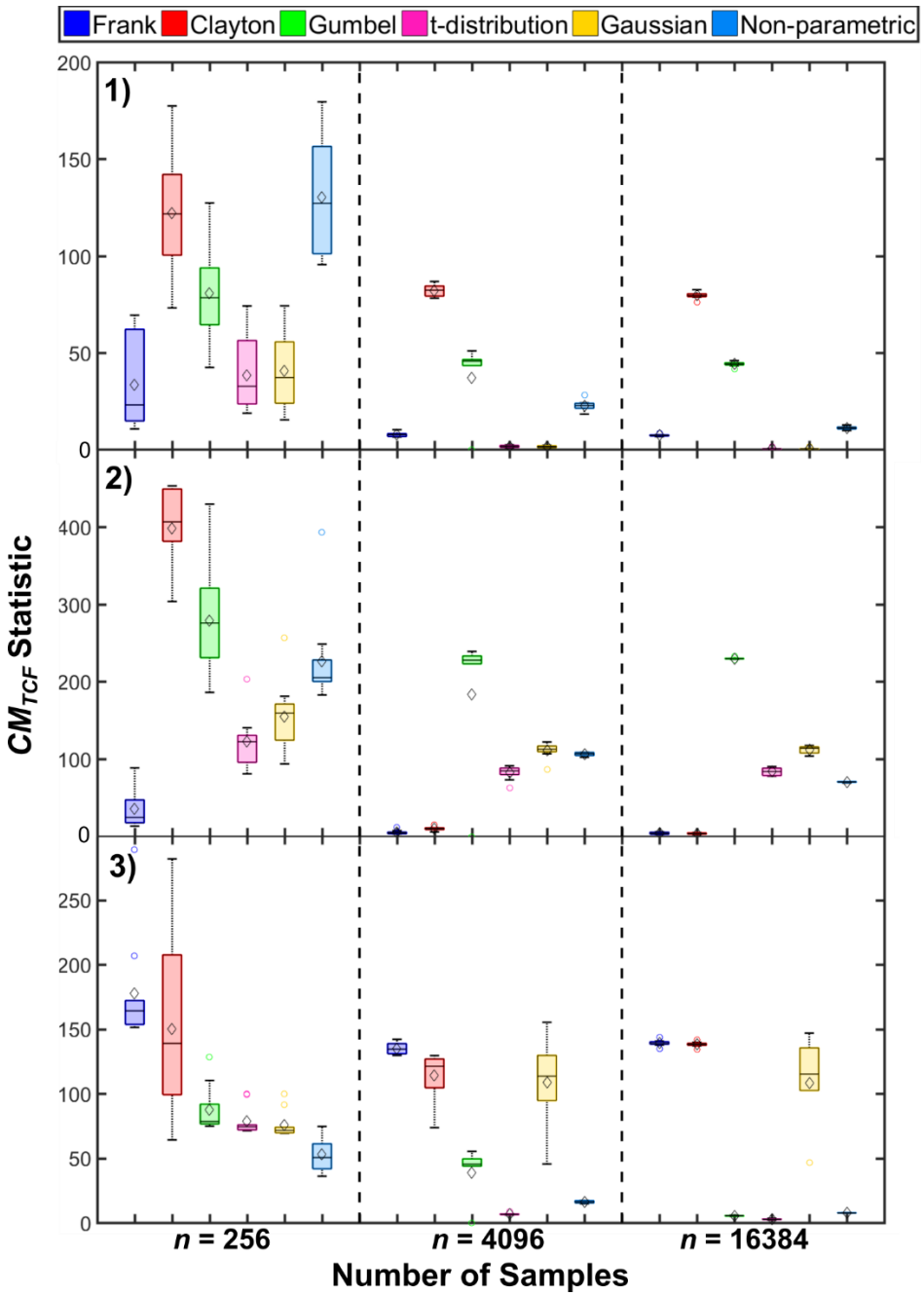

Figure 50. *Boxplot distributions of the tail fits for several parametric (and one non-parametric) copula models. The diamond symbols indicate the mean of the modified Cramér-von Mises distance statistic after ten independent realizations were performed, and the black line represents the median of these realizations. Results are presented row-wise for Test Functions 1, 2, and 3, where the number of samples used to construct each copula was varied from n = 256, 4096, to 16384. Results are also presented for the most influential model input variable (i.e., input variable X1, X1, and X2 for test functions 1,2, and 3, respectively). The legend coloring identifies the different copula models.*

3.3 The Effect of Alternative Sampling Schemes

Figure 51 plots the evolution of the mean absolute error as a function of the number of samples used to construct and sample the copula models and shows that the choice of sampling scheme noticeably affected the accuracy of the estimated MI sensitivity indices. For Test Cases 1 and 2, the application of QMC-CDM sampling methods significantly improved the accuracy of the semi-parametric method developed in this study. This result agrees with previous studies finding optimal results with QMC copula sampling-based methods over those based on pseudo random number generators (Cambou et al. 2017). Comparably, the use of the density resampling approach on Test Cases 1 and 2 resulted in poor approximation of the MI sensitivity indices (Figure 51).

In general, the density-based sampling approach performed much better for Test Case 3 compared to the other CDM sampling methods (Figure 51). Although the approximation error was lower using this resampling method, this approach produced importance rankings that were not entirely in line with those obtained from the analytical solution (data not shown). For example, the importance rankings obtained from the density resampling method indicated that the third variable was second most influential to the model output, whereas the analytical solution indicated that the first variable was the second most influential to the model output. This result may be due to similarities in the copula probability density estimates between both the first and third input variables, which results in relatively equal selection probability during the resampling step.

The QMC-MO algorithm generally demonstrated similar, if not more variable results for Test Case 2 as compared to the QMC-CDM algorithm (Figure 51). The slightly worse performance and higher variability observed for the QMC-MO algorithm over the QMC-

CDM algorithm may be due to the approximation of the inverse Laplace-Stieljes transform using a logarithmic, discrete probability density function. This approximation was observed to be highly variable when the strength of the dependency between the input variable/model output (as determined by Kendall's tau) was greater than 0.95 (and θ values for the Frank copula were large ~50 or higher). The use of the MO algorithm was especially problematic for the third test function (where no results were obtained), in which the resulting dependency between model inputs and output after monotonization was higher than the empirically determined threshold of 0.95 above. Ultimately, these results confirm the use of the CDM algorithm with QMC samples in order to ensure stable and accurate estimation of MI sensitivity indices.

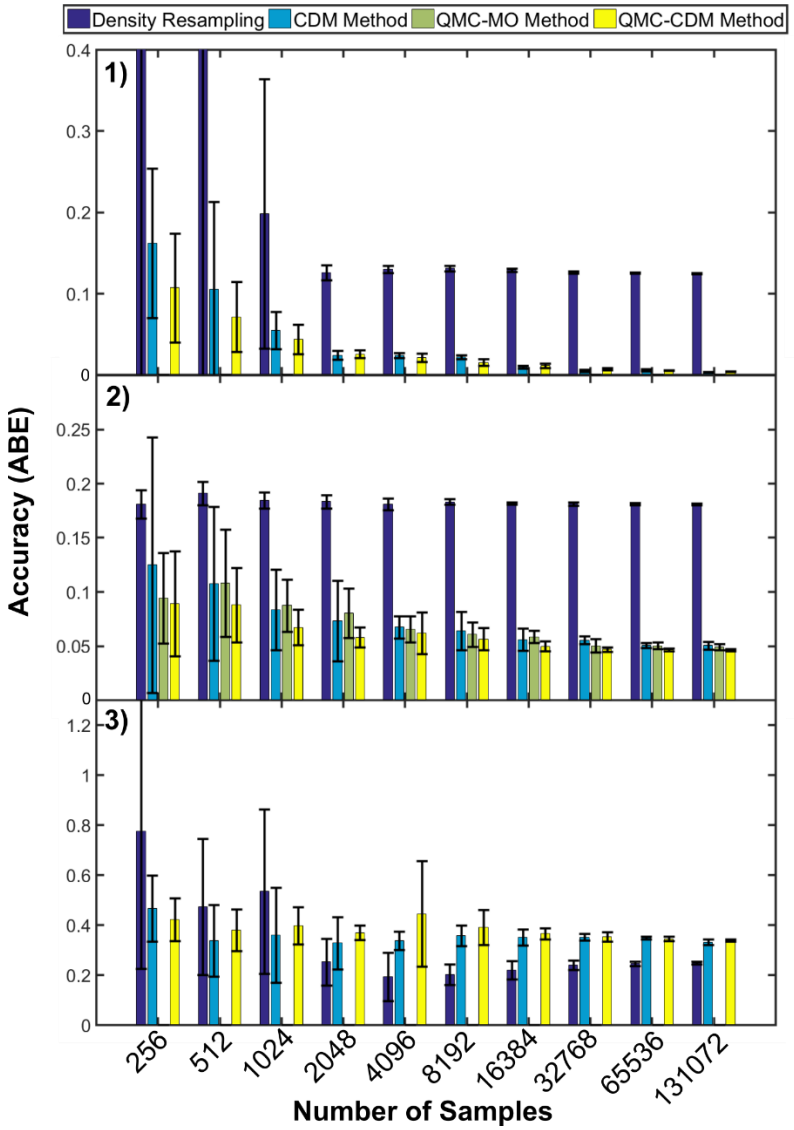

Figure 51. *Comparison of the accuracy (mean absolute error between analytical MI sensitivity indices and experimentally determined indices) of each sampling scheme as a function of the number of QMC samples used to construct/sample each copula model. Results are presented for Test Cases 1)-3), where the best performing parametric copula model (i.e., Gaussian copula for Test Case 1 and Frank copula for Test Case 2 and 3) was used. The error bars denote the standard deviation of the absolute error over ten independent realizations of each sampling scheme. The different sampling schemes investigated are differentiated by color, as indicated in the legend above. The standard sampling scheme used as a basis for comparison against all alternative sampling schemes was the CDM method.*

3.4 Evaluation of Copula Symmetry

Comparison of the modified Cramér-von Mises test statistics (S_n), which provide a quantitative indication as to the degree of diagonal symmetry between model input/output

dependencies, indicated that as the number of QMC samples increased, the asymmetry of the dependencies increased for all input variables and for both of the analyzed asymmetric test functions (Figure 52). The magnitude of the diagonal asymmetry (as revealed by the higher S_n values) was greatest for input variables in test function 2 as compared to test function 3 (Figure 52). Results for Test Case 2 demonstrated that the second input variable had the most asymmetric dependence structure, followed by the fifth or fourth input variable, whereas input variables 1 and 3 were marked by the most asymmetric dependence structures for test function 3 (Figure 52). The variability of the S_n test statistics, as summarized by the standard deviation and coefficient of variation (COV), generally decreased as the QMC sample size increased (Tables E4 and E5), indicating that the degree of asymmetry became more uniform as more samples were included in the analysis.

Using the modified Monte Carlo method presented in Genest et al. (2012), p-values were calculated to assess the statistical significance of the diagonal symmetry between the dependence structure(s) of the model input variables and output. A p-value less than 0.05 rejected the null hypothesis that the dependence structure was symmetrical. P-value calculations for Test Case 2 indicated that the dependence structure along the diagonal was indeed asymmetrical for all input variables excluding variable 1 as the number of QMC samples increased to 4096. Statistical significance was not reached, however, for the dependencies existing in test function 3, signifying that the dependencies remained symmetric, despite an increase in sample size and magnitude of the S_n statistic (Figure 52).

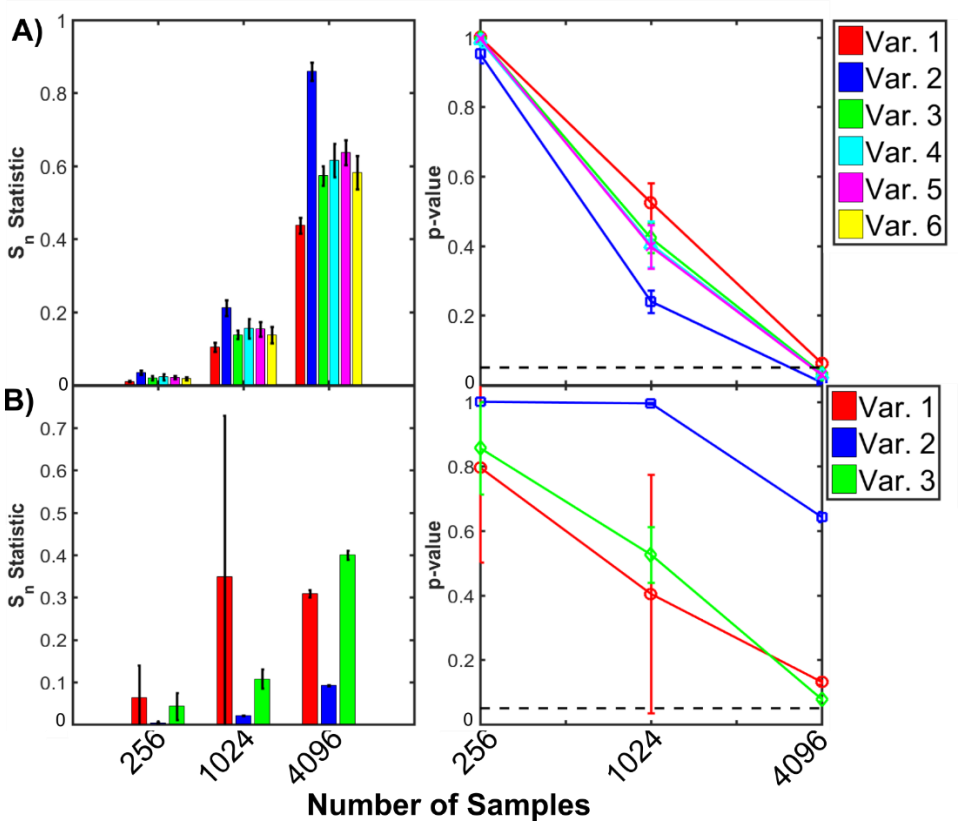

Figure 52. *Calculated Sn statistics and p-values as a function of QMC samples (256-4096) for evaluation of Copula asymmetry. Results are presented for test problems 2 (A) and 3 (B), where the input variables for each test function are denoted by a certain color indicated in the legend. The error bars indicate the standard deviation of the Sn and p-values over ten independent realizations of the asymmetry testing. The dashed black line on the plots in the second column indicate the statistical significance threshold of 0.05.*

The performance of the asymmetrical version of the Frank copula when estimating the MI sensitivity indices for Test Cases 2 and 3 was generally poor compared to the symmetrical Frank copula, in terms of both accuracy and precision (Figure 53). For all QMC construction and sampling numbers, the asymmetrical Frank copula maintained both a high average absolute error and standard deviation across replicate experiments, especially for Test Case 2 (Figure 53A). Overall, the MI sensitivity index estimation performance was generally better for the asymmetric Frank copula for Test Case 3 as compared to Test Case 2 (Figure 53).

Although Figure 52, Table E4, and Table E5 originally indicated that asymmetry was present for some model input and output dependencies for both test functions (along with statistical significance to validate this asymmetry), the asymmetric copula model fits may not have been adequate for some realizations using the optimization scheme and parameter bounds presented. For example, the optimization scheme was more complex for Test Case 2 as compared to Test Case 3, where 18 parameters required optimization (2 for each input variable/output dependency). Even though convergence was generally reached within the allotted number of function evaluations using the global, evolutionary approach (LSHADE-EpSin), some θ parameters, which describe the strength of the dependency between model input/output for the Frank Archimedean copula, were approaching the lower or upper bounds (-100, 100). For reference, the corresponding magnitude of values for θ were on the order of -0.961 to 0.961 in terms of Kendall's tau. Thus, since the parameter values were restricted during optimization, the accuracy and precision of the asymmetric Frank copula method generally suffered. These challenges observed during optimization were magnified for Test Case 2, in which the asymmetric dependency structure modelled between input variable 5 and the model output was suboptimal (data not shown).

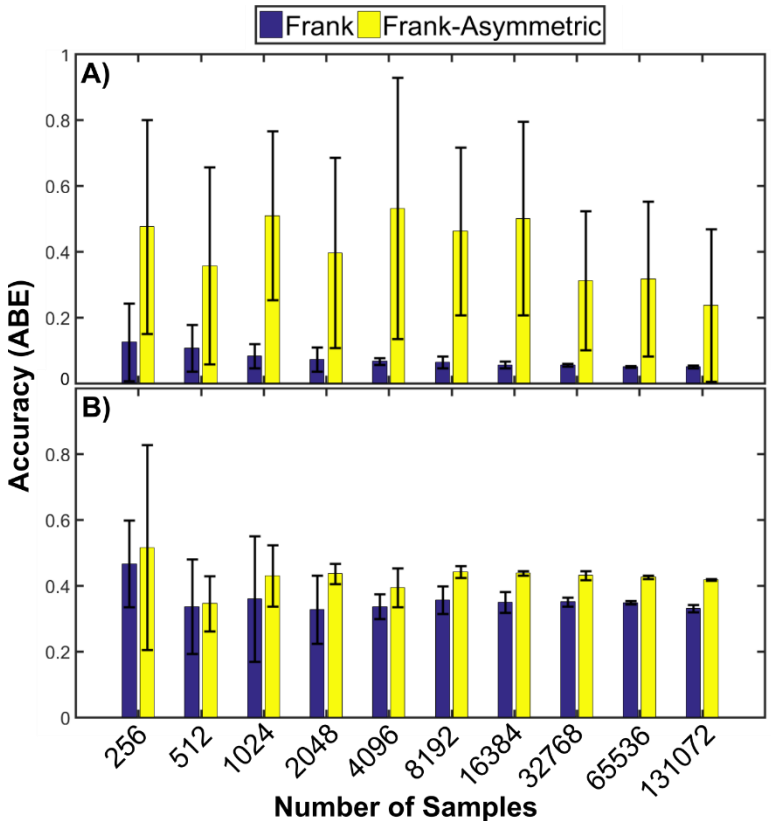

Figure 53. *Comparison of the accuracy (mean absolute error between analytical MI sensitivity indices and experimentally determined indices) between the Frank (blue) and asymmetrical Frank copula models as a function of the number of QMC samples used to construct/sample each copula model. Results are presented for test functions 2) (A) and 3) (B). The error bars denote the standard deviation of the absolute error over ten independent realizations of each copula model method.*

3.5 Comparison of Semi-Parametric MI Algorithm Performance

The semi-parametric method developed in this study outperformed existing MI algorithms across the linear, nonlinear, and non-linear/nonmonotonic set of test functions investigated (Figure 54, Panel 1 and 2). For Test Case 1, the average absolute error across ten independent realizations was lowest for the semi-parametric method after approximately 2048 QMC samples, where the average error remained the lowest of all algorithms tested until the highest number of QMC samples was reached (n = 131072). Comparably, for Test Case 2, the average absolute error was lowest for the semi-parametric method across all QMC sample sizes surveyed (Figure 54). The results for Test Case 3 were

more variable than previous test functions, in which the semi-parametric method was the second-best performing algorithm behind the NPIS single loop approach. Across all test functions, the single loop and non-parametric copula methods were more precise, but significantly less accurate, whereas the semi-parametric method and the NPIS method were more accurate, but less precise, especially at small QMC sample numbers (Figure 54).

The convergence efficiency was assessed for each MI sensitivity algorithm across all analytical test functions through calculation of the 95% confidence interval widths of the absolute errors estimated between the experimental and analytical solutions. Formal convergence was reached when the width of the 95% confidence intervals describing the variation of the absolute error dropped below 0.05 (Sarrazin et al. 2016). As observed in Figure 54, the convergence efficiencies of each algorithm were relatively similar for Test Case 1 but diverged for Test Cases 2 and 3. For Test Case 1, after approximately 2048 to 4096 QMC samples, all algorithms appeared to formally converge. However, for Test Case 2, approximately 8192 to 16384 samples were required for each algorithm to formally converge except for the NPIS method, which did not formally converge, even after the application of 131072 QMC samples. Finally, the results for Test Case 3 indicated that approximately 32768 to 65536 QMC samples were required for each algorithm to formally converge, with the semi-parametric method demonstrating the highest variability (Figure 54).

Analysis of the convergence behavior of each input variable was quite different between the semi-parametric, NPIS, and non-parametric copula/single loop MC estimators for the more complex test functions (2 and 3). Figures E4 and E5 qualitatively portray the convergence behavior and factor rankings according to each input variable for Test Cases 2

and 3. Focusing on the semi-parametric method (Figure E4), from the smallest number of QMC samples (n = 256) and onward, the medians of the boxplots depicting the distribution in MI sensitivity indices across ten realizations were close to the analytical solutions for each input variable. However, the medians of the distributions of estimated sensitivity indices for the remaining algorithms were very far away from the analytical solutions, even after the largest number of QMC samples were applied (Figure E4).

Similar convergence behavior was observed for the non-linear, non-monotonic test function 3 (Figure E5), in which the non-parametric copula and single loop methods could not adequately resolve the analytical solutions. For these two methods, the ranking of the most sensitive input variables was also relatively skewed (with the ranking of variable 3 often greater than variable 1), which was most likely an artefact of the non-monotonic, yet highly non-linear dependency observed between the first/third model input variables and the corresponding model output. Although the semi-parametric method demonstrated some trouble with approximating the analytical solutions of the final test function, the factor ranking order was always preserved. This result was attributed to the integration of the Rolling Pin method into the approach developed in this study, which always ensured that the dependency structure between each input variable and model output was strictly positive and monotonic. It is important to note that the non-parametric method also demonstrated a significantly improved convergence performance for Test Case 3 as compared to Test Case 2 (Figure E4 vs. Figure E5).

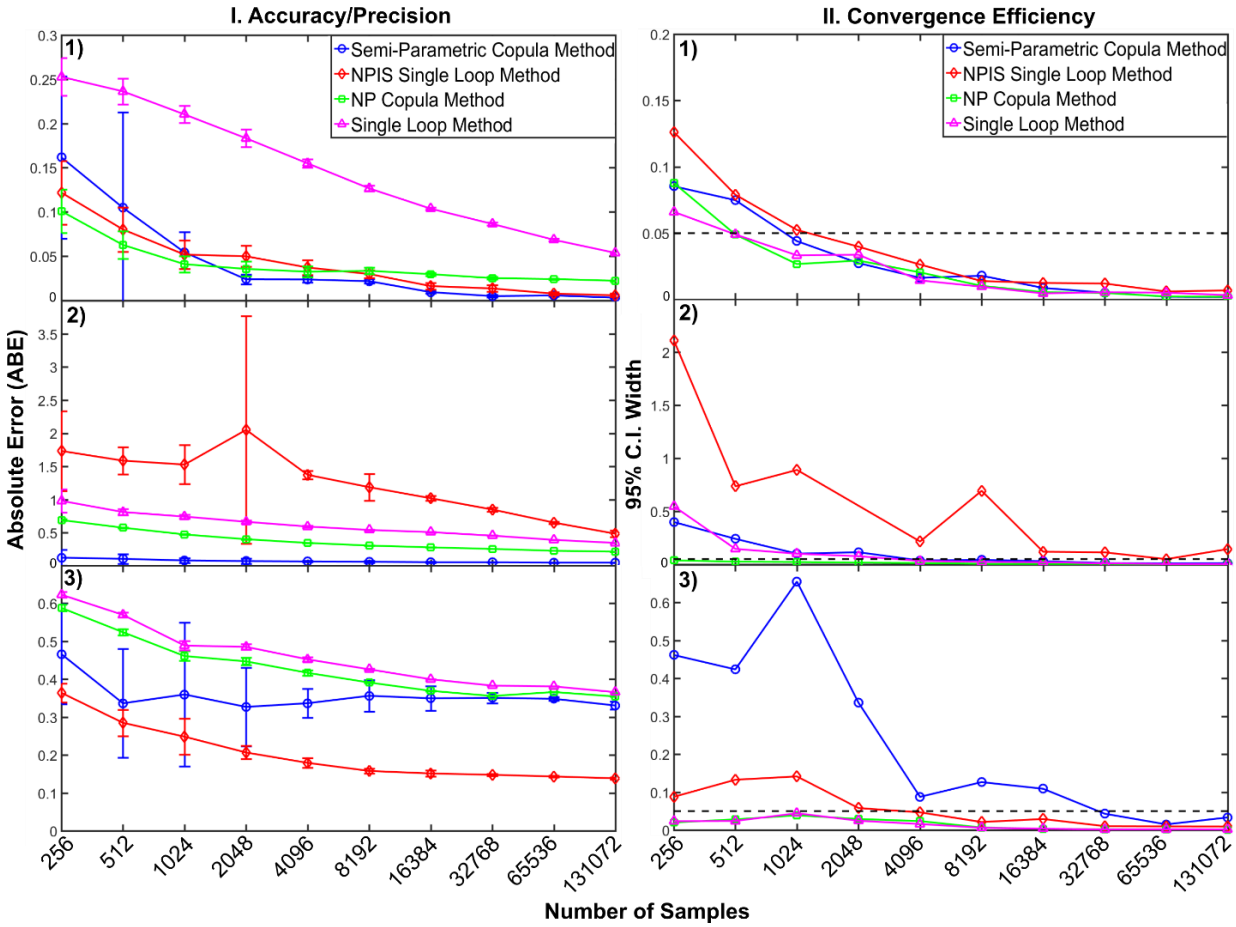

Figure 54. *Comparison of the I. accuracy/precision (mean absolute error between analytical MI sensitivity indices and experimentally determined indices) and II. convergence efficiencies (width of the 95% confidence intervals of the absolute error) between the different MI Borgonovo sensitivity methods as a function of the number of QMC samples. Results are presented for test functions 1-3. The error bars denote the standard deviation of the absolute error over ten independent realizations of each method. The dashed black line on the plots in the second column indicate the convergence threshold of 0.05.*

3.6 Application of the Semi-Parametric Method to an Environmental Model

The semi-parametric method developed in this study was applied to a well-known unstructured kinetic model describing microcystin biodegradation by isolated bacterial populations. As observed in Tables E6 and E7, the strength of correlation between many input parameters (aside from μ_{max} for substrate concentrations and Y for cell concentrations) was generally weak (|Kendall's tau| $<$ 0.30) and many dependencies existing between model input parameters and output variables were non-monotonic (or

decreasing) in nature. These aspects describing the dependency between model input-output relationships, as indicated from the analytical test function results in the previous section, challenged current fully non-parametric techniques for estimating accurate and reliable MI sensitivity indices. The semi-parametric method developed in this study, however, was equipped with the capability to monotonize the dependencies existing between certain input-output relationships and, in most cases, could reliably discern acute differences in MI sensitivity indices among different input variables and simulated timepoints for this environmental model.

Results presented in Tables E8 and E9 highlight that the optimal monotonization parameters obtained for this study were relatively small (<0.15, on a scale from 0 to 1, where 0 indicates no monotonization should be performed), indicating that variable monotonization was generally not required to model the dependency between input parameters and output variables for this environmental model. In addition, the estimated MI sensitivity indices were observed to converge around n = 16384 QMC samples for both model output variables, where the width of the 95% confidence intervals over ten realizations dropped below the previously specified threshold of 0.05 (Figures E6 and E7) (Sarrazin et al. 2016).

Figure 55 depicts the MI sensitivity indices, as a function of simulation time, calculated for both model outputs by applying the semi-parametric method developed in this study. Over all simulated time points, the semi-parametric method determined the following factor ranking, from the most to least influential model parameters affecting *substrate* concentration predictions: 1) μ_{max}, 2) n, 3) Y, 4) K_s, 5) k_d (Figure 55A). Comparably, the factor rankings obtained for *cell* concentration predictions were as

follows, again from the most to least influential model parameters: 1) Y, 2) μ_{max}, 3) k_d, 4) n, 5) K_s. In general, the dynamic trends in calculated MI sensitivity indices were contradictory when comparing both substrate and cell concentration predictions (Figure 55). For example, as simulated time progressed, μ_{max} was observed to increase in influence when predicting substrate concentrations and became significantly less influential when describing cell concentrations (Figure 55). Similar trends were observed for K_s and n model parameters (Figure 55). Moreover, some model parameters, such as Y (Figure 55B) and n (Figure 55A) increased in influence at moderate time points (around 5-6 days) across the simulated time period.

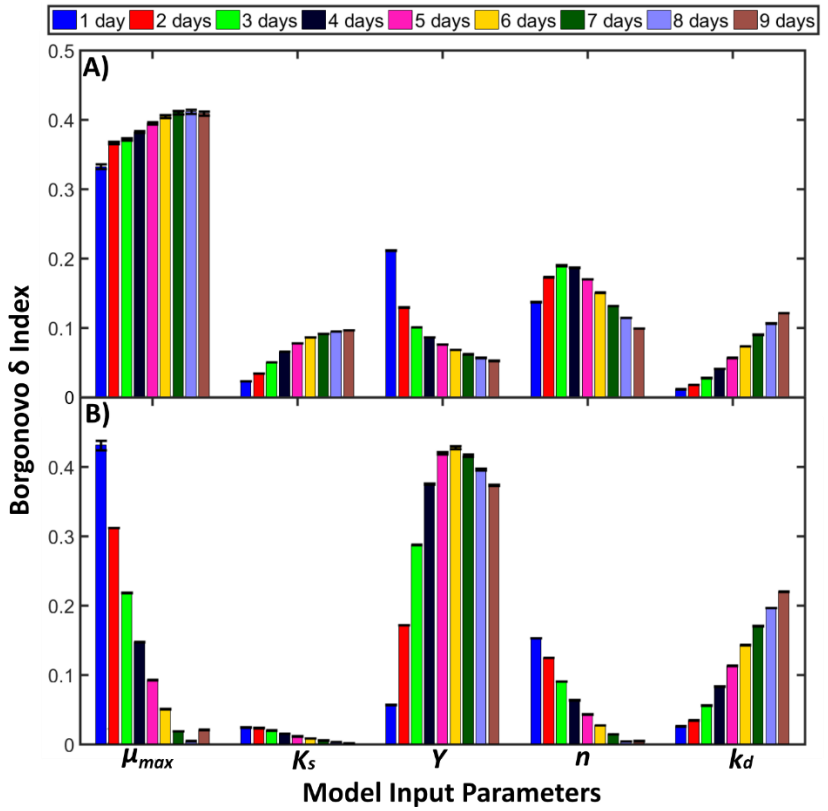

Figure 55. *MI Borgonovo (δ) sensitivity indices calculated using the semi-parametric method developed in this study (n = 16384) as a function of the simulation time (1-9 days) and the model input parameters. The colors in the legend correspond to different simulation times, and panels A and B correspond to either the predicted substrate or cell concentrations, respectively. Standard deviations of the calculated δ indices (over 10 realizations) are presented as error bars in the Figure.*

To further demonstrate the efficacy of the semi-parametric method, the copula density predictions afforded from the Frank model were qualitatively compared to the empirical copula densities of the QMC samples (Figure 56). The empirical results were generally in agreement with the parametric model predictions, as the density of the empirical estimates clustered in similar locations where the model predictions indicated higher densities should exist (Figure 56). Stronger dependencies between model input parameters and output variables, such as those observed between μ_{max} and cell or substrate concentration predictions, corresponded with more influential model parameters identified in Figure 55, as expected intuitively. Similar to the results portrayed in Figure 55, the direction of the dependence (positive or negative) was, at times, completely reversed when comparing the two model outputs (i.e., as observed for μ_{max} and Y) (Figure 56).

The GOF results for this model application were also qualitatively and quantitatively checked using comparisons of the empirical and parametric lambda functions (similar to the Kendall distribution functions examined above). Qualitatively, it appeared that the bivariate dependency between the most sensitive parameter (μ_{max}) and substrate concentration predictions agreed, whereas the input/output relationship between the most sensitive parameter (Y) and predicted cell concentrations were somewhat different (Figure E8). These results were confirmed quantitively, in which average values of the Cramér-von Mises distance statistic (across ten realizations) were an order of magnitude larger for the Y input and cell concentration dependence as compared to the μ_{max} input and substrate concentration dependence structures (i.e., 684 vs. 3,857). Upon more careful inspection of Figure 56, there was also a divergence between the empirical and modelled densities for the Y input and cell concentration dependence structure, as the empirical densities

appeared more homogenous and evenly dispersed across the copula variable space. Therefore, for this model application, some non-linearities existed between the model inputs and outputs in which the Frank copula could not fully resolve.

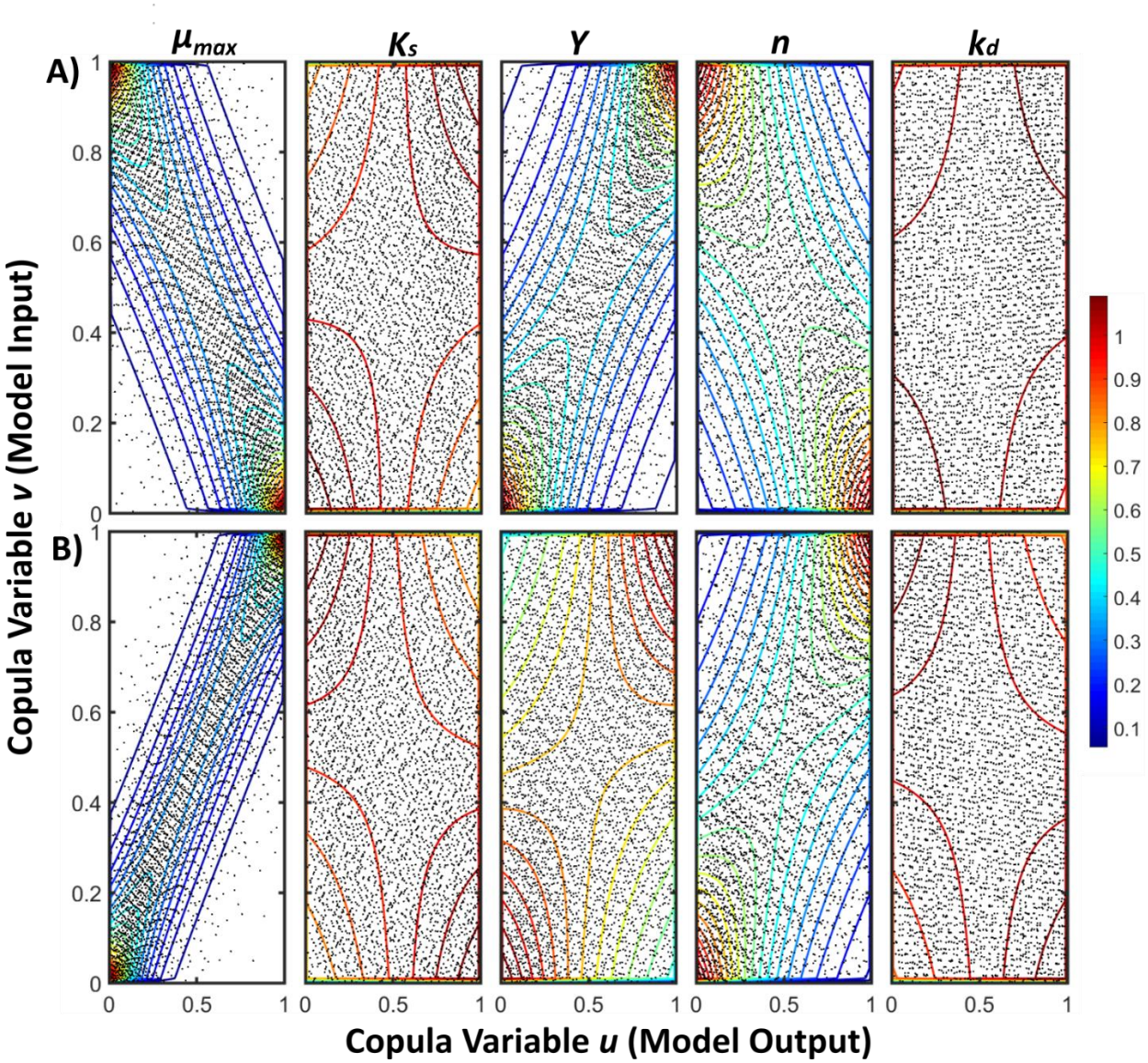

Figure 56. *Empirical copula densities (plotted as black dots) overlaid with the predicted Frank copula densities (contour lines) using the results from the Moser model (t = 1 day, n = 4096 QMC sampling points, transformed variables only). The copula density results are categorized according to the input parameter (columns) and the model output variable, substrate (A), or cells (B). The color bar corresponds to the magnitude of the predicted copula density values, where darker colors (i.e., red) are indicative of higher predicted copula densities. Copula variable u corresponds to the model output variable, whereas copula variable v corresponds to the model input parameter.*

4. Discussion

4.1 Study Contribution, Advantages, and Limitations of the Semi-Parametric Method

This is the first study, to the best of our knowledge, to successfully integrate parametric copula models into a MI global sensitivity analysis framework. Compared to previous non-parametric MI methods, including those based on copulas (Wei et al. 2014), this method greatly improved the overall accuracy of the MI sensitivity indices when applied to a range in suitable analytical test functions (i.e., linear, non-linear, non-linear and non-monotonic). The improvements in accuracy gained through the application of parametric copula models to estimate MI sensitivity indices can be attributed to the enhanced definition of the dependency structures formed between model inputs and output(s) over existing non-parametric methods. Simply put, the dependency structure (or correlation) can be directly modelled as a function of the input marginal cumulative probability densities of both variables, which is a significant advantage over non-parametric methods. In addition, the model structure of many parametric copulas provides greater flexibility over non-parametric methods, as the dependency structure can be easily decomposed into different sub-regions, for example, the lower tail, diagonal, and upper tails, in which the dependencies within these sub-regions of a given multivariate distribution can be modelled explicitly.

As non-parametric copula methods mainly rely on density to model dependency, they cannot resolve the complete underlying structure of the dependence between model inputs and outputs, even with a sufficiently large number of QMC samples. For example, the non-parametric copula method repeatedly encountered trouble reproducing the empirical TCFs of the analytical test functions, which suggests that different sub-regions of the

dependency structure formed between model inputs and output (i.e., around the tail regions) are not accurately modelled using non-parametric methods (Figure E2). Parametric copula models, however, can resolve tail dependencies quite well (as demonstrated in Figure E2), and models such as the Clayton and Gumbel families can account for differences in correlation strength between the upper and lower tails of a given bivariate (or even multivariate) distribution.

Even though significant improvements were made in accuracy over existing non-parametric methods, the convergence efficiency and precision of the semi-parametric approach was similar to, if not worse than (i.e., Test Case 3 results), previous fully non-parametric methods. Issues with the precision and convergence efficiency are directly related to the number of QMC samples used to construct as well as sample each parametric copula prior to calculation of the MI sensitivity indices. To be impartial in our comparison against previous non-parametric methods, we kept the number of QMC samples used to construct the copula equivalent to the number of samples drawn from the copula. To improve the precision and convergence efficiency, it would be advantageous to draw significantly more samples than initially used to construct the copula to provide greater coverage of the joint PDF between model input(s) and output(s). However, to some extent, the number and design of QMC samples (i.e., Sobol sets, Latin Hypercube Sampling) used to construct the initial parametric copula is an important factor that can also be addressed to improve convergence efficiency and precision of the semi-parametric method developed herein.

An important limitation of the semi-parametric method developed in this study is that it can only address the sensitivity of single model parameter or input on the resulting

model predictions. Ultimately, previous non-parametric methods that can compute MI Borgonovo delta sensitivity indices are able to resolve the interactive effects of combined groups of input parameters on the model output (i.e., Wei et al. 2013a). These calculations are important, as the full sensitivity of the model inputs on model output predictions cannot be realized unless all potential groupings of input parameters are considered in the analysis. However, we argue that the semi-parametric method developed in this study can readily accommodate the effect of groups of input parameters on the model output through application of multivariate parametric copula models to describe the joint PDF between a specific group of input parameters and the model output response. Hierarchal or nested Archimedean parametric copula classes have been found to be more computationally attractive to handle multivariate copula distributions (Hofert 2011, Okhrin et al. 2013). Thus, Equation 8 would be modified to include the marginal PDFs of all input parameters in a specific grouping in addition to the joint PDF between the group of input parameters and the model output response. Although most parametric copula models can accommodate higher dimensions, both the application of the Rolling Pin method and the fitting of a multivariate parametric copula model will surely increase the complexity and the computational burden of the semi-parametric method developed herein.

Another limitation to consider is whether the current semi-parametric copula method explicitly accounts for the effect of correlated input parameters on the MI sensitivity analysis. Some previous methods, including the single loop and NPIS single loop methods can explicitly account for the effect of correlated inputs on the estimated MI sensitivity indices (Wei et al. 2013a, Derennes et al. 2018). Since the framework of the semi-parametric method is based off that presented in Wei et al. (2013a) and Derennes et

al. (2018), we can offer a tentative conclusion that even if parameter inputs are correlated, there will be no significant effect on the estimation of singular Borgonovo delta sensitivity indices (i.e., without considering grouping of model input parameters). The main reasoning that supports this conclusion is the fact that the copula model can dissect and isolate the joint PDF as a function of the marginals of the input parameters only and in the calculation presented in Equation 8, input parameter correlation should have a negligible effect on the calculated sensitivity indices. However, this reasoning may not be valid when calculating delta indices for groupings of input variables. Future studies involving this semi-parametric method should provide a focused investigation into the effect of input parameter correlation on the calculation of accurate and reliable MI Borgonovo delta sensitivity indices.

Compared to the previous non-parametric methods, the semi-parametric method developed in this study presents some challenges to computational efficiency (i.e., CPU time). The first challenge affecting computational efficiency is related to the optimization procedure to determine the monotonization parameters. Depending on the problem of interest (i.e., the number of dimensions) and number of QMC samples used, the computational efficiency may become a burden when applied to real world problems. Importantly, in the problems investigated in this study, the number of dimensions was limited to six input parameters or less and the range in QMC samples from n = 256 to 131072. For the optimization procedure, the CPU time and memory requirements were adequate on a standard three core, 64-bit *Intel* processor up to n = 16384-32768 QMC samples, the standard number of QMC samples required to reach convergence. However, we relied on the high-performance computing system available at the University of

California, Irvine (UCI) for handling QMC samples beyond 32768. It is important to note that the code developed for this method was vectorized and took advantage of parallel computation.

The second challenge affecting computational efficiency was running the KDE routines provided by the MATLAB program, especially for a high number of QMC samples. The MATLAB KDE routine was ultimately chosen in this study due to the greater stability it afforded when calculating the MI sensitivity indices compared to alternative KDE methods. The algorithm developed in this study relies on three calls to the KDE routine, an initial call to find the KDE of the monotonized samples used to construct the copula, a second call to find the KDE of the sampled estimates from the copula, and a third call to estimate the KDE of the transformed samples that were originally sampled from the copula. Given the significant reliance on the KDE routine provided by MATLAB, the semi-parametric method was observed to significantly slow at n = 65536 QMC samples and beyond. To circumvent these issues, an alternative calculation can be used (Equation 20, where *c(u, v)* is the copula density) that avoids the cost of computing the marginal KDE density estimates of the model input parameters and solely relies on accurate estimation of the copula density, reducing the number of KDE calls to 2 (Wei et al. 2014). Alternative KDE tools can also be considered to improve computational efficiency, including the method of Botev et al. (2010). However, the application of these alternative KDE estimators may compromise the stability of the semi-parametric method, as these methods, although more computationally efficient than the MATLAB routine, cannot adequately resolve the probability density estimates (for both the PDF and CDF) at or close to the tails of the KDE distributions.

$$\delta_i = \frac{1}{2N} \sum_{k=1}^{N} \left| 1 - \frac{1}{c(u,v)_k} \right| \tag{17}$$

A final limitation of the parametric copula model developed in this study is the inability of the model to practically address non-scalar model outputs. This is an important issue to address, as most environmental models are temporally, or spatially varying and sensitivity methods developed for these applications must consider this aspect. Although the example model application we have included in this study was dynamic in nature, with multiple model outputs corresponding to different simulation times, the computational burden imposed by non-scalar model outputs was found to be impractical. In our application, we were required to run this method sequentially, once for each time point, which required t different optimization calls (t representing the number of simulated time points). Clearly, this number of optimizations is impractical, especially for models with much higher resolution and finer grid spacing. Thus, time varying parametric copula models, which can model either how the copula function or model parameters change with respect to time, can be implemented as a practical solution to address the issue of non-scalar model outputs from many environmental models (Manner and Reznikova 2012).

4.2 General Guidelines for Practical Implementation of the Semi-Parametric Method

Even though we have offered a detailed overview of the numerical implementation of this developed method, since this method relies on the use of parametric methods, the practical application of this method still will require some formal tailoring to a given problem of interest. To achieve gains in accuracy for MI sensitivity indices, we stress in the development of this method that this is not a simple drop in, one-size fit all replacement to MI sensitivity analysis that fully non-parametric methods offer. In this section, we present some insight as to how to most efficiently apply this method to improve MI sensitivity index accuracy for any problem of interest. We give a detailed overview of several

necessary steps required to avoid problems previously observed during the development of this method. Using these steps as a general guideline, this method can be adapted to any problem of interest.

The selection of an appropriate parametric copula to describe the dependency structure between model inputs and outputs is the first necessary pre-requisite to practical implementation of this method. We found that the range in copula models presented in the MATLAB statistics toolbox were an adequate starting point for determining the most appropriate copula model. If access to the MATLAB copula routines is an issue, we refer the reader to a recently developed, comprehensive and convenient copula toolbox that can be applied to model any multivariate dependency structure (Sadegh et al. 2017). This toolbox contains at least 26 different parametric copula models (spanning a wide range in copula families) that can be fit using Bayesian regression. Importantly, this program can determine a posterior distribution in copula parameter estimates and can easily compare and rank the performance of each competing parametric copula model (Sadegh et al. 2017). Overall, we determined that the Frank Archimedean copula family provided a robust approximation of most of the dependence structures encountered in the analytical test functions and should be considered as a basis of comparison for any initial copula model screening. In addition, the choice of copula model did not have to be altered to describe the dependencies between other model inputs or outputs for a given test function. This is important as the complexity of this method was greatly reduced for not having to choose several different parametric copula models for describing different model input and output relationships for a given model. As part of this initial screening (if not using the toolbox

above), we also recommend the use of a quantitative metric, such as the Cramér-von Mises distance to compare the overall GOF of each of the copula models reviewed.

Following review of the appropriate parametric copula model/family, an additional check of the copula fit to the tail regions is recommended. This step can be achieved by computing and comparing the empirical and parametric TCFs as defined in Appendix E, section 7. This step will both reinforce whether the selection of the copula model above is appropriate and determine whether another copula model family should be investigated that explicitly models the tail regions of the multivariate copula distribution (i.e., the Gumbel or Clayton Copula families). Again, we recommend the use of a quantitative metric to assess the tail fits among the copulas compared.

Other than overall and tail GOF, the sampling strategy and symmetry of a given dependency structure should be evaluated as third and fourth final steps to tailor the semi-parametric method to a certain problem of interest. In this study, we observed that QMC sampling designs (over pseudo-random numbers) improved the accuracy and convergence efficiencies of the estimated MI sensitivity indices. Moreover, the CDM method was observed to be the most suitable sampling scheme for both the Elliptical and Archimedean classes of parametric copulas. Symmetry along the diagonal of the copula is also an important criterium to review to improve the accuracy and convergence efficiency of this method. Transforming a certain parametric copula model to account for asymmetric dependence along the diagonal may be more complex but could offer great advancements in the accuracy of MI sensitivity indices. Although some asymmetry was observed in the test functions reviewed in this study, it was not significant enough to warrant the use of more complex copula models that explicitly account for asymmetry along the diagonal.

Helpful quantitative metrics, like the S_n metric, and statistical hypothesis testing, like the method adopted in this study, are available to assist in the evaluation of symmetry for a given dependence structure (Genest et al. 2012).

As a final suggestion, we urge that the preliminary step of determining the appropriate copula model through comparison of the overall GOF should be conducted as the primary means to improve accuracy for any given test problem. We highlight that this step within this method allows great flexibility to model many different types of multivariate dependence structures necessary for the computation of MI sensitivity indices. The following steps (2-4), although potentially helpful for understanding the complexity behind modelling the dependence structure, are auxiliary tools that can be applied as other options to improve the accuracy and reliability of this method. Additional technical improvements to this algorithm and workflow will be discussed in the subsequent section to further the applicability of this method to many different problems of interest.

4.3 Possible Improvements to the Semi-Parametric Copula Method

Results from both the analytical test function 3 (Ishigami function) and the environmental model application indicated that there was still ample room for technical improvement of the semi-parametric copula model presented in this study. Most of these issues regarding the accuracy of this method were attributed to the inability of the parametric copula model to account for the high non-linearities present within the dependence structures formed from the model inputs and outputs. Here, we give an overview of several technical improvements that can be considered to improve the accuracy and precision of this method, focusing on improvements to the sampling scheme,

modelling non-linearities, and improving the estimation of the marginal probability distributions.

Importance sampling (a class of variance reduction techniques) of parametric copulas has recently emerged as a powerful tool to improve convergence efficiency of Monte Carlo based estimators like those relied upon in MI sensitivity analysis (Arbenz et al. 2014, Arbenz et al. 2018). The main theory behind importance-based sampling regarding parametric copulas presented by these authors is to oversample sub regions of the copula distribution that contribute more to improving the overall precision of the approximation. This technique has been previously applied to Elliptical copulas, and a new importance sampling framework was recently introduced for the Archimedean copula class (Arbenz et al. 2018). Future study of this semi-parametric copula approach will consider technical improvements through integration of innovative sampling schemes that serve to improve the convergence efficiency and precision.

Although asymmetrical transformations were shown to have a negligible impact on the accuracy of this developed method, polynomial transformations using the lambda function, $\lambda(t)$, (a function of the Kendall distribution function presented herein) are yet another integral tool to improve the accuracy of copula models to describe the dependence between model inputs and outputs in MI sensitivity analysis (Michiels et al. 2011, Michiels and De Schepper 2012). Polynomial transformations of the Archimedean class of parametric copulas have been shown to greatly improve the overall GOF for some copula families, and to handle distinct non-linearities between variables, including the Frank family (Michiels et al. 2011, Michiels and De Schepper 2012). Michiels and De Schepper (2012) introduced a concordance invariant and tail preserving family of polynomial

transformations, where this terminology signifies that even with the integration of a polynomial function into the copula model structure, the strength and nature of the dependence (including the tail dependence) will be similar to the original structure afforded by the non-transformed model. In this same study, polynomials as high as order 6 (with three shape parameters) were introduced that offered statistically significant improvements to the accuracy of the copula model fits. A similar framework, that provides for a concordance invariant and tail-preserving polynomial transform of Archimedean copula models, should be investigated in future studies to improve the accuracy of the semi-parametric method developed herein.

A final potential area to improve the accuracy of this semi-parametric method would be to advance the non-parametric estimation of the marginal probability distributions for the model output variables. The method used in this study, which is based on a rule of thumb for determining optimal bin widths for KDE, is relatively naïve and in some cases, cannot handle modelling extremely skewed or multi modal empirical probability distributions. Maximum entropy methods focus on approximating a PDF or CDF of a distribution using the statistical integer (i.e., the mean, standard deviation, skewness, or kurtosis) or fractional moments of a given distribution (Zhang et al. 2014, 2015c). In this way, maximum entropy methods rely on approximating a PDF through maximization of Shannon's entropy principle, in which the optimization can be constrained through use of the statistical moments. Rajan et al. (2018) presented an improved moment constrained, maximal entropy approach that can account for the use of multiple moments (greater than 4) when constructing the approximation of the PDF, which allows the method to fit distributions that may be highly skewed or multi-modal. Although computationally more

intensive, this moment constrained maximum entropy method could greatly improve the approximation of the PDFs and CDFs required for accurate estimation of the Borgonovo delta sensitivity indices using the semi-parametric method developed in this study.

5. Conclusions

A novel semi-parametric method based on copulas was developed in this study to estimate MI Borgonovo delta sensitivity indices. Comparison of this developed method against previously existing non-parametric methods over a range of analytical test functions (ranging from linear, to non-linear, to highly non-linear and nonmonotonic) indicated improved accuracy for most of the test functions reviewed. However, the overall convergence efficiency and precision of this method was comparable to existing non-parametric methods across all test functions reviewed. Application of this method to an environmental model further highlighted the ability of this method to reliably distinguish the sensitivities among certain input parameters in which the strength of the input and output dependency was weak and, in some cases, non-monotonic or highly non-linear. The integration of a monotonization technique (i.e., the Rolling Pin method) as a major framework in this method not only allowed non-monotonic dependence to be modelled, but also any parametric copula model could be easily assimilated and compared, leading to great flexibility and improvements in overall accuracy of the MI sensitivity indices calculated.

Potential challenges with the generalization of the semi-parametric method to other specific problems of interest were thoroughly discussed, including the observation that much of the inaccuracy stemmed from the inability of one parameter copula models (i.e.,

the Frank copula) to model the high-nonlinearities present for some dependence structures reviewed. Other potential challenges investigated in this study included the ability of each parametric copula to model tail dependence, the effect of certain sampling schemes (i.e., the CDM method vs. the MO algorithm), and explicitly accounting for the presence of asymmetry in some of the bivariate dependencies modelled. Based on the results, addressing most of these challenges identified above were concluded to be more auxiliary as compared to the importance of selecting an appropriate parametric copula model to properly predict the dependency structure between model inputs and outputs. To improve the accuracy and precision of this semi-parametric method, importance sampling schemes, concordance invariant and tail preserving polynomial transformations focused on the lambda function, as well as the integration of maximum entropy methods for reliable estimation of marginal densities can be considered for future study. Overall, this study provides the first attempt to integrate complex parametric models to predict the multivariate joint PDFs required in MI Borgonovo sensitivity analysis calculations.

6. List of Abbreviations

Abbreviation	Meaning
MI	Moment Independent
GSA	Global Sensitivity Analysis
ABE	Absolute Error
PDF	Probability Distribution Function
CDF	Cumulative Distribution Function
CDM	Conditional Distribution Method
MO	Marshall-Olkin

QMC	Quasi Monte Carlo
KDE	Kernel Density Estimation
KDF	Kendall Distribution Function
TCF	Tail Concentration Function
GOF	Goodness of Fit
NPIS	Non-Parametric Importance Sampling
MC	Monte Carlo
ML	Maximum Likelihood
CMLE	Canonical Maximum Likelihood Estimation
CM	Cramér-von Mises Overall Goodness of Fit Statistic
$\boldsymbol{CM_{TCF}}$	Cramér-von Mises Tail Goodness of Fit Statistic

Chapter 7: Optimal Design of Experiments for Identification of Unstructured Kinetic Model Parameters Describing Microcystin Biodegradation

Abstract: Unstructured kinetic models have been recently found to provide practical and reliable predictions of microcystin (MC) removal and bacterial growth in drinking water biological treatment applications. However, the main challenge to improve the overall statistical certainty of kinetic model predictions lies in how to improve model parameter identification, which depends on both the model structure and quality of the experimental data collected. In this study, a structural and practical identifiability analysis was conducted to determine whether parameters of the Moser kinetic model could be uniquely estimated and to what extent optimally designed experiments could lead to datasets with maximal information content and parameter decorrelation for improved parameter estimation. The results demonstrated that parameters of the Moser model were locally, structurally identifiable, signifying that a global, unique parameter set describing MC biodegradation was not mathematically achievable. The practical identifiability analysis, through reliance on global, optimal experimental design, indicated that the statistical confidence of the parameter estimates can be significantly improved if a fed batch reactor experimental configuration with an optimal dynamic feed rate profile is applied to study MC biodegradation as compared to uninformed batch experiments. Overall, it was found that model-based design of experiments are a valuable tool to arrive at experimental datasets with maximal information content and minimal parameter correlation for optimal parameter identification of unstructured kinetic models.

1. Introduction and Background

The rapid advance of global climate change, fueled by ongoing anthropogenic activities and the combustion of fossil fuels, has posed both great challenges and unique opportunities to augment the supply and quality of drinking water resources. Across drought prone and temperate regions worldwide, many municipalities and governments are stressing to address the dwindling supply and deteriorating quality of freshwater resources to sustain the growing population (Postel 1996, Postel 2014). Of the many issues challenging the quality of drinking water resources on a local to global scale, harmful cyanobacterial blooms (HCBs) have emerged as a formidable issue confronting humanity at large (Paerl and Huisman 2009, Pearl and Paul 2012, O'Neill et al. 2012).

Over the past decade, warming global temperatures, intense storm events, and prolonged drought periods, along with non-point source nutrient pollution originating from intensive commercial agricultural practices, have led to an increase in the frequency, severity, and persistence, as well as the geographical spatiotemporal dominance of freshwater HCB events (Paerl and Huisman 2009, Pearl and Paul 2012, O'Neill et al. 2012). During and following HCB events, various species of toxic cyanobacteria (i.e., *Microcystis, Anabaena, Planktothrix, Cylindrospermopsis*) produce and excrete a suite of biotoxins into receiving water bodies (Huisman et al. 2006, Cheung et al. 2013, Pearl and Otten 2013). The impact of these toxic bloom events is far-reaching; ranging from transformations to aquatic, even surrounding terrestrial, biodiversity and primary production on the micro to macro scales, to diminishing recreational opportunities and contamination of drinking water resources (Cheung et al. 2013, Otten and Paerl 2015).

Of the extremely wide variety of biotoxins excreted by these microalgae, microcystin (MC), produced primarily by toxic species of *Microcystis*, *Anabaena*, *Planktothrix*, and *Nostoc*, has been detected most frequently and abundantly in the environment (Harke et al. 2016, Pelaez et al. 2010). MC is termed a cyclical heptapeptide, in which seven amino acids, two of which are variable across different congeners, form a ring-like molecular structure (Huisman et al. 2006, Edwards and Lawton 2009). Ultimately, this uniquely crafted molecular structure of MC renders it highly resistant to both physical and chemical deterioration in the environment (Westrick et al. 2010). To date, over 100 structural congeners of MC have been identified and detected in the environment, where MC-LR (*L* and *R* standing for Leucine and Arginine as the two conserved amino acids, respectively) has been confirmed as the most common and toxic (Huisman et al. 2006, Puddicke et al. 2014). Given that most MCs, such as MC-LR, are both hepatotoxic and known human carcinogens, the World Health Organization (WHO) and US EPA have developed guidelines for total MCs in drinking water set at 1 μg/L (US EPA 2015a).

During these bloom events, MC toxins have been recognized to accumulate to lethal concentrations (for human exposure) in water bodies routinely relied on for drinking water provision. Past examples ranging from the Lake Taihu and Toledo water crises, have demonstrated that "mega" blooms of toxic *Microcystis* and perhaps other genera can overwhelm, even shut down, local drinking water treatment facility operations, leaving millions stranded without potable water for time periods varying from days to months (Qin et al. 2009a, Ho and Michalak 2015). Although conventional drinking water treatment technologies (such as coagulation, flocculation, sedimentation) can effectively remove the cellular portion of biotoxins from the water, the dissolved (or extracellular) portions are

sparingly removed (Westrick 2008, Westrick et al. 2010). Advanced treatment technologies, such as ozonation, UV treatment, or granular activated carbon, have been developed to supplement conventional technologies and reliably remove total cyanotoxins from drinking water. However, these advanced technologies are energy-intensive, cost-ineffective, subject to some inherent treatment variability, and are difficult to maintain and operate (Westrick et al. 2010, Ho et al. 2012a).

The immediate and omnipresent threat of toxic cyanobacterial blooms has prompted the development of unique and sustainable solutions to effectively treat MC toxins in drinking water. Biological treatment options, such as biological filtration, have received a great amount of interest and recent research attention, as MCs have been found to already be naturally metabolized as a carbon (perhaps nitrogen) and energy source by a diverse range in native bacterial populations endemic to drinking water sources (Ho et al. 2006, Bourne et al. 2006, Ho et al. 2012a, Li et al. 2017). Even though biodegradation of MCs is naturally mediated, variability in treatment kinetics and efficiencies attributed to a wide array of environmental factors (i.e., temperature, pH, the presence of exogenous nutrients, bacterial community composition) have limited the full-scale application of bioremediation-based treatment technologies (Ho et al. 2012a, Li et al. 2017). The main challenge to the advent of bio-based treatment technologies, thus, lies in offsetting these environmental factors to truly harness, stabilize, and augment this natural treatment ability in a systematic and "engineered" manner (Lauderdale et al. 2012).

Effectively "engineering" these biologically based MC treatment systems relies on a practical, predictive understanding of the microbial growth kinetics associated with MC metabolism. Drawing from the founding principles of biochemical engineering,

unstructured kinetic growth models, such as the well-known Monod model, can guide researchers and practitioners alike as to the optimal behavior of these MC degrading populations in settings ranging from engineered reactors to the environment (Esener et al. 1983, Kovárová-Kovar and Egli 1998, Alexander 1999, Shuler and Kargi 2002, Tchobanoglous et al. 2003, Okpokwasili and Neweke 2006). However, as past research has indicated with biological wastewater treatment design and operation of activated sludge or anaerobic digestion systems, predictions from these simplified models can often be misleading (Koch et al. 1982, Robinson 1985, Grady et al. 1996, Kovárová-Kovar and Egli 1998, Knightes and Peters 2000). The utility of unstructured kinetic models can ultimately be diminished if, for example: 1) the underlying mechanisms of the model structure describing MC metabolism are not sufficient; 2) the parameters associated with these model structures are improperly calibrated or estimated without quantitative estimates of certainty; or 3) the parameters are not structurally nor practically identifiable given the quality of the experimental data.

In a previous study, we addressed issue 1) identified above as to what extent and which model structures better predicted MC metabolism and growth kinetics of isolated degrading populations (Manheim et al. 2019), concluding that the Moser model well outperformed existing unstructured kinetic models. Regarding issue 2) identified above, we further developed a reliable, global, and fully Bayesian parameter estimation protocol to arrive at stable posterior distributions in parameter estimates (Manheim et al. 2019). It was clear from this study that unstructured kinetic models (i.e., the Moser model structure) could accurately and precisely predict MC removal and growth kinetics; however, reliable parameter estimates could not always be achieved - even with a well devised parameter

estimation protocol. We attributed this lack of parameter definition to the quality of the experimental data, which was insufficient to uniquely estimate all model parameters (5 out of 6 at best). As the quality of the experimental data is directly associated with the experimental design, we focus our attention in this study on how to best devise an experiment to achieve maximal information content for parameter identification of unstructured kinetic models describing MC biodegradation.

To achieve this end, computational techniques such as optimal experimental design (OED) can be implemented to obtain experiments that, through careful parameter estimation procedures, result in reliable and uniquely identifiable estimates of model parameters (Rodriguez-Fernandez et al. 2007, Chu and Hahn 2010, 2013, Banga and Canto 2008, Balsa-Canto et al. 2008, 2016). OED relies on optimizing the experimental conditions (i.e., experimental method, initial state conditions, sampling time or frequency) for maximal information content using some summary criterion (or multiple criteria) of the Fisher Information Matrix (i.e., A-D optimality criteria), constructed using sensitivity index estimates of the simulated model output to changes in the model input parameters (Dette et al. 2003, 2005, Franceschini and Macchietto 2008, McLean and McAuley 2012). Experimental designs that maximize (or minimize) these criteria ultimately lead to improved practical identifiability of model parameters. Therefore, in this study we applied a recently developed, computationally efficient, global OED approach to investigate the following pertinent research questions:

1) Are the unstructured kinetic model structures first globally, structurally identifiable? By “globally, structurally” identifiable we mean that, a priori, given the

model structure (and noise free data), can we estimate unique (singular) values of each parameter?

2) What experimental designs lead to improved practical identifiability of unstructured kinetic model parameters? By "experimental designs," we specifically refer to what experimental approaches used (i.e., batch reactor, fed-batch reactor, continuously stirred tank reactor, CSTR), the initial state variable conditions employed (i.e., initial substrate/biomass concentrations, fed-batch feed profile, etc.).
3) How much improvement in parameter definition can we expect (compared to existing, non-optimal experimental designs) if we apply the optimal experimental designs achieved above in practice?

In this study, two contrasting approaches were incorporated to address both structural and practical identifiability of kinetic parameters underlying the Moser model. First, a symbolic, generating series approach to structural identifiability of the model parameters was applied to investigate to what extent the model structure itself limits parameter identification. Next, a global approach to optimal experimental design, based on a derivative based global sensitivity measure, was employed using both single and multiple objective optimization frameworks to examine which experimental conditions lead to parameter decorrelation and maximum information content. This model-based design of experiments approach is expected to provide great insight as to which experimental method is most suitable for practically identifying parameters of the Moser model for describing microcystin biodegradation.

2. Materials and Methods

2.1 Summary of Selected Unstructured Kinetic Model to Describe MC Biodegradation

Unstructured kinetic models describing dynamic MC biodegradation ($\frac{dC}{dt}$) and corresponding bacterial cell growth ($\frac{dX}{dt}$) in a batch reactor setting consist of two coupled ordinary differential equations (ODEs), in which first order endogenous decay is explicitly incorporated (Equations 1 and 2). Importantly, unstructured kinetic models are based on the governing assumption that there is a single substrate (i.e., MC) that is limiting bacterial growth. It is important to note that the form of Equations 1 (substrate balance) and 2 (cell balance) will change when considering different experimental approaches in the following section.

$$\frac{dC}{dt} = -\frac{1}{Y}\mu X \quad (1)$$

$$\frac{dX}{dt} = \mu X - k_d X \quad (2)$$

Where C is the limiting substrate concentration (mg/L), X is the biomass concentration (mg/L), μ is the specific growth rate of bacterial cells (1/hr), Y is the cell yield coefficient (unitless) and k_d is the endogenous decay coefficient (1/hr).

As presented in Manheim et al. (2019), there are numerous mathematical relationships devised to describe the relationship between bacterial specific growth rate (μ) in Equations 1 and 2 and substrate concentration (C). Based on statistical evidence in favor of the Moser model structure and associated cellular growth mechanisms in a previous study, we chose to select this model structure as the basis for study hereafter (Moser 1958). The Moser model structure presents the specific growth rate of bacterial cells (μ) involved in biodegradation as a sigmoidal function of substrate concentration (C)

with three main parameters: the maximum specific growth rate, half saturation constant, the yield coefficient, and the interaction coefficient (μ_{max}, K_s, Y, n) (Equation 3).

$$\mu = \frac{\mu_{max} C^n}{K_s + C^n} \quad (3)$$

The maximum specific growth rate (μ_{max}) represents the maximum growth rate the bacterial cells achieve when the substrate is saturating ($C >> K_s$) (1/hr). The half saturation constant is defined as the substrate concentration (mg/L) existing at one half the maximum specific growth rate and is described as the relative affinity of the degrading organism for a limiting substrate. The yield coefficient (Y) is defined as the mass of bacterial cells produced per mass of substrate consumed (mg biomass/mg substrate). The interaction parameter n accounts for the interactions between binding sites on the enzyme molecule, analogous to Hill's equation in enzymology. Values of $n > 1$ indicated cooperative interactive effects between binding sites, whereas values of $n < 1$ signified competitive (non-cooperative) interactive effects between binding sites (Panikov and Pirt 1978).

2.2 Experimental Approaches for Optimal Parameter Estimation

In this study, we investigated and compared four different approaches for defining an experimental design for improved biokinetic parameter estimation of unstructured growth models describing MC biodegradation including a batch reactor, fed-batch reactor, chemostat, and continuously stirred tank reactor (CSTR) (Figure 57, Table 17). For all experimental approaches, the time rate of change of three primary state variables are considered including the substrate concentration (C), biomass concentration (X), and the liquid media volume (V). During all experiments (which are assumed to be performed in the laboratory on a benchtop scale), a standard liquid medium (i.e., M9 mineral salts medium) supplied with MC as the sole carbon and energy source is assumed, where all

other nutrients (i.e., nitrogen, phosphorus, trace metals) are non-limiting. In addition, sterile air is supplied at a constant rate via a diffuser to ensure that oxygen is not limited inside each reactor configuration (Figure 57). Finally, all reactors are equipped with a mixer (programmed at a defined mixing intensity), sampling ports, and are fully insulated to ensure optimum temperature control. Moreover, during these idealized experiments, the pH, temperature, and dissolved oxygen are monitored, and air input and temperature can be adjusted accordingly as part of a preprogrammed, closed feedback loop (Figure 57).

Across all experiments, time varying MC concentrations will be measured using a solid phase extraction assisted LC-MS/MS standard protocol for optimal accuracy, precision, and sensitivity (US EPA 2015b). This LC-MS/MS protocol for MC quantification has been well established in the scientific literature and has a detection limit of 1.2 ng/L (for MC-RR) (US EPA 2015b). However, achieving accurate, precise, and sensitive quantification of active MC-degrading biomass is expected to be challenging for these experiments. Based on previous research, ATP concentrations have provided the most accurate, stable and sensitive determinations of active biomass in drinking water treatment applications (Velten et al. 2007, 2011). This method developed assumes an adequate conversion from ATP to dry weight (in terms of cellular carbon) is available, where median values of this conversion factor can be used as suggested in (Graça et al. 2007). Although there may be some uncertainty in this conversion factor (i.e., variation across different bacterial populations), the ability of the ATP method to differentiate between active and decaying biomass and the sensitivity of this method is critical for the correct determination of viable MC-degrading cells.

Even though a detection limit was not specified in Velten et al. (2007, 2011), a theoretical detection limit was calculated assuming: a) the sensitivity of the fluorescence detector reported by a commercial microbial ATP kit (10E-18 mol ATP/50 µL sample, BioThema 2018); b) the molar mass of ATP (507.18 g/mol), the average ATP content per cell as reported in Velten et al. (2007) (6.7 E-17 g ATP/cell); and the theoretical weight of a microcystin degrading bacterial cell (6 fg/cell, Mou et al. 2013). Applying these conversions resulted in a theoretical detection limit of 0.0179 ng/L, which theoretically corresponds to the weight of 5 MC degrading bacterial cells per L of solution (BioThema 2018). Clearly, this protocol was considerably more sensitive than optical density, dry or wet weight, and colony count methods.

A batch reactor, perhaps the simplest experimental approach, consists of a closed, fixed volume reactor apparatus ($\frac{dV}{dt} = 0$), in which the dissolved oxygen, temperature, pH are tightly controlled (Figure 57, Table 17). The initial concentrations of substrate (C_0) and MC-degrading microorganisms (X_0) are the only experimental variables that can be used to effectively design an experiment for optimal parameter estimation (Table 17). After adding the initial MC and MC-degrading cells to the reactor, samples of both MC and MC-degrading biomass (i.e., a pre-determined volume) were assumed to be taken from the sampling ports at designated sampling times during each experiment.

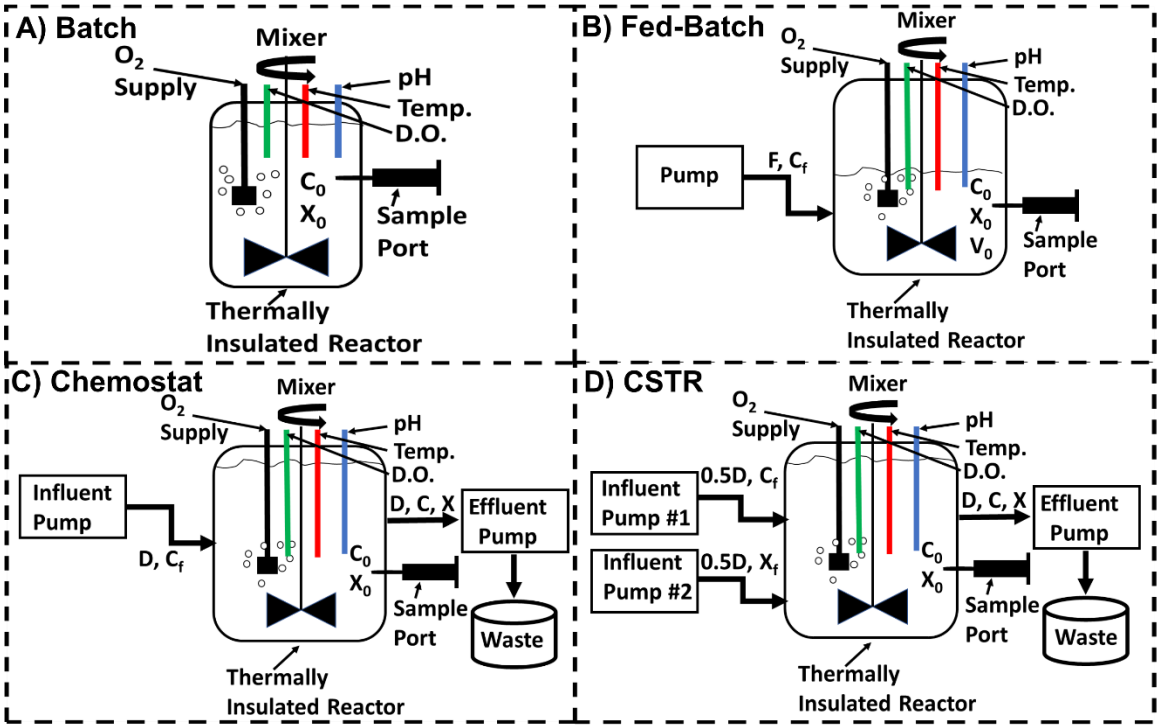

Figure 57. *Qualitative illustration of the laboratory, benchtop scale experimental configurations used to estimate biokinetic parameters for unstructured kinetic models describing MC biodegradation. Configurations are presented for A) a batch reactor, B) a fed-batch reactor, C) a chemostat, and D) a continuously stirred tank reactor (CSTR). The symbols C_0, X_0 and V^0 refer to the initial MC substrate concentration, MC-degrading cell concentration, and media volume (inside the reactor) used for each experiment. For the fed-batch reactor, F and Cf stand for the dynamically varying feed rate profile and feed substrate concentration, respectively. For both the chemostat and CSTR, D, C_f, an X_f refer to the dilution rate (constant), feed concentration of substrate, and feed concentration of MC-degrading cells, whereas C, and X refer to the concentration of MC and MC-degrading cells exiting the reactors.*

Comparably, a fed batch reactor is a partially open system, in that the substrate (sterile) is continuously fed according to a certain feed rate (F/V) profile into the batch reactor (Figure 57). In this approach, the volume of liquid media is not fixed within the reactor, but dynamic ($\frac{dV}{dt}$ = F) and there is some effect of cell dilution to account for ($-\frac{F}{V}$X). In addition, the fed-batch system explicitly accounts for the initial concentration of MC substrate and degrading cell biomass within the reactor (C_0, X_0) as well as the concentration of the feed entering the reactor (C_f) (Figure 57, Table 17). In this study, we

considered a dynamically varying feed rate profile for a fed-batch type reactor system and constrained the volume of the reactor to 1 L (maximum volume for bench top scale) during all optimization runs. Using a form of control vector parameterization (CVP), the feed rate profile was discretized into twenty uniform time intervals of approximately 14 hours each. Mathematically, the input feed rate profile was a continuous piecewise function, where during each time interval a constant feed rate was assumed (which could vary across all 14 time intervals) (Chu and Hahn 2013).

Chemostats and CSTRs are both fully open systems, as liquid media is configured to flow into and out of the reactor apparatus (Figure 57C and 57D). Since the volumetric flow rate (Q) is held constant, there is no accumulation of liquid within the reactor ($\frac{dV}{dt} = 0$). Ultimately, the dilution rate ($D = Q/V$) controls the specific growth rate the organisms can grow at within these reactor configurations (Bailey and Ollis 1976, Shuler and Kargi 2002). The primary difference between the chemostat and CSTR is that the chemostat maintains a sterile feed, whereas the CSTR maintains cell inputs within the feed to avoid possible cell washout during operation due to any unforeseen circumstances such as abrupt shifts in feed conditions (Figure 57, Bailey and Ollis 1976, Shuler and Kargi 2002). The CSTR most closely resembles a controlled environmental system as compared to the other experimental reactor configurations.

Table 17 *- Comparison of experimental approaches, associated structural equations for parameter estimation, and the corresponding design variables that can be optimized using OED.*

Experimental Method	Substrate Balance	Cell Balance	Volume Balance	Design Variables
Batch Reactor	$\frac{dC}{dt} = -\frac{1}{Y}\mu X$	$\frac{dX}{dt} = \mu X - K_d X$	$\frac{dV}{dt} = 0$	C_0, X_0,
Fed-Batch Reactor	$\frac{dC}{dt} = -\frac{1}{Y}\mu X + \frac{F}{V}(C_0 - C)$	$\frac{dX}{dt} = \mu X - K_d X - \frac{F}{V}X$	$\frac{dV}{dt} = F$	C_0, X_0, $F(t)$, C_f
Chemostat	$\frac{dC}{dt} = -\frac{1}{Y}\mu X + \frac{Q}{V}(C_0 - C)$	$\frac{dX}{dt} = \mu X - K_d X - \frac{Q}{V}(X)$	$\frac{dV}{dt} = 0$	C_0, X_0, D, C_f
CSTR	$\frac{dC}{dt} = -\frac{1}{Y}\mu X + \frac{Q}{V}(C_0 - C)$	$\frac{dX}{dt} = \mu X - K_d X + \frac{Q}{V}(X_0 - X)$	$\frac{dV}{dt} = 0$	C_0, X_0, D, C_f, X_f

2.3 Structural Identifiability Analysis

GenSSI, a software toolbox for structural identifiability analysis of biological models (V. 2.0) was adopted in this study to assess whether the models investigated were globally, structurally identifiable (Chis et al. 2011a, 2011b, Ligon et al. 2017). By definition, global, structural identifiability means that there exists a unique solution, or a single parameter combination, that is optimal for a given experimental condition. In contrast, a model can also be classified as locally, structurally identifiable, which means that a certain finite number (or neighborhood) of unique parameter combinations may exist for a given experimental condition. Lastly, if there are many, non-unique parameter combinations that exist for a given experimental condition, the model is classified as structurally unidentifiable (Villaverde and Banga 2017).

The GenSSI software approach is based on an analytical, generating series method coupled with identifiability tableaus for estimating structural identifiability of a given model (Chis et al. 2011a, 2011b, Ligon et al. 2017). The GenSSI method is based on

analytical computation of successive Lie derivatives of the model output function to generate a non-linear system of equations on the model parameters (Chis et al. 2011a, Villaverde and Bang 2017). If the solution of this non-linear system of equations is unique, then the model is concluded to be globally, structurally identifiable (Chis et al. 2011a). The degree of structurally identifiability of a given model can be qualitatively visualized through generation of identifiability tableaus, which illustrate the mathematical dependence of the Lie derivatives on each model parameter (where black areas are indicative of dependence). Ideally, if the model is globally, structurally identifiable, the tableau will visually appear like a staircase, in which each Lie derivative mathematically depends on only one model parameter at a time.

In general, the GenSSI analysis depends on the number of lie derivatives used in the calculation as well as the initial conditions of the system. GenSSI (v 2.0) allows the use of both generic and numeric initial conditions, where structural identifiability can be assessed for multiple experimental conditions. In this study, we have evaluated structural identifiability of the Moser model using both a batch and fed-batch reactor experimental configuration as a contrasting example. The analysis was carried out for only generic experimental conditions, as the built-in multiple experiment option provided by the software cannot handle dynamic input controls. For all runs, the number of lie derivatives was set to 10, a number twice the number of model parameters, which is consistent with what was recommend by reference literature (Chis et al. 2011a, Ligon et al. 2017). With the number of lie derivatives fixed, the initial conditions were set to generic variable values for each experimental configuration (i.e., batch vs. fed-batch).

2.4 Practical Identifiability: Optimal Experimental Design Approach

2.4.1 General Description of the OED-GSA Procedure

An OED approach based on global sensitivity analysis (GSA) was adopted in this study to ascertain the best experimental conditions for parameter identifiability of unstructured kinetic models describing microcystin biodegradation (Rodriguez Fernandez et al. 2007, Chu and Hahn 2008, 2010). The application of GSA is advantageous over local sensitivity methods as it allows the full range in input parameter uncertainty to be incorporated into the design of experiments, as opposed to just nominal values of the parameters (Rodriguez Fernandez et al. 2007, Banga and Balsa-Canto 2008, Bandara et al. 2009). This aspect of GSA is critical as in most cases, the optimal parameters describing the model are often unknown prior to conducting an experiment (Franceschini and Macchietto 2008). Therefore, GSA has become a valuable tool in OED to limit the amount of experimentation required before model calibration takes place and to improve model parameter practical identifiability.

Quantitative OED relies on accurate and precise calculation of the partial derivatives of the model response variables with respect to each input parameter (i.e., the local sensitivities, Equation 1, where *f* represents a model response variable and x_i the *i*th model parameter). In this study, a Monte Carlo, derivative based approach to GSA (DBGS) was adopted, which considers the average and standard deviation of the local sensitivities of the model response variables with respect to each input parameter over the entire input parameter space (Equations 2-4, where *k* indicates the index of the *n* number of QMC samples, and *i* is the index for the *d* number of parameters, Kucherenko et al. 2009). In effect, the final DBGS indices ($\bar{G}_i$), which were used in the OED calculations, are normalized

so that the sum of all parameters for a given timepoint is equal to unity (Equation 7). Importantly, this approach can be modified for dynamic model outputs, where DBGS indices can be calculated for any number of simulated timepoints. As this is a MC approach, a certain number of QMC samples (using Sobol's sequences) was required for the calculated DBGS indices to formally converge (Sarrazin et al. 2016). Based on a rigorous test of convergence, we found that approximately 8,192 QMC samples were needed for each model describing different experimental approaches to formally converge (see Appendix F, section 5).

$$E_i = \frac{\partial f}{\partial x_i} \tag{4}$$

$$\bar{M}_i = \frac{1}{n} \sum_{k=1}^{n} \left| E_{i,k} \right| \tag{5}$$

$$\bar{\Sigma}_i = \sqrt{\frac{1}{n-1} \sum_{k=1}^{n} \left(\left| E_{i,k} \right| - \overline{M_\iota} \right)^2} \tag{6}$$

$$\bar{G}_i = \frac{\bar{M}_i^{\,2} + \bar{\Sigma}_i^{\,2}}{\sum_{i=1}^{d} \bar{M}_i^{\,2} + \bar{\Sigma}_i^{\,2}} \tag{7}$$

The Fisher Information Matrix (FIM) has been routinely applied as an indicator for quantitatively comparing the quality of different experimental designs by summarizing the information content of a given experiment. The FIM summarizes both the uncertainty of the experimental measurements as well as the uncertainty of the estimated parameters expected from the model calibration process (and is *d*x*d* in dimension, where *d* represents the number of model parameters) (Dette et al. 2003, 2005, Franceschini and Macchietto 2008, McLean and McAuley 2012). In general, experiments that maximize information content are optimal, and calculations to derive singular representations of the FIM are often conducted in OED (i.e., the determinant), as explained in the upcoming paragraphs.

To construct the FIM, the sensitivity matrix (S) and the weighting matrix (Q) must be specified a priori (Equation 8).

$$FIM = S^T Q S \tag{8}$$

The sensitivity matrix is typically formed from the partial derivatives of the model response variables with respect to each model parameter for each simulated time point for a dynamic model. It is important to note that in this study $\bar{G}_{i,}$ which represents the global sensitivity of the model output response across the entire parameter uncertainty range, has replaced the local sensitivity calculations (Equation 9, where C and X indices refer to the sensitivity with respect to substrate or cell concentration state variables, N the total number of simulated time points, and d, the number of parameters to be estimated). In this study, the resulting sensitivity matrix (S) is twice the number of simulated time points long ($2*N$) by number of parameters (d) wide (Equation 9). However, for the fed-batch experimental designs, the sensitivity matrix was expanded to also account for the volume of liquid media within the reactor (V), resulting in a length of $3*N$.

$$S = \begin{bmatrix} \bar{G}_{C,1}(t_1) & \bar{G}_{C,2}(t_1) & \dots & \bar{G}_{C,d}(t_1) \\ \bar{G}_{C,1}(t_2) & \bar{G}_{C,2}(t_2) & \dots & \bar{G}_{C,2}(t_2) \\ \vdots & \vdots & \vdots & \vdots \\ \bar{G}_{C,1}(t_N) & \bar{G}_{C,2}(t_N) & \dots & \bar{G}_{C,d}(t_N) \\ \bar{G}_{X,1}(t_1) & \bar{G}_{X,2}(t_1) & \dots & \bar{G}_{X,d}(t_1) \\ \bar{G}_{X,1}(t_2) & \bar{G}_{X,2}(t_2) & \dots & \bar{G}_{X,d}(t_2) \\ \vdots & \vdots & \vdots & \vdots \\ \bar{G}_{X,1}(t_N) & \bar{G}_{X,2}(t_N) & \dots & \bar{G}_{X,d}(t_N) \end{bmatrix} \tag{9}$$

The square weighting matrix, Q, represents the expected variance-covariance matrix of the measurement errors, and can be used to place more emphasis on the measurement uncertainty of certain variables (Dette et al. 2003, 2005, Franceschini and Macchietto 2008, McLean and McAuley 2012). In general, it is assumed that the covariance between

measured variables is negligible, measurement errors are homoscedastic, and that the measurement error can be simulated as a Gaussian distribution, with zero mean and unit variance (i.e., Gaussian white noise) (McLean and McAuley 2012, Li et al. 2018). Here, we adopt these same assumptions commonly used in OED, and, due to lack of experimental measurement knowledge, make the assumption that the measurement variability is of similar magnitude when measuring both substrate and cell concentrations as well as the volume of liquid within the reactor configuration.

To perform quantitative OED, singular mathematical descriptions of the FIM are warranted for ease of optimization and interpretation. The alphabetical criteria (*A*-*E*), which describe different aspects of the FIM, have been presented as the most well-known indices applied for optimization. For example, the *D* criterion maximizes the determinant of the FIM (corresponding to minimizing the geometric mean of the parameter estimation error), whereas the *A* and *E* criteria minimize either the mean of the parameter estimation errors or the largest parameter error (disregarding all other parameters), respectively. Geometrically speaking, maximizing the *D* criterion is equivalent to minimizing the volume of the elliptical joint confidence region between the parameters, while minimizing the A criterion can be interpreted as minimizing the enclosing frame around the joint confidence region between the parameters. Furthermore, minimizing the E criterion is interpreted as reducing the length of the major axis of the elliptical joint confidence region between parameters. Modified criteria have also been introduced, including the modified E criterion, which minimizes the condition number of the FIM (Telen et al. 2012, Maheshwari et al. 2013). Due to its widespread and successful application, we have chosen the *D* criterion as

a suitable metric for optimization in this study (where the objective function (OF_1) is the maximization of the determinant of the FIM, Equation 10).

$$OF_1 = \max(|FIM|) \tag{10}$$

Although many criteria have been introduced to decompose the FIM into a singular value, previous OED research has suggested that optimizing one of these metrics alone (i.e., only focusing on maximizing information content) will not always produce experimental designs that result in parameter decorrelation (Maheshwari et al. 2013). It is crucial to explicitly address parameter correlation during the OED process in the case of unstructured kinetic models, as previous practical identifiability experiments have characteristically identified correlation among certain parameters such as μ_{max} and K_s (Nihtilä and Virkkunen 1977, Holmberg 1982, Robinson and Tiejde 1983, Liu and Zachara 2001). Therefore, in addition to optimizing the information content of a certain experiment, we have adopted a decorrelation metric previously introduced by Maheshwari et al. (2013) and transformed the OED into a multi-objective optimization problem (Equation 11). Here, *Corr* refers to the matrix norm of the parameter correlation matrix, as defined by Maheshwari et al. (2013), which is achieved through inversion and transformation of the FIM. The OED is thus specified by designing the experiment as a tradeoff between maximizing information content and minimizing parameter correlation, where, in a multi-objective optimization framework, the primary objective is to find an optimal Pareto front of non-dominated solutions. In addition to multi-objective optimization, we also performed single objective optimization, where each objective was optimized independently, as a means to benchmark the convergence of the Mo results.

$$OF_2 = \min(Corr) \tag{11}$$

2.4.2 General Numerical Procedure for Performing OED-GSA

Figure 58 demonstrates the main workflow for numerical application of the single and multi-objective OED-GSA algorithms. Before the optimization algorithms were initiated, the first step of the workflow was to initialize the parameter ranges, obtain the parameter QMC samples, and define the feasible search space for the experimental design criteria (Figure 58). The overall posterior distribution in parameters obtained from Manheim et al. (2019), which calibrated the Moser model using several different MC biodegradation datasets, was incorporated in this study to bound the certainty range of the parameter estimates (Table F1 provides a summary of the parameter estimates for reference). Next, the parameter samples (n = 8192) were obtained using a Sobol sequence to acquire uniform, quasi-random draws from the constrained parameter space.

As a continuation of Step 1, the feasible search space for experimental design criteria was initialized for application in the OED optimization and varied according to the reactor configuration (Appendix F, section 1, Table F2). For example, the initial substrate and MC-degrading cell concentrations were restricted to a range from 0 to 1000 (mg/L) for each configuration. For all practicality, this range was deemed reasonable since purified MC is currently very expensive and difficult to obtain or prepare in sufficient quantity. Given this accessibility issue, it may be challenging to grow a population of sufficient density (i.e., past 1 g/L) using MC as the sole carbon and energy source. However, the feed concentration of MC-degrading cells was increased to 10 g/L for the CSTR configuration, as the optimization results continually attempted to breach the upper bound of 1 g/L. Similarly, the dilution rates were restricted from 0 to 6.59 (1/day), the upper bound on the maximum growth rate of the MC-degrading bacteria, as to avoid washout. Importantly, the

feed rate profile was constrained during optimization so that the theoretical volume added to the reactor throughout the course of the experiment would not exceed 1 L (a practical upper threshold on the volume of a bench scale, laboratory reactor system).

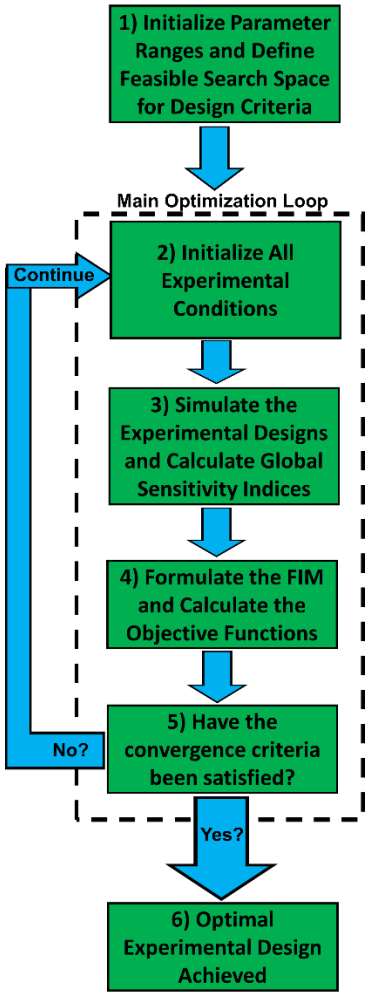

Figure 58. *Example workflow for numerical implementation of the OED-GSA algorithm applied in this study.*

Since the optimization problem for OED is notoriously difficult, noisy, and non-convex, local, gradient based search methods, such as MATLAB's *fmincon* suffer from premature convergence or may become trapped in local solutions (Banga et al. 2004). Therefore, we relied on stochastic, evolutionary algorithms with global search capabilities such as LSHADE-NLS and NSGA-III to perform both single and multi-objective optimization,

respectively (Awad et al. 2016, Deb and Jain 2014). Both LSHADE-NLS and NSGA-III are based on the theory of differential evolution or metaheuristics, in which a population of individuals (potential solutions to an optimization problem) are evolved based on their fitness and random probabilities of acceptance and or mutation (i.e., control parameters). The NSGA-III algorithm was slightly different as it relies on optimizing a Pareto front, or non-dominated solution set, as opposed to a population of individuals, as was the case in single objective optimization. Further details behind the LSHADE-NLS and NSGA-III control settings and run conditions are presented in Appendix F, section 2 for reference.

OED-GSA depended on both rapid and accurate simulation of the representative ODEs and the corresponding local sensitivities used in the DBGS calculations. As part of Step 2 in the workflow (Figure 58), our experience with the *ODE15s* and related solvers in the MATLAB environment were that they were much to slow to be incorporated in an OED optimization framework. Therefore, we relied on a MATLAB wrapper developed by van Riel (2012) to efficiently apply the *CVodes* differential equation solver developed by LLNL for systems biology models. This wrapper further allowed the ODE function that was coded in MATLAB to be conveniently transformed to C code for rapid evaluation (van Riel 2012). Specifications of the solver tolerances and steps applied for the *CVodes* approach are presented in the SI for reference. These work arounds, in combination with code vectorization and maximal reliance on parallel computing (as facilitated by the UCI high performance computing system), allowed efficient and accurate simulation of the ODEs and calculation of the corresponding sensitivity indices from the MATLAB environment for use in OED.

After formulation of the FIM and calculation of the corresponding objective functions (Step 4), it was necessary to monitor convergence for both the single and multi-objective optimizers (Step 5). Convergence of the single objective optimizers was monitored by comparing the range in the solution sets for all members of the population (threshold of 1E-10 was set), as commonly performed in differential evolution (Storn and Price 1997). However, monitoring the convergence of the MO algorithm was much more complicated and involved integrating a previously developed, specialized statistical approach (Trautman et al. 2009, Wagner et al. 2009). This online convergence monitoring approach for a multi-objective framework relied on four different indicator metrics that are commonly applied to assess the quality and accuracy of multi objective, non-dominated Pareto fronts including: hypervolume, epsilon, R2, and diversity metrics (Trautman et al. 2009, Wagner et al. 2009). The description of each index, along with details concerning the statistical approach for monitoring convergence, and an example application of this approach are presented in Appendix F, section 3 for reference. Overall, if the single or multi objective optimization algorithms met the convergence criteria, or exceeded the number of allotted generations, the OED process was terminated, and an OED was achieved (Step 6, Figure 1).

2.4.3 Application of the OED-GSA Numerical Method

The OED-GSA numerical method was first applied to gauge differences in the experimental approaches between reactor configurations. This involved running the OED-GSA method for three different repetitions (in which the Sobol QMC sequence was varied), to assess the reproducibility of the results, for both the single and multi-objective algorithms. For these initial sets of experiments, the sampling times were fixed to 1-day

intervals for a simulation period ranging from 0 to 11 days. For the fed batch experimental configuration, the dynamic feed rate profile was randomly initialized, making sure that the volume injected over the course of the experiment was always below 1 L prior to the start of the optimization procedure. Similarly, the initial conditions for each of the experimental designs for the remaining experimental configurations were taken as uniform, random draws within the uncertainty range of the experimental design criteria.

2.5 Post-Processing of OED Results

Many previous studies have successfully relied on comparison of experimental designs returned by the OED procedure using the FIM singular values (i.e., the A-E criteria) and confidence intervals of the parameters derived from the FIM using the Cramér-Rao inequality (Chu and Hahn 2010, 2013). Thus, to effectively evaluate to what extent the OED improved parameter identification in this study, we relied on the transformation of the optimal FIM obtained in the previous optimization procedures to obtain the variance-covariance matrix (CM) of the parameter estimates, where $CM = FIM^{-1}$ (Banga and Balsa Canto 2008).

Once an estimate of the optimal CM was reached, the statistical certainty in the parameter estimates and the degree of parameter correlation were analyzed through application of confidence ellipses. Theoretically, the CM matrix represents a "cloud" of parameter values, or a hyper ellipsoid of *d* dimensions, that can be quantitatively analyzed through application of principal component analysis (PCA). This analysis is generally conducted for combinations of pairs of parameter values (i.e., θ_i, θ_j), in which the hyper ellipsoid achieved from the PCA analysis can be projected onto multiple 2D planes. Similar to what was proposed in Balsa-Canto et al. (2008), we have calculated several intuitive

metrics to facilitate the comparison of the quality of experimental designs returned by this OED procedure including:

- The overall pseudo volume of the hyper ellipsoid, Θ, which is determined through multiplication of the semi-axes (radii of the semi-major axes) obtained from the PCA. Smaller values of the pseudo volume are indicative of an improved experimental design.
- The maximum and mean eccentricity, ε and ε_a, which are simply the maximum or average ratios of all semi-major to semi-minor ellipse axes across every parameter combination. Again, values closer to 0 (i.e., more circular) are indicative of an improved experimental design.
- The length of the 95% confidence intervals for each parameter, η_i, which describes the magnitude of the remaining uncertainty of each parameter value achieved for a given experimental design. Again, smaller interval lengths quantitatively indicate the parameter estimates are of higher certainty and correspond to improved experimental designs.

3. Results

3.1 Structural Identifiability of Kinetic Parameters

The GenSSI analysis for both the batch and fed-batch experimental configurations determined that the Moser model was locally, structurally identifiable. This conclusion was the same, regardless of the experimental configuration used, as the GenSSI analysis could not account for a dynamic feed rate profile for the fed-batch reactor when conducting the Lie derivatives. Ultimately, if this analysis could account for a dynamic feed rate profile, then improved structural identifiability of the Moser model would be expected. The conclusion of

local, structural identification meant that, given the experimental configurations evaluated, all parameters (i.e., μ_{max}, K_s, Y, k_d, and n) were locally, structurally identifiable and had at least a finite number (non-unique) of valid solutions for a given experimental design.

The reduced identifiability tableau returned by the GenSSI structural identifiability analysis indicated that all model parameters were very interdependent on one another (Figure 59). For example, the third through fifth Lie Derivatives all mathematically depended on all the model parameters. If a given model was globally, structurally identifiable, there would be more white-shaded regions on the identifiability tableau, indicating good mathematical independence of each parameter. However, in the case of the Moser model, it appeared that all input parameters were inherently very structurally correlated, as most of Figure 2 is shaded in blue. Mathematical correlation seemed to be strongest among μ_{max}, K_s, Y and n as well as μ_{max}, K_s, k_d, and n parameter groupings, as observed from the identifiability tableau for the first and second Lie derivatives (Figure 59).

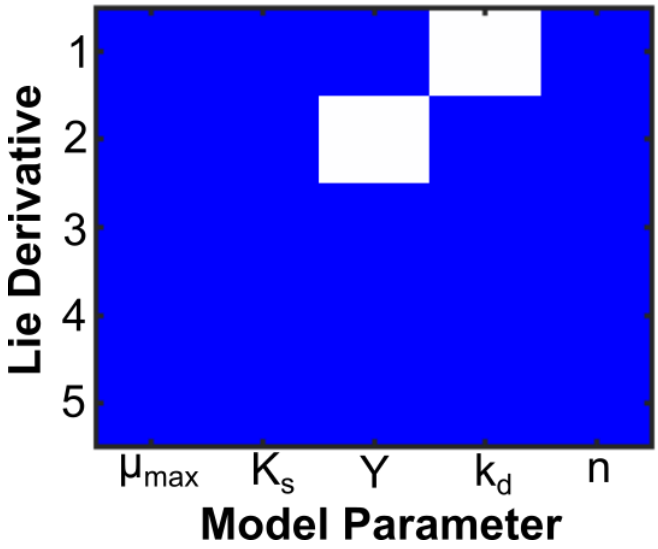

Figure 59. *Reduced identifiability tableau returned by the GenSSI structural identifiability analysis program for both the batch and fed-batch experimental configurations. Shaded blue areas indicate that the Lie derivatives mathematically depend on the model parameters, whereas white shading indicates no mathematical dependence.*

3.2 Practical Identifiability of Kinetic Parameters

After reviewing the structural identifiability of the Moser model, we now illustrate the practical identifiability of the Moser model kinetic parameters through analysis of the OEDs obtained from both the single and multi-objective optimization frameworks. Importantly, the OED results are presented separately for both the single and multi-objective optimization frameworks. For the single objective optimization framework, results pertaining to both the D-criterion and decorrelation criterion are presented independently to highlight differences in the optimization schemes. Finally, the best multi-objective OED is compared to that of an uninformed experimental design to demonstrate the improvements in parameter identification and decorrelation achieved through application of OED principles.

3.2.1 Single Objective OED Results: The D-criterion

As recommended by Balsa-Canto et al. (2016), it is important to first identify the sensitivity rankings of the kinetic parameters of the Moser model to help elucidate which experimental designs are in fact *practically* optimal (as opposed to theoretically optimal). In any model based experimental design scenario, the OED process could return an acceptable overall alphabetical criterion value, but lead to poor identification of the most sensitive model parameters. This result is troublesome, as the highest priority in the model identification process should be to reduce the uncertainty of the most sensitive model parameters, as these parameters contribute more to the overall uncertainty of model predictions. In the case of the Moser model, μ_{max} and k_d were observed to be the most sensitive model parameters across all simulated timepoints (Figure F6); therefore, special

emphasis will be given to OED results that reduce the uncertainty of these model parameters in particular.

Under the D-criterion, single objective framework, which seeks to minimize the volume of the hyper-ellipsoid of the parameter uncertainties (or maximize information content), there was a noticeable impact of the experimental configuration on the achieved results (Table 18). Overall, the fed-batch and batch systems resulted in experiments with the highest and lowest information content, respectively, as initially expected (Table 18). In addition, high information content was achieved from the chemostat experimental reactor configuration as compared to the CSTR configuration. Interestingly, the calculated pseudo-volume of the 95% CI hyper ellipsoid was orders of magnitude higher for the batch system as compared to the fed-batch system (Table 18). Comparably, the confidence ellipses were significantly more eccentric for the batch design as compared to all other designs, with maximum and average eccentricity values approaching 1, signifying high degrees of parameter correlation (Table 18). For the batch experiment, parameter correlation was greatest between K_s and n model parameters, in which a significant negative correlation was observed (data not shown). The expected 95% confidence interval lengths for the batch experiment were also very high for μ_{max} and n model parameters, demonstrating that this design was sub-optimal in terms of reducing the overall uncertainty of model predictions, as discussed above.

Table 18 *- OED statistical results using the D-criterion for optimization. Results are summarized for the best repetition (out of 3 independent realizations) for each experimental configuration.*

Experimental Configuration	D-Criterion	Θ	ε	ε_a	η_1 (μ_{max})	η_2 (K_s)	η_3 (Y)	η_4 (k_d)	η_5 (n)
Batch	0.0171	1.04 E06	1	0.934	13.10	5.48	10.1	2.00	31.3
Fed-Batch	19.1	5.40	0.944	0.760	4.54	3.50	3.26	2.19	6.49
Chemostat	12.6	38.1	0.987	0.862	9.90	2.99	5.16	1.58	3.46
CSTR	1.32	1.13 E04	1	0.920	4.97	8.18	5.00	1.52	16.6

Table 19 summarizes the initial conditions and experimental design criteria obtained from the best experimental designs using the D-criterion for single objective optimization. Across all experimental design configurations, the initial concentration of substrate (MC) and degrading microorganisms were disproportionate in the sense that the substrate concentration was sometimes order of magnitudes higher than the bacterial cell concentrations (Table 19). This result was especially apparent for the batch reactor and chemostat experimental configurations. The optimal dilution rate for the chemostat experiment was also relatively high compared to the highest expected specific growth rate of MC degrading microorganisms (6.60 day^{-1}), which was close to washout of the cells from the reactor. For both the CSTR and fed-batch reactors, the feed concentration of substrate was relatively high relative to the initial concentration of degrading cells inoculated in both reactors (Table 19).

Table 19 - *Initial conditions and experimental design criteria obtained using the D-criterion for optimization. Results are summarized for the best repetition (out of 3 independent realizations) for each experimental configuration.*

Experimental Configuration	C_0 (mg/L)	X_0 (mg/L)	V_0 (L)	D (1/day)	C_f (mg/L)	X_f (mg/L)
Batch	1.60	9.94E-05	-	-	-	-
Fed-Batch	0.858	0.102	0.00041	-	104.7	-
Chemostat	58.9	0.000251	-	5.06	0.00035	-
CSTR	165.1	0.471	0.767	0.153	50.5	51.9

When applying the D-criterion for optimization, the best OED achieved for all experimental configurations (i.e., the fed-batch configuration) was simulated and presented qualitatively in Figure 60. As observed in Figure 60, the substrate (MC) and degrading cell concentration profiles are quite dynamic, demonstrating at least three to four regions of distinct fluctuation over the course of the simulated experiment. In addition, there was high variability in the predicted responses of both state variables when applying the GSA approach for different parameter combinations (as indicated by the extensive uncertainty regions, Figure 60). The high variability observed among different parameter combinations may be due to the wide a priori uncertainty in the parameter estimates of kinetic models describing MC biodegradation. Although the parameter uncertainty intervals were relatively constrained to realistic boundaries from previous model calibration efforts (i.e., Manheim et al. 2019), the high diversity in MC degrading bacterial kinetics may have contributed to this increased variability in simulations. The liquid volume predicted within the reactor, however, remained constant across different simulations, as the liquid volume was only affected by the feed rate profile, which was fixed for each simulation. Lastly, the optimal feed rate profile was not very dynamic, where there was a relatively gradual step in concentration of substrate from 5-7 days followed by a noticeable jump around 7-8 days of simulation (Figure 60).

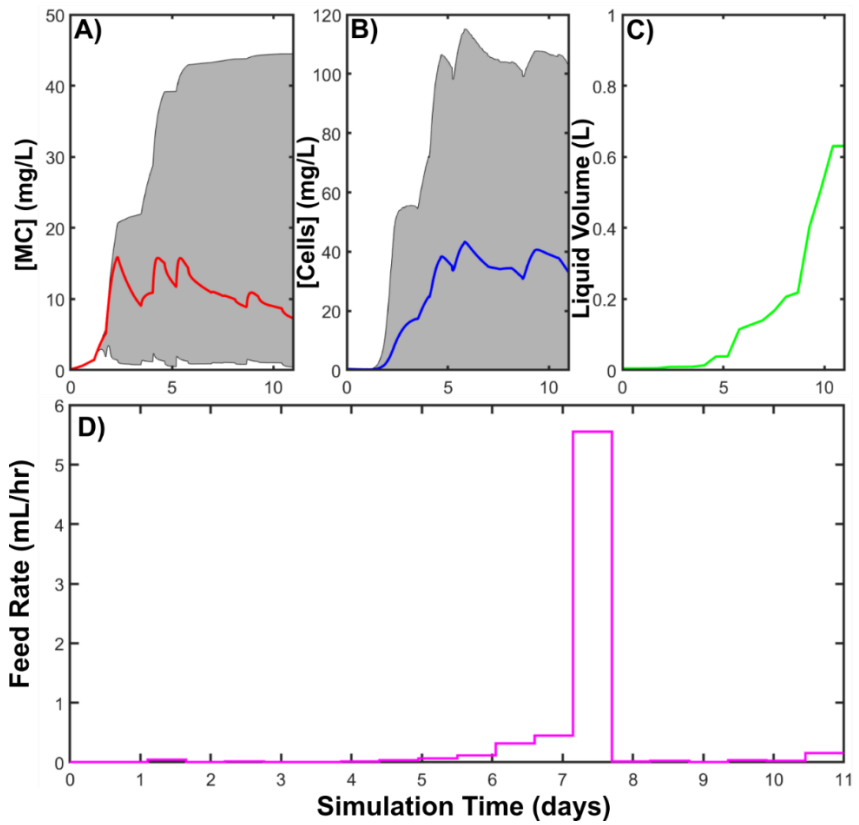

Figure 60. *Simulated optimal experimental design for the fed-batch reactor configuration using the D-criterion for single objective optimization. This figure displays the predicted MC concentration, degrading cell concentration, and liquid volume of the reactor system as a function of simulation time. The red, blue and green lines represent the mean predictions across 8192 different parameter combinations used in the GSA, while the grey region indicates the 95% CI achieved across all 8192 model predictions. Panel D portrays the optimal feed rate profile of the fed-batch reactor system.*

3.2.2 Single Objective OED Results: The Decorrelation Criterion

OED statistical results using the parameter decorrelation criterion showed that the uncertainty in some of the parameter estimates was considerably higher compared to the use of the D-criterion (Table 18 vs. Table 20). In fact, the pseudo-volume (Θ) of the confidence hyper ellipsoid was orders of magnitude larger (i.e., E17-39) for the optimal experiments determined using the decorrelation criterion over the D-criterion (Table 18 vs. Table 20). The length of the uncertainty intervals for K_s and n model parameters also severely increased when the decorrelation criterion was applied during single objective

optimization (Table 20). This increase in uncertainty observed for K_s and n model parameters was most likely at the expense of reducing the correlation existing between the most sensitive parameters (i.e., μ_{max} and k_d) and either K_s or n model parameters. Although the orientation of the confidence ellipsoids was near perpendicular and parallel to the x-axis (indicating little correlation, data not shown), the extremely high eccentricity values confirmed that there was high uncertainty in several model parameters that optimizing the decorrelation metric alone could not explicitly account for (Table 20).

Table 20 *- OED statistical results using the decorrelation criterion for optimization. Results are summarized for the best repetition (out of 3 independent realizations) for each experimental configuration.*

Experimental Configuration	Decorrelation Criterion	Θ	ε	ε_a	η_1 (μ_{max})	η_2 (K_s)	η_3 (Y)	η_4 (k_d)	η_5 (n)
Batch	0.923	7.24E39	1	0.999	2.55	2.29E06	43.8	1.54	4855
Fed-Batch	0.823	7.53E21	1	0.997	2.68	1.13E04	30.0	1.54	127
Chemostat	0.976	2.01E18	1	0.994	3.31	1.86E03	25.0	1.54	79.7
CSTR	0.878	2.86E17	1	0.994	2.45	3.58E03	9.65	1.56	42.6

Similar to results presented in the previous section, the fed-batch reactor was able to decorrelate the model parameters to the greatest extent (Table 20). However, the difference in magnitude of the optimal decorrelation criteria reached was quite similar among the experimental configurations presented in Table 20. This result may suggest that the experimental configuration may have less of an effect on controlling correlation among parameters as compared to statistical certainty. In addition, the use of the chemostat was observed to reduce correlation among model parameters the least, which was contradictory to the results observed for the D-criterion optimization.

As compared to the optimal experimental conditions obtained using the D-criterion, the use of the decorrelation criterion resulted in initial concentrations of substrate and

degrading cells that were considerably higher, especially for the batch and fed-batch configurations (Table 19 vs. Table 21). For both the batch and fed-batch configurations, the initial concentration of degrading cells was approaching the theoretical practical limit of 1000 mg/L, where lower values of the decorrelation criterion may have been achieved if this limit was increased. In addition, the magnitude of the initial concentrations of substrate and degrading cells were quite similar for the optimization involving the decorrelation criterion as compared to the D-criterion (Table 21). Moreover, the optimal dilution rates obtained from the decorrelation criterion experiments were much smaller as compared to the previous experiments with the D-criterion (Table 21).

Table 21 *- Initial conditions and experimental design criteria obtained using the Decorrelation criterion for optimization. Results are summarized for the best repetition (out of 3 independent realizations) for each experimental configuration.*

Experimental Configuration	C_0 **(mg/L)**	X_0 **(mg/L)**	V_0 **(L)**	D **(1/day)**	C_f **(mg/L)**	X_f **(mg/L)**
Batch	697	999.8	-	-	-	-
Fed-Batch	774	999.5	0.221	-	38.6	-
Chemostat	456	233	-	0.505	1.47	-
CSTR	203	0.536	-	0.0483	13.7	1224

The efficacy of the decorrelation optimization scheme to reduce the correlation existing between model parameters can be observed visually in Figure 61 that depicts the correlation matrices for optimal fed-batch experiments using either optimization criteria. Correlations between parameters Y and n were significantly reduced when using the decorrelation criterion for single objective optimization (Figure 61). In addition, correlations between μ_{max} and Y as well as μ_{max} and k_d were reduced to a noticeable extent when applying the decorrelation criterion as an objective function (Figure 61). However, there was a slight increase in the correlations existing between μ_{max} and K_s as well as

between k_d and n when optimizing using the decorrelation criterion instead of the D-criterion (Figure 61).

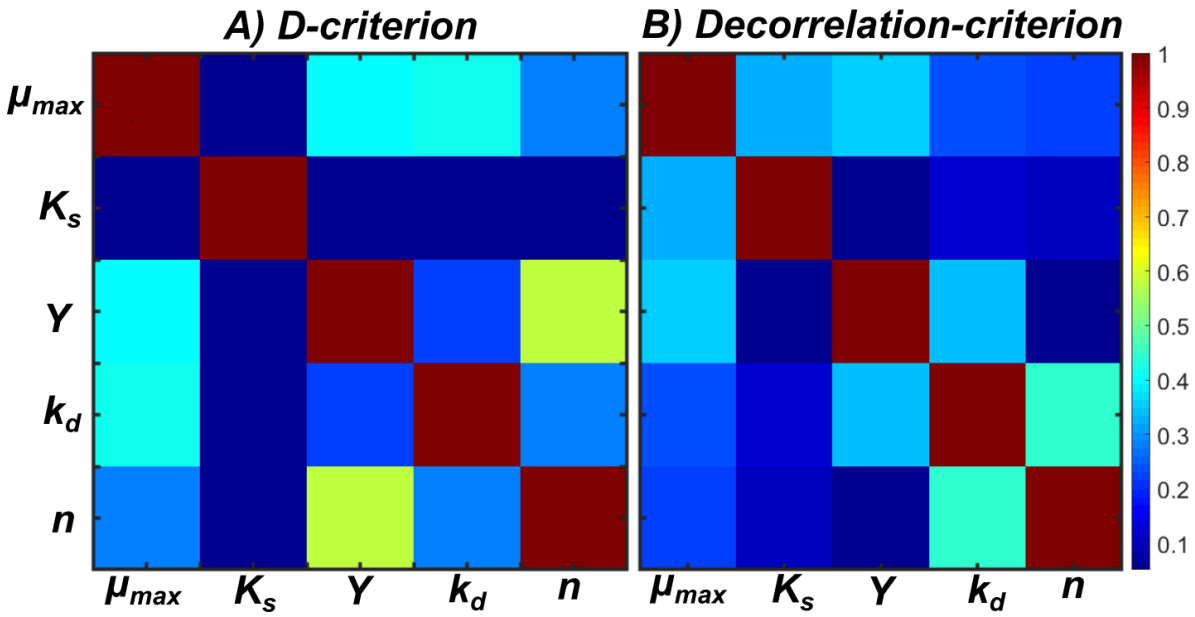

Figure 61. *Comparison of the parameter correlation between optimal fed batch experiments achieved from single objective optimization using either A) the D-criterion or B) the decorrelation criterion as objective functions to maximize or minimize. The color scale (blue to red) reflects the magnitude of Spearman's correlation coefficient (ranging from 0-1) between model parameters.*

Again, simulations of the optimal experimental design (for the fed batch reactor configuration) were visualized for all relevant parameter combinations used in the GSA analysis for the decorrelation criterion optimization scheme (Figure 62). Compared to Figure 60 (using the D-criterion), the simulations that attempted to decorrelate the model parameters appeared much less dynamic (Figure 62). In the previous D-criterion experiments, both substrate and cell concentrations were observed to increase for much of the experiment; however, both substrate and cell concentrations were observed to decline in the decorrelation run of experiments (Figure 62). As noted by the large uncertainty regions, there was still some variability in the OED simulations when predicting cell concentrations across the different parameter combinations used for the GSA (Figure 62). In addition, the feed rate profile was observed to maintain several sharp

pulses (both at the onset, Day 1, and towards the duration of the experiment, Day 7), which was different than the series of step pulses observed for the D-criterion experiments around days 6-8 of experimentation (Figure 62D). Lastly, the liquid volume of the reactor was observed to increase past the theoretical limit of 1 L, which was due to the higher magnitude of the feed rate pulses (up to 35 mL/hr) applied for the decorrelation criterion experiments over the D-criterion experiments.

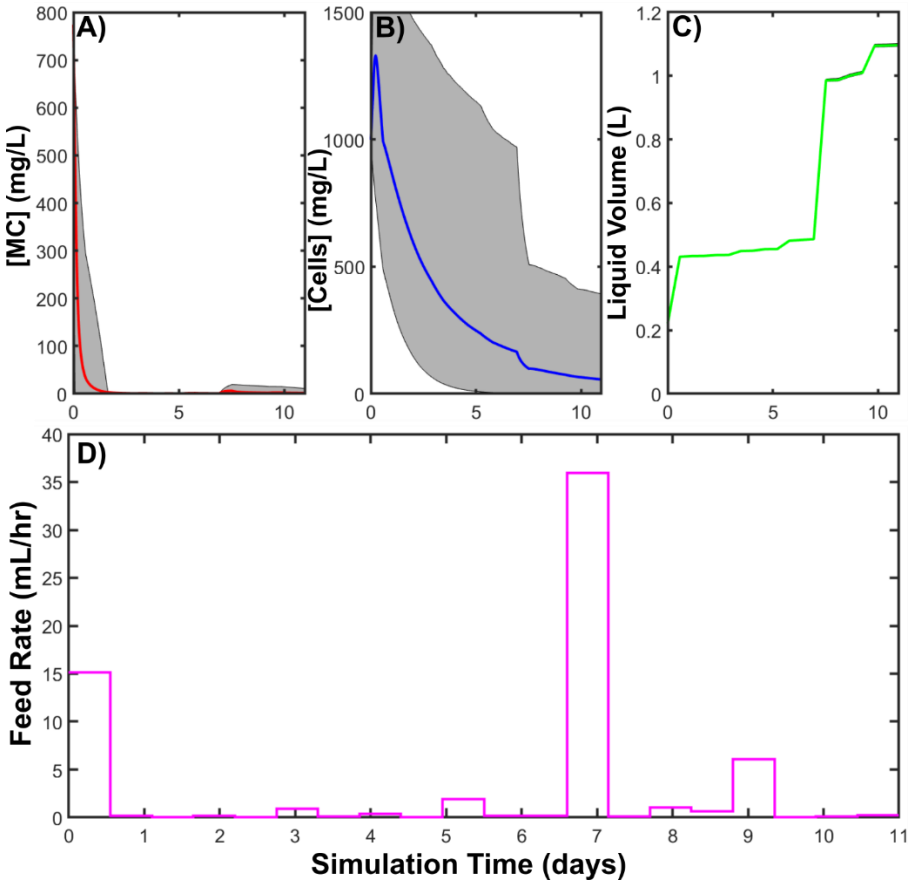

Figure 62. *Simulated optimal experimental design for the fed-batch reactor configuration using the decorrelation-criterion for single objective optimization. This figure displays the predicted MC concentration, degrading cell concentration, and liquid volume of the reactor system as a function of simulation time. The red, blue and green lines represent the mean predictions across 8192 different parameter combinations used in the GSA, while the grey region indicates the 95% CI achieved across all 8192 model predictions. Panel D portrays the optimal feed rate profile of the fed-batch reactor system.*

3.2.3 Multi-Objective OED Results

The multi-objective OED results indicated that the fed-batch reactor configuration produced the best tradeoff between maximum information content and minimum correlation among input parameters as the pseudo volume of the hyper ellipsoid was lowest and the confidence interval lengths were, on average, smallest out of all experimental configurations tested (Table 22). Although the pseudo volumes of the confidence ellipsoids were reduced from the decorrelation, single objective optimization experiments, they were still very high compared to the D-criterion optimization experiments, indicating that the Pareto fronts were possibly more biased towards reducing parameter decorrelation over maximizing information content. This observation was supported by the fact that the diversity of solutions along the Pareto optimal front for each experimental reactor configuration was very unstable (and still did not converge after 5000 generations for most runs) (Figures F7 and F8).

Even though the fed-batch experimental configuration produced the best tradeoff OED, the eccentricity and parameter uncertainty concerning the Y parameter were still relatively concerning for the OED of the fed-batch reactor to be considered a valid Pareto tradeoff solution. This inconsistency was most likely due to the multi-objective optimization requiring a larger number of generations for the Pareto front to formally converge than what was conducted in this study (i.e., 5,000 or more required compared to only 1,000 conducted). This inconsistency was further confirmed when comparing the D-criterion optimization results to the multi-objective results, in which the decorrelation criterion was lower for the single objective results (0.8659 compared to 1.10). On the other

hand, the optimal Pareto fronts for all other experimental configurations were observed to converge when monitoring the hypervolume, R2 and delta convergence indices (Figure F8).

Table 22 *- OED statistical results using multi-objective criteria for optimization. Results are summarized for the best repetition (out of 3 independent realizations) for each experimental configuration.*

Experimental Configuration	**D-Criterion**	**Decorr. Criterion**	$\boldsymbol{\Theta}$	$\boldsymbol{\varepsilon}$	$\boldsymbol{\varepsilon_a}$	$\boldsymbol{\eta_1}$ (μ_{max})	$\boldsymbol{\eta_2}$ (K_s)	$\boldsymbol{\eta_3}$ (Y)	$\boldsymbol{\eta_4}$ (k_d)	$\boldsymbol{\eta_5}$ (n)
Batch	4.23 E-07	1.22	5.30 E20	1	0.987	5.38	1.65 E04	2.47	1.44	27.0
Fed-Batch	1.82	1.10	7959	1	0.899	3.50	5.25	21.7	1.41	5.91
Chemostat	0.295	1.01	27790	1	0.935	6.32	2.87	9.96	1.69	23.4
CSTR	0.37	1.08	66477	1	0.922	7.01	2.40	7.33	1.77	34.2

Table 23 summarizes the initial conditions and experimental design criteria obtained from the multi-objective optimization framework. These experimental design results appeared to be somewhat in line with those obtained for both the D-criterion and decorrelation criterion experiments. For example, the initial substrate to cell concentration ratios for the batch and fed batch configurations were approximately the same when comparing the decorrelation results to the multi-objective results, albeit the initial concentrations were somewhat smaller for the multi-objective optimization results (Table 19 vs. 23). Initial conditions (concentrations of substrate and biomass) for the chemostat and CSTR were comparable to those obtained for the D-criterion optimization results (i.e., very low concentration of cell biomass compared to the concentration of substrate).

Table 23*- Initial conditions and experimental design criteria obtained using the multi-objective criteria for optimization. Results are summarized for the best repetition (out of 3 independent realizations) for each experimental configuration.*

Experimental Configuration	C_0 (mg/L)	X_0 (mg/L)	V_0 (L)	D (1/day)	C_f (mg/L)	X_f (mg/L)
Batch	165	539	-	-	-	-
Fed-Batch	75.4	137	0.0109	-	0.855	-
Chemostat	357	0.000141	-	1.40	0.279	-
CSTR	885	3.49E-06	-	2.06	0.268	0.0250

The simulations of the OED achieved from the multi-objective optimization framework (for the fed batch reactor configuration) are depicted in Figure 63. Compared to the other experimental designs obtained from the single objective criteria, the simulations for the multi-objective results were the least dynamic, where the substrate concentration is observed to decline in a first order fashion, whereas the MC degrading cells grow slightly, then decay for the remaining duration of the experiment (Figure 63). The liquid volume within the reactor was observed to increase exponentially during the latter portion of the experiment and plateaus around 10 days at a volume well below the upper limit of the volume of the reactor (1 L was the upper limit). The magnitude of the feed rate was larger than that obtained for the D-criterion experiment (but similar in magnitude to the decorrelation experiment), where the feed rate profile demonstrated a 3-step pulse during days 8-10 of the experiment (Figure 63).

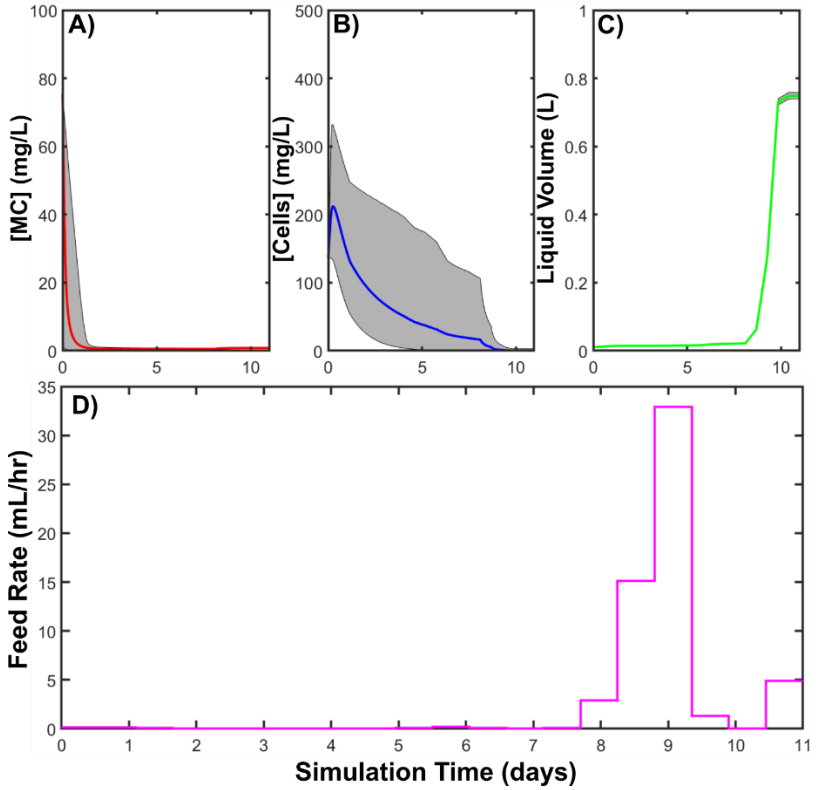

Figure 63. *Simulated optimal experimental design for the fed-batch reactor configuration using the multi-objective for single objective optimization. This figure displays the predicted MC concentration, degrading cell concentration, and liquid volume of the reactor system as a function of simulation time. The red, blue and green lines represent the mean predictions across 8192 different parameter combinations used in the GSA, while the grey region indicates the 95% CI achieved across all 8192 model predictions. Panel D portrays the optimal feed rate profile of the fed-batch reactor system.*

3.2.4 Comparison of the OEDs to an Uninformed Experimental Design

In this section, we compare the best overall OED returned by the fed-batch reactor experimental configuration to that of an uniformed batch reactor experiment to demonstrate the extent of improvement in model parameter statistical certainty. The uniformed experiment was modelled directly after Xiao and coworkers (2011) study, examining the batch degradation of MC-LR by an isolated *Sphingopyxis sp.* USTB-05.The experimental design of this particular study (C_0 = 28.8, X_0 = 7.39 mg/L) resulted in the

worst parameter identification for the Moser model (out of four studies) after a fully Bayesian model comparison and selection procedure was conducted.

As observed in Figure 64, the parameter uncertainty was considerably reduced through implementation of the fed-batch OED achieved in this study. The confidence ellipses were observed to be orders of magnitude smaller for the informed experimental design as compared to the uninformed experimental designs, for all parameter combinations (Figure 64). This improvement was especially apparent for the μ_{max} and n as well as the k_d and Y model parameter combinations, where the uninformed experiments demonstrated a significant positive and negative correlation structure (Figure 64, subplot 3 and 8). However, application of the optimal OED almost eliminated the parameter correlation and greatly reduced the area of the ellipse when projected onto the 2D plane. This result was promising as μ_{max} and k_d were both identified to be very influential parameters when predicting substrate removal and bacterial growth kinetics. However, as indicated in Figure 64, subplot 9, there was still some residual correlation between Y and n model parameters for the informed OED using the fed batch configuration. In addition, although the projected area of most of the confidence ellipses was reduced through the informed OED, some of the ellipses were marked by high eccentricity, signifying that the parameter certainty was not uniformly distributed among all of the model parameters (Figure 64, subplot 1, 5, and 6).

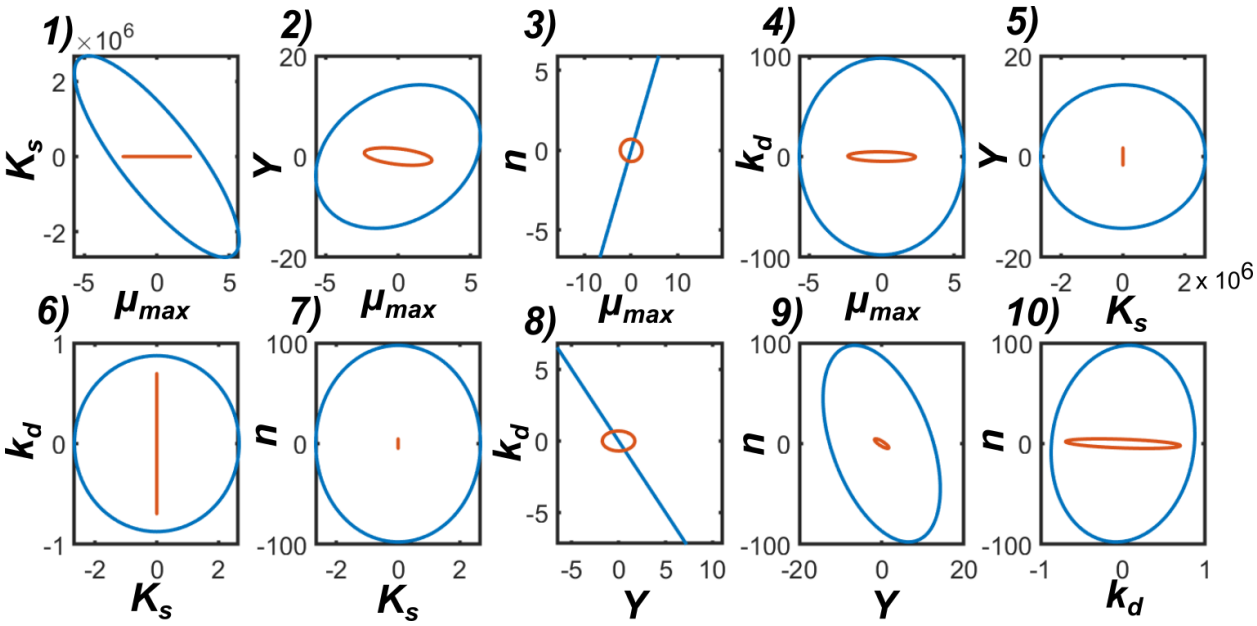

Figure 64. *Comparison of 95% confidence ellipses returned for an uniformed batch experiment (blue) and a fed-batch configuration OED (blue).*

Table 24 quantitatively demonstrates that the informed experiment using the fed batch reactor leads to a substantial reduction in pseudo-volume of the 95% CI hyper ellipsoid of the parameter certainty, which varied by approximately 37 orders of magnitude. The length of the confidence intervals were considerably higher for K_s and n model parameters for the uninformed experiment as compared to the informed experiment. Moreover, critical differences in both FIM singular criteria were observed, where the D-criterion is approximately 16 orders of magnitude larger than the uninformed batch experiment. The results help solidify the notion that model based design of experiments can considerably improve the information content of experiments for improved parameter identification.

Table 24 *- Comparison of the OED statistical results between the informed (fed batch reactor) and uninformed (batch reactor) experimental designs.*

Experimental Configuration	D-Criterion	Decorr. Criterion	Θ	ε	ε_a	η_1 (μ_{max})	η_2 (K_s)	η_3 (Y)	η_4 (k_d)	η_5 (n)
Batch (uninformed)	9.30E-15	1.998	1.22 E37	1	0.991	10.99	5.17 E06	27.5	1.68	188
Fed-Batch (informed)	19.1	0.8596	5.40	0.944	0.760	4.54	3.50	3.26	2.19	6.49

4. Discussion

4.1 Study Contribution

This is the first study, to the best of our knowledge, to apply global optimal experimental design principles to improve the parameter identification of unstructured kinetic models describing microcystin biodegradation. Compared to uninformed experimental designs, the application of OED experiments can produce experimental datasets that drastically increase the information content, substantially reduce parameter correlation, and greatly improve overall parameter identification. The results demonstrated that through the best OED achieved, all parameters could be successfully identified, as the rank of the resulting FIM was equivalent to the number of model parameters. Overall, the resulting statistical variance of the estimated parameters was relatively uniform and low in magnitude, and the highest uncertainty for the best OED was observed for both μ_{max} and n model parameters. Improvements could be made targeting the eccentricity of the confidence ellipses achieved from all OEDs, which could be resolved by minimizing, in a multi-objective framework, the modified E-criterion (i.e., the condition number of the FIM) along with the D-criterion and decorrelation criterion applied in this study. This framework would theoretically allow for improved uniformity in the confidence region obtained for all parameter estimates.

More importantly, it was observed that accounting for different metrics during optimization, such as the information content or decorrelation criteria, produced considerably different estimates of the statistical parameter confidence region. This result is in agreement with other OED studies, in which OED experiments were observed to differ according to the objective function used during optimization (Telen et al. 2012, Maheshwari et al. 2013). Although explicitly accounting for both objective functions in a multi-objective framework showed to

provide some tradeoff between both criteria, the information content was still not as high as that achieved by the single objective experiments targeting the D-criterion during optimization. This result signified that the magnitude of the reduction in parameter decorrelation was generally not proportional to the information content gained from the OEDs returned by the tradeoff solutions from the multi-objective framework. Thus, in the case of the Moser model, it may be better to rely on one criterion in a single objective framework to obtain reliable experimental designs, as the relative degree of parameter correlation was observed to indirectly decrease when the information content of the experiments was maximized.

4.2 Optimal Experimental Design: From Theory to Practice

Even though the statistical results were promising, it is important to make clear that the fed batch experiments proposed in this study were not easy to carry out in practice (especially when working with MC) and are subject to some practical limitations (Cappuyns et al. 2007). To highlight the practical limitations identified with the experimental designs proposed, we will examine the initial conditions of the best OED for the fed-batch experimental configuration. Given the initial volume of 0.00041 L identified by this OED, the initial biomass that should be inoculated into the reactor concentrations is extremely low, on the order of 0.0418 μg of cells. In practice, it may be quite difficult to measure the biomass of MC degrading cells (using the ATP method) down to the sub μg level and with the desired precision. This would involve a complicated dilution procedure that may not be practically feasible. Similar difficulties would be expected for the initial MC concentration, where optimal initial conditions required inoculating 0.352 ug of MC into the reactor system.

The theoretical constraints of the experimental conditions that could be applied in practice was also relatively arbitrary in this study. As of current, no studies have actually measured the biomass of these degrading organisms when grown on MC as the sole carbon and energy source. We limited the upper bound of the initial biomass concentration in all experiments to 1 g/L, which seemed reasonable given that MC may not be a preferential carbon source in the environment for many of these organisms. In addition, a previous study by Manheim and coworkers (2018) demonstrated that biomass growth was relatively insignificant when a degrading community was supplied with 200 μg/L of microcystin, suggesting that this MC as a substrate may be suboptimal for rapid and intensive bacterial growth. When setting this theoretical upper bound on the initial experiment conditions, it will be important to consider what substrate (MC) concentration threshold actually results in saturation of bacterial growth for different degrader populations, as there is a theoretical biomass that can be derived assuming this limiting concentration.

Similarly, due to the high adsorption potential of microcystin on most plastic materials, the experimental equipment will require either glass, stainless steel, or Teflon tubing and fittings (Hyenstrand et al. 2001a, 2001b). Investing in this type of hardware and finding the correct fittings could become expensive and difficult when considering the practical application of these experiments. Moreover, the price and availability of pure MC may limit the practical applicability of these experiments, as MC is notoriously difficult to isolate and extract from toxic cyanobacterial cultures (Ramanan et al. 2000, Lawton and Edwards 2001). However, if proper attention is not given to these small details, there could be substantial losses of MC due to adsorption alone. Lastly, it will be critical to keep the

feed lines sterile during the fed batch experiments. In practice, as the feed rate is varied over several orders of magnitude, there is a chance that bacteria can enter and contaminate the feed line from the batch reactor chamber, especially if the feed rate is kept below the optimal specific growth rate. To avoid potential contamination the inlet to the reactor can be fixed with a non-reactive filter of fixed pore size (with material that limits adsorption of MC and bacterial cells) that prohibits bacterial contamination but ensures the same feed rate profile as initially designed.

Lastly, there are theoretical considerations concerning the OED of the feed rate profile that should be taken into consideration as to avoid violation of unstructured kinetic model assumptions. In this study, we found that the optimal feed rate profile was quite dynamic around 7-10 days of experimentation. The feed rate profile was observed to have a very high gradient for this part of the experiment, which may violate the assumption of balanced growth upheld by the Moser model. This assumption states that the environmental conditions are not changing too rapidly as to induce large variations in the physiological composition of a bacterial cell. Ultimately, if the feed rate profile is too dynamic, it may induce fast, non-physical dynamic physiological responses of the bacteria cells that are not described by unstructured kinetic models (Baltes et al. 1994, Versyck and Impe 1998, Cappuyns et al. 2007). It is unknown in this study to what extent the gradient presented for this experimental design obeys or disobeys the constraints of unstructured kinetic models, but it certainly is a valid topic for future study.

4.3 General Statistical Considerations of the Validity of the OED Performed in this Study

The OED procedure performed in this study made several simplifying statistical assumptions that must be adequately recognized and discussed. First and foremost, due to lack of information concerning the variability of experimental measurements (for substrate and cell concentrations), we assumed that: 1) the measurement noise of both the substrate and cell concentration measurements in the derivation of the FIM were equal (i.e., standard normal distribution – 0 mean and unit variance); 2) measurement noise was homoscedastic; and 3) that there was no covariance among the measured variables. This may not be the case in practice, as it is expected that the measurement noise associated with cell biomass measurements should be greater in magnitude than substrate concentration measurements. For example, measurements of MC degrading cell density using colony counts (CFU/mL) or even optical density was quite noisy in practice (where replications are generally few and far between) (Valeria et al. 2006, Wang et al. 2010, Xiao et al. 2011). Although our simulated experiments assumed that cell biomass was determined using ATP measurements (which is considerably more accurate and marked by higher precision than the aforementioned methods) there is still uncertainty regarding the conversion from ATP content to cellular carbon (dry weight) content in which this series of OED experiments did not explicitly address. In this conversion, two metrics are needed, one to convert ATP concentrations to cell concentrations (ATP/cell), then another to convert from cell concentration to biomass (cell/biomass). A similar conversion factor, used to convert OD to dry weight, was shown to influence the uncertainty of model predictions in a previous study (Manheim et al. 2019), where correlations were observed between this conversion factor and other influential model parameters. Thus, future studies should

address to what extent these conversion factors contribute to the overall parameter and model predictive uncertainty of the Moser kinetic model.

The assumption of homoscedasticity of the measurement error for both variables as well as covariance among state variables are also important factors to consider. From practical experience, it is expected that as the concentration of a species of interest increases, the measurement noise associated with the given measurement system or technique should also increase accordingly (Holmberg 1982). Thus, the measurement error should theoretically decrease over the simulated experiments for substrate concentrations (as substrate is removed from the system) and increase over the simulated experiments for biomass concentrations (as growth is expected). However, the assumption made in this study neglected this heteroscedasticity in measurement error over time. Furthermore, in future studies, it may be important to account for covariance among observed variables, as state variables in many experiments have been known to covary (where explicit assumptions have been made to account for this covariance during ML optimization, Knightes and Peters 2000, 20003). In our defense, making these statistical adjustments was deemed difficult and perhaps unnecessary without actually having performed an experiment using the measurement methods specified and acquiring practical expertise with the measurement systems relied upon. We further highlight that these adjustments can be made by simply changing the specifications of the weighting matrix (W) during formulation of the FIM (i.e., $FIM = S' * W * S$).

4.4 Specific Considerations of the Validity of the OED Performed in this Study

It is important to first highlight that the parameter uncertainty bounds for the global sensitivity analysis performed in this study were relatively wide compared to that expected

in practice. We specifically maintained the bounds of the parameter uncertainty to the feasible space determined for four different isolated bacterial populations degrading MC, as we were interested in a holistic understanding of the generalized experimental conditions that would result in improved parameter identification encompassing all potential degrader populations (Manheim et al. 2019). In experimental practice, the feasible parameter space will be much narrower than that applied herein (as the experiments will be conducted for an individual population of bacteria), especially if an initial, uninformed experiment is conducted, and a Bayesian posterior distribution in parameter estimates can be obtained prior to performing the optimal experimental design.

Incorporating a wider parameter uncertainty interval was observed to produce some strange artefacts in the optimization process. For example, the dynamic sensitivity estimates were observed to change to some degree when different QMC samples were used, which resulted in somewhat different estimates of optimal experimental designs among the independent realizations performed (when the sample size was fixed at 8192). Even though a sufficient number of samples was chosen for each of these GSA sensitivity indices to converge, there were still differences in the time varying sensitivity estimates among different QMC samples. This result may be due to the wide range in parameter combinations obtained for each QMC sample set. In addition, the solver sometimes encountered parameter combinations that were mathematically infeasible to solve and produced results with complex number sets. These solutions were ultimately thrown out of the GSA when conducting the OED optimization and may have affected the results, to some degree.

It is more likely that differences in the OED experiments achieved from different QMC sample sets may be due to issues with the structural identifiability of the Moser model. Through application of the GenSSI generating series approach, it was clear that the Moser model was locally, structurally identifiable. This result signified that there were multiple parameter combinations that could have been optimal for a given experimental design, which was a result of the high dependency at play between model parameters. Therefore, this result shows that there was not a "global" OED solution across the objective space analyzed and that, potentially, there were multiple OEDs that produced similar improvements in parameter identification. This result helps to prove that faults with the model structure, as opposed to details of the practical identifiability analysis, led to the observed differences in OEDs achieved from independent realizations utilizing different QMC sample sets.

In order to perform each of the OEDs in an acceptable time frame (3-4 day period), the absolute and relative tolerances of the *CVodes* solver had to be adjusted to find an optimal balance between accuracy and efficiency. In this study, we found that a relative tolerance of 1E-3 and an absolute tolerance of 1E-6 provided the best balance between accuracy and computational efficiency. Running with these tolerances on multiple cores and in parallel implementation (up to 32 cores) greatly improved the speed of these simulations. However, the tolerances used may have resulted in model predictions that were sub optimal for some parameter combinations, which may have also increased the uncertainty of the results obtained. Future studies should consider comparing OEDs returned when different tolerances are set by the user to ensure that little numerical discrepancies exist between resulting simulations.

Furthermore, it is important to note that the confidence ellipses were developed based on the Cramér-Rao bound, which may be unreliable in the case of highly non-linear models (such as the Moser model), as the FIM is derived from linearization of the least squares optimization of the parameter values (Balsa-Canto et al. 2008). Thus, to reliably evaluate to what extent the OED improved parameter identification in this study, a robust identifiability analysis (RIA) could be carried out (Balsa-Canto et al. 2008). The basis of this RIA analysis is to perform a Monte Carlo analysis, where many different experimental datasets are simulated using the optimal design criteria determined from the OED step and a randomly selected parameter combination. In addition, the experimental datasets are simulated assuming some theoretical measurement noise. The objective of this analysis is then to perform repeated model calibration efforts to arrive at an empirical parameter cloud that describes the joint confidence region of the parameter estimates. Although this analysis is more robust than the statistical analysis performed in this study, the main drawbacks are that it is very computationally intensive to perform a large number of model calibrations (> 10000) using a reliable global optimization scheme.

Lastly, this study did not explicitly address improvements in the experimental design that could be reached through considering the sampling times and frequencies of each experiment. It is likely that the OED could have been further improved if the sampling times were optimized along with the sampling frequencies of each experiment. In this study, we assumed the sampling times were uniform and conducted on daily (24 hr) intervals. However, in practice, once an OED is reached, it may be necessary to further determine which sampling times and frequencies result in experiments with maximal information content and minimal parameter correlation. Importantly, this step can be

conducted independently of the initial OED to determine the initial conditions and relevant design parameters to ensure that the optimization process is as efficient as possible, as inclusion of sampling times/frequencies may significantly expand the dimensions of the feasible search space (i.e., optimizing 8 design variables is more efficient as opposed to 16 variables).

5.0 Conclusions

This study has successfully applied both a structural identifiability and OED principles to improve parameter identification of the Moser model for describing MC biodegradation. The Moser model was determined to be structurally, locally identifiable, indicating that a finite number of optimal parameter solutions are possible when calibrating a given model for a certain experimental condition. The practical identifiability analysis determined that a fed batch experimental configuration with a dynamic feed rate profile was optimal over all other experimental configurations reviewed. The use of a multi-objective framework allowed the determination of an OED that resulted in a tradeoff between maximal information content and minimum correlation among model parameters. The application of this OED was demonstrated to significantly improve the parameter certainty of the Moser model as compared to a simple, uninformed batch reactor experiment. However, it is important to note that achievements in statistical certainty of the model parameters can only be realized if the practical constraints on running the OED can be overcome. The practical identifiability analysis of the Moser model was observed to be affected by the structural identification properties of the model, in which independent realizations of the same optimization problems utilizing different QMC sample sets

converged to multiple global minima. Overall, it is expected that the improved confidence in the parameter estimates will greatly improve the overall predictive certainty of the Moser model predictions.

MAIN CONCLUSIONS AND FUTURE DIRECTIONS

Biological drinking water treatment strategies targeting the removal of algal biotoxins, such as biological filtration, offer the potential to provide safe drinking water during harmful algal bloom periods at a fraction of the cost of current advanced physico-chemical methods and with the goal of sustaining the environment in mind. This dissertation has provided ample evidence that individual bacterial populations as well as more complex microbial communities isolated from natural lake or reservoir environments can effectively degrade microcystin, one of the most common and toxic algal biotoxins produced during these harmful bloom events. However, the kinetics of treatment (on the order of days) and variability in environmental conditions such as temperature, pH, availability of exogenous nutrients, and microbial community composition, have challenged the advent of biofiltration in full scale drinking water treatment practice.

Ultimately, developing a more stable and robust bio-based drinking water treatment system relies on improving our predictive understanding of the microorganisms involved in microcystin biodegradation. If the eventual goal is to fully "engineer" these treatment systems and to target the complete removal of algal biotoxins from drinking water, we must be able to successfully model how these bacterial communities grow, interact with one another, and respond to the surrounding environmental conditions and the presence of other higher trophic order organisms (i.e., protozoa). The bottom line achieved from preliminary research was that the use of simple zero or first order kinetic models were not descriptive enough to further this predictive understanding of microcystin biodegradation and that more advanced models needed to be developed and applied. Clearly, as was demonstrated in this dissertation research, developing a comprehensive and practical

model describing any biological based treatment system is an extremely complex (perhaps lifelong) task and depends on first understanding many different factors, ranging from comprehension of the structural or practical identifiability of a given model to Bayesian model selection and optimal experimental design.

Overall, there were four main modelling approaches applied in this dissertation that were geared towards improving the current predictive understanding of the microorganisms involved in microcystin biodegradation: a) a holistic, systems approach; b) a top down approach; c) a mechanistic approach; and D) a bottom up approach. Each of these models was developed or applied to answer some very specific questions ranging from microcystin biodegradation on a cellular level to the larger fate and transport of these biotoxins in drinking water treatment systems. In this section, we shed some light behind the main conclusions drawn from each study and offer some food for thought for future research direction.

The holistic, system modelling approach, where a probabilistic materials flow analysis was conducted for a SWRO facility on a larger scale of analysis, was shown to be very useful to answer questions as to the fate and transport of these toxins within drinking water treatment facilities and the potential human health effects from ingesting treated drinking water during harmful algal blooms periods. The modelling results indicated that the treatment system configuration and operational practices considered had a statistically significant impact on the removal and fate of algal biotoxins within these facilities, where minimal acute human health effects were predicted due to the reliance on reverse osmosis membranes as a final treatment step. The uncertainty of this system model was perhaps the highest out of all the models developed or applied in this research, as many logical

assumptions were made concerning the removal efficiency of these toxins in various treatment systems as well as the algal toxin loadings (i.e., intracellular toxin content), and cell breakage experienced in these mechanized treatment systems.

Future studies related to this system modelling approach should consider acquiring experimental data from these facilities (i.e., measuring biotoxin concentrations) at different steps of the treatment train to first corroborate model predictions presented in this study. Moreover, routine monitoring of the algal composition and toxin loadings to these facilities is a key factor to further reduce the uncertainty of the system model developed. In addition, this system modelling framework can be applied to freshwater drinking water treatment systems targeting cyanobacterial biotoxin removal. Since these facilities do not rely on RO treatment systems, it would be interesting to apply this probabilistic modelling approach to reevaluate the acute, and even chronic, human health effects from ingesting treated drinking water during HAB periods. What is more, predicting to what extent drinking water treatment operations must prepare themselves in the future to combat the harmful effects of climate change and the increasing frequency and intensity of these blooms is critical to address.

The "top-down" or community scale modelling approach refers to the metagenomic study of several microcystin degrading bacterial communities (Chapter 2), which focused on understanding the degradation kinetics and taxonomic identity of the community members. In this study, we isolated several natural bacterial communities that possessed the ability to degrade microcystin and exposed these communities to an alternative, readily bio-available organic carbon source (i.e., ethanol) to evaluate the relative stability of these communities to external environmental factors. The 16S rRNA

pyrosequencing analysis also provided insight as to how, taxonomically, the communities were changing under this environmental pressure. It was found that these communities were extremely sensitive to the presence of an alternative organic carbon source other than microcystin, in which the diversity and microcystin degradation kinetics declined to a statistically significant extent. The taxonomic composition of each community consisted of both microcystin degrading and non-degrading community members, where exact identification or differentiation of the presence or quantity of each population within these greater factions was lacking. An unstructured kinetic model was applied to model the degradation half-lives of microcystin mediated by the entire community. Although the kinetic model was able to reproduce the bi-phasic degradation of each community, it could not account for important mechanisms such as higher order community member interactions or substrate competition (i.e., between microcystin and ethanol) within microcystin degrading bacterial populations.

Future directions for this research should first aim at improving the isolation and culturing process of the microcystin degrading communities. The reliance on a batch culturing system and a chemically defined medium for cultivation of each community was considerably far removed from actual settings in the environment. Firstly, application of a batch system for culturing resulted in unintended shifts in the community composition, where, as the number of sub-cultures progresses, the more the community will select for more "fit" community members, which will eventually dominate over the natural population. The use of a continuous culture system (i.e., a chemostat) from the onset of isolation should allow a more refined and representative look into the taxonomic membership of microcystin degrading communities present in the environment. In this

study, there was little observable growth of each community on microcystin as the sole organic carbon source, which is again atypical of environmental settings. Therefore, the chemically defined medium could be replaced with filtered (sterile) lake water, that has key, albeit low levels, of organic carbon to help bolster the growth of these microorganisms to simulate natural conditions (i.e., Li and Pan 2014). Furthermore, in addition to 16S rRNA, the use of 16S shotgun sequencing should be pursued to identify the key metabolic fingerprints of each community. This analysis should be conducted in conjunction with the *mlrA* quantitative gene profiling of each community to gain further insight into what task each member is performing and how community members may be interacting. Finally, a more complex, or top down modelling approach based on dynamic flux balances of the bacterial populations (i.e., Song et al. 2014) within each community will help link experimental data with an improved, predictive understanding of each microcystin degrading community.

The development of a mechanistic model to describe biofiltration of microcystin toxins was, unlike the previous kinetic models, focused on the inclusion of all the important underlying mechanisms affecting the fate, transport, and degradation of microcystin within a theoretical biofilter. The steady state, numerical model developed in this research was focused on predicting the physical-chemical and biological removal of microcystin in the filter along with growth, decay, and transformation of aqueous and solid bacterial biofilms, both of which were comprised of microcystin degrading and non-degrading populations. Importantly, the growth kinetics of aqueous and solid biofilm components were differentiated in the model structure, and the model only accounted for growth, decay, and transformation of microcystin degrading populations out of the total bacterial populations

present. In addition, the physical-biological feedback mechanism of "bioclogging" was explicitly modelled to determine to what extent the formation of the biofilms was altering the hydraulic conductivity within a hypothetical biofiltration treatment system. A 1D version of this numerical model was developed and successfully verified against a series of analytical solutions. Initial experimental efforts were conducted to calibrate several physical transport parameters of the model, including parameters related to physical-chemical adsorption and dispersion. However, initial model predictions could not be achieved since the remaining model parameters describing transport and growth of the degrading bacteria were unknown and subject to future calibration.

In addition to experimental investigations targeting the calibration of the biokinetic parameters describing growth, decay, and transformation of aqueous cells and solid biofilms containing microcystin degrading populations, the numerical model should be expanded to include at least two dimensions. The drawback of the current model is that it cannot account for fluid transport in the lateral direction of the biofilter, which will be very important to consider when bioclogging prevents fluid flow vertically in some areas of the simulated filter. Of course, expanding the model to 2D will require an additional run of model verification experiments to ensure that all elements of the numerical solution are functioning as expected (in terms of accuracy and stability). Lastly, in order to make informed predictions of the removal of microcystin toxins within biofilters, the numerical model will be validated against a series of 2D, laboratory-based flow cell experiments, in which the bacterial growth can be visually monitored and quantified for comparison of the numerical simulation with experimental results. Ultimately, this model can be applied to investigate certain operational conditions and design elements of biofiltration systems that

are favorable for microcystin removal and may provide insight as to which of these strategies may progress biofiltration systems from passive to more fully engineered treatment systems.

As a final attempt to improve the current predictive understanding of biological degradation of microcystin toxins, a bottom up modelling approach, commonly used in the fields of bioremediation and wastewater treatment (i.e., Alexander 1999, Tchobanoglous et al. 2003), was explored in this dissertation research. As compared to the top down modelling approach, the bottom up modelling approach focused on understanding how an individual bacterial population behaves within the greater community. This approach was found to be more advantageous and intuitive over the top-down approach since it allowed the model framework to start with the necessary complexity as a foundation and successively build upon this complexity to increase the practical utility. In this dissertation research, the ultimate goal was to develop a comprehensive and practical kinetic model to describe microcystin biodegradation by natural bacterial communities in the environment.

To lay an effective foundation for a practical kinetic model describing microcystin biodegradation, it was first important to comprehend the bacterial growth kinetics of isolated microcystin degrading populations. The adoption of unstructured kinetic models over structured kinetic models to describe cellular growth and substrate consumption was clear, as unstructured kinetic models are associated with a limited number of parameters, avoided unnecessary complexity, and were well established in the fields of bioremediation and water/wastewater treatment. Of the wide range in kinetic models available, the main challenge was determining which model structure was most appropriate when predicting microcystin biodegradation as well as arriving at accurate and precise estimates of the

model parameters. Thus, a fully Bayesian model comparison and selection approach was applied to compare the predictive accuracy and certainty of several prominent unstructured models describing microcystin biodegradation. The Moser model well reproduced several experimental datasets obtained from the literature, and up to 5 out of 6 model parameters were practically identifiable. Aside from model selection and parameter identification, the physical meaning of the model parameters was discussed, and the Moser model was presumed to be an important predictor of the rate-limiting enzymatic reaction involved in the first step of the linearization of the microcystin ring structure. This was an important observation, as unstructured kinetic models attempt to reconcile millions of potential enzymatic reactions that are catalyzed by the cell. This observation also provided a theoretical basis for the further investigation of more complex enzyme-kinetic models to describe the growth of microcystin degrading bacterial populations (Noel and Narang 2009). Furthermore, some important and inherent limitations of the Moser model were addressed, including the ability of this model to incorporate other physical mechanisms such as substrate competition, temperature, pH, as well as model interactions between community members using Lotka-Volterra predator-prey relationships.

Despite the progress made with model selection and parameter calibration, there were still lingering issues associated with parameter correlation and identification that needed to be resolved. In this way, the parameter sensitivity of the Moser model was explored in depth to ascertain techniques to improve parameter identification and to reduce parameter correlation. The development of a novel semi-parametric, global sensitivity analysis technique represented a preliminary attempt to improve the estimation of parameter sensitivities and to assess the overall predictive certainty of unstructured

kinetic models. The semi-parametric method was beneficial as it avoided the dependence of the sensitivity analysis on statistical moments of the output distribution and relied on a more direct and practical mathematical relationship between the model parameters and the model predictions. This method was shown to improve the overall accuracy and reliability afforded by existing, fully non-parametric approaches to moment independent, global sensitivity analysis. In addition, when applied to the Moser model, the resulting sensitivity indices were accurate and converged efficiently, where a small to moderate computational effort was required. Overall, this method refined the existing approach to model the joint probability distribution function of the model input parameters and the model predictions which is ultimately required for calculation of the moment independent sensitivity indices.

Optimal experimental design, which was yet another avenue for improving parameter identification of the Moser model, was examined in the final chapter of this dissertation research. In this final study, the structural and practical identifiability of the Moser model were investigated in detail through application of an analytical, generating series approach, and a global OED procedure focused on optimization of either singular or multiple criteria of the Fisher information matrix. This approach determined that the parameters of the Moser model were all locally, structurally identifiable meaning that non-unique, yet finite, optimal parameter combinations existed when calibrating a model using a dataset generated from any array of experimental and initial conditions. The practical identifiability analysis determined that the fed batch experimental configuration resulted in experimental datasets with both maximal information content and minimum parameter correlation. The experiments identified by this practical identifiability analysis were

observed to significantly improve the a priori statistical certainty surrounding the parameter estimates as compared to a uniformed batch experiment. Although these experiments were identified as harder to practically carry out, the reward in terms of improvements in overall model predictive certainty are expected to be well worth the effort for going through the initial a priori practical identifiability analysis. Future experiments will be aimed at replicating these optimal experimental designs with isolated microcystin degrading populations to verify if the predictions made by this preliminary practical identifiability analysis are in fact achievable.

Above all, transforming these bio-based treatment systems into truly engineered systems, where the treatment efficacy can be tightly controlled, relies on the notion of "reverse" engineering (Villaverde and Banga 2014). As a whole, this concept of reverse engineering is contrary to what is typically expected of Civil and Environmental Engineers, as we are not engineering a system to produce a given response but are "engineering" a response from the system of interest; more specifically, we are seeking to tightly control the environmental conditions as to improve microbial growth and metabolic activity directed towards the degradation of algal toxins. Thus, this notion of reverse engineering cannot be accomplished unless we fully understand how the system responds to a full range in environmental conditions, which can be facilitated by understanding how the building block of the system (the MC degrading bacterial cell) responds to an array of environmental stimuli. In this research, we have obtained some fundamental understanding of how the MC degrading bacterial cell will function in a controlled setting. However, expanding this knowledge to account for the plethora of environmental

conditions or microbial interactions affecting MC degrading bacteria in treatment practice still remains as the next piece of the puzzle to ascertain.

Although the research results presented in this dissertation have demonstrated that there are optimal models describing microcystin biodegradation, parameter sets, and experiments to go about better identifying the model parameters for more informed model predictions, it is likely that there will still be some deviation from the behavior observed in real world experiments. The bulk of this dissertation has been focused on reducing uncertainty through statistical means and trying to quantify the expected degree of deviation from real world data; however, one aspect that was generally missing was an opportunity to verify and validate the results of these model simulations and algorithms designed to reduce uncertainty on real world experiments. In general, it was cost-prohibitive to use microcystin for long term, steady state experiments and it was very difficult to extract and isolate enough microcystin toxin to use for these experiments. Unfortunately, this lack of microcystin for use in laboratory experiments halted many of the proposed experimental efforts, including complete calibration of the biokinetic parameters within the numerical biofiltration model. Thus, it is expected that future research on this subject will involve experimental efforts to help validate the theoretical results presented in this research and to provide a direct link to practical application in full scale drinking water treatment practice.

REFERENCES

Ahmad, R., & Amirtharajah, A., (1998), "Detachment of particles during biofilter backwashing," Journal of the American Water Works Association, 90(12).

Alagappan, G., and Cowan, R. M., (2004), "Effect of temperature and dissolved oxygen on the growth kinetics of *Pseudomonas putida* F1 growing on benzene and toluene," Chemosphere, 54(8), pp. 1255–1265.

Alamri, S. A., (2010), "Biodegradation of microcystin by a new *Bacillus sp.* isolated from a Saudi freshwater lake," African Journal of Biotechnology, 9(39), pp. 6552–6559.

Alamri, Saad A., (2012), "Biodegradation of microcystin-RR by *Bacillus flexus* isolated from a Saudi freshwater lake," Saudi Journal of Biological Sciences, 19(4), pp. 435–440.

Alexander, M. (1999). *Biodegradation and Bioremediation* (2nd ed.). Academic Press.

Al-Khalid, T., and El-Naas, M. H., (2012), "Aerobic Biodegradation of Phenols: A Comprehensive Review," Critical Reviews in Environmental Science and Technology, 42(16), pp. 1631–1690.

Allen, J. I., Smyth, T. J., Siddorn, J. R., & Holt, M., (2008), "How well can we forecast high biomass algal bloom events in a eutrophic coastal sea?" Harmful Algae, 8(1), pp. 70–76.

Amade, P., Mehiri, M., & Lewis, R. J., (2014), "Outstanding Marine Biotoxins: STX, TTX, and CTX," In S. L. Barre & J.-M. Kornprobst (Eds.), Outstanding Marine Molecules (pp. 23–44). Wiley-VCH Verlag GmbH & Co. KGaA.

Anderson, T. W., and Darling, D. A., (1954), "A Test of Goodness of Fit," Journal of the American Statistical Association, 49(268), pp. 765–769.

Anderson, D. M., Glibert, P. M., & Burkholder, J. M., (2002), "Harmful algal blooms and eutrophication: Nutrient sources, composition, and consequences," Estuaries, 25(4), pp. 704–726.

Anderson, P. D., (2012), "Bioterrorism: Toxins as Weapons," Journal of Pharmacy Practice, 25(2), pp. 121–129.

Annuar, M. S. M., Tan, I. K. P., Ibrahim, S., and Ramachandran, K. B., (2008), "A kinetic model for growth and biosynthesis of medium-chain-length poly-(3-hydroxyalkanoates) in *Pseudomonas putida*," Brazilian Journal of Chemical Engineering, 25(2), pp. 217–228.

Arbenz, P., Cambou, M., and Hofert, M., (2014), "An importance sampling approach for copula models in insurance," ArXiv:1403.4291 [q-Fin, Stat].

Arbenz, P., Cambou, M., Hofert, M., Lemieux, C., and Taniguchi, Y., (2018), "Importance Sampling and Stratification for Copula Models," In J. Dick, F. Y. Kuo, & H. Woźniakowski (Eds.), Contemporary Computational Mathematics - A Celebration of the 80th Birthday of Ian Sloan (pp. 75–96). Cham: Springer International Publishing.

Ascough, J. C., Maier, H. R., Ravalico, J. K., and Strudley, M. W., (2008), "Future research challenges for incorporation of uncertainty in environmental and ecological decision-making," Ecological Modelling, 219(3), pp. 383–399.

Aune, T., Sørby, R., Yasumoto, T., Ramstad, H., and Landsverk, T., (2002), "Comparison of oral and intraperitoneal toxicity of yessotoxin towards mice," Toxicon, 40(1), pp. 77–82.

Avnimelech, Y., Ritvo, G., Meijer, L. E., and Kochba, M., (2001), "Water content, organic carbon and dry bulk density in flooded sediments," Aquacultural Engineering, 25(1), pp. 25–33.

Awad, N. H., Ali, M. Z., Suganthan, P. N., and Reynolds, R. G., (2016), "An ensemble sinusoidal parameter adaptation incorporated with L-SHADE for solving CEC2014 benchmark problems," In 2016 IEEE Congress on Evolutionary Computation (CEC) (pp. 2958–2965).

Awad, N. H., Ali, M. Z., and Suganthan, P. N., (2017), "Ensemble sinusoidal differential covariance matrix adaptation with Euclidean neighborhood for solving CEC2017 benchmark problems," In 2017 IEEE Congress on Evolutionary Computation (CEC) (pp. 372–379).

Azeloglu, E. U., and Iyengar, R., (2015)., "Good practices for building dynamical models in systems biology," Sci. Signal., 8(371), pp. fs8–fs8.

Azzeh, J., Taylor-Edmonds, L., & Andrews, R. C., (2015), "Engineered biofiltration for ultrafiltration fouling mitigation and disinfection by-product precursor control," Water Science and Technology: Water Supply, 15(1), pp. 124–133.

Babel, W., and Müller, R. H., (1985), "Mixed Substrate Utilization in Micro-organisms: Biochemical Aspects and Energetics," Microbiology, 131(1), pp. 39–45.

Babel, S., and Takizawa, S., (2010), "Microfiltration membrane fouling and cake behavior during algal filtration," Desalination, 261(1–2), pp. 46–51.

Back, T., (1996). *Evolutionary Algorithms in Theory and Practice: Evolution Strategies, Evolutionary Programming, Genetic Algorithms*. Oxford University Press.

Bailey, J. E., and Ollis, D. F., (1976). *Biochemical Engineering Fundamentals*. Chemical Engineering Education.

Balsa-Canto, E., Alonso, A. A., and Banga, J. R., (2008), "Computational procedures for optimal experimental design in biological systems," IET Systems Biology, 2(4), pp. 163–172.

Balsa-Canto, E., Henriques, D., Gábor, A., and Banga, J. R., (2016), "AMIGO2, a toolbox for dynamic modeling, optimization and control in systems biology," Bioinformatics, 32(21), pp. 3357–3359.

Baltes, M., Schneider, R., Sturm, C., and Reuss, M., (1994), "Optimal Experimental Design for Parameter Estimation in Unstructured Growth Models," Biotechnology Progress, 10(5), pp. 480–488.

Bandara, S., Schlöder, J. P., Eils, R., Bock, H. G., and Meyer, T., (2009), "Optimal Experimental Design for Parameter Estimation of a Cell Signaling Model," PLOS Computational Biology, 5(11), pp. e1000558.

Banga, J. R., Moles, C. G., and Alonso, A. A., (2004), "Global Optimization of Bioprocesses using Stochastic and Hybrid Methods," In Frontiers in Global Optimization (pp. 45–70). Springer, Boston, MA.

Banga, J. R., and Balsa-Canto, E., (2008), "Parameter estimation and optimal experimental design," Essays In Biochemistry, 45, pp. 195–210.

Bard, Y. (1974). *Nonlinear Parameter Estimation*. Academic Press.

Bargu, S., Powell, C. L., Wang, Z., Doucette, G. J., & Silver, M. W., (2008), "Note on the occurrence of *Pseudo-nitzschia australis* and domoic acid in squid from Monterey Bay, CA (USA)," Harmful Algae, 7(1), pp. 45–51.

Baroni, G., and Tarantola, S., (2014), "A General Probabilistic Framework for uncertainty and global sensitivity analysis of deterministic models: A hydrological case study," Environmental Modelling & Software, 51, pp. 26–34.

Bar-Zeev, E., Berman-Frank, I., Liberman, B., Rahav, E., Passow, U., & Berman, T., (2009), "Transparent exopolymer particles: Potential agents for organic fouling and biofilm formation in desalination and water treatment plants," Desalination and Water Treatment, 3(1–3), pp. 136–142.

Bar-Zeev, E., Belkin, N., Liberman, B., Berman, T., & Berman-Frank, I., (2012), "Rapid sand filtration pretreatment for SWRO: Microbial maturation dynamics and filtration efficiency of organic matter," Desalination, 286, pp. 120–130.

Bar-Zeev, E., Belkin, N., Liberman, B., Berman-Frank, I., & Berman, T., (2013), "Bioflocculation: Chemical free, pre-treatment technology for the desalination industry," Water Research, 47(9), pp. 3093–3102.

Bear, J., (2013). *Dynamics of fluids in porous media*. Courier Corporation.

Bear, J., and Cheng, A. H. D., (2010). *Modeling Groundwater Flow and Contaminant Transport*. Springer Science & Business Media.

Behrenfeld, M. J., O'Malley, R. T., Siegel, D. A., McClain, C. R., Sarmiento, J. L., Feldman, G. C., … Boss, E. S., (2006), "Climate-driven trends in contemporary ocean productivity," Nature, 444(7120), pp. 752–755.

Bekins, B. A., Warren, E., and Godsy, E. M., (1998), "A Comparison of Zero-Order, First-Order, and Monod Biotransformation Models," Ground Water, 36(2), pp. 261–268.

Benner, J., Helbling, D. E., Kohler, H.-P. E., Wittebol, J., Kaiser, E., Prasse, C., … Boon, N., (2013), "Is biological treatment a viable alternative for micropollutant removal in drinking water treatment processes?" Water Research, 47(16), pp. 5955–5976.

BioThema, (2018). *Microbial ATP Kit: Prod. No. 266-112*. Retrieved from https://biothema.com/shop/kits/atp-biomass-kit-hs/

Billam, M., Tang, L., Cai, Q., Mukhi, S., Guan, H., Wang, P., … Wang, J. S., (2006), "Seasonal variations in the concentration of microcystin-LR in two lakes in western Texas, USA," Environmental Toxicology and Chemistry, 25(2), pp. 349–355.

Billen, G., Servais, P., Ventresque, C., and Bouillot, P., (1992), "Functioning of biological filters used in drinking-water treatment: the CHABROL model," Journal of Water Supply: Research and Technology - Aqua, 41(4), pp. 231-241.

Blackman, F.F., (1905), "Optima and Limiting Factors," Annals of Botany, 19, pp. 281–295.

Bodegom, P. van., (2007), "Microbial Maintenance: A Critical Review on Its Quantification," Microbial Ecology, 53(4), pp. 513–523.

Boere, J. A., (1991), "Reduction of oxidants by granular activated carbon filtration," Proceedings of the 10th Ozone World Congress, Monaco.

Boerlage, S., and Nada, N., (2015), "Algal toxin removal in seawater desalination processes," Desalination and Water Treatment, 55(10), pp. 2575–2593.

Bolster, C. H., Mills, A. L., Hornberger, G. M., & Herman, J. S., (2001), "Effect of surface coatings, grain size, and ionic strength on the maximum attainable coverage of bacteria on sand surfaces," Journal of Contaminant Hydrology, 50(3–4), pp. 287–305.

Borgonovo, E., (2007), "A new uncertainty importance measure," Reliability Engineering & System Safety, 92(6), pp. 771–784.

Borgonovo, E., Castaings, W., and Tarantola, S., (2011), "Moment Independent Importance Measures: New Results and Analytical Test Cases," Risk Analysis, 31(3), pp. 404–428.

Borgonovo, E., Castaings, W., and Tarantola, S., (2012), "Model emulation and moment-independent sensitivity analysis: An application to environmental modelling," Environmental Modelling & Software, 34, pp. 105–115.

Borgonovo, E., and Plischke, E., (2016), "Sensitivity analysis: A review of recent advances," European Journal of Operational Research, 248(3), pp. 869–887.

Botev, Z. I., Grotowski, J. F., and Kroese, D. P., (2010), "Kernel density estimation via diffusion," The Annals of Statistics, 38(5), pp. 2916–2957.

Bourne, D. G., Jones, G. J., Blakeley, R. L., Jones, A., Negri, A. P., & Riddles, P., (1996), "Enzymatic pathway for the bacterial degradation of the cyanobacterial cyclic peptide toxin microcystin LR," Applied and Environmental Microbiology, 62(11), pp. 4086–4094.

Bourne, D. G., Riddles, P., Jones, G. J., Smith, W., & Blakeley, R. L., (2001), "Characterization of a gene cluster involved in bacterial degradation of the cyanobacterial toxin microcystin LR," Environmental Toxicology, 16(6), pp. 523–534.

Bourne, D. G., Blakeley, R. L., Riddles, P., and Jones, G. J., (2006), "Biodegradation of the cyanobacterial toxin microcystin LR in natural water and biologically active slow sand filters," Water Research, 40(6), 1294–1302.

Bouzat, J. L., Hoostal, M. J., and Looft, T., (2013), "Spatial patterns of bacterial community composition within Lake Erie sediments," Journal of Great Lakes Research, 39(2), pp. 344–351.

Box, G. E. P., (1994). *Time Series Analysis: Forecasting and Control*. Prentice Hall.

Brent, R. P., (2013). *Algorithms for Minimization Without Derivatives*. Courier Corporation.

Breusch, T. S., and Pagan, A. R., (1979), "A Simple Test for Heteroscedasticity and Random Coefficient Variation," Econometrica, 47(5), pp. 1287–1294.

Brovelli, A., Malaguerra, F., and Barry, D. A., (2009), "Bioclogging in porous media: Model development and sensitivity to initial conditions," Environmental Modelling & Software, 24(5), pp. 611–626.

Bugg, T., Foght, J. M., Pickard, M. A., and Gray, M. R., (2000), "Uptake and Active Efflux of Polycyclic Aromatic Hydrocarbons by *Pseudomonas fluorescens* LP6a," Applied and Environmental Microbiology, 66(12), PP. 5387–5392.

Burns, J. M., and Ferry, J. L., (2007), "Adsorption of domoic acid to marine sediments and clays," Journal of Environmental Monitoring, 9(12), pp. 1373.

Burns, J. M., Hall, S., and Ferry, J. L., (2009), "The adsorption of saxitoxin to clays and sediments in fresh and saline waters," Water Research, 43(7), pp. 1899–1904.

Byrd, R., Hribar, M., and Nocedal, J., (1999), "An Interior Point Algorithm for Large-Scale Nonlinear Programming," SIAM Journal on Optimization, 9(4), pp. 877–900.

California Department of Water Resources (CDWR), (2013). California Water Plan Update 2013: Volume 3-Resource Management Strategies-Chapter 10 Desalination (Brackish and Seawater); CDWR, Sacramento, CA, USA.

Cambou, M., Hofert, M., and Lemieux, C., (2017), "Quasi-random numbers for copula models," Statistics and Computing, 27(5), pp. 1307–1329.

Campinas, M., and Rosa, M. J., (2010), "Evaluation of cyanobacterial cells removal and lysis by ultrafiltration," Separation and Purification Technology, 70(3), pp. 345–353.

Campolongo, F., Saltelli, A., and Cariboni, J., (2011), "From screening to quantitative sensitivity analysis: A unified approach," Computer Physics Communications, 182(4), pp. 978–988.

Caporaso, J. G., Kuczynski, J., Stombaugh, J., Bittinger, K., Bushman, F. D., Costello, E. K., … Knight, R., (2010), "QIIME allows analysis of high-throughput community sequencing data," Nature Methods, 7(5), pp. 335–336.

Cappuyns, A. M., Bernaerts, K., Smets, I. Y., Ona, O., Prinsen, E., Vanderleyden, J., and Impe, J. F. V., (2007), "Optimal Fed Batch Experiment Design for Estimation of Monod Kinetics of *Azospirillumbrasilense*: From Theory to Practice," Biotechnology Progress, 23(5), pp. 1074–1081.

Caron, D. A., Garneau, M.-È., Seubert, E., Howard, M. D. A., Darjany, L., Schnetzer, A., … Trussell, S., (2010), "Harmful algae and their potential impacts on desalination operations off southern California," Water Research, 44(2), pp. 385–416.

Castaing, J. B., Massé, A., Séchet, V., Sabiri, N.-E., Pontié, M., Haure, J., & Jaouen, P., (2011), "Immersed hollow fibres microfiltration (MF) for removing undesirable micro-algae and protecting semi-closed aquaculture basins," Desalination, 276(1–3), pp. 386–396.

Castaings, W., Borgonovo, E., Morris, M. D., and Tarantola, S., (2012), "Sampling strategies in density-based sensitivity analysis," Environmental Modelling & Software, 38, pp. 13–26.

Chao, A., and Jost, L., (2008). *Diversity Analysis*. Taylor & Francis: Milton Keynes, United Kingdom.

Chao, A., Chiu, C.-H., and Jost, L., (2014), "Unifying Species Diversity, Phylogenetic Diversity, Functional Diversity, and Related Similarity and Differentiation Measures Through Hill Numbers," Annual Review of Ecology, Evolution, and Systematics, 45(1), pp. 297–324.

Charpentier, A., Fermanian, J., and Scaillet, O., (2007), "The estimation of copulas : Theory and practice," In Jörn Rank (Ed.), Copulas: From theory to application in finance (pp. 35-64). London: Risk Books. Retrieved from https://archive-ouverte.unige.ch/unige:41917

Chaudhary, D. S., Vigneswaran, S., Ngo, H.-H., Shim, W. G., & Moon, H., (2003), "Biofilter in water and wastewater treatment," Korean Journal of Chemical Engineering, 20(6), pp. 1054–1065.

Chaudhary, A., Kauser, I., Ray, A., and Poretsky, R., (2018), "Taxa-driven functional shifts associated with stormflow in an urban stream microbial community," BioRxiv, pp. 300699.

Chen, G., & Strevett, K. A., (2003), "Microbial surface thermodynamics and interactions in aqueous media," Journal of Colloid and Interface Science, 261(2), pp. 283–290.

Chen, S. X., and Huang, T.-M., (2007), "Nonparametric Estimation of Copula Functions for Dependence Modelling," The Canadian Journal of Statistics / La Revue Canadienne de Statistique, 35(2), pp. 265–282.

Chen, W., Song, L., Peng, L., Wan, N., Zhang, X., and Gan, N., (2008), "Reduction in microcystin concentrations in large and shallow lakes: Water and sediment-interface contributions," Water Research, 42(3), pp. 763–773.

Chen, J., Hu, L. B., Zhou, W., Yan, S. H., Yang, J. D., Xue, Y. F., and Shi, Z. Q., (2010), "Degradation of Microcystin-LR and RR by *a Stenotrophomonas sp.* Strain EMS Isolated from Lake Taihu, China," International Journal of Molecular Sciences, 11(3), pp. 896–911.

Cheng, R., Jin, Y., Olhofer, M., and Sendhoff, B., (2016), "A Reference Vector Guided Evolutionary Algorithm for Many-Objective Optimization," IEEE Transactions on Evolutionary Computation, 20(5), pp. 773–791.

Cheung, M. Y., Liang, S., and Lee, J., (2013), "Toxin-producing cyanobacteria in freshwater: A review of the problems, impact on drinking water safety, and efforts for protecting public health," Journal of Microbiology, 51(1), pp. 1–10.

Chiș, O., Banga, J. R., and Balsa-Canto, E., (2011a), "GenSSI: a software toolbox for structural identifiability analysis of biological models," Bioinformatics, 27(18), pp. 2610–2611.

Chiș, O. T., Banga, J. R., and Balsa-Canto, E., (2011b), "Structural Identifiability of Systems Biology Models: A Critical Comparison of Methods," PLOS ONE, 6(11), pp. e27755.

Chorus, I., and Bartel, H., (2006), "Retention and elimination of cyanobacterial toxins (microcystins) through artificial recharge and bank filtration," "Algae" group: Federal Environmental Agency of Germany (UBA).

Christensen, B. E., Trønnes, H. N., Vollan, K., Smidsrød, O., & Bakke, R., (1990), "Biofilm removal by low concentrations of hydrogen peroxide," Biofouling, 2(2), pp. 165–175.

Christensen, R., Johnson, W., Branscum, A., and Hanson, T. E., (2011). *Bayesian Ideas and Data Analysis: An Introduction for Scientists and Statisticians*. Boco Raton, FL: CRC Press.

Christoffersen, K., Lyck, S., and Winding, A., (2002), "Microbial activity and bacterial community structure during degradation of microcystins," Aquatic Microbial Ecology, 27(2), pp. 125–136.

Chu, Y., and Hahn, J., (2010), "Quantitative Optimal Experimental Design Using Global Sensitivity Analysis via Quasi-Linearization," Industrial & Engineering Chemistry Research, 49(17), pp. 7782–7794.

Chu, Y., and Hahn, J., (2013), "Necessary condition for applying experimental design criteria to global sensitivity analysis results," Computers & Chemical Engineering, 48, pp. 280–292.

Chudoba, P., Capdeville, B., and Chudoba, J., (1992), "Explanation of Biological Meaning of the So/Xo Ratio in Batch Cultivation," Water Science and Technology, 26(3–4), pp. 743–751.

Clement, T. P., Hooker, B. S., and Skeen, R. S., (1996), "Macroscopic Models for Predicting Changes in Saturated Porous Media Properties Caused by Microbial Growth," Ground Water, 34(5), pp. 934–942.

Coe, R., (2002), "It's the Effect Size, Stupid: What Effect Size is and why it is important," Presented at the Annual Conference of the British Educational Research Association, University of Exeter, England, 12–14 September 2002.

Coffey, B. M., Krasner, S. W., Sclimenti, M. J., Hacker, P. A., & Gramith, J. T., (1996), "A comparison of biologically active filters for the removal of ozone by-products, turbidity, and particles," American Water Works Association, Denver.

Cohlberg, J. A., (1979), "Km as an apparent dissociation constant," Journal of Chemical Education, 56(8), pp. 512.

Contois, D. E., (1959), "Kinetics of Bacterial Growth: Relationship between Population Density and Specific Growth Rate of Continuous Cultures," Microbiology, 21(1), pp. 40–50.

Cordier, S., Monfort, C., Miossec, L., Richardson, S., and Belin, C., (2000), "Ecological Analysis of Digestive Cancer Mortality Related to Contamination by Diarrhetic Shellfish Poisoning Toxins along the Coasts of France," Environmental Research, 84(2), pp. 145–150.

Costa, L. G., Giordano, G., and Faustman, E. M., (2010), "Domoic acid as a developmental neurotoxin," NeuroToxicology, 31(5), pp. 409–423.

Cotruvo, J. A., (1988), "Drinking water standards and risk assessment," Regulatory Toxicology and Pharmacology, 8(3), pp. 288–299.

Cotruvo, J, Couper, M., Cunliffe, D.; Fawell, J., Giddings, M., Ohanian, E., Ong, C. N., Sanderson, H., Simizaki, D., (2011), "Pharmaceuticals in Drinking Water," World Health Organization: Geneva, Switzerland.

Cousins, I. T., Bealing, D. J., James, H. A., and Sutton, A., (1996), "Biodegradation of microcystin-LR by indigenous mixed bacterial populations," Water Research, 30(2), pp. 481–485.

Cromwell, J. B., Labys, W. C., and Terraza, M., (1994). *Univariate Tests for Time Series Models*. SAGE.

A. de la Cruz, A., G. Antoniou, M., Hiskia, A., Pelaez, M., Song, W., E. O'Shea, K., … D. Dionysiou, D., (2011), "Can We Effectively Degrade Microcystins? - Implications on Human Health," Anti-Cancer Agents in Medicinal Chemistry, 11(1), pp. 19–37.

Dabes, J. N., Finn, R. K., and Wilke, C. R., (1973), "Equations of substrate-limited growth: The case for blackman kinetics," Biotechnology and Bioengineering, 15(6), pp. 1159–1177.

Dahm, C. N., (2010). Consequences of Climate Variability and Human Water Demand on Freshwater Ecosystems: A Mediterranean Perspective from the United States. In S. Sabater & D. Barceló (Eds.), Water Scarcity in the Mediterranean (pp. 55–71). Springer Berlin Heidelberg.

Daniel, P., & Teefy, S., (1995), "Biological filtration: Media, quality, operations, and cost," Proceedings of the 1995 AWWA Annual Conference, Anaheim, California.

Dang, J. S., Harvey, D. M., Jobbagy, A., and Grady, C. L., (1989), "Evaluation of biodegradation kinetics with respirometric data," Research Journal of the Water Pollution Control Federation, pp. 1711–1712.

Davis, T. W., Berry, D. L., Boyer, G. L., & Gobler, C. J., (2009), "The effects of temperature and nutrients on the growth and dynamics of toxic and non-toxic strains of Microcystis during cyanobacteria blooms," Harmful Algae, 8(5), pp. 715–725.

Dawoud, M. A., (2005), "The role of desalination in augmentation of water supply in GCC countries," Desalination, 186(1), pp. 187–198.

Deb, K., (2001). *Multi-Objective Optimization Using Evolutionary Algorithms*. John Wiley & Sons.

Deb, K., and Jain, H., (2014), "An Evolutionary Many-Objective Optimization Algorithm Using Reference-Point-Based Nondominated Sorting Approach, Part I: Solving Problems With Box Constraints," IEEE Transactions on Evolutionary Computation, 18(4), pp. 577–601.

Dehwah, A. H. A., Al-Mashharawi, S., Kammourie, N., and Missimer, T. M., (2015), "Impact of well intake systems on bacterial, algae, and organic carbon reduction in SWRO desalination systems, SAWACO, Jeddah, Saudi Arabia," Desalination and Water Treatment, 55(10), pp. 2594–2600.

de Maagd, P. G.-J., Hendriks, A. J., Seinen, W., and Sijm, D. T. H. M., (1999), "pH-Dependent hydrophobicity of the cyanobacteria toxin microcystin-LR," Water Research, 33(3), pp. 677–680.

Derennes, P., Morio, J., and Simatos, F., (2018), "A nonparametric importance sampling estimator for moment independent importance measures," Reliability Engineering & System Safety.

Dette, H., Melas, V. B., Pepelyshev, A., and Strigul, N., (2003), "Efficient design of experiments in the Monod model," Journal of the Royal Statistical Society: Series B (Statistical Methodology), 65(3), pp. 725–742.

Dette, H., Melas, V. B., Pepelyshev, A., and Strigul, N., (2005), "Robust and efficient design of experiments for the Monod model," Journal of Theoretical Biology, 234(4), pp. 537–550.

DiLiberto, T., (2015), "Record setting bloom of toxic algae in the North Pacific," NOAA, last accessed May 6th, 2016. https://www.climate.gov/news-features/event-tracker/record-setting-bloom-toxic-algae-north-pacific.

Dittmann, E., and Wiegand, C., (2006), "Cyanobacterial toxins – occurrence, biosynthesis and impact on human affairs," Molecular Nutrition & Food Research, 50(1), pp. 7–17.

Dixon, M. B., Richard, Y., Ho, L., Chow, C. W. K., O'Neill, B. K., and Newcombe, G., (2011), "A coagulation–powdered activated carbon–ultrafiltration – Multiple barrier approach for removing toxins from two Australian cyanobacterial blooms," Journal of Hazardous Materials, 186(2–3), pp. 1553–1559.

Dominguez, H. J., Paz, B., Daranas, A. H., Norte, M., Franco, J. M., and Fernández, J. J., (2010), "Dinoflagellate polyether within the yessotoxin, pectenotoxin and okadaic acid toxin groups: Characterization, analysis and human health implications," Toxicon, 56(2), pp. 191–217.

Donohue, J., and Zavaleta, J.O., (2003), "Toxicological Basis for Drinking Water Risk Assessment," In Drinking Water Regulation and Health; Pontius, F., Ed.; John Wiley & Sons, New York, NY, USA, pp. 133–160.

Doran, P. M. (1995). *Bioprocess Engineering Principles*. Academic Press.

Drikas, M., Chow, C. W. K., House, J., and Burch, M. D., (2001), "Using Coagulation, Flocculation, and Settling to Remove Toxic cyanobacteria," Journal of the American Water Works Association, 93(2), pp. 100–111.

Dullien, F. A., (2012). Porous media: fluid transport and pore structure. Academic press.

Durante, F., (2009), "Construction of non-exchangeable bivariate distribution functions," Statistical Papers, 50(2), pp. 383–391.

Durante, F., Fernández-Sánchez, J., and Pappadà, R., (2015), "Copulas, diagonals, and tail dependence," Fuzzy Sets and Systems, 264, pp. 22–41.

Dutta, K., Venkata Dasu, V., Mahanty, B., and Anand Prabhu, A., (2015), "Substrate Inhibition Growth Kinetics for Cutinase Producing *Pseudomonas cepacia* Using Tomato-peel Extracted Cutin," Chemical and Biochemical Engineering Quarterly, 29(3), pp. 437–445.

Dziga, D., Wasylewski, M., Szetela, A., Bocheńska, O., & Wladyka, B., (2012), "Verification of the Role of MlrC in Microcystin Biodegradation by Studies Using a Heterologously Expressed Enzyme," Chemical Research in Toxicology, 25(6), pp. 1192–1194.

Dziga, D., Wasylewski, M., Wladyka, B., Nybom, S., & Meriluoto, J., (2013), "Microbial Degradation of Microcystins," Chemical Research in Toxicology, 26(6), pp. 841–852.

Dziga, D., Lisznianska, M., and Wladyka, B., (2014), "Bioreactor Study Employing Bacteria with Enhanced Activity toward Cyanobacterial Toxins Microcystins," Toxins, 6(8), pp. 2379–2392.

Edwards, C., Graham, D., Fowler, N., and Lawton, L. A., (2008), "Biodegradation of microcystins and nodularin in freshwaters," Chemosphere, 73(8), pp. 1315–1321.

Edwards, C., and Lawton, L.A., (2009), "Bioremediation of Cyanotoxins," In Advances in Applied Microbiology; Laskin, A., Sariaslani, S., Gadd, G., Eds.; Academic Press: San Diego, California, USA; Volume 67, pp. 109–129.

Efron, B., and Tibshirani, R. J., (1994). *An Introduction to the Bootstrap*. CRC Press.

Egli, T., (1995), "The Ecological and Physiological Significance of the Growth of Heterotrophic Microorganisms with Mixtures of Substrates," In Advances in Microbial Ecology; Jones, J.G., Ed.; Plenum Press: New York, New York, USA; pp. 305–386,

Egli, T., (2010), "How to live at very low substrate concentration," Water Research, 44(17), pp. 4826–4837.

Eleutario, L. and Batista, J. R., (2010), "Biodegradation studies and sequencing of microcystin-LR degrading bacteria isolated from a drinking water biofilter and fresh water lake," Toxicon, Vol.55, pp.1434-1442.

Elimelech, M., & O'Melia, C. R., (1990), "Kinetics of deposition of colloidal particles in porous media," Environmental Science & Technology, 24(10), pp. 1528–1536.

El-Naas, M. H., Acio, J. A., and El Telib, A. E., (2014), "Aerobic biodegradation of BTEX: Progresses and Prospects," Journal of Environmental Chemical Engineering, 2(2), pp. 1104–1122.

Engle, R. F., Lilien, D. M., and Robins, R. P., (1987), "Estimating Time Varying Risk Premia in the Term Structure: The Arch-M Model," Econometrica, 55(2), pp. 391–407.

Eltawil, M. A., Zhengming, Z., & Yuan, L., (2009), "A review of renewable energy technologies integrated with desalination systems," Renewable and Sustainable Energy Reviews, 13(9), pp. 2245–2262.

Emelko, M. B., Huck, P. M., Coffey, B. M., and Smith, E. F., (2006), "Effects of media, backwash, and temperature on full-scale biological filtration," Journal of the American Water Works Association, Vol.98(12), pp. 61-73.

Engesgaard, P., Holm, J., Jensen, K. H., Henze, M., & Albrechtsen, H. J., (2002). Development of preferential flow in bioclogging of porous media. In R. J. S. S. Majid Hassanizadeh William G. Gray and George F. Pinder (Ed.), Developments in Water Science (Vol. 47, pp. 803–810). Elsevier.

Engesgaard, P., Seifert, D., & Herrera, P., (2006). Bioclogging in Porous Media: Tracer Studies. In S. A. Hubbs (Ed.), Riverbank Filtration Hydrology (pp. 93–118). Springer Netherlands.

Enzweiler, H., Visioli, L. J., Muneron de Mello, J. M., Guelli Ulson de Souza, S. M. de A., Ulson de Souza, A. A., Silva, A. da, … Schwaab, M., (2014), "Statistical Evaluation of Biochemical Kinetic Models for BTX Degradation," Industrial & Engineering Chemistry Research, 53(50), pp. 19416–19425.

Esener, A. A., Roels, J. A., and Kossen, N. W. F., (1983), "Theory and applications of unstructured growth models: Kinetic and energetic aspects," Biotechnology and Bioengineering, 25(12), pp. 2803–2841.

Evans, P. J., Opitz, E. M., Daniel, P. A., & Schulz, C. R., (2010b), "Biological drinking water treatment perceptions and actual experiences in North America," Water Research Foundation, Denver.

Evans, P. J., Smith, J. L., LeChavillier, M. W., Schneider, O.D., Weinrich, L. A., and Jjemba, P. K., (2013a), "Biological Filtration Monitoring and Control Toolbox: Guidance Manual," Water Research Foundation, Denver.

Evans, P. J., Smith, J. L., LeChavillier, M. W., Schneider, O.D., Weinrich, L. A., and Jjemba, P. K., (2013b), "A Monitoring and Control Toolbox for Biological Filtration," Water Research Foundation, Denver.

Falk, M., Seto, P. F., and Walter, J. A., (1991), "Solubility of domoic acid in water and in non-aqueous solvents," Canadian Journal of Chemistry, 69(11), pp. 1740–1744.

Faust, K., and Raes, J., (2012), "Microbial interactions: from networks to models," Nature Reviews Microbiology, 10(8), pp. 538–550.

Feng, K., Lu, Z., Pang, C., and Yun, W., (2018), "An efficient computational method of a moment-independent importance measure using quantile regression," Mechanical Systems and Signal Processing, 109, pp. 235–246.

Ferguson, D. W., McGuire, M. J., Koch, B., Wolfe, R. L., & Aieta, E., (1990), "Comparing PEROXONE and ozone for controlling taste and odor compounds, disinfection by-products, and microorganisms," Journal of the American Water Works Association, 82(4), pp. 181-191.

Finley, B., and Paustenbach, D., (1994), "The Benefits of Probabilistic Exposure Assessment: Three Case Studies Involving Contaminated Air, Water, and Soil," Risk Analysis, 14(1), pp. 53–73.

Flemming, H.-C., & Wingender, J., (2001), "Relevance of microbial extracellular polymeric substances (EPSs) - Part I: Structural and ecological aspects," Water Science and Technology, 43(6), pp. 1–8.

Forsythe, G. E., Malcolm, M. A., and Moler, C. B., (1977). *Computer methods for mathematical computations*. Englewood Cliffs, NJ: Prentice-Hall.

Fowle, J.R., and Dearfield, K.L., (2000), "Risk Characterization Handbook; EPA 100-B-00-002," U.S. EPA Science Policy Council, Washington, DC, USA.

Franceschini, G., and Macchietto, S., (2008), "Model-based design of experiments for parameter precision: State of the art," Chemical Engineering Science, 63(19), pp. 4846–4872.

Franchi, A., & O'Melia, C. R., (2003), "Effects of Natural Organic Matter and Solution Chemistry on the Deposition and Reentrainment of Colloids in Porous Media," Environmental Science & Technology, 37(6), pp. 1122–1129.

Francy, D. S., Graham, J. L., Stelzer, E. A., Ecker, C. D., and Brady, A. M., (2015). *Water Quality, Cyanobacteria, and Environmental Factors and Their Relations to Microcystin Concentrations for Use in Predictive Models at Ohio Lake Erie and Inland Lake Recreational Sites, 2013-14* (Scientific Investigations Report No. 2015–5120) (p. 58). United States Geological Survey. Retrieved from http://dx.doi.org/10.3133/sir20155120.

Frappart, M., Massé, A., Jaffrin, M. Y., Pruvost, J., & Jaouen, P., (2011), "Influence of hydrodynamics in tangential and dynamic ultrafiltration systems for microalgae separation," Desalination, 265(1–3), pp. 279–283.

Fredrickson, A. G., Ramkrishna, D., and Tsuchiya, H. M., (1971), "The Necessity of Including Structure In Mathematical Models of Unbalanced Microbial Growth," Chemical Engineering Symposium Series, 67(108), pp. 53–59.

Fux, E., (2008). *Development and Evaluation of Passive Sampling And LC-MS Based Techniques For The Detection And Monitoring Of Lipophilic Marine Toxins in Mesocosm and Field Studies* (Doctoral Dissertation). Retrieved from http://arrow.dit.ie/cgi/viewcontent.cgi?article=1054&context=sciendoc.

Geisser, S., and Eddy, W. F., (1979), "A Predictive Approach to Model Selection," Journal of the American Statistical Association, 74(365), pp. 153–160.

Gelfand, A. E., and Dey, D. K., (1994), "Bayesian model choice: asymptotics and exact calculations," Journal of the Royal Statistical Society: Series B (Methodological), pp. 501–514.

Gelman, A., Carlin, J., Stern, H., Vehtari, A., Dunson, D. B., and Rubin, D. B., (2014). *Bayesian Data Analysis* (3rd ed.). Boco Raton, FL: CRC Press.

Genest, C., and Rivest, L. P., (1993), "Statistical Inference Procedures for Bivariate Archimedean Copulas," Journal of the American Statistical Association, 88(423), pp. 1034–1043.

Genest, C., Ghoudi, K., and Rivest, L. P., (1998), "Discussion of ''understanding relationships using copulas'' by E. W. Frees and E. A. Valdez," North Am. Act. J. 2(3), pp. 143–149.

Genest, C., Rémillard, B., and Beaudoin, D., (2009), "Goodness-of-fit tests for copulas: A review and a power study," Insurance: Mathematics and Economics, 44(2), pp. 199–213.

Genest, C., Nešlehová, J., and Quessy, J. F., (2012), "Tests of symmetry for bivariate copulas," Annals of the Institute of Statistical Mathematics, 64(4), pp. 811–834.

Ghaffour, N., Missimer, T. M., & Amy, G. L., (2013a), "Technical review and evaluation of the economics of water desalination: Current and future challenges for better water supply sustainability," Desalination, 309, pp. 197–207.

Ghaffour, N., Missimer, T. M., and Amy, G. L. (2013b). Combined desalination, water reuse, and aquifer storage and recovery to meet water supply demands in the GCC/MENA region. Desalination and Water Treatment, 51(1–3), 38–43.

Ghernaout, B., Ghernaout, D., and Saiba, A., (2010), "Algae and cyanotoxins removal by coagulation/flocculation: A review," Desalination and Water Treatment, 20(1–3), pp. 133–143.

Ghovvati, M., Khayati, G., Attar, H., and Vaziri, A., (2015), "Comparison across growth kinetic models of alkaline protease production in batch and fed-batch fermentation using hybrid genetic algorithm and particle swarm optimization," Biotechnology & Biotechnological Equipment, 29(6), pp. 1216–1225.

Giaramida, L., Manage, P. M., Edwards, C., Singh, B. K., & Lawton, L. A., (2013), "Bacterial communities' response to microcystins exposure and nutrient availability: Linking degradation capacity to community structure," International Biodeterioration & Biodegradation, 84, pp. 111–117.

Gibbons, J. D., (1996). *Nonparametric Methods for Quantitative Analysis* (3rd edition). Columbus, Ohio: Amer Sciences Pr.

Gijsbertsen-Abrahamse, A. J., Schmidt, W., Chorus, I., and Heijman, S. G. J., (2006), "Removal of cyanotoxins by ultrafiltration and nanofiltration," Journal of Membrane Science, 276(1–2), pp. 252–259.

Gokulakrishnan, S., and Gummadi, S. N., (2006), "Kinetics of cell growth and caffeine utilization by *Pseudomonas sp.* GSC 1182," Process Biochemistry, 41(6), pp. 1417–1421.

Gong, Z. L., Zhang, C. F., Jin, R., and Zhang, Y. Q., (2016), "*Steroidobacter flavus*, a microcystin-degrading Gammaproteobacterium isolated from soil," Antonie van Leeuwenhoek, 109(8), pp. 1073–1079.

Gottschalk, F., Scholz, R. W., & Nowack, B., (2010a), "Probabilistic material flow modeling for assessing the environmental exposure to compounds: Methodology and an application to engineered nano-TiO2 particles," Environmental Modelling & Software, 25(3), pp. 320–332.

Gottschalk, F., Sonderer, T., Scholz, R. W., & Nowack, B., (2010b), "Possibilities and limitations of modeling environmental exposure to engineered nanomaterials by probabilistic material flow analysis," Environmental Toxicology and Chemistry, 29(5), pp. 1036–1048.

Goudar, C. T., and Strevett, K. A., (2000), "Estimating in-situ Monod biodegradation parameters using a novel explicit solution of a one-dimensional contaminant transport equation," Ground Water, 38(6), pp. 894.

Graça, M. A. S., Bärlocher, F., and Gessner, M. O., (2007). *Methods to Study Litter Decomposition: A Practical Guide*. Springer Science & Business Media.

Grady, C. P. L., Smets, B. F., and Barbeau, D. S., (1996), "Variability in kinetic parameter estimates: A review of possible causes and a proposed terminology," Water Research, 30(3), pp. 742–748.

Graneli, E., and Turner, J. (Eds.), (2006), "Part C: The Ecology and Physiology of Harmful Algae," In The Ecology of Harmful Algae (Vol. 189, pp. 215–239). Springer Berlin Heidelberg.

Grasso, D., Subramaniam, K., Butkus, M., Strevett, K., and Bergendahl, J., (2002), "A review of non-DLVO interactions in environmental colloidal systems," Reviews in Environmental Science and Biotechnology, 1(1), pp. 17–38.

Grattan, L. M., Boushey, C., Tracy, K., Trainer, V., Roberts, S. M., Schluterman, N., and Morris, J. G., (2016), "The association between razor clam consumption and memory in the CoASTAL Cohort," Harmful Algae, 57(B), pp. 20–25.

Grützmacher, G., Böttcher, G., Chorus, I., and Bartel, H., (2002), "Removal of microcystins by slow sand filtration," Environmental Toxicology, 17(4), pp. 386–394.

Grützmacher, G., Wessel, G., Klitzke, S., & Chorus, I., (2010), "Microcystin Elimination During Sediment Contact," Environmental Science & Technology, 44(2), pp. 657–662.

Guastalli, A. R., Simon, F. X., Penru, Y., de Kerchove, A., Llorens, J., & Baig, S., (2013), "Comparison of DMF and UF pre-treatments for particulate material and dissolved organic matter removal in SWRO desalination," Desalination, 322, pp. 144–150.

Gupta, H., and Razavi, S., (2017), "Chapter 20 - Challenges and Future Outlook of Sensitivity Analysis," In G. P. Petropoulos & P. K. Srivastava (Eds.), Sensitivity Analysis in Earth Observation Modelling (pp. 397–415). Elsevier.

Hallé, C., Huck, P. M., Peldszus, S., Haberkamp, J., & Jekel, M., (2009), "Assessing the Performance of Biological Filtration As Pretreatment to Low Pressure Membranes for Drinking Water," Environmental Science & Technology, 43(10), pp. 3878–3884.

Hallegraeff, G. M., Anderson, D. M., Cembella, A. D., and Enevoldsen, H. O., (2003). *Manual on Harmful Marine Microalgae*. Unesco.

Hallegraeff, G. M., (2010), "Ocean Climate Change, Phytoplankton Community Responses, and Harmful Algal Blooms: A Formidable Predictive Challenge," Journal of Phycology, 46(2), pp. 220–235.

Hamilton, J. D., (1994). *Time Series Analysis*. Princeton University Press.

Hamm, C. E., Merkel, R., Springer, O., Jurkojc, P., Maier, C., Prechtel, K., and Smetacek, V., (2003), "Architecture and material properties of diatom shells provide effective mechanical protection," Nature, 421(6925), pp. 841–843.

Harada, K., Imanishi, S., Kato, H., Mizuno, M., Ito, E., & Tsuji, K., (2004), "Isolation of Adda from microcystin-LR by microbial degradation," Toxicon, 44(1), pp. 107–109.

Harke, M. J., Steffen, M. M., Gobler, C. J., Otten, T. G., Wilhelm, S. W., Wood, S. A., and Paerl, H. W., (2016), "A review of the global ecology, genomics, and biogeography of the toxic cyanobacterium, *Microcystis spp.,*" Harmful Algae, 54, pp. 4–20.

Hashimoto, E. H., Kato, H., Kawasaki, Y., Nozawa, Y., Tsuji, K., Hirooka, E. Y., & Harada, K., (2009), "Further Investigation of Microbial Degradation of Microcystin Using the Advanced Marfey Method," *Chemical Research in Toxicology*, 22(2), pp. 391–398.

Heijnen, J. J., and Romein, B., (1995), "Derivation of Kinetic Equations for Growth on Single Substrates Based on General Properties of a Simple Metabolic Network," Biotechnology Progress, 11(6), pp. 712–716.

Heiskary, S., Lindon, M., and Anderson, J., (2014), "Summary of microcystin concentrations in Minnesota lakes," Lake and Reservoir Management, 30(3), pp. 268–272.

Heisler, J., Glibert, P. M., Burkholder, J. M., Anderson, D. M., Cochlan, W., Dennison, W. C., … Suddleson, M., (2008), "Eutrophication and harmful algal blooms: A scientific consensus," Harmful Algae, 8(1), pp. 3–13.

Heitzer, A., Kohler, H. P., Reichert, P., and Hamer, G., (1991), "Utility of phenomenological models for describing temperature dependence of bacterial growth," Applied and Environmental Microbiology, 57(9), pp. 2656–2665.

Helton, J. C., and Davis, F. J., (2002), "Illustration of Sampling-Based Methods for Uncertainty and Sensitivity Analysis," Risk Analysis, 22(3), pp. 591–622.

Hengy, M. H., Horton, D. J., Uzarski, D. G., and Learman, D. R., (2017), "Microbial community diversity patterns are related to physical and chemical differences among temperate lakes near Beaver Island, MI," PeerJ, 5, pp. e3937.

Hill, M. O., (1973), "Diversity and Evenness: A Unifying Notation and Its Consequences," Ecology, 54(2), pp. 427–432.

Hoefel, D., Adriansen, C. M. M., Bouyssou, M. A. C., Saint, C. P., Newcombe, G., & Ho, L., (2009), "Development of an mlrA Gene-Directed TaqMan PCR Assay for Quantitative Assessment of Microcystin-Degrading Bacteria within Water Treatment Plant Sand Filter Biofilms," Applied and Environmental Microbiology, 75(15), pp.5167–5169.

Hoeger, S. J., Shaw, G., Hitzfeld, B. C., and Dietrich, D. R., (2004), "Occurrence and elimination of cyanobacterial toxins in two Australian drinking water treatment plants," Toxicon, 43(6), pp. 639–649.

Hoeger, S. J., Hitzfeld, B. C., and Dietrich, D. R., (2005), "Occurrence and elimination of cyanobacterial toxins in drinking water treatment plants," Toxicology and Applied Pharmacology, 203(3), pp. 231–242.

Hofert, M., (2008), "Sampling Archimedean copulas," Computational Statistics & Data Analysis, 52(12), pp. 5163–5174.

Hofert, M., (2011), "Efficiently sampling nested Archimedean copulas," Computational Statistics & Data Analysis, 55(1), pp. 57–70.

Hollister, J. W., and Kreakie, B. J., (2016), "Associations between chlorophyll a and various microcystin health advisory concentrations," F1000Research, 5.

Holmberg, A., (1982), "On the practical identifiability of microbial growth models incorporating Michaelis-Menten type nonlinearities," Mathematical Biosciences, 62(1), pp. 23–43.

Ho, J. C., & Michalak, A. M., (2015), "Challenges in tracking harmful algal blooms: A synthesis of evidence from Lake Erie," Journal of Great Lakes Research, 41(2), pp. 317–325.

Ho, L., Meyn, T., Keegan, A., Hoefel, D., Brookes, J., Saint, C. P., and Newcombe, G., (2006), "Bacterial degradation of microcystins within a biologically active sand filter," Water Research, Vol.40, pp. 768-774.

Ho, L., Hoefel, D., Saint, C. P., & Newcombe, G., (2007a), "Degradation of Microcystin-LR through Biological Sand Filters," Practice Periodical of Hazardous, Toxic, and Radioactive Waste Management, 11(3), pp. 191–196.

Ho, L., Gaudieux, A.-L., Fanok, S., Newcombe, G., & Humpage, A. R., (2007b), "Bacterial degradation of microcystin toxins in drinking water eliminates their toxicity," Toxicon, 50(3), pp. 438–441.

Ho, L., Hoefel, D., Saint, C. P., and Newcombe, G., (2007c), "Isolation and identification of a novel microcystin-degrading bacterium from a biological sand filter," Water Research, 41(20), pp. 4685–4695.

Ho, L., Hoefel, D., Palazot, S., Sawade, E., Newcombe, G., Saint, C. P., & Brookes, J. D., (2010), "Investigations into the biodegradation of microcystin-LR in wastewaters," Journal of Hazardous Materials, 180(1–3), pp. 628–633.

Ho, L., Sawade, E., & Newcombe, G., (2012a), "Biological treatment options for cyanobacteria metabolite removal – A review," Water Research, 46(5), pp. 1536–1548.

Ho, L., Tang, T., Monis, P. T., and Hoefel, D., (2012b), "Biodegradation of multiple cyanobacterial metabolites in drinking water supplies," Chemosphere, 87(10), pp. 1149–1154.

Homma, T., and Saltelli, A., (1996), "Importance measures in global sensitivity analysis of nonlinear models," Reliability Engineering & System Safety, 52(1), pp. 1–17.

Howard, M. D. A., Silver, M., & Kudela, R. M., (2008), "Yessotoxin detected in mussel (*Mytilus californicus*) and phytoplankton samples from the U.S. west coast," Harmful Algae, 7(5), pp. 646–652.

Howard, M. D. A., Nagoda, C., Kudela, R. M., Hayashi, K., Tatters, A., Caron, D. A., … Stein, E. D., (2017), "Microcystin Prevalence throughout Lentic Waterbodies in Coastal Southern California," Toxins, 9(7), pp. 231.

Howd, R.A., Brown, J.P., and Fan, A.M., (2004), "Risk Assessment for Chemicals in Drinking Water: Estimation of Relative Source Contribution," The Toxicologist 2004, 78 , pp. 1-10.

Hozalski, R. M., Bouwer, E. J., & Goel, S., (1999), "Removal of natural organic matter (NOM) from drinking water supplies by ozone-biofiltration," Water Science and Technology, 40(9), pp. 157–163.

Hozalski, R. M., & Bouwer, E. J., (2001a), "Non-steady state simulation of BOM removal in drinking water biofilters: Model development," Water Research, 35(1), pp. 198–210.

Hozalski, R. M., & Bouwer, E. J., (2001b), "Non-steady state simulation of BOM removal in drinking water biofilters: applications and full-scale validation," Water Research, 35(1), pp. 211–223.

Huang, X., Min, J. H., Lu, W., Jaktar, K., Yu, C., & Jiang, S. C., (2015a), "Evaluation of methods for reverse osmosis membrane integrity monitoring for wastewater reuse," Journal of Water Process Engineering, 7, pp. 161–168.

Huang, X., Liu, L., Wen, T., Zhu, R., Zhang, J., and Cai, Z., (2015b), "Illumina MiSeq investigations on the changes of microbial community in the *Fusarium oxysporum cubense* infected soil during and after reductive soil disinfestation," Microbiological Research, 181, pp. 33–42.

Huang, X., Zhao, Z., Hernandez, D., and Jiang, S. C., (2016), "Near Real-Time Flow Cytometry Monitoring of Bacterial and Viral Removal Efficiencies during Water Reclamation Processes," Water, 8(10), pp. 464.

Huang, W., Chen, X., Jiang, X., and Zheng, B., (2017), "Characterization of sediment bacterial communities in plain lakes with different trophic statuses," MicrobiologyOpen, 6(5).

Huband, S., Hingston, P., Barone, L., and While, L., (2006), "A review of multiobjective test problems and a scalable test problem toolkit," IEEE Transactions on Evolutionary Computation, 10(5), pp. 477–506.

Huck, P. M., Fedorak, P. M., & Anderson, W. B., (1991), "Formation and removal of assimilable organic carbon during biological treatment," Journal of the American Water Works Association, pp. 69-80.

Huck, P. M., (2000). Optimizing Filtration in Biological Filters. American Water Works Association.

Huisman, L., & Wood, W. E., (1974). Slow sand filtration (Vol. 16). Geneva: World Health Organization.

Huismann, J., Matthijs, H. C. P., and Visser, P. M., (2006). Harmful Cyanobacteria. Springer Science & Business Media.

Hu, L. B., Yang, J. D., Zhou, W., Yin, Y. F., Chen, J., and Shi, Z. Q., (2009), "Isolation of a *Methylobacillus sp.* that degrades microcystin toxins associated with cyanobacteria," New Biotechnology, 26(3), pp. 205–211.

Hu, L., Zhang, F., Liu, C., and Wang, M., (2012), "Biodegradation of Microcystins by *Bacillus sp.* strain EMB," Energy Procedia, 16(Part C), pp. 2054–2059.

Hyenstrand, P., Metcalf, J. S., Beattie, K. A., and Codd, G. A., (2001a), "Effects of adsorption to plastics and solvent conditions in the analysis of the cyanobacterial toxin microcystin-LR by high performance liquid chromatography," Water Research, 35(14), pp. 3508–3511.

Hyenstrand, P., Metcalf, J. S., Beattie, K. A., and Codd, G. A., (2001b), "Losses of the cyanobacterial toxin microcystin-LR from aqueous solution by adsorption during laboratory manipulations," Toxicon, 39(4), pp. 589–594.

Hyenstrand, P., Rohrlack, T., Beattie, K. A., Metcalf, J. S., Codd, G. A., and Christoffersen, K., (2003), "Laboratory studies of dissolved radiolabelled microcystin-LR in lake water," Water Research, 37(14), pp. 3299–3306.

Igel, C., Hansen, N., and Roth, S., (2007), "Covariance Matrix Adaptation for Multi-objective Optimization," Evolutionary Computation, 15(1), pp. 1–28.

Imanishi, S., Kato, H., Mizuno, M., Tsuji, K., and Harada, K., (2005), "Bacterial Degradation of Microcystins and Nodularin," Chemical Research in Toxicology, 18(3), pp. 591–598.

Ingram, L. O., (1986), "Microbial tolerance to alcohols: role of the cell membrane," Trends in Biotechnology, 4(2), pp. 40–44.

Ingram, L. O., (1990), "Ethanol tolerance in bacteria," Critical Reviews in Biotechnology, 9(4), pp. 305–319.

Iooss, B., and Lemaître, P., (2015), "A Review on Global Sensitivity Analysis Methods," In G. Dellino & C. Meloni (Eds.), Uncertainty Management in Simulation-Optimization of Complex Systems: Algorithms and Applications (pp. 101–122). Boston, MA: Springer US.

Ishii, H., Nishijima, M., and Abe, T., (2004), "Characterization of degradation process of cyanobacterial hepatotoxins by a gram-negative aerobic bacterium," Water Research, 38(11), pp. 2667–2676.

Ishigami, T., and Homma, T., (1991), "An importance quantification technique in uncertainty analysis for computer models," In [1990] Proceedings. First International Symposium on Uncertainty Modeling and Analysis (pp. 398–403). College Park, MD, USA: IEEE Comput. Soc. Press.

Izaguirre, G., Jungblut, A. D., and Neilan, B. A., (2007), "Benthic cyanobacteria (*Oscillatoriaceae*) that produce microcystin-LR, isolated from four reservoirs in southern California," Water Research, 41(2), pp. 492–498.

Jacoby, W. G., (2000), "Loess: - a nonparametric, graphical tool for depicting relationships between variables," Electoral Studies, 19(4), pp. 577–613.

Jain, H., and Deb, K., (2014), "An evolutionary many-objective optimization algorithm using reference-point based nondominated sorting approach, Part II: Handling constraints and extending to an adaptive approach," IEEE Transactions on Evolutionary Computation, 18(4), pp. 602–622.

Janssens, G. K., and Pangilinan, J. M., (2010), "Multiple Criteria Performance Analysis of Non-dominated Sets Obtained by Multi-objective Evolutionary Algorithms for Optimisation," In Artificial Intelligence Applications and Innovations (pp. 94–103). Springer, Berlin, Heidelberg.

Jeffery, B., Barlow, T., Moizer, K., Paul, S., and Boyle, C., (2004), "Amnesic shellfish poison," Food and Chemical Toxicology, 42(4), pp. 545–557.

Jeong, S., Bae, H., Naidu, G., Jeong, D., Lee, S., and Vigneswaran, S., (2013), "Bacterial community structure in a biofilter used as a pretreatment for seawater desalination," Ecological Engineering, 60, pp. 370–381.

Jester, R., Lefebvre, K., Langlois, G., Vigilant, V., Baugh, K., and Silver, M. W., (2009a), "A shift in the dominant toxin-producing algal species in central California alters phycotoxins in food webs," Harmful Algae, 8(2), pp. 291–298.

Jester, R. J., Baugh, K. A., & Lefebvre, K. A., (2009b), "Presence of *Alexandrium catenella* and paralytic shellfish toxins in finfish, shellfish and rock crabs in Monterey Bay, California, USA," Marine Biology, 156(3), pp. 493.

Jewett, D. G., Hilbert, T. A., Logan, B. E., Arnold, R. G., & Bales, R. C., (1995), "Bacterial transport in laboratory columns and filters: Influence of ionic strength and pH on collision efficiency," Water Research, 29(7), pp. 1673–1680.

Jiang, Y., Shao, J., Wu, X., Xu, Y., & Li, R. (2011). Active and silent members in the mlr gene cluster of a microcystin-degrading bacterium isolated from Lake Taihu, China. FEMS Microbiology Letters, 322(2), 108–114.

Jiao, S., Chen, W., Wang, E., Wang, J., Liu, Z., Li, Y., and Wei, G., (2016), "Microbial succession in response to pollutants in batch-enrichment culture," Scientific Reports, 6, pp. srep21791.

Jimbo, Y., Okano, K., Shimizu, K., Maseda, H., Fujimoto, N., Utsumi, M., & Sugiura, N., (2010), "Quantification of Microcystin-degrading Bacteria in a Biofilm from a Practical Biological Treatment Facility by Real-time PCR," Journal of Water and Environment Technology, 8(3), pp. 193–201.

Jin, H., Chen, L., Wang, J., and Zhang, W., (2014), "Engineering biofuel tolerance in non-native producing microorganisms," Biotechnology Advances, 32(2), pp. 541–548.

Jing, W., Sui, G., and Liu, S., (2014), "Characteristics of a Microcystin-LR Biodegrading Bacterial Isolate: *Ochrobactrum sp.* FDT5," Bulletin of Environmental Contamination and Toxicology, 92(1), pp. 119–122.

Jochimsen, E. M., Carmichael, W. W., An, J., Cardo, D. M., Cookson, S. T., Holmes, C. E. M., … Jarvis, W. R., (1998), "Liver Failure and Death after Exposure to Microcystins at a Hemodialysis Center in Brazil," New England Journal of Medicine, 338(13), pp. 873–878.

Joe, H., (1990), "Multivariate concordance," Journal of Multivariate Analysis, 35(1), pp. 12–30.

Joe, H., (1997). *Multivariate Models and Multivariate Dependence Concepts*. CRC Press.

Jones, G. J., and Orr, P. T., (1994), "Release and degradation of microcystin following algicide treatment of a Microcystis aeruginosa bloom in a recreational lake, as determined by HPLC and protein phosphatase inhibition assay," Water Research, 28(4), pp. 871–876.

Jones, G. J., Bourne, D. G., Blakeley, R. L., and Doelle, H., (1994b), "Degradation of the cyanobacterial hepatotoxin microcystin by aquatic bacteria," Natural Toxins, 2(4), pp. 228–235.

Jost, L., (2006), "Entropy and diversity," Oikos, 113(2), pp. 363–375.

Jost, L., (2007), "Partitioning Diversity into Independent Alpha and Beta Components," Ecology, 88(10), pp. 2427–2439.

Jost, L., (2009), "Mismeasuring biological diversity: Response to Hoffmann and Hoffmann (2008)," Ecological Economics, 68(4), pp. 925–928.

Jurczak, T., Tarczynska, M., Izydorczyk, K., Mankiewicz, J., Zalewski, M., and Meriluoto, J., (2005), "Elimination of microcystins by water treatment processes—examples from Sulejow Reservoir, Poland," Water Research, 39(11), pp. 2394–2406.
Kansole, M. M. R., and Lin, T. F., (2016), "Microcystin-LR Biodegradation by *Bacillus sp.*: Reaction Rates and Possible Genes Involved in the Degradation," Water, 8(11), pp. 508.

Kargi, F., (2009), "Re-interpretation of the logistic equation for batch microbial growth in relation to Monod kinetics," Letters in Applied Microbiology, 48(4), pp. 398–401.

Kato, H., Imanishi, S. Y., Tsuji, K., & Harada, K., (2007), "Microbial degradation of cyanobacterial cyclic peptides," Water Research, 41(8), pp. 1754–1762.

Keir, G., Jegatheesan, V., & Vigneswaran, S., (2009), "Deep bed filtration: modeling theory and practice," Water and Wastewater Treatment Technologies, V. Saravanamuthu, ed., Eolss Publishers, Oxford, UK, pp. 263-307.

Kildsgaard, J., and Engesgaard, P., (2001), "Numerical analysis of biological clogging in two-dimensional sand box experiments," Journal of Contaminant Hydrology, 50(3–4), pp. 261–285.

Kim, H.-J., Miller, A. J., McGowan, J., & Carter, M. L. ,(2009), "Coastal phytoplankton blooms in the Southern California Bight," Progress in Oceanography, 82(2), pp. 137–147.

Kim, S.-H., Min, C.-S., & Lee, S., (2011), "Application of dissolved air flotation as pretreatment of seawater desalination," Desalination and Water Treatment, 33(1–3), pp. 261–266.

Kim, D., Chung, S., Lee, S., and Choi, J., (2012), "Relation of microbial biomass to counting units for Pseudomonas aeruginosa," African Journal of Microbiology Research, 6(21), pp. 4620–4622.

Kirk, P. D. W., Babtie, A. C., and Stumpf, M. P. H., (2015), "Systems biology (un)certainties," Science, 350(6259), pp. 386–388.

Knight, R., Jansson, J., Field, D., Fierer, N., Desai, N., Fuhrman, J. A., … Gilbert, J. A., (2012), "Unlocking the potential of metagenomics through replicated experimental design," Nature Biotechnology, 30(6), pp. 513–520.

Knightes, C. D., and Peters, C. A., (2000), "Statistical analysis of nonlinear parameter estimation for monod biodegradation kinetics using bivariate data," Biotechnology and Bioengineering, 69(2), pp. 160–170.

Knightes, C. D., and Peters, C. A., (2003), "Aqueous Phase Biodegradation Kinetics of 10 PAH Compounds," Environmental Engineering Science, 20(3), pp. 207–218.

Koch, A. L., (1982), "Multistep kinetics: Choice of models for the growth of bacteria," Journal of Theoretical Biology, 98(3), pp. 401–417.

Kooij, D. van der, Oranje, J. P., and Hijnen, W. A., (1982), "Growth of *Pseudomonas aeruginosa* in tap water in relation to utilization of substrates at concentrations of a few micrograms per liter," Applied and Environmental Microbiology, 44(5), pp. 1086–1095.

Kooij, D. van der, and Hijnen, W. A. M., (1984), "Substrate Utilization by an Oxalate-Consuming *Spirillum* Species in Relation to Its Growth in Ozonated Water," Applied and Environmental Microbiology, 47(3), pp. 551–559.

Kooij, D. van der, and Hijnen, W. A., (1985), "Determination of the concentration of maltose- and starch-like compounds in drinking water by growth measurements with a well-defined strain of a *Flavobacterium* species," Applied and Environmental Microbiology, 49(4), pp. 765–771.

Kosten, S., Huszar, V. L. M., Bécares, E., Costa, L. S., van Donk, E., Hansson, L.-A., … Scheffer, M., (2012), "Warmer climates boost cyanobacterial dominance in shallow lakes," Global Change Biology, 18(1), pp. 118–126.

Kovárová, K., Zehnder, A.J., and Egli, T., (1996), "Temperature-dependent growth kinetics of *Escherichia coli* ML 30 in glucose-limited continuous culture," Journal of Bacteriology 178, pp. 4530–4539.

Kovárová-Kovar, K., and Egli, T., (1998), "Growth Kinetics of Suspended Microbial Cells: From Single-Substrate-Controlled Growth to Mixed-Substrate Kinetics," Microbiology and Molecular Biology Reviews, 62(3), pp. 646–666.

Krasner, S.W., Sclimenti, M. J., and Cofffey, B. M., (1993), "Testing biologically active filters for removing aldehydes formed during ozonation," Journal of the American Water Works Association, 85(5).

Kruschke, J. K., (2011), "Bayesian Assessment of Null Values Via Parameter Estimation and Model Comparison," Perspectives on Psychological Science, 6(3), pp. 299–312.

Kruschke, J. K., (2013), "Bayesian Estimation Supersedes the t Test," Journal of Experimental Psychology: General, 142(2), pp. 573–603.

Kucherenko, S., Rodriguez-Fernandez, M., Pantelides, C., and Shah, N., (2009), "Monte Carlo evaluation of derivative-based global sensitivity measures," Reliability Engineering & System Safety, 94(7), pp. 1135–1148.

Kucherenko, S., Tarantola, S., and Annoni, P., (2012), "Estimation of global sensitivity indices for models with dependent variables," Computer Physics Communications, 183(4), pp. 937–946.

Kudela, R. M., Mioni, C., Peacock, M., Schraga, T., and Senn, D., (2015). Assessing SPATT in San Francisco Bay; SFEI Contract 1051 Final Report; University of California, Santa Cruz (UCSC). http://sfbaynutrients.sfei.org/sites/default/files/SPATT%20Final%20Report%20May2015.pdf (last accessed on 8/21/17).

Kurowicka, D., and Cooke, R. M., (2006). *Uncertainty Analysis with High Dimensional Dependence Modelling*. John Wiley & Sons.

Ladner, D. A., Vardon, D. R., & Clark, M. M., (2010), "Effects of shear on microfiltration and ultrafiltration fouling by marine bloom-forming algae," Journal of Membrane Science, 356(1–2), pp. 33–43.

Laloy, E., and Vrugt, J. A., (2012), "High-dimensional posterior exploration of hydrologic models using multiple-try DREAM(ZS) and high-performance computing," Water Resources Research, 48(1), pp. W01526.

Lam, A. K. Y., Fedorak, P. M., and Prepas, E. E., (1995a), "Biotransformation of the cyanobacterial hepatotoxin microcystin-LR, as determined by HPLC and protein phosphatase bioassay," Environmental Science & Technology, 29(1), pp. 242–246.

Lam, Angeline K. Y., Prepas, E. E., Spink, D., & Hrudey, S. E., (1995b), "Chemical control of hepatotoxic phytoplankton blooms: Implications for human health," Water Research, 29(8), pp. 1845–1854.

Landa, M., Cottrell, M. T., Kirchman, D. L., Kaiser, K., Medeiros, P. M., Tremblay, L., … Obernosterer, I., (2014), "Phylogenetic and structural response of heterotrophic bacteria to dissolved organic matter of different chemical composition in a continuous culture study," Environmental Microbiology, 16(6), pp. 1668–1681.

Landsberg, J. H., (2002), "The effects of harmful algal blooms on aquatic organisms," Reviews in Fisheries Science, 10(2), pp. 113-390.

Lane, J. Q., Roddam, C. M., Langlois, G. W., & Kudela, R. M., (2010), "Application of Solid Phase Adsorption Toxin Tracking (SPATT) for field detection of the hydrophilic phycotoxins domoic acid and saxitoxin in coastal California," Limnology and Oceanography: Methods, 8(11), pp. 645–660.

Lau, R. K. L., Kwok, A. C. M., Chan, W. K., Zhang, T. Y., and Wong, J. T. Y., (2007), "Mechanical Characterization of Cellulosic Thecal Plates in Dinoflagellates by Nanoindentation," Journal of Nanoscience and Nanotechnology, 7(2), pp. 452–457.

Lauderdale, C., Chadik, P., Kirisits, M. J., & Brown, J., (2012), "Engineered biofiltration: Enhanced biofilter performance through nutrient and peroxide addition," Journal - American Water Works Association, 104.

Laurent, P., Prévost, M., Cigana, J., Niquette, P., and Servais, P., (1999), "Biodegradable organic matter removal in biological filters: evaluation of the CHABROL model," Water Research, 33(6), pp. 1387–1398.

Lavallée, B., Lessard, P., and Besser, C., (2002), "Decay rate variability of active heterotrophic biomass," Water Science and Technology, 46(1–2), pp. 423–430.

Lawton, L. A., and Edwards, C., (2001), "Purification of microcystins," Journal of Chromatography A, 912(2), pp. 191–209.

Lawton, L. A., Welgamage, A., Manage, P. M., & Edwards, C., (2011), "Novel bacterial strains for the removal of microcystins from drinking water," *Water Science & Technology*, 63(6).

Laycock, M. V., Anderson, D. M., Naar, J., Goodman, A., Easy, D. J., Donovan, M. A., Alshihi, R., (2012), "Laboratory desalination experiments with some algal toxins," Desalination, 293, pp. 1–6.

Lee, J., and Walker, H. W., (2006), "Effect of Process Variables and Natural Organic Matter on Removal of Microcystin-LR by PAC–UF," Environmental Science & Technology, 40(23), pp. 7336–7342.

Lee, J., and Walker, H. W., (2008), "Mechanisms and factors influencing the removal of microcystin-LR by ultrafiltration membranes," Journal of Membrane Science, 320(1–2), pp. 240–247.

Lefebvre, K. A., Powell, C. L., Busman, M., Doucette, G. J., Moeller, P. D. R., Silver, J. B., … Tjeerdema, R. S., (1999), "Detection of domoic acid in northern anchovies and california sea lions associated with an unusual mortality event," Natural Toxins, 7(3), pp. 85–92.

Lefebvre, K. A., Trainer, V. L., and Scholz, N. L., (2004), "Morphological abnormalities and sensorimotor deficits in larval fish exposed to dissolved saxitoxin," Aquatic Toxicology, 66(2), pp. 159–170.

Lefebvre, K. A., Bill, B. D., Erickson, A., Baugh, K. A., O'Rourke, L., Costa, P. R., … Trainer, V. L., (2008), "Characterization of Intracellular and Extracellular Saxitoxin Levels in Both Field and Cultured *Alexandrium* spp. Samples from Sequim Bay, Washington," Marine Drugs, 6(2), pp. 103–116.

Lefebvre, K. A., and Robertson, A., (2010), "Domoic acid and human exposure risks: A review," Toxicon, 56(2), pp. 218–230.

Lefebvre, K. A., Frame, E. R., Gulland, F., Hansen, J. D., Kendrick, P. S., Beyer, R. P., … Marcinek, D. J., (2012), "A Novel Antibody-Based Biomarker for Chronic Algal Toxin Exposure and Sub-Acute Neurotoxicity," PLoS ONE, 7(5), pp. e36213.

Lefebvre, K. A., Kendrick, P. S., Ladiges, W., Hiolski, E. M., Ferriss, B. E., Smith, D. R., and Marcinek, D. J., (2017), "Chronic low-level exposure to the common seafood toxin domoic acid causes cognitive deficits in mice," Harmful Algae, 64, pp. 20–29.

Lehman, P. W., Boyer, G., Hall, C., Waller, S., & Gehrts, K., (2005), "Distribution and toxicity of a new colonial Microcystis aeruginosa bloom in the San Francisco Bay Estuary, California," Hydrobiologia, 541(1), pp. 87–99.

Lehman, P. W., Teh, S. J., Boyer, G. L., Nobriga, M. L., Bass, E., & Hogle, C., (2009), "Initial impacts of Microcystis aeruginosa blooms on the aquatic food web in the San Francisco Estuary," Hydrobiologia, 637(1), pp. 229–248.

Lehman, P. W., Marr, K., Boyer, G. L., Acuna, S., & Teh, S. J., (2013), "Long-term trends and causal factors associated with Microcystis abundance and toxicity in San Francisco Estuary and implications for climate change impacts," Hydrobiologia, 718(1), pp. 141–158.

Lemes, G. A. F., Kersanach, R., da S. Pinto, L., Dellagostin, O. A., Yunes, J. S., and Matthiensen, A., (2008), "Biodegradation of microcystins by aquatic *Burkholderia sp.* from a South Brazilian coastal lagoon," Ecotoxicology and Environmental Safety, 69(3), pp. 358–365.

Lemes, G. A., Kist, L. W., Bogo, M. R., and Yunes, J. S., (2015), "Biodegradation of [D-Leu1] microcystin-LR by a bacterium isolated from sediment of Patos Lagoon estuary, Brazil," Journal of Venomous Animals and Toxins Including Tropical Diseases, 21, pp. 4.

Leparc, J., Rapenne, S., Courties, C., Lebaron, P., Croué, J. P., Jacquemet, V., & Turner, G., (2007), "Water quality and performance evaluation at seawater reverse osmosis plants through the use of advanced analytical tools," Desalination, 203(1–3), pp. 243–255.

Levin, E. D., Pizarro, K., Pang, W. G., Harrison, J., and Ramsdell, J. S., (2005), "Persisting behavioral consequences of prenatal domoic acid exposure in rats," Neurotoxicology and Teratology, 27(5), pp. 719–725.

Levin, E. D., Pang, W. G., Harrison, J., Williams, P., Petro, A., and Ramsdell, J. S., (2006), "Persistent neurobehavioral effects of early postnatal domoic acid exposure in rats," Neurotoxicology and Teratology, 28(6), pp. 673–680.

Lewitus, A. J., Horner, R. A., Caron, D. A., Garcia-Mendoza, E., Hickey, B. M., Hunter, M., … Tweddle, J. F., (2012), "Harmful algal blooms along the North American west coast region: History, trends, causes, and impacts," Harmful Algae, 19, pp. 133–159.

Lezcano, M. Á., Morón-López, J., Agha, R., López-Heras, I., Nozal, L., Quesada, A., and El-Shehawy, R., (2016), "Presence or Absence of mlr Genes and Nutrient Concentrations Co-Determine the Microcystin Biodegradation Efficiency of a Natural Bacterial Community," Toxins, 8(11), pp. 318.

Liao, X., Chen, C., Zhang, J., Dai, Y., Zhang, X., & Xie, S., (2014), "Operational performance, biomass and microbial community structure: impacts of backwashing on drinking water biofilter," Environmental Science and Pollution Research, 22(1), pp. 546–554.

Liebscher, E., (2008), "Construction of asymmetric multivariate copulas," Journal of Multivariate Analysis, 99(10), pp. 2234–2250.

Ligon, T. S., Fröhlich, F., Chiş, O. T., Banga, J. R., Balsa-Canto, E., and Hasenauer, J., (2018), "GenSSI 2.0: multi-experiment structural identifiability analysis of SBML models," Bioinformatics, 34(8), pp. 1421–1423.

Li, J., Shimizu, K., Utsumi, M., Nakamoto, T., Sakharkar, M. K., Zhang, Z., & Sugiura, N., (2011a), "Dynamics of the functional gene copy number and overall bacterial community during microcystin-LR degradation by a biological treatment facility in a drinking water treatment plant," Journal of Bioscience and Bioengineering, 111(6), pp. 695–701.

Li, J., Shimizu, K., Maseda, H., Lu, Z., Utsumi, M., Zhang, Z., & Sugiura, N., (2011b), "Investigations into the biodegradation of microcystin-LR mediated by the biofilm in wintertime from a biological treatment facility in a drinking-water treatment plant," Bioresource Technology, 106, pp. 27–35.

Li, J., Shimizu, K., Sakharkar, M. K., Utsumi, M., Zhang, Z., and Sugiura, N., (2011c), "Comparative study for the effects of variable nutrient conditions on the biodegradation of microcystin-LR and concurrent dynamics in microcystin-degrading gene abundance," Bioresource Technology, 102(20), pp. 9509–9517.

Li, X., Rui, J., Mao, Y., Yannarell, A., and Mackie, R., (2014a), "Dynamics of the bacterial community structure in the rhizosphere of a maize cultivar," Soil Biology and Biochemistry, 68, pp. 392–401.

Li, M., Yang, S., and Liu, X., (2014b), "Shift-Based Density Estimation for Pareto-Based Algorithms in Many-Objective Optimization," IEEE Transactions on Evolutionary Computation, 18(3), pp. 348–365.

Li, H., and Pan, G., (2014), "Enhanced and continued degradation of microcystins using microorganisms obtained through natural media," Journal of Microbiological Methods, 96(Supplement C), pp. 73–80.

Li, J., Shimizu, K., Akasako, H., Lu, Z., Akiyama, S., Goto, M., Utsumi, M., and Sugiura, N., (2015a), "Assessment of the factors contributing to the variations in microcystins

biodegradability of the biofilms on a practical biological treatment facility," Bioresource Technology, Vol.175, pp. 463-472.

Li, K., Deb, K., Zhang, Q., and Kwong, S., (2015b), "An Evolutionary Many-Objective Optimization Algorithm Based on Dominance and Decomposition," IEEE Transactions on Evolutionary Computation, 19(5), pp. 694–716.

Li, H., Ai, H., Kang, L., Sun, X., and He, Q., (2016), "Simultaneous *Microcystis* Algicidal and Microcystin Degrading Capability by a Single *Acinetobacter* Bacterial Strain," Environmental Science & Technology, 50(21), pp. 11903–11911.

Li, J., Li, R., and Li, J., (2017), "Current research scenario for microcystins biodegradation – A review on fundamental knowledge, application prospects and challenges," Science of The Total Environment, 595, pp. 615–632.

Li, Z., Lu, P., Zhang, D., and Zhang, T., (2018), "Practical Identifiability Analysis and Optimal Experimental Design for the Parameter Estimation of the ASM2d-Based EBPR Anaerobic Submodel," Mathematical Problems in Engineering, pp. 1–9.

Linz, A. M., Crary, B. C., Shade, A., Owens, S., Gilbert, J. A., Knight, R., and McMahon, K. D., (2017), "Bacterial Community Composition and Dynamics Spanning Five Years in Freshwater Bog Lakes," MSphere, 2(3), pp. e00169-17.

Liu, Q., and Homma, T., (2009), "A new computational method of a moment-independent uncertainty importance measure," Reliability Engineering & System Safety, 94(7), pp. 1205–1211.

Liu, Y., & Tay, J.-H., (2001), "Detachment forces and their influence on the structure and metabolic behaviour of biofilms," World Journal of Microbiology and Biotechnology, 17(2), pp. 111–117.

Liu, J. R., Liu, C. T., Edwards, E. A., and Liss, S. N., (2006), "Effect of phosphorus limitation on microbial floc structure and gene expression in activated sludge," Water Science and Technology, 54(1), pp. 247–255.

Liu, Y., and Li, J., (2008), "Role of Pseudomonas aeruginosa Biofilm in the Initial Adhesion, Growth and Detachment of Escherichia coli in Porous Media," Environmental Science & Technology, 42(2), pp. 443–449.

Liu, C., and Zachara, J. M., (2001), "Uncertainties of Monod Kinetic Parameters Nonlinearly Estimated from Batch Experiments," Environmental Science & Technology, 35(1), pp. 133–141.

Liu, G., Qian, Y., Dai, S., and Feng, N., (2008), "Adsorption of Microcystin LR and LW on Suspended Particulate Matter (SPM) at Different pH," Water, Air, and Soil Pollution, 192(1–4), pp. 67–76.

Loftin, K. A., Graham, J. L., Hilborn, E. D., Lehmann, S. C., Meyer, M. T., Dietze, J. E., and Griffith, C. B., (2016), "Cyanotoxins in inland lakes of the United States: Occurrence and potential recreational health risks in the EPA National Lakes Assessment 2007," Harmful Algae, 56, pp. 77–90.

Lopes, A. R., Manaia, C. M., & Nunes, O. C., (2014), "Bacterial community variations in an alfalfa-rice rotation system revealed by 16S rRNA gene 454-pyrosequencing," FEMS Microbiology Ecology, 87(3), pp. 650–663.

López Rodas, V., Maneiro, E., Martínez, J., Navarro, M., & Costas, E., (2006), "Harmful algal blooms, red tides and human health: Diarrhetic shellfish poisoning and colorectal cancer," *Anales de la Real Academia Nacional de Farmacia*, 72, pp. 391–408.

Losic, D., Short, K., Mitchell, J. G., Lal, R., and Voelcker, N. H., (2007), "AFM Nanoindentations of Diatom Biosilica Surfaces," Langmuir, 23(9), pp. 5014–5021.

Lovanh, N., Hunt, C. S., and Alvarez, P. J. J., (2002), "Effect of ethanol on BTEX biodegradation kinetics: aerobic continuous culture experiments," Water Research, 36(15), pp. 3739–3746.

MacKenzie, L., Beuzenberg, V., Holland, P., McNabb, P., & Selwood, A., (2004), "Solid phase adsorption toxin tracking (SPATT): a new monitoring tool that simulates the biotoxin contamination of filter feeding bivalves," Toxicon, 44(8), pp. 901–918.

MacKenzie, L., Beuzenberg, V., Holland, P., McNabb, P., Suzuki, T., & Selwood, A., (2005), "Pectenotoxin and okadaic acid-based toxin profiles in *Dinophysis acuta* and *Dinophysis acuminata* from New Zealand," Harmful Algae, 4(1), pp. 75–85.

Maghsoudi, E., Fortin, N., Greer, C., Maynard, C., Pagé, A., Vo Duy, S., … Dorner, S., (2016), "Cyanotoxin degradation activity and mlr gene expression profiles of a *Sphingopyxis sp.* isolated from Lake Champlain, Canada," Environmental Science: Processes & Impacts, 18(11), pp. 1417–1426.

Maheshwari, V., Rangaiah, G. P., and Samavedham, L., (2013), "Multiobjective Framework for Model-based Design of Experiments to Improve Parameter Precision and Minimize Parameter Correlation," Industrial & Engineering Chemistry Research, 52(24), pp. 8289–8304.

Malagoli, D., Marchesini, E., and Ottaviani, E., (2006), "Lysosomes as the target of yessotoxin in invertebrate and vertebrate cell lines," Toxicology Letters, 167(1), pp. 75–83.

Manage, P. M., Edwards, C., Singh, B. K., & Lawton, L. A., (2009), "Isolation and Identification of Novel Microcystin-Degrading Bacteria," Applied and Environmental Microbiology, 75(21), pp. 6924–6928.

Manerio, E., Rodas, V. L., Costas, E., and Hernandez, J. M., (2008), "Shellfish consumption: A major risk factor for colorectal cancer," Medical Hypotheses, 70(2), 409–412.

Manheim, D., Cheung, Y.-M., and Jiang, S., (2018), "The Effect of Organic Carbon Addition on the Community Structure and Kinetics of Microcystin-Degrading Bacterial Consortia," Water, 10(11), pp. 1523.

Manheim, D. C., and Detwiler, R., (2018), "Accurate and Reliable Estimation of Kinetic Parameters for Environmental Engineering Applications: A Global, Multi Objective, Bayesian Optimization Approach," MethodsX (In Press).

Manheim, D. C., Detwiler, R., and Jiang, S. C., (2019), "Application of Unstructured Kinetic Models to Predict Microcystin Biodegradation: Towards A Practical Approach for Drinking Water Treatment," Water Research, 149(1), pp. 617-631.

Mankiewicz-Boczek, J., Gągała, I., Jurczak, T., Jaskulska, A., Pawełczyk, J., and Dziadek, J., (2015), "Bacteria homologus to *Aeromonas* capable of microcystin degradation," Open Life Sciences, 10(1).

Manner, H., and Reznikova, O., (2012), "A Survey on Time-Varying Copulas: Specification, Simulations, and Application," Econometric Reviews, 31(6), pp. 654–687.

Mara, T. A., Tarantola, S., and Annoni, P., (2015), "Non-parametric methods for global sensitivity analysis of model output with dependent inputs," Environmental Modelling & Software, 72, pp. 173–183.

Marshall, A. W., and Olkin, I., (1988), "Families of Multivariate Distributions," Journal of the American Statistical Association, 83(403), pp. 834–841.

Marshall, A. W., and Olkin, I., (1997), "A new method for adding a parameter to a family of distributions with application to the exponential and Weibull families," Biometrika, 84(3), pp. 641–652.

Marsili-Libelli, S., (1992), "Parameter estimation of ecological models," Ecological Modelling, 62(4), pp. 233–258.

Maruyama, T., Park, H.-D., Ozawa, K., Tanaka, Y., Sumino, T., Hamana, K., … Kato, K., (2006), "*Sphingosinicella microcystinivorans*, a microcystin-degrading bacterium," International Journal of Systematic and Evolutionary Microbiology, 56(1), pp. 85–89.

Matott, L. S., Babendreier, J. E., and Purucker, S. T., (2009), "Evaluating uncertainty in integrated environmental models: A review of concepts and tools," Water Resources Research, 45(6).

McDowall, B., Ho, L., Saint, C., & Newcombe, G., (2007), "Removal of geosmin and 2-methylisoborneol through biologically active sand filters," International Journal of Environment and Waste Management, 1(4), pp. 311–320.

McDowall, B., Hoefel, D., Newcombe, G., Saint, C. P., & Ho, L., (2009), "Enhancing the biofiltration of geosmin by seeding sand filter columns with a consortium of geosmin-degrading bacteria," Water Research, 43(2), pp. 433–440.

McDowell-Boyer, L. M., (1992), "Chemical mobilization of micron-sized particles in saturated porous media under steady flow conditions," Environmental Science & Technology, 26(3), pp. 586–593.

McKie, M. J., Taylor-Edmonds, L., Andrews, S. A., & Andrews, R. C., (2015), "Engineered biofiltration for the removal of disinfection by-product precursors and genotoxicity," Water Research, 81, pp. 196–207.

McLean, K. A. P., and McAuley, K. B., (2012), "Mathematical modelling of chemical processes—obtaining the best model predictions and parameter estimates using identifiability and estimability procedures," The Canadian Journal of Chemical Engineering, 90(2), pp. 351–366.

Merel, S., Walker, D., Chicana, R., Snyder, S., Baurès, E., and Thomas, O., (2013), "State of knowledge and concerns on cyanobacterial blooms and cyanotoxins," Environment International, 59, pp. 303–327.

Meyerhofer, P., Desormeaux, E., Luckenbach, H., 2010. *Seawater Reverse Osmosis Desalination Pilot Test Program Report*. Santa Cruz Water District: Santa Cruz, CA, USA.

Michels, M. H. A., Goot, A. J. van der, Norsker, N.-H., and Wijffels, R. H., (2010), "Effects of shear stress on the microalgae *Chaetoceros muelleri*," Bioprocess and Biosystems Engineering, 33(8), pp. 921–927.

Michiels, F., Koch, I., and Schepper, A. D., (2011), "A New Method for the Construction of Bivariate Archimedean Copulas Based on the λ Function," Communications in Statistics - Theory and Methods, 40(15), pp. 2670–2679.

Michiels, F., and De Schepper, A., (2012), "How to improve the fit of Archimedean copulas by means of transforms," Statistical Papers, 53(2), pp. 345–355.

Missimer, T. M., Ghaffour, N., Dehwah, A. H. A., Rachman, R., Maliva, R. G., and Amy, G., (2013), "Subsurface intakes for seawater reverse osmosis facilities: Capacity limitation, water quality improvement, and economics," Desalination, 322, pp. 37–51.

Mohseni Ahooyi, T., Arbogast, J. E., and Soroush, M., (2014), "Rolling Pin Method: Efficient General Method of Joint Probability Modeling," Industrial & Engineering Chemistry Research, 53(52), pp. 20191–20203.

Mohseni Ahooyi, T., Arbogast, J. E., and Soroush, M., (2015), "Applications of the Rolling Pin Method. 1. An Efficient Alternative to Bayesian Network Modeling and Inference," Industrial & Engineering Chemistry Research, 54(16), pp. 4316–4325.

Monod, J., (1949), "The growth of bacterial cultures," Annual Review of Microbiology, 3.

Morales, V. L., Gao, B., & Steenhuis, T. S., (2009), "Grain Surface-Roughness Effects on Colloidal Retention in the Vadose Zone," Vadose Zone Journal, 8(1).

Moser, H., (1958), "The dynamics of bacterial populations maintained in the chemostat," Carnegie Institution of Washington.

Motulsky, H., and Christopoulos, A., (2004). *Fitting Models to Biological Data Using Linear and Nonlinear Regression: A Practical Guide to Curve Fitting*. Oxford University Press.

Mou, X., Lu, X., Jacob, J., Sun, S., & Heath, R., (2013), "Metagenomic Identification of Bacterioplankton Taxa and Pathways Involved in Microcystin Degradation in Lake Erie," PLOS ONE, 8(4).

Mu, R., He, Y., Liu, S., Wang, X., and Fan, Z., (2009), "The Algicidal Characteristics of One Algae-Lysing FDT5 Bacterium on Microcystis aeruginosa," Geomicrobiology Journal, 26(7), pp. 516–521.

Myers, J. A., Curtis, B. S., and Curtis, W. R., (2013), "Improving accuracy of cell and chromophore concentration measurements using optical density," BMC Biophysics, 6, pp. 4.

Naidu, G., Jeong, S., Vigneswaran, S., and Rice, S. A., (2013), "Microbial activity in biofilter used as a pretreatment for seawater desalination," Desalination, 309, pp. 254–260.

Nelsen, R. B., (2007). *An Introduction to Copulas*. Springer Science & Business Media.

Newton, R. J., and McLellan, S. L., (2015), "A unique assemblage of cosmopolitan freshwater bacteria and higher community diversity differentiate an urbanized estuary from oligotrophic Lake Michigan," Frontiers in Microbiology, 6.

Ng, H. Y., and Elimelech, M., (2004), "Influence of colloidal fouling on rejection of trace organic contaminants by reverse osmosis," Journal of Membrane Science, 244(1), pp. 215–226.

Nguyen, M. L., Westerhoff, P., Baker, L., Hu, Q., Esparza-Soto, M., and Sommerfeld, M., (2005), "Characteristics and Reactivity of Algae-Produced Dissolved Organic Carbon," Journal of Environmental Engineering, 131(11), pp. 1574–1582.

Nihtilä, M., and Virkkunen, J., (1977), "Practical identifiability of growth and substrate consumption models," Biotechnology and Bioengineering, 19(12), pp. 1831–1850.

Nishijima, W., & Speitel Jr., G. E., (2004), "Fate of biodegradable dissolved organic carbon produced by ozonation on biological activated carbon," Chemosphere, 56(2), pp. 113–119.

Nishiwaki-Matsushima, R., Ohta, T., Nishiwaki, S., Suganuma, M., Kohyama, K., Ishikawa, T., … Fujiki, H., (1992), "Liver tumor promotion by the cyanobacterial cyclic peptide toxin microcystin-LR," Journal of Cancer Research and Clinical Oncology, 118(6), pp. 420–424.

Noel, J. T., and Narang, A., (2009), "Gene Regulation in Continuous Cultures: A Unified Theory for Bacteria and Yeasts," Bulletin of Mathematical Biology, 71(2), pp. 453–514.

Norton, J. P., (2008), "Algebraic sensitivity analysis of environmental models," Environmental Modelling & Software, 23(8), pp. 963–972.

Nybom, Sonja M. K., Salminen, S. J., and Meriluoto, J. A. O., (2007), "Removal of microcystin-LR by strains of metabolically active probiotic bacteria," FEMS Microbiology Letters, 270(1), pp. 27–33.

Nybom, Sonja M. K., Salminen, S. J., and Meriluoto, J. A. O., (2008a), "Specific strains of probiotic bacteria are efficient in removal of several different cyanobacterial toxins from solution," Toxicon, 52(2), pp. 214–220.

Nybom, Sonja M. K., Collado, M. C., Surono, I. S., Salminen, S. J., and Meriluoto, J. A. O., (2008b), "Effect of Glucose in Removal of Microcystin-LR by Viable Commercial Probiotic Strains and Strains Isolated from Dadih Fermented Milk," Journal of Agricultural and Food Chemistry, 56(10), pp. 3714–3720.

Nybom, S. M. K., Dziga, D., Heikkilä, J. E., Kull, T. P. J., Salminen, S. J., and Meriluoto, J. A. O., (2012), "Characterization of microcystin-LR removal process in the presence of probiotic bacteria," Toxicon, 59(1), pp. 171–181.
OECD, (2000), "Test No. 106: Adsorption -- Desorption Using a Batch Equilibrium Method," OECD Guidelines for the Testing of Chemicals, Section 1, OECD Publishing, Paris,

Okano, K., Shimizu, K., Kawauchi, Y., Maseda, H., Utsumi, M., Zhang, Z., … Sugiura, N., (2009), "Characteristics of a Microcystin-Degrading Bacterium under Alkaline Environmental Conditions," Journal of Toxicology, 2009.

Okhrin, O., Okhrin, Y., and Schmid, W., (2013), "On the structure and estimation of hierarchical Archimedean copulas," Journal of Econometrics, 173(2), pp. 189–204.

Okpokwasili, G. C., and Nweke, C. O., (2006), "Microbial growth and substrate utilization kinetics," African Journal of Biotechnology, 5(4), pp. 305–317.

O'Melia, C. R., & Stumm, W., (1967), "Theory of water filtration," Journal of the American Water Works Association, 59(11), pp. 1393-1412.

O'Neil, J. M., Davis, T. W., Burford, M. A., and Gobler, C. J., (2012), "The rise of harmful cyanobacteria blooms: The potential roles of eutrophication and climate change," Harmful Algae, 14, pp. 313–334.

Otten, T. G., and Paerl, H. W., (2015), "Health Effects of Toxic Cyanobacteria in U.S. Drinking and Recreational Waters: Our Current Understanding and Proposed Direction," Current Environmental Health Reports, 2(1), pp. 75–84.

Ouiroga, J. M., Perales, J. A., Romero, L. I., and Sales, D., (1999), "Biodegradation kinetics of surfactants in seawater," Chemosphere, 39(11), pp. 1957–1969.

Padilla, I. Y., Yeh, T.-C. J., and Conklin, M. H., (1999), "The effect of water content on solute transport in unsaturated porous media," Water Resources Research, 35(11), pp. 3303–3313.

Paerl, H. W., & Huisman, J., (2009), "Climate change: a catalyst for global expansion of harmful cyanobacterial blooms," Environmental Microbiology Reports, 1(1), pp. 27–37.

Paerl, H. W., Xu, H., McCarthy, M. J., Zhu, G., Qin, B., Li, Y., & Gardner, W. S., (2011), "Controlling harmful cyanobacterial blooms in a hyper-eutrophic lake (Lake Taihu, China): The need for a dual nutrient (N & P) management strategy," Water Research, 45(5), pp. 1973–1983.

Paerl, H. W., & Paul, V. J., (2012), "Climate change: Links to global expansion of harmful cyanobacteria," Water Research, 46(5), pp. 1349–1363.

Paerl, H. W., & Otten, T. G., (2013), "Harmful Cyanobacterial Blooms: Causes, Consequences, and Controls," Microbial Ecology, 65(4), pp. 995–1010.

Pallmann, P., Schaarschmidt, F., Hothorn, L. A., Fischer, C., Nacke, H., Priesnitz, K. U., and Schork, N. J., (2012), "Assessing group differences in biodiversity by simultaneously testing a user-defined selection of diversity indices," Molecular Ecology Resources, 12(6), pp. 1068–1078.

Panikov, N., and Pirt, S. J., (1978), "The Effects of Cooperativity and Growth Yield Variation on the Kinetics of Nitrogen or Phosphate Limited Growth of *Chlorella* in a Chemostat Culture," Microbiology, 108(2), pp. 295–303.

Panikov, N. (1995). *Microbial Growth Kinetics* (1st ed.). London, United Kingdom: Chapman & Hall.

Paredes, I., Rietjens, I. M. C. M., Vieites, J. M., & Cabado, A. G., (2011), "Update of risk assessments of main marine biotoxins in the European Union," Toxicon, 58(4), pp. 336–354.

Pardieck, D. L., Bouwer, E. J., and Stone, A. T., (1992), "Hydrogen peroxide use to increase oxidant capacity for in situ bioremediation of contaminated soils and aquifers: A review," Journal of Contaminant Hydrology, 9(3), pp. 221–242.

Park, H.-D., Sasaki, Y., Maruyama, T., Yanagisawa, E., Hiraishi, A., and Kato, K., (2001), "Degradation of the cyanobacterial hepatotoxin microcystin by a new bacterium isolated from a hypertrophic lake," Environmental Toxicology, 16(4), pp. 337–343.

Parks, D. H., Tyson, G. W., Hugenholtz, P., and Beiko, R. G., (2014), "STAMP: statistical analysis of taxonomic and functional profiles," Bioinformatics, 30(21), pp. 3123–3124.

Parlange, J. Y., Starr, J. L., Barry, D. A., and Braddock, R. D., (1984), "Some Approximate Solutions of the Transport Equation With Irreversible Reactions," Soil science, 137(6), pp. 434-442.

Patton, A. ,(2013), "Copula Methods for Forecasting Multivariate Time Series," Handbook of Economic Forecasting, 2, pp. 899–960.

Paz, B., Riobó, P., Luisa Fernández, M., Fraga, S., and Franco, J. M., (2004), "Production and release of yessotoxins by the dinoflagellates *Protoceratium reticulatum* and *Lingulodinium polyedrum* in culture," Toxicon, 44(3), pp. 251–258.

Paz, B., Daranas, A. H., Norte, M., Riobó, P., Franco, J. M., and Fernández, J. J., (2008), "Yessotoxins, a Group of Marine Polyether Toxins: an Overview," Marine Drugs, 6(2), pp. 73–102.

Pelaez, M., Antoniou, M. G., He, X., Dionysiou, D. D., de la Cruz, A. A., Tsimeli, K., … Westrick, J., (2010), "Sources and Occurrence of Cyanotoxins Worldwide," In D. Fatta-Kassinos, K. Bester, & K. Kümmerer (Eds.), Xenobiotics in the Urban Water Cycle: Mass Flows, Environmental Processes, Mitigation and Treatment Strategies (pp. 101–127). Dordrecht: Springer Netherlands.

Pereira, R. P. A., Peplies, J., Brettar, I., & Höfle, M. G., (2017), "Development of a genus-specific next generation sequencing approach for sensitive and quantitative determination of the *Legionella* microbiome in freshwater systems," BMC Microbiology, 17(1), pp. 79.

Pharand, L., Van Dyke, M. I., Anderson, W. B., & Huck, P. M., (2014), "Assessment of biomass in drinking water biofilters by adenosine triphosphate," Journal of the American Water Works Association, 106(10), pp. E433–E444.

Phujomjai, Y., and Somdee, T., (2013), "Isolation and Characterization of Microcystin-Degrading Bacterium," Journal of Life Sciences and Technologies, 1(4).

Phujomjai, Y., Somdee, A., and Somdee, T., (2016), "Biodegradation of microcystin [Dha7]MC-LR by a novel microcystin-degrading bacterium in an internal airlift loop bioreactor," Water Science and Technology, 73(2), pp. 267–274.

Pianosi, F., and Wagener, T., (2015), "A simple and efficient method for global sensitivity analysis based on cumulative distribution functions," Environmental Modelling & Software, 67, pp. 1–11.

Pianosi, F., Beven, K., Freer, J., Hall, J. W., Rougier, J., Stephenson, D. B., and Wagener, T., (2016), "Sensitivity analysis of environmental models: A systematic review with practical workflow," Environmental Modelling & Software, 79, pp. 214–232.

Pilloni, G., Granitsiotis, M. S., Engel, M., and Lueders, T., (2012), "Testing the Limits of 454 Pyrotag Sequencing: Reproducibility, Quantitative Assessment and Comparison to T-RFLP Fingerprinting of Aquifer Microbes," PLOS ONE, 7(7), pp. e40467.

Plantier, S., Castaing, J.-B., Sabiri, N.-E., Massé, A., Jaouen, P., & Pontié, M., (2013), "Performance of a sand filter in removal of algal bloom for SWRO pre-treatment," Desalination and Water Treatment, 51(7–9), pp. 1838–1846.

Plischke, E., Borgonovo, E., and Smith, C. L., (2013), "Global sensitivity measures from given data," European Journal of Operational Research, 226(3), pp. 536–550.

Postel, S., (1996), "Dividing the waters: food security, ecosystem health, and the new politics of scarcity.," Worldwatch Institute, 132, 76.

Postel, S., (2014). *The Last Oasis: Facing Water Scarcity*. Routledge.

Powell, E.O., (1967), "The growth of microorganisms as a function of substrate concentration," In: Evans, C.G.T., Strange, R.E., Tempest, D.W. (Eds.), Microbial Physiology and Continuous Culture. HMSO, London, United Kingdom.

Powell, M. J. D., (1978), "A fast algorithm for nonlinearly constrained optimization calculations," In Numerical Analysis (pp. 144–157). Springer, Berlin, Heidelberg.

Prassopoulou, E., Katikou, P., Georgantelis, D., and Kyritsakis, A., (2009), "Detection of okadaic acid and related esters in mussels during diarrhetic shellfish poisoning (DSP) episodes in Greece using the mouse bioassay, the PP2A inhibition assay and HPLC with fluorimetric detection," Toxicon, 53(2), pp. 214–227.

Puddick, J., Prinsep, M. R., Wood, S. A., Kaufononga, S. A. F., Cary, S. C., and Hamilton, D. P., (2014), "High Levels of Structural Diversity Observed in Microcystins from Microcystis CAWBG11 and Characterization of Six New Microcystin Congeners," Marine Drugs, 12(11), pp. 5372–5395.

Qin, A. K., and Suganthan, P. N., (2005), "Self-adaptive differential evolution algorithm for numerical optimization," In 2005 IEEE Congress on Evolutionary Computation (Vol. 2, pp. 1785-1791 Vol. 2).

Qin, B., Zhu, G., Gao, G., Zhang, Y., Li, W., Paerl, H. W., & Carmichael, W. W., (2009a), "A Drinking Water Crisis in Lake Taihu, China: Linkage to Climatic Variability and Lake Management," Environmental Management, 45(1), pp. 105–112.

Qin, A. K., Huang, V. L., and Suganthan, P. N., (2009b), "Differential Evolution Algorithm With Strategy Adaptation for Global Numerical Optimization," IEEE Transactions on Evolutionary Computation, 13(2), pp. 398–417.

Qiongqiong, X., Wei, C., and Xingcan, Z., (2008), "Modeling of NOM-removal in drinking water biofilters," Water Science and Technology: Water Supply, 8(5), pp. 499–504.

Rahman, I., Dyke, M. I. V., Anderson, W. B., Jin, X., Ndiongue, S., & Huck, P. M., (2016), "Effect of phosphorus addition on biofiltration pre-treatment to reduce ultrafiltration membrane fouling," Desalination and Water Treatment, 0(0), pp. 1–13.

Rajagopalan, R., and Tien, C., (1976), "Trajectory analysis of deep-bed filtration with the sphere-in-cell porous media model," AIChE Journal, 22(3), pp. 523–533.

Rajan, A., Kuang, Y. C., Ooi, M. P., Demidenko, S. N., and Carstens, H., (2018), "Moment-Constrained Maximum Entropy Method for Expanded Uncertainty Evaluation," IEEE Access, 6, pp. 4072–4082.

Ramanan, S., Tang, J., and Velayudhan, A., (2000), "Isolation and preparative purification of microcystin variants," Journal of Chromatography A, 883(1), pp. 103–112.

Ramkrishna, D., Fredrickson, A. G., and Tsuchiya, H. M., (1967), "Dynamics of microbial propagation: Models considering inhibitors and variable cell composition," Biotechnology and Bioengineering, 9(2), pp. 129–170.

Ramani, A., Rein, K., Shetty, K. G., and Jayachandran, K., (2012), "Microbial degradation of microcystin in Florida's freshwaters," Biodegradation, 23(1), pp. 35–45.

Rapala, J., Lahti, K., Sivonen, K., and Niemelä, S. I., (1994), "Biodegradability and adsorption on lake sediments of cyanobacterial hepatotoxins and anatoxin-a," Letters in Applied Microbiology, 19(6), pp. 423–428.

Rapala, J., Berg, K. A., Lyra, C., Niemi, R. M., Manz, W., Suomalainen, S., … Lahti, K., (2005), "*Paucibacter toxinivorans*, a bacterium that degrades cyclic cyanobacterial hepatotoxins microcystins and nodularin," International Journal of Systematic and Evolutionary Microbiology, 55(4), pp. 1563–1568.

Rasheed, A., Amirtharajah, A., Al-Shawwa, A., & Huck, P. M., (1998), "Effects of backwashing on biological filters," Journal of the American Water Works Association, 90(12).

Rastogi, R. P., Sinha, R. P., & Incharoensakdi, A., (2014), "The cyanotoxin-microcystins: current overview," Reviews in Environmental Science and Bio/Technology, 13(2), pp. 215–249.

Razavi, S., and Gupta, H. V., (2015), "What do we mean by sensitivity analysis? The need for comprehensive characterization of "global" sensitivity in Earth and Environmental systems models," Water Resources Research, 51(5), pp. 3070–3092.

Razavi, S., and Gupta, H. V., (2016a), "A new framework for comprehensive, robust, and efficient global sensitivity analysis: 1. Theory," Water Resources Research, 52(1), pp. 423–439.

Razavi, S., and Gupta, H. V., (2016b), "A new framework for comprehensive, robust, and efficient global sensitivity analysis: 2. Application," Water Resources Research, 52(1), pp. 440–455.

Reardon, K. F., Mosteller, D. C., and Bull Rogers, J. D., (2000), "Biodegradation kinetics of benzene, toluene, and phenol as single and mixed substrates for *Pseudomonas putida* F1," Biotechnology and Bioengineering, 69(4), pp. 385–400.

Reardon, K. F., Mosteller, D. C., Rogers, J. B., DuTeau, N. M., and Kim, K. H., (2002), "Biodegradation kinetics of aromatic hydrocarbon mixtures by pure and mixed bacterial cultures," Environmental Health Perspectives, 110(Suppl 6), pp. 1005–1011.

Redman, J. A., Walker, S. L., & Elimelech, M., (2004), "Bacterial Adhesion and Transport in Porous Media: Role of the Secondary Energy Minimum," Environmental Science & Technology, 38(6), pp. 1777–1785.

Refsgaard, J. C., van der Sluijs, J. P., Højberg, A. L., and Vanrolleghem, P. A., (2007), "Uncertainty in the environmental modelling process – A framework and guidance," Environmental Modelling & Software, 22(11), pp. 1543–1556.

Remize, P.-J., Laroche, J.-F., Leparc, J., & Schrotter, J.-C., (2009), "A pilot-scale comparison of granular media filtration and low-pressure membrane filtration for seawater pretreatment," Desalination and Water Treatment, 5(1–3), pp. 6–11.

Ren, J., Packman, A. I., and Welty, C., (2000), "Correlation of colloid collision efficiency with hydraulic conductivity of silica sands," Water Resources Research, 36(9), pp. 2493–2500.

Riquelme, N., Lücken, C. V., and Baran, B., (2015), "Performance metrics in multi-objective optimization," In 2015 Latin American Computing Conference (CLEI) (pp. 1–11).

Rittmann, B. E., and McCarty, P. L., (1980), "Model of steady-state-biofilm kinetics," Biotechnology and Bioengineering, 22(11), pp. 2343–2357.

Rittmann, B. E., (1982a), “Comparative performance of biofilm reactor types,” Biotechnology and Bioengineering, 24(6), pp. 1341–1370.

Rittman, B. E., (1982b), “The effect of shear stress on biofilm loss rate,” Biotechnology and Bioengineering, 24(2), pp. 501–506.

Rittmann, B. E., Crawford, L., Tuck, C. K., and Namkung, E., (1986), “In situ determination of kinetic parameters for biofilms: Isolation and characterization of oligotrophic biofilms,” Biotechnology and Bioengineering, 28(11), pp. 1753–1760.

Rittmann, B. E., (1987), “Aerobic biological treatment in Water treatment processes,” Environmental Science & Technology, 21(2), pp. 128–136.

Rittmann, B. E., Huck, P. M., and Bouwer, E. J., (1989), “Biological treatment of public water supplies,” Critical Reviews in Environmental Control, 19(2), pp. 119–184.

Rittmann, B. E., (1990), “Analyzing biofilm processes used in biological filtration,” Journal of the American Water Works Association, pp. 62-66.

Rittmann, B. E., and Stilwell, D., (2002), “Modelling biological processes in water treatment: the integrated biofiltration model,” Journal of Water Supply: Research and Technology - Aqua, 51(1), pp. 1–14.

Rittmann, B. E., Stilwell, D., & Ohashi, A., (2002), “The transient-state, multiple-species biofilm model for biofiltration processes,” Water Research, 36(9), pp. 2342–2356.

Robinson, J. A., and Tiedje, J. M., (1983), “Nonlinear estimation of Monod growth kinetic parameters from a single substrate depletion curve,” Applied and Environmental Microbiology, 45(5), pp. 1453–1458.

Robinson, J. A., (1985), “Determining Microbial Kinetic Parameters Using Nonlinear Regression Analysis,” In Advances in Microbial Ecology (pp. 61–114). Springer, Boston, MA.

Rodriguez-Fernandez, M., Kucherenko, S., Pantelides, C., and Shah, N., (2007), “Optimal experimental design based on global sensitivity analysis,” In V. Pleşu and P. Ş. Agachi (Eds.), Computer Aided Chemical Engineering (Vol. 24, pp. 63–68). Elsevier.

Rogers, R. S., and Rapoport, H., (1980), “The pKa’s of saxitoxin,” Journal of the American Chemical Society, 102(24), pp. 7335–7339.

Romanowicz, K. J., Freedman, Z. B., Upchurch, R. A., Argiroff, W. A., and Zak, D. R., (2016), “Active microorganisms in forest soils differ from the total community yet are shaped by the same environmental factors: the influence of pH and soil moisture,” FEMS Microbiology Ecology, 92(10).

Ross, C., Santiago-Vázquez, L., & Paul, V., (2006), "Toxin release in response to oxidative stress and programmed cell death in the cyanobacterium Microcystis aeruginosa," Aquatic Toxicology, 78(1), pp. 66–73.

Rosso, L., Lobry, J. R., and Flandrois, J. P., (1993), "An Unexpected Correlation between Cardinal Temperatures of Microbial Growth Highlighted by a New Model," Journal of Theoretical Biology, 162(4), pp. 447–463.

Rosso, L., Lobry, J. R., Bajard, S., and Flandrois, J. P., (1995), "Convenient Model To Describe the Combined Effects of Temperature and pH on Microbial Growth," Applied and Environmental Microbiology, 61(2), pp. 610–616.

Rubin, D. B., and Gelman, A., (1992), "Inference from Iterative Simulation Using Multiple Sequences," *Statistical Science*, 7, pp. 457–472.

Sabiri, N. E., Castaing, J. B., Massé, A., & Jaouen, P., (2012), "Performance of a sand filter in removal of micro-algae from seawater in aquaculture production systems," Environmental Technology, 33(6), pp. 667–676.

Sadegh, M., and Vrugt, J. A., (2014), "Approximate Bayesian Computation using Markov Chain Monte Carlo simulation: DREAM(ABC)," Water Resources Research, 50(8), pp. 6767–6787.

Sadegh, M., Ragno, E., and AghaKouchak, A., (2017), "Multivariate Copula Analysis Toolbox (MvCAT): Describing dependence and underlying uncertainty using a Bayesian framework," Water Resources Research, 53(6), pp. 5166–5183.

Saito, T., Okano, K., Park, H.-D., Itayama, T., Inamori, Y., Neilan, B. A., Sugiura, N., (2003), "Detection and sequencing of the microcystin LR-degrading gene, mlrA, from new bacteria isolated from Japanese lakes," FEMS Microbiology Letters, 229(2), pp. 271–276.

Saitou, T., Sugiura, N., Itayama, T., Inamori, Y., and Matsumura, M., (2003), "Degradation characteristics of microcystins by isolated bacteria from Lake Kasumigaura," Journal of Water Supply: Research and Technology - Aqua, 52(1), pp. 13–18.

Saltelli, A., Ratto, M., Andres, T., Campolongo, F., Cariboni, J., Gatelli, D., … Tarantola, S., (2008). *Global Sensitivity Analysis: The Primer*. John Wiley & Sons.

Saltelli, A., Annoni, P., Azzini, I., Campolongo, F., Ratto, M., & Tarantola, S., (2010), "Variance based sensitivity analysis of model output. Design and estimator for the total sensitivity index," Computer Physics Communications, 181(2), pp. 259–270.

Sarrazin, F., Pianosi, F., and Wagener, T., (2016), "Global Sensitivity Analysis of environmental models: Convergence and validation," Environmental Modelling & Software, 79, pp. 135–152.

Sasaki, T., Okabe, J., Henmi, M., Hayashi, H., and Iida, Y., (2013), "Cesium (Cs) and strontium (Sr) removal as model materials in radioactive water by advanced reverse osmosis membrane," Desalination and Water Treatment, 51(7–9), pp. 1672–1677.

Sawyer, L. K., & Hermanowicz, S. W., (1998), "Detachment of biofilm bacteria due to variations in nutrient supply," Water Science and Technology, 37(4–5), pp. 211–214.

Scavia, D., Field, J. C., Boesch, D. F., Buddemeier, R. W., Burkett, V., Cayan, D. R., Titus, J., G. (2002), "Climate change impacts on U.S. Coastal and Marine Ecosystems," Estuaries, 25(2), 149–164.

Scheibe, T. D., Dong, H., and Xie, Y., (2007), "Correlation between bacterial attachment rate coefficients and hydraulic conductivity and its effect on field-scale bacterial transport," Advances in Water Resources, 30(6–7), pp. 1571–1582.

Schiffler, M., (2004), "Perspectives and challenges for desalination in the 21st century," Desalination, 165, pp. 1–9.

Schmidt, S. K., and Alexander, M., (1985), "Effects of dissolved organic carbon and second substrates on the biodegradation of organic compounds at low concentrations," Applied and Environmental Microbiology, 49(4), pp. 822–827.

Schmidt, W., Willmitzer, H., Bornmann, K., and Pietsch, J., (2002), "Production of drinking water from raw water containing cyanobacteria—pilot plant studies for assessing the risk of microcystin breakthrough," Environmental Toxicology, 17(4), pp. 375–385.

Schmidt, W., Petzoldt, H., Bornmann, K., Imhof, L., and Moldaenke, C., (2009), "Use of cyanopigment determination as an indicator of cyanotoxins in drinking water," Water Science and Technology: A Journal of the International Association on Water Pollution Research, 59(8), pp. 1531–1540.

Schmidt, J. R., Wilhelm, S. W., and Boyer, G. L., (2014), "The Fate of Microcystins in the Environment and Challenges for Monitoring," Toxins, 6(12), pp. 3354–3387.

Schnetzer, A., Miller, P. E., Schaffner, R. A., Stauffer, B. A., Jones, B. H., Weisberg, S. B., … Caron, D. A., (2007), "Blooms of *Pseudo-nitzschia* and domoic acid in the San Pedro Channel and Los Angeles harbor areas of the Southern California Bight, 2003–2004," Harmful Algae, 6(3), pp. 372–387.

Scholl, M. A., Mills, A. L., Herman, J. S., & Hornberger, G. M., (1990), "The influence of mineralogy and solution chemistry on the attachment of bacteria to representative aquifer materials," Journal of Contaminant Hydrology, 6(4), pp. 321–336.

Scott, J. T., Cotner, J. B., & LaPara, T. M., (2012), "Variable stoichiometry and homeostatic regulation of bacterial biomass elemental composition," Front. Microbiol, 3(42), pp. 10-3389.

Seifert, D., and Engesgaard, P., (2012), "Sand box experiments with bioclogging of porous media: Hydraulic conductivity reductions," Journal of Contaminant Hydrology, 136–137, pp. 1–9.

Servais, P., Billen, G., Bouillot, P., & Benezet, M., (1992), "A pilot study of biological GAC filtration in drinking water," Aqua, 41, pp. 163-168.

Seubert, E. L., Trussell, S., Eagleton, J., Schnetzer, A., Cetinić, I., Lauri, P., Caron, D. A., (2012), "Algal toxins and reverse osmosis desalination operations: Laboratory bench testing and field monitoring of domoic acid, saxitoxin, brevetoxin and okadaic acid," Water Research, 46(19), pp. 6563–6573.

Seubert, E. L., Gellene, A. G., Howard, M. D. A., Connell, P., Ragan, M., Jones, B. H., … Caron, D. A., (2013), "Seasonal and annual dynamics of harmful algae and algal toxins revealed through weekly monitoring at two coastal ocean sites off southern California, USA," Environmental Science and Pollution Research, 20(10), pp. 6878–6895.

Shimizu, Y., Hsu, C.-P., and Genenah, A., (1981), "Structure of saxitoxin in solutions and stereochemistry of dihydrosaxitoxins," Journal of the American Chemical Society, 103(3), pp. 605–609.

Shimizu, K., Maseda, H., Okano, K., Kurashima, T., Kawauchi, Y., Xue, Q., … Sugiura, N., (2012), "Enzymatic pathway for biodegrading microcystin LR in Sphingopyxis sp. C-1," Journal of Bioscience and Bioengineering, 114(6), pp. 630–634.

Shuler, M. L., and Kargi, F. K., (2002). *Bioprocess Engineering: Basic Concepts* (2nd ed.). Upper Saddle River, NJ: Prentice Hall.

Shumway, S. E., Allen, S. M., and Dee Boersma, P., (2003), "Marine birds and harmful algal blooms: sporadic victims or under-reported events?" Harmful Algae, 2(1), pp. 1–17.

Simkins, S., and Alexander, M., (1984), "Models for mineralization kinetics with the variables of substrate concentration and population density," Applied and Environmental Microbiology, 47(6), pp. 1299–1306.

Simon, F. X., Rudé, E., Llorens, J., and Baig, S., (2013), "Study of Seawater Biofiltration by Measuring Adenosine Triphosphate (ATP) and Turbidity," Water, Air, & Soil Pollution, 224(5), pp. 1568.

Sobol, I. M., (2001), "Global sensitivity indices for nonlinear mathematical models and their Monte Carlo estimates," Mathematics and Computers in Simulation, 55(1), pp. 271–280.

Somdee, T., (2010). *Biodegradation of cyanobacterial hepatotoxins [Dha7]MC-LR and MC-LR by natural aquatic bacteria*: *a thesis submitted for fulfillment of the requirements for the*

degree of Doctor of Philosophy in Microbiology. Institute of Food, Nutrition and Human Health, College of Sciences, Massey University at Wellington, New Zealand.

Song, H. S., Cannon, W. R., Beliaev, A. S., and Konopka, A., (2014), "Mathematical Modeling of Microbial Community Dynamics: A Methodological Review," Processes, 2(4), pp. 711–752.

Song, X., Zhang, J., Zhan, C., Xuan, Y., Ye, M., and Xu, C., (2015), "Global sensitivity analysis in hydrological modeling: Review of concepts, methods, theoretical framework, and applications," Journal of Hydrology, 523, pp. 739–757.

Stewart, J. E., Marks, L. J., Gilgan, M. W., Pfeiffer, E., and Zwicker, B. M., (1998), "Microbial utilization of the neurotoxin domoic acid: blue mussels (*Mytilus edulis*) and soft shell clams (*Mya arenaria*) as sources of the microorganisms," Canadian Journal of Microbiology, 44(5), pp. 456–464.

Storn, R., and Price, K., (1997), "Differential Evolution – A Simple and Efficient Heuristic for global Optimization over Continuous Spaces," Journal of Global Optimization, 11(4), pp. 341–359.

Strigul, N., Dette, H., and Melas, V. B., (2009), "A practical guide for optimal designs of experiments in the Monod model," Environmental Modelling & Software, 24(9), pp. 1019–1026.

Suarez, M. P., and Rifai, H. S., (1999), "Biodegradation Rates for Fuel Hydrocarbons and Chlorinated Solvents in Groundwater," Bioremediation Journal, 3(4), pp. 337–362.

Subhash, G., Yao, S., Bellinger, B., and Gretz, M. R., (2005), "Investigation of Mechanical Properties of Diatom Frustules Using Nanoindentation," Journal of Nanoscience and Nanotechnology, 5(1), pp. 50–56.

Subramani, A., Badruzzaman, M., Oppenheimer, J., & Jacangelo, J. G., (2011), "Energy minimization strategies and renewable energy utilization for desalination: A review," Water Research, 45(5), pp. 1907–1920.

Suganthan, P. N., Hansen, N., Liang, J. J., Deb, K., Chen, Y. P., Auger, A., and Tiwari, S., (2005), *Problem Definitions and Evaluation Criteria for the CEC 2005 Special Session on Real-Parameter Optimization* (KanGAL Report No. 2005005). Kanpur Genetic Algorithms Laboratory, IIT Kanpur).

Sun, J., Zhang, Q., Zhou, J., and Wei, Q., (2014), "Illumina Amplicon Sequencing of 16S rRNA Tag Reveals Bacterial Community Development in the Rhizosphere of Apple Nurseries at a Replant Disease Site and a New Planting Site," PLOS ONE, 9(10), pp. e111744.

Surono, I. S., Collado, M. C., Salminen, S., and Meriluoto, J., (2008), "Effect of glucose and incubation temperature on metabolically active *Lactobacillus plantarum* from dadih in removing microcystin-LR," Food and Chemical Toxicology, 46(2), pp. 502–507.

Takenaka, S., and Watanabe, M. F., (1997), "Microcystin LR degradation by *Pseudomonas aeruginosa* alkaline protease," Chemosphere, 34(4), pp. 749–757.

Tanabe, R., and Fukunaga, A., (2013), "Success-history based parameter adaptation for Differential Evolution," In 2013 IEEE Congress on Evolutionary Computation (pp. 71–78).

Tanabe, R., and Fukunaga, A. S., (2014), "Improving the search performance of SHADE using linear population size reduction," In 2014 IEEE Congress on Evolutionary Computation (CEC) (pp. 1658–1665).

Tanabe, R., Ishibuchi, H., and Oyama, A., (2017), "Benchmarking Multi- and Many-Objective Evolutionary Algorithms Under Two Optimization Scenarios," IEEE Access, 5, pp. 19597–19619.

Tarantola, S., Giglioli, N., Jesinghaus, J., and Saltelli, A., (2002), "Can global sensitivity analysis steer the implementation of models for environmental assessments and decision-making?" Stochastic Environmental Research and Risk Assessment, 16(1), pp. 63–76.

Taylor, S. W., and Jaffé, P. R., (1990), "Biofilm growth and the related changes in the physical properties of a porous medium: 3. Dispersivity and model verification," Water Resources Research, 26(9), pp. 2171–2180.

Tchobanoglous, G., Burton, F. L., and Stensel, H. D., (2003). *Wastewater Engineering: Treatment and Reuse* (4th ed.). New York, NY: McGraw Hill.

Teixeira, M. R., & Rosa, M. J., (2005), "Microcystins removal by nanofiltration membranes," Separation and Purification Technology, 46(3), pp. 192–201.

Telen, D., Logist, F., Van Derlinden, E., Tack, I., and Van Impe, J., (2012), "Optimal experiment design for dynamic bioprocesses: A multi-objective approach," Chemical Engineering Science, 78, pp. 82–97.

Telgmann, U., Horn, H., & Morgenroth, E., (2004), "Influence of growth history on sloughing and erosion from biofilms," Water Research, 38(17), pp. 3671–3684.

Tessier, G., (1942), "Croissance des populations bactériennes et quantité d'aliment disponible," Rev. Sci. Paris 80.

Thode, H. C. (2002). *Testing For Normality*. CRC Press.

Thomas, T., Gilbert, J., and Meyer, F., (2012), "Metagenomics - a guide from sampling to data analysis," Microbial Informatics and Experimentation, 2(1), pp. 3.

Thullner, M., Mauclaire, L., Schroth, M. H., Kinzelbach, W., and Zeyer, J., (2002a), "Interaction between water flow and spatial distribution of microbial growth in a two-

dimensional flow field in saturated porous media," Journal of Contaminant Hydrology, 58(3–4), pp. 169–189.

Thullner, M., Zeyer, J., and Kinzelbach, W., (2002b), "Influence of Microbial Growth on Hydraulic Properties of Pore Networks," Transport in Porous Media, 49(1), pp. 99–122.

Thullner, M., Schroth, M. H., Zeyer, J., & Kinzelbach, W., (2004), "Modeling of a microbial growth experiment with bioclogging in a two-dimensional saturated porous media flow field," Journal of Contaminant Hydrology, 70(1–2), pp. 37–62.

Thullner, M., (2010), "Comparison of bioclogging effects in saturated porous media within one- and two-dimensional flow systems," Ecological Engineering, 36(2), pp. 176–196.

Tian, Y., Zhang, X., Cheng, R., and Jin, Y., (2016), "A multi-objective evolutionary algorithm based on an enhanced inverted generational distance metric," In 2016 IEEE Congress on Evolutionary Computation (CEC) (pp. 5222–5229).

Tian, Y., Cheng, R., Zhang, X., and Jin, Y., (2017), "PlatEMO: A MATLAB Platform for Evolutionary Multi-Objective Optimization [Educational Forum]," IEEE Computational Intelligence Magazine, 12(4), pp. 73–87.

Trainer, V. L., Cochlan, W. P., Erickson, A., Bill, B. D., Cox, F. H., Borchert, J. A., & Lefebvre, K. A., (2007), "Recent domoic acid closures of shellfish harvest areas in Washington State inland waterways," Harmful Algae, 6(3), pp. 449–459.

Trainer, V. L., Bates, S. S., Lundholm, N., Thessen, A. E., Cochlan, W. P., Adams, N. G., & Trick, C. G., (2012), "*Pseudo-nitzschia* physiological ecology, phylogeny, toxicity, monitoring and impacts on ecosystem health," Harmful Algae, 14, 271–300.

Trautmann, H., Wagner, T., Naujoks, B., Preuss, M., and Mehnen, J., (2009), "Statistical Methods for Convergence Detection of Multi-Objective Evolutionary Algorithms," Evolutionary Computation, 17(4), pp. 493–509.

Trigueros, D. E. G., Módenes, A. N., Kroumov, A. D., and Espinoza-Quiñones, F. R., (2010), "Modeling of biodegradation process of BTEX compounds: Kinetic parameters estimation by using Particle Swarm Global Optimizer," Process Biochemistry, 45(8), pp. 1355–1361.

Trussell, R. R., Anderson, H. A., Archuleta, E. G., Crook, J., Drewes, J. E., Fort, D. D., Haas, C. H., Haddad, B. M., Huggett, D. B., Jiang, S. C., Sedlak, D. L., Snyder, S. A., Whittaker, M. H., Whittington, D., (2012). Water Reuse: Potential for Expanding the Nation's Water Supply through Reuse of Municipal Wastewater. The National Academies Press: Washington, DC, USA.

Tsao, S., Wei, D.-J., Chang, Y.-T., and Lee, J. F., (2017), "Aerobic biodegradation of microcystin-LR by an indigenous bacterial mixed culture isolated in Taiwan," International Biodeterioration & Biodegradation, 124, pp. 101-108.

Tubaro, A., Dell'Ovo, V., Sosa, S., and Florio, C., (2010), "Yessotoxins: A toxicological overview," Toxicon, 56(2), pp. 163–172.

Tufenkji, N., & Elimelech, M., (2005), "Breakdown of Colloid Filtration Theory: Role of the Secondary Energy Minimum and Surface Charge Heterogeneities," Langmuir, 21(3), pp. 841–852.

Tufenkji, N., (2007), "Modeling microbial transport in porous media: Traditional approaches and recent developments," Advances in Water Resources, 30(6–7), pp. 1455–1469.

Tuomisto, H., (2010), "A consistent terminology for quantifying species diversity? Yes, it does exist," Oecologia, 164(4), pp. 853–860.

Tyagi, M., Fonseca, M. M. R. da, and Carvalho, C. C. C. R. de., (2010), "Bioaugmentation and biostimulation strategies to improve the effectiveness of bioremediation processes," Biodegradation, 22(2), pp. 231–241.

Urfer, D., Huck, P. M., Booth, S. D., & Coffey, B. M., (1997), "Biological filtration for BOM and particle removal: a critical review," Journal of the American Water Works Association, 89(12).

Urfer, D., & Huck, P. M., (2000), "A Study of the Impacts of Periodic Ozone Residuals on Biologically Active Filters," Ozone: Science & Engineering, 22(1), pp. 77–97.

Ursell, T., (2016), "Generate Random Numbers from a 2D Discrete Distribution," MATLAB Central File Exchange. Retrieved October 18th, 2018. https://www.mathworks.com/matlabcentral/fileexchange/35797

US EPA, (2015a), "Drinking Water Health Advisory for the Cyanobacterial Microcystin Toxins," (No. 820R15100), last accessed May 24th, 2016. https://www.epa.gov/sites/production/files/2015-06/documents/microcystins-report-2015.pdf

US EPA, (2015b). Method 544: Determination of Microcystins and Nodularin in Drinking Water By Solid Phase Extraction and Liquid Chromatography/Tandem Mass Spectrometry (LC/MS/MS). Washington, DC., USA.

US EPA, (2016a), "Guidelines and Recommendations for Cyanobacteria or Cyanotoxins in Drinking Water," last accessed May 24th, 2016. https://www.epa.gov/nutrient-policy-data/guidelines-and-recommendations#what3

US EPA, (2016b). *National Lakes Assessment 2012: A Collaborative Survey of Lakes in the United States*; US EPA: Washington, DC., USA.

Valdiglesias, V., Fernández-Tajes, J., Méndez, J., Pásaro, E., and Laffon, B., (2013), "The marine toxin okadaic acid induces alterations in the expression level of cancer-related genes in human neuronal cells," Ecotoxicology and Environmental Safety, 92, pp. 303–311.

Valeria, A. M., Ricardo, E. J., Stephan, P., and Alberto, W. D., (2006), "Degradation of Microcystin-RR by *Sphingomonas sp.* CBA4 isolated from San Roque reservoir (Córdoba – Argentina)," Biodegradation, 17(5), pp. 447–455.

Vandanjon, L., Rossignol, N., Jaouen, P., Robert, J. M., & Quéméneur, F., (1999), "Effects of shear on two microalgae species. Contribution of pumps and valves in tangential flow filtration systems," Biotechnology and Bioengineering, 63(1), pp. 1–9.

Vandenberghe, S., Verhoest, N. E. C., and Baets, B. D., (2010), "Fitting bivariate copulas to the dependence structure between storm characteristics: A detailed analysis based on 105 year 10 min rainfall," Water Resources Research, 46(1).

Vandevivere, P., and Baveye, P., (1992), "Relationship between Transport of Bacteria and Their Clogging Efficiency in Sand Columns," Applied and Environmental Microbiology, 58(8), pp. 2523–2530.

Vandevivere, P., (1995), "Bacterial clogging of porous media: A new modelling approach," Biofouling, 8(4), pp. 281–291.

Van Genuchten, M. T., and Alves, W. J., (1982). *Analytical solutions of the one-dimensional convective-dispersive solute transport equation* (No. 157268). United States Department of Agriculture, Economic Research Service.

van Riel, N., (2012), "Speeding up simulations of ODE models in Matlab using CVode and MEX files," *Eindhoven University of Technology.* Retrieved from http://bmi.bmt.tue.nl/~nvriel/software/Speeding%20up%20simulations%20of%20ODE%20models%20in%20Matlab%20using%20CVode%20and%20MEX%20files.pdf

Vanrolleghem, P. A., and Keesman, K. J., (1996), "Identification of Biodegradation models under model and data uncertainty," Water Science and Technology, 33(2), pp. 91–105.

Velten, S., Hammes, F., Boller, M., and Egli, T., (2007), "Rapid and direct estimation of active biomass on granular activated carbon through adenosine tri-phosphate (ATP) determination," Water Research, 41(9), pp. 1973–1983.

Velten, S., Boller, M., Köster, O., Helbing, J., Weilenmann, H.-U., and Hammes, F., (2011), "Development of biomass in a drinking water granular active carbon (GAC) filter," Water Research, 45(19), pp. 6347–6354.

Verliefde, A. R. D., Cornelissen, E. R., Heijman, S. G. J., Petrinic, I., Luxbacher, T., Amy, G. L., … van Dijk, J. C., (2009), "Influence of membrane fouling by (pretreated) surface water on

rejection of pharmaceutically active compounds (PhACs) by nanofiltration membranes," Journal of Membrane Science, 330(1), pp. 90–103.

Versyck, K. J., and Impe, J. F. V., (1998), "Trade-offs in design of fed-batch experiments for optimal estimation of biokinetic parameters," In Proceedings of the 1998 IEEE International Conference on Control Applications (Cat. No.98CH36104) (Vol. 1, pp. 51–55 vol.1).

Villacorte, L. O., Tabatabai, S. A. A., Dhakal, N., Amy, G., Schippers, J. C., & Kennedy, M. D., (2015a), "Algal blooms: an emerging threat to seawater reverse osmosis desalination," Desalination and Water Treatment, 55(10), pp. 2601–2611.

Villacorte, L. O., Tabatabai, S. A. A., Anderson, D. M., Amy, G. L., Schippers, J. C., & Kennedy, M. D., (2015b), "Seawater reverse osmosis desalination and (harmful) algal blooms," Desalination, 360, pp. 61–80.

Villarini, G., Serinaldi, F., and Krajewski, W. F., (2008), "Modeling radar-rainfall estimation uncertainties using parametric and non-parametric approaches," Advances in Water Resources, 31(12), pp. 1674–1686.

Villaverde, A. F., and Banga, J. R., (2014), "Reverse engineering and identification in systems biology: strategies, perspectives and challenges," Journal of The Royal Society Interface, 11(91), pp. 20130505.

Villaverde, A. F., and Banga, J. R., (2017), "Dynamical compensation and structural identifiability of biological models: Analysis, implications, and reconciliation," PLOS Computational Biology, 13(11), pp. e1005878. https://doi.org/10.1371/journal.pcbi.1005878

Volk, C., Renner, C., Roche, P., Paillard, H., and Joret, J. C., (1993), "Effects Of Ozone On The Production Of Biodegradable Dissolved Organic Carbon (BDOC) During Water Treatment," Ozone: Science & Engineering, 15(5), pp. 389–404.

Voutchkov, N., (2010), "Considerations for selection of seawater filtration pretreatment system," Desalination, 261(3), pp. 354–364.

Voutchkov, N. (2013). Desalination Engineering: Planning and Design (1 edition). New York: McGraw-Hill Education.

Vrugt, J. A., and Robinson, B. A., (2007), "Improved evolutionary optimization from genetically adaptive multimethod search," Proceedings of the National Academy of Sciences, 104(3), pp. 708–711.

Vrugt, J. A., Robinson, B. A., and Hyman, J. M., (2009), "Self-Adaptive Multimethod Search for Global Optimization in Real-Parameter Spaces," IEEE Transactions on Evolutionary Computation, 13(2), pp. 243–259.

Vrugt, J. A., (2016), "Markov chain Monte Carlo simulation using the DREAM software package: Theory, concepts, and MATLAB implementation," Environmental Modelling & Software, 75, pp. 273–316.

Vu, B., Chen, M., Crawford, R. J., & Ivanova, E. P., (2009), "Bacterial Extracellular Polysaccharides Involved in Biofilm Formation," Molecules, 14(7), pp. 2535–2554.

Wagner, T., Trautmann, H., and Naujoks, B., (2009), "OCD: Online Convergence Detection for Evolutionary Multi-Objective Algorithms Based on Statistical Testing," In M. Ehrgott, C. M. Fonseca, X. Gandibleux, J.-K. Hao, & M. Sevaux (Eds.), Evolutionary Multi-Criterion Optimization (pp. 198–215). Springer Berlin Heidelberg.

Wang, H., Ho, L., Lewis, D. M., Brookes, J. D., and Newcombe, G., (2007), "Discriminating and assessing adsorption and biodegradation removal mechanisms during granular activated carbon filtration of microcystin toxins," Water Research, 41(18), pp. 4262–4270.

Wang, J., Wu, P., Chen, J., and Yan, H., (2010), "Biodegradation of Microcystin-RR by a New Isolated *Sphingopyxis sp.* USTB-05," Chinese Journal of Chemical Engineering, 18(1), pp. 108–112.

Wang, J., Chen, L., Tian, X., Gao, L., Niu, X., Shi, M., and Zhang, W., (2013), "Global Metabolomic and Network analysis of *Escherichia coli* Responses to Exogenous Biofuels," Journal of Proteome Research, 12(11), pp. 5302–5312.

Wang, X., Utsumi, M., Gao, Y., Li, Q., Tian, X., Shimizu, K., and Sugiura, N., (2016), "Influences of metal ions on microcystin-LR degradation capacity and dynamics in microbial distribution of biofilm collected from water treatment plant nearby Kasumigaura Lake," Chemosphere, 147(Supplement C), pp. 230–238.

Wang, H., Jin, Y., and Yao, X., (2017), "Diversity Assessment in Many-Objective Optimization," IEEE Transactions on Cybernetics, 47(6), pp. 1510–1522.

Warmink, J. J., Janssen, J. A. E. B., Booij, M. J., and Krol, M. S., (2010), "Identification and classification of uncertainties in the application of environmental models," Environmental Modelling & Software, 25(12), pp. 1518–1527.

Wei, P., Lu, Z., and Yuan, X., (2013a), "Monte Carlo simulation for moment-independent sensitivity analysis," Reliability Engineering & System Safety, 110, pp. 60–67.

Wei, P., Lu, Z., Wu, D., and Zhou, C., (2013b), "Moment-independent regional sensitivity analysis: Application to an environmental model," Environmental Modelling & Software, 47, pp. 55–63.

Wei, P., Lu, Z., and Song, J., (2014), "Moment-Independent Sensitivity Analysis Using Copula," Risk Analysis, 34(2), pp. 210–222.

Wei, P., Lu, Z., and Song, J., (2015), "Variable importance analysis: A comprehensive review," Reliability Engineering & System Safety, 142, pp. 399–432.

Welker, M., Steinberg, C., and Jones, G. J., (2001), "Release and Persistence of Microcystins in Natural Waters," In Cyanotoxins: Occurence, Causes, Consequences (pp. 83–102). Springer Berlin Heidelberg.

Wells, M. J. M., and Yu, L. Z., (2000), "Solid-phase extraction of acidic herbicides," Journal of Chromatography A, 885(1–2), pp. 237–250.

Wells, M. J. M., (2006), "Log DOW: Key to Understanding and Regulating Wastewater-Derived Contaminants," Environmental Chemistry, 3(6), pp. 439–449.

Westrick, J. A., (2008), "Cyanobacterial toxin removal in drinking water treatment processes and recreational waters," In H. K. Hudnell (Ed.), Cyanobacterial Harmful Algal Blooms: State of the Science and Research Needs (pp. 275–290). Springer New York.

Westrick, J. A., Szlag, D. C., Southwell, B. J., & Sinclair, J., (2010), "A review of cyanobacteria and cyanotoxins removal/inactivation in drinking water treatment," Analytical and Bioanalytical Chemistry, 397(5), pp. 1705–1714.

White, H., (1980), "A Heteroskedasticity-Consistent Covariance Matrix Estimator and a Direct Test for Heteroskedasticity," Econometrica, 48(4), pp. 817–838.

WHO, (2003), "Cyanobacterial Toxins: Microcystin-LR in Drinking Water," Background Document for development of WHO Guidelines for Drinking-water Quality, last accessed May 24th, 2016.
http://www.who.int/water_sanitation_health/waterquality/guidelines/chemicals/cyanobactoxins.pdf?ua=1

Wilcox R., (2005). *Kolmogorov–Smirnov Test*. Encyclopedia of Biostatistics.

Winters, A. D., Marsh, T. L., Brenden, T. O., and Faisal, M., (2014), "Molecular characterization of bacterial communities associated with sediments in the Laurentian Great Lakes," Journal of Great Lakes Research, 40(3), pp. 640–645.

Wobus, A., Bleul, C., Maassen, S., Scheerer, C., Schuppler, M., Jacobs, E., and Röske, I., (2003), "Microbial diversity and functional characterization of sediments from reservoirs of different trophic state," FEMS Microbiology Ecology, 46(3), pp. 331–347.

Wöhling, T., Vrugt, J. A., and Barkle, G. F., (2008), "Comparison of Three Multiobjective Optimization Algorithms for Inverse Modeling of Vadose Zone Hydraulic Properties," Soil Science Society of America Journal, 72(2), pp. 305–319.

Wong, A. W., Emelko, M., Walton, T., (2014), "Simple filter capping approaches for enhanced biological filtration performance," Ontario Water Works Association, last accessed May 25th, 2016. http://www.owwa.ca/wp-content/uploads/2014/06/1.-Simple-Filter-Capping-Approaches-for-Enhanced-Biological-Filtration-Performance-Paper1.pdf.

Woodhouse, J. N., Ziegler, J., Grossart, H.-P., and Neilan, B. A., (2018), "Cyanobacterial Community Composition and Bacteria–Bacteria Interactions Promote the Stable Occurrence of Particle-Associated Bacteria," Frontiers in Microbiology, 9.

Wooldridge, J. M., (2015). *Introductory Econometrics: A Modern Approach*. Cengage Learning.

Xiao, C., Yan, H., Wang, J., Wei, W., Ning, J., and Pan, G., (2011), "Microcystin-LR biodegradation by *Sphingopyxis sp.* USTB-05," Frontiers of Environmental Science & Engineering in China, 5(4), pp. 526–532.

Xu, P., Drewes, J. E., Kim, T.-U., Bellona, C., & Amy, G., (2006), "Effect of membrane fouling on transport of organic contaminants in NF/RO membrane applications," Journal of Membrane Science, 279(1), pp. 165–175.

Xu, H., Wang, H., Xu, Q., Lv, L., Yin, C., Liu, X., … Yan, H., (2015), "Pathway for Biodegrading Microcystin-YR by *Sphingopyxis sp.* USTB-05," PLOS ONE, 10(4), pp. e0124425.

Yang, X., Chen, X., Qian, H., and Xiao, B., (2008), "Effects of nutrient elements on the biodegradation of microcystin under aerobic conditions," Journal of Agro-Environment Science, 28, pp. 2385–2388.

Yang, F., Zhou, Y., Yin, L., Zhu, G., Liang, G., and Pu, Y., (2014a), "Microcystin-Degrading Activity of an Indigenous Bacterial Strain *Stenotrophomonas acidaminiphila* MC-LTH2 Isolated from Lake Taihu," PLOS ONE, 9(1), pp. e86216.

Yang, F., Zhou, Y., Sun, R., Wei, H., Li, Y., Yin, L., and Pu, Y., (2014b), "Biodegradation of microcystin-LR and-RR by a novel microcystin-degrading bacterium isolated from Lake Taihu," Biodegradation, 25(3), pp. 447–457.

Yannarell, A. C., and Triplett, E. W., (2005), "Geographic and Environmental Sources of Variation in Lake Bacterial Community Composition," Applied Environmental Microbiology, 71(1), pp. 227–239.

Yao, K.-M., Habibian, M. T., & O'Melia, C. R., (1971), "Water and waste water filtration: Concepts and applications," Environmental Science & Technology, 5(11), pp. 1105–1112.

Yen, G. G., and He, Z., (2014), "Performance Metric Ensemble for Multiobjective Evolutionary Algorithms," IEEE Transactions on Evolutionary Computation, 18(1), pp. 131–144.

Yoon, H., Klinzing, G., and Blanch, H. W., (1977), "Competition for mixed substrates by microbial populations," Biotechnology and Bioengineering, 19(8), pp. 1193–1210.

You, D. J., Chen, X. G., Xiang, H. Y., Ouyang, L., and Yang, B., (2014), "Isolation, identification and characterization of a microcystin-degrading bacterium *Paucibacter sp.* strain CH," Huan Jing Ke Xue, 35(1), pp. 313–318.

Yu, X., Zhang, X., Liu, X., Zhao, X., & Wang, Z., (2003a), "Phosphorus limitation in biofiltration for drinking water treatment," Journal of Environmental Sciences, 15(4), pp. 494–499.

Yu, X., Zhang, X.-J., & Wang, Z.-S., (2003b), "Improving removal efficiency of organic matters by adding phosphorus in drinking water biofiltration treatment," Biomedical and Environmental Sciences: BES, 16(1), pp. 29–39.

Yudianto, D., and Yuebo, X., (2010), "A comparison of some numerical methods in solving 1-D steady-state advection dispersion reaction equation," Civil Engineering and Environmental Systems, 27(2), pp. 155–172.

Yun, W., Lu, Z., Jiang, X., and Zhang, L., (2018), "Borgonovo moment independent global sensitivity analysis by Gaussian radial basis function meta-model," Applied Mathematical Modelling, 54, pp. 378–392.

Yürekli, K., Kurunç, A., and Öztürk, F., (2005), "Testing the Residuals of an ARIMA Model on the Çekerek Stream Watershed in Turkey," Turkish Journal of Environmental Engineering and Science, 29(2), pp. 61–74.

Zabaglo, K., Chrapusta, E., Bober, B., Kaminski, A., Adamski, M., & Bialczyk, J., (2016), "Environmental roles and biological activity of domoic acid: A review," Algal Research, 13, pp. 94–101.

Zar, J. H., (2010). *Biostatistical Analysis*. Prentice Hall.

Zhai, Q., Yang, J., Xie, M., and Zhao, Y., (2014), "Generalized moment-independent importance measures based on Minkowski distance," European Journal of Operational Research, 239(2), pp. 449–455.

Zhang, S., and Huck, P. M., (1996), "Removal of AOC in biological water treatment processes: A kinetic modeling approach," Water Research, 30(5), pp. 1195–1207.

Zhang, Q., and Li, H., (2007), "MOEA/D: A Multiobjective Evolutionary Algorithm Based on Decomposition," IEEE Transactions on Evolutionary Computation, 11(6), pp. 712–731.

Zhang, M., Pan, G., & Yan, H., (2010), "Microbial biodegradation of microcystin-RR by bacterium Sphingopyxis sp. USTB-05," Journal of Environmental Sciences, 22(2), pp. 168–175.

Zhang, Y., Tian, J., Nan, J., Gao, S., Liang, H., Wang, M., & Li, G., (2011a), "Effect of PAC addition on immersed ultrafiltration for the treatment of algal-rich water," Journal of Hazardous Materials, 186(2–3), pp. 1415–1424.

Zhang, M. L., Yan, H., and Pan, G., (2011b). Microbial degradation of microcystin-LR by Ralstonia solanacearum. Environmental Technology, 32(15), 1779–1787.

Zhang, L., Lu, Z., Cheng, L., and Fan, C., (2014), "A new method for evaluating Borgonovo moment-independent importance measure with its application in an aircraft structure," Reliability Engineering & System Safety, 132, pp. 163–175.

Zhang, F., Lee, J., Liang, S., & Shum, C., (2015a), "Cyanobacteria blooms and non-alcoholic liver disease: evidence from a county level ecological study in the United States," Environmental Health, 14, pp. 14-41.

Zhang, J., Shi, H., Liu, A., Cao, Z., Hao, J., & Gong, R. (2015b). Identification of a New Microcystin-Degrading Bacterium Isolated from Lake Chaohu, China. Bulletin of Environmental Contamination and Toxicology, 94(5), 661–666.

Zhang, L., Lu, Z., Cheng, L., and Hong, D., (2015c), "Moment-independent regional sensitivity analysis of complicated models with great efficiency," International Journal for Numerical Methods in Engineering, 103(13), pp. 996–1014.

Zhou, J., Yan, H., He, H., Zhong, G., Lin, H., and Zhang, C., (2006), "Activity of *Delftic acidovorans* for the Biodegradation of microcystins," Science Technology & Engineering, 2.

Zhou, Y., Yang, F., Liang, G., Yin, L., and Pu, Y, (2008), "Biodegradation of Microcystin LR and RR by an indigenous bacterial strain MC-LTH11 isolated from Lake Taihu," Journal of Southeast University, 30, pp. 68–71.

Zhou, S., Shao, Y., Gao, N., Deng, Y., Li, L., Deng, J., and Tan, C., (2014), "Characterization of algal organic matters of *Microcystis aeruginosa*: Biodegradability, DBP formation and membrane fouling potential," Water Research, 52, pp. 199–207.

Zhou, X., and Wu, F., (2018), "Vanillic acid changed cucumber (*Cucumis sativus L.*) seedling rhizosphere total bacterial, *Pseudomonas* and *Bacillus spp.* Communities," Scientific Reports, 8(1), pp. 4929.

Zhu, I. X., Bates, B. J., & Anderson, D. M., (2014), "Removal of *Prorocentrum minimum* from seawater using dissolved air flotation," Journal of Applied Water Engineering and Research, 2(1), pp. 47–56.

Zhu, X., Shen, Y., Chen, X., Hu, Y. O. O., Xiang, H., Tao, J., and Ling, Y., (2016), "Biodegradation mechanism of microcystin-LR by a novel isolate of *Rhizobium sp.* TH and the evolutionary origin of the mlrA gene," International Biodeterioration & Biodegradation, 115, pp. 17–25.

Zitzler, E., Deb, K., and Thiele, L., (2000), “Comparison of Multiobjective Evolutionary Algorithms: Empirical Results,” Evolutionary Computation, 8(2), pp. 173–195.

Zitzler, E., and Künzli, S., (2004), “Indicator-Based Selection in Multiobjective Search,” In Parallel Problem Solving from Nature - PPSN VIII (pp. 832–842). Springer, Berlin, Heidelberg.

Zwirglmaier, K., Keiz, K., Engel, M., Geist, J., and Raeder, U., (2015), “Seasonal and spatial patterns of microbial diversity along a trophic gradient in the interconnected lakes of the Osterseen Lake District, Bavaria,” Frontiers in Microbiology, 6.

Appendix A: *Investigation of Algal Biotoxin Removal during SWRO Desalination through a Materials Flow Analysis* - Supplementary Materials

I. Supplementary Methods

1. Calculation of Process Flows

1.1 GMF Process Flow Calculations

Operational parameters for a single unit conventional GMF are listed in Table A1. For a 50 MGD plant, we estimated 10 GMF units considering the influent water flow rate is twice the permeate flow rate (8 units plus an additional two units to that are offline during backwashing). The maximum upper limit in water use for these eight operating units is thus 5,000 m^3/day (1.32 MGD). Thus, the process flow calculations resulted in a total backwash water volumetric flow rate of approximately 38,400 m^3/day (10.1 MGD) assuming 10 GMF units was sufficient for the 50 MGD facility.

Table A1 *- Summary of engineering operational parameters for a 50 MGD SWRO with conventional GMF pretreatment systems (Villacorte et al. 2015b, Voutchkov 2013)*

Design Parameter	Practical Value
Filtration Rate (HLR-m/hr)	10
Areal Footprint of One Unit (m^2)	192
Number of Filters in Operation	8
Filter Run Time (hrs)	24
Ratio Backwash Rate: Filtration Rate	5
Backwash Time (min)	30
Filtered Volume (Q)/hr/unit (m^3)	9,600
Total Volume of Water Consumed during Backwash Operation (m^3)	38,400

Similar process design calculations were conducted for pressurized GMF systems for a 50 MGD plant operating at a theoretical intake rate of 100 MGD (Table A2). Pressurized systems would be expected to operate at a HLR of 25 m/hr with a much smaller areal footprint than conventional GMF systems, leading to a higher number of

filters in operation (24 filters total, 2 for redundancy during backwashing). The required volume of water to backwash these units was calculated to be 12,441 m^3/day (3.29 MGD), approximately three times less than conventional GMF systems (Table A2).

Table A2 *- Summary of engineering operational parameters for a 50 MGD SWRO with pressurized GMF pretreatment systems (Villacorte et al. 2015b, Voutchkov 2013)*

Design Parameter	Practical Value
Filtration Rate (HLR-m/hr)	25
Areal Footprint of One Unit (m^2)	28
Number of Filters in Operation	22
Filter Run Time (hrs)	24
Ratio Backwash Rate: Filtration Rate	4
Backwash Time (min)	30
Filtered Volume (Q)/hr/unit (m^3)	1,131
Total Volume of Water Consumed during Backwash Operation (m^3)	12,441

1.2 MF/UF Process Flow Calculations

The estimated volume of water consumed per day for the pressurized UF system depended on the specifications of the manufacturer and reported practical experience from pilot testing of pressurized UF systems (Table A3) *(*Voutchkov 2013). This study used UF system parameters given by Norit (Pentair X-Flow) Seaguard SXL 225 systems, with hollow fiber PES membranes of 0.02 to 0.025 µm pore sizes and operating in an inside out configuration. These systems have 40 m^2 surface area per membrane module. Each pressure vessel houses 4 membrane modules in a horizontal configuration and 48 vessels are configured per train. We considered that the Norit system would be operating at a median pressure of 1 bar and a design flux (from pilot testing) of 65 L/m^2/hour and a filter run time of 75 minutes. To meet this design flux, 6 percent standby capacity was incorporated for one train to be offline for backwashing and another potentially offline for cleaning purposes. Incorporating this standby capacity resulted in an average flux of 64 L/m^2/hour. From the average flux, backwash rate, backwash time, and frequency, a total of

50,505 m^3/day (13.3 MGD) of water was estimated to be used for UF backwashing purposes alone (Table A3).

Table A3 *- Summary of engineering operational parameters for a 50 MGD SWRO with pressurized SWRO UF pretreatment systems (Villacorte et al. 2015b, Voutchkov 2013)*

Design Parameter	Practical Value
Average Flux (L/m^2/hr)	64.2
Total Membrane Area Required (m^2)	245,760
Number of Modules Required	6,435
Number of Vessels Required	1,609
Number of Trains	34
Filter Run Time (min)[1]	75
Ratio Backwash Rate: Filtration Rate	10
Backwash Time (min)	1
Backwash cycles/day [2]	19
Total Volume of Water Consumed during Backwash Operation (m^3)	50,505
Pressure Loss (TMP) (bar)	1

[1]Taken as median value presented in Voutchkov 2013
[2]Calculated based on a 24-hour period

The vacuum driven submerged UF system was based off a design using GE Zenon ZeeWeed 1000 V-3 model and practical experience of a pilot testing of this product (Voutchkov 2013). The Zenon ZeeWeed product is a hollow fiber membrane system operating with outside in configuration. The operating pressure of this system, 0.4 bar, was assumed to be much lower than the standard operating pressure for comparison purposes with the pressurized membrane systems. Voutchkov (2010) stated that operating submerged vacuum systems during algal bloom periods at 0.4 bars resulted in half of the run time of normal systems. If we assume that the run time of the submerged systems were identical to pressurized systems, then the run time of this system would be 37.5 minutes, increasing the backwash frequency to 38 times per day (Table A4). From a design flux of 40 L/m^2/hr, a total of 7,148 membrane modules are required along with 149 cassettes (48 modules per cassette) and 30 tanks (assuming each tank houses 5 cassettes). The resulting water usage for backwash processes is approximately double the usage of pressurized systems at 101,010 m^3/day (26.7 MGD) (Table A4).

Table A4 *- Summary of engineering operational parameters for a 50 MGD SWRO with submerged SWRO UF pretreatment systems (Villacorte et al. 2015b, Voutchkov 2013)*

Design Parameter	Practical Value
Average Flux (L/m^2/hr)	40
Total Membrane Area Required (m^2)	394,571
Number of Modules Required	7,148
Number of Cassettes Required	149
Number of Tanks	30
Filter Run Time (min)[1]	37.5
Ratio Backwash Rate: Filtration Rate	10
Backwash Time (min)	1
Backwash cycles/day [2]	38
Total Volume of Water Consumed during Backwash Operation (m^3)	101,010
Pressure Loss (TMP) (bar)	0.4

[1]Taken as median value presented in Voutchkov 2013
[2]Calculated based on a 24-hour period

2. Identification of algal blooms and total toxic algal cell concentrations in the desalination intake

Field data collected and posted to the Southern California Ocean Observing System (SCOOS, http://www.sccoos.org/) database were used to identify the pattern and intensity of algal blooms. Specifically, we compiled chlorophyll-a, dissolved domoic acid, as well as algal cell concentrations for the following algae: *Akashiwo sanguinea*, *Alexandrium sp.*, *Prorocentrum sp.*, *Dinophysis sp.*, *Lingulodinium polyedrum*, *Pseudo-nitzschia delicatissima* size class and *Pseudo-nitzschia seriata* size class from a three-year period (2012-2015). The monitoring data for chlorophyll-a was first used as a surrogate for identifying algal blooms, where prolonged periods with chlorophyll-a levels > 12 µg/L (the mean across the 3-year period) were identified as blooms. From this analysis, eight distinct bloom periods of varying duration were observed at the Santa Monica Pier (Figure A1). We have noted that even if the chlorophyll concentration is elevated, it does not directly imply an elevation of toxin producing algae in water. Nontoxic blooms have been known to frequent the region

and are generally associated with non-toxic species of the genus *Prorocentrum* (*Prorocentrum micans*) (Caron et al. 2010).

To identify the toxic blooms, domoic acid weekly concentrations reported by SCOOS were analyzed over the same three-year period to assess the blooms that were dominated by *Pseudo nitzschia sp.* (Figure A1). Several large spikes of DA were observed in late spring and early summer months and corresponded with some algal bloom periods identified by chlorophyll (more notably Bloom 4). Generally, DA concentrations were observed to peak right at the onset of some bloom periods. Correlation between the bloom period and the presence of DA suggests that these bloom periods (1 and 4) were dominated by *Pseudo nitzschia* species.

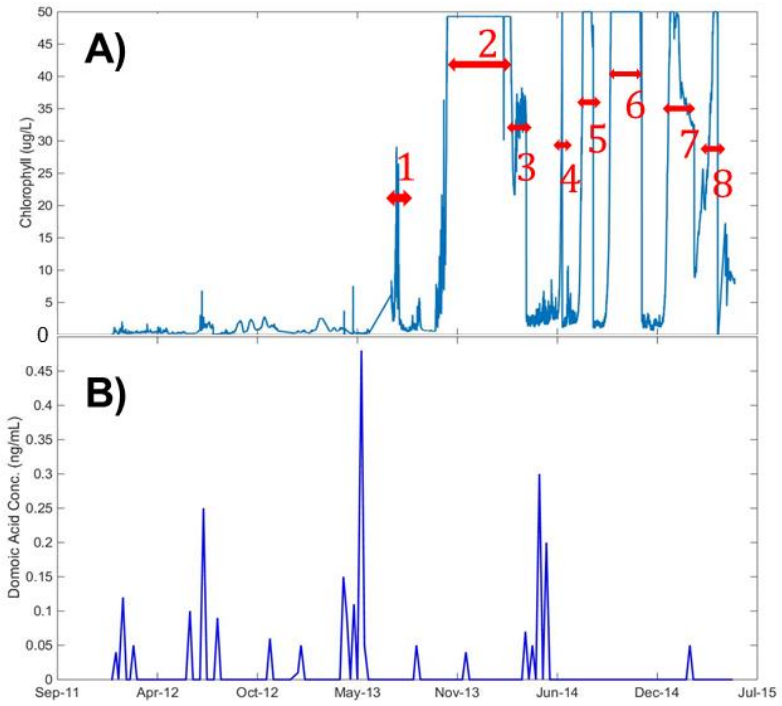

Figure A1. *A) Chlorophyll and B) Domoic acid concentrations over a three-year period at the Santa Monica Pier (2012-2015)*

The marine algal species and concentration at the Santa Monica location was then compiled over the course of three years for each distinct bloom period (Figure A2). Figure

A2 portrays the average logarithmic cell concentration for each of eight respective bloom periods.

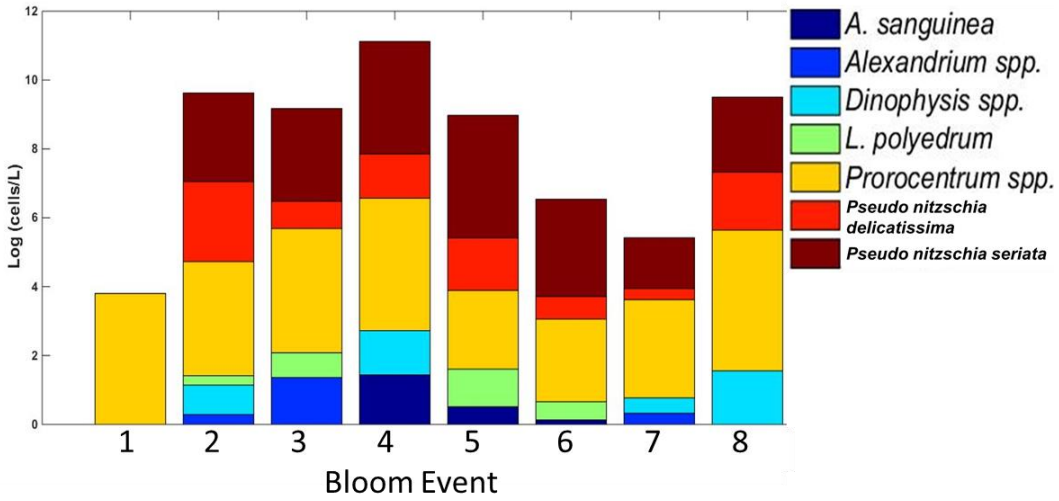

Figure A2. *Average cell concentration for all monitored algal species during eight identified algal blooms at the Santa Monica Pier between 2012 and 2015. The timing of the eight algal blooms is indicated in Figure A1.*

Of the different algal species reported, only some species of *Alexandrium* (producer of Saxitoxin, STX), *Dinophysis* (producer of Okadaic acid, OA), *Lingolidinium polyedrum* (producer of Yessotoxin, YTX), and *Pseudo-nitzschia* (producer of domoic acid, DA) are known to produce toxins (Lewitus et al. 2012). Therefore, only those toxic species and their associated toxins DA, STX, OA, and YTX were included in the pMFA. The toxic effects of each toxin are presented below and their health effects are summarized in Table A5.

DA is an amino acid derivative of the kainoid class of compounds that is associated with amnesic shellfish poisoning (ASP) (Caron et al. 2010). The most common route of human exposure to DA is through ingestion of contaminated shellfish. The acute health effects include short term memory loss, gastroenteritis (vomiting, stomach pains, cramps), and neurological symptoms such as confusion, disorientation, seizures, and in some cases, death (Zabaglo et al. 2016). ASP is also a serious threat to marine wildlife as there have

been reports of more than one thousand deaths and/or intoxication episodes of marine mammals or sea birds, especially off the coast of California (Lefebvre et al. 1999, Lewitus et al. 2012).

STX is one of the most powerful toxins comprising most marine algal blooms and possibly one of the most toxic poisons on earth other than some select venoms and bacterial toxins (Anderson 2012). STX is classified in the group of paralytic shellfish poisons (PSPs) in that consumption (either through food or drinking contaminated water) can lead to severe, acute health effects such as gastro-intestinal symptoms, paralysis, and in the worst cases, death (Caron et al. 2010, Amade et al. 2014). These toxins have also been associated with marine wildlife mortalities, affecting species of fish, marine mammal, and seabird populations (Shumway et al. 2003, Lefebvre et al. 2004, Lefebvre et al. 2008). However, no unusual animal mortality has been recorded from STX off the California coast (Jester et al. 2009b).

OA is classified as a diarrhetic shellfish poison (DSP) due to the acute symptoms it causes in humans including gastrointestinal inflammation, abdominal pain, and diarrhea (Hallegraeff et al. 2003). OA has also been observed to be tumor forming, although there is no specification of whether OA is cancerous to humans as no chronic health effects have been studied or reported in the published literature (Dominguez et al. 2010, Valdiglesias et al. 2013). There have been no documented cases of DSP poisoning from OA on the West Coast, but analysis of shellfish tissue from established monitoring programs has indicated the presence of OA in shellfish found throughout the region (Caron et al. 2010).

YTX has been commonly classified as a DSP since it was observed in the natural environment with other DSP toxins, but some studies have shown that it does not produce

these gastrointestinal effects in the human body (Paz et al. 2004, Paz et al. 2008). In fact, the human health effects of YTX, both acute and chronic, are not yet fully understood (Tubaro et al. 2010). Other studies have suggested that YTX is a potent cardiotoxin, while others have shown that YTX targets the lysosomes, immunes system, and the thymus of the human body (Aune et al. 2002, Malagoli et al. 2006).

Table A5 *- Summary of Human Health Effects of Various Algal Toxins Endemic to Southern California*[1]

Toxin	Classification	Exposure Route	Acute Symptoms
Domoic Acid	Amnesiac Shellfish Poison (ASP)	Contaminated Shellfish/Fish, Recreation, Desalinated Drinking Water	Gastroenteritis (vomiting, stomach pains, cramps), memory loss, confusion, disorientation, seizures, and death
Saxitoxin	Paralytic Shellfish Poison (PSP)	Contaminated Shellfish/Fish, Recreation, Desalinated Drinking Water	Gastrointestinal symptoms, paralysis, death
Okadaic Acid	Diarrhetic Shellfish Poison (DSP)	Contaminated Shellfish/Fish, Recreation, Desalinated Drinking Water	Gastrointestinal inflammation, abdominal pain, and diarrhea (potentially carcinogenic)
Yessotoxin	Diarrhetic Shellfish Poison (DSP)[2]	Contaminated Shellfish/Fish, Recreation Desalinated Drinking Water	Not fully understood (studies report gastrointestinal symptoms and cardiotoxicity)

[1]Information is summarized from following references: Caron et al. 2010, Zabaglo et al. 2016, Anderson 2012, Amade et al. 2014, Hallegraeff et al. 2003, Dominguez et al. 2010, Valdiglesias et al. 2013, Tubaro et al. 2010, Aune et al. 2002, Malagoli et al. 2006

[2]Some studies report that Yessotoxin is not toxic to humans Paz et al. 2004, Paz et al. 2008

Cell concentration data as summarized in Figure A2 was used to derive a probability distribution as input to the pMFA. The visual inspection of the histograms of the cell concentrations (Figure A3) indicated that the cell distributions appeared to be nonparametric and not suitable to fit to any parametric statistical distribution (i.e., normal, gamma, beta, etc.). In addition, the number of observations for each species was relatively low over the three-year period, given that only bloom conditions were considered, further hindering the use of parametric probability distributions. Therefore, a nonparametric estimate of the empirical cumulative probability distribution (ECDF) was applied in this study.

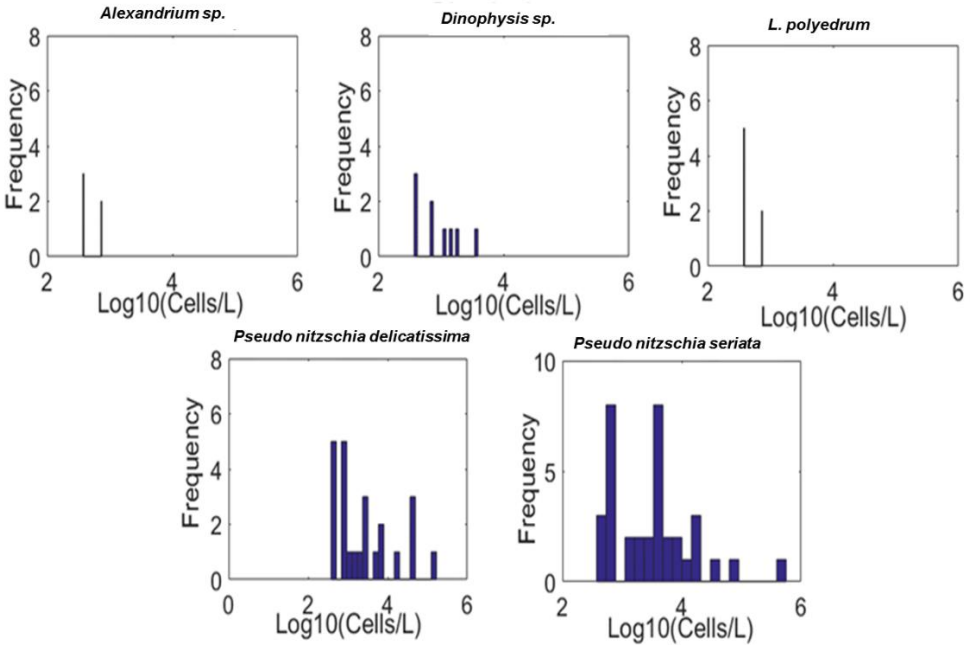

Figure A3. *Histograms of the cell distributions of each algal species over a three-year period.*

Nonparametric estimates of the CDF were achieved by linearly interpolating the stair step function of the ECDF through the breakpoints located at the midpoints of each characteristic jump (Figure A4). The ECDF was then inverted to obtain a plot of the ECDF output probability (x-axis) plotted against the logarithm of the cell concentration (y-axis). Thus, a uniform random number generator was used to select a number between 0 and 1, which was then applied in the inverse ECDF to randomly select a cell concentration, taking the full probability of the observations into account. As observed in Figure A4, algal species with fewer observations have a steeper inverse ECDF as compared to algal species with a larger amount of observations and the probability distribution is much narrower.

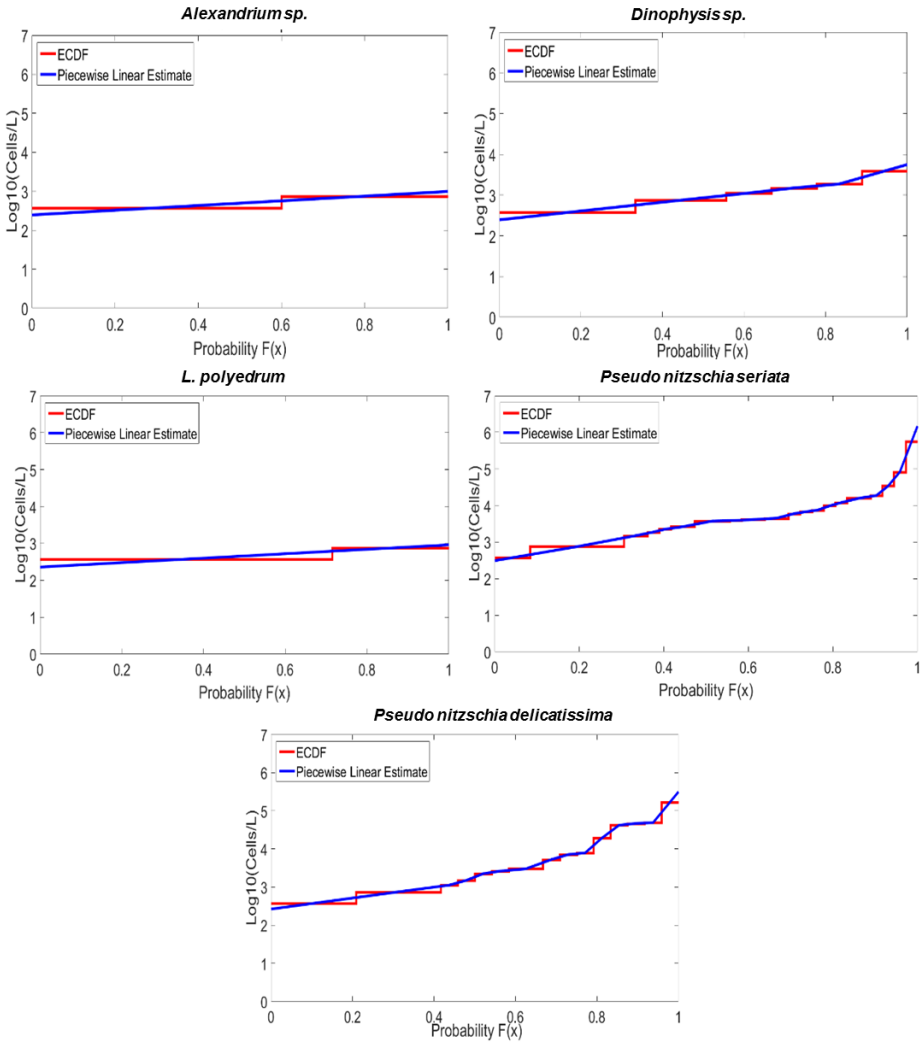

Figure A4. *Inverse CDF Plots for all algal species. The red line is the stair step function of the ECDF, whereas the blue line is the piece wise linear interpolation of the ECDF.*

3. Estimation of dissolved marine toxin removal

3.1 Physical and chemical properties of algal toxins

Information on dissolved marine algal toxin removal through water treatment processes is sparse in comparison with the removal of algal cells containing the intracellular toxins for most conventional process (Villacorte et al. 2015b). To understand the removal efficiency of these toxins, the properties of marine toxins were compared with the cyanotoxin microcystin-LR (MC-LR), a well-studied algal toxin present during most

cyanobacterial harmful algal blooms (confined to fresh and some brackish waters). Figure A5 shows the molecular structure of the four marine toxins together with MC-LR.

DA consists of a tricarboxylic amino acid parent group (three carboxyl groups) with one secondary amino group (Figure A5-A). All four groups are charged at neutral pH (Figure A5-A). The secondary amino group is generally positively charged, whereas the carboxylic acid groups contribute to a net negative charge of the compound. Protonation as the pH increases yields five different protonated isomers of DA including isodomoic acid A-H and the domoic acid 5'-distereomer (Jeffery et al. 2004).

STX consists of a tricyclic core that is very rigid and stable in most environmental solutions, similar to the hepatotoxins common to the Microcystis genus (Figure A5-B). Two amino groups exist at either side of the cyclic structure, which impart a net positive charge at neutral pH of 7.7 (Shimizu et al. 1981).

YTX is rather complex but consists of a series of cyclic polyether structures (11) that compose a ladder-like formation. YTX molecules are disulfated at one end of the structure, which counteracts the lipophilic nature of the ether structure, lending to an amphoteric behavior (Paz et al. 2008) (Figure A5-C).

OA consists of a monocarboxylic group attached to a linear chain of polyether structure (hence it is a monocarboxylic acid, Figure A5-D). OA can be observed in natural water samples in a polar and non-polar (esteric) form. At neutral pH, one can expect OA to be relatively water soluble due to the presence of a carboxylic acid (anionic charge) (Prassopoulou et al. 2009).

MC-LR is a monocyclic heptapeptide in that it consists of seven amino acids in a ring-like structure, which impart a large stability in most environmental conditions

(Bourne et al. 2006). MC-LR is a structural variant of the group of MC toxins, which has a leucine (L) and arginine (R) amino acid in the second and fourth amino acid position of the ring structure (Figure A5-E). Two ionizable carboxylic acid groups on D-glutamate and D-erthyro-β-methylaspartic acid as well as one ionizable amino on the arginine group contribute to MC-LR's high water solubility (Teixeira and Rosa 2005). In addition, the ADDA group attached to MC-LR's ring structure is relatively hydrophobic, which contributes to an appreciable solubility in organic solvents.

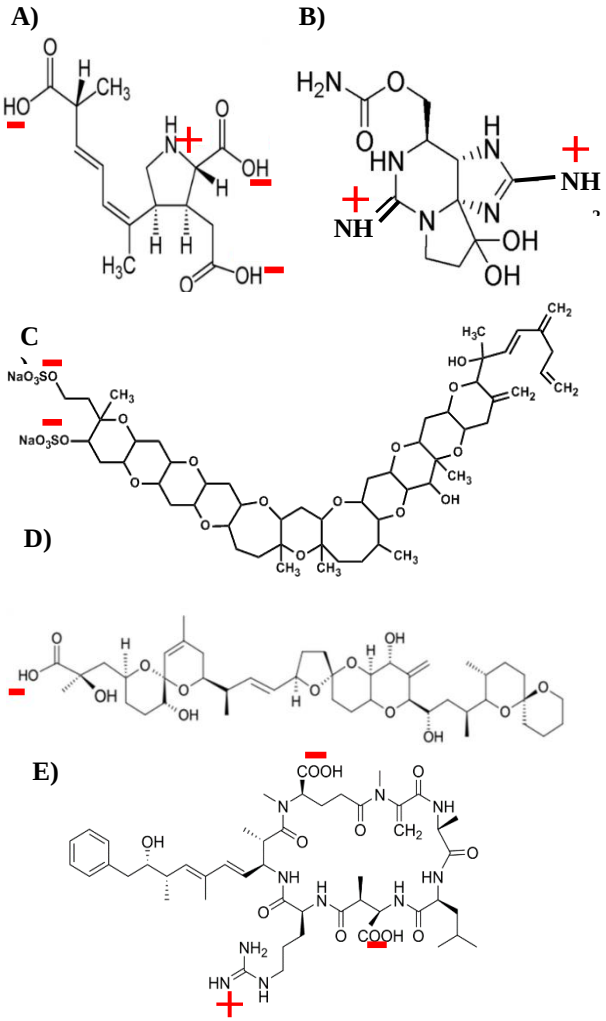

Figure A5. *Molecular structure of the common marine toxins a) Domoic acid, b) Saxitoxin, c) Yessotoxin, d) Okadaic acid, and e) Microcystin-LR*

The comparison of molecular structures provided insights to the physical and chemical properties of each marine toxin in terms of the water solubility and adsorption characteristics. Information summarized in Table A6 revealed that all toxins are chemically stable and heat resistant at operational pH (7-9). MC-LR, STX, and DA are considered hydrophilic compounds, whereas OA and YTX are lipophilic. All of the compounds are polar, to varying degrees. The majority of the compounds possess net negative charges (MC-LR, DA, OA, YTX), which vary in strength due to the presence, protonation, and de-protonation of certain functional groups (i.e., amino, carboxylic acid, etc.) as a function of pH and ionic strength (i.e., presence of sodium and chloride ions) of the water, as discussed in the previous section. Only the STX toxins are net positively charged at operating pH, due to the presence of two amino functional groups.

To quantitatively assess both the water solubility and potential sorption characteristics of the marine toxins, the partition coefficient (LogKOw) and distribution coefficients (LogDOw) were compared to that of MC-LR (Table A6). In general, the LogDOw is more predictive than the LogKOw because it depends on the pH of the solution and considers the ionization potential of compounds in solution (Wells 2006). Species with LogDOw values < 1 are considered strongly lipophilic and are more likely dissolved in non-polar solvents, absorbed in fatty tissues, or adsorbed onto organic matter present on soils (Wells and Yu 2000, Wells et al. 2006). A majority of the distribution coefficients presented in Table A6 were experimentally determined. As compared to predictions based on the molecular structure, a greater confidence was vested in the experimentally derived values (Fux 2008). The distribution coefficients also were presented for a pH range of 7-8.5 for all studies, which was similar to that expected during operation of a SWRO facility. Based on

the trends in the LogDOw, the water solubility for the toxins from highest water solubility to lowest water solubility was summarized as follows: STX> DA>MC-LR>OA>YTX. Although YTX appeared to be more polar than OA (based on chemical structure alone), experimental results suggested otherwise (Fux 2008).

The more water-soluble compounds are expected to be removed sparingly from conventional treatment processes such as conventional coagulation, flocculation (C/F), and GMF (Drikas et al. 2001). This is due to the fact that the predominant negative charge of these molecules resists charge neutralization of traditional coagulants. Further, the small molecular size of dissolved toxins may hinder the formation or adherence to flocs of appreciable density to be removed by gravitational settling, especially at the low hydraulic retention times used in conventional practice. Moreover, the presence of natural organic matter (NOM) or algal organic matter will most likely consume most of the coagulant dosage, especially at practical operational doses (Ghernaout et al. 2010). Studies have shown that even at large coagulant additions to promote sweep flocculation, complete removal of the dissolved fraction of MC-LR was not achieved (Ghernaout et al. 2010). Thus, since large doses of coagulants (to promote sweep flocculation) are not practical from an operational and economical viewpoint, we can expect the removal of most marine toxins to be relatively small from conventional C/F processes alone. STX may prove to be an exception to this inference during certain conditions of C/F. For example, alkaline conditions and the presence of oxygen may favor the transformation of STX into less toxic components, and may, to some extent, be removed by conventional C/F processes (Amade et al. 2014).

The partition between octanol and water for MC-LR has been studied as a function of pH and is a significant factor controlling the fate and transport in soil (conventional GMF) and near surfaces/boundary layers of membranes (MF/UF) (de Maagd et al. 1999, Liu et al. 2008). The soil in most conventional granular media filtration systems will contain an appreciable amount of organic material and biomass on the surface that cannot be removed by backwashing, especially near the top layers of the filter media (Emelko et al. 2006). Similarly, MF/UF practices create a cake layer due to compression of and breakage of algal cells as a result of high transmembrane pressures (Babel and Takizawa 2010, Castaing et al. 2011). When assuming the LogDOw as the main factor for sorption behavior on soils and/or hydrophobic membranes, then an approximate trend in the adsorption potential to soil (GMF) or hydrophobic membranes from highest to lowest can be summarized as follows: YTX>OA>MC-LR>DA> STX.

Table A6 *- Summary of Physico-Chemical Properties of Marine Algal Toxins*

Toxin	MW[a] (g/mol)	Water Solubility	Other Observations	Charge @ Operat. pH, Net Charge[b]	B. P. (ºC)[c]	pKa	$LogKO_w$	$LogDO_w$	Kd/Kf (L/g)
STX	299	Soluble	High oxidative degradation potential, unstable under alkaline pH	Polar, +	693	8.22, 11.28[1]	-4.53[2]	-5.492[2]	6.9 E-07[3]
DA	311.3	Soluble	Crystalline, acidic at neutral pH	Polar, -	321	2.1,3.72, 4.93,9.82[4]	-2.43[4]	-2.39[4]	2.63[5]
MC-LR	995.17	Soluble	Cyclic structure, extremely stable	Polar, -	N/A	2.09, 2.19, 12.48[6]	0.248[6]	-1.55[6]	0.0116[7]
OA	805	Slightly soluble	Lipophilic, potential to bioaccumulate	Polar, slight -	921.6	4.9[8]	1.64[8]	0.036[8]	N/A
YTX	1187.3	Slightly soluble	Lipophilic, potential to bioaccumulate	Polar, slight -	N/A	6.9[8]	4.57[8]	3.26[8]	N/A

[a,c]Adapted from Boerlage and Nada 2015
[b]Operational pH for seawater was assumed to range between 7 and 8.5, charge of dominant ionized species
[1]Experimentally determined by Rogers and Rapoport 1980
[2]Predicted by ACD/Labs from Molecular Structure, pH 7.4
[3]Experimentally determined by Burns et al. 2009, Santa Barbara sediments, saltwater
[4]Experimentally determined by Falk et al. 1991
[5]Experimentally determined by Burns and Ferry 2007, Santa Barbara sediments, saltwater
[6]Experimentally determined by de Maagd et al. 1999, extrapolated values at pH 8.46
[7]Experimentally determined by Grützmacher et al. 2010 for slow sand filter material, freshwater

[8]Experimentally determined by Fux 2008, extrapolated values at pH 8.81
[N/A] Not available in the literature

3.2 Removal Coefficient for MC-LR as a Reference

To set the reference removal coefficient, we determined the removal ranges of dissolved MC-LR from the literature for both GMF and MF/UF processes (Figure A6). Data mining results showed that MC-LR removal efficiencies varied over a wide range but were lower for GMF as compared to MF/UF processes. Since the reports did not clearly separate the processes with or without coagulation pretreatment, we assumed that the lower interquartile range corresponded to removal efficiencies without coagulation; and the upper interquartile ranges represent processes with coagulation (Figure A6). This assumption was justified by experimental reports on improvement of dissolved toxin removal with coagulation (Ghernaout et al. 2010, Meyerhofer et al. 2010, Campinas and Rosa 2010, Dixon et al. 2011).

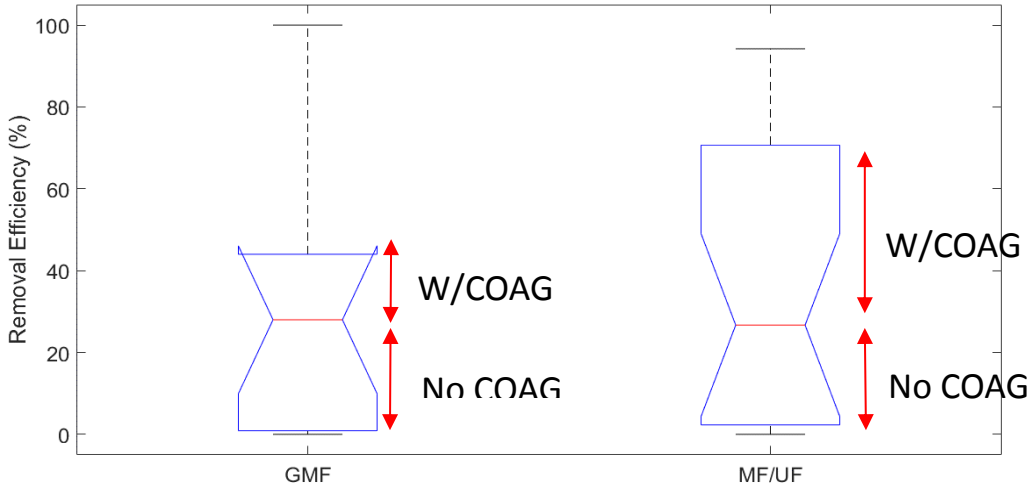

Figure A6. *Summary of reported removal efficiencies of dissolved MCLR (Dixon et al. 2011, Lee and Walker 2006, Lee and Walker 2008, Hoeger et al. 2004, Hoeger et al. 2005, Schmidt et al. 2002, Schmidt et al. 2009, Jurczak et al. 2005, Drikas et al. 2001, Gijsbertsen-Abrahamse et al. 2006, Zhang et al. 2011a)*

3.3 Dissolved Toxin Removal Coefficients by GMF Systems

The ranges in each dissolved marine algal toxin removal were developed from the relative similarity or differences in physical chemical properties to MC-LR and the expected removal mechanisms within the treatment system. Two main mechanisms: electrostatic interactions (chemical adsorption) and phase partitioning of the toxin (based on logDOw), contribute to the removal of dissolved toxins during GMF. We assumed that the physical mechanisms of retention, such as straining, interception, or impaction did not apply as the dissolved toxins have a very small molecular weight. Similarly, diffusive or dispersive processes were neglected due to the high operational interstitial velocities employed by most pretreatment filtration processes.

Electrostatic interactions may occur between the charged functional groups of each toxin at operational pH (7.7-8) and the media surface. In most cases, the filter media will have organic matter previously attached to the surface and not completely removed by backwashing processes (Emelko et al. 2006). This organic matter consists of weak organic acids that become deprotonated within the operational pH range and contribute to a net negative charge. Therefore, toxins with a net positive charge, such as STX, may chemically sorb to the media surface, whereas other toxins that are net negatively charged may become repelled. Other factors such as the strength of the net charge of functional groups may affect the sorption potential. Taking these factors into account, the relative ranking in potential removal by electrostatic interactions is as follows: STX>DA>MC-LR>YTX>OA.

The above trend is confirmed by experimental studies that have reported the adsorption coefficients for the toxins of interest onto natural beach sediments or quartz

sands (Burns and Ferry 2007, Burns et al. 2009, Grützmacher et al. 2010). A low relative adsorption potential of MC-LR was observed in both batch and column engineering filtration studies in the laboratory (Grützmacher et al. 2002, Grützmacher et al. 2010). However, STX demonstrated a much higher adsorption potential than both DA and MC-LR onto natural beach sediments (in artificial seawater, neutral pH), due to the increased electrostatic interactions between positively charged functional groups and either the sediments surface (negative charge) or the organic matter present on the surface (negative charge) (Figure A7) (Burns and Ferry 2007, Burns et al. 2009).

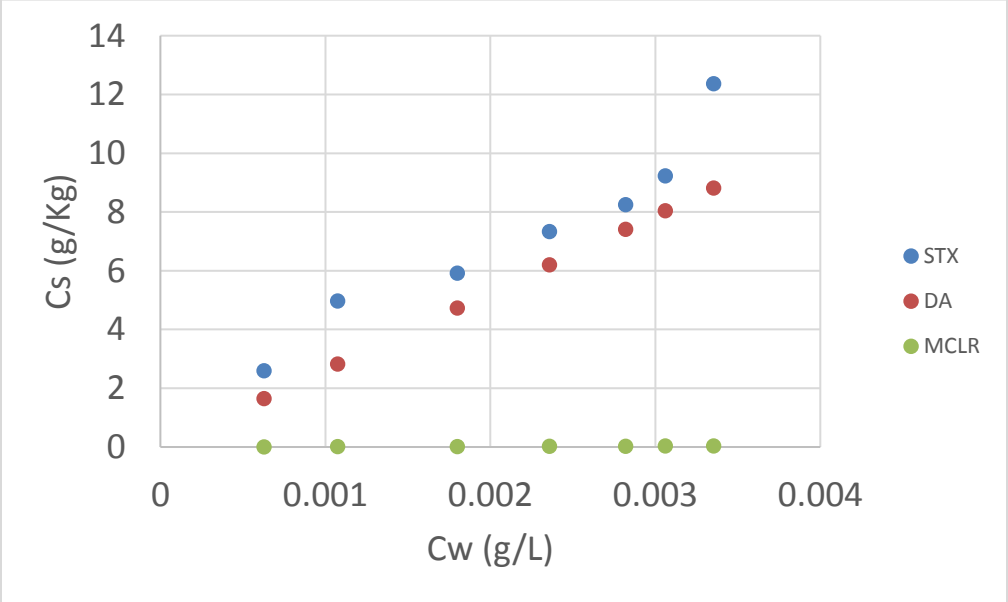

Figure A7. *Adsorption isotherms for different algal toxins onto natural sediments (graph is based on data reported in Burns and Ferry 2007 and Burns et al. 2009)*

Regarding phase partitioning, the relative ranking from most hydrophobic to most hydrophilic was determined as: YTX>OA>MC-LR>DA> STX. This ranking does not reflect electrostatic interactions, which may potentially outweigh the potential for phase partitioning. Longer chain, lipophilic toxins such as YTX and OA would be more affected by phase partitioning removal mechanisms, while the smaller and hydrophilic toxins, DA and

STX, would depend much more on electrostatic interactions (chemical adsorption) between the organic matter present in GMF systems and the charged functional groups. Therefore, the ultimate removal in GMF systems, weighted by physical chemical properties of the toxins and proposed mechanisms of removal, is as follows: STX>YTX>OA>MC-LR>DA. STX exhibits the highest removal due to the relatively strong, net positive charge, whereas YTX and OA are likely to partition to organic matter on the filter media due to the high distribution coefficients at operational pH. DA is most likely repelled by the net negative charge of the organic matter, and due to its small molecular weight is the toxin rejected the most by GMF systems.

The final dissolved marine toxin removal ranges in GMF processes follow the trend postulated above and in reference to MC-LR is shown in Table A7. As evidenced in the table, the lower and upper limit of the ranges in dissolved MC-LR removal were adjusted by an increment of 2% based on the trend in removal predicted. A value of 2% was chosen as an increment as a conservative estimate of the change in the expected removal efficiency. Coagulation based processes have the potential to remove a greater extent of dissolved toxins and were given the highest range in removals for all treatment processes. Both pressurized and conventional GMF processes without coagulant addition had relatively similar ranges in dissolved toxin removal, although pressurized systems were slightly higher than conventional systems (Table A7).

Table A7*. Summary of removal efficiencies for dissolved marine toxins in GMF treatment systems*

Treatment Process	MC-LR (%)	DA (%)	OA (%)	YTX (%)	STX (%)
No Coag	0.9-28	0-27.1	2.9-30	4.9-32	6.9-34
Pressurized, No Coag	8.6-34	6.6-32	10.6-36	12.6-38	14.6-40
W/Coag	28-44	26-42	30-46	32-48	34-50

3.4 Dissolved Toxin Removal Coefficients by MF/UF Systems

The main mechanisms for dissolved solutes removal during membrane filtration processes include size exclusion, electrostatic interactions, phase partitioning, and diffusion (Lee and Walker 2008). Although the major rejection mechanism of most dissolved solutes is through physical sieving or size exclusion alone, the molecular weight cutoff (MWCO) of all MF or UF membranes (0.1 to 0.02 μm) is considerably larger than the molecular weight of all marine algal toxins. Therefore, size exclusion should be ruled out as a major removal mechanism.

During algal blooms, the accumulation of organic matter at the MF/UF membrane surface is inevitable due to the transmembrane pressures employed and associated cell breakage (Voutchkov 2010). The relative thickness and development of this organic fouling layer depends on the membrane surface properties such as hydrophobicity, roughness, and charge (Lee and Walker 2008). Thus, similar to the GMF process, the same two main mechanisms: electrostatic interactions and phase partitioning, are responsible for dissolved marine toxin removal in MF/UF. An equivalent trend in removal proposed for GMF systems is also applied to MF/UF systems: STX>YTX>OA>MCLR>DA.

To be consistent with GMF systems, an increment of 2% was added or subtracted from the higher and lower boundaries of each range from the reference toxin MC-LR

removal range (Table A8). In general, MF/UF processes with coagulation were observed to have a much higher removal of extracellular toxins than processes without coagulation (Table A8). In this study, dissolved toxin removals were assumed to be comparable for MF/UF configurations (i.e., pressurized vs. submerged).

Table A8 *- Summary of removal efficiencies for dissolved marine toxins in MF/UF treatment systems*

Treatment Process	MC-LR (%)	DA (%)	OA (%)	YTX (%)	STX (%)
No Coag	2.3-26.7	0.3-24.7	4.3-28.7	6.3-30.7	8.3-32.7
W/Coag	26.7-70.7	24.7-68.7	28.7-72.7	30.7-74.7	32.7-76.7

3.5 Dissolved Toxin Removal Coefficients by RO Systems

Pore size exclusion was identified as the primary removal mechanism of RO membranes for most molecular compounds, although the relative hydrophobicity and membrane material may influence the formation of boundary layers/concentration polarization and biological fouling (Voutchkov 2013). The size exclusion range of most RO membranes is 0.6 to 0.7 nm and the molecular weight cutoff is generally 100-300 Daltons (Sasaki et al. 2013). Similar to MF/UF membranes, RO membranes can be either negatively charged (hydrophilic) or positively charged (hydrophobic).

Complete removal of YTX (1000 Da) and OA (>800 Da) are expected based on the RO size exclusion mechanism alone (Boerlage and Nada 2015). These theoretical predictions were confirmed in a variety of laboratory and pilot scale studies, assessing the removal efficiency of OA in the feed and permeate water (Laycock et al. 2012, Seubert et al. 2012) (Table A9). However, removal of YTX by RO membranes, to the best of our knowledge, has not been presented in the published literature.

Prediction of RO rejection for the smaller toxins, STX and DA (~300 Da), is much more complex and depends on several factors such as the condition of the membrane surface, as well as the ionic strength, and pH of the feed water (Boerlage and Nada 2015). Increased biological or organic membrane fouling may lead to increased DA rejection due to formation of chemical bounds with the carboxylic acid group on DA. Physical adsorption of STX may occur due to the hydrophilic properties of the membrane (negative charge), leading to increased rejection. Despite these complications in prediction ability during RO removal of the smaller toxins, laboratory and pilot scale studies have indicated that the removal of STX and DA ranges between 99.4->99.9 and 99.0 to >99.9 % removal for each toxin, respectively (Table A9).

Table A9 *- Summary of RO rejection of dissolved marine toxins*

Scale	Dissolved % Toxin Removal					Reference
	STX	**PbTX**	**DA**	**OA**	**YTX**	
Lab	99.4	99.9	99.0	99.7	N/A	[50]
Lab	>99.9	>99.9	>99.9	>99.9	N/A	[51]
Pilot[1]	>99.9	>99.9	>99.9	>99.9	N/A	
Pilot[1]			>99.9			[42]
Pilot[2]			99.8			

N/A = Not reported, [1]Proceeding UF treatment, [2]Proceeding slow sand filter treatment

3.6 Ranges in Algal Cell Breakage

The percentage of cells that break during each pretreatment were estimated based on Voutchkov (2010), in which 0.4 bars was used as a pressure threshold of significant cell breakage. The transmembrane pressure (TMP, rather than shear) of each pretreatment process at general operational conditions was used to relate the percentage of cell breakage with pressure. With general assumptions of TMP >0.4 bar for pressurized MF/UF and GMF, 0.4 bar for submerged MF/UF and <<0.4 bar for conventional GMF processes, cell

breakage was estimated to range between 75-100%, 25-50% and 0-25%, respectively. Coagulation based processes were assumed to decrease the impact of cell breakage for each treatment process.

4. Derivation of Acute Reference Doses for Algal Toxins in Drinking Water

The acute RfDs for STX, DA, and OA were derived from LOAELs of human exposure events, whereas acute RfDs for YTX were established from NOAELs of animal testing (Table A10). The uncertainty factors (UF1) of 3 as used by Paredes and co-workers (2011) were applied to extrapolate the LOAEL to NOAEL for STX, DA, and OA toxins (Table A10). To be conservative, an additional uncertainty factor for intra-species variation (UF2) of 3 was used for both STX and OA. The UF2 of 10 was applied to DA; and 3 and 100 (was used for YTX for extrapolation from animal to human data (Paredes et al. 2011). In all the RfD calculations, a body weight of 70 kg, instead of 60 kg, was used, which is more concurrent with US EPAs quantitative chemical risk assessment framework (Fowle and Dearfield 2000).

Table A10 *- Summary of values and benchmarks used in risk assessments*

Toxin	LOAEL (µg/kg)	UF1	NOAEL (µg/kg)	UF2	Acute RfD (µg/kg/d)	Acceptable Level (µg/L)
STX	1.71	3	0.571	3	0.19	3.32
DA	900	3	300	10	30	525
OA	0.714	3	0.238	3	0.08	1.4
YTX	-	-	5000	3 &100	16.7	292

II. Supplementary Results

5. Algal Toxin Concentrations in Difference Sources

5.1 Inlet Toxin Concentration Distributions

The inlet toxin concentration distributions (TCDs) entering the SWRO pretreatment systems varied dramatically by toxin type (Figure A8, STX, DA, OA, YTX). For all pretreatment train scenarios, DA and YTX concentration distributions were much higher (with a mean of 200 and 75 µg/L) than the STX and OA concentration distributions (with a mean of 0.5 and 3 µg/L) (Figure A8). The variability of the influent distributions of DA and YTX, with standard deviation of 11 and 9 µg/L, was also much higher than the influent distributions of STX and OA, with standard deviations of 0.061 and 0.3 µg/L, respectively.

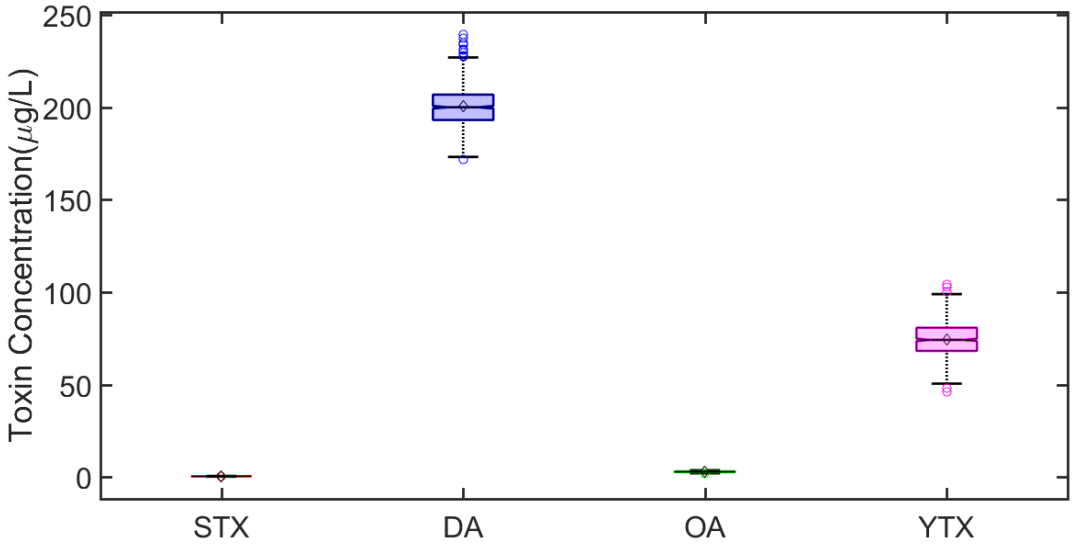

Figure A8. *Influent toxin concentration distributions for a singular pretreatment train (GMF alone)*

5.2 Toxin Concentration Factors in Backwash and Brine Reject

Relative mean toxin concentration factors were calculated by normalizing the model output concentration in the backwash/brine water by the inlet toxin concentrations and compared among pretreatment train configurations (Figure A9). The calculated toxin concentration factors for both backwash and RO rejects ranged from 2 to 10 times the inlet toxin concentrations for all pretreatment train scenarios (Figure A9). STX toxins demonstrated the largest magnitude in concentration factors among all toxin types in this study. Pressurized GMF processes generally produced the higher range in observed toxin concentration factors, whereas processes without coagulation resulted in much lower concentration factors.

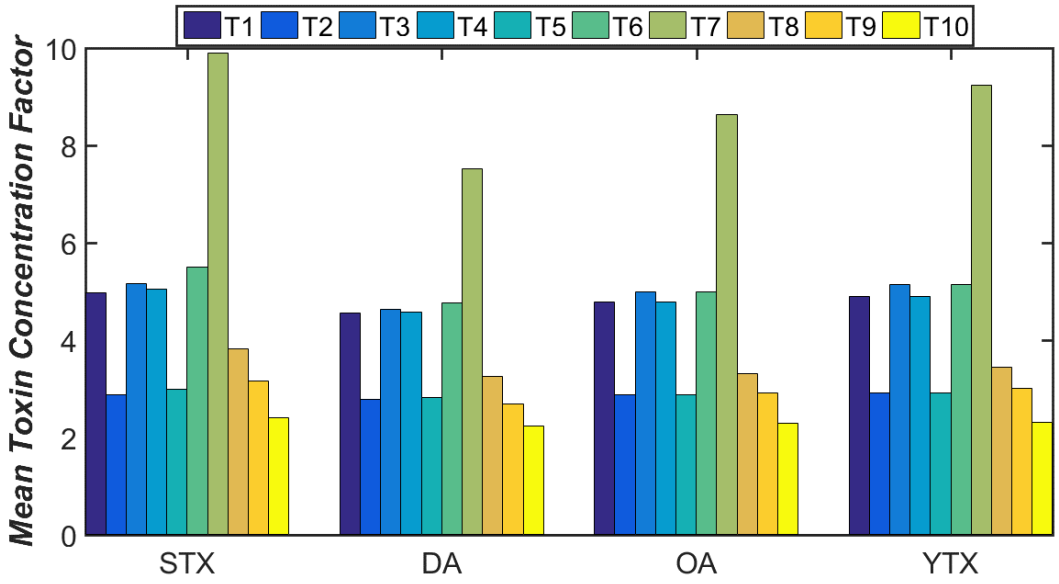

Figure A9. *Mean toxin concentration factors for various algal toxins as a function of pretreatment configuration. T1-T10 refer to the same ten treatment train configurations evaluated in the pMFA.*

5.3 Toxicity Fraction: Backwash Water vs. RO Reject

The contribution of either the backwash or brine waters to the overall toxicity of the pretreatment system waste streams was assessed for all pretreatment processes (Figure A10). For all toxin types, the backwash water was observed to contribute the most to the overall toxicity of the concentrated waste stream, which varied from 50 to 85% of the total toxicity. However, treatment processes without coagulation had a much higher contribution from the RO concentrate to the overall toxicity as compared to the backwash waters. The magnitude of the contribution to overall toxicity from backwash waters originating from processes without coagulation were much higher for DA toxins than STX, OA, and YTX alike (ranging from 55 to 80% of the total toxicity).

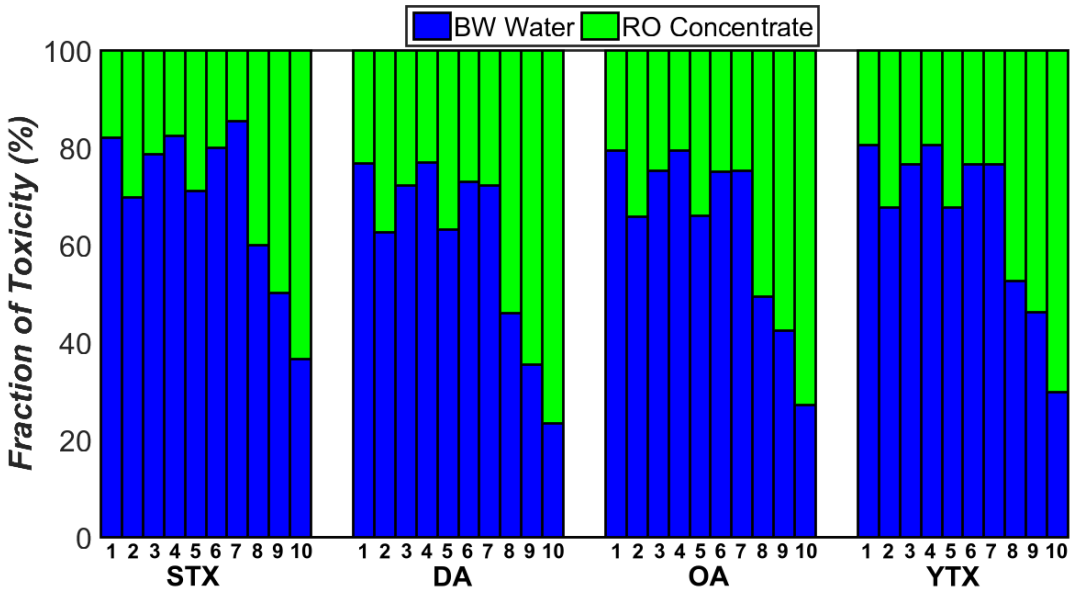

Figure A10. *Relative fraction of toxicity of Backwash water and RO Concentrate for various algal toxins. T1-T10 refer to the same ten treatment train configurations evaluated in the pMFA.*

6. Summary of p-values from ANOVA Testing

The p-values generated from the Tukey post hoc analysis comparing individual treatment trains (T1-T10) using the toxin concentration distributions of the permeate and backwash/brine reject waters are tabulated in Table A15. The results are organized according to toxin type (i.e., STX, DA, OA, YTX), toxin concentration distribution (permeate or brine/backwash waters) and treatment train comparison (i.e., T1 vs. T2). The grey shading indicates comparisons that were not statistically significant (p value < 0.05), while the remaining (no-shading) cells represent statistically significant comparisons. In addition, box and whisker plots summarizing the p-value results of the grouped comparisons (i.e., No Coag. Vs. Coag.) for backwash/brine reject waters are presented in Figure A11.

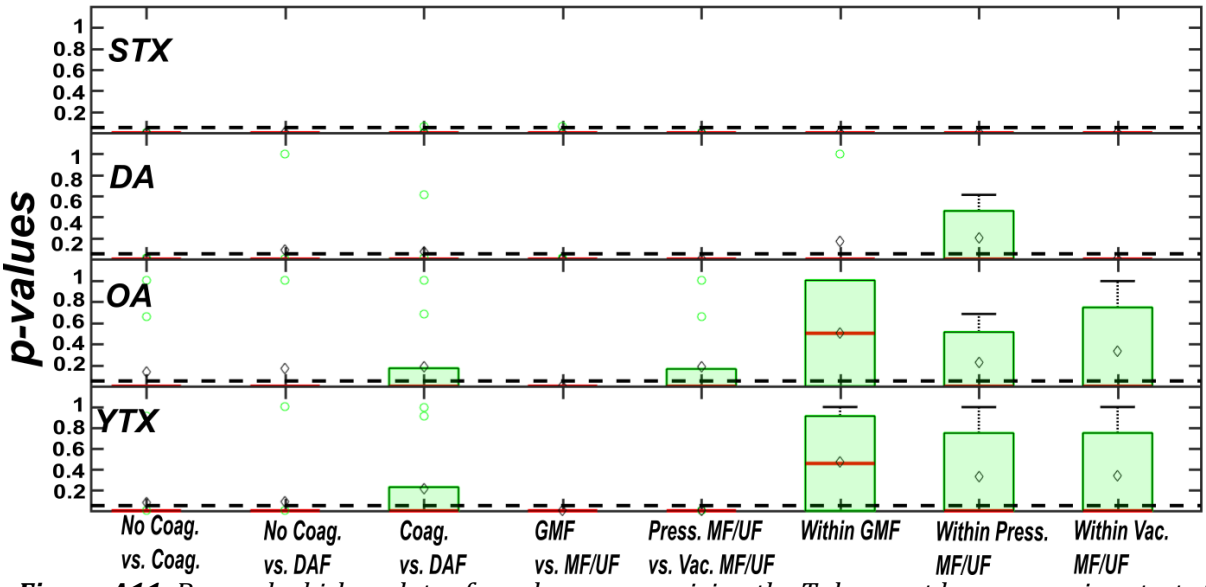

Figure A11. *Box and whisker plots of p-values summarizing the Tukey post hoc comparison tests for the backwash/brine reject waters of each toxin (i.e., STX, DA, OA, YTX). The black dashed lines illustrate the significance level (0.05), while the red lines and black diamonds indicate the median and mean of p-values for each group, respectively. Circles represent outlying p-values from each comparison group.*

Table A11. *Tabulated p-values for the Tukey post hoc comparisons of T1-T10 treatment trains using permeate and backwash/brine water toxin concentration distributions. Grey shading indicates non-significant (p-value < 0.05) comparisons.*

	Permeate Water				***Backwash/Brine Water***			
	STX	**DA**	**OA**	**YTX**	**STX**	**DA**	**OA**	**YTX**
Overall	0	0	0	0	0	0	0	0
T1 vs. T2	0.676	0.509	1	0.993	1.27E-07	1.27E-07	1.27E-07	1.27E-07
T1 vs. T3	1.27E-07	1.27E-07	1.27E-07	1.27E-07	1.27E-07	1.82E-06	1.27E-07	1.27E-07
T1 vs. T4	0.999	0.999	0.999	1	0.00388	0.611	0.682	0.999
T1 vs. T5	0.456	0.0928	1	1	1.27E-07	1.27E-07	1.27E-07	1.27E-07
T1 vs. T6	1.27E-07	1.27E-07	1.27E-07	1.27E-07	1.27E-07	1.27E-07	1.27E-07	1.27E-07
T1 vs. T7	1.27E-07	1.27E-07	1.27E-07	1.27E-07	1.27E-07	1.27E-07	1.27E-07	1.27E-07
T1 vs. T8	1.27E-07	1.27E-07	1.27E-07	1.27E-07	1.27E-07	1.27E-07	1.27E-07	1.27E-07
T1 vs. T9	1.27E-07	1.27E-07	1.27E-07	1.27E-07	1.27E-07	1.27E-07	1.27E-07	1.27E-07
T1 vs. T10	1.27E-07	1.27E-07	1.27E-07	1.27E-07	1.27E-07	1.27E-07	1.27E-07	1.27E-07
T2 vs. T3	1.27E-07	1.27E-07	1.27E-07	1.27E-07	1.27E-07	1.27E-07	1.27E-07	1.27E-07
T2 vs. T4	0.178	0.771	1	0.998	1.27E-07	1.27E-07	1.27E-07	1.27E-07
T2 vs. T5	1	0.998	1	1	0.0016	2.81E-05	0.992	1
T2 vs. T6	1.27E-07	1.27E-07	1.27E-07	1.27E-07	1.27E-07	1.27E-07	1.27E-07	1.27E-07
T2 vs. T7	1.27E-07	1.27E-07	1.27E-07	1.27E-07	1.27E-07	1.27E-07	1.27E-07	1.27E-07
T2 vs. T8	1.27E-07	1.27E-07	1.27E-07	1.27E-07	1.27E-07	1.27E-07	1.27E-07	1.27E-07
T2 vs. T9	1.27E-07	1.27E-07	1.27E-07	1.27E-07	1.27E-07	1.27E-07	0.996	1.60E-04
T2 vs. T10	1.27E-07	1.27E-07	1.27E-07	1.27E-07	1.27E-07	1.27E-07	1.27E-07	1.27E-07
T3 vs. T4	1.27E-07	1.27E-07	1.27E-07	1.27E-07	0.065	0.016	1.27E-07	1.27E-07
T3 vs. T5	1.27E-07	1.27E-07	1.27E-07	1.27E-07	1.27E-07	1.27E-07	1.27E-07	1.27E-07
T3 vs. T6	1	1	1	0.928	1.27E-07	1.27E-07	1	0.913
T3 vs. T7	1.27E-07	1	1	1	1.27E-07	1	1	1
T3 vs. T8	1.27E-07	1.27E-07	1.27E-07	1.27E-07	1.27E-07	1.27E-07	1.27E-07	1.27E-07
T3 vs. T9	1.27E-07	1.27E-07	1.27E-07	1.27E-07	1.27E-07	1.27E-07	1.27E-07	1.27E-07
T3 vs. T10	1.27E-07	1.27E-07	1.27E-07	1.27E-07	1.27E-07	1.27E-07	1.27E-07	1.27E-07
T4 vs. T5	0.0808	0.235	1	1	1.27E-07	1.27E-07	1.27E-07	1.27E-07
T4 vs. T6	1.27E-07	1.27E-07	1.27E-07	1.27E-07	1.27E-07	1.27E-07	1.27E-07	1.27E-07
T4 vs. T7	1.27E-07	1.27E-07	1.27E-07	1.27E-07	1.27E-07	0.016	1.27E-07	1.27E-07
T4 vs. T8	1.27E-07	1.27E-07	1.27E-07	1.27E-07	1.27E-07	1.27E-07	1.27E-07	1.27E-07
T4 vs. T9	1.27E-07	1.27E-07	1.27E-07	1.27E-07	1.27E-07	1.27E-07	1.27E-07	1.27E-07
T4 vs. T10	1.27E-07	1.27E-07	1.27E-07	1.27E-07	1.27E-07	1.27E-07	1.27E-07	1.27E-07
T5 vs. T6	1.27E-07	1.27E-07	1.27E-07	1.27E-07	1.27E-07	1.27E-07	1.27E-07	1.27E-07
T5 vs. T7	1.27E-07	1.27E-07	1.27E-07	1.27E-07	1.27E-07	1.27E-07	1.27E-07	1.27E-07
T5 vs. T8	1.27E-07	1.27E-07	1.27E-07	1.27E-07	1.27E-07	1.27E-07	1.27E-07	1.27E-07
T5 vs. T9	1.27E-07	1.27E-07	1.27E-07	1.27E-07	2.02E-07	1.27E-07	0.654	0.0018
T5 vs. T10	1.27E-07	1.27E-07	1.27E-07	1.27E-07	1.27E-07	1.27E-07	1.27E-07	1.27E-07
T6 vs. T7	1.27E-07	1	1	0.928	1.27E-07	1.27E-07	1	0.913

T6 vs. T8	1.27E-07	1.27E-07	1.27E-07	1.27E-07	1.27E-07	1.27E-07	1.27E-07	1.27E-07
T6 vs. T9	1.27E-07	1.27E-07	1.27E-07	1.27E-07	1.27E-07	1.27E-07	1.27E-07	1.27E-07
T6 vs. T10	1.27E-07	1.27E-07	1.27E-07	1.27E-07	1.27E-07	1.27E-07	1.27E-07	1.27E-07
T7 vs. T8	1.27E-07	1.27E-07	1.27E-07	1.27E-07	1.27E-07	1.27E-07	1.27E-07	1.27E-07
T7 vs. T9	1.27E-07	1.27E-07	1.27E-07	1.27E-07	1.27E-07	1.27E-07	1.27E-07	1.27E-07
T7 vs. T10	1.30E-07	1.27E-07	1.27E-07	1.27E-07	1.27E-07	1.27E-07	1.27E-07	1.27E-07
T8 vs. T9	1.55E-03	1.30E-07	0.994	1	1.27E-07	1.27E-07	1.27E-07	1.27E-07
T8 vs. T10	0.912	0.030	1	0.987	1.27E-07	1.27E-07	1.27E-07	1.27E-07
T9 vs. T10	1.26E-06	0.0501	0.999	0.967	1.27E-07	1.27E-07	1.27E-07	1.27E-07

Appendix B: *The Effect of Organic Carbon Addition on the Community Structure and Kinetics of Microcystin-Degrading Bacterial Consortia* - Supplementary Materials

I. Supplementary Results and Methods

1. ELISA and UPLC-MS/MS Results

Figures B1 and B2 depict typical calibration curves used in both the ADDA-ELISA analysis and UPLC-MS/MS confirmations of microcystin (MC) concentration. Excellent agreement was observed between the standard concentrations and the response of either measurement technique for all replicate experiments (r^2 approaching 1). These results ensured that each measurement of MC concentration was reproducible and subject to low variability.

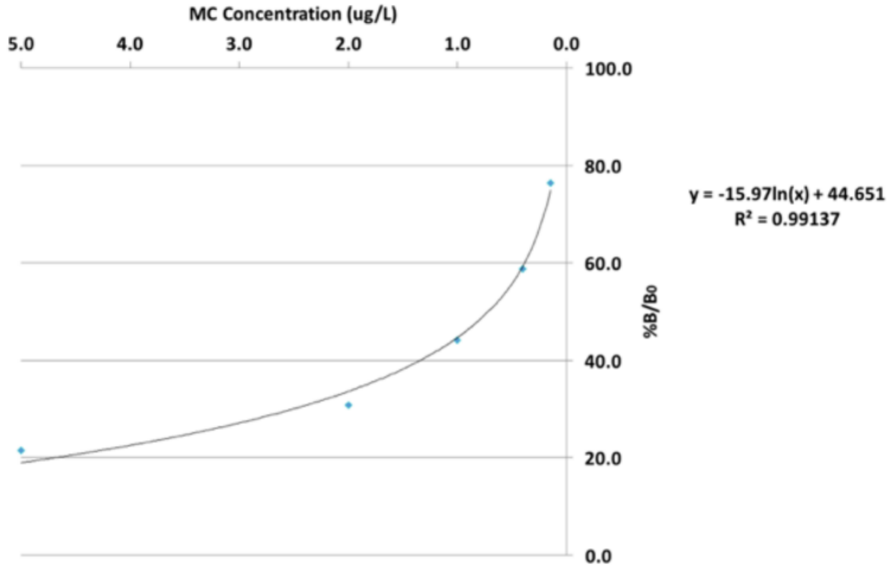

Figure B1. *Sample calibration curve for ELISA tests for determination of MC concentration in batch degradation experiments. The correlation coefficient in this case was 0.99137, indicating good agreement between measured and standard concentrations.*

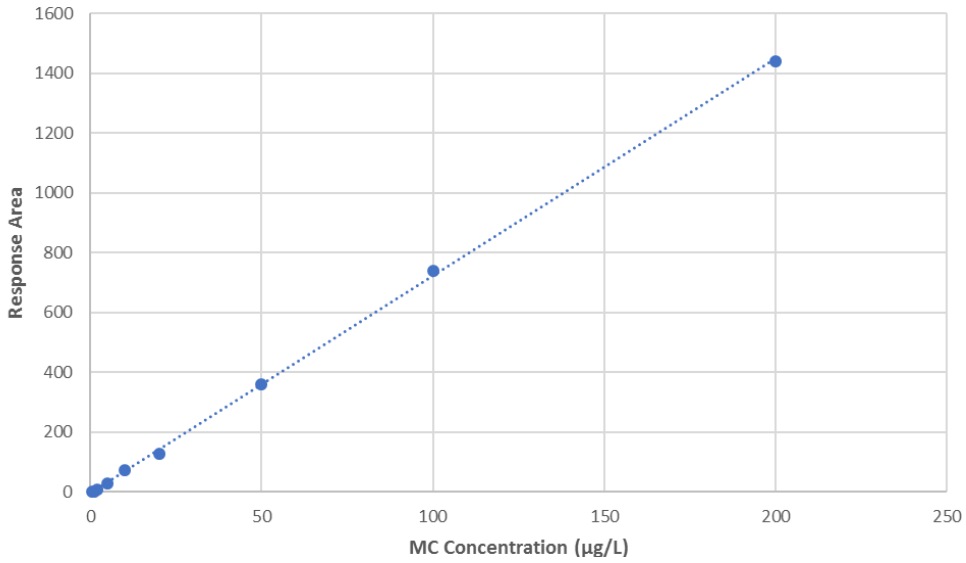

Figure B2. *Sample calibration curve for UPLC-MS/MS tests for comparison against ELISA tests. The correlation coefficient in this was 0.9997, indicating very good agreement between measured and standard concentrations.*

2. Flow Cytometry Results

For consortia cultured without the presence of ethanol, optical density was not sensitive enough to detect changes in the concentration of MC-degrading bacterial cells. Therefore, flow cytometry was used to qualify the changes in cell counts during additional batch biodegradation experiments or each consortium in the presence of MC-LR. In brief, a Novocyte Flow cytometer (ABEA Biosciences) equipped with a single 488 nm excitation laser was used for bacterial cell detection. The cells were diluted, fixed, and stained with fluorescent SYBR Gold dye following a similar procedure presented by Huang et al. (2016). Based on the SYBR Gold fluorescent properties, the forward scatter (FSC-H), side scatter (SSC-H), and main fluorescence intensity (FITC-H) channels were monitored during measurement. Flow cytometer settings were set to the following for each run: slow flow rate, 35 µL of sample injection, and FSC-H/FITC-H cutoffs at 150 and 500. respectively. These cutoffs were empirically determined to properly separate the bacterial signal from the smaller virus or debris particle signal.

Figure B3 illustrates the results of the 11B consortia degrading MC-LR at an initial concentration of 100 μg/L after three replicate experiments. Other consortia (i.e., 10B and LSB) shared similar cell growth behavior of the 11B consortium (data not shown). MC-LR was rapidly degraded by 11B consortium 2-4 days after the initial inoculation. Cell growth was highly variable for this consortium after 27, 66, and 98 hours (1, 3, and 4 days) of the duration of the experiment. However, there was relatively low variability in measured MC concentrations throughout the course of the experiment, indicating that MC metabolism was similar across each replicate experiment. Differences in cell growth may be attributed to a wide range in factors, including the composition of the initial inoculum. Although the initial cell counts were relatively equivalent across replicates (as intended), it was difficult to control, for example, the ratio of the initial number of MC degrading organisms to non-degrading organisms, which may have substantially influenced the cell growth profiles. Overall, the flow cytometry data was useful as it indicated that cell growth was occurring in each consortium using MC as the sole carbon and energy source and that the initial bacterial cell concentrations were relatively uniform across each experimental replicate.

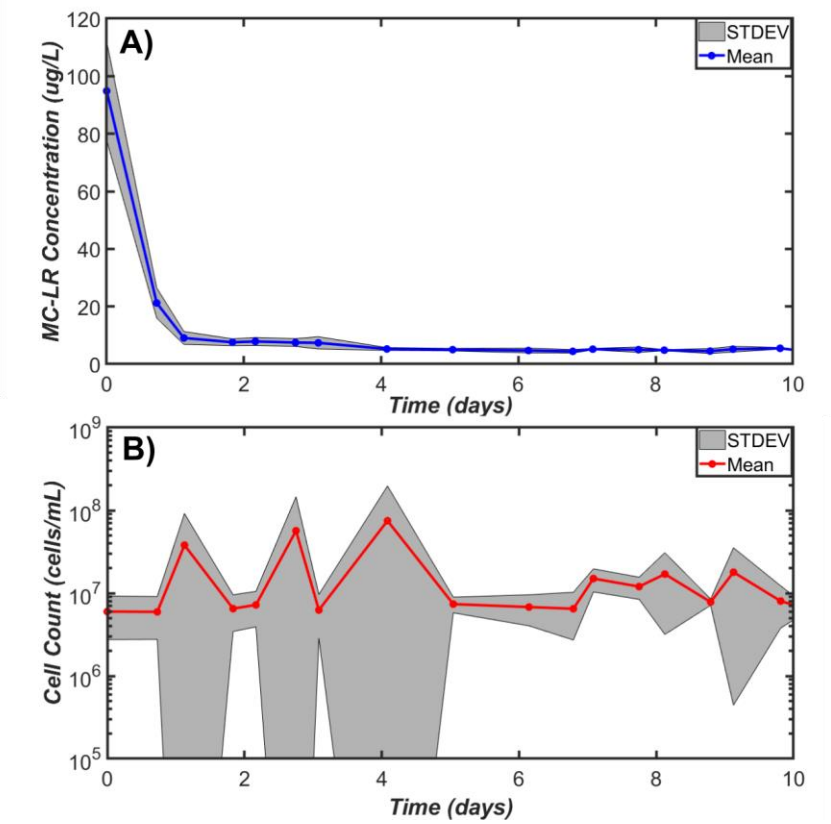

Figure B3. *MC-LR batch biodegradation experiment for the 11B consortia cultured without ethanol. Both the A) concentration of MC-LR (blue) measured using ELISA and B) cell counts (red) measured by flow cytometry are reported. Solid lines indicate the mean of three individual replicates, whereas grey shading indicates one standard deviation of the replicated measurements. The y-axis for cell count concentration is plotted on a log (base 10)-scale.*

3. MC-LR Abiotic Degradation Experiments

Control experiments (MC-LR without added consortia or ethanol) were run in triplicate to assess the effect of abiotic degradation potentially taking place during the batch biodegradation experiments (Figure B4). Experimental conditions for these experiments were kept identical to those described for batch biodegradation; however, monitoring was only performed for 4-days (shaken, room temperature, same volume and sterile tissue flasks used, 200 µg/L MC-LR initial concentration). As observed in Figure B4, there was a slight decline in MC-LR during experimentation, with some variation observed across replicates. The decline in MC concentrations may be attributed to sorption to the tissue flask rather than

abiotic degradation as the experiments were performed in the dark and under room temperature (ruling out photo or thermal degradation) and the stability of MC is very high compared to other chemicals or toxicants.

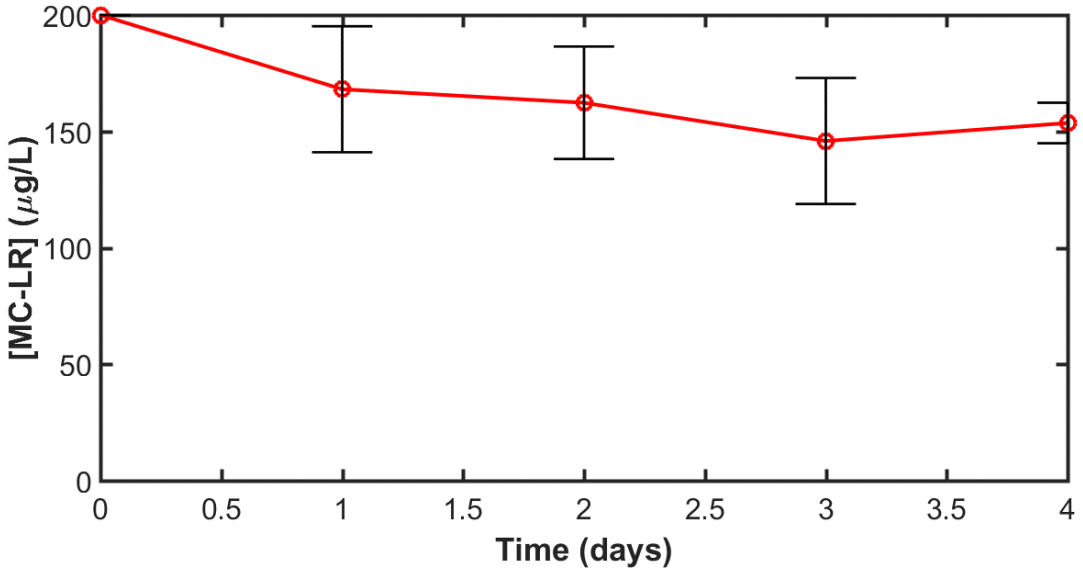

Figure B4. *Concentration of MC-LR as observed during the batch control experiments.*

4. Derivation of the Bi-Phasic Kinetic Model

The derivation of the analytical solution for the bi-phasic kinetic model presented in Equation 1 is shown below and is similar to that presented by Ouiroga and co-workers (1999).

$$\frac{dC}{dt} = -KCX \tag{1}$$

First, a substitution is made for the microorganism concentration (X) given that the substrate (MC concentration) is rate limiting by introducing the cell yield coefficient (Y), resulting in Equation 2.

$$Y = \frac{X - X_0}{C_0 - C} \tag{2}$$

$$X = Y(C_0 - C) + X_0 \quad (3)$$

$$\frac{dC}{dt} = -KYC^2 + C(KX_0 + KYC_0) \quad (4)$$

The proposed model also considers some fraction of the initial substrate (MC) to be non-biodegradable, which is realistic given that complete degradation of MC often is not performed by the degrader population (and depends on the non-degrader population present).

$$C_T = C_B + C_{NB} \ \ and \ \ C_{T0} = C_{B0} + C_{NB} \quad (5)$$

where C_T is the total substrate, C_B is the biodegradeable substrate, and C_{NB} is the non-biodegradable substrate portion, C_{T0} is the initial total susbtrate, C_{B0} is the initial biodegradeable substrate, in which the non-biodegradeable substrate remains non-transformed during degradation.

Substituting the above relations for total substrate and grouping together like terms, three rate coefficients are observed, K_0, K_1, and K_2. The mathematical meanings of each of these kinetic constants are described below (Equations 7-9).

$$\frac{dC}{dt} = K_2C^2 + K_1C + K_0 \quad (6)$$

$$K_2 = -KY \quad (7)$$

$$K_1 = KY\left(\frac{X_0}{Y} + (C_{T0} - C_{NB}) + 2C_{NB}\right) \quad (8)$$

$$K_0 = -KY\left(\frac{X_0}{Y}C_{NB} + (C_{T0} - C_{NB})C_{NB} + {C_{NB}}^2\right) \quad (1)$$

The physical meaning of each of these constants can be determined by factoring Equation 6 and defining a new set of model parameters, p, q, and h. It can be shown mathematically that h is one limiting solution of the quadratic equation and represents one solution where biodegradation rates are at a minimum (dc/dt = 0). In this way, h is termed the maximum amount of substrate available for biodegradation. On the other hand, q is

another limiting case from the quadratic equation where biodegradation rates reach a minimum. Thus, q signifies the non-biodegradable fraction of substrate remaining when the biodegradable substrate is exhausted. Finally, when substituting K_1, K_2, and K_0 into Equation 10, it is evident that the p value represents the maximum specific growth rate of the microorganisms ($\frac{1}{X}\frac{dX}{dt}$).

$$p = \sqrt{(K_1^2 - 4K_2K_0)} \quad (2)$$

$$q = \frac{-K_1 + p}{2K_2} \quad (3)$$

$$h = \frac{-K_1 - p}{2K_2} \quad (12)$$

where h represents the maximum amount of substrate (MC-LR) available for biodegradation (μg/L), q represents the non-biodegradable portion of MC-LR (μg/L), and p represents the maximum growth rate of the microorganisms (1/day).

5. Summary of Model-Data Fitting Procedure and Metrics

DREAM$_{ZS}$ (v1.0), a variant of the well-known Bayesian, Differential Evolution Adaptive Metropolis (*DREAM*) algorithm, was used to estimate the posterior distribution of model parameters and associated half-lives. *DREAM$_{ZS}$* differs from *DREAM* in that it samples from the past states of each designated Markov chain exploring the specified parameter space and was selected for this study for the following advantages: a) a smaller number of chains is required to search the parameter space (reducing CPU time); b) the CPU time can be further reduced since each chain can run on a different processor (better parallel distribution); and c) outlier chains do not need as forceful of treatment as compared to *DREAM* (Vrugt 2016). Advantage c) was particularly important since the parameter space for this kinetic model was marked by a very large number of local minima.

The specific settings used to run the *DREAM$_{ZS}$* algorithm are described in Table B1. The choice of objective function was set to Gaussian likelihood without measurement error (with the assumption that the error residuals are normal, independent, and homoscedastic), as the sample size (n=3) was small. With a smaller number of replicates, the standard deviation will vary considerably by chance; therefore, weighting by the measurement error should, in most cases, always be avoided (Motulsky and Christopoulos 2004).

Table B1 *– DREAM_ZS settings for Model-Data Fitting Procedure.*

Parameter Setting	Nominal Value
Objective Function	Gaussian Likelihood: measurement error integrated out
Number of Markov Chains (N)	6
Number of Generations (T)	50,000
Prior Distribution	Uniform
Boundary Handling	Reflection
Number of Crossover Values (nCR)	3
Number of Chain Pairs for Proposal (δ)	3
Random Error for Ergodicity (λ)	0.05
Randomization (ζ)	0.05
Probability of Jump Rate	1
Adapt Selection Probability Crossover	Yes
Scaling Factor of Jump Rate ($b0$)	0.75

For all cases, a small number of chains (~6-15) and a high number of generations (50K-200K) resulted in convergence of the search algorithm for all datasets (Figure B5). The number of chains for low-dimensional problems (d<10) in *DREAM$_{ZS}$* was recommended to at least 3; therefore, between 6-15 were used to be as conservative as possible. For runs requiring greater than 6 chains to reach convergence, outlying chains (with poor progress to the global minimum solution) were removed so that the number of chains compared was always consistent between experiments (6). In addition, the number of posterior samples (n) used after each fitting procedure was set to 25,000 (discarding

half of samples for "burn in"). If the number of generations required to reach convergence was greater than 50,000, the last 25,000 samples were used to keep the number of posterior samples consistent between experiments. Convergence of the search algorithm to the target distribution was observed when the multivariate R_{hat} statistic, which compares the variance of the parameter distributions both within and between chains, reached a value below the threshold value of 1.2 (Vrugt 2016, Rubin and Gelman 1992) (Figure B5).

The prior distribution was set to a uniform range between 195-205, 0-10, and 0-10 for the three parameters *h*, *q*, and *p* due to lack of information provided in the literature concerning the typical range in these parameters. The scaling factor jump rate (*b0*) was another parameter that was changed from the default value, where it was reduced from 1 to 0.75 to allow improved mixing and acceptance probabilities for each chain (Vrugt 2016). The remaining settings used in *DREAM*$_{ZS}$ were all default values, as pre-specified by the algorithm.

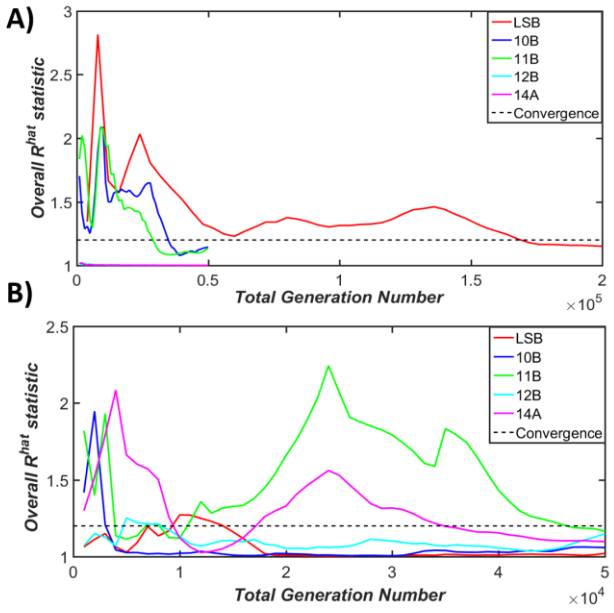

Figure B5. *Evolution of the multivariate convergence statistic (Rhat) using the DREAM_ZS algorithm for a) consortia without and b) consortia with the presence of ethanol.*

A summary of the best performing parameter sets (maximum log-likelihood) and the mean/95% credible intervals for the parameter estimations is presented in Tables B2 and B3. In addition, the marginal densities of the posterior parameter distributions are plotted in Figure B6. To reiterate the meaning of each model parameter, *h* represents the maximum amount of substrate (MC-LR) available for biodegradation (μg/L), *q* represents the non-biodegradable portion of MC-LR (μg/L), and *p* represents the maximum growth rate of the microorganisms (1/day). The credible intervals were generally widest (highest uncertainty) for the non-biodegradable fraction of MC (*q*), especially for 10B, 12B, and LSB without the presence of ethanol (Table B3). These results can be observed visually (Figure B6) as the spread of the distribution for some model-data fits for q appears uniform across the specified interval of the prior parameter distributions. This wide interval suggests that there was an array of potential local minimum solutions in the parameters search space, and possibly some correlation between parameters. The posterior distributions for the maximum specific growth rates (*p*) and the initial concentration of biodegradable substrate (*h*) were well defined for all model-data fitting procedures (with best performing parameters close to the peak of all distributions), with reasonable credible intervals observed (Table B3). The shape of the posterior parameter distributions for p appeared gaussian for most consortia, with and without ethanol, while the shape of the parameter distributions for h were negatively skewed, with many parameter values congregating close to the initial concentration of 200 μg/L. The posterior distribution of half-lives for MC biodegradation were well defined for most cases; however, some discontinuities in the distributions were observed for both the 11B with ethanol and LSB without ethanol cases (Figure B6).

Table B2 *– Best Performing Parameter Sets and Associated Fitting Metrics.*

Consortia ID	h (µg/L)	q (µg/L)	p (1/day)	$t^{1/2}$ (days)	r^2	RMSE
LR-NE-10B	200.0003	1.82	6.80	1.98	1.00	0.4299
LR-NE-11B	200.0001	1.63	6.69	2.12	1.00	0.4526
LR-NE-12B	204.9624	0.098	1.27	2.94	0.745	39.10
LR-NE-14A	204.9597	0.419	1.36	2.75	0.672	44.99
LR-NE-LSB	200.0001	1.69	6.81	2.15	1.00	0.3141
LR-WE-10B	200.0004	1.44	3.87	3.38	0.975	14.52
LR-WE-11B	200.0000	2.43	8.05	2.27	1.00	0.1451
LR-WE-12B	200.0000	0.169	4.58	3.43	0.995	6.943
LR-WE-14A	200.0000	1.97	9.87	2.45	1.00	0.2539
LR-WE-LSB	200.0016	0.710	2.64	4.43	0.975	12.63

Table B3 *– Summary of Posterior Parameter Distributions.*

Consortia	h (µg/L)		q (µg/L)		p (1/day)		$t^{1/2}$ (days)	
ID	µ	95% C.I.	µ	95% C.I.	µ	95%C.I.	µ	95%C.I.
LR-NE-10B	200.0025	[200.0003,200.0121]	1.78	[1.08,2.43]	5.97	[4.93,6.78]	1.976	[1.967,1.981]
LR-NE-11B	200.001	[200.0002,200.0052]	1.57	[0.604,2.43]	6.03	[4.88,6.65]	2.14	[2.12,2.18]
LR-NE-12B	202.4767	[199.9905,204.8917]	4.99	[0.238,9.74]	1.99	[1.05,6.28]	2.74	[0.733,4.01]
LR-NE-14A	202.3028	[197.6178,204.8869]	5.10	[0.252,9.76]	2.71	[1.14,8.13]	2.14	[0.56,3.67]
LR-NE-LSB	200.0004	[200.0000,200.0012]	1.61	[0.912,2.26]	6.47	[5.53,7.40]	2.16	[2.14,2.19]
LR-WE-10B	201.353	[200.0012,204.706]	4.71	[0.219,9.69]	1.92	[1.08,3.59]	3.28	[2.55,3.96]
LR-WE-11B	200.0000	[200.0000,200.0000]	2.34	[1.88,2.69]	7.59	[6.96,8.07]	2.30	[2.27,2.35]
LR-WE-12B	201.0049	[200.0000,204.594]	4.64	[0.199,9.67]	2.22	[1.07,4.58]	3.37	[2.68,4.00]
LR-WE-14A	200.0184	[200.0000,200.0042]	1.95	[0.135,6.43]	7.48	[4.36,9.72]	2.47	[2.38,2.56]
LR-WE-LSB	201.269	[200.0020,204.643]	4.72	[0.204,9.72]	1.41	[0.806,2.64]	4.41	[3.82,5.12]

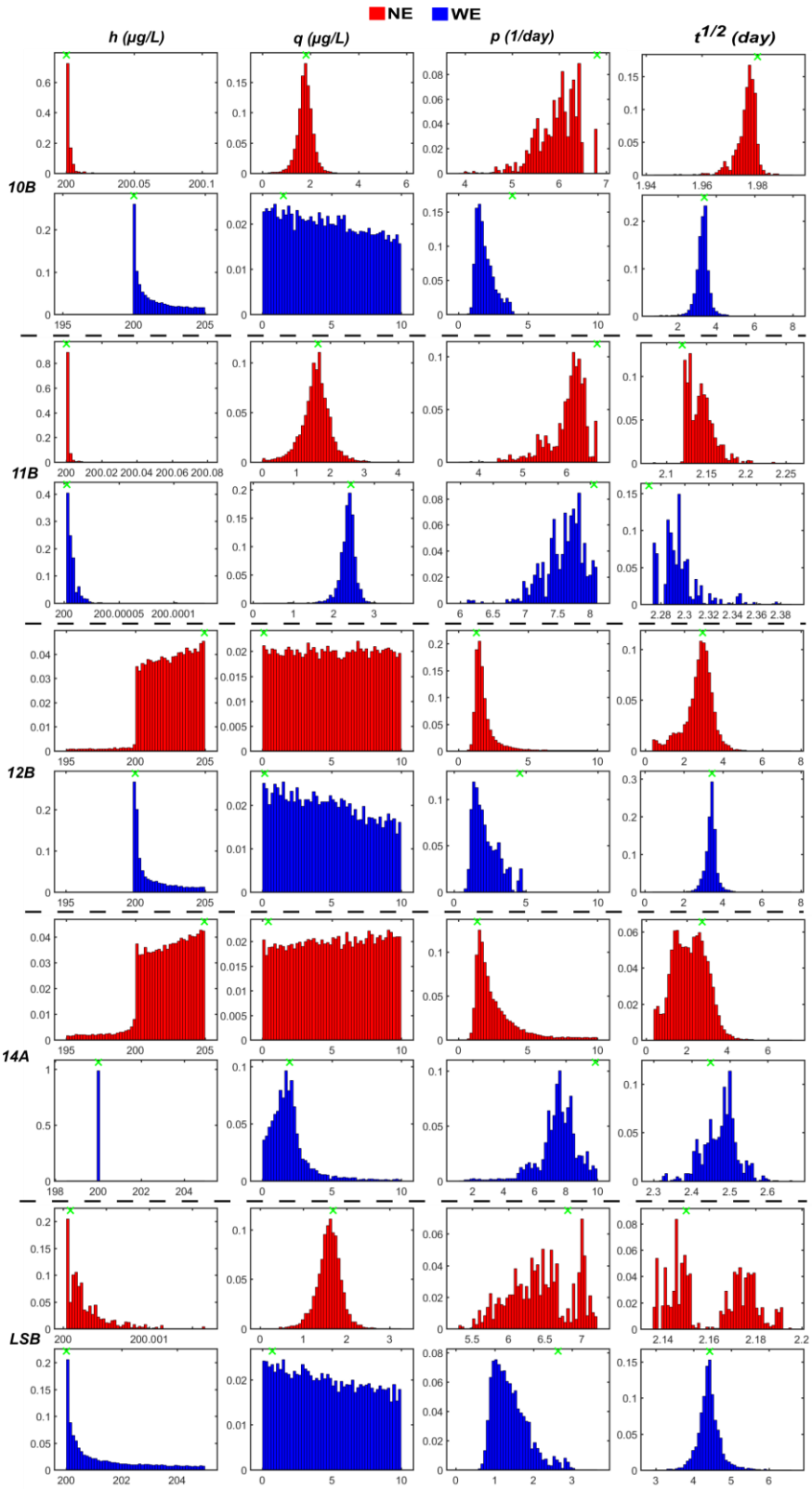

Figure B6. *Marginal densities of parameters and half-lives developed from DREAM_ZS for each consortium without (red) and with (blue) the presence of ethanol. Green crosses (on the top of each plot) indicate the best performing parameters (and half-lives) associated with each distribution.*

A potential reason for the lack of definition of the posterior distribution of some parameters (most often the non-biodegradable fraction of MC, q) may be due to either structural issues of the model (structural identifiability) or the quality of the data collected (practical identifiability) (McLean and McAuley 2012). Since the model structure used was relatively simplistic and previous studies have determined that the Monod kinetic model is globally identifiable, we can assume that the main problem is not due to structural identifiability, but rather parameter estimability (Holmberg 1982). In the case of estimability, we are concerned with whether we can estimate unique values of each parameter given the quality of the experimental data collected (McLean and McAuley 2012). For many empirical models, such as the well-known Monod kinetic model, the initial conditions of the experiment (i.e., the initial biomass or substrate concentrations) have a drastic effect on whether unique parameters can be estimated (Holmberg 1982, Nihtilä, M., and Virkkunen 1977, Robinson and Tiedje 1983, Liu and Zachara 2001). In addition, a parameter may not be estimable if a) the model predictions are not sensitive to the parameter value or b) the effect of the parameter on model predictions is correlated with the effects of other parameters, where the latter is generally the case for unstructured bacterial growth models (McLean and McAuley 2012, Robinson and Tiedje 1983).

Thus, the degree of linear correlation between parameter values was evaluated using Pearson's correlation coefficients to assess whether parameter correlation was the main issue affecting estimability. This analysis indicated that there was a strong, significant negative correlation between the parameters h and p for all consortia, with and without ethanol (Table B4). For most cases, there was also a slight positive correlation between the parameters q and p, and a slight negative correlation between parameters h and q for all

consortia, with and without ethanol (Table B4). These results indicate that, due to some inherent correlations between parameter values, the parameter estimability was low for some experimental data. The presence of these correlations provides evidence as to why in some cases the distribution of the non-biodegradable fraction of microcystin, *q*, was ill-defined.

Table B4 *– Summary of Pearson's correlation and p-values for different model parameters.*

Consortia I.D.	h vs. q		h vs. p		q vs. p	
	rho	p-value	rho	p-value	rho	p-value
10B-NE	-0.1510	0	-0.6810	0	0.1726	0
10B-WE	0.0174	1.54E-11	-0.6776	0	9.85E-04	0.7026
11B-NE	-0.1649	0	-0.6198	0	0.2690	0
11B-WE	-0.3956	0	-0.7708	0	0.3797	0
12B-NE	-0.0146	1.55E-08	-0.4813	0	0.0457	3.70E-70
12B-WE	0.0646	3.15E-138	-0.6766	0	-0.1002	0
14A-NE	-0.0389	3.06E-51	-0.5214	0	0.0533	1.17E-94
14A-WE	0.1515	0	-0.3655	0	-0.2825	0
LSB-NE	-0.3259	0	-0.8949	0	0.3398	0
LSB-WE	0.01	1.02E-04	-0.7529	0	-0.0118	4.78E-06

6. Monte Carlo Simulations for Comparison of Alpha Diversity Metrics

Monte Carlo (MC) simulations were carried out to arrive at statistical distributions in true Alpha diversity metrics. The first step of this process was to develop an empirical relationship between mean relative abundance and the standard deviation expected among experimental replicates for corresponding taxa within a given community. By "experimental" replicates we refer to the combination of biological and technical replicate classes. Biological replicates can be defined as sampling multiple times at a given location and then performing identical 16S rRNA processing on the replicated samples (Knight et al. 2012, Thomas et al. 2012). The 16S rRNA processing protocol includes everything from sample preparation and DNA extraction, to pyrosequencing and downstream analysis (i.e.,

QIIME). Biological replication includes uncertainty related to the heterogeneity of the bacterial populations at the location of sampling as well as uncertainty related to the measurement/processing techniques. Technical replicates, however, are defined as processing a single sample from a location or treatment multiple times to solely assess the uncertainty in the measurement/processing technique (Knight et al. 2012, Thomas et al. 2012). We focused our search to obtain relevant data from studies analyzing bacterial community structure, as opposed to other microbes (from environmental samples only). Both mean relative abundances and standard deviations of relative abundances were compiled from these studies (from at least 2 technical replicates) to develop the empirical model described above (Table B5).

A total of 10 metagenomic studies (Chaudhary et al. 2018, Landa et al. 2014, Lopes et al. 2014, Li et al. 2014a, Pereira et al. 2017, Pilloni et al. 2012, Sun et al. 2014, Romanowicz et al. 2016, Huang et al. 2015b, Zhou and Wu 2018) were ultimately used to develop the empirical relationship between taxon mean relative abundance and expected standard deviation among replicates (Table B5). The pooled data from all these studies provided a sufficient number of samples to develop the empirical model (N = 1,188). Ideally, studies that performed biological replicates were more desirable, as they included uncertainty corresponding to both the community composition at the sampling location and the potential measurement error. However, very few studies that conducted biological replicates were found in the literature that presented relative abundance data on the genus level of analysis. In this way, we supplemented studies that performed biological replicates (5) with those that only performed technical replicates to aid in the development of this empirical model (5).

As observed in Table B5, the studies selected sampled a diverse array of environmental media for conducting the bacterial community analyses, ranging from drinking water, wastewater, seawater, soil, and aquifer sediments. The studies selected were split evenly between sequencing platforms, where half used the 454-pyrosequencing technology (as in this study) and the other half relied on Illumina MiSeq technologies. A majority of studies targeted the V4 region of the 16S rRNA, which was close to the region targeted in this study. In addition, most of the studies incorporated the QIIME/Greengenes analysis pipeline and reference database, which was nearly identical to that selected in this study (Table B5).

Table B5 *– Summary of studies selected to develop the empirical model.*

Reference	Source Location	Environ. Media	Seq. Platform	16S Region	Analysis Pipeline / Ref Database	Tax. Level	# Replicates	Type of Replicate
Chaudhary et al. 2018	North Shore Channel, Chicago, USA	Storm/ Wastewater	Illumina MiSeq	V1-V3	QIIME/ Greengenes	Genus	2	Biological
Landa et al. 2014	Laboratory cultures, isolated from Mediterranean Sea	Seawater	454-FLX Titanium	V2-V3	QIIME/ Greengenes	Genus	3	Technical
Lopes et al. 2014	Farm in Portugal	Soil	454-FLX Titanium	V3-V4	QIIME/ Greengenes	Genus	3	Biological
Li et al. 2014a	Energy Farm, University of Illinois, USA	Soil	454-FLX Titanium	V4-V5	RDP Pipeline	Genus	4	Biological
Pereira et al. 2017	Helmholtz Centre for Infection Research, Germany	Drinking Water	Illumina MiSeq	V3-V4	SILVA Pipeline	Genus	3	Technical
Pilloni et al. 2012	Tar oil contaminated aquifer, Germany	Aquifer Sediments	454-FLX Titanium	Unknown	GS Run Processor/ Greengenes	Genus	3	Biological

Sun et al. 2014	Orchard near Beijing, China	Soil	Illumina MiSeq	V4	QIIME/ Greengenes	Genus	3	Technical
Romanowicz et al. 2016	Forest floor samples, Upper Michigan, USA	Soil	PacBio RS II	Unknown	MOTHUR Pipeline	Order	4	Biological
Huang et al. 2015b	Laboratory grown cultures	Soil	Illumina MiSeq	V4	QIIME/ Greengenes	Genus	3	Technical
Zhou and Wu 2018	Experimental Station, Harbin, China	Soil	Illumina MiSeq	V3-V4	QIIME/ Greengenes	Genus	3	Technical

A non-linear, yet monotonic, relationship between taxon mean relative abundance and standard deviation of replicate measurements was observed from the compiled data. This monotonic relationship makes sense intuitively, as the abundance of a given taxon increases, the associated variability across replicate samples should also increase. The dependency structure between the mean relative abundance and standard deviation was deemed significant as the magnitude of Spearman's rho was high (0.84). To be as objective as possible, a non-parametric regression model (LOESS) was used to describe the compiled data. LOESS stands for locally weighted polynomial regression and is a simple, but powerful tool to model unknown, empirical relationships between variables (Jacoby 2000). LOESS provides a smooth interpretation of the relationship between two variables through use of two main model parameters, the polynomial order (λ) and the spanning parameter (α). In general, the polynomial order dictates what shapes the curve can take, while the spanning parameter balances "overfitting" vs. "smoothing" of the data (Jacoby 2000). Larger values of α (close to 1) will provide a smoother curve at the cost of a poorer fit, while smaller values of α (close to 0) provide an optimal fit, but a very haphazard (and non-generalizable) curve. In this study, we selected a polynomial of order two ($\lambda = 2$) and an

optimal spanning parameter of 0.85 based on the procedure outlined in (Jacoby 2000). A bootstrap re-sampling approach (using N = 10,000 samples) was used to estimate both the 95% confidence and prediction intervals for the LOESS regression model. The algorithm presented by (Efron and Tibshirani 1994) was implemented in this study to develop the 95% confidence and prediction intervals of the empirical model.

Figure B7 portrays the results of the LOESS nonparametric regression and bootstrapping analysis. Given that the main underlying trend in the observed data is captured by the LOESS prediction, the regression model was concluded to satisfactorily predict the nonlinear relationship between mean relative abundance and standard deviation among experimental replicates. As observed in Figure B7, several data points fall outside the 95% prediction and confidence intervals and may be considered outliers in this analysis. In addition, most of the data points are clustered towards the origin of Figure B7 (where corresponding certainty in the regression is higher). This result was expected given that, on the genus level of analysis, most of the identified taxa among studies had low relative abundances (<10%). The uncertainty in the model predictions rises substantially when the mean relative abundance increases to 30% and beyond (Figure B7). This result was a direct consequence of the small number of data points compiled from the literature that were above a mean relative abundance of 30%. Since this was a locally weighted regression analysis, higher confidence would be achieved if the density of points above this mean relative abundance threshold of 30% was greater.

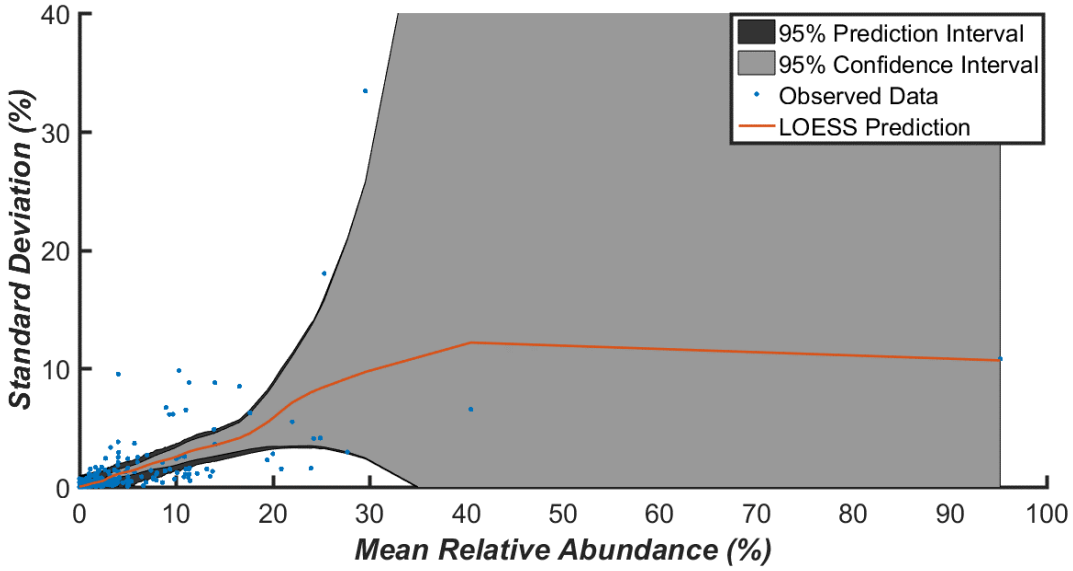

Figure B7. *Empirical relationship developed between mean relative abundance and expected standard deviation among experimental replicates using the LOESS regression approach. Dark and light grey shading indicate the 95% bootstrapped prediction and confidence intervals for the LOESS predictions. The blue dots and red line correspond to the observed data points and best fitting prediction of* the LOESS regression.

With the main empirical relationship between taxon mean relative abundance and expected standard deviation established, the main approach behind the MC simulations to determine distributions in true Alpha diversity metrics will now be described. The objective of the MC simulations was to randomly and repeatedly generate a new bacterial community composition, given the known extrapolated uncertainty in the experimental measurements, and calculate Alpha diversity metrics for each of these re-sampled communities. Figure B8 describes the main workflow of the MC simulations from start to finish. First, the experimental data containing the identified genus (rows) vs. absolute abundances (columns) for a given community is loaded and transformed into relative abundances (on a scale from 0-1).

After entering the main Monte Carlo loop (which is performed for N_{max} = 20,000 times), the following two steps (2, 3) involve sampling the relative taxonomic abundances

for all genera within the community (Figure B8). We first assume that the measurement error (which includes uncertainty about the heterogeneity of each community within each location and the measurement methodology) is normally distributed. In addition, we center each normal distribution describing the uncertainty in taxonomic abundance from each location around the observed relative abundances obtained from the experimental results. Thus, given the mean relative abundance from step 1, step 2 involves randomly sampling the 95% prediction intervals of the LOESS regression to obtain the expected standard deviation across replicates. The 95% prediction intervals were approximated by a kernel density estimation (KDE) since the distribution of the predictions within each interval appeared to be non-parametric and multi-modal (data not shown). Using the obtained standard deviation, step 3 involves randomly sampling a relative abundance value from this normal distribution. Steps 2 and 3 are repeated until relative abundances have been sampled for all existing genera within the original community.

As the sampled standard deviations can vary, there is a possibility of selecting either a negative standard deviation or a negative relative abundance. To circumnavigate this issue, we only sample positive standard deviations from the empirical model. However, it is important to note the significance of a negative relative abundance draw. Instead of only sampling positive values (the right side of the normal distribution) for relative abundance, we assume that a negative relative abundance is indicative of several replicates (out of how many were conducted) that may have demonstrated relative abundance values of 0. Thus, when a negative relative abundance value is obtained, we assume that this draw was effectively 0 (and not a member of the simulated community). Importantly, this step allows the MC simulations the probability of not drawing relative abundances for genera that were

in fact experimentally observed, providing some measure of variability for richness-based measures of Alpha diversity for each community (true Alpha diversity measures of order 0).

The final two steps within the MC loop involve the re-sampling (4) and calculation of true Alpha diversity metrics (5) (Figure B8). With the relative abundances of the simulated community now sampled, a weighted re-sampling of the original community is performed to obtain absolute abundances for each genus (using a weighted random sample with replacement). Step (4) is essentially the main bootstrapping component of this procedure. Finally, the true Alpha diversity metrics are calculated using the absolute abundances sampled during the previous weighted bootstrapping step. This series of sampling and calculations is effectively repeated (N_{max} = 20,000 times) and a final distribution in true diversity metrics is obtained (Figures B9 and B10, Tables B6 and B7).

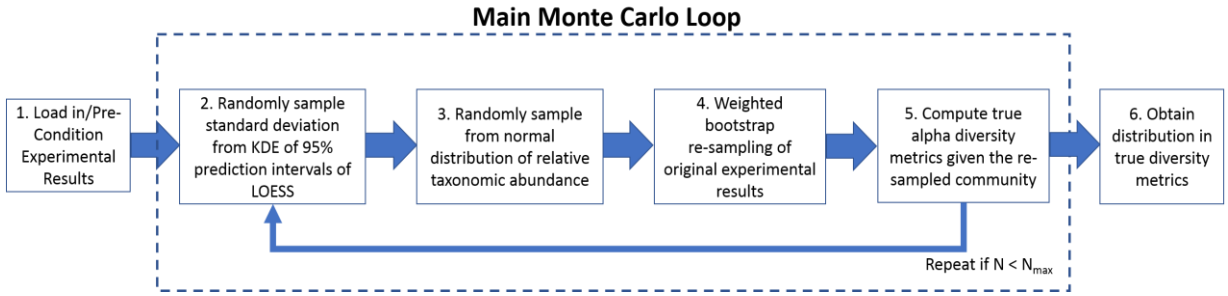

Figure B8. *The MC algorithm developed to simulate distributions in true Alpha diversity metrics*

Typically, in many MC applications, N = 10,000 MC samples are enough to arrive at a parametric and stable distribution (Gottschalk et al. 2010a). In this study, we found that 20,000 samples were necessary to arrive at a series of stable distributions for each true diversity order, all of which qualitatively appeared distinctly normal (Figures B9 and B10, Tables B6 and B7). The lack of extreme outliers (low kurtosis values) and characteristic bell shape of the plotted histograms indicated satisfactory fits to a normal distribution for

most diversity orders describing each MC-degrading community. It is important to note that for some higher order diversity indices (q = 1-3) describing communities with the addition of ethanol, the resulting distributions were slightly right skewed, more notably for 10B and 12B consortia. This skew was confirmed with the relatively higher coefficient of variations observed for 10B (with ethanol) for the higher order diversity metrics (1-3) (Table B7). Otherwise, variability in simulated metrics generally increased moving from the far-right side of both Tables B6 and B7 (q =3) to the far-left side (q = -1), as the magnitude of the indices increased. Both the 10B and 12B communities (in the presence of ethanol), contained genera that had higher relative abundances (>30%) than the other MC-degrading communities analyzed. As the empirical model demonstrated higher uncertainty in predicting the standard deviations in replicated measurements for high relative abundances (>30%), deviation from a perfectly normal distribution was as expected. However, other, more complex parametric distributions were not applied in this study to account for the skew in these aforementioned probability distributions.

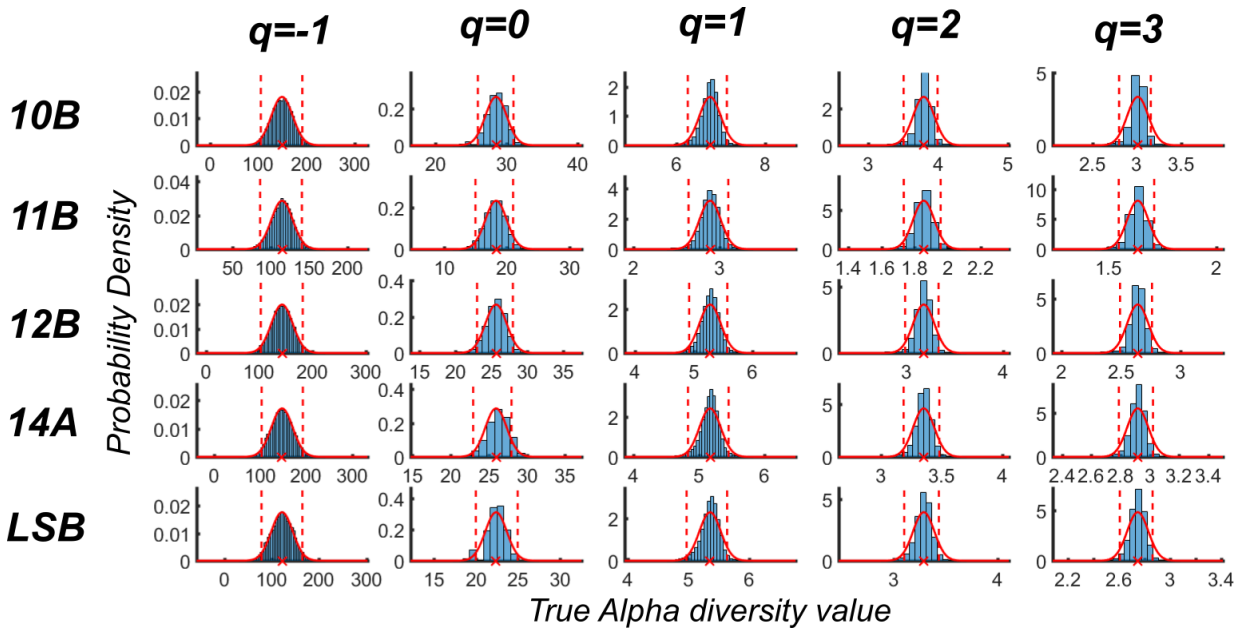

Figure B9. *Resulting probability distributions in simulated true Alpha diversity metrics of orders -1,0,1,2,3 (column-wise) grouped by MC degrading community (row-wise) without the addition of ethanol. The solid red line indicates the normal probability distribution function fitted to the data, whereas the dashed red line indicates the 95% confidence interval for the distribution of each diversity order. The 'x' indicates the mean of each distribution.*

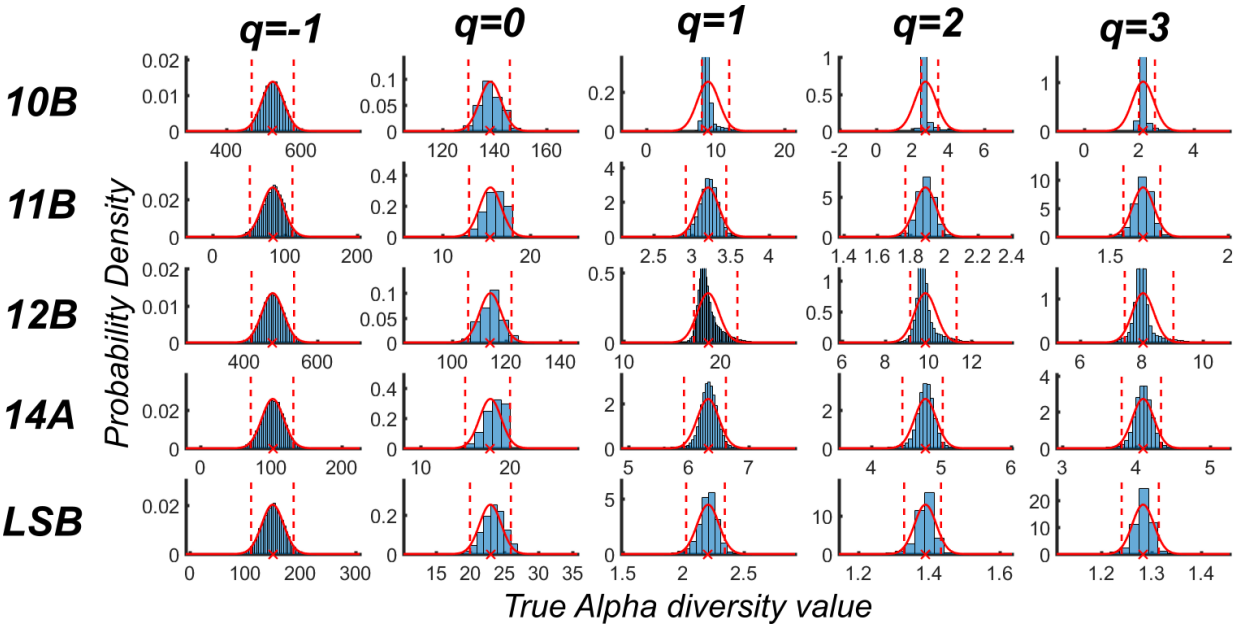

Figure B10. *Resulting probability distributions in simulated true Alpha diversity metrics of orders -1,0,1,2,3 (column-wise) grouped by MC degrading community (row-wise) with the addition of ethanol. The solid red line indicates the normal probability distribution function fitted to the data, whereas the dashed red line indicates the 95% confidence interval for the distribution of each diversity order. The 'x' indicates the mean of each distribution.*

Table B6 *– Summary of normal distributions fitted to the MC simulation output in calculated Alpha diversity orders for consortia without ethanol addition.*

Consortia ID	Metric	True Alpha diversity order				
		q = -1	**q = 0**	**q = 1**	**q = 2**	**q = 3**
10B	μ	149	28.6	6.76	3.79	3.01
	σ	22.1	1.50	0.241	0.152	0.119
	COV	14.8	5.2	3.6	4.0	4.0
11B	μ	115	18.3	2.89	1.85	1.64
	σ	13.9	1.70	0.125	0.0641	0.0493
	COV	12.1	9.3	4.3	3.5	3.0
12B	μ	143	25.7	5.28	3.18	2.64
	σ	20.1	1.49	0.182	0.110	0.0895
	COV	14.0	5.8	3.5	3.4	3.4
14A	μ	147	26.0	5.17	3.35	2.92
	σ	23.2	1.39	0.164	0.0872	0.0727
	COV	15.7	5.4	3.2	2.6	2.5
LSB	μ	122	22.4	5.36	3.29	2.75
	σ	22.6	1.28	0.175	0.102	0.0832
	COV	18.5	5.7	3.3	3.1	3.0

Table B7 *– Summary of normal distributions fitted to the MC simulation output in calculated Alpha diversity orders for consortia with ethanol addition.*

Consortia ID	Metric	True Alpha diversity order				
		q = -1	**q = 0**	**q = 1**	**q = 2**	**q = 3**
10B	μ	524	138	8.95	2.73	2.16
	σ	29.1	4.19	1.57	0.597	0.394
	COV	5.6	3.0	17.5	21.9	18.3
11B	μ	83.6	15.4	3.21	1.89	1.64
	σ	15.0	1.24	0.140	0.0644	0.0459
	COV	18.0	8.1	4.4	3.4	2.8
12B	μ	478	114	18.78	9.88	8.05
	σ	29.8	4.01	1.13	0.502	0.355
	COV	6.2	3.5	6.0	5.1	4.4
14A	μ	102	17.8	6.32	4.77	4.09
	σ	15.4	1.21	0.180	0.155	0.147
	COV	15.1	6.8	2.8	3.2	3.6
LSB	μ	150	23.0	2.21	1.39	1.28
	σ	19.7	1.59	0.0896	0.0307	0.0216
	COV	13.1	6.9	4.1	2.2	1.7

When comparing simulated diversity profiles of each MC-degrading community, with and without the addition of ethanol, there were distinct differences in trends across communities (Figure B11). For example, as diversity order increased, the dominance of certain genera (with higher relative abundance) increased for both the 10B and LSB

communities (Figure B11). An opposing trend was observed for the 12B and 14A species, where the addition of ethanol may have an evening effect on the more abundant genera, as the slope of the diversity profile (with ethanol) is not as steep as compared to without (Figure B11). In addition, the differences in the diversity profiles for 11B consortium appear to be insignificant to make any definitive conclusions. These results confirm that ethanol addition had a unique effect on both the abundance and presence of certain genera within each community, either increasing the evenness, increasing the dominance, or exerting a negligible effect as evidenced in Figure B11.

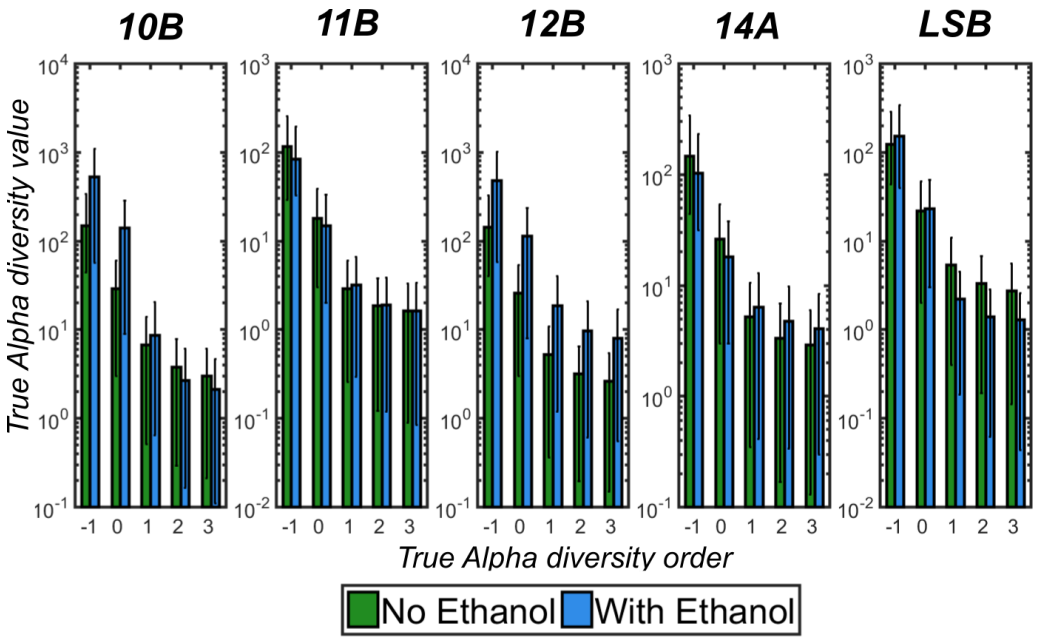

Figure B11. *True Alpha diversity profiles for MC-degrading communities cultured with and without ethanol addition. The bar charts signify the median and 95% confidence intervals for the distributions of the true Alpha diversity values as a function of diversity order. The y-axis is plotted on a Log_{10}-scale to highlight the differences in diversity profiles between treatments.*

We also present a summary of the "raw" Alpha diversity values as returned by the QIIME pipeline (Table B8). The "raw" indices include Shannon index, Simpson's Dominance, and Equitability values. These values were included as reference to

existing studies that have reported similar "raw" indices for bacterial communities isolated from lakes of different trophic statuses.

Table B8 *- Summary of "raw" Alpha diversity metrics for MC-LR degrading bacterial consortia without (NE) and with (WE) ethanol addition. Individual values of each metric are calculated for each of the five consortia within a given treatment.*

Consortia ID	Culture Condition	Shannon Index	Simpson Dominance	Equitability
10B	NE	3.20	0.236	0.540
	WE	4.03	0.356	0.462
11B	NE	2.89	0.207	0.547
	WE	3.22	0.177	0.633
12B	NE	3.07	0.231	0.520
	WE	4.88	0.079	0.599
14A	NE	3.30	0.196	0.550
	WE	2.70	0.207	0.606
LSB	NE	3.82	0.104	0.666
	WE	3.18	0.208	0.545

7. Quality Control of QIIME Analysis

A total of 66,716 16S rRNA gene reads were qualified for further QIIME metagenomics analysis from ten individual consortia samples after initial de-multiplexing, denoising, chimera removal and quality checking. The average number of 16S rRNA gene reads per sample was 6,672, ranging from 2,212 to 13,659 across all samples (Table B9). The average length of individual reads was approximately 488 base pairs, in which a majority of reads ranged between 300 to 500 base pairs in length (data not shown). A high percent recovery (OTU assignment/filtering retrieval) was observed for the Usearch quality filtering, clustering, and OTU picking. An average of 96% of the total reads were assigned to 690 distinct operational taxonomic units (Table B9).

Table B9*- Summary of the consortia samples analyzed and the general results of the QIIME/Usearch analysis pipelines.*

Consortia ID	Number of Reads Qualified	Number of Reads Retrieved	% Reads Retrieved
LR-NE-10B	6,790	6,527	96
LR-NE-11B	2,212	2,180	99
LR-NE-12B	5,758	5,390	94
LR-NE-14A	8,011	7,834	98
LR-NE-LSB	6,731	6,582	98
LR-WE-10B	13,659	12,384	91
LR-WE-11B	2,496	2,431	97
LR-WE-12B	12,380	11,364	92
LR-WE-14A	3,462	3,315	96
LR-WE-LSB	5,217	4,949	95
Total	66,716	62,956	96[1]

[1]This represents the average of the percentage of reads that were retrieved.

8. Rarefaction Analysis

The Shannon indices as a function of the number of sequences retrieved by the QIIME module were investigated in the rarefaction analysis. It is evident that the sequencing depth was adequate for all consortia, as the Shannon indices were observed to plateau (Figure B12).

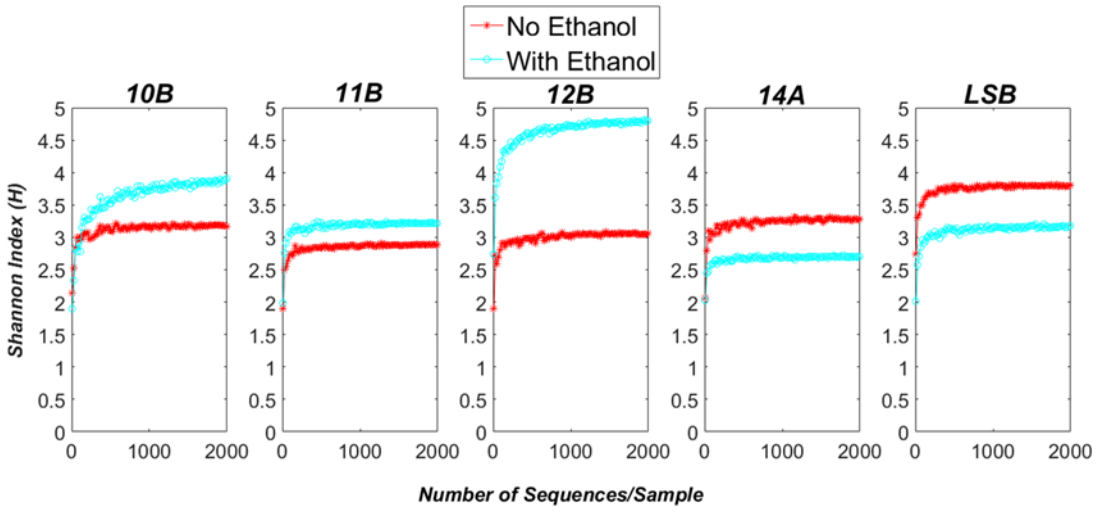

Figure B12. *Rarefaction plots showing Shannon Diversity indices for microcystin-LR degrading consortia.*

9. Taxonomic Summary of MC-Degrading Communities on the Genera Level of Analysis

Figures B13-B15 further dissect the taxonomic composition of each MC-LR degrading community in the absence of ethanol on the genera level of analysis and are grouped by each representative order (i.e., *Rhizobiales*, *Burkholderiales*, *Xanthomonadales, or* "Other"). These orders were selected for grouping each taxon since they represent a large proportion of taxa within each community. Figure B13, B14, and B15 depict the proportions of all detected genera within the *Rhizobiales Burkholderiales,* and *Xanthomonadales* orders. It is important to note that all of these genera were obtained by filtering out extremely underrepresented taxa from each consortium (relative abundance < 0.001 %).

As observed in each Figure below, there appears to be similar genera present (albeit in different proportions) within the sediment samples (10B-14A) as compared to the lake water sample (LSB). It is important to note that in Figure B16 the proportion of taxa on the genera level of analysis are portrayed from all remaining orders (i.e., the residuals not contained within *Rhizobiales Burkholderiales,* or *Xanthomonadales*). In addition, to better illustrate differences in composition, Figure B16 includes the taxonomic composition without the *Pseudomonas* (for 10B, 11B, 14A, LSB only) or *Azospirillum* (for 12B only) genera, as these taxa dominate the composition (>90%) of each community.

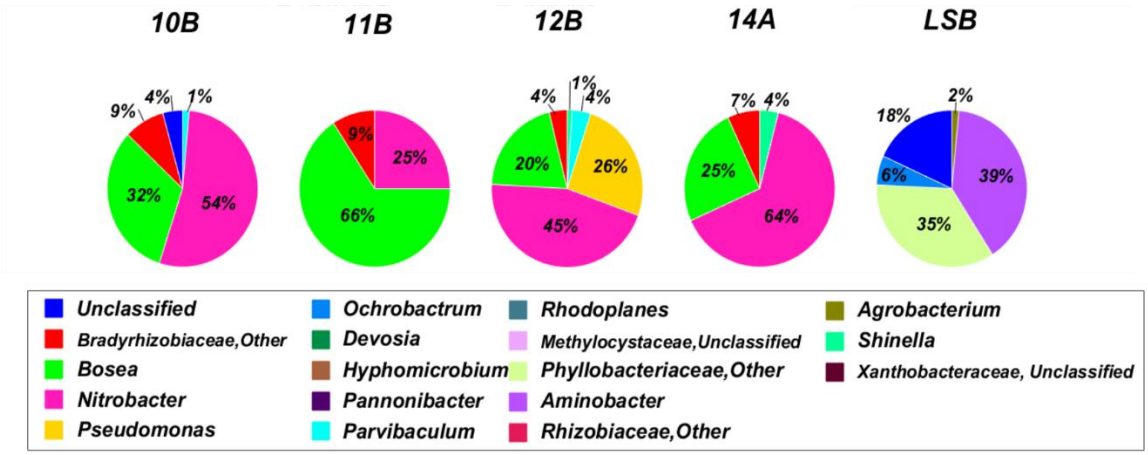

Figure B13. *Pie charts depicting the taxonomic composition of MC-LR degrading communities (in the absence of ethanol) on the genera level of analysis within the Rhizobiales order.*

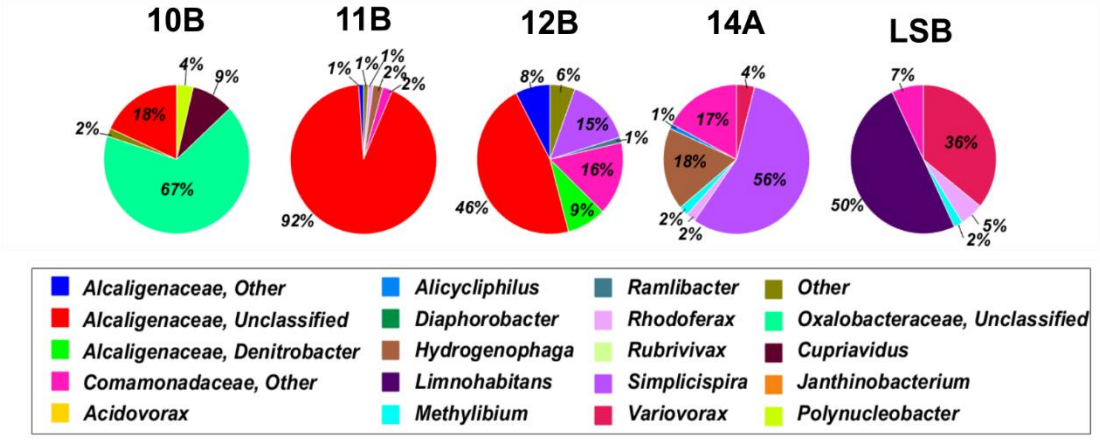

Figure B14. *Pie charts depicting the taxonomic composition of MC-LR degrading communities (in the absence of ethanol) on the genera level of analysis within the Burkholderiales order.*

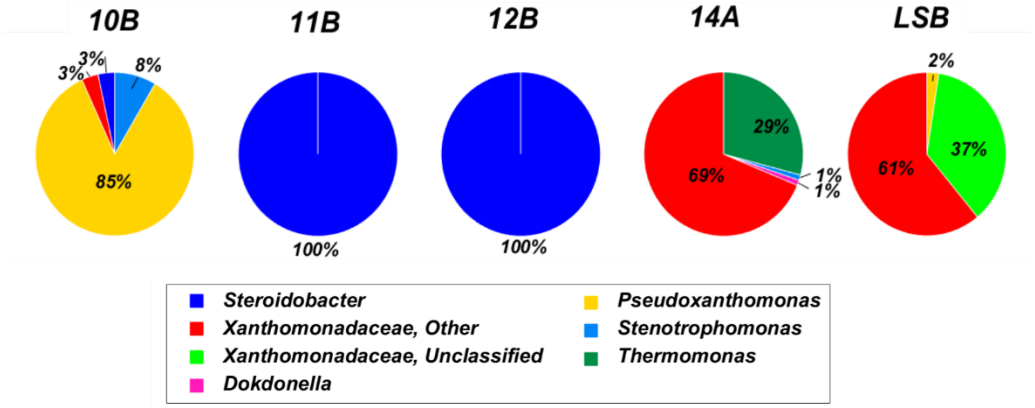

Figure B15. *Pie charts depicting the taxonomic composition of MC-LR degrading communities (in the absence of ethanol) on the genera level of analysis within the Xanthomonadales order.*

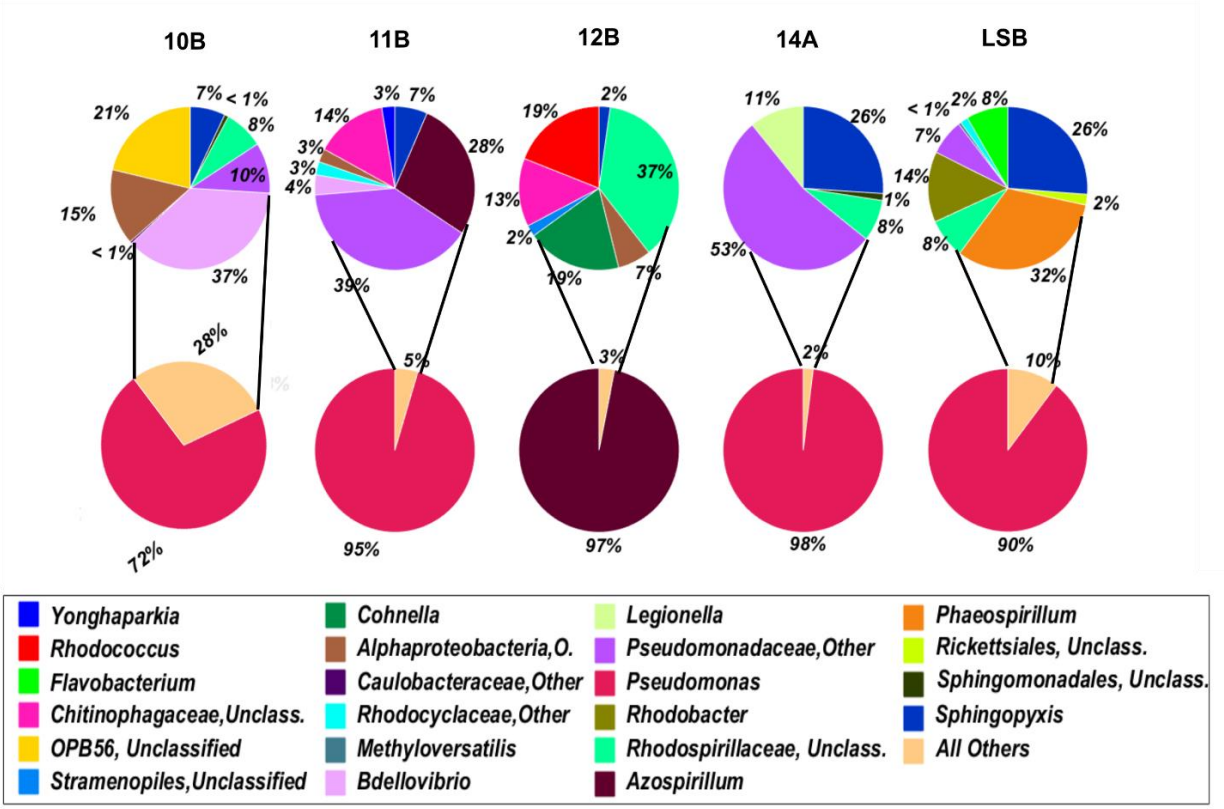

Figure B16. *Pie charts depicting the taxonomic composition of MC-LR degrading communities (in the absence of ethanol) on the genera level of analysis within all remaining orders (other than Rhizobiales, Burkholderiales, or Xanthomonadales). It is important to note that the Pseudomonas genera (pictured here on the bottom row of pie charts) makes up 71.6, 95.3, 98, and 89% of the genera for the "Other" orders grouping for 10B,11B,14A, and LSB, respectively. In addition, the Azospirillum genera comprises 96.8% of the "Other" orders grouping for the 12B consortia. Thus, the pie charts on the top row above depict the proportions of the other genera without Pseudomonas (for 10B,11B,14A, and LSB only) or Azosprillum (for 12B only) included to highlight differences in the less representative taxa.*

10. Summary of Affiliated MC-Degrading Genera With and Without Ethanol Addition

Table B10 summarizes the bacterial genera present in different consortia that have been associated with species of MC-degrading bacteria. The bacterial genera identified within each consortium included the following: *Sphingopyxis*, *Sphingomonas*, *Acinetobacter*, *Aeromonas*, *Sphingomonas*, *Novosphingobium*, *Pseudomonas*, *Stenotrophomonas*, *Ochrobactrum*, *Rhodococcus*, and *Steroidobacter*. Although 10 distinct genera were initially identified, not all genera were present in each consortium, as

indicated in the "Consortia Detected" column. Several genera are affiliated with species that degrade MC using the well-known mlr gene pathway; however, several degrading pathways are either unknown or have not been detected (Table B10).

Table B10 *– Bacterial genera identified within each consortium that have been previously affiliated with species of MC-degrading bacteria.*

Bacterial Genera	Consortia Detected	*mlr* pathway?	Reference(s)
Ochrobactrum	14A-NE LSB-NE 10B-WE 14A-WE	Unknown	(Jing et al. 2014, Mu et al. 2009)
Pseudomonas	10B-NE 11B-NE 14A-NE LSB-NE 10B-WE 11B-WE 14A-WE LSB-WE	Unknown	(Lemes et al. 2015, Li and Pan 2014)
Steroidobacter	10B-NE 11B-NE 12B-NE LSB-NE 10B-WE	Unknown	(Gong et al. 2016)
Stenotrophomonas	10B-NE 14A-NE 10B-WE 12B-WE 14A-WE	+	(Chen et al. 2010)
Sphingomonas	10B-NE 14A-NE 12B-NE	+	(Jones et al. 1994b, Harada et al. 2004, Imanishi et al. 2005, Ishi et al. 2004, Maruyama et al. 2006, Park et al. 2001, Saitou et al. 2003, Somdee 2010)
Sphingopyxis	10B-NE 11B-NE 12B-NE 14A-NE LSB-NE 10B-WE 12B-WE	+	(Wang et al. 2010, Xiao et al. 2011, Xu et al. 2015, Okano et al. 2009, Maghsoudi et al. 2016)
Rhodococcus	12B-NE 12B-WE	-	(Lawton et al. 2011, Manage et al. 2009)
Novosphingobium	12B-WE	+	(Jiang et al. 2011)
Acinetobacter	10B-WE 12B-WE	Unknown	(Li and Pan 2014)
Aeromonas	10B-WE 12B-WE	-	(Mankiewicz-Boczek et al. 2015)

Aside from the *Pseudomonas* genera, the relative abundance of the potential known MC degrading bacteria within each community was found to be relatively small and sometimes quite variable across each consortium (below 0.5-1%) With the addition of ethanol, the proportion of sequences from genera affiliated with MC biodegradation was observed to change significantly (Figure B17). In general, the relative abundance of bacterial species associated with the *Sphingopyxis* genera was observed to significantly decline across all consortia, whereas the relative abundance of bacterial species associated with the *Stenotrophomonas* was observed to significantly increase in the presence of ethanol (Figure B17). In addition, in the presence of ethanol, the relative abundance was observed to generally increase for the following bacterial genera: *Aeromonas*, *Acinetobacter*, *Novosphingobium*, and *Ochrobactrum* across all consortia. Some of these increases in relative abundance were not statistically significant (Figure B17). Trends in relative abundance were less apparent for the remaining genera affiliated with MC degradation across all consortia. For example, the relative abundance of *Steroidobacter* increased for 10B consortia in the presence of ethanol but decreased for 11B and 12B consortia. Similar mixed results were detected for the *Pseudomonas* genera with and without the addition of ethanol (Figure B17).

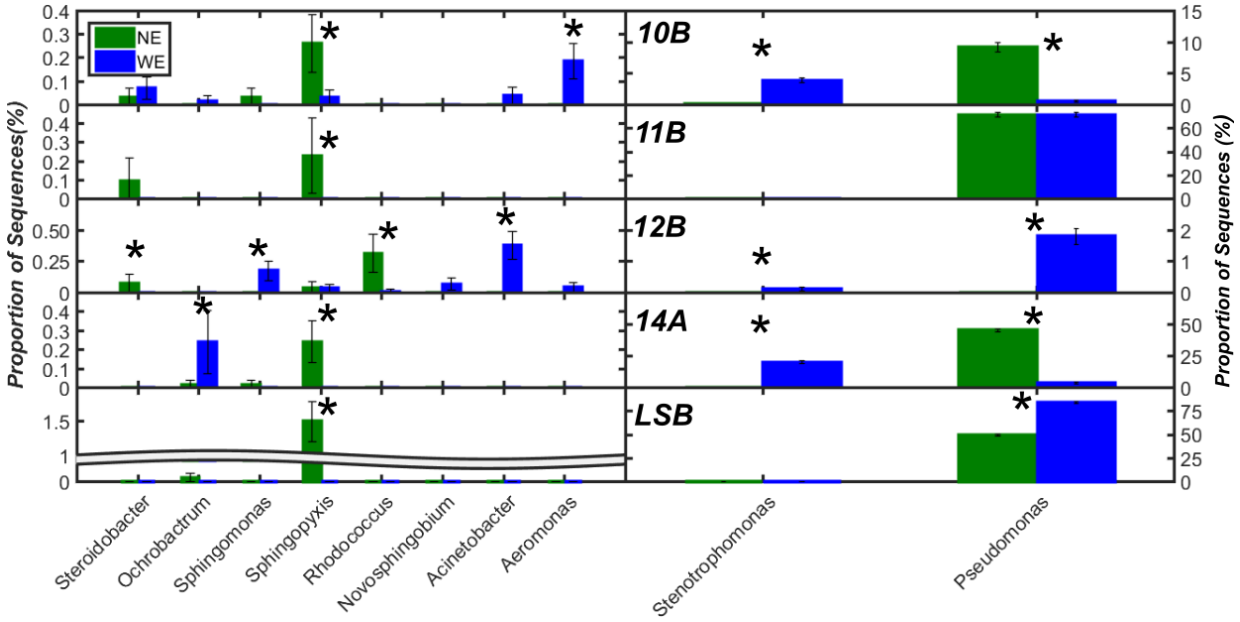

Figure B17. *Differences in relative abundance of the phylogenetic genera previously affiliated with MC degradation that were identified within consortia treated with (WE) and without ethanol (NE). Statistically significant differences in relative abundance are marked with an asterisk (p-value < 0.05, Bonferroni corrected).*

11. Summary of Reported MC Biodegradation Half Lives

A detailed review of studies examining MC biodegradation kinetics was conducted to compare the half-lives for isolated MC degrading bacterial populations against those reported for enriched MC degrading consortia. The reported half-lives were estimated by each study using three unique approaches a) simply interpolating the time until 50% of the initial substrate was degraded (Lawton et al. 2011); b) fitting a zero-order model to the kinetic data (Li et al. 2015a) (Equations 13-14); or c) fitting a first-order model to the kinetic data (Jones et al. 1994b) (Equations 15-16). If the study did not report a half-life value, we fitted a simple 0-order model to predict the MC biodegradation half-lives using the data provided in the study. A total of 50 (Lawton et al. 2011, Jones et al. 1994b, Alamri 2010, Alamri 2012, Chen et al. 2010, Eleuterio and Batista 2010, Harada et al. 2004, Ho et al. 2007c, Ho et al. 2012b, Hu et al. 2009, Hu et al. 2012, Imanishi et al. 2005, Ishii et al.

2004, Jiang et al. 2011, Jing et al. 2014, Kansole and Lin 2016, Lemes et al. 2008, Lemes et al. 2015, Lezcano et al. 2016, Li et al. 2016, Li and Pan 2014, Maghsoudi et al. 2016, Manage et al. 2009, Mankiewicz-Boczek et al. 2015, Maruyama et al. 2006, Mu et al. 2009, Nybom et al. 2007, 2008a, 2008b, 2012, Park et al. 2001, Phujomjai and Somdee 2013, Phujomjai et al. 2016, Ramani et al. 2012, Rapala et al. 2005, Saitou et al. 2003, Somdee 2010, Takenaka and Watanabe 1997, Valeria et al. 2006, Wang et al. 2010, Xiao et al. 2011, Xu et al. 2015, Yang et al. 2014a, 2014b, You et al. 2014, Zhang et al. 2015b, Zhang et al. 2011b, Zhou et al. 2006, Zhou et al. 2008, Zhu et al. 2016) and 23 (Jones et al. 1994b, Bourne et al. 2006, Chen et al. 2008, Christoffersen et al. 2002, Cousins et al. 1996, Edwards et al. 2008, Edwards and Lawton 2009, Grützmacher et al. 2010, Ho et al. 2010, Ho et al. 2006, Hoefel et al. 2009, Hyenstrand et al. 2003, Jones et al. 1994a, Lam et al. 1995a, Lam et al. 1995b, Li et al. 2011a, 2011b, 2011c, 2015, Rapala et al. 1994, Tsao et al. 2017, Wang et al. 2016, Welker et al. 2001) studies were compiled for MC degrading isolates and consortia, respectively. Only studies that focused on aerobic (not anaerobic) MC biodegradation through *bacterial* activity were incorporated in this analysis. All half-lives were included from each study for each experimental condition tested, regardless of environmental condition studied (i.e., pH, temperature, initial MC concentration), giving rise to a higher number of half-lives reported over studies compiled (i.e., N=167 vs. 27 studies). Comparably, we did not make a distinction between aqueous and biofilm MC degrading bacterial communities when compiling the reported half-lives for isolated consortia.

$$t_{1/2,0} = \frac{C_0}{2 * K_0} \quad (13)$$

Where C_0 is the initial concentration of MC (µg/L) and K_0 is the zero-order rate constant (µg/L/day) determined using Eq. 2.

$$K_0 = \frac{(C_0 - C_F)}{\Delta t} \quad (4)$$

Where C_F is the final concentration of MC (µg/L, usually 0), and Δt is the total time elapsed until C_F is reached.

$$t_{1/2,1} = \frac{\ln(2)}{K_1} \quad (15)$$

Where K_1 (1/day) is the first order rate constant that is derived from fitting the experimental data to the first order kinetic equation. In the absence of non-linear curve fitting tools, K_1 can be estimated from Equation 4 using the natural logarithm of MC concentration.

$$K_1 = \frac{ln(C_0) - \ln(C_F)}{\Delta t} \quad (5)$$

Where C_F is the final concentration of MC (µg/L, usually 0), and Δt is the total time elapsed until C_F is reached.

In general, isolated degrading populations demonstrated faster biodegradation kinetics than the enriched consortia studied (Figure B18). The statistical results of a two-tailed t-test with homoscedastic error variance (α = 0.05) indicated that the MC biodegradation half-lives for isolated degrading populations were significantly faster than those for enriched consortia (p = 2.45E-14). The distribution of reported biodegradation half-lives for isolated populations was also much narrower as compared to consortia (small interquartile range and whiskers), indicating that the biodegradation behavior was more consistent and less variable than isolated consortia. The range of half-lives predicted for consortia isolated in this study (without organic carbon) was within the 25-50% interquartile range for isolated consortia, signifying that the biodegradation kinetics were

fast as compared to other kinetics reported in the literature for various consortia (Figure B18). However, the range of half-lives predicted for consortia isolated in this study (without organic carbon) was above the 50-75% interquartile range for isolated consortia, implying that the biodegradation kinetics for consortia may not be as rapid or comparable in efficiency to isolated degrading populations (Figure B18).

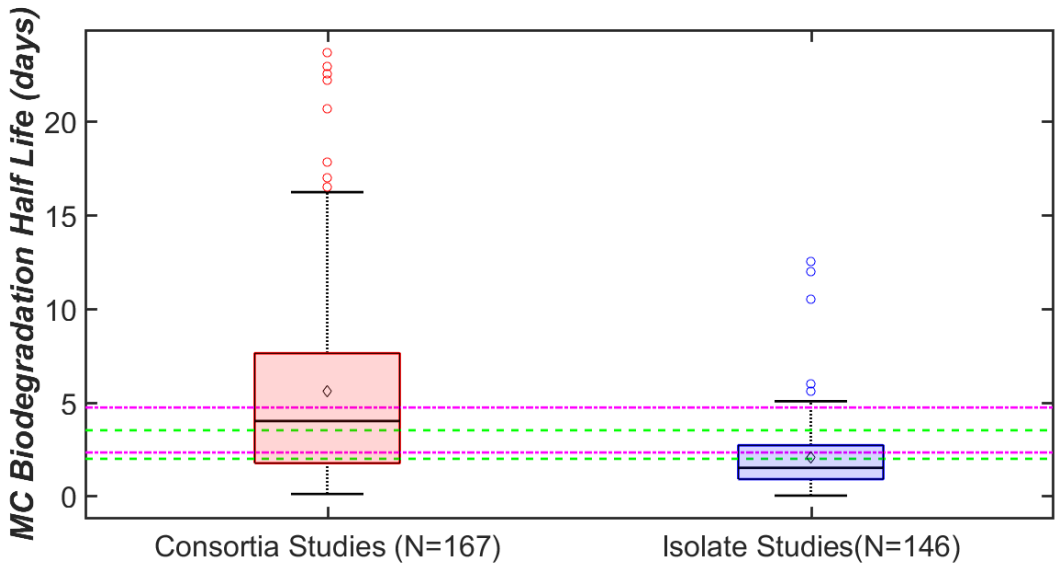

Figure B18. *Boxplot summary of reported MC biodegradation half-lives in the literature for studies involving both enriched consortia and isolated degradation populations. The green and magenta dashed/dot-dashed lines indicate the range (average value ± 1 standard deviation) in predicted half-lives determined in this study for consortia without and with ethanol, respectively. The number of reported half lives used to develop each distribution is indicated in the x-axis title (i.e., N value). Black diamonds indicate mean biodegradation half-lives for each distribution.*

12. Monte Carlo Analysis to Assess the Effect of Sampling Frequency

In this section, we investigate to what extent the number of data points used in model calibration (which depends on the sampling frequency) will affect the main conclusions presented in Chapter 2 of this dissertation. This analysis was conducted out of our own mindfulness that the sampling frequency used in this study may not have been high enough to provide meaningful data. Ultimately, we argue that no matter how many

data points are acquired during experimentation that may “fill the missing gaps” between existing data points (serving as “partials”), the main conclusions presented in Chapter 2 will not change significantly.

To prove our point, we have run a brief Monte Carlo (MCA) simulation using experimental results from the 11B consortium as an example. The 11B consortium was used since it demonstrated very similar MC-LR degradation kinetic profiles between the two treatments. We performed this MCA by simulating (or re-creating) our experimental dataset with a greater number of data points included (changing from N=7 to N=13) to represent the “what if” scenario of collecting more data points during experimentation. For example, using the original dataset as a foundation, three data points were simulated between Days 1 and 2 and three data points were simulated between Days 2 and 3, effectively doubling the number of datapoints in the dataset. Data points were added in the timeframe from Day 1 to Day 3 since this was the most dynamic portion of the experiment.

To run these MCA simulations, the simulated datapoints were taken as random, uniform draws using 0 and 200 (µg/L) as lower and upper boundaries of the selection interval. The selection of this interval for MCA sampling allows many different types of degradation behavior to be simulated during this time period. In addition, new selections were made from the existing data using normal, random draws (assuming the measurement error was normally distributed and using the mean and standard deviation obtained from the original measurements). Once the dataset was re-sampled, we performed non-linear, least squares regression to obtain a best-fitting parameter estimate and determined the half-lives from the best fitting prediction accordingly. This procedure was repeated for 50,000 unique simulations to arrive at a distribution in half-lives for

statistical comparison between each treatment. Significant differences in predicted half-lives between both simulated datasets (between consortia with and without ethanol) were assessed using a two-sample t-test (two-sided, unequal variance). The effect size was also calculated to evaluate the magnitude of difference between both distributions (see Equation 4 in Chapter 2).

The results of the MCA analysis indicated that the addition of new data points to the existing dataset did not change our initial conclusion presented in Chapter 2, as MC-LR biodegradation half-lives between treatments remained significantly different (Table B11, under "MCA" tab). However, the standard deviations of the distribution in half-lives increased an order of magnitude with the introduction of new data points in the MCA analysis (Table B11). In addition, the values of the effect sizes presented for the original dataset were larger than those observed for the MCA modified datasets, suggesting that MCA simulation created more variability in the simulated MC-LR removal kinetics (i.e., with/without ethanol) (Table B11). This result provides enough quantitative evidence that even if we increased the sampling intensity between the time periods that demonstrated the most change, the main conclusions reached would not be drastically different.

Table B11 *– Statistical comparison of simulated half-lives between treatments (with vs. without ethanol) for both original and MC analysis datasets.*

Criteria	**Original**		**MCA**	
	11B-NE	**11B-WE**	**11B-NE**	**11B-WE**
μ	2.14	2.30	2.05	2.16
σ	0.017	0.016	0.314	0.293
p-value	<1E-08		<1E-08	
Effect Size	9.693		0.348	

Figure B19 visually demonstrates that the distribution in 50,000 simulated MC-LR degradation curves is relatively uniform (especially for panel B), despite the extremely

wide range in concentrations sampled from (i.e., 0-200 µg/L) for each of the three time points between Days 1-2 or 2-3 of analysis. The relatively narrow 25-75% confidence interval bands indicate that although the concentrations of MC-LR in the simulated datasets were drastically changing, the model response was relatively similar across different MCA simulations. This result is because, mechanistically, the model cannot account for the very dynamic (perhaps up and down) degradation behavior simulated in the MCA analysis. Similar results were observed for the 12B and 14A consortia (without ethanol) in Figure 14 of Chapter 2, where the best fits of the model would pass through data points for Days 2 and 3 of analysis. Therefore, we can conclude (after assessing statistical and qualitative data) that even if we sampled more data points between Days 1-2 and 2-3, our initial conclusions would not change significantly. This result is due to the fact that the model is not sophisticated enough to mechanistically account for very dynamic changes in MC-LR concentrations over time.

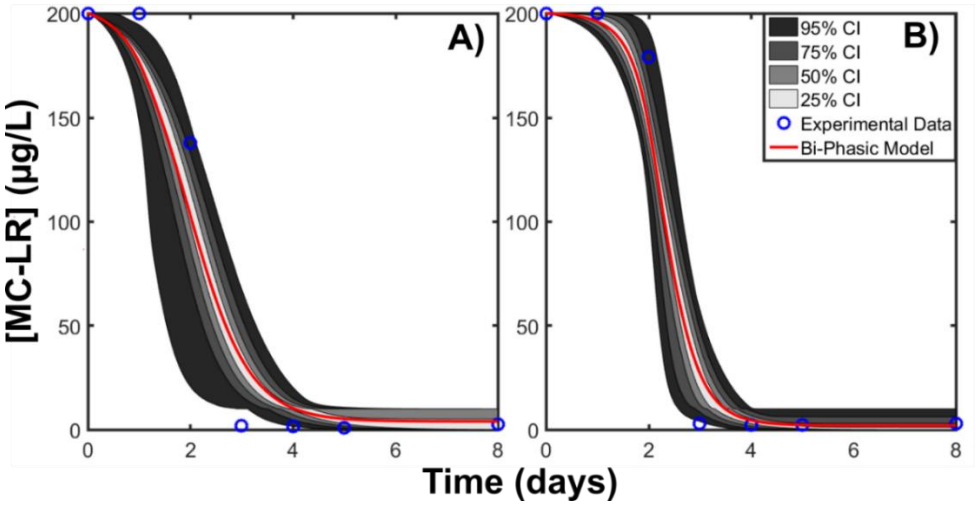

Figure B19. *Distribution in simulated MC-LR biodegradation kinetics obtained from the MC analysis for consortia treated A) without ethanol and B) with ethanol. The shading indicates the nonparametric confidence intervals (25, 50, 75, and 95%) estimated from the distribution of kinetic curves obtained from the MC analysis. The blue circles represent the experimental data, whereas the red line indicates the mean of the 50,000 simulated MC-LR removal curves.*

Appendix C: *Application of Unstructured Kinetic Models to Predict Microcystin Biodegradation: Towards A Practical Approach for Drinking Water Treatment* – Supplementary Materials

I. Supplementary Results and Methods

1. Realistic Parameter Ranges for Model Data-Fitting Approach

The realistic parameter ranges for all model parameters used in this study are summarized in Table C1, including the references used to develop the lower and upper bounds. Experimental parameters were taken from a wide array of sources including studies from the fields of bioprocess/biochemical engineering, wastewater treatment engineering, and bioremediation to be as comprehensive as possible. Two parameter ranges are given for the scaling parameters to account for differences in conversions between OD and CFU/mL cell concentrations (Table C1). We make the important distinction between units for the $\propto_{1,2}$ and n parameter values that correspond to the Dabes et al. (1973), Powell (1967), and Moser (1949), and Heijnen-Romein (1995) kinetic model structures (Table C1). Since there were few studies that have estimated parameters for the Heijnen, Dabes, and Powell kinetic models, we used a similar range to that developed for the Moser (1958) model structure (i.e., 0.0001 to 10). These values of the lower and upper bounds encompass all the very few parameter values reported for the Heijnen, Dabes, and Powell kinetic models in the literature. Negative values were excluded for the n range in values (for both the Moser and Heijnen model structures) to avoid issues with complex numbers commonly observed from predictions involving negative exponents.

Table C1 *– Summary of realistic parameter ranges developed for parameter estimation*

Parameter	References	Unit	Lower Bound	Upper Bound
μ_{max}	Rittmann et al. 1986, Kovárová-Kovar and Egli 1998, Suarez and Rifai 1999, Tchobanoglous et al. 2003, Okpokwasili and Nweke 2006, Al-Khalid and El-Naas 2012, El-Naas et al. 2014	Day^{-1}	0.01	50
K_s	Kooij et al. 1982, Kooij and Hijnen 1984, 1985, Schmidt and Alexander 1985, Rittmann et al. 1986, Doran 1995, Suarez and Rifai 1999, Tchobanoglous et al. 2003, Okpokwasili and Nweke 2006, Al-Khalid and El-Naas 2012, El-Naas et al. 2014	mg/L	0.0001	220
Y	Doran 1995, Shuler and Kargi 2002, Tchobanoglous et al. 2003, Suarez and Rifai 1999	mg biomass/ mg substrate	0.01	3.5
n	Annuar et al. 2008, Gokulakrishnan and Gummadi 2006, Ghovvati et al. 2015, Dutta et al. 2015, Enzweiler et al. 2014	None	0.0001	10
$\propto_1$	Dabes et al. 1973	(mg*day)/L		
$\propto_2$	Powell 1967	1/day		
b_1	Kim et al. 2012, Myers et al. 2013	(g DW/L) / OD	1.00E-08	2
b_2		(g DW/L) / (CFU/mL)	1.00E-15	1.00E-07
K_d	Knightes and Peters 2000, Lavallée et al. 2002, Tchobanoglous et al. 2003	Day^{-1}	0.01	1

2. Bayesian Model Comparison and Selection Calculations

The following information criteria were estimated using the posterior distribution in model parameters after the fitting process: Akaike Information Criterion (AIC), Bayes Information Criterion (BIC), Deviance Information Criterion (DIC), and Watanabe-Akaike Information Criterion (WAIC). AIC is the simplest criterion to compute, corrects for the bias induced by the number of parameters to fit the model, and is based on the posterior solution with the highest log-likelihood (θ_{mle}) (Equation 1), where k is the number of effective parameters.

$$AIC = -2\log(p(y|\theta_{mle}) - 2k \quad (1)$$

BIC considers both the number of effective parameters (k) and the size of the dataset used to fit the model (n) when correcting for bias (Equation 2).

$$BIC = -2\log(p(y|\theta_{mle}) + klog(n) \quad (2)$$

DIC is a more Bayesian estimate of AIC, where the θ_{mle} is replaced by the mean of the posterior parameter distribution (θ_{Bayes}) and the calculation of the effective number of parameters is altered to $2p_{DIC}$ (where p_{DIC} is defined in Gelman et al. 2014) (Equation 3).

$$DIC = -2\log(p\left(y\middle|\theta_{Bayes}\right) + 2p_{DIC} \quad (3)$$

WAIC is the "fullest" Bayesian information criterion and is calculated from the difference between the log posterior predictive density (LPPD) and the effective number of free parameters from the simulation (P), both of which are computed according to Gelman et al. 2014 (Equation 4).

$$WAIC = -2(\text{LPPD} - \text{P}) \quad (4)$$

For the second approach, the log pseudo marginal likelihood (LPML) was estimated using the posterior distribution in parameters (and corresponding simulations) as described first by Gelfand and Dey (1994) and summarized by Christensen et al. (2011). First, the inverse conditional predictive ordinate (CPO_i) was calculated according to Equation 5, using the pointwise estimate for the likelihood after drawing a single set of parameters from the posterior distribution (and repeating *N* times, where *N* is the size of the posterior distribution, *M* is the model under consideration). The average of the CPO values was then used to derive the LPML for a given model.

$$CPO_i^{-1} = \frac{1}{N}\sum_{k=1}^{N}\frac{1}{f_i\left(y_i\middle|\theta^k, M\right)} \quad (5)$$

3. Bayesian Hypothesis Testing

As the basis for the BEST approach, DREAM_ZS (Laloy and Vrugt 2012) was used to fit the t-distributions to the posterior log-likelihood data for each study and model combination. Overall, the estimation of 5 parameters was required including the mean and standard deviations of the posterior log-likelihood values as well as *ν*, which describes the weight of the distribution tails (μ_1, μ_2, σ_1, σ_2, and ν) (Kruschke 2011, 2013). It is important to note that the *ν* value was shared between both distributions as specified in (Kruschke 2011, 2013). We only present results for the t-test comparisons between the best and next best performing model observed for each study.

The DREAM_ZS analysis was run using similar specifications as defined in the ABC parameter estimation procedure above, except that the number of generations was reduced to 20,000 and the prior distributions of model parameters consisted of the following: normal distribution for μ_1 and μ_2; uniform distribution for σ_1 and σ_2; and a shifted exponential distribution for ν (Kruschke 2011, 2013) (Table C2). The mean and

standard deviation of the prior distribution for μ_1 and μ_2 were set to the mean and 1000 times the standard deviation of the posterior log-likelihood values for each study (Kruschke 2011, 2013). Upper and lower bounds for the uniform distribution for σ_1 and σ_2 were set to 1/1000 and 1000 times the standard deviation of the posterior log-likelihood values (Kruschke 2011, 2013). Finally, λ, for the shifted exponential was set to 29, to balance the selection of nearly normal distributions ($\nu > 30$) with heavy tailed distributions ($\nu < 30$) (Kruschke 2011, 2013). For reference, all the settings for the DREAM-ZS analysis are summarized in Table C2.

Table C2 *– DREAM-ZS Parameter Settings for BEST Analysis*

Parameter Setting	**Nominal Value**
Number of Parameters (D)	5
Objective Function	Log-Likelihood (Option 2)
Number of Markov Chains (N)	6
Number of Generations (T)	20,000
Prior Distribution	Normal, Uniform, Normal, Uniform, Shifted Exponential
Boundary Handling	None
Number of Crossover Values (nCR)	3
Number of Chain Pairs for Proposal (δ)	3
Random Error for Ergodicity (λ_E)	0.1
Randomization (ζ)	10E-12
Probability of Jump Rate	0.2
Adapt Selection Probability Crossover	Yes
Scaling Factor of Jump Rate (b_0)	1

The overall convergence statistic of Rubin and Gelman (1992) was summarized for each study to verify that the DREAM-ZS algorithm was running through enough generations to reach a stable estimate of the posterior distribution in parameters for the BEST approach (Figure C1). For all studies (a-d), convergence appeared to be reached after 20,000 generations (corresponding to 120K overall for 6 chains), where the R-statistics converge to a stable value below the 1.2 threshold for each parameter (Figure C1). These results indicate that the model-data fitting procedure was valid for applying the Bayesian

hypothesis testing approach described in Kruschke (2013), as reliable posterior distributions in parameters have been achieved.

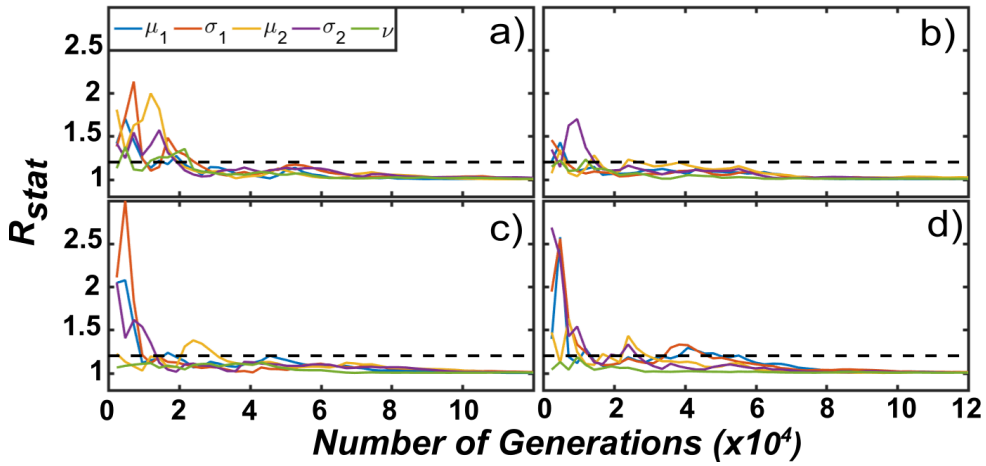

Figure C1. *Evolution of the Rubin and Gelman R-statistic for the DREAM-ZS algorithm when applied to a t-test probability distribution model for use in the BEST hypothesis testing approach. The letters a-d correspond to Studies 1-4 and the parameters refer to the mean, standard deviation and nu values of the t-distribution fitted to the posterior distribution in log-likelihood values. The dashed line indicates the convergence threshold of 1.2.*

4. Bayesian, Linear Correlation Analysis

DREAM-ZS was used to fit Pearson's linear correlation model to the posterior parameter distributions for each study and model combination. Overall, the estimation of 5 parameters was required including the mean and standard deviations of the posterior parameter values being compared as well as the correlation coefficient (rho) parameter (μ_1, μ_2, σ_1, σ_2, and ρ) (Kruschke 2011, 2013). We only present the most significant correlations observed between posterior parameter distributions for the Moser model (Studies 1-3) and the Heijnen model (Study 4).

The DREAM-ZS analysis was run using similar specifications as defined in the ABC and BEST parameter estimation procedures above, except that the number of generations was set to 50,000 and the prior distributions of model parameters consisted of the following: normal distribution for μ_1 and μ_2; uniform distribution for σ_1 and σ_2; and a

uniform distribution for ρ (Table C3). The mean and standard deviation of the prior distribution for μ_1 and μ_2 were set to the mean of the posterior distribution in parameter values and 1000, respectively, for each study. Upper and lower for σ_1 and σ_2 were set to vary uniformly between 0 and 1000. Finally, the rho parameter was set to vary uniformly between the feasible range of correlation coefficients (-1, 1). For reference, all the settings for the DREAM-ZS analysis are summarized in Table C3.

Table C3 *– DREAM-ZS Parameter Settings for Correlation Analysis*

Parameter Setting	**Nominal Value**
Number of Parameters (D)	5
Objective Function	Log-Likelihood (Option 2)
Number of Markov Chains (N)	6
Number of Generations (T)	50,000
Prior Distribution	Normal, Uniform, Normal, Uniform, Uniform
Boundary Handling	None
Number of Crossover Values (nCR)	3
Number of Chain Pairs for Proposal (δ)	3
Random Error for Ergodicity (λ_E)	0.1
Randomization (ζ)	10E-12
Probability of Jump Rate	0.2
Adapt Selection Probability Crossover	Yes
Scaling Factor of Jump Rate (b_0)	1

The convergence statistic of Rubin and Gelman (1992) was summarized for each study to verify that the DREAM-ZS algorithm was running through enough generations to reach a stable estimate of the posterior distribution in parameters for the linear correlation model (Figure C2). For all studies (a-d), convergence appeared to be reached after 50,000 generations (corresponding to 300K overall for 6 chains), where the R-statistics converge to a stable value below the 1.2 threshold for each parameter (Figure C2). These results indicated that the model-data fitting procedure was valid, as reliable posterior distributions in parameters were achieved for Pearson's linear correlation model application.

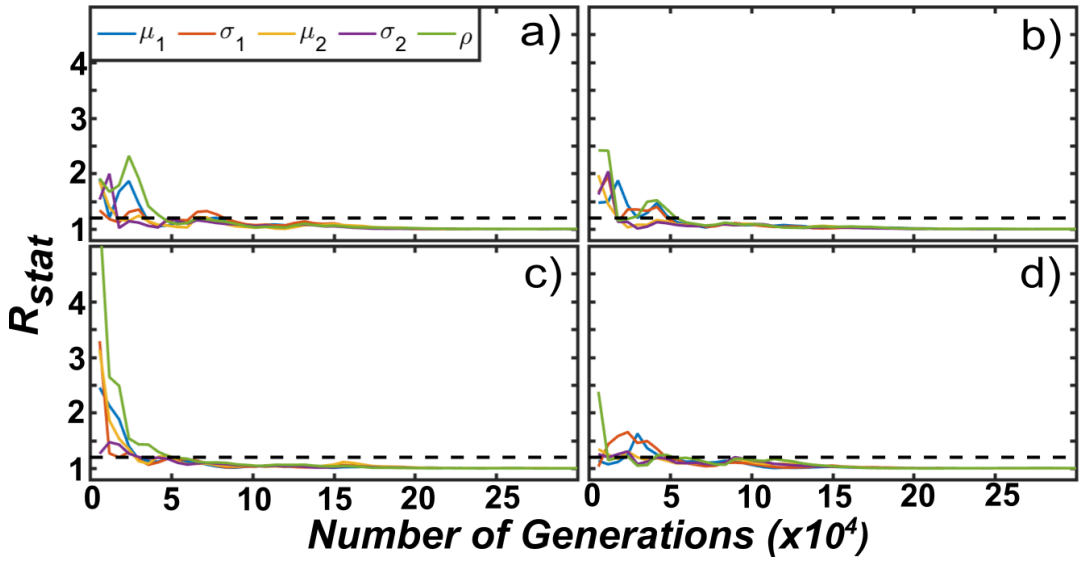

Figure C2. *Evolution of the Rubin and Gelman R-statistic for the DREAM-ZS algorithm when applied to Pearson's linear correlation model for use in the correlation analysis. The letters a-d correspond to Studies 1-4 and the parameters refer to the mean, standard deviation and Pearson's correlation coefficient values for the most significant correlations only. The dashed line indicates the convergence threshold of 1.2.*

5. Variance Based Global Sensitivity Analysis (VBGSA) Approach with Dependent Inputs

VBGSA methods are based on analysis of changes in the model output variance when varying one or more input parameters across their full range in parameter uncertainty. These methods are based on decomposing the total "unconditional" model output variance (using ANOVA) by the average conditional variances obtained by fixing one parameter input and allowing the remaining inputs to vary across their full uncertainty ranges (termed the main effect) (Saltelli et al. 2008, 2010). Thus, parameters are deemed sensitive if the difference between the total unconditional output variance and average conditional variance is high (and insensitive if low). In addition, Homma and Saltelli (1996) determined that if multiple parameters are fixed at a time, higher order interactive effects can be assessed between parameters. From this analysis, two indices can be calculated to quantify the sensitivity fractions of each parameter: the first order sensitivity (S_i) and total

order sensitivity (ST_i) (Equations 6 and 7). The first order sensitivity (S_i) accounts for the "main effect" as described above (fixing one variable only), whereas the total order sensitivity (ST_i) reflects the influence of higher order interactions among parameter inputs.

$$S_i = \frac{V_{Xi}(E_{X\sim i}(Y|X_i))}{V(Y)} \quad (6)$$

$$S_{T,ind} = 1 - \frac{V_{X\sim i}(E_{Xi}(Y|X_{\sim i}))}{V(Y)} \quad (7)$$

Where X_i is the parameter value of interest, $X_{\sim i}$ represents every other parameter but X_i, Y is the model output corresponding to the set of input parameters X, $V_{Xi}()$ and $E_{Xi}()$ refer to the variance or mean (expectation) of the argument taken over X_i alone, and $V_{X\sim i}()$ and $E_{X\sim i}()$ refer to the variance or mean of the argument taken over all parameters but X_i.

One of the main principles of Sobol's method and corresponding VBGSA approaches is that to effectively decompose the variance, the parameter distributions must be independent of each other. To circumvent this issue, several recent VBGSA approaches have been developed that can dissect the main effect and total order sensitivity indices into full (correlated + uncorrelated), correlated, and independent (uncorrelated) indices only (Kucherenko et al. 2012, Mara et al. 2015). This allows the sensitivity analysis to be conducted unobstructed from the correlations that may be present between input variables, allowing two new unique indices to be derived (Equations 8, 9). The full first order effect (S_i) and total order independent effect ($S_{T,ind}$) are calculated using identical estimates as presented in Equations 6 and 7. However, the independent first order effect ($S_{i,\,ind}$) and full total order effect ($S_{T,i}$) can be estimated using the new equations developed by Mara et al. 2015 (where the overbar signifies a conditional distribution). Although we

calculate all four indices, it is important to note that this study is limited to the analysis of the independent (uncorrelated) first and total order effect indices (Equations 7 and 8) only.

$$S_{i,ind} = \frac{V_{Xi}(E_{X\sim i}\left(Y\middle|(\overline{X_i}|X_{\sim i})\right))}{V(Y)} \quad (8)$$

$$S_{T,i} = 1 - \frac{V_{X\sim i}(E_{Xi}\left(Y\middle|(\overline{X_{\sim i}}|X_i)\right))}{V(Y)} \quad (9)$$

5.1 VBGSA Algorithm Specifications and Run Settings

To estimate the four sensitivity indices presented in Mara et al. (2015) the algorithm was slightly modified to allow for individual indices to be calculated at different simulated time points. In Mara's approach, QMC (using Sobol's sequences) sampling was used to cover the entire parameter uncertainty range. Bootstrapped predictions were obtained to assess the stability in sensitivity estimates across simulated time points by resampling the results 100 times. The posterior distribution in model parameters achieved from the DREAM-ABC algorithm was used as the uncertainty range input. In addition, Mara's method required the Spearman's rank correlation matrix for each study to be provided as input. Formal convergence to stable parameter estimates was reached when the maximum widths of the 95% confidence intervals of each parameter summarized across all simulated time points was below 0.05 (Sarrazin et al. 2016). For both model structures, the number of model evaluations required to formally converge was approximately 1,572,864 for Studies 1 and 3 and 12,582, 912 for Studies 2 and 4 (see section 5.2).

5.2 Convergence Analysis of the VBGSA Approach

The main objective of this section was to ascertain the number of samples (and corresponding model evaluations) required by the VBGSA method to converge to reliable sensitivity indices. Since the model output was bivariate (substrate and cell

concentrations) and dynamic in nature, we reviewed the variance of the indices returned for each time step as opposed to a composite sensitivity index. We assessed the sensitivity indices returned by each approach after a fixed number of samples (N ~ 64, 128, 256, 512, 1024, 2048, 4096, 8192…) using either the Moser (Studies 1-3) or Heijnen and Romein (Study 4) kinetic models as the experimental test cases. In line with QMC sampling, N values had to be an exponent with base 2. In place of experimental repetitions, bootstrapping was used to evaluate the precision of each approach (using Nboot = 100 for this method). Importantly, the initial conditions (biomass and substrate concentrations) for each model were kept identical to the experimental conditions employed by each study. Convergence to a stable sensitivity estimate was judged quantitatively, using the following criteria: the maximum width of the 95% confidence intervals obtained from bootstrapping the sensitivity index for each input parameter should be below 0.05 (Sarrazin et al. 2016). The results indicated that convergence for the VBGSA method was reached for most studies at approximately 1,572,864 model evaluations or higher (Figure C3).

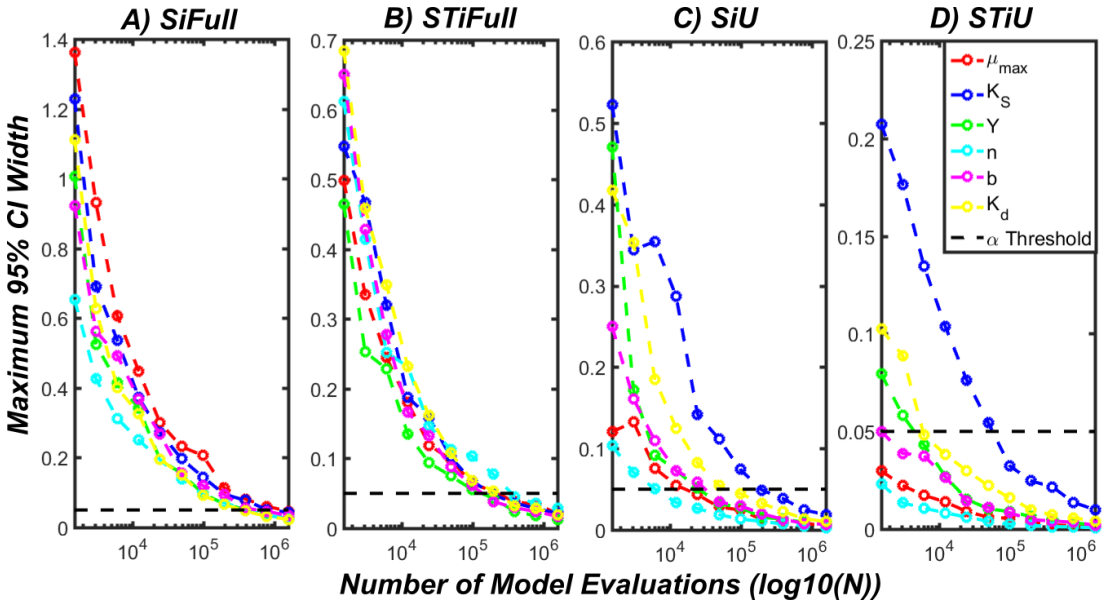

Figure C3. *Convergence of variance-based sensitivity indices accounting for correlation among input parameters (using the Moser model, Study 1 conditions, showing substrate only). Subplots A, B, C, and*

D refer to the full first order, total order, uncorrelated first order (aka independent), and uncorrelated total order variance-based sensitivity indices. The sensitivity index corresponding to each input parameter is denoted by the color in the legend. The threshold maximum CI width for convergence is shown at 0.05 (black dashed lines).

5.3 Ranking System of the VBGSA Approach

Distributions of the parameter sensitivities were obtained by employing one hundred bootstrapped replicates for each simulated time point and then re-combining these results across all time points. Ranking of the sensitivity (both first and total order) for various input parameters can be facilitated by comparing statistics on three levels of analysis, including: the 1) medians, 2) lengths of the upper quartiles (i.e., 50-75%) of the boxplots, and 3) the upper whisker lengths. For example, parameter sensitivities can first be compared across studies using the median of the distributions; if comparing the medians alone results in equivalent rankings for several different parameters, the upper quartile lengths would serve as the second level of comparison, and so on. Given that the rankings varied noticeably across studies (with no clear trend after examining Figure 8), we obtained an "overall" parameter ranking (from most to least influential or interactive) based on the system proposed above.

6. Bayesian Model Comparison and Selection

The Bayesian model selection criteria for studies 1-4 are summarized in Tables C4-C7. The color shading indicates the best rankings for each model, where red, green, and blue indicate 1st, 2nd, and 3rd place respectively (full rankings are given in a separate column). The ranking was based on a point scaling from 0-840, where points were weighted (i.e., increased) by more reliable Bayesian selection estimates (i.e., LPML (5) > WAIC (4) > DIC (3) > BIC (2) > AIC (1)). The first-place finishers received the full available points (56), where the next best and so on would be deducted 8 points. This point value would then be multiplied by the corresponding weighting factor identified above. This

point-based selection method allowed a fully objective ranking of the models compared in this study. For these selection criteria, lower numbers of AIC, BIC, DIC, and WAIC and higher values of LPML were desired (Table C4-C7).

Table C4– *Tabulated Bayesian Model Selection Criteria for Study 1 (Zhang et al. 2015)*

Model	AIC	BIC	DIC	WAIC	LPML	Ranking
1	-30.5	-25.5	-35.4	-115	51.1	8
2	-31.0	-26.1	-35.8	-121	51.2	5
3	**-45.4**	**-40.4**	**-64.5**	**-135**	**55.8**	**2**
4	-31.7	-26.8	-36.7	-117	50.9	7
5	-35.0	-29.0	-65.3	-114	52.5	4
6	-29.7	-23.7	-63.7	-119	51.0	6
7	**-55.5**	**-49.5**	**-68.9**	**-132**	**56.0**	**1**
8	**-46.8**	**-40.8**	**-47.1**	**-130**	**54.6**	**3**

Table C5 – *Tabulated Bayesian Model Selection Criteria for Study 2 (Wang et al. 2010)*

Model	AIC	BIC	DIC	WAIC	LPML	Ranking
1	10.3	11.8	0.637	-35.9	16.6	4
2	9.40	10.9	-0.201	-33.6	15.7	5
3	**8.66**	**10.2**	**-10.3**	**-37.8**	**15.6**	**2**
4	8.53	10.0	-1.06	-30.9	14.9	6
5	9.12	10.9	-4.25	-30.1	14.2	7
6	10.3	12.2	1.05	-29.5	12.6	8
7	**6.85**	**8.67**	**-4.51**	**-36.2**	**17.0**	**1**
8	**7.77**	**9.6**	**-4.09**	**-33.3**	**15.2**	**3**

Table C6 – *Tabulated Bayesian Model Selection Criteria for Study 3 (Valeria et al. 2006)*

Model	AIC	BIC	DIC	WAIC	LPML	Ranking
1	0.401	1.91	-8.73	-33.4	15.0	7
2	0.346	1.86	-8.72	-31.6	15.3	6
3	0.512	2.03	-24.0	-31.9	15.1	5
4	**-0.704**	**0.809**	**-9.55**	**-40.6**	**16.9**	**3**
5	1.38	3.19	-9.67	-33.2	16.2	4
6	1.91	3.72	-26.4	-31.5	15.1	8
7	**-13.5**	**-11.7**	**-21.6**	**-46.1**	**21.3**	**1**
8	**-5.42**	**-3.60**	**-37.3**	**-43.7**	**19.1**	**2**

Table C7 *– Tabulated Bayesian Model Selection Criteria for Study 4 (Xiao et al. 2011)*

Model	AIC	BIC	DIC	WAIC	LPML	Ranking
1	19.9	21.4	10.0	-20.6	10.0	8
2	19.6	21.1	9.78	-22.9	10.6	4
3	22.7	24.2	0.903	-21.9	10.6	6
4	**19.1**	**20.7**	**9.30**	**-27.1**	**11.7**	**3**
5	21.2	23.0	11.9	-24.3	9.23	7
6	21.3	23.1	9.32	-22.8	11.1	5
7	**-21.1**	**-19.3**	**-1.69**	**-40.9**	**16.4**	**2**
8	**-11.9**	**-10.1**	**-59.9**	**-49.9**	**21.2**	**1**

7. Summary of Best Performing Parameter Values

Table C8 summarizes the best performing parameter values achieved for each study along with the associated minimum objective function, r^2, and Root-Mean Square Error (RMSE) fitting metrics. For Studies 1-4, the best and second-best performing models were as follows: Moser and Contois; Moser and Contois; Moser and Heijnen; as well as Heijnen and Moser.

Table C8 *– Best Performing Parameter Values and Fitting Metrics for Studies 1-4*

Study	μ_{max} (1/day)	K_s (mg/L)	Y	K_d (1/day)	b	n	MinOF	r^2	RMSE
1	1.04	218	2.39	0.135	0.00863	2.24	0.0342	0.979	0.0413
2	6.08	0.100	2.68	0.715	0.0682	9.71	0.5997	0.932	0.245
3	1.27	0.000108	2.68	0.0115	1.12E-10	2.25	0.0781	0.988	0.0883
4	3.25	34.4	2.86	0.309	0.465	1.99	0.0923	0.998	0.0961

8. Summary of C_0/X_0 ratio guideline values

Table C9 summarizes the theoretical C_0/X_0 ratios calculated for each study. The conversions to COD were made using the following balanced chemical oxidation reactions (Eqautions 10 and 11) below. The first equation describes the oxidation of microcystin-LR, whereas the second equation describes the oxidation of cellular biomass. These equations result in the following conversion factors between MC and biomass concentrations and theoretical chemical oxygen demands (1.7386 g O_2/g MCLR and 1.982 g O_2/g biomass).

$$C_{49}H_{74}N_{10}O_{12} + 54O_2 \rightarrow 22H_2O + 49CO_2 + 10NH_3 \quad (10)$$

$$C_5H_7NO_2 + 7O_2 \rightarrow 3H_2O + 5CO_2 + NO_3^- + H^+ \quad (11)$$

Table C9 *– Calculated Theoretical S_0/X_0 Ratios for Studies 1-4*

Study	C_0 (mg/L)	X_0 (mg/L)	K_s (mg/L)	C_0 COD (mg/L)	X_0 COD (mg/L)	K_s COD (mg/L)	C_0/X_0
1	15	4.83	188	26.0	9.58	326	2.72
2	42.3	0.248	3.93	73.4	0.492	6.82	149
3	0.2	0.1152	0.0002	0.3472	0.228	0.0003	1.52
4	28.8	7.39	30.1	50.0	14.6	52.3	3.41

Appendix D: *Accurate and Reliable Estimation of Kinetic Parameters for Environmental Engineering Applications: A Global, Multi Objective, Bayesian Optimization Approach* – Supplementary Materials

I. Supplementary Results and Methods

1. Formal Comparison of Single Objective Optimization Algorithms

Several genetic, evolutionary algorithms were benchmarked against 15 standard test functions to evaluate and compare their inherent optimization performance. This comparison was deemed necessary before testing took place on actual data sets as some algorithms (saDE) were coded from scratch and the performance of AMALGAM-SO and LSHADE-cnEpSin was relatively unknown. The standard test functions for benchmarking included unimodal, multimodal, and hybrid composition functions clearly defined in Suganthan et al. (2005) and referred to by Vrugt and Robinson (2007). The following optimization algorithms were assessed in detail: classical differential evolution (DE) (Storn and Price 1997); self-adaptive differential evolution (saDE) (Qin and Suganthan 2005, Qin et al. 2009); AMALGAM-SO, a multi-method evolutionary single objective optimization algorithm (Vrugt et al. 2009); and LHSHADE-cnEpSin, an enhanced adaptive evolutionary algorithm (Tanabe and Fukunga 2013, 2014, Awad et al. 2016, Awad et al. 2017).

1.1 Run Conditions and Control Settings for Single Objective Algorithms

Specifications of the exact run conditions and control parameters used in each of these algorithms are specified below. AMALGAM-SO was run using the following three specified algorithms: CMA-ES, PSO, and GA, based on results presented in (Vrugt et al. 2009). The control settings for each algorithm (i.e., PSO and GA) are identical to those

presented in Table 3 of Vrugt et al. (2009). Similarly, the number of population members in AMALGAM-SO was set to evolve from 10, 20, 40, 80, 160, 320.

saDE was run using a learning period value of 20 generations and a median initialized cross-over value of 0.5 (with standard deviation of 0.1), which was the only parameter that was adapted, as specified by Qin et al. (2009). The following five mutation strategies were used in our version of saDE: DE/rand/1/bin; DE/rand2best/2/bin; DE/rand/2/bin; DE/current2rand/1; and original DE as defined in (Storn and Price 1997). Stochastic universal selection (SUS) sampling was used to select the mutation strategies and the control parameters lambda and F_{de} were selected from a normal random distribution (using a mean of 0.5 and standard deviation of 0.3) as specified by (Qin et al. 2009). The number of population members per generation was fixed to 50 for each optimization run for the saDE algorithm.

The LSHADE-cnEpSin algorithm was run using mostly identical settings to those specified in Awad et al. (2017). Initialized values of the adapted scaling parameter (F_{de}), crossover probability (CR), and the frequency of the sinusoidal search function were all set to 0.5. The memory size for adaptive storage and learning period, as specified in Awad et al. (2017) was set to 5 and 20, respectively. The mutation strategy for LSHADE-cnEpSin was set to current2pbest/1, as used in Awad et al. (2016, 2017). The probability of performing crossover using covariance matrix adaptation (p_c) and the proportion of individuals used to generate the covariance matrix was set to 0.4 and 0.5, respectively, based on results presented in Awad et al. (2017). The initial size of the population and the minimum size of the population (after population size reduction) were set to 50 and 4, respectively. All other control settings were identical to those reviewed in Awad et al. (2017).

1.2 Testing Procedure for Single Objective Algorithms

The testing procedure involved running the specified optimization algorithm on each individual test function for a total of 25 individual runs, where the random number generator was offset for each run to ensure that performance was varied for each run. All the problems were solved in D=10 dimensions, which was sufficient compared to the number of parameters used in realistic model simulations presented in this study. A predefined tolerance limit, as specified by Suganthan et al. (2005) was used to monitor the convergence of each run. The maximum number of function evaluations was set to 100,000, which was of similar order of magnitude to that previously specified (Suganthan et al. 2005). The total number of function evaluations required to reach the specified tolerance was recorded along with the minimum function value for each run for adequate comparison between optimization algorithms. Similar parameters were calculated as specified in Vrugt and Robinson (2007) to quantitatively evaluate the performance of each algorithm, including the probability of success (P_s), *SP1* value, as well as the average and standard deviation of successful runs.

1.3 Results of the Formal Benchmarking for Single Objective Algorithms

The results of the benchmark comparison indicated that the AMALGAM-SO optimization algorithm was, on average, superior to the saDE, LSHADE-cnEpSin, and DE algorithms for locating the global minimum for most test functions, which agrees with what was originally expected (Figure D1). This performance was especially apparent for the unimodal test functions, where AMALGAM-SO could quickly and efficiently locate the global minimum values (especially for function # 3, Figure D1). However, as indicated by the high spread of the standard deviation values, it was clear that the performance was quite

variable for each algorithm, due to the stochastic nature of each search algorithm. All the algorithms had difficulty solving the multimodal and expanded test functions 8, 13, and 14, which is similar to results presented for other evolutionary optimization algorithms (Vrugt and Robinson 2007, Qin et al. 2009*)*. The self-adaptive variant of DE, which switches between mutation strategies based on a stored memory of performance outperformed the AMALGAM-SO algorithm for test function 9 (shifted Rastrigin's function) as well as test function 15 (the 1st hybrid composition function) (Figure D1). However, the performance of saDE was relatively hindered on the rotated benchmark functions (3, 10, 11), where AMALGAM-SO generally performed well (Figure D1).

The LSHADE-cnEpSin global, single objective optimization algorithm, which relies on a more complex approach to adapt the DE control parameters than saDE or DE (using an ensemble approach with sinusoidal increasing or decreasing adjustments), could outperform both the saDE and DE variants for a variety of the unimodal test problems (1-5, especially apparent for 3) (Figure D1). This algorithm can effectively balance the exploitation of already achieved "best" solutions along with exploration of non-visited regions of the search space and is better equipped to handle search spaces with correlated parameter values as compared to the saDE and DE versions (Awad et al. 2016). However, for multimodal functions 6 and 7, saDE performs slightly better than LSHADE (Figure D1). Notably, on average, LSHADE outperforms the AMALGAM-SO algorithm for test functions 9, 13, and 15 (Figure D1).

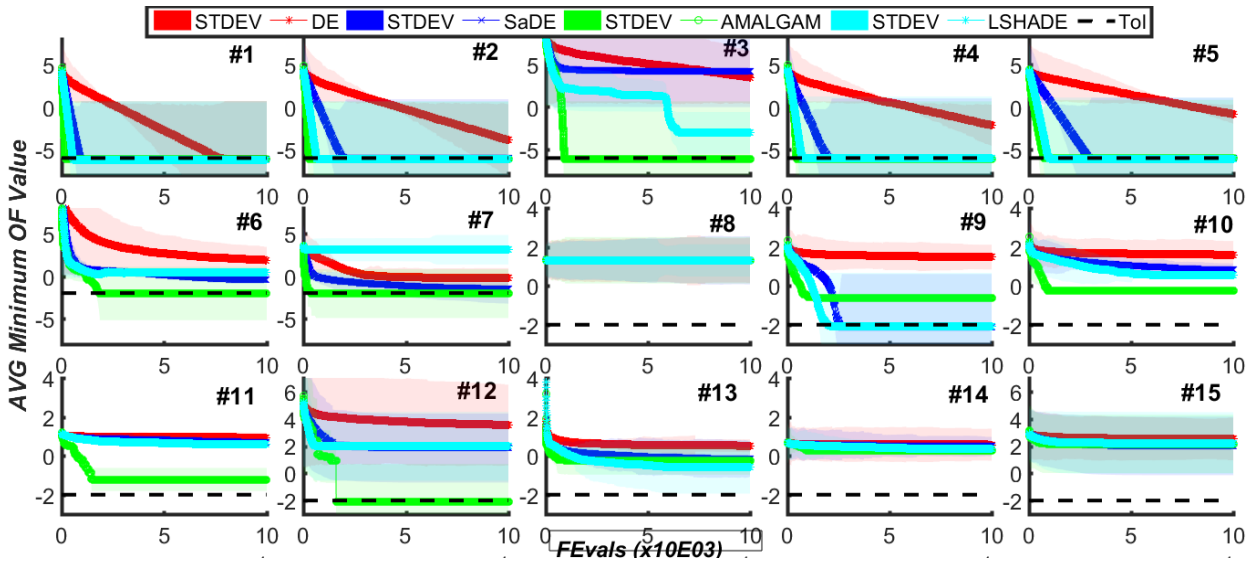

Figure D1. *Comparison of DE, saDE, AMALGAM-SO, and LSHADE-cnEpSin optimization algorithms tested on 15 benchmark functions*

The calculated values of optimization performance were in general agreement with trends illustrated in Figure D1, as demonstrated in Tables D1, D2, D3, and D4. As expected, *SP1* values were generally lower for unimodal as compared to more complex multimodal test functions. The classical DE optimization algorithm was only able to solve test function #1 in the allotted number of function evaluations. All optimization algorithms were unable to solve (at least once) test functions 8, 13, and 14 (with SP1 values and function evaluations approaching 4000 and 100,000 respectively). These results were similar to those observed by Vrugt et al. (2009), where no combinations of algorithms of AMALGAM-SO were able to solve these rather complex arrays of hybrid composition test functions. The AMALGAM-SO algorithm used in this benchmark approach performed differently than what was reported in Vrugt et al. (2009). For example, AMALGAM-SO (with CMAES-PSO-GA) did not perform as well on test functions 9, 10, 11, and 15. The reason for these inconsistencies is relatively unknown.

AMALGAM-SO was able to solve the remaining test functions (1-7, 9-12, 15) with a relatively higher probability (P_s) than both the saDE and LSHADE-cnEpSin algorithms (Tables D2 and D3). Exceptions to this trend included test functions 9 and 15, which was similar to what was depicted qualitatively in Figure D1. In addition, AMALGAM-SO was reflected by lower standard deviation values over LSHADE-cnEpSin or saDE, suggesting that the search performance was more reproducible and less stochastic in nature (Tables D2 and D3). Compared to saDE, AMALGAM-SO generally took a much smaller number of function evaluations to reach the global minimum, most likely due to the higher search efficiency afforded by the combination of three premier evolutionary search algorithms. Finally, the average minimum objective function values (MinAVG) and associated standard deviations were generally smaller for the AMALGAM-SO algorithm over saDE or LSHADE-cnEpSin (exceptions for problems 9 and 15). After comparing trends in tabulated *Ps* and MinSTDEV values, the LSHADE algorithm was slightly more variable in performance than the saDE algorithms, due in part to the adaptation procedure in LSAHDE-cnEpSin (Tables D2 and D4). Overall, AMALGAM-SO demonstrated a more reliable optimization performance than the LSHADE-cnEpSin, saDE and classical DE alone, where the following classification can be concluded: AMALGAM-SO>LSHADE-cnEpSin>saDE>DE.

Table D1 *– Tabulated results of classical DE on 15 benchmark test functions*

Test Function	Ps	SP1	AVG	STDEV	MinAVG	MinSTDEV
1	1	3048	76192	6577	8.1046E-07	1.58211E-07
2	0	4000	-	-	1.23E-04	5.54096E-05
3	0	4000	-	-	2966	1195
4	0	4000	-	-	7.09E-03	3.86E-03
5	0	4000	-	-	1.43E-01	7.98E-02
6	0	4000	-	-	74	35.25
7	0	4000	-	-	6.37E-01	7.46E-02
8	0	4000	-	-	20	7.03E-02
9	0	4000	-	-	30	4.29
10	0	4000	-	-	39.54	5.05
11	0	4000	-	-	8.74	0.56
12	0	4000	-	-	3502	921
13	0	4000	-	-	3.26	4.70E-01
14	0	4000	-	-	3.72	1.50E-01
15	0	4000	-	-	326	36

Table D2 *– Tabulated results of saDE on 15 benchmark test functions*

Test Function	Ps	SP1	AVG	STDEV	Tolerance	MinAVG	MinSTDEV
1	1	362	9042	296	1E-06	8.25E-07	1.72E-07
2	1	712	17788	1657	1E-06	8.66E-07	1.05E-07
3	0	4000	-	-	1E-06	14019	14316
4	1	708	17704	1993	1E-06	8.78E-07	8.706E-08
5	1	1166	29146	870	1E-06	9.16E-07	7.39E-08
6	1	3002	75042	15524	1E-06	3.32E-01	1.10
7	0.52	3180	60581	22162	1E-02	2.94E-02	1.95E-02
8	0	4000	-	-	1E-02	20	5.90E-02
9	1	908	22712	1550	1E-02	8.48E-03	1.04E-03
10	0	4000	-	-	1E-02	6.44	2.20
11	0.04	3998	98900	-	1E-02	4.78	1.36
12	0.68	2128	31176	17704	1E-02	71	338
13	0	4000	-	-	1E-02	6.75E-01	1.24E-01
14	0	4000	-	-	1E-02	3.03	3.24E-01
15	0.36	2968	35644	9907	1E-02	101	141

Table D3 *– Tabulated results of AMALGAM-SO on 15 benchmark test functions*

Test Function	Ps	SP1	AVG	STDEV	Tolerance	MinAVG	MinSTDEV
1	1	69	1737	97	1E-06	7.82E-07	1.57E-07
2	1	108	2688	132	1E-06	7.78E-07	1.87E-07
3	1	326	8152	504	1E-06	7.92E-07	1.73E-07
4	1	126	3160	376	1E-06	7.59E-07	1.67E-07
5	1	280	6997	329	1E-06	8.71E-07	1.32E-07
6	1	423	10568	9319	1E-06	8.98E-03	7.40E-04
7	1	316	7908	6913	1E-02	8.54E-03	1.38E-03
8	0	4000	-	-	1E-02	20.368	0.064
9	0.72	2348	42628	18906	1E-02	2.25E-01	6.50E-01
10	0.52	3118	57615	18282	1E-02	5.61E-01	6.44E-01
11	0.96	1264	28745	17857	1E-02	6.04E-02	2.56E-01
12	1	894	22348	18753	1E-02	7.71E-03	1.63E-03
13	0	4000	-	-	1E-02	5.41E-01	1.99E-01
14	0	4000	-	-	1E-02	1.793	0.613
15	0.08	3935	79420	15061	1E-02	143.200	136.926

Table D4 *– Tabulated results of LSHADE-cnEpSin on 15 benchmark test functions*

Test Function	Ps	SP1	AVG	STDEV	Tolerance	MinAVG	MinSTDEV
1	1	223	5568	59	1E-06	6.61E-07	1.9E-07
2	1	265	6634	0	1E-06	6.89E-07	1.38E-07
3	0.8	3027	69608	32699	1E-06	3.95E-05	7.85E-05
4	1	293	7313	72	1E-06	9.38E-07	5.4E-08
5	1	390	9740	195	1E-06	7.54E-07	5.94E-08
6	0.32	3129	31959	4839	1E-06	2.71E+00	1.89
7	0.52	4000	100000	0	1E-02	1.21E+03	7.23E+01
8	0	4000	-	-	1E-02	20	8.73E-02
9	1	644	16098	1594	1E-02	8.17E-03	1.77E-03
10	0.04	3999	99530	-	1E-02	3.58	1.60
11	0	4000	-	-	1E-02	3.81	1.03
12	0.52	2083	7838	2731	1E-02	97	336
13	0	4000	-	-	1E-02	2.20E-01	4.40E-02
14	0	4000	-	-	1E-02	2.24	6.05E-01
15	0.44	2716	27057	13519	1E-02	161	189

2. Formal Testing of the Model Prediction Residuals

This section confirms the validity of several assumptions made when deriving the maximum likelihood function used for the GSO and GMO algorithms in this study. The four main assumptions made in this derivation were as follows:

1. The error residuals are normally distributed with zero mean;
2. The error residuals are independent;
3. The error residuals are homoscedastic (constant variance).

Regarding the first assumption, quantile-quantile (QQ) plots of the best performing parameter sets for each study (using the Moser model for Studies 1-3 and Heijnen model for Study 4) indicated that the error residuals for both substrate and cell concentration predictions were normally distributed, as all residuals fell close to the QQ line plot (Figure D2) (Anderson and Darling 1954, Thode 2002). In addition, an Anderson-Darling (AD), one-sample Komolgorov-Smirnov (KS) test, and D'Agostino Pearson K2 test were performed to quantitatively assess if the error residuals were normally distributed (Thode 2002, Wilcox 2005, Zar 2010). Both the AD and KS tests evaluate the significance of the departure of an empirical cumulative distribution function (CDF) created from the data from the CDF of a hypothetical normal distribution (where the KS significance test is nonparametric and the AD test places more emphasis on the tails of the empirical distribution), whereas the K2 test evaluates the normality based on measures of skewness and kurtosis of the data alone (Thode 2002, Wilcox 2005, Zar 2010).

The results demonstrated that for most Studies (2-4), the null hypothesis that the distribution of error residuals was normal was not rejected, as the calculated p-values were mostly greater than 0.05 (Table D5). Although rejection of the null hypothesis was not

observed for the AD test for Study 1, the KS test indicated otherwise (Table D5). Similarly, the null hypothesis was rejected for the cell concentration residuals obtained from Study 2, indicating the distribution of residuals was not normal based on measures of skewness and kurtosis alone (Table D5). We also quantitatively checked if the mean of the residuals for each Study was significantly different from 0 using the F-test statistical approach presented in (Knightes and Peters 2000). The confidence level values calculated ranged from 61% to 92%, indicating that there was generally high certainty (greater than 90% for Studies 1,2 and 4) that the mean of the error residuals was 0; however, these results were generally not statistically significant using the 0.05 significance level.

Table D5 – *Results of the normality testing significance (p) values for residuals from predicted substrate and cell concentrations*

Study	AD Test		KS Test		K2 Test	
	p-value (Substrate)	**p-value (Cells)**	**p-value (Substrate)**	**p-value (Cells)**	**p-value (Substrate)**	**p-value (Cells)**
1	0.297	0.149	0.0148	0.0095	0.463	0.291
2	0.527	0.092	0.264	0.276	0.691	0.0378
3	0.869	0.257	0.228	0.131	0.858	0.158
4	0.581	0.749	0.236	0.141	0.694	0.564

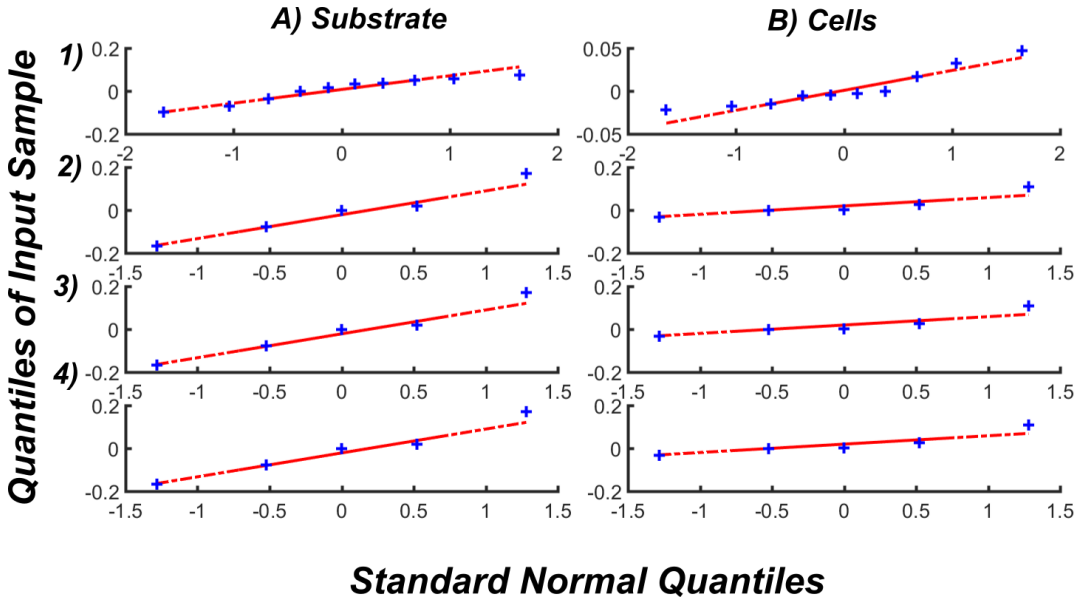

Figure D2. *Quantile-quantile plots for the best fitting parameter sets obtained for studies 1-4, separated by residuals pertaining to A) substrate and B) cell concentration variables.*

To check if the error residuals were independent, several methods were investigated. Autocorrelation plots were first developed to qualitatively inspect whether the error residuals were independent and non-correlated (Figure D3) (Box 1994, Hamilton 1994). As observed in Figure D2, most of the autocorrelation values were close to 0, especially for Studies 2-4, which demonstrates that there was little temporal similarity among error residuals. In addition, most of the autocorrelation estimates ranged within the 95% standard error bounds, signifying that the autocorrelation response was relatively uniform across different lag time periods. For some initial lag periods (i.e., 1), the autocorrelation values were high, especially for Study 1; however, the values seemed to dampen as the number of lag periods progressed, which was indicative of independent residual distributions for both predicted substrate and cell concentrations.

The Ljung Box Q, Runs test, and Turning point tests were used to quantitatively assess the independence of the residual errors for each study (Box 1994, Cromwell et al.

1994, Gibbons 1996, Yürekli et al. 2005). The Ljung Box Q test investigates the null hypothesis that the residuals are not autocorrelated using a chi-squared statistical test (Box 1994). This test depends on the number of lags (L) incorporated, where we varied the number of lags from 1 to the number of observations and reported the minimum p-value from these estimates. Based on Table D6, a majority of the p-values were greater than 0.05, suggesting that the null hypothesis was not rejected and that the residuals are indeed not autocorrelated. The only exception to these results was the error residuals obtained from the substrate concentration predictions in Study 1, which resulted in a rejection of the null hypothesis.

The Runs test, on the other hand, tests the null hypothesis that the residuals come in random order, and can help support the hypothesis that they are independently distributed in time or space (Cromwell et al. 1994, Gibbons 1996, Yürekli et al. 2005). For all studies, the p-value was greater than 0.05, signifying that the null hypothesis was not rejected, and that the error residuals were indeed in random, independent ordering (Table D6).

Finally, the Turning test (based on the number of up or down turns) tests the null hypothesis that the set of residuals are independent and identically distributed, random values. If the value of the *Nt* statistic calculated from this test is greater than 1.96, then the null hypothesis is rejected, and the values do not come from an independent, identically distributed set of random numbers (Cromwell et al. 1994, Gibbons 1996, Yürekli et al. 2005). The results in Table D6 indicated that most of the residuals were indeed independent and identically distributed random numbers, except for the residuals obtained from the substrate predictions in Study 1, as the Nt statistic values were generally below the 1.96 critical threshold.

Table D6 *– Results of the independence testing significance (p) values for residuals from predicted substrate and cell concentrations*

Study	Ljung Box Q Test		Runs Test		Turning Test	
	p-value (Substrate)	p-value (Cells)	p-value (Substrate)	p-value (Cells)	Nt-value (Substrate)	Nt-value (Cells)
1	0.0204	0.0931	0.095	0.167	2.98	0.916
2	0.166	0.485	1	1	1.76	0
3	0.0977	0.859	1	1	1.76	1.76
4	0.139	0.899	1	1	0	1.76

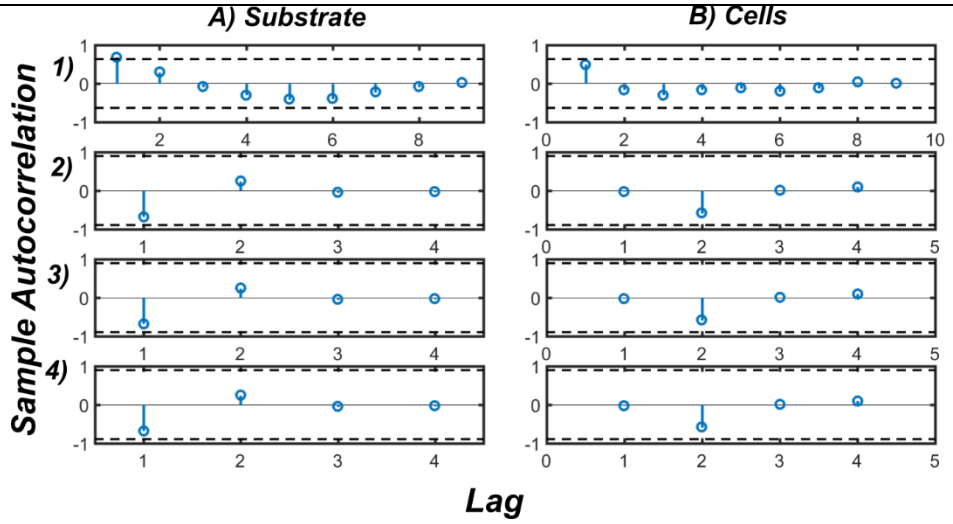

Figure D3. *Autocorrelation plots for the best fitting parameter sets obtained for studies 1-4, separated by residuals pertaining to A) substrate and B) cell concentration variables.*

To check for homoscedasticity, Engle's ARCH test (Engle et al. 1987), the Bresuch and Pagan (1979), and the White test (White 1980, Wooldridge 2015) methods were applied. Engle's ARCH test tests the null hypothesis that a series of residuals exhibits no conditional heteroscedasticity by fitting an ARCH(L) model to the residuals, where L represents the number of lags included (Engle et al. 1987). Similar to the Ljung Box Q Test, we varied the number of lags included to fit/develop the ARCH model from 1 to the number of observations and reported the minimum p-value from these estimates. Based on this test, the null hypothesis was not rejected for any study, as the distribution of p-values never dropped below the 0.05 significance level (Table D7). Thus, we can conclude with high statistical certainty that there was no conditional heteroscedasticity to the residuals obtained from the predictions of substrate or cell concentrations for each study.

The Breusch-Pagan and White methods test whether the variance of the error residuals from a regression are dependent on the values of the independent "predictors," indicating heteroscedasticity (Engle et al. 1987, Breusch and Pagan 1979, White 1980, Wooldridge 2015). Here, the "predictors" are the predicted substrate and cell concentrations from the nonlinear kinetic models. The Breusch-Pagan method differs from the White method as it considers a simple, additive linear regression between the squared residuals and the predictors, whereas the White method considers a more complex quadratic regression between the squared residuals and predictors. Both tests test the null hypothesis that the error residuals are homoscedastic using a chi-squared statistical significance test. Different results were observed between the two methods, as the White test generally did not reject the hypothesis that the error residuals were homoscedastic (as all p-values > 0.05), whereas the Breusch-Pagan test rejected the null hypothesis for the residuals obtained from substrate predictions for Studies 2-4 (Table D7). Clearly, if the datasets were not so sparse, and included higher resolution at more dynamic portions of the kinetic curves, the validity of these statistical tests would be greatly improved. However, despite this uncertainty in the experimental datasets acquired, it is generally safe to make a preliminary conclusion that in the majority of cases the error residuals were proven to be homoscedastic, as initially assumed.

Table D7 *– Results of the heteroscedasticity testing significance (p) values for residuals from predicted substrate and cell concentrations*

Study	Engle's ARCH Test		Breusch-Pagan Test		White Test	
	p-value (Substrate)	p-value (Cells)	p-value (Substrate)	p-value (Cells)	p-value (Substrate)	p-value (Cells)
1	0.0643	0.255	0.132	0.551	0.246	0.475
2	0.183	0.223	0.0275	0.667	0.0827	0.098
3	0.165	0.223	0.0278	0.552	0.088	0.566
4	0.0981	0.223	0.0284	0.271	0.087	0.532

3. Formal Comparison of Multi Objective Optimization Algorithms

A total of 10 evolutionary, multi-objective optimization algorithms (EMOA) were formally benchmarked against 13 test functions. The EMOA algorithms selected for screening in this study were considered from the results presented in Tanabe et al. (2017) (for M = 2 objective functions, similar conditions to our problem herein), which benchmarked 21 recent and classical EMOA algorithms using the WFG suite of test functions. The 10 selected algorithms included: MO-CMA-ES (the multi-objective version of CMA-ES (Igel et al. 2007); NSGA-III (Deb and Jain 2014); MOEA/D (Zhang and Li 2007); MOEA/DD (Li et al. 2015b); SPEA2-SDEA (Li et al. 2014b); IBEA (Zitzler and Künzli 2004); RVEA (Cheng et al. 2016); MOEA/IGDNS (Tian et al. 2016); AMALGAM-MO (Vrugt and Robinson 2007); and A-NSGA-III (Jain and Deb 2014). For the MO benchmark tests, we selected test functions that were both non-convex (WFG 1-9) and convex (MaF3, MaF5, MaF11, MaF15), multi-modal, biased, separable, and non-separable to gain a full perspective of the performance of each algorithm. Importantly, the ratio of convex to concave problems was set at 1:1 to ensure that performance evaluations were equally split between these two specific categories of test problems (even though the MO problems in this study were convex). Each of these test algorithms and problems (except AMALGAM-MO) were compiled by Tian et al. (2017) in a convenient platform for testing and comparison (PlatEMO v.3.0), which was utilized in this study.

The metrics used to compare the EMOA algorithms differed significantly from the SO algorithms, as it is impossible to judge the performance of an EMOA using one singular criterium. Similar to criteria reviewed by Zitzler et al. (2000), the EMOA algorithms were compared using the final, non-dominated Pareto solution sets returned by each

optimization run (which was different than criteria presented by Tanabe et al. (2017)). The algorithms were judged based on three categories: accuracy and convergence (how close the solution sets were to the exact Pareto front), diversity (distribution of solutions and spread/coverage), and the number of nondominated solutions in the experimental solution set (Zitzler et al. 2000). Accuracy and convergence were evaluated based on five primary parameters: set coverage (C, higher number is better), final generational distance (GD, lower number), inverted generational distance (IGD, lower number), hypervolume (HV, higher number), and normalized hypervolume (NHV, higher number), described in detail elsewhere (Huband et al. 2006, Janssensand Pangilinan 2010, Riquelme et al. 2015, Yen and He 2014, Wang et al. 2017). It is important to note that C, IGD. HV, and NHV metrics also consider diversity/uniformity of solution sets in addition to accuracy and convergence. Diversity or uniformity of solution sets were judged using the following parameters: spacing (S), spread (Sp), and pure diversity (PD). The number of nondominated solutions in the experimental Pareto front was assessed using the RNI metric (ratio of nondominated solution sets) (Yen and He 2014). In addition, the CPU time was compared among algorithms, yet another factor to benchmark for each test function.

To fairly assess the performance of each algorithm over the wide range in test problems, a scoring system was constructed for each metric (excluding coverage and RNI statistics). In this approach, a score on the scale of 1-10 (10 being 'excellent' and 1 being 'poor') was delegated to each algorithm after sorting the calculated results for each metric (in either ascending or descending order, depending on the metric chosen). For this scoring method, a perfect performance would be equivalent to a score of 1040 (first place for each problem and metric), whereas a very poor performance would be equivalent to 0. The

coverage and RNI scores were excluded from this comparison as each algorithm reported many similar values for each of these metrics, making it difficult to find a rank for comparison.

3.1 Run Conditions and Control Settings for Multi-Objective Algorithms

The AMALGAM-MO run conditions and control settings used in this study are summarized in Table D8. Run conditions were kept identical to those developed for the other two MO algorithms (fixed population and generations). All the control settings required to run this algorithm were identical to the default values presented in Vrugt (2016), including all the recombination methods listed. Latin hypercube sampling was used for sampling from the initial prior distribution. Boundary handling was set to the reflect option, where mutated values outside the feasible range were reflected an equal distance back into the feasible parameter space. DE scaling factors (i.e., F_{de}) and PSO inertia factors were set to uniform distributions (U) using the ranges specified in Table D8.

Table D8 *– Run conditions and control settings for the AMALGAM-MO application*

Parameter Setting	Nominal Value
Number of Parameters (D)	6
Population Size (N)	100
Number of Generations (T)	20,000
Number of Objective Functions (m)	2
Prior Distribution	Latin
Boundary Handling	Reflect
Recombination Methods	GA, PSO, AMS, DE
NSGA Crossover Probability	0.9
NSGA Mutation Probability	1/6
NSGA Cross Distribution Index	10
NSGA Mutation Distribution Index	50
AMS Jump Rate	0.9440
DE Scaling Factor – DE Variant 1	U[0.6,1]
DE Scaling Factor – DE Variant 2	U[0.2,0.6]
PSO Social Factor	1.5
PSO Cognitive Factor	1.5
PSO Inertia Factor	U[0.5,1]
Thinning Rate	1
Minimum Selection Probability	0.05

EMOA run conditions were fixed for each test problem to settings that resembled the unique problems presented in this study including M=2 objective functions, d = 6 "parameters", N = 100 population members, and $50*10^4$ function evaluations. The SBX crossover and polynomial mutation functions were selected for each run, as suggested by (Tian et al. 2017) and provided by the PlatEMO user interface. The user settings for the crossover and mutation functions were identical to those presented in Tanabe et al. (2017) (pc = 1, nc = 30, pm = 1/d, and nm = 20). Importantly, each algorithm was run for five individual replicates and an average metric was computed and recorded for each test problem to gain some statistical significance in the comparison evaluation.

The results of the formal comparison demonstrated that the NSGA-III algorithm was the most robust multi objective optimizer to the wide range in test problems encountered, whereas the adaptive NSGA-III algorithm performed the worst (Table D9). Interestingly, although AMALGAM-MO combines several different algorithms (i.e., PSO, NSGA-II, DE) to improve MO performance, it was still outperformed by the NSGA-III algorithm. This result was unexpected; however, the relatively short run time (50,000 function evaluations) may have hindered the performance of the AMALGAM-MO algorithm. Future comparisons should be made between all algorithms at a higher number of function evaluations to clarify this point. The recently introduced MOEA/IGD-NS algorithm also showed a good overall performance across the 13 benchmark test functions (Table D9).

In addition, the percent contribution of each metric to the total score is summarized in Table D9. For the top two performing algorithms, the contribution from each metric to the total score was relatively equivalent (ranging from 9-14%). NSGA-III was slightly more accurate (with higher contributions from HV/NHV metrics) as compared to AMALGAM-MO.

However, the distribution of solutions along the pareto front were perhaps more uniform (higher Spacing contribution) and diverse (higher PD contribution) for AMALGAM-MO over NSGAIII. The MOEA/IGD-NS algorithm suffered from a high CPU-time and accuracy (low CPU/GD contribution) but gained a competitive advantage in the distribution and diversity criteria (PD, Spacing, Spread) of the experimental solution sets generated. The remaining algorithms demonstrated a wider spread in the contribution from each metric to the total score as compared to the top three performing algorithms (from 6-37%), where higher contributions came from CPU time or diversity/distribution metrics as opposed to accuracy metrics.

Table D9 *– Comparison of the MO algorithms performance against 13 benchmark test functions*

Rank	Algorithm	Total Score	CPU Time (%)	GD (%)	IGD (%)	Spacing (%)	Spread (%)	HV (%)	NHV (%)	PD (%)
1	NSGA-III	774	13	13	14	11	11	14	14	9
2	AMALGAM-MO	747	12	10	14	14	11	13	13	14
3	MOEA/IGDNS	673	4	11	14	16	18	11	11	14
4	RVEA	643	20	8	12	11	15	11	11	13
5	SPEA2-SDE	574	7	15	13	11	10	17	17	11
6	MOEA-DD	568	3	16	17	10	14	16	16	9
7	IBEA	536	14	16	9	10	7	14	14	17
8	MOEA-D	470	10	11	11	17	19	10	10	10
9	MO-CMA	421	16	9	11	12	13	10	10	20
10	A-NSGAIII	314	37	18	6	15	5	6	6	6

Visual inspection of the performance of the best performing algorithm (NSGA-III) qualitatively confirms the high accuracy and precision of the NSGA-III MO algorithm (Figure D4). Average results from each independent run (from N=5 repetitions) showed that the experimental, non-dominated solutions from the NSGA-III algorithm well approximate the true Pareto front for many of the test functions, both concave and convex in nature. The largest error between the true Pareto front and the experimental front was

observed for the WFG-8 test function, which was similar to the performance among all other algorithms. In addition, the coverage of solutions for the WFG1 and 2 as well as MaF11 staircase functions is relatively sparse at lower values of objective function 1 (higher values of objective function 2), where the lack of diversity in NSGA-III solutions for some test problems was similarly confirmed in Table 2 above (Figure D4). These results highlight NSGA-III as a reliable and consistent multi-objective optimization algorithm that will be used as a primary algorithm for model-data calibration in this study.

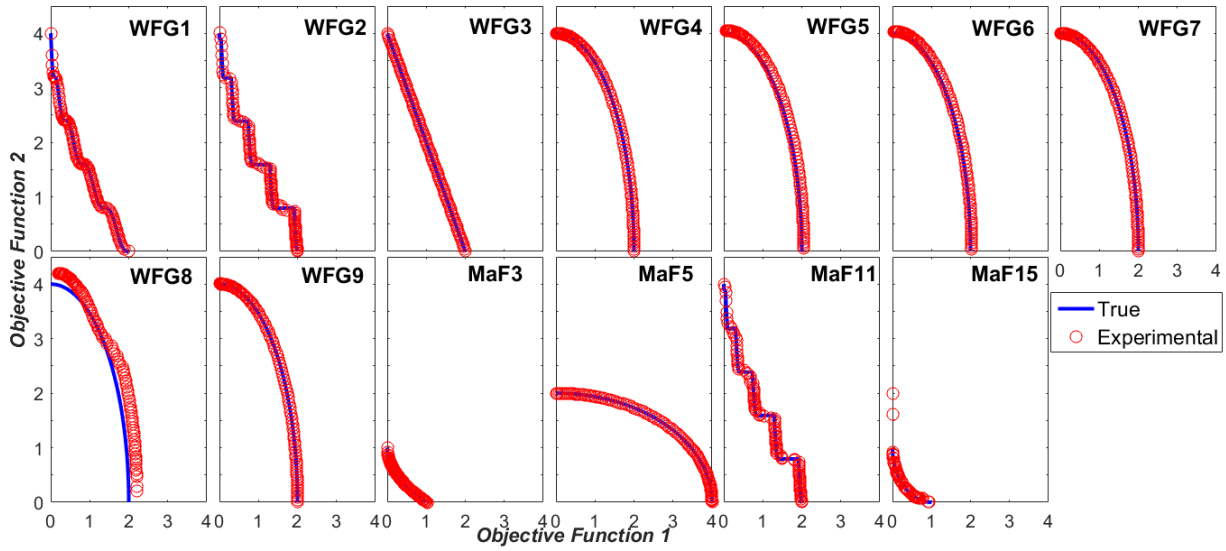

Figure D4. *NSGA-III MO performance when benchmarked against 13 test functions (for M=2 objective functions). The blue line indicates the true Pareto front, whereas the red circles indicate the experimental Pareto front as determined using the NSGAIII algorithm.*

4. DREAM-ZS Run Conditions: Approximate Bayesian Computation

The DREAM-ZS run conditions for the Approximate Bayesian Computation algorithm are summarized in Table D10. To run the ABC component within DREAM-ZS, the ABC objective function had to be explicitly specified in the DREAM-ZS calling script. Of the two functions provided, the distance function was chosen with a threshold (ε_j) value set to 0.025 as recommended in Sadegh and Vrugt (2014). Depending on the model structure and the experimental dataset applied, the number of generations was varied from 50,000 to

400,000 until convergence was formally reached (using the Gelman-Rubin convergence statistic threshold, Rubin and Gelman 1992). The prior distribution of model parameters was always set to a uniform distribution within the specified realistic uncertainty range. The remaining parameter values specified in Table D10 were found to be optimal to improve convergence speed and were primarily based on information presented in Vrugt (2016) and by trial and error approaches.

Table D10 *– DREAM-ZS Parameter Settings for the ABC Analysis*

Parameter Setting	**Nominal Value**
Number of Parameters (D)	6
Objective Function	ABC Distance Function (Option 22)
Number of Markov Chains (N)	6
Number of Generations (T)	50,000-400,000
Prior Distribution	Uniform
Boundary Handling	Reflect
Number of Crossover Values (nCR)	3
Number of Chain Pairs for Proposal (delta)	3
Random Error for Ergodicity (lambda)	0.1
Randomization (zeta)	10E-12
Probability of Jump Rate	0.2
Adapt Selection Probability Crossover	Yes
Scaling Factor of Jump Rate (b0)	1
Epsilon Value	0.025

5. Constrained Boundaries for Improved FMINCON Search

Lower and upper parameter boundaries for the improved FMINCON local search are presented in Table D11 for reference. The limits on each parameter were set very close to the optimal parameter sets determined by the global optimization algorithms to gauge the optimization performance of the local search methods around the global optimum.

Table D11 *– Summary of constrained lower (top row) and upper (bottom row) parameter boundaries for the improved FMINCON optimization tests*

Study	μ_{max}	K_s	Y	K_d	b	n
1	1.06	219	2.60	0.12	0.01	2.17
	1.08	220	2.80	0.13	0.011	2.19
2	6	0.07	3	0.8	0.07	9
	7	0.09	4	0.9	0.08	10
3	1.2	0.0001	1.7	0.01	0.000000000075	2.2
	1.3	0.0002	1.8	0.02	0.00000000008	2.3
4	2.7	0.0001	3.3	0.02	0.6	2.6
	2.8	0.0002	3.4	0.03	0.7	2.7

6. Formal Convergence of DREAM-ABC vs. DREAM-GL (Gaussian Likelihood) Bayesian Optimization Approaches

In this section, the formal convergence efficiency of the Approximate Bayesian Computational (ABC) variant of the Bayesian optimization approach DREAM was compared to that of the standard DREAM variant incorporating a formal Gaussian Likelihood objective function. The results are specifically presented for the Moser model calibration. Both the mean and standard deviation from five independent realizations of the overall R statistic of [49] were used to compare the convergence efficiency and reliability for both approaches. For all studies (a-d), the DREAM-GL (Gaussian Likelihood) approach demonstrated improved formal convergence efficiency over the DREAM-ABC approach (Figure D5). Both approaches formally converged by at least 50,000 generations, except for Study 3, which clearly required a larger number of generations before convergence was feasible using both approaches (Figure D5). Apart from Study 3 results, the DREAM-ABC

approach was marked by a more consistent optimization performance as compared to the DREAM-GL approach, as reflected by the small standard deviation in the R-statistic across the repetitions performed (Figure D5).

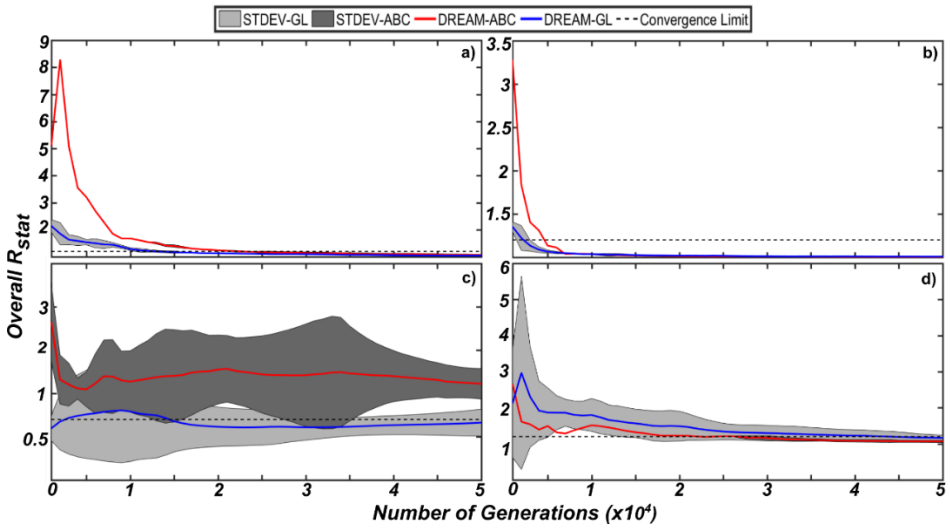

Figure D5. *Evolution of the overall Gelman and Rubin R-statistic for both the DREAM-ZS (ABC) algorithm (red) and the DREAM-ZS (Gaussian Likelihood) algorithm when calibrated against the Moser model for each corresponding dataset (1-4). The letters a-d correspond to Studies 1-4. The solid lines and grey shaded areas indicate the mean value and one standard deviation from the mean value across five independent realizations. The dashed line indicates the convergence threshold of 1.2.*

7.0 Parameter Identifiability of DREAM-ABC vs. DREAM-GL (Gaussian Likelihood) Bayesian Optimization Approaches

Figures D6-D8 summarize the experimental results comparing the parameter identifiability between the DREAM-ABC and DREAM-GL approaches for Studies 1-3, respectively. For all studies, the parameter identifiability and definition were drastically improved using the DREAM-ABC approach. It is apparent that the Bayesian optimization has not converged for Study 3, as the mean parameter values from the ABC approach were not homogenous, especially for μ_{max}, K_s, and Y model parameters. In addition, some parameters were not identifiable, even when the DREAM-ABC approach was used, as observed for most Y values and some K_d values across all studies (Figures D6-D8).

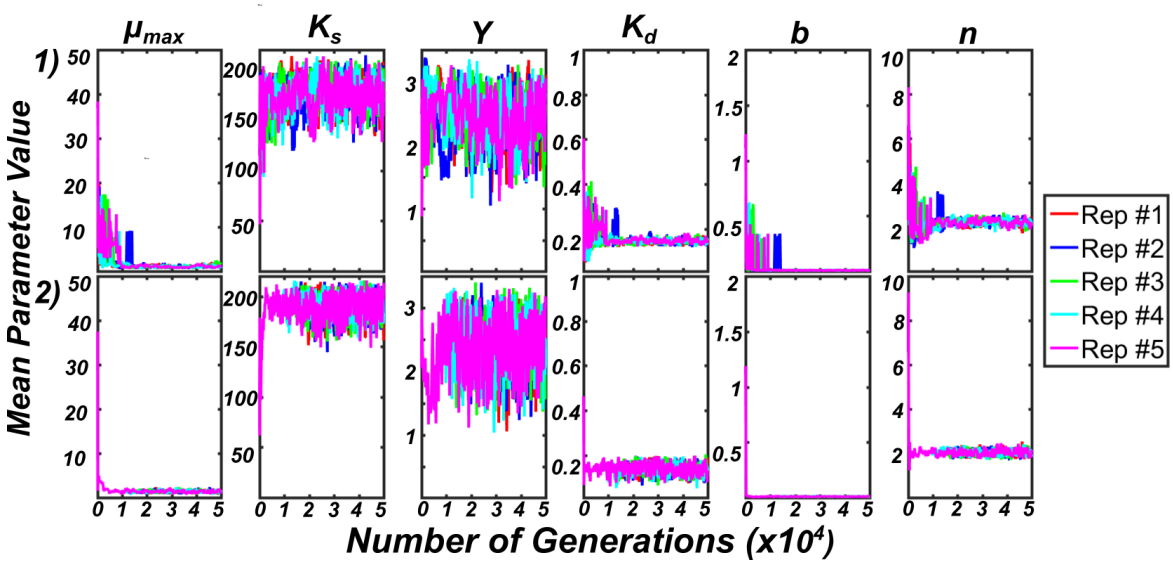

Figure D6. *Evolution of the mean (across all Markov chains) parameter values for both the 1) DREAM-ZS (Gaussian Likelihood) and 2) the DREAM-ZS (ABC) algorithms when calibrated against the Moser model using the first experimental dataset. The results of five independent repetitions are presented, as differentiated by the color scale of the legend.*

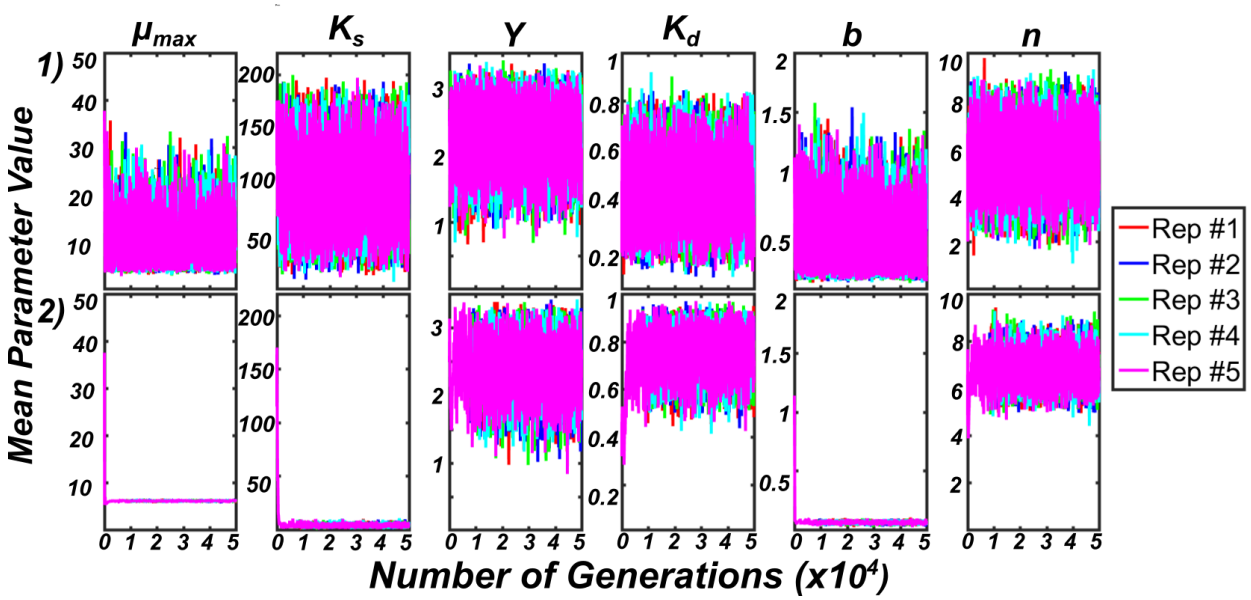

Figure D7. *Evolution of the mean (across all Markov chains) parameter values for both the 1) DREAM-ZS (Gaussian Likelihood) and 2) the DREAM-ZS (ABC) algorithms when calibrated against the Moser model using the second experimental dataset. The results of five independent repetitions are presented, as differentiated by the color scale of the legend.*

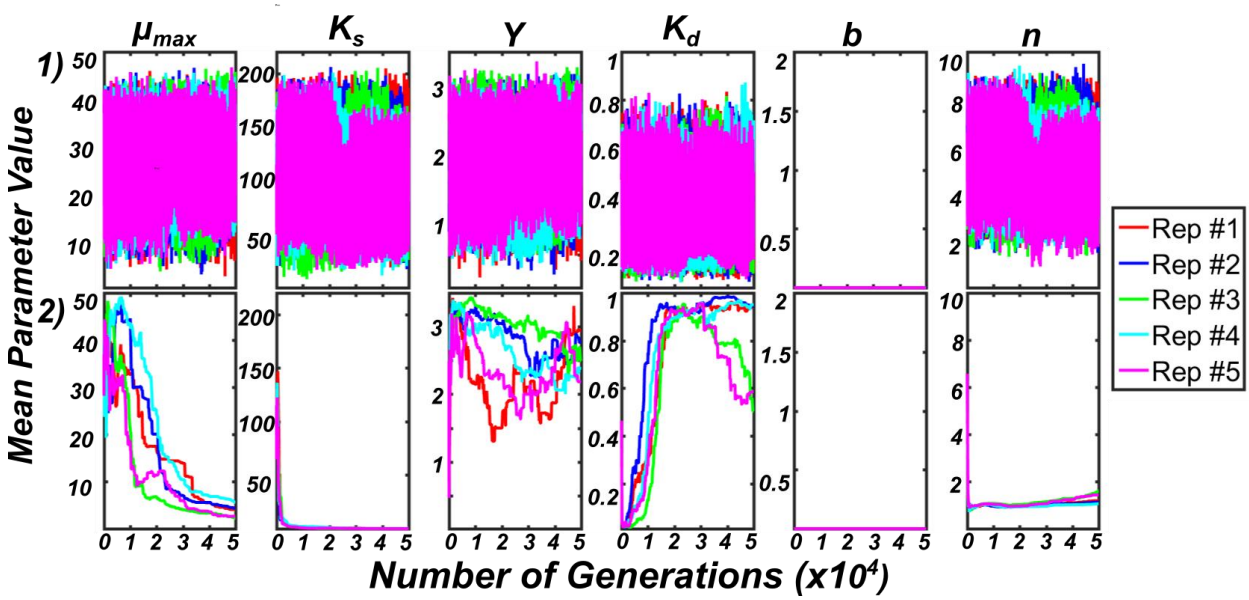

Figure D8. *Evolution of the mean (across all Markov chains) parameter values for both the 1) DREAM-ZS (Gaussian Likelihood) and 2) the DREAM-ZS (ABC) algorithms when calibrated against the Moser model using the third experimental dataset. The results of five independent repetitions are presented, as differentiated by the color scale of the legend.*

Appendix E: *A Reliable and Efficient Semi-Parametric Approach to Moment Independent Global Sensitivity Analysis Based on Copulas* – Supplementary Materials

I. Supplementary Results and Methods

1. Rolling Pin Method: Maximum Likelihood Optimization

In this section of the dissertation, we briefly describe the details behind the maximum likelihood (ML) optimization to learn the monotonization variables required by the Rolling Pin method. It is important to note that the learning of these parameters was particularly fast using any global optimization approach, with complexity O(d^2) (where d is the dimension of the problem) (Mohseni Ahooyi et al. 2014). The ML method simultaneously optimizes the monotonization parameter for each transformed model output according to Equation 1, where *c()* represents the copula probability density function taking as input the CDF values (F_y/F_x) of model input and output and f_y/f_x signify the marginal PDF values of the output and inputs, respectively. In this example, α_1 is being optimized (as $\alpha_2 = 0$ for the reference variable) for the pairwise dependency between Y_i (model input) and X_i (model output) over k number of samples. Equation 1 is summed over i ranging from 1 to the number of dimensions (d) considered in the model to obtain the total log-likelihood, where different values of α_1 are considered for each dimension.

$$\ln\big(L(\alpha_1)\big) = \sum_{k=1}^{n} \ln(c(F_{Y,i}(Y_{i,k}), F_{X,i}(X_{i,k}))) + \sum_{k=1}^{n} \left[\ln\left(f_{yi}\big(Y_{i,k}\big)\right) + \ln\left(f_{xi}\big(X_{i,k}\big)\right)\right] + n[\ln(1-\alpha_1) + \ln(1-\alpha_2)] \quad (1)$$

The LSHADE-EpSin algorithm, developed by Awad et al. (2016) was selected in this study to perform the ML optimization procedure. LSHADE-EpSin is based on the theory of differential evolution or metaheuristics, in which a population of individuals (potential solutions to an optimization problem) are evolved based on their fitness and random

probabilities of acceptance and or mutation (i.e., control parameters). The LSHADE algorithm exploits a novel adaptation of the control parameters by using two sinusoidal formulas, one fixed decreasing adjustment and an adaptive history based increasing adjustment to achieve quick convergence to the global optimum solution (Awad et al. 2016). The algorithm was set to run for a maximum of 20,000 function evaluations with an initial population size of N = 50. Convergence was reached when either the maximum number of function evaluations was exceeded or the range of the fitness values for the entire population was less than 1E-06 (usually around 10-12K function evaluations). All other control parameters and algorithm settings were identical to those specified in Awad et al. (2016).

The objective function for running the ML optimization approach required an approximation of the CDF and PDF of the model output and inputs (Fy(Y), Fx(X), fy(Y), fx(X)). The CDFs were used to fit a parametric copula to estimate a copula density, as required in Equation 8 (in Chapter 6). Fitting of the parametric copula was achieved using a modified maximum likelihood approach (described in Section 2.1.3). The PDF estimates were used directly in Equation 8 (Chapter 6) for both model inputs and outputs, alike. Both CDFs and PDFs for the model outputs were estimated using a well-established, accurate, and computationally efficient kernel density estimation method (Botev et al. 2010). The method developed by Botev et al. (2010) is an improved KDE method that can account for distributions that may be highly skewed or multi-modal. It is important to note that the input variables followed a standard normal distribution; therefore, they did not require KDE using the method developed by Botev et al. (2010).

2. Fitting of the Parametric Copula Models: Canonical Maximum Likelihood Approach

A canonical maximum likelihood estimation (CMLE) method, which is provided as a routine in MATLAB's statistics toolbox (r2015b), was ultimately used for fitting each parametric copula model to the QMC training points originally selected in Step 1, Figure 48 of Chapter 6. This method is termed "canonical" as it relies on CDF values from each variate that were estimated non-parametrically (using a KDE approach). The CMLE method relies on finding the optimal value of the parametric copula parameter (θ_{opt}) through maximization of the log-likelihood of the copula density function, $c(u_{1,}u_2;\theta)$, where, the value of θ is limited to the ranges defined in Table 1 in the main manuscript (Equation 2). The copula density function for the Frank copula is presented in Equation 3 as an example (Charpentier et al. 2007). MATLAB's built in *fminbnd* algorithm (using default tolerances, maximum function evaluations, and iterations), which relies on golden section search and parabolic interpolation (Forsythe et al. 1977, Brent 2013), was used to fit the parametric copula to the QMC training samples. This particular algorithm has proved very effective for maximum log likelihood optimization of nonlinear functions with a single parameter.

$$\theta_{opt} = \arg\max_{\theta\in\Theta} \sum_{i=1}^{n} \log\left[c(u_{1,}u_2;\theta)\right] \tag{2}$$

$$c\left(u_{1,}u_2;\theta\right) = \frac{\theta(1-e^{-\theta})e^{-\theta(u_1+u_2)}}{\left[(1-e^{-\theta})-(1-e^{-\theta u_1})(1-e^{-\theta u_2})\right]^2} \tag{3}$$

3. General Procedure for Sampling from the Parametric Copula Models

The elliptical copulas (i.e., Gaussian and t distributions) were sampled using the inverse cumulative distribution function method. This procedure involved sampling from a multivariate normal or t-distribution, using the model parameters (correlation matrices (Σ) and degrees of freedom (ν)) obtained from the previous step. First, MATLAB's multivariate normal (*mvnrnd*) or t random sampling functions (*mvtrnd*), which rely on the Cholesky

decomposition of the correlation matrix for sampling, were utilized for initially sampling from these distributions. Then, the inverse normal or t-distribution functions (*norminv* or *tinv*) were used to compute the copula CDF values, which were the targeted outputs of the sampling procedure.

The conditional distribution method (CDM), which is available as a MATLAB routine, was implemented to sample from each parametric copula. The CDM algorithm, which is also conveniently built into MATLAB's statistics toolbox, relies on a closed form of the inverse conditional CDF of each parametric copula (Equation 4). The three steps for implementing the CDM algorithm were as follows (Joe 1997, Nelsen 2007):

1) Generate two independent, standard uniform variates u_1 and t;
2) Use the closed form, inverse of the conditional CDF derived (i.e., for the Frank copula) (Equation 4) to generate samples from the copula CDF: $v = \emptyset^{-1}(u_1, t)$;

$$\emptyset^{-1}(u_1, t) = -\frac{1}{\theta} log\left[\frac{((e^{-\theta u_1})\left(\frac{1-t}{t}\right)+e^{-\theta})}{(1+e^{-\theta u_1}\left(\frac{1-t}{t}\right))}\right] \quad (4)$$

3) The pair (u_1, v) is now a sample from the parametric copula.

4. Alternative Procedures for Sampling from the Parametric Copula Models

Several alternative parametric copula sampling methods (other than the inverse conditional distribution method (CDM)) were compared in this study to improve the accuracy and convergence efficiency. The alternative methods investigated can be classified into approaches that sample directly from the copula as well as those that re-sample from the samples already obtained from the copula. For the Archimedean copulas, both classes of sampling methods were implemented. However, only the re-sampling class of alternative

methods were implemented for the elliptical copulas. In this section, we review the sampling algorithms for the alternative methods investigated in this study.

Under the class of approaches sampling directly from the copula model, we reviewed two alternative sampling schemes, including: 1) the quasi Monte Carlo (QMC)-CDM approach (as opposed to pseudo random sampling-CDM) and 2) the Marshall-Olkin approach. The QMC-CDM method was identical to the CDM method described in the main manuscript, instead QMC samples were selected instead of pseudo random samples. Importantly, the QMC sample range that was selected for constructing and training the copula model were ultimately used for sampling. The Marshall-Olkin (MO) approach defines a class of sampling algorithms that were expected to sample more efficiently from the Archimedean class of copulas as compared to the CDM approach (Joe 1997, Marshall and Olkin 1988, 1997, Hoefert 2008). The MO approach relies on the inverse Laplace-Stieltjes transform ($LS^{-1}(\psi)$) of the Archimedean generator functions ($\psi(t)$) for the Clayton, Gumbel, and Frank copula families (Joe 1997; Marshall and Olkin 1988, 1997; Hoefert 2008). The following three steps demonstrate how the MO algorithm is implemented, which applies to each copula family (i.e., Clayton, Frank, Gumbel):

1) Sample $V \sim F = LS^{-1}(\psi)$
2) Sample uniform, independently distributed numbers $X_i \sim U[0,1]$ $i \in \{1,..d\}$
3) Return (U_1, .., U_d) after evaluating $U_i = \psi\left(-log\left(\frac{X_i}{V}\right)\right)$ $i \in \{1,..d\}$

The corresponding Archimedean generator functions (ψ) as well as the inverse Laplace Stieltjes transform (LS^{-1}) previously derived for each parametric copula family are presented in Table E1 for reference. In addition, the domain over which the MO algorithm

will work (i.e., acceptable θ values) are summarized in Table E1. For the Clayton family, *V* is a randomly generated sample from the Gamma probability distribution with shape factor of $\frac{1}{\theta}$ and a scale parameter equal to unity. For the Frank family, *V* is a randomly generated sample from the log series distribution (discrete), where the parameter of this distribution is as follows: $\left(1-e^{-\theta}\right)$. Lastly, for the Gumbel family, V is a randomly generated sample from the Stable probability distribution with α, β, γ, and δ equal to $\frac{1}{\theta}$, 1, $\cos\left(\frac{\pi}{2\theta}\right)^{\theta}$, and 0, respectively. It is important to note that θ can only take on positive values (nonzero for the Gumbel family) for this sampling algorithm to be effective.

Table E1 *– Summary of inverse Laplace-Stieltjes transforms and generator functions for the Archimedean copula families investigated in this study.*

Family	**θ**	$\boldsymbol{\psi(t)}$	**F**
Clayton	(0,∞)	$(1+t)^{-\frac{1}{\theta}}$	$\Gamma(\frac{1}{\theta},1)$
Frank	(0,∞)	$-\frac{1}{\theta}\log(e^{-t}\left(e^{-\theta}-1\right)+1)$	$y_k=\frac{(1-e^{-\theta})^k}{k\theta}\ k\in\aleph$
Gumbel	[1,∞)	$e^{-t^{\frac{1}{\theta}}}$	$S(\frac{1}{\theta},1,\cos\left(\frac{\pi}{2\theta}\right)^{\theta},0)$

Under the class of re-sampling techniques, we investigated a density re-sampling approach initially presented by Kurowicka and Cooke (2006). After first sampling from the copula using the pseudo-random CDM approach, a new population is obtained from re-sampling based on the probability density of the copula model. The following steps indicate how this algorithm is implemented:

1) Obtain N samples from the copula model using the pseudo-random CDM approach (where $N = 4*N_{evalpts}$ in our study)

   Note that the $N_{evalpts}$ was the number of QMC samples originally used to construct the copula

2) Determine the probability density of the N samples using MATLAB's *copulapdf*

3) Calculate the weights for re-sampling using the Equation 5 below:

$$w_i = \frac{c(u_i,v_i)}{\sum_{i=1}^{N} c(u_i,v_i)} \quad (5)$$

4) Use a weighted re-sampling approach without replacement and return $N_{evalpts}$ samples (this can be accomplished using MATLAB's built in *datasample* function).

This approach is similar to importance sampling in that it is re-sampling from areas of the density that have higher associated probability. However, this sampling method may not fully consider the magnitude of variance reduction that may be achieved to ultimately improve the approximation accuracy and convergence efficiency of the Monte Carlo integration regarding the shifts in probability densities between the unconditional/conditional distributions.

As presented in the Materials and Methods section of Chapter 6 (section 2), each sampling method was run for the following range of initial Sobol QMC samples (using the same sequence starting point): 2^8, 2^9,2^{10},2^{11},2^{12},2^{13},2^{14},2^{15},2^{16}, and 2^{17} in which 10 independent runs were performed for each method to assess the statistical precision. For each sampling method, the number of points sampled was equivalent to the range in initial Sobol QMC samples used to construct and train each parametric copula model. The accuracy of each approach was benchmarked using the absolute error (ABE), calculated between the approximate analytical solution ($\delta_{i,A}$) and the solution obtained after each run ($\delta_{i,E}$) (Equation 12, Chapter 6). The precision of each approach was assessed using the standard deviation of all delta indices acquired across runs (Equation 13, Chapter 6).

5. Summary of Approximate Analytical Solutions

Table E2 *– Summary of the approximate analytical solutions determined for each test function and corresponding input variable.*

Test Function	Variable 1	Variable 2	Variable 3	Variable 4	Variable 5	Variable 6
1	0.1192	0.1283	0.1377	0.1474	0.1574	0.1678
2	0.4319	0.1547	0.0889	0.03368	0.02413	0.01705
3	0.3169	0.4319	0.2872	-	-	-

6. Comparison of Overall Parametric Copula Goodness of Fits

The ability of 5 representative parametric copulas and 1 empirical copula to model the dependency structure between the original model input parameters and output (for all test functions) was compared through application of the well-known copula calibration approach developed by Genest and Rivest (1993). This approach compares the distance between an empirical Kendall distribution function (KDF) and that derived/estimated by the respective parametric copula method. The KDF describes the cumulative probability that a random selection from a given parametric copula function will be less than or equal to a given variable t (on the unit range, 0 to 1) (Genest and Rivest 1993).

$$K(t) = P[C(U,V) \leq t] \tag{6}$$

Initially, this approach relies on construction of an empirical KDF for the model input-output dependency under consideration. As detailed in Genest and Rivest (1993), the empirical KDF is computationally derived as described in the following steps.

- For i = 1 to n (number of samples), Z_i was computed as the proportion of observations in the lower quadrant, with upper corner (X_i, Y_i) (Equation 7).

$$Z_i = \frac{1}{n-1}\sum_{j \neq i} 1(X_j < X_i, Y_j < Y_i) \tag{7}$$

- The upper corner, (X_i, Y_i) was changed, n number of times and the empirical distribution function (MATLAB, r 2015b) was used to estimate the empirical KDF ($K_E(t)$) using the Z_i values as a basis of calculation.

Next, the parametric KDF ($K_V(t)$) for the model input-output dependency was calculated for comparison against the empirical KDF (Equation 8). This calculation required knowledge of the lambda function for each parametric copula ($\lambda(t)$), which is simply the Archimedean generator function normalized by the inverse of the Archimedean generator function ($\lambda(t) = \frac{\varphi(t)}{\varphi^{-1}(t)}$). Genest and Rivest (1993) have presented several derivations of the lambda function ($-\lambda(t)$) for the Frank, Gumbel, and Clayton Archimedean copulas, which were applied in this study (Table E3).

$$K_V(t) = t - \lambda(t) \tag{8}$$

To calculate the parametric KDF, first Kendall's tau was estimated to describe the relative strength of correlation between the model input parameter(s) and model output. Then, the conversion presented in Table E3 was used to estimate the θ parameter corresponding to each parametric copula model. Finally, given a range in t values (0 to 1), the parametric estimate of the KDF ($K_V(t)$) was reached using Equation (8) and the lambda functions previously derived in Table E3.

For the elliptical copulas (Student's t and Gaussian), no explicit generator or inverse generator function is known or presented in the literature ($\varphi(t)$) (Table E3). Therefore, the "parametric" estimates of the KDFs for these particular copulas were determined using a sampling-based methodology. For the Gaussian copula, Kendall's tau was first estimated to describe the dependency between model input parameter(s)/output and converted to

Pearson's linear correlation coefficient for use in the sampling procedure. The Gaussian copula was then sampled, *n* number of times (in this case *n* = 256, 4096, 16384) by applying the multivariate normal random number generator (in this case bi-variate) available in MATLAB (r2015b) and calculating the normal CDF values of these estimates. A comparable sampling procedure was employed to estimate the parametric KDF for the Student's t copula. Briefly, a Student's t copula was fit (to estimate linear correlation coefficient, ρ and ν values) using the maximum likelihood approach described in the manuscript. Again, the Student's t copula was then sampled, *n* number of times (*n* = 256, 4096, 16384) by applying the multivariate *t* random number generator (bi-variate) available in MATLAB (r2015b) and calculating the *t*-distributed CDF values of these estimates.

Table E3 *– Summary of lambda functions and Kendall's $\tau/\theta/\rho$ relationships for the Archimedean copulas used in this study.*

Family	$-\boldsymbol{\lambda}(\boldsymbol{t})$	$\boldsymbol{\tau}$
Frank	$\frac{1-e^{(-\theta t)}}{\theta e^{(-\theta t)}}\log\left[\frac{1-e^{(-\theta)}}{1-e^{(-\theta t)}}\right]$	$1+4\frac{\{D_1(\theta)-1\}^*}{\theta}$
Gumbel	$\frac{-tlog(t)}{(\theta+1)}$	$\frac{\theta}{(\theta+1)}$
Clayton	$\frac{t(1-t^{\theta})}{\theta}$	$\frac{\theta}{(\theta+2)}$
Student's t	N/A	N/A
Gaussian	N/A	$\frac{2}{\pi}\arcsin(\rho)$

*D_1 stands for the Debye function of order, $D_1(\theta) = \int_0^{\theta}\left\{\frac{t}{\theta(e^t-1)}\right\}dt$

A non-parametric copula method was incorporated to further compare the ability of both parametric and non-parametric methods to model the dependencies between model input parameter(s) and output. Similar to the method presented in Wei et al. (2014), a 2D kernel density estimation (KDE), relying on the method of Botev et al. (2010) was used to empirically model the dependency structure. First, the CDF values were calculated for each

variate, and a 2D KDE was constructed. Next, the 2D KDE was sampled, *n* number of times (*n* = 256, 4096, 16384) using a 2D discrete probability distribution sampling approach, given that the returned estimates from Botev et al. (2010) were not continuous in nature (Ursell 2016). Lastly, a non-parametric KDF estimate ($K_{E2}(t)$) was constructed from the samples obtained in the previous step using the computational method described above.

Ultimately, the goodness of fit of each copula model was assessed through application of the Cramér-von Mises distance between the empirically estimated KDF and the parametric/non-parametric estimated KDFs (Equation 9) (Genest and Rivest 1993, Genest et al. 2009). In general, large values of the CM distance implicated poor overall copula fits, whereas small values of the CM distance indicated improved copula fits to the dependency structure. In this study, we compared the CM metrics obtained from each copula fit for the three preliminary test functions described in the manuscript. A total of ten independent realizations were used to assess the variability of the CM fitting metrics. In addition, three different sampling numbers (*n* = 256, 4096, 16384) were chosen to evaluate how these metrics changed with an increasing number of quasi Monte Carlo samples. Importantly, we ran the goodness of fit analyses using the *transformed* variables as a basis for comparison (using the Rolling Pin method). This required running the MLE optimization scheme described in the manuscript multiple times (10 times for each sampling number) to determine the optimal monotonization parameters for each of the different Parametric copula models. The optimized monotonization parameters were then applied to transform the variables before each Parametric copula was fit. It is important to note that the variables were not monotonized for the non-parametric copula model described above before testing the goodness of fit.

$$CM = \int_0^1 \left[\sqrt{n} * (K_v(t) - K_E(t)\right]^2 \quad (9)$$

Qualitative results for this fitting procedure are presented in Figure E1 below, which compares the GOF for the Frank, Clayton, Gumbel, t-distribution, Gaussian, and non-parametric copulas (for n = 4096, most sensitive model inputs). As observed in Figure E1, the Frank and t-distribution copulas produced excellent fitting results for the three test problems investigated. In addition, the non-parametric method demonstrated a similar performance to these parametric copulas. The Clayton and Gumbel copulas struggled to provide optimal fits for most of the test problems investigated, whereas the Gaussian copula demonstrated some inherent variability on the last test problem. It is also important to note that the variability associated with many of the parametric copulas was relatively insignificant, as the 95% confidence intervals were narrow for many of the test problems investigated. In addition, as the test functions progressed, the dependence of each copula on the monotonic transformation provided by the Rolling Pin method seemed to increase. In general, the KDF appeared more linear for test function 3 as compared to more nonlinear for test functions 1-2. This result is directly related to the magnitude of the monotonization parameters, which increased in magnitude from the initial to the final test problem.

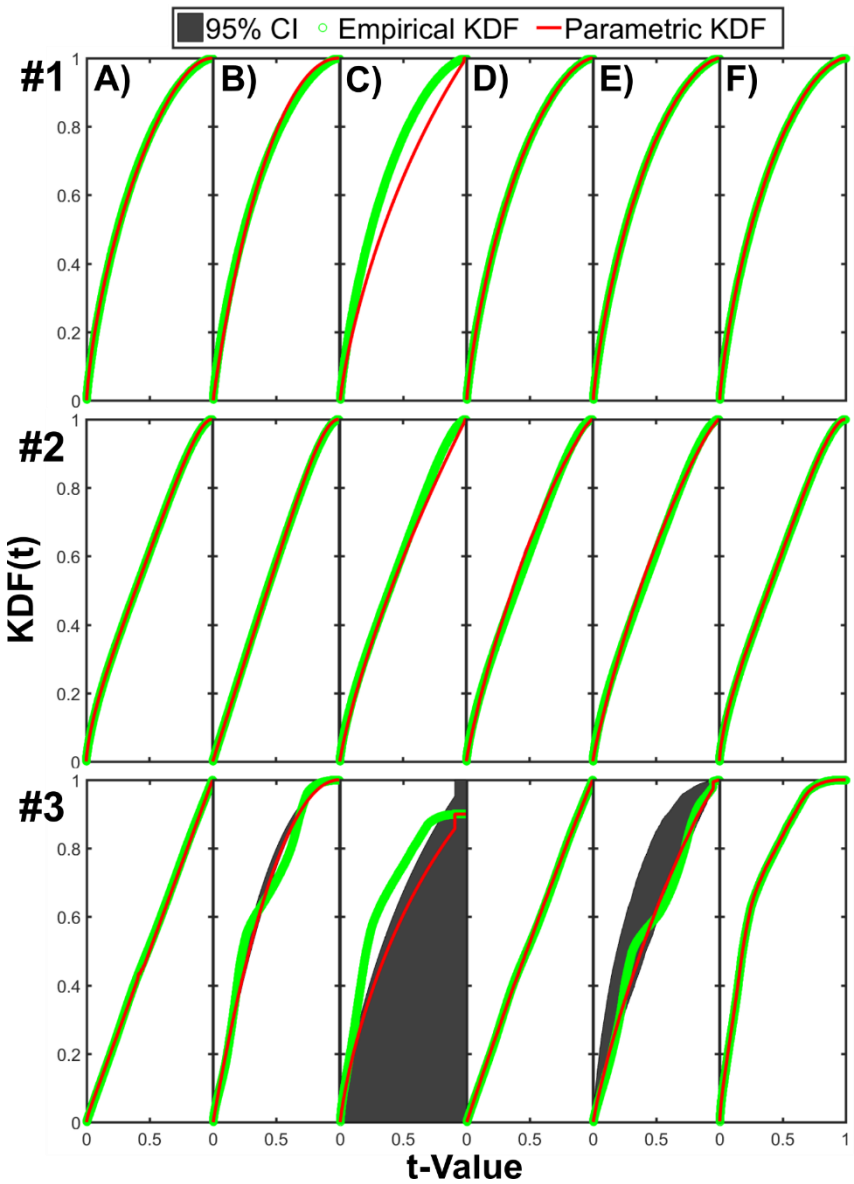

Figure E1. *Copula GOF test results portraying the qualitative fit of the parametric KDF (red lines) to the empirical KDF (green circles). Results are depicted for the most influential input variable (X_1, X_1, X_2) model output combination for each of the three test problems reviewed. The number of QMC samples used to construct each plot was set to n = 4096. The columns depict the fitting results from the following copulas: a) Frank, b) Clayton, c) Gumbel, d) t-distribution, E) Gaussian, and F) the non-parametric method.*

7. Comparison of Parametric Copula Tail Dependence

The tail concentration function is a suitable technique to compare how well each parametric copula can fit the tails of the bivariate dependency structure between the model input(s) and output. Joe (1990) was the first to suggest the use of a strong tail dependence index (λ) for evaluating the tail fits of parametric copulas, differentiating between both lower and upper tail dependence. For both the lower and upper tail fits, the definition of the tail dependence index varies, where *C(u, u)* is the copula CDF and *C*(1-u,1-u)* is the survival copula associated with the copula CDF (Equations 10 and 11).

$$\lambda_L = \lim_{u \to 0} \frac{C(u,u)}{u} \tag{10}$$

$$\lambda_U = \lim_{u \to 0} \frac{C^*(1-u,1-u)}{1-u} \tag{11}$$

The empirical estimation of the λ tail concentration functions ($TCF_{L,E}$ *or* $TCF_{U,E}$) above provides the first basis for comparison of the tail fitting performance among the bivariate parametric copulas investigated in this study. Equations 10 and 11 can be estimated empirically through use of the following sampling procedure. First, the empirical copulas were constructed from the transformed model input(s) (V) and output data (U) (where d empirical copulas are constructed). Next, Equations 12 and 13 were used to estimate the empirical lower and upper tail concentration functions. Here, *Zi* is an incremental copula CDF value, ranging from 0 to 1. Ultimately, the tail concentration function is evaluated over n, uniformly spaced points (Zi) between 0 and 1 (in our study, n = 10,000).

$$TCF_{L,E} = \frac{\sum_{i=1}^{n} 1[U_i \leq Z_i \,\&\, V_i \leq Z_i]}{\sum_{i=1}^{n} 1[U_i \leq Z_i]} \tag{12}$$

$$TCF_{U,E} = \frac{\sum_{i=1}^{n} 1[U_i \geq 1-Z_i \,\&\, V_i \geq 1-Z_i]}{\sum_{i=1}^{n} 1[U_i \geq 1-Z_i]} \tag{13}$$

Parametric estimation of the λ tail concentration functions $TCF_{L,A}$ *or* $TCF_{U,A}$) was conducted in addition to the empirical method as a second step for evaluating the tail fitting performance. Similar to the Kendall distribution function estimation, Kendall's tau was first estimated between the transformed model input(s) and output. This procedure then involved determination of the parametric copula parameter value(s) using the relationship between Kendall's tau and Spearman's rho (for Gaussian only), the previously fitted values of rho and nu (for the t copula only), or the unique relationship between Kendall's tau and the parameter θ for all the Archimedean copulas investigated (Table E3). The parametric tail concentration functions were then evaluated for n number of equidistributed points between 0 and 1 (u) through application of Equations 14 and 15 below. The equations describing the copula CDF ($C(u, u)$) for each parametric copula investigated in this study are presented in Table 15 in Chapter 6 for reference.

$$TCF_{L,A} = \frac{C(u,u)}{u} \tag{14}$$

$$TCF_{U,A} = \frac{1-2(1-u)+C(1-u,1-u)}{(1-u)} \tag{15}$$

A non-parametric tail concentration function using techniques implemented by Wei et al. (2014) was further derived for comparison against the parametric methods. The non-parametric tail concentration function was derived through application of a 2D KDE approximation method by Botev et al. (2010), which was also applied in Wei et al. (2014). However, since the 2D KDE approximation estimated the copula PDF (or density) of the dependency structure, it was numerically integrated (in two dimensions) using MATLAB's *cumtrapz* function to arrive at a non-parametric estimate of the copula CDF ($C(u, u)$). The copula CDF was then estimated through interpolation (MATLAB's interp2d, nearest neighbor setting), using the integration results as baseline points and the equidistributed u

or 1-u values as query points. Finally, the tail concentration functions were approximated using Equations 8 and 9 above. It is important to reiterate that for the non-parametric tail concentration function, the model output was not transformed, similar to that presented above for the non-parametric estimate of the Kendall distribution function.

The overall tail fit (combining both the upper and lower tails) of each copula model was assessed through application of a modified Cramér-von Mises distance calculation, as initially presented in Durante et al. (2015) (Equation 16). Again, large values of the CM_{TCF} distance implicated poor tail fits, whereas small values of the CM_{TCF} distance indicated improved copula tail fits. Similar to section 1 above, we compared the $CM_{TCF\ metrics}$ obtained from each copula fit for the three preliminary test functions described in the manuscript. A total of ten independent realizations were used to assess the variability of the CM_{TCF} fitting metrics. In addition, three different sampling numbers (n = 256, 4096, 16384) were chosen to evaluate how these metrics changed with an increasing number of quasi Monte Carlo samples. Importantly, we ran the tail fit analyses incorporating the *transformed* variables as a basis for comparison (using the Rolling Pin method) of the parametric copula models. We simply applied the results achieved previously for the monotonization parameters to development of the tail concentration functions described herein.

$$CM_{TCF} = \int_0^1 [(\lambda_E - \lambda_A)]^2 \tag{16}$$

Qualitative results of the tail fitting procedure for all three test problems are presented in Figure E2 for reference. These plots portray the mean empirical TCF overlaid with the mean parametric TCF, along with the 95% confidence intervals achieved from ten independent realizations. As observed in Figure E2, the tail GOF (for both the lower, left side, and upper, right side) varied greatly across test functions. For Test Case 1, the Clayton

and Gumbel copulas overestimate the empirical TCF for the lower and upper tails of the dependency structure. In addition, the non-parametric copula method exhibited great difficulty when trying to replicate both the lower and upper tails of the dependency structure (for both Test Case 1 and 2); however, the non-parametric method greatly improved the tail GOF for Test Case 3, which caused the greatest difficulty in tail GOF for all copulas (i.e., wide 95% CI, Figure E2). The results for Test Case 2 demonstrated that the Clayton copula was able to accurately reproduce the asymmetry existing in the lower tail, whereas the Gumbel copula reproduced the high tail dependencies in both the upper and lower tails for Test Case 3 (Figure E2). Both the t-distribution and Frank copulas were able to replicate the tail dependencies across a wide range in test functions (Figure E2).

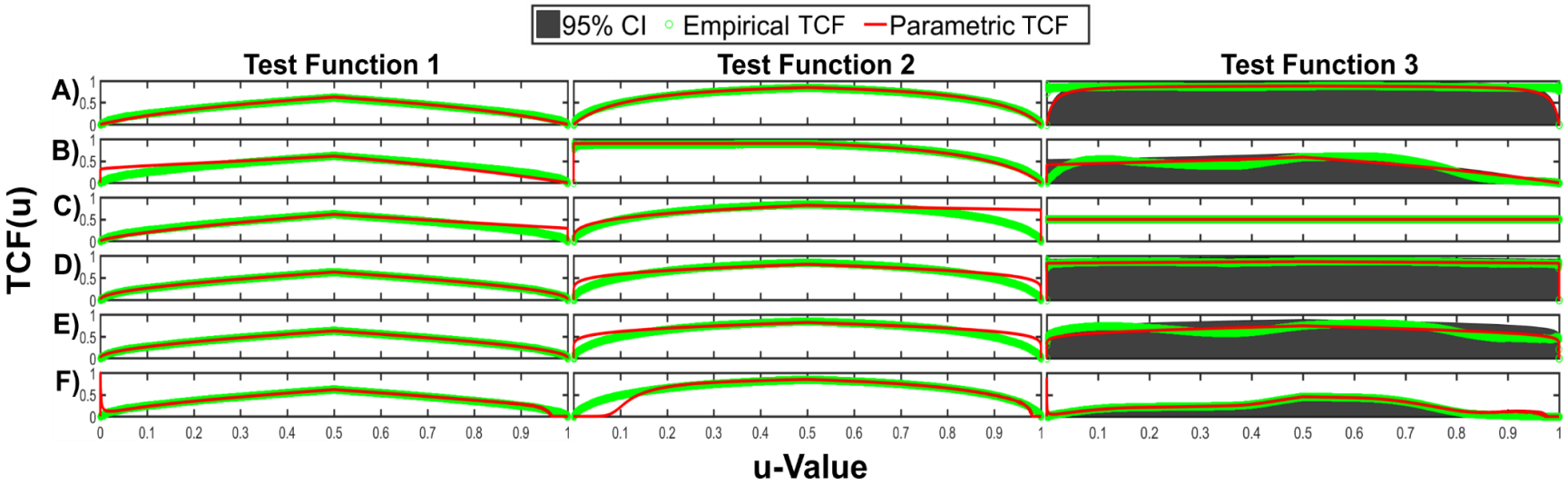

Figure E2. *Copula tail GOF test results portraying the qualitative fit of the parametric TCF (red lines) to the empirical TCF (green circles). Results are depicted for the most influential input variable (X_1, X_1, X_2) model output combination for each of the three test problems reviewed. The number of QMC samples used to construct each plot was set to n = 4096. The rows depict the fitting results from the following copulas: a) Frank, b) Clayton, c) Gumbel, d) t-distribution, E) Gaussian, and F) the non-parametric method.*

8. Evaluation of Parametric Copula Symmetry

The symmetry of the dependency structure formed between the model input(s) and output was further examined as yet another potential opportunity to improve the parametric copula fits. In general, the parametric copula models (including the Archimedean and Elliptical families) assume that the dependency structure under review is symmetric in nature. Symmetry is often defined by mathematically reviewing the concept of exchangeability, where variables are deemed exchangeable if the order of the dependency structure has little effect on the copula cumulative density evaluation (i.e., $C(u, v) = C(v, u)$) (Liebscher 2008, Durante 2009, Genest et al. 2012). There are ample statistical techniques available in the literature to determine if the dependency between two variables are symmetric or not, including the method introduced by Genest et al. (2012). This method depends on comparing a modified Cramér-von Mises distance statistic, similar to the GOF and TCF testing introduced above. Briefly, a sample of size n is obtained from each parametric copula and the empirical copula is formed for $C_n(u, v)$ and $C_n(v, u)$. Next, the S_n value (which was chosen considering its strength as determined in Genest et al. 2012) can be calculated according to Equation 17 below, which measures the degree of similarity between both empirical copula distributions (where smaller values are indictive of more symmetric dependencies between variables). In this case, S_n represents a rank-based analogue of the Cramér-von Mises statistic (Genest et al. 2012).

$$S_n = \int_0^1 \int_0^1 \{C_n(u, v) - C_n(v, u)\}^2 \, dC_n(u, v) \tag{17}$$

A novel Monte Carlo method introduced by Genest et al. (2012) was adopted in this study to assess the statistical significance of the modified Cramér-von Mises test statistic, S_n for each input variable-output combination (see Genest et al. 2012 for full details). This

method relies on an innovative bootstrap resampling approach to calculate S_n and returns a P-value to compare with any given statistical significance level. The null hypothesis assumed that the dependency between variables u and v was symmetric, where P-values below the 0.05 significance level were deemed statistically significant to conclude asymmetric dependence between both variables. The algorithm presented in Genest et al. (2012) was run for M = 1,000 bootstrapped resamples for test functions 2 and 3 only, which qualitatively showed some potential asymmetry, using the best performing Frank parametric copula. Importantly, the transformed model output-input dependency was used in this analysis of symmetry. To obtain some idea of how the symmetry may change when the sample size increases, we varied the number of samples (n = 256, 4096, and 16384) for all ten independent realizations and recorded the average S_n and P-values for comparison.

Aside from evaluating the statistical significance of the symmetry between both model inputs and output, we compared the performance of an asymmetrized version of the Frank copula to the unmodified version when computing MI sensitivity indices. An asymmetrized version of the Frank copula was derived using the Khoudraji transformation as defined in Vandenberghe et al. (2010) and Genest et al. (1998). First, the asymmetric copula family of Durante (2009) was selected as the basis for this transformation, as shown in Equation 18 below. This asymmetric family is composed of a multiplicative combination of two copula functions, C_1 and C_2, where two additional tuning parameters are introduced (α and β). The Khoudraji transformation is applied by simply inserting the independence copula for C_1 and the Frank copula for C_2, forming Equation 19 below, where the generator function and inverse generator function correspond to that of the Frank copula. Equation 19 contains a third parameter, θ, that describes the dependency between the two variables,

similar to the original θ parameter used in the Frank copula. The parameters α and β are restricted to the range [0,1], with the following condition: $\alpha \neq 0.5, \beta \neq 0.5$, while the range for the θ parameter is the following: $(-\infty, \infty)$.

$$C_{\alpha,\beta}(u,v) = C_1(u^{\alpha}, v^{\beta})C_2(u^{1-\alpha}, v^{1-\beta}) \quad (18)$$

$$C(u,v) = u^{\alpha}v^{\beta}\varphi^{-1}(\varphi(u^{1-\alpha}) + \varphi(v^{1-\beta})) \quad (19)$$

Although the copula cumulative density is rather easy to derive analytically, the asymmetrized Frank copula density (which is used in the MI sensitivity calculation) was more challenging. To derive the copula density, we performed the mixed partial derivative with respect to model parameters *u* and *v* using *Mathematica* ($c(u,v,\theta,\alpha,\beta) = \frac{\partial^2 C(u,v,\theta,\alpha,\beta)}{\partial u \partial v}$) (similar method to that proposed by Vanderberghe et al. 2010). Importantly, the equation that was obtained from *Mathematica* was double-checked to ensure that the copula density was correctly derived before we incorporated it into the MI sensitivity calculations.

The asymmetrized copula was fit to the available data through application of a modified Canonical Maximum Likelihood approach. Instead of relying on the *MATLAB* optimization routine, we integrated the LSHADE-EpSin algorithm to determine the optimal parameters θ, α, β. Of course, with a more sophisticated parametric copula approach, as the dimension of the problem (i.e., the number of input variables) increases, the number of parameters also will increase (in this case the number of parameters tripled with an increase in dimension size). Thus, to improve efficiency, we solved for all required parameters simultaneously through a combined maximum likelihood optimization routine. Importantly, this procedure was performed directly after the Rolling Pin method, which used the monotonization parameters determined for the symmetric parametric copulas.

After determining the optimal parameters using a modified Canonical Maximum Likelihood approach, the asymmetric copula was sampled, and sensitivity indices determined using identical steps as described in Section 2.1 in the main manuscript.

To sample from the asymmetrized copula, the following algorithm, as recommended by Nelsen (2007), was adopted in this study. This algorithm is based on a "combination" approach by sampling each copula independently and then combining results using the maximum operator.

1) Sample two uniform random distributions (on the interval 0 to 1), u_1 and v_1 (this is the same approach for sampling from the independence copula)
2) Sample from the Frank copula using the dependency parameter theta derived during the fitting step to obtain u_2 and v_2 (here we used the CDM with pseudo random number generation)
3) Form two matrices, g_1 and g_2 below, by combining u_1, v_1, u_2, and v_2:

$$g_1 = [u_1^{\frac{1}{\alpha}}, u_2^{\frac{1}{(1-\alpha)}}] \; g_2 = [v_1^{\frac{1}{\beta}}, v_2^{\frac{1}{(1-\beta)}}]$$

4) Take the maximum value, row-wise, to end up with the final asymmetric copula samples, *u* and *v.*

9. Application of the Semi-Parametric Method to an Environmental Model

The MI sensitivity indices were estimated for the Moser model using the following simulation framework. First, the biodegradation simulations were performed assuming that microcystin was the main contaminant of interest (present at 25 mg/L), that isolated bacterial populations were available (present at 1 mg/L) and in sufficient physiological condition for biodegradation to commence, and that other environmental conditions, such

as optimal pH, temperature, as well as oxygen and nutrient availability were non-limiting. Next, the parameter ranges previously defined by Manheim et al. (2019) were used to restrict the feasible parameter space for μ_{max}, K_s, Y, n, and k_d model parameters. Lastly, the model simulations were run for a 10-day period (typical time period for complete biodegradation of MC to occur), where sampling for the determination of bacterial cell and substrate concentrations was conducted daily.

The semi-parametric copula method developed in this study was applied sequentially for each simulated time point and run independently for each variable (i.e., substrate or cell concentrations). As the Frank parametric copula demonstrated the most well-rounded GOF performance on each analytical test function investigated, it was employed to model the dynamic bivariate dependency structure between each model input parameter and model output.

10. Summary of Statistical Testing for Copula Symmetry

Table E4 *– Summary of S_n statistics and p-values for the copula symmetry testing (test problem 2). The first row of the table heading indicates the number of QMC samples (i.e., 256, 1024, and 4096), while the second row of the table heading indicates the input variables (i.e., 1-6). The symbols μ, σ, and COV refer to the mean, standard deviation and coefficient of variation of each metric calculated for ten independent realizations of the symmetry testing.*

Test		n = 256						n = 1024						n = 4096					
Statistic		1	2	3	4	5	6	1	2	3	4	5	6	1	2	3	4	5	6
S_n	μ	0.009	0.034	0.019	0.022	0.021	0.017	0.104	0.211	0.138	0.155	0.153	0.138	0.437	0.859	0.573	0.616	0.637	0.58
	σ	0.002	0.006	0.005	0.008	0.004	0.005	0.012	0.021	0.011	0.026	0.020	0.022	0.022	0.025	0.026	0.046	0.034	0.046
	COV	17	16	28	38	20	27	12	10	8	17	13	16	5	3	5	7	5	8
p-val.	μ	1.000	0.953	0.997	0.991	0.998	0.999	0.525	0.240	0.422	0.404	0.398	0.456	0.063	0.007	0.033	0.030	0.029	0.04
	σ	0.000	0.026	0.004	0.019	0.002	0.003	0.056	0.032	0.041	0.066	0.062	0.069	0.008	0.002	0.007	0.007	0.006	0.00
		0	5	1	4	8	4	7	2	3	6	7	3	1	9	3	1	2	97
	COV	0	3	0	2	0	0	11	13	10	16	16	15	13	42	22	24	22	23

Table E5 *– Summary of S_n statistics and p-values for the copula symmetry testing (test problem 3). The first row of the table heading indicates the number of QMC samples (i.e., 256, 1024, and 4096), while the second row of the table heading indicates the input variables (i.e., 1-3). The symbols μ, σ, and COV refer to the mean, standard deviation and coefficient of variation of each metric calculated for ten independent realizations of the symmetry testing.*

Test		**n = 256**			**n = 1024**			**n = 4096**		
Statistic		**1**	**2**	**3**	**1**	**2**	**3**	**1**	**2**	**3**
S_n	**μ**	0.0518	0.0034	0.0365	0.3015	0.0206	0.1133	0.3076	0.0923	0.4021
	σ	0.0774	0.0016	0.0315	0.3804	0.0010	0.0224	0.0089	0.0019	0.0105
	COV	149	48	86	126	5	20	3	2	3
p-value	**μ**	0.836	1.000	0.885	0.464	0.994	0.503	0.133	0.639	0.076
	σ	0.294	0.000	0.144	0.370	0.003	0.086	0.008	0.016	0.007
	COV	35	0	16	80	0	17	6	2	9

11. MI Sensitivity Index Convergence Plots: Analytical Test Functions 1-3

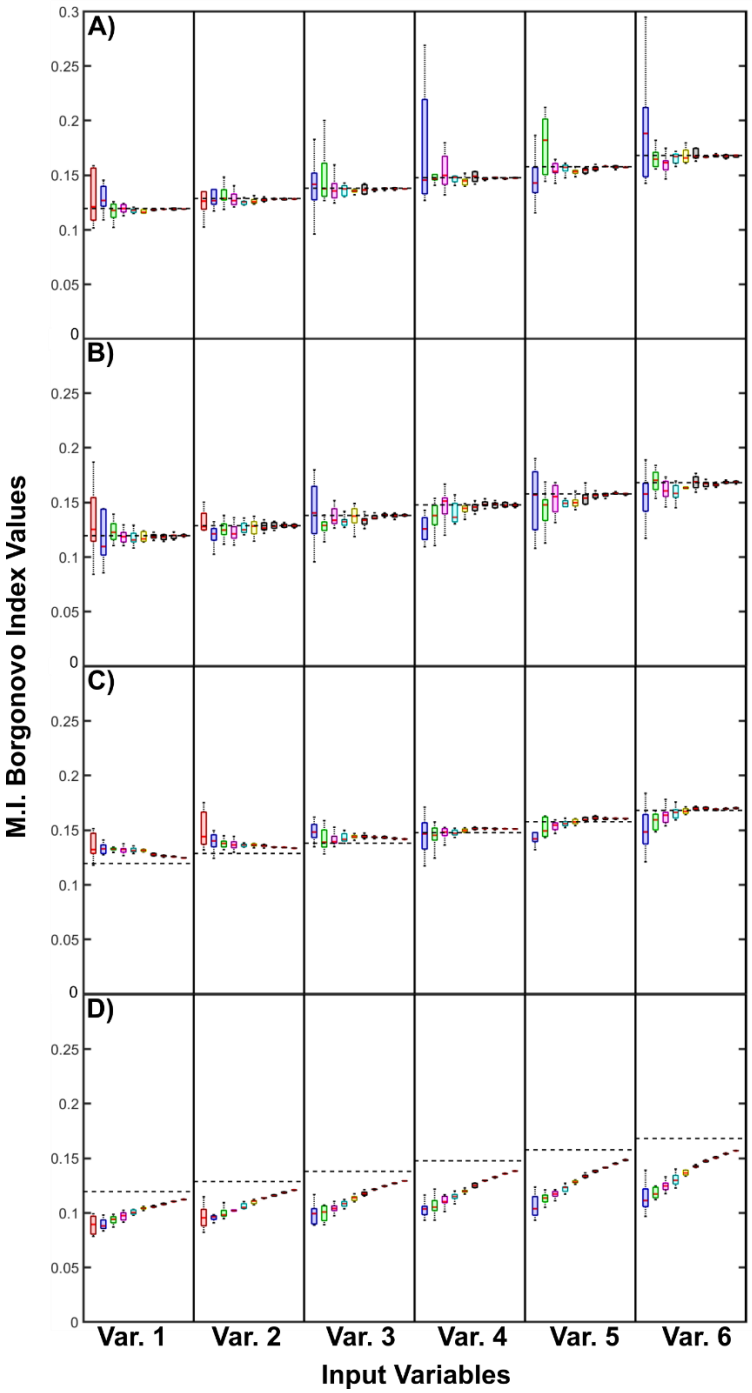

Figure E3. *MI Borgonovo sensitivity index convergence plots for analytical test function 1. Each subplot for a given input variable (i.e., 1-6) illustrates the distribution of each estimated sensitivity index (across ten realizations) as a function of the number of QMC samples used (boxplots are color coded to differentiate between QMC sample numbers, n = 256 to 131072). The rows depict the convergence results using the following methods: A) Semi-Parametric copula Method, B) NPIS Method, c) NP copula Method, and d) Single Loop Method. In all subplots, the analytical solutions for each input variable are indicated by the dashed black line.*

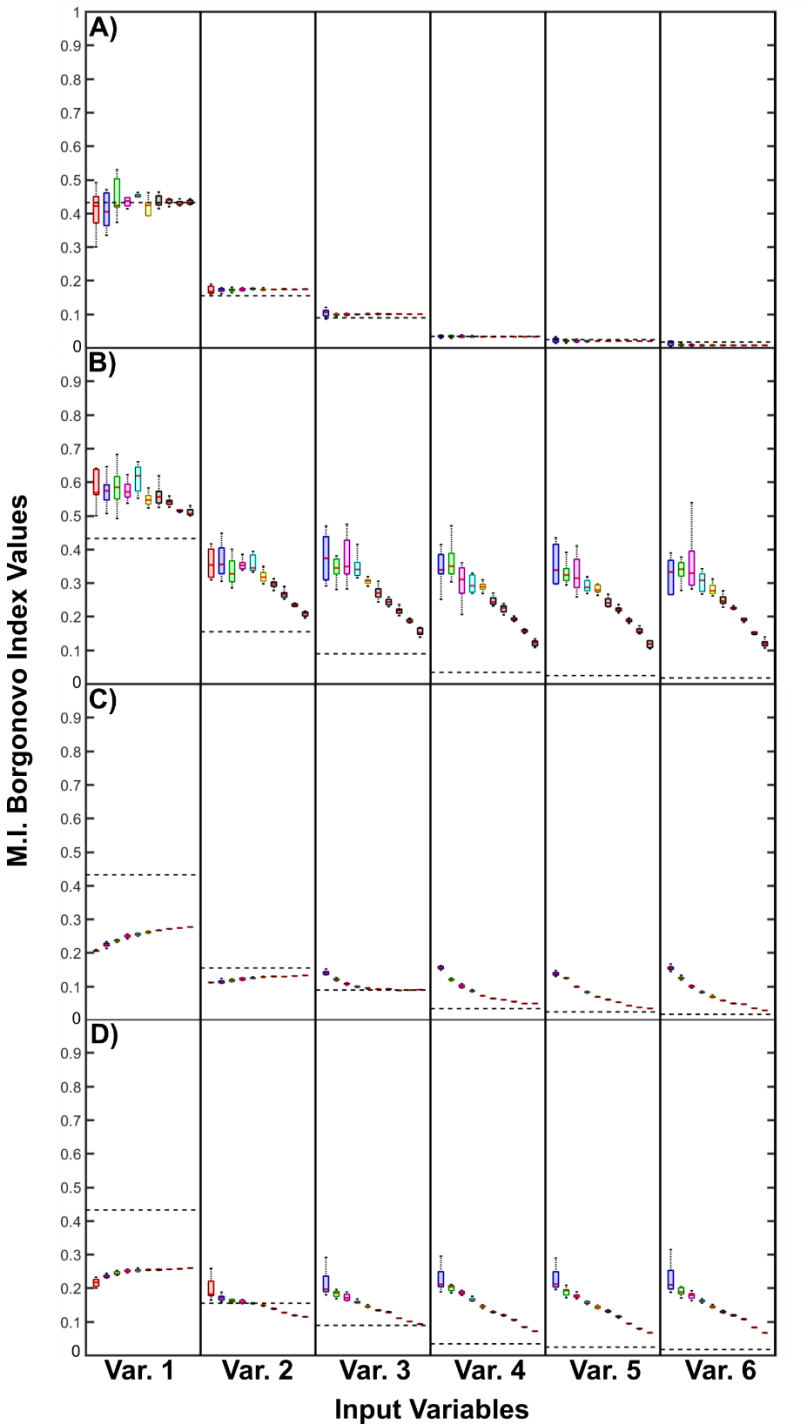

Figure E4. *MI Borgonovo sensitivity index convergence plots for analytical test function 2. Each subplot for a given input variable (i.e., 1-6) illustrates the distribution of each estimated sensitivity index (across ten realizations) as a function of the number of QMC samples used (boxplots are color coded to differentiate between QMC sample numbers, n = 256 to 131072). The rows depict the convergence results using the following methods: A) Semi-Parametric copula Method, B) NPIS Method, c) NP copula Method, and d) Single Loop Method. In all subplots, the analytical solutions for each input variable are indicated by the dashed black line.*

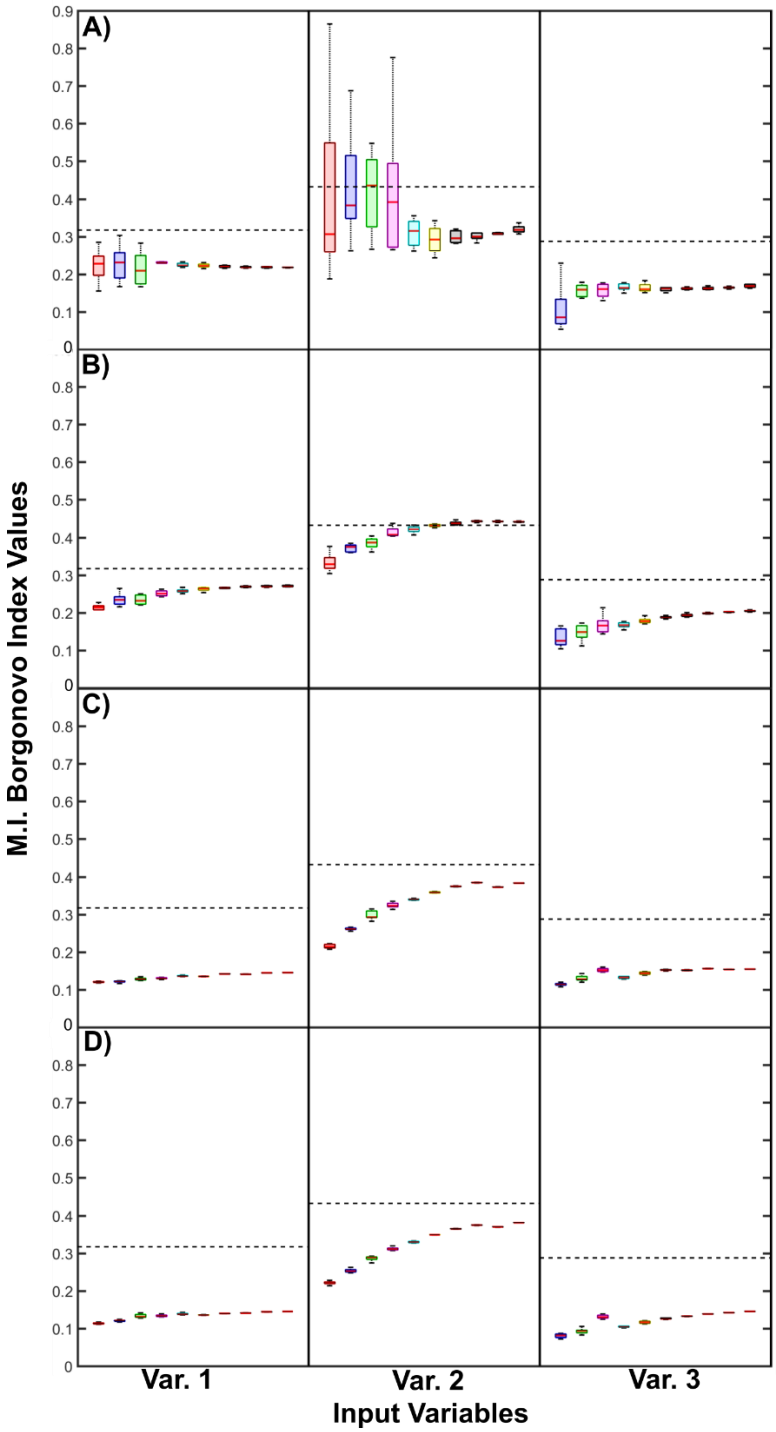

Figure E5. *MI Borgonovo sensitivity index convergence plots for analytical test function 3. Each subplot for a given input variable (i.e., 1-3) illustrates the distribution of each estimated sensitivity index (across ten realizations) as a function of the number of QMC samples used (boxplots are color coded to differentiate between QMC sample numbers, n = 256 to 131072). The rows depict the convergence results using the following methods: A) Semi-Parametric copula Method, B) NPIS Method, c) NP copula Method, and d) Single Loop Method. In all subplots, the analytical solutions for each input variable are indicated by the dashed black line.*

12. Model Application: Supporting Results

Table E6 *– Summary of average Kendall's tau estimates (across ten realizations) for quantitatively describing the strength of the model input-output relationships for model inputs (top row) and output (substrate concentration) variables. The number of QMC samples used for these calculations was set to 4096.*

Time Point	μ_{max}	K_s	Y	n	k_d
1	-0.5297	0.0409	0.3528	-0.2414	0.0205
2	-0.5687	0.0661	0.2320	-0.3088	0.0335
3	-0.5741	0.0948	0.1804	-0.3254	0.0514
4	-0.5839	0.1201	0.1527	-0.3115	0.0755
5	-0.5957	0.1397	0.1343	-0.2839	0.1032
6	-0.6051	0.1533	0.1204	-0.2522	0.1322
7	-0.6104	0.1619	0.1092	-0.2208	0.1608
8	-0.6112	0.1668	0.0999	-0.1921	0.1880
9	-0.6084	0.1691	0.0922	-0.1668	0.2133

Table E7 *– Summary of average Kendall's tau estimates (across ten realizations) for quantitatively describing the strength of the model input-output relationships for model inputs (top row) and output (cell concentration) variables. The number of QMC samples used for these calculations was set to 4096.*

Time Point	μ_{max}	K_s	Y	n	k_d
1	0.6465	-0.0459	0.1055	0.2693	-0.0541
2	0.5018	-0.0428	0.3232	0.2197	-0.0691
3	0.3636	-0.0361	0.4931	0.1602	-0.1059
4	0.2499	-0.0281	0.5852	0.1120	-0.1534
5	0.1586	-0.0210	0.6248	0.0755	-0.2036
6	0.0869	-0.0153	0.6334	0.0476	-0.2520
7	0.0321	-0.0104	0.6238	0.0252	-0.2964
8	-0.0085	-0.0063	0.6042	0.0068	-0.3356
9	-0.0378	-0.0029	0.5798	-0.0084	-0.3702

Table E8 *– Summary of optimal monotonization parameter estimates acquired during the rolling pin method for model inputs (top row) and output (substrate concentration) variables. The results presented in each table were averaged across ten realizations. The number of QMC samples used for these calculations was set to 4096.*

Time Point	μ_{max}	K_s	Y	n	k_d
1	1.38E-01	2.97E-03	2.27E-04	3.54E-02	2.85E-03
2	1.19E-01	1.05E-04	4.72E-05	9.62E-02	9.91E-04
3	4.07E-02	8.94E-05	1.81E-04	3.48E-02	3.15E-04
4	1.93E-02	5.99E-05	2.24E-04	2.97E-04	2.25E-04
5	8.89E-03	4.70E-05	1.18E-04	1.20E-04	7.28E-05
6	1.49E-03	5.02E-06	6.65E-04	4.15E-05	3.25E-05
7	1.21E-03	4.82E-05	3.75E-04	3.37E-05	2.41E-05
8	5.88E-04	7.35E-05	5.09E-04	1.19E-05	2.41E-05
9	7.60E-04	1.87E-04	1.35E-03	7.23E-06	5.32E-05

Table E9 *– Summary of optimal monotonization parameter estimates acquired during the rolling pin method for model inputs (top row) and output (cell concentration) variables. The results presented in each table were averaged across ten realizations. The number of QMC samples used for these calculations was set to 4096.*

Time Point	μ_{max}	K_s	Y	n	k_d
1	5.78E-04	2.05E-02	9.54E-03	1.20E-03	8.57E-02
2	5.17E-03	4.49E-02	3.37E-03	1.26E-03	1.69E-01
3	5.18E-02	5.31E-02	2.67E-03	6.33E-03	2.32E-01
4	1.15E-01	1.85E-02	2.12E-03	1.04E-02	2.14E-01
5	1.19E-01	5.74E-02	2.72E-04	4.28E-02	2.12E-01
6	8.66E-02	4.66E-02	1.98E-04	4.71E-02	1.76E-01
7	6.71E-02	2.13E-02	7.00E-04	3.75E-02	1.22E-01
8	2.98E-02	3.73E-02	7.65E-04	3.75E-02	8.17E-02
9	2.85E-02	3.53E-02	4.72E-04	5.37E-02	8.94E-02

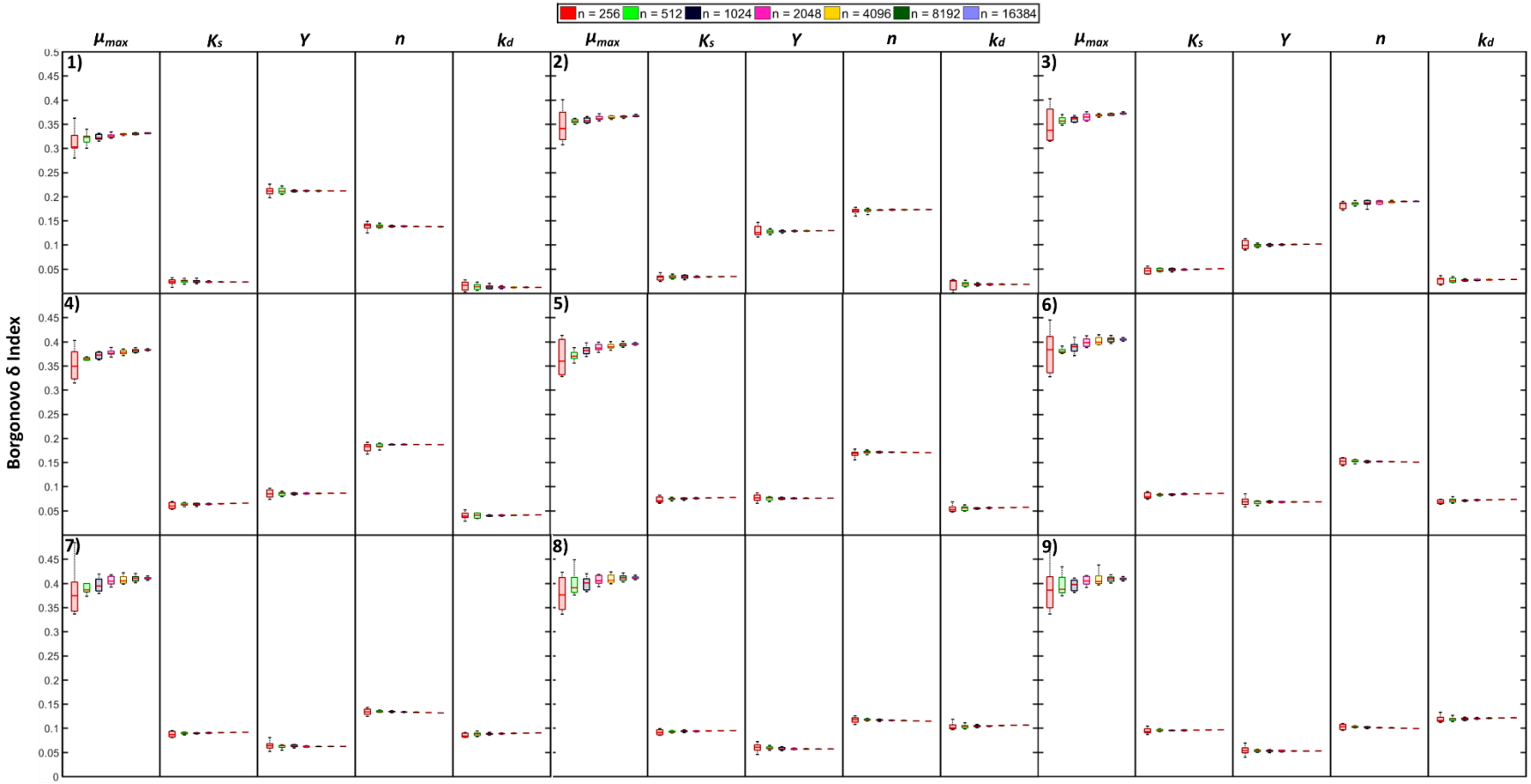

Figure E6. *MI Borgonovo sensitivity index convergence plots for the Moser model application. All Borgonovo sensitivity indices are estimated for the substrate concentration model output variable. Each subplot for a given model input parameter illustrates the distribution of each estimated sensitivity index (across ten realizations) as a function of the number of QMC samples used (boxplots are color coded to differentiate between QMC sample numbers, n = 256 to 16384). The subplots, organized row-wise, depict the convergence results for time points simulated from 1 to 9 days.*

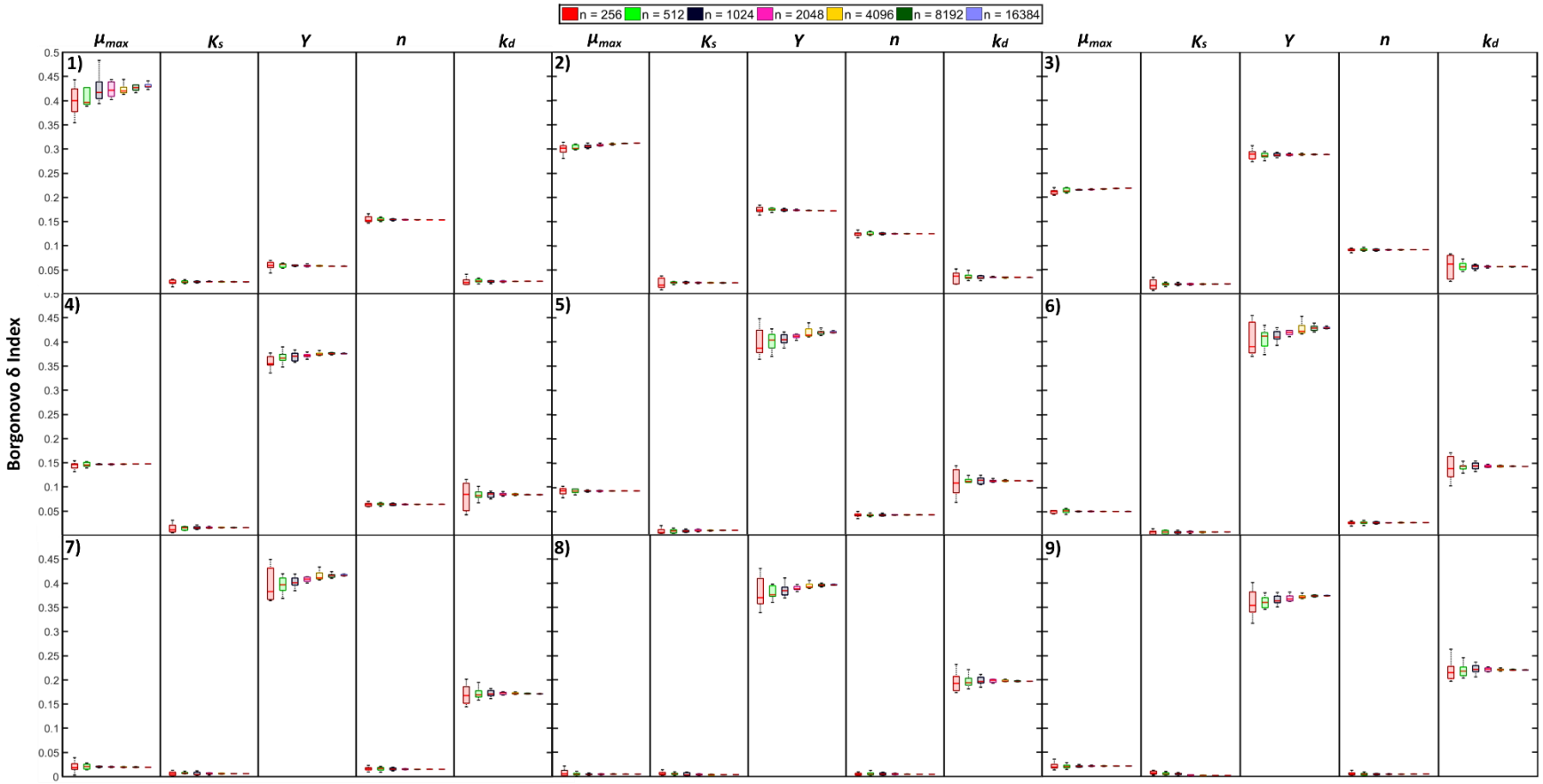

Figure E7. *MI Borgonovo sensitivity index convergence plots for the Moser model application. All Borgonovo sensitivity indices are estimated for the cell concentration model output variable. Each subplot for a given model input parameter illustrates the distribution of each estimated sensitivity index (across ten realizations) as a function of the number of QMC samples used (boxplots are color coded to differentiate between QMC sample numbers, n = 256 to 16384). The subplots, organized row-wise, depict the convergence results for time points simulated from 1 to 9 days.*

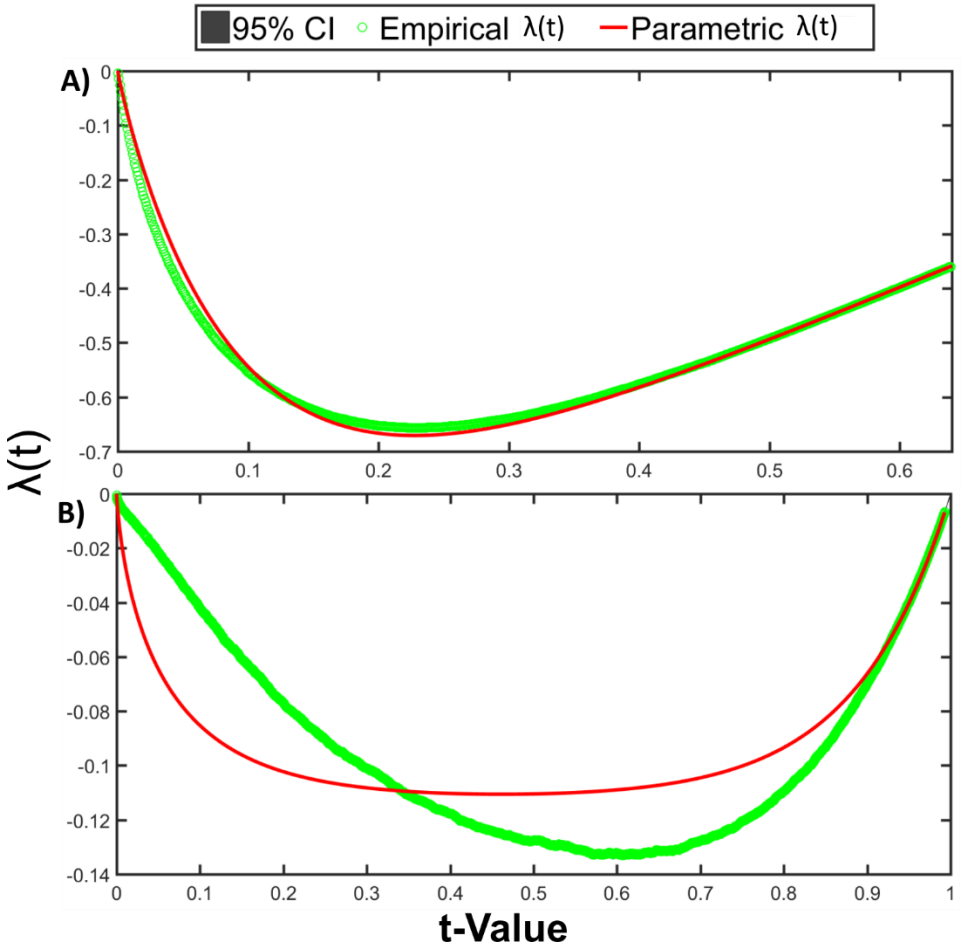

Figure E8. *Comparison of empirical (green circles) and parametric (red lines) lambda functions for the Moser model application. Results are presented for the most sensitive parameter (μmax in panel A and Y in panel B) and simulated timepoint (timepoint 9 for panel A and 7 for panel B). The number of QMC samples used to construct each plot was set to n = 4096.*

Appendix F: *Optimal Design of Experiments for Identification of Unstructured Kinetic Model Parameters Describing Microcystin Biodegradation* – Supplementary Materials

I. Supplementary Results and Methods

1. Parameter Ranges and Feasible Search Space for Experimental Design Criteria Applied in OED Procedure

Table F1 *– Summary of parameter bounds applied in the OED procedure in this study*

Bound	μ_{max} (1/day)	K_s (mg/L)	Y (unitless)	k_d (1/day)	N (unitless)
Lower	0.659	0.0001	0.433	0.014	1.49
Upper	6.59	219	3.48	0.991	9.73

Table F2 *– Summary of the feasible search space applied to constrain the experimental designs in the OED procedure in this study*

Experimental Configuration	Bound	C_0 (mg/L)	X_0 (mg/L)	F (L/day)	D (1/day)	C_f (mg/L)	X_f (mg/L)
Batch	Lower	0	0	-	-	-	-
	Upper	1000	1000	-	-	-	-
Fed-Batch	Lower	0	0	sum(dt*F)	-	0	-
	Upper	1000	1000	< 1	-	1000	-
Chemostat	Lower	0	0	-	0	0	-
	Upper	1000	1000	-	6.59	1000	-
CSTR	Lower	0	0	-	0	0	0
	Upper	1000	1000	-	6.59	1000	10000

2. Control Settings and Run Conditions for the Single and Multi-Objective OED Experiments

When running the single objective OED experiments, the LSHADE-NLS (NLS stands for No Local Search) algorithm was run using mostly identical settings to those specified in Awad et al. (2016). Initialized values of the adapted scaling parameter (Fde), crossover probability (CR), and the frequency of the sinusoidal search function were all set to 0.5. The memory size for adaptive storage and learning period, as specified in Awad et al. (2016) was set to 5 and 20, respectively. The mutation strategy for LSHADE-cnEpSin was set to

current2pbest/1, as used in Awad et al. (2016). The probability of performing crossover using covariance matrix adaptation (pc) and the proportion of individuals used to generate the covariance matrix was set to 0.4 and 0.5, respectively, based on results presented in Awad et al. (2016). In addition, the linear population size reduction functionality available in the most current LSHADE-EpSin version was not included in this optimization framework. The initial size of the population was set to 20 and 10 for single objective experiments running with the decorrelation criterion or D-criterion, respectively. The population size was reduced for the D-criterion experiments as convergence was observed to improve when the population size declined. The single objective experiments were set to run for 5,000 generations for the batch, chemostat, and CSTR experiments and 1,000 generations for the fed-batch experiments. Termination was reached when either the number of generations was exceeded, or the range in best and worst objective function values for the current generation were below a user specified threshold of 1E-10. All other control settings were identical to those reviewed in Awad et al. (2016).

For the multi-objective optimization framework, the NSGA-III run conditions were fixed to M=2 objective functions, d = 2-24 parameters (depending on the experimental configuration), N = 20 population members, and 5,000 generations. Similar to the single objective framework, the number of generations was reduced to 1,000 for the fed batch experimental reactor configuration due to running time constraints on the high-

performance computing cluster at UCI. SBX crossover and polynomial mutation function strategies were selected for each run, as suggested by Tanabe et al. (2017) and provided by the PlatEMO user interface. The user settings for the crossover and mutation functions were identical to those presented in Tanabe et al. (2017) (pc = 1, nc = 30, pm = 1/d, and nm = 20). Termination was reached when either the number of generations was exceeded, or the termination criteria described in the next section was met.

3. Termination Criteria for Multi-Objective Evolutionary Algorithms (MOEA)

Since the optimal design of experiments method required a multi-objective optimization approach, valid stopping criteria for the multi-objective algorithms needed to be developed and applied. The online convergence detection (OCD) approach (Trautman et al. 2009) was found to be the most reliable method available in the literature for properly stopping and detecting convergence of multi-objective algorithms and was formally applied in this study. The OCD approach focused on formal statistical testing on performance indicators calculated from the non-dominated pareto fronts from each generation during the MOEA search process. Convergence was reached when the statistical tests on each performance indicator were below a specified significance level ($\alpha = 0.05$).

Trautman et al. 2009 observed that three MOEA performance indicators including the hypervolume, additive epsilon, and R2 statistic were comprehensive enough to assess convergence of the MOEA to the true nondominated Pareto solution. We also found that including the delta spread performance indicator (Deb 2001) was necessary to ensure that each solution of the Pareto front also accounted for diversity on top of accuracy (i.e., convergence to the true solution). Either the variance of each of the performance indicators

or the linear regression coefficients obtained from regressing the performance indicators over a certain number of generations (*nPreGen*) were used as a proxy for statistical testing in the OCD method. Either convergence criteria relied on the use of a chi-squared or t-test to assess whether the differences were significant enough for convergence to be reached. For formal convergence to be reached, *all* of the above criteria had to be met for each performance indicators assessed. For the regression approach, we chose the option to compute a linear regression over all performance indicators (combined) to speed up the runtime of the optimization algorithm.

Control settings for MOEA termination were kept identical to those recommended by Trautman et al. (2009) and Wagner et al. (2009). The number of previous generations (*nPreGen*) used for performing the statistical testing was set to 16. The significance level (α) was set to 0.05 for each of the statistical tests performed. Lastly, the square root of the variance limit was set to 1E-03 for all performance indicators.

The OCD termination approach was first formally benchmarked against the ZDT class (1-4, 6) of test functions (which have two objective functions) to understand how the approach could be applied to the optimization of the Vt values for this study. For these initial tests, we kept the dimensionality of the test functions set to 1. The population size was set to 100 and the number of generations was limited to 200 (20,000 function evaluations). The NSGA-III algorithm was used over all other available MOEAs (in the PLATEMO suite) since it demonstrated superior performance over several other prominent MOEAs, including AMALGAM-MO and RVEA (see Manheim and Detwiler 2018). The NSGA-III approach relies on SB crossover and polynomial mutation, with the following specified parameter settings: probability of crossover (1), probability of mutation (0.167), crossover

distribution index (30), and mutation distribution index (20). Ten independent realizations were performed to assess the variability in the termination results for each test function.

The results of the OCD testing indicated that each performance metric (i.e., hypervolume, epsilon, R2) was approaching convergence as the number of generations before termination was reached (Figure F1, F2). Test problem number one (ZDT1), which is concave up in shape, took the largest number of generations for the NSGA-III algorithm to converge, where the median number of generations until termination was approximately 40 for the one-dimensional problem investigated (Figure F2). Test problem number 2 (ZDT2) was solved using the smallest number of generations (median number of generations until termination was approximately 22), which is convex in structure (Figure F2). In addition, all the solutions of the Pareto fronts achieved from the NSGA-III algorithm for each of the ten different realizations that were terminated using the OCD approach were very accurate and well distributed across the true Pareto fronts (Figure F1). The standard deviation of the Pareto front estimates across all ten realizations was also very small (on the order of 0.001) for all test problems investigated, demonstrating that the OCD method returned solutions that were both precise and accurate (data not shown). These results confirm that the termination criteria implemented in the OCD approach were consistently valid and reliable.

In general, the linear regression termination criteria as opposed to the performance metric criteria dictated when the MOEA search was stopped, as 96% out of all 50 runs performed across each test function were terminated using the linear regression criterion. This result was most likely due to faster convergence of several performance metrics over the others. As observed in Figure F2, the hypervolume and R2 performance metrics were

less variable and approached convergence sooner than both the epsilon and delta spread indices. Generally, the epsilon metric was the most variable metric over the ten realizations, especially for test problems 1 and 2. Differing convergence results between performance indices may be directly related to the stability and complexity of the calculation involved for each index as well as the level of difficulty of the ZDT test functions evaluated.

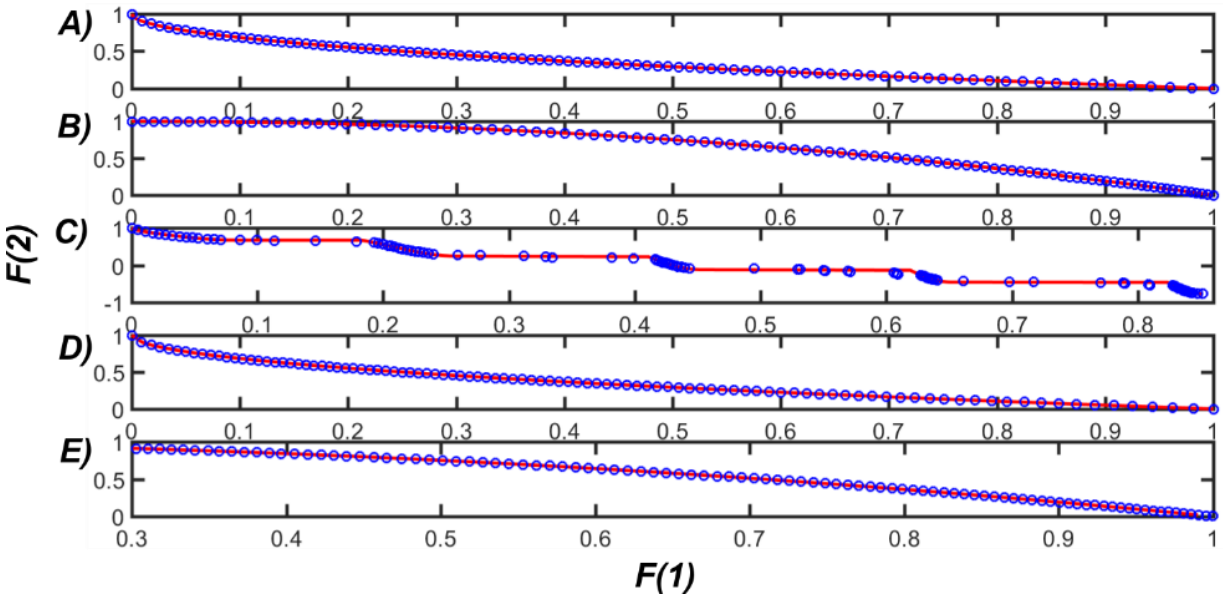

Figure F1. *Accuracy and precision of the OCD termination method when benchmarked on the A) ZDT1, B) ZDT2, C) ZDT3, D) ZDT4, and E) ZDT6 test problems. The blue circles represent the mean of the Pareto fronts achieved from ten independent realizations, whereas the red line indicates the true Pareto front solution.*

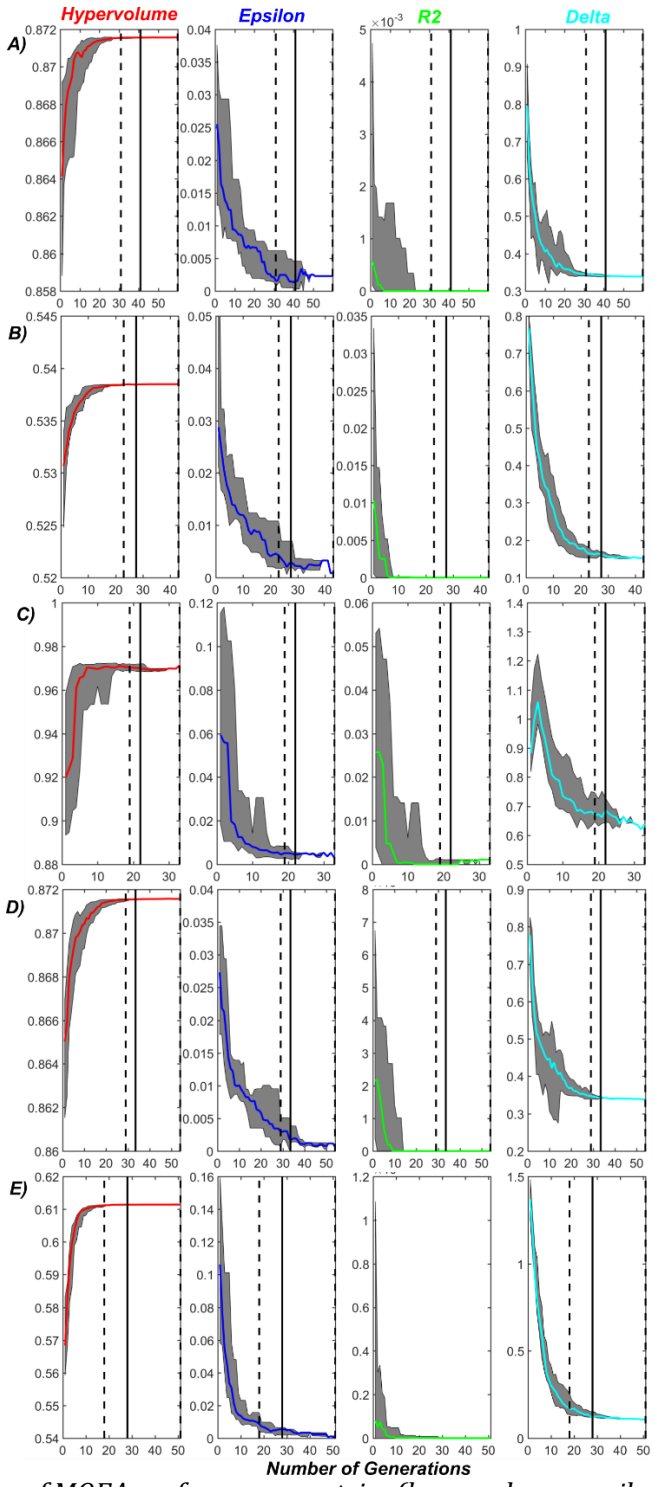

Figure F2. *Convergence of MOEA performance metrics (hypervolume, epsilon, R2, and delta spread) for the A) ZDT1, B) ZDT2, C) ZDT3, D) ZDT4, and E) ZDT6 test problems using the OCD termination method. The colored lines and grey regions represent the median and 95% confidence regions for each performance metric and test problem over 10 independent realizations. The black and dashed lines represent the median and 95% confidence interval for the generation of MOEA search termination for each test problem.*

4. Comparison of Derivative Based Global Sensitivity Analysis Methods

In this study, two derivative based global sensitivity analysis (GSA) methods were compared as the basis for the optimal design of experiments investigation. The two GSA approaches belonging to the derivative based classes compared in this study were the elementary effects (Morris) method and the mean partial derivative method (DBGSM) (Kucherenko et al. 2009).

As a first step, a formal comparison of GSA methods was conducted to ascertain the accuracy and precision of each approach using standard GSA test functions available in the literature. More importantly, since each method was based on a Monte Carlo, quasi Monte Carlo, we were also concerned with the convergence of each method and the number of samples (N) required to reach this convergence. Here we define the convergence criteria as the number of samples necessary for identification of "stable" sensitivity indices (Serrazin et al. 2016). For the derivative based class of GSA methods (Morris and DBGSM), we used the Mi^* and Σ_i^* indices as defined by Kucherenko et al. (2009) and Campolongo et al. (2011), as the corresponding analytical solutions of each index for each test function were conveniently provided by the references indicated above.

To compare the convergence of all methods, we used both visual inspection of the mean and variation in absolute error (MAE) (a relative measure of accuracy and precision, Equation 1, $\widehat{S_{T,i}}(j)$ represents the sensitivity index predicted by the GSA method and $S_{T,j}$ is the analytically derived sensitivity index value and comparison of the widths of the 95% confidence intervals of the sensitivity indices for each input factor over 50 repetitions of each test function. If the maximum of the widths of the confidence intervals across all input factors were below a set threshold (0.05), the sensitivity approach was deemed to

converge. This method proved to be effective as the computational demand of each analytical test function was low as compared to actual real-world models, allowing for many repetitions to be run at various sample numbers (N).

$$MAE = \frac{1}{50}\sum_{j=1}^{50}\sum_{i=1}^{k}\left|\widehat{S_{T,i}}(j) - S_{T,j}\right| \quad (1)$$

Importantly, Kucherenko et al. (2011) classified three major types of analytical test functions (A, B, and C) based on the ratio of the first order effect to total order effect levels. Type A functions were defined as functions not having equally important variables (most commonly encountered in practice); Type B functions were classified as those with dominant low order terms; and Type C functions were defined as those with dominant high order interaction terms (Kucherenko et al. 2008). Therefore, the objective of this testing procedure was to choose a wide range in analytical test functions that covered all of the different classes defined by Kucherenko et al. 2009. In this way, the analytical test functions selected were based off five common structures presented in the GSA literature: Sobol's G function (can be a type A or B), the K-function (strictly type A), the B-function (strictly type B), the Ishigami function (type C), the Roos and Arnold Function (type C), the B1 factor function (type B), the C1 factor function (type C), and the Morris test function (Type A) (Table F3).

To provide a wider platform of GSA test functions, we incorporated both the original and modified forms of Sobol's G function (Table F3). Sobol's G function was modified to include a curvature and shift factor as described by Saltelli et al. (2010) to avoid giving the tested design an "unfair" advantage. In the G function mathematical description, δ_i is the shift factor (random number generated $\in$ [0, 1]), α_i is the curvature parameter ($\alpha_i > 0$), X_i is the ith input factor (out of k total model parameters), I[$X_i + \delta_i$] represents the integer

part of the input factor added to the shift factor, and a_i represents the relative importance of each model parameter or input factor (lower values signify greater importance). For this particular test function, several test cases can be prepared. An "easy" test case would involve several a_i values that are small (around 0), and all remaining values are large (a_i = 9), as there are just two important input factors and a two way interaction. The most difficult test case, on the other hand, would involve all k input factors set to weights of 0 (a_i = 0), where each factor is very important and subject to multiple higher order interactions with the other parameters.

The K function is more self-explanatory than the other functions (X_j is the jth input factor) and is generally more difficult in the interactions that it presents as opposed to the importance between each sensitivity value (Table F3). The B function, however, places the difficulty on the importance over the interactions between sensitivity values. In this particular function, both X_i and ω_i represent draws from a normal distribution with fixed standard deviations that are prespecified by the user. The remaining functions (Ishigami/Roos and Arnold) were important to include as they were more similar to real world test cases (Ishigami) or presented more difficulty in the way of higher order interactions between parameter values, as demonstrated by the Roos and Arnold function (Type C).

Table F3 *– Summary of analytical test functions used to compare each derivative based GSA approach*

Analytical Test Function	Mathematical Description
Sobol's G	$G = \prod_{i=1}^{k} g_i$ $g_i = \frac{\lvert 4 * X_i - 2 \rvert + a_i}{1 + a_i}$
Sobol's G*	$G^* = \prod_{i=1}^{k} g_i^*$ $g_i^* = \frac{(1 + \alpha_i) * \lvert 2(X_i + \delta_i - I[X_i + \delta_i]) - 1 \rvert^{\alpha_i} + a_i}{1 + a_i}$
K	$\sum_{i=1}^{k} (-1)^i \prod_{j=1}^{i} X_j$
B	$\sum_{i=1}^{m} X_i * \omega_i$
Ishigami (I)	$\sin(X_1) + asin^2(X_2) + bX_3{}^4 \sin(X_1)$
Roos & Arnold (R)	$\prod_{i=1}^{k} \lvert 4X_i - 2 \rvert$
B1	$\prod_{i=1}^{n} \frac{n - X_j}{n - 0.5}$
C1	$2^n \prod_{i=1}^{n} X_i$
Morris Test Function (M)	$\sum_{i=1}^{4} \beta_i \omega_i + \sum_{i \le j}^{4} \beta_{ij} \omega_i \omega_j + \sum_{i \le j \le k}^{4} \beta_{ijk} \omega_i \omega_j \omega_k$

Based on these analytical test functions, eleven individual test cases have been constructed to formally benchmark each derivative based GSA approach, respectively. The test cases selected are nearly identical to those presented by Saltelli et al. 2010, as well as Kucherenko et al. 2009 (Table F4). Each test case is presented for k = 10 dimensions

(except for the Ishigami function), similar to the order of the models tested in this study (number of parameters ranged from 5-6). For most test cases, we considered the prior distribution of each parameter to be uniformly distributed on the interval 0 to 1 (except for the Ishigami case, [-pi, pi], and the B-function case, [~N(0,SD)]). We also set the number of samples (N) for each approach to a fixed interval, ranging from 70 to 50,000. Importantly, for each GSA method using a quasi Monte Carlo approach, we vary the Sobol's sequence for each iteration at each sampling level. Each test case was strategically constructed to evaluate each approach over a range of difficulties. For example, Sobol's modified test cases range in difficulty from relatively easy (1-2) to very difficult (5-6) based on the magnitude of the curvature factor (a_i) and the a_i terms (i.e., test case 1 is slightly less difficult than 2). Similarly, the difficulty of the K test function is comparable to Sobol's G* case number 6, whereas the difficulty of the B test function is comparable to Sobol's G* case number 5.

Table F4 *– Collection of individual test cases used to compare each derivative based GSA approach*

Test Case #	Analytical Test Function	Parameter Settings
1	Sobol's G	a_i = [0, 0, 9, 9, 9, 9, 9, 9, 9]
2		a_i = [0, 0.1, 0.2, 0.3, 0.4, 0.8, 1, 2, 3, 4]
3		a_i = [0, 0, 0, 0, 0, 0, 0,0, 0]
4		a_i = [0, 0, 6.52, 6.52, 6.52, 6.52, 6.52, 6.52, 6.52, 6.52]
5		a_i = [50, 50, 50, 50, 50, 50, 50, 50, 50]
6		a_i = [0, 0, 0.1, 0.1, 0.2, 0.2, 0.3, 0.3, 0.4, 0.4]
7	K	None to be specified
8	R	None to be specified
9	B1	None to be specified
10	C1	None to be specified
11	M	The β matrices are identical to those specified in Kucherkenko et al. 2010

The results of the derivative based GSA approaches demonstrated that the DBGSM was far superior to the Morris method in terms of both accuracy and precision (Figure F3). In most analytical test cases, the magnitude of the absolute error using the DBGSM method

is far below that obtained using the Morris method (especially for test cases 1-6, 8, and 11). This result was expected since the DBGSM method evaluates the partial derivative of the function using a refined numerical approach as opposed to a finite difference approximation in which the elementary effects of the Morris method represent. Although the Morris method suffered from inaccuracy for a majority of test cases, the performance was comparable to the DBGSM method for test cases 7, 9, and 10 (Figure F3). The precision of each method was generally high, as the error bars for 50 iterations were low (and cannot be observed on each plot), even for a low number of samples. This precision was confirmed quantitatively, where each method was observed to converge (maximum range in 95% ~ 0) after 50K samples (Table F5). Again, for most cases, the DBGSM method appeared to converge before the Morris method (at around N = 10K samples). Based on these results, it is clear that the DBGSM method should be considered as the most reliable method among the derivative based GSA approaches investigated in this study.

Table F5 *– Maximum range in 95% confidence intervals after 50K samples and 50 iterations on each test function (sigma, Σi^*).*

Test Function	Morris	DBGSM
1	0.00805	0.0003018
2	0.03401	0.01265
3	0.2113	0.10971
4	0.008762	0.0004722
5	0.000244	5.76E-08
6	0.08832	0.0553
7	0.00019	0.000122
8	0.2185	0.10971
9	5.121E-06	2.801E-06
10	0.07665	0.0578
11	0.0188	0.00996

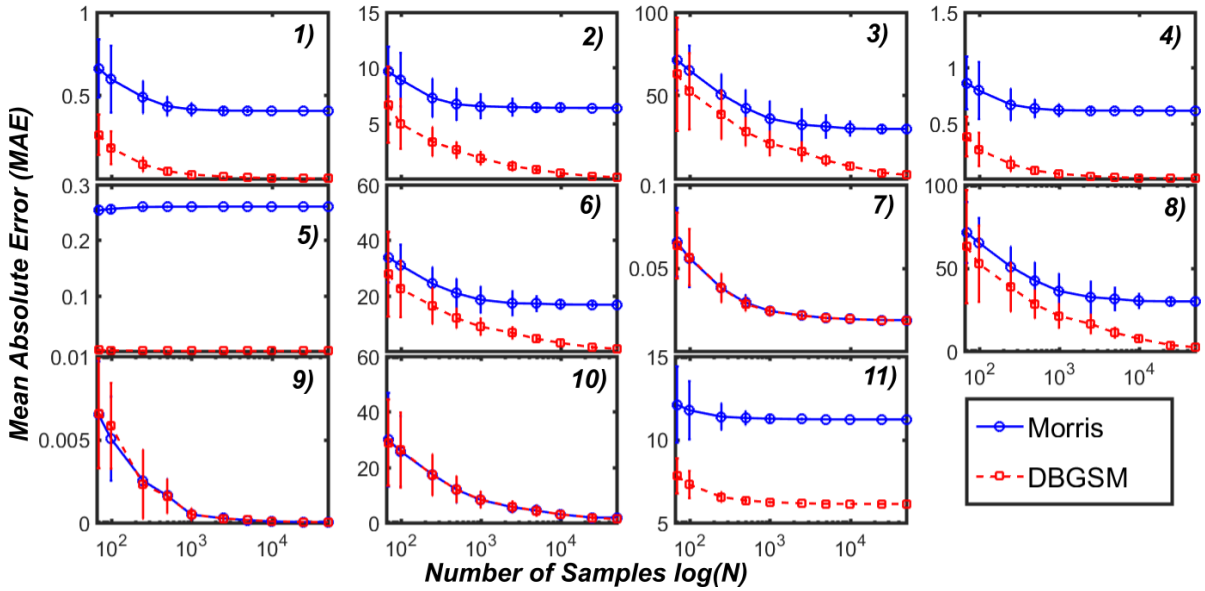

Figure F3. *Mean absolute error (MAE) achieved after benchmarking the Morris (blue) and DBGSM (red) derivative based GSA methods on analytical test functions 1-11 (sigma, Σi*).*

5. Application of the DBGSM Approach to the Moser Model

The DBGSM approach was initially applied to the Moser Model to ascertain the number of QMC samples required to reach formal convergence of the estimated sensitivity indices at each simulated time point. Again, formal convergence was defined as the number of QMC samples required to reduce the width of 95% empirical confidence intervals to less than a threshold value of 0.05 (Sarrazin et al. 2016). The determination of the number of QMC samples to reach convergence for each sensitivity index (describing each model parameter) at each simulated time point was critical, as it affected the number of model evaluations required during the optimal experimental design procedure. These initial runs were performed for all four experimental designs presented in the main manuscript (Batch, Fed-Batch, CSTR, and Chemostat). Importantly, for the Fed-Batch system, we only tested a random binary feed rate profile with a constant feed concentration. The initial experimental design variables were held constant for each of the experimental designs considered and are briefly reviewed here for reference (Table F6). For all experiments, an

initial substrate/cell concentration of 10/1 mg/L, which were relatively high concentrations to those employed in practice in order to make the simulations as dynamic and variable as possible. The feed and dilution rates were set to relatively slow rates, an order of magnitude smaller than those typically used for fast growing organisms (as the biokinetics for MC degrading bacteria are relatively slow compared to most heterotrophic organisms). Simulations were run for a total of 11 days and the DBGSM indices were calculated at the following number of QMC samples: n = 256, 512, 1024, 2048, 4096, 8192, 16384. Ten independent realizations using different QMC sample sets were run to assess the variability and convergence of the DBGSM method when applied to the Moser model.

Table F6 *– Summary of fixed experimental variables used during the initial convergence testing*

<table>
<tr><th>Experimental Design</th><th>Initial Substrate Concentration (mg/L)</th><th>Initial Cell Concentration (mg/L)</th><th>Feed Rate (1/day)</th><th>Dilution Rate (1/day)</th><th>Feed Substrate Concentration (mg/L)</th><th>Feed Cell Concentration (mg/L)</th></tr>
<tr><td>Batch Reactor</td><td rowspan="3">10</td><td rowspan="3">1</td><td>N/A</td><td rowspan="2">N/A</td><td>N/A</td><td rowspan="2">N/A</td></tr>
<tr><td>Fed-Batch Reactor</td><td>0.5</td><td rowspan="2">5</td></tr>
<tr><td>Chemostat</td><td rowspan="2">N/A</td><td rowspan="2">0.2</td><td rowspan="2">1</td></tr>
<tr><td>CSTR</td></tr>
</table>

The convergence results are presented in Figures F4 and F5, in which the precision (width of the 95% Cis across ten realizations) is plotted as a function of the number of QMC samples. Results are presented independently for both substrate (Figure F4) and cell (Figure F5) concentration predictions and were organized according to the experimental design (columns) as well as the model parameters (rows). The results indicated that the sensitivity indices related to substrate concentration predictions took longer to converge (n = 8192) as compared to the cell concentration predictions (n = 1024). For both the substrate and cell concentration predictions, μ_{max}, k_d, and n were the most variable, as indicated by the high precision values across all QMC sample numbers, which further

implied that these parameters were the most sensitive when predicting either substrate or cell concentrations. The DBGSM indices estimated for the parameters Y and K_s, however, were very precise, as indicated by the small precision values across all AMC sampling numbers, suggesting that these parameters may not have been very influential on the model output (Figures F4 and F5).

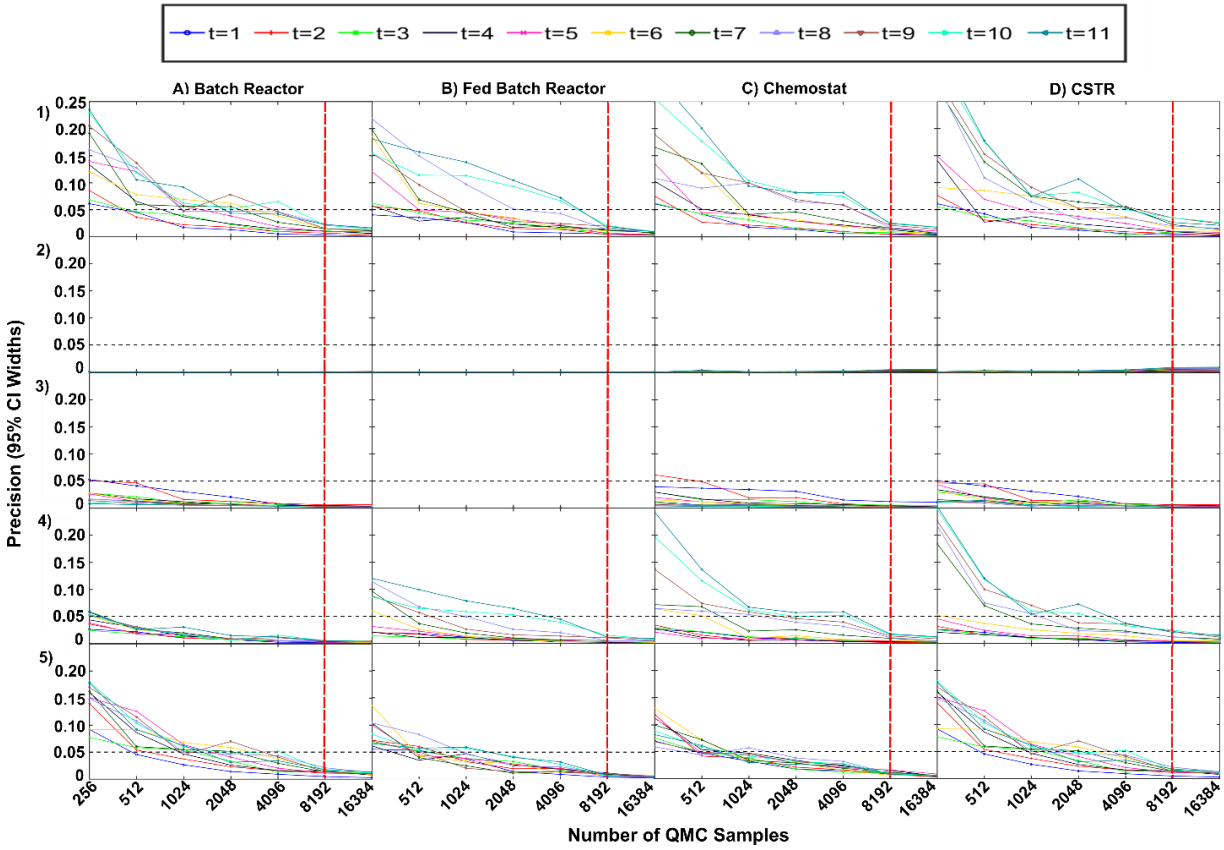

Figure F4. *Convergence plots for the derivative based global sensitivity analysis when applied to the Moser model. In this Figure, the precision of the DBGSM (as determined by the width of the 95% confidence intervals) is qualitatively compared as a function of the number of QMC samples. Results are presented detailing the sensitivity of the model parameters when predicting substrate concentration only. The columns of this Figure indicate the results of certain experimental designs (batch reactor, fed-batch, etc.), whereas the rows (1-5) correspond to the following model input parameters: μ_{max}, K_s, Y, k_d, and n. The colors of the lines in the legend correspond to different simulated time points for which the DBGSM indices were calculated (i.e., 1-11 days). The black dashed line indicates the threshold for formal convergence, whereas the dashed red line indicates the number of QMC samples required to reach convergence.*

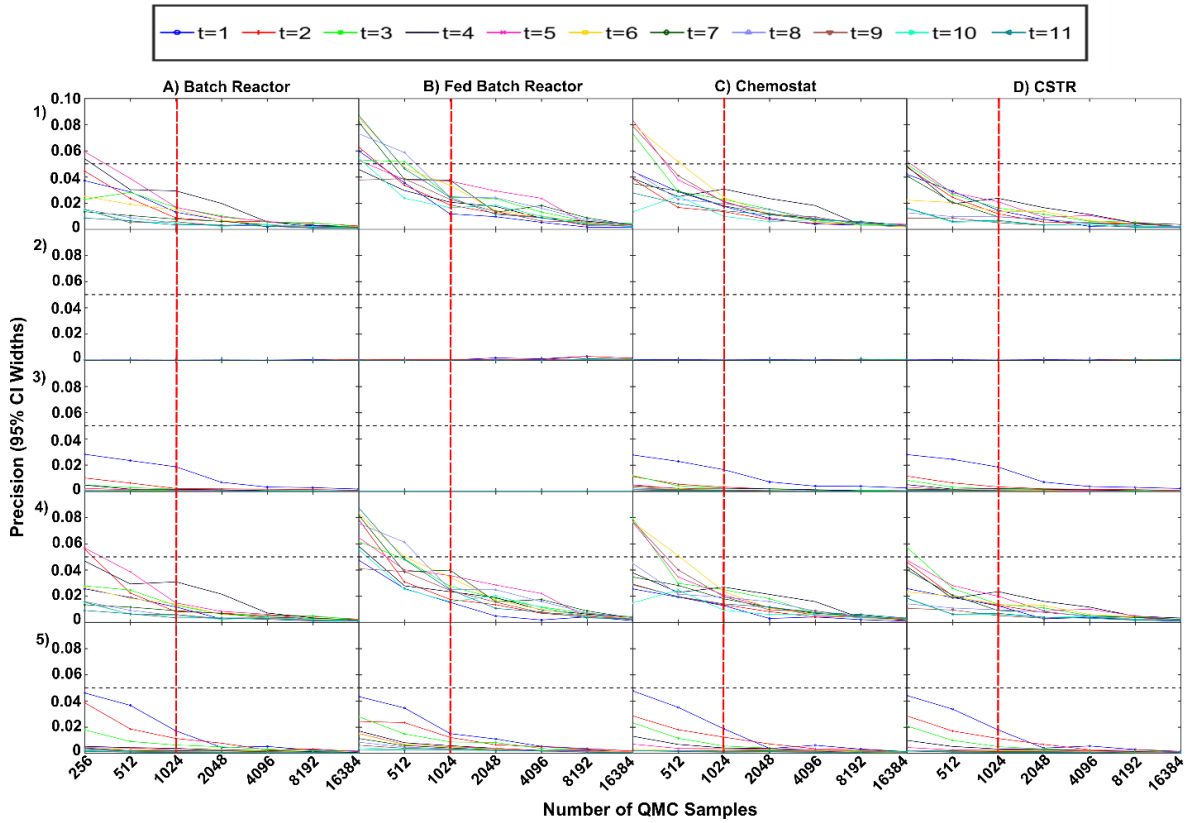

Figure F5. *Convergence plots for the derivative based global sensitivity analysis when applied to the Moser model. In this Figure, the precision of the DBGSM (as determined by the width of the 95% confidence intervals) is qualitatively compared as a function of the number of QMC samples. Results are presented detailing the sensitivity of the model parameters when predicting cell concentrations only. The columns of this Figure indicate the results of certain experimental designs (batch reactor, fed-batch, etc.), whereas the rows (1-5) correspond to the following model input parameters:* μ_{max}, K_s, Y, k_d, *and n. The colors of the lines in the legend correspond to different simulated time points for which the DBGSM indices were calculated (i.e., 1-11 days). The black dashed line indicates the threshold for formal convergence, whereas the dashed red line indicates the number of QMC samples required to reach convergence.*

Using the initial conditions specified in Table F6, the calculated DBGSM indices were plotted *as* a function of the simulation time (Figure F6). For substrate concentration predictions, μ_{max} was the most influential parameter at early simulation times, while k_d was the most influential parameter at later times (Figure F6). Both n and Y were also relatively influential at early time points when predicting substrate concentrations (Figure F6). Regarding cell concentration predicitons, k_d was the most influential parameter across all simulation times. The parameters Y, μ_{max}, and n were also relatively influential at earlier

timepoints when predicting cell concentrations (Figure F6). These results confirm initial presumptions made above that more variable parameters were likely more sensitive model inputs.

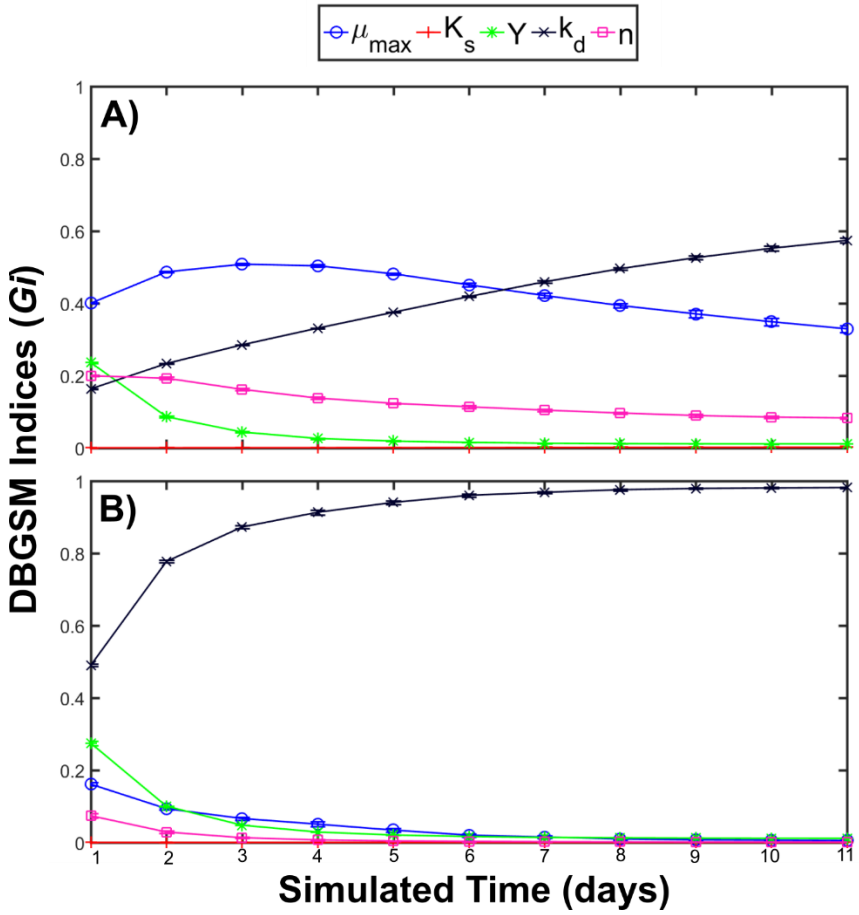

Figure F6. *Differences in calculated DBGSM indices as a function of simulation time. Panel A) corresponds to substrate concentration predictions (at n = 8192), whereas Panel B) corresponds to cell concentration predictions (at n = 1024). The legend indicates which line corresponds to which model parameter.*

6. Optimal Pareto Fronts of the Multi-Objective OEDs

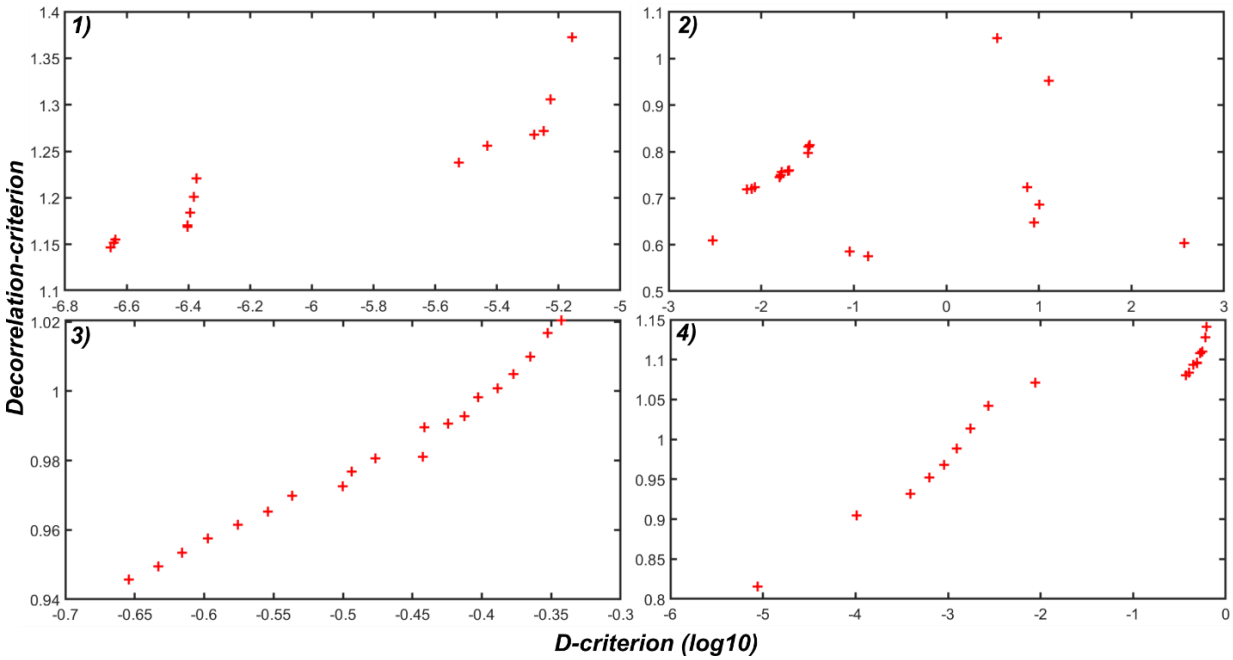

Figure F7. *Pareto optimal fronts obtained for the MO optimization framework for the 1) Batch, 2) Fed Batch, 3) Chemostat, and 4) CSTR experimental configurations. The decorrelation criterion is plotted on the y-axis, whereas the D-criterion (in log scale) is presented on the x-axis.*

7. Convergence Plots for the MO OEDs

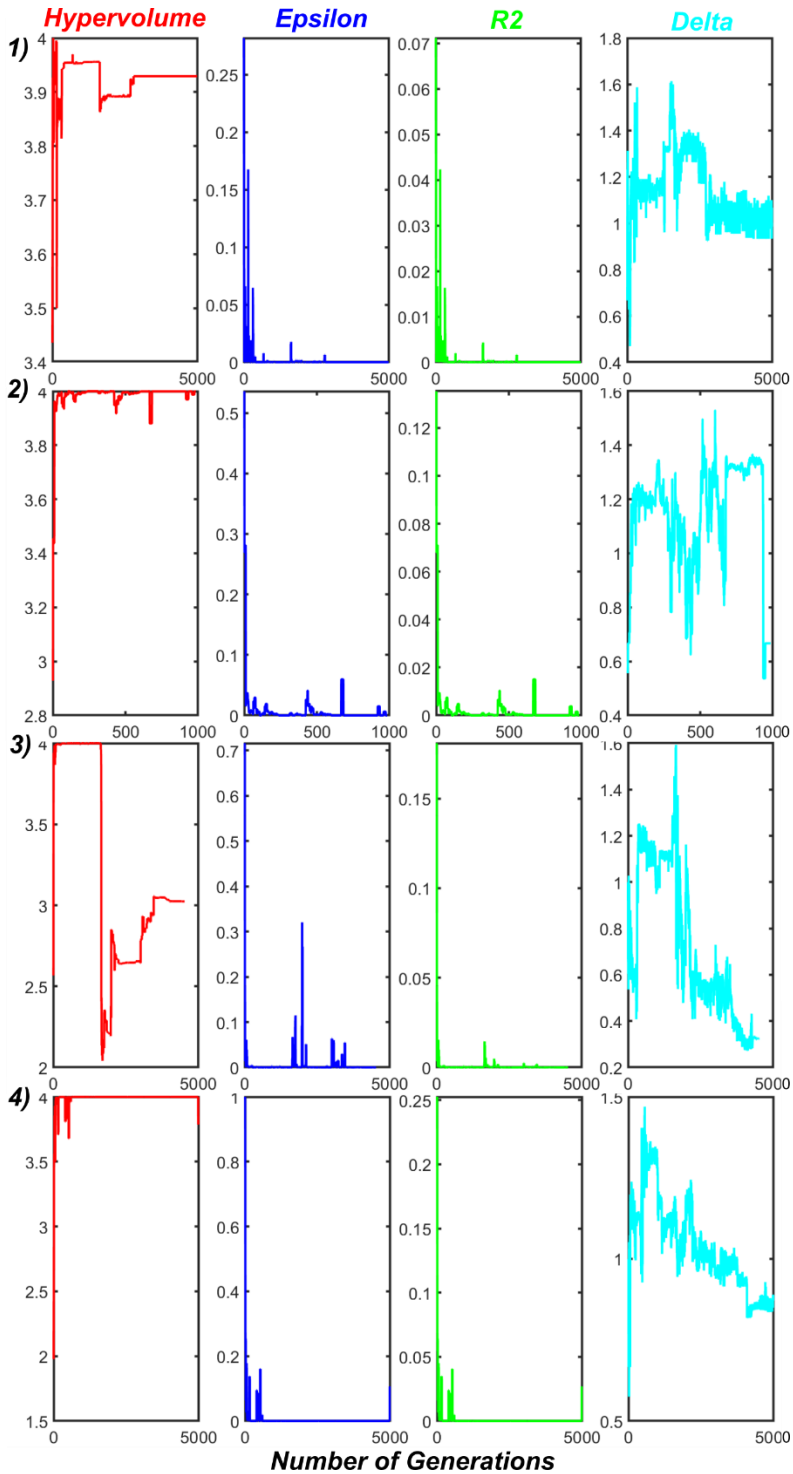

Figure F8. *Convergence of MOEA performance metrics (hypervolume, epsilon, R2, and delta spread) for the 1) Batch, 2) Fed Batch, 3) Chemostat, 4) CSTR experimental configurations using the OCD termination method. The colored lines differentiate between difference performance metrics.*